Applied Scientific Research

An International Journal on
the Applications of Fluid Dynamics

Special Double Issue

A Tribute to Mårten T. Landahl

Guest Editors
P. HENRIK ALFREDSSON, FRITZ H. BARK & ARNE V. JOHANSSON
Department of Mechanics
Royal Institute of Technology
Stockholm, Sweden

Special Double Issue

Selected Papers from a IUTAM Symposium entitled
"Eddy Structure Identification in Free Turbulent Shear Flows",
held at Poitiers, France, 12–14 October 1992

Guest Editors

J.P. BONNET & M.N. GLAUSER

A Sketch of a Portrait of Mårten T. Landahl

This issue of *Applied Scientific Research* has the form of a festschrift in the honor of Professor Mårten T. Landahl on the occasion of his sixty-fifth birthday. The papers making up the festschrift are all written by former graduate students of his. Although Mårten's pioneering scientific achievements in fluid mechanics, some of which are classical, are certainly well known, his role as a successful graduate supervisor, both in Sweden and the US, is perhaps less known. This part of his scientific career has resulted in an unusually large number of tenured professors in both countries. The papers in this issue, some of which report on new results whereas others are of review character, intend to give credit to an enthusiastic and

highly esteemed teacher, whose capacity to see things in unconventional ways, never renouncing high scientific standards, impressed and inspired us all.

Mårten Teodor Landahl was born in 1928 in Noraström in the rural part of Northern Sweden. He received his *studentexamen* (matriculation) from the Högre Allmänna Läroverket in Östersund in 1946 and, in 1951, his engineering degree from the School of Aeronautics and Naval Architecture at the Royal Institute of Technology (KTH) in Stockholm. In 1959, after having worked as a senior research engineer at the Swedish Aeronautical Research Institute and in the Department of Aeronautics and Astronautics at the Massachusetts Institute of Technology, Mårten received his doctoral degree at KTH. His thesis, which dealt with unsteady transonic flow, was one of outstanding quality and he was awarded a docentship in the same year as his dissertation. Between 1960 and 1963, he served as an Associate Professor in the aforementioned department at MIT, in which he became a tenured Professor in 1963. During the period from 1967 to 1988, Mårten also held a position as Professor of Mechanics at KTH.

The early work by Mårten Landahl on unsteady transonic flow was one of the major break-throughs in that research area and rapidly lead to his international recognition. In 1961, shortly after his dissertation, his thesis was published as a book by Pergamon Press and has recently been republished by Cambridge University Press in the Classic Science Series. For some years after his dissertation, Mårten extended his research in aeronautics and gave significant contributions to several other aspects of the subject, examples are wing-body interactions and lifting surface theory. With Holt Ashley, one of his colleagues in the aeronautics department at MIT at that time, he wrote the textbook "Aerodynamics of Wings and Bodies", which was first published by Addison-Wesley in 1965 and by Dover Publications in 1985.

In the late fifties, some experimental evidence regarding the possibility to reduce drag on water vehicles, perhaps due to delay of transition, by using flexible surfaces appeared in the literature. In view of its potential engineering importance, this finding spurred a series of theoretical studies. A significant contribution to the understanding of this phenomenon was made by Mårten Landahl in a most elucidating paper on the hydrodynamic stability of flow over a flexible surface (*J. Fluid Mech.* **13**, 609, 1962). In this paper Mårten explained, among other things, the stabilizing or, in certain regions of parameter space, destabilizing effect of wall damping. During this period, the interest in various aspects of hydrodynamic stability was growing strongly. Accurate numerical integration of the Orr-Sommerfeld equation was still a very difficult problem. Together with R.E. Kaplan, one of his graduate students, Mårten constructed an ingenious and widely used numerical scheme, based on physical rather than mathematical concepts, to obtain accurate solutions with limited computer accuracy. The scheme was documented in Kaplan's thesis.

A considerable part of Mårten Landahl's research efforts has been spent on turbulence. In the middle of the sixties, he took the brave step to use methods of

linear theory of hydrodynamic stability to describe fluctuations in fully developed turbulent shear flows. This was some years after the so-called "spanwise streaks" and "turbulent bursts" were experimentally recorded by S.J. Kline and co-workers at Stanford University, who also demonstrated experimentally that most of the production of turbulent energy is localized in time and space to the bursts. Mårten's idea was, indeed, an appealing one and his model can, very briefly in his own words, be described as "linear ringing due to nonlinear banging". Using this concept, Mårten was able to compute wall pressure correlations in good agreement with observations (*J. Fluid Mech.* **27**, 433, 1967). In the late sixties and early seventies, Mårten and co-workers used this "wave guide model" of his to explain different aspects of turbulent drag reduction due to addition of minute amounts of long chain polymers. Albeit in somewhat modified form, Mårten is still using this approach to model phenomena in turbulent flows, notably the streaky structure of the wall region. Some results from these studies are documented in his book "Turbulence and Random Phenomena in Fluids" (Camb. Univ. Press, 1986), written with Erik Mollo-Christensen, another former colleague in the MIT aeronautics department. This book is in its second edition.

Mårten Landahl's interest in hydrodynamic stability itself has been oscillatory in time. Ten years after his work on effects of compliant surfaces appeared, he published an exciting, and, to some researchers, provocative theory of transition in boundary layer flows (*J. Fluid Mech.* **56**, 775, 1972). As is always the case in Mårten's work, the physical concept is simple even though the mathematics is perhaps not altogether so. The model essentially proposes that, at transition, a nonlinearly distorted Tollmien-Schlichting wave makes the laminar boundary layer velocity distribution *locally* unstable to linear small scale waves. Furthermore, the small scale waves are subject to wave focussing in a very small region of space, which leads to the spiky structure that has been observed experimentally. Mårten's theory gave results in very good agreement with experiments. Although details of the theory were disputed, the basic concept of local secondary instability is still used in research on hydrodynamic stability.

Eight years later, Mårten Landahl published another seminal paper on hydro-dynamic stability (*J. Fluid Mech.* **98**, 243, 1980). This time, he stressed properties of the linear inviscid stability problem. The perhaps most important result of this work is that, even though perturbations may not grow exponentially, there is, for a wide class of initial conditions, a linear growth in time of the streamwise component of the velocity perturbation. In later papers, Mårten used this result to give a very reasonable explanation of the success of the classical mixing length theory of Prandtl and, as was mentioned above, other aspects of the structure of the wall layer in turbulent shear flows. The results of this paper were later extensively elaborated upon by several of Mårten's graduates, who, among other things, showed that Mårten's somewhat heuristically obtained results for the inviscid case are indeed limits of corresponding viscous cases for infinite values of the Reynolds number. Again, Mårten's ability to simplify a difficult and physically relevant mathematical

problem by intuition was verified. It should be pointed out that the 1980 *JFM* paper has inspired numerous recent efforts to analyze the so-called by-pass mechanism for transition, which is a new field in transition research.

Although being a theoretician, who only to some minor extent has participated in experimental work, Mårten always stresses the physical aspects of his work. The conceptual understanding of results in terms of simple concepts such as convection, amplification by stretching and diffusion of vorticity etc. are always of prime importance, the mathematics itself being secondary. Formal justification is left to others and has so far, in almost all cases, provided verification. Another characteristic quality of Mårten's work is that, whenever possible, he spends great efforts to validate his theoretical predictions by comparisons with observations. Mårten is also an excellent speaker and, as a member of audiences at seminars and lectures, his broad knowledge in the natural sciences and his ability to draw striking analogies, in combination with his pleasure of opposition and speed of thought, gives life to any discussion.

Aside from his own scientific achievements, Mårten Landahl's ability to initiate and conduct research programs has been of profound importance for the development of research, not only in fluid mechanics, particularly in Sweden. During the late sixties and the seventies, there was a momentous national program in Sweden to develop technology for centrifugal separation of gaseous uranium hexaflouride for the production of nuclear reactor fuel. Within this program, together with his colleague Professor S.B. Berndt of KTH, Mårten set up an extensive research program on basic phenomena in rotating flows, in particular gases that are rotating at hypersonic speeds. Several people, both from Sweden and the US, participated in this research. Although this program was terminated not long after the Harrisburg incident, it had a definite impact on certain parts of Swedish industry, footprints that remain today. Mårten has been instrumental in guiding also other national research programs in fluid mechanics. During the period from 1984 to 1990, he was the Head Secretary of the Research Council at the National Swedish Board for Technical Development.

In general, theoreticians have only a modest interest in experimental studies as such but in Mårten's case this is not so. He has been responsible for the build up, from scratch, of two well equipped modern laboratories, one at KTH and the other one at MIT.

The authors of the papers in this issue of *Applied Scientific Research*, as well as friends and colleagues around the world, wish Mårten and Christine a good life and all the best.

FRITZ H. BARK

Publications of Mårten T. Landahl

Induced drag for swept wings at supersonic speed (in Swedish). Flygplanbyran, MF 3-Proj-39, 1949.

Moment coefficients for delta wings with a trailing edge flap at supersonic speeds (in Swedish). Flygplanbyran, MF 3-Aero-5, 1950.

Some electrical analogies for solving common wing problems for incompressible flow (in Swedish). Masters thesis, Royal Institute of Technology, 1951.

(with H. Merbt) Aerodynamic forces on oscillating low aspect ratio wings in compressible flow. KTH, AERO TN 30, 1953.

(with H. Merbt) The oscillating wing of low aspect ratio – results and tables of auxiliary functions. KTH, AERO TN 31, 1953.

Analysis of some wing-body vertical tail interference problems for non-symmetric steady flow using steady-body theory. KTH, AERO TN 32, 1953.

(with V.J.E. Stark) An electrical analogy for solving the oscillating surface problem for incompressible non-viscid fluid. KTH, AERO TN 34, 1953.

Aerodynamic forces on oscillating slender bodies in compressible flow (in Swedish). KTH, AERO Report F1, 1953.

(with P H. Skogstad) Theoretical investigation of three-dimensional non-symmetric transonic flow patterns in lift and yaw Transonic aircraft control project No. 2, Tech. Rep., Dep. Aero & Astro, MIT, 1953.

The flow around oscillating low aspect ratio wings at transonic speeds. KTH, AERO TN 40, 1954.

(with E Mollo-Christensen & H Ashley) Parametric studies of viscous and non-viscous unsteady flows. OSR Technical Report No. 55–13, 1955.

Forces and moments on oscillating slender wing-body combinations at sonic speed. OSR Technical Note No. 56–109, 1956.

(with F Mollo-Christensen & H Ashley) On approximate solutions for the compressible flow around oscillating thin wings. JAS, 22, p. 581, 1955.

Unsteady flow around thin wings at high Mach numbers. JAS, 24, p. 33, 1957.

A strip theory for oscillating thin wings with subsonic leading and supersonic trailing edges. OSR TN 56–155, 1956.

The flow around oscillating low-aspect ratio wings and wing-body combinations at transonic speeds. Proc. of the 9th int. congress of applied mechanics, Brussels, 1956, p. 103, Université de Bruxelles, 1957.

(with E. Mollo-Christensen and J.R Martuccelli) A short static pressure probe independent of Mach number. JAS, 24, p. 625, 1957.

Aerodynamic derivatives for oscillating three-dimensional wings in transonic flow. Presented at the 1st int. congress of the aeronautical sciences, Madrid, 1958.

Adv. Aero. Sci., 1, p. 255, Pergamon Press, 1959.

Theoretical studies of unsteady transonic flow. Ph.D. thesis, KTH, Stockholm, 1959.

(with G. Drougge and B. Beane) Theoretical and experimental investigation of second-order supersonic wing-body interference JAS, 27, p. 694, 1960.

The interference between two intersecting perpendicular two-dimensional supersonic flow fields. FFA Report AU–II–93: 3, 1960.

Unsteady transonic flow. Pergamon Press, Oxford, 1961.

On the stability of a laminar incompressible boundary layer over a flexible surface. J. Fluid Mech. 13, p. 609, 1962.

Some free surface effects on unsteady hydrodynamic loads and hydroelasticity. Presented at the 4th symp. on naval hydrodynamics, 1962.

Linearized theory for unsteady transonic flow. Tech. Rep., Dep. Aero & Astro, MIT 1962.

Inviscid hypersonic flow. Hypersonic flow research (ed. F.R. Ridell), Progress in astronautics and rocketry, 7, p. 319, 1962.

(with S. Widnall) Digital calculation of steady and oscillatory hydrofoil loads including free surface effects. Proc. int. symp. on analogue and digital techniques applied to aeronautics, Liege, 1963, p. 161, 1964.

Linearized theory for unsteady transonic flow. Symp. transsonicum (ed. K. Oswatitsch), p. 414, Springer, 1964.

Graphical technique for analyzing marginally stable dynamic systems. J. Aircraft, 1, p. 293, 1964.

(with H. Ashley) Aerodynamics of wings and bodies. Addison-Wesley, 1965.

Recent developments in boundary layer research (presented at AGARD specialists meeting on recent developments in boundary layer research, Naples). AGARDograph 97, p. 353, 1965.

(with R.E. Kaplan) The effect of compliant walls on boundary layer stability and transition. AGARDograph 97, p. 363, 1965.

(with H. Ashley & Sheila Widnall) New directions in lifting surface theory. AIAA Journal 3, p. 3, 1965.

(with P.E. Rubbert) Solution of nonlinear flow problems through parametric differentiation. Phys. Fluids, 10, p. 831, 1967.

A wave-guide model for turbulent shear flow. J. Fluid Mech., 29, p. 441, 1967.

(with P.E. Rubbert) Solution of the transonic airfoil problem through parametric differentiation. AIAA Journal, 5, p. 470, 1967.

Kernal function for nonplanar oscillating surfaces in a subsonic flow. AIAA Journal, 5, p. 1045, 1967.

(with J.J. Kacprzynski) Recent developments in the supersonic flow over axisymmetric bodies with continuous slope. AIAA–67–5, 1967.

(with A.K. Gupta & E.L. Mollo-Christensen) Experimental and theoretical investigation of the stability of air flow over a water surface. J. Fluid Mech., 33, p. 673, 1968.

Pressure-loading functions for oscillating wings with control surfaces. AIAA Journal, 6, p. 345, 1968.

(with B. White) Effect of gaps on the loading distribution of planar lifting surfaces. AIAA Journal, 6, p. 626, 1968.

(with V.J.E. Stark) Numerical lifting-surface theory – problems and progress. AIAA Journal, 6, p. 2049, 1968.

(with I. Ryhming & L. Hilding) Nonlinear effects on sonic boom intensity. Proc. 2nd conf. on sonic boom, NASA SP–180, p. 117, 1968.

Results of parallel-flow stability calculations obtained by time-sharing computations. Phys. Fluids Suppl. II, p. 146, 1969.

(with H.J. Obremski & M.V. Morkovin) A portfolio of stability characteristics of incompressible boundary layers. AGARDograph 134, 1969.

(with H. Ashley) Thickness and boundary layer effects. AGARD manual on aeroelasticity, vol. 2, chapter 9, 1969.

Hydrodynamic stability. Fluid dynamics transactions, 6, part I, p. 293, 1971.

Gas centrifuges for isotope separation. FFA TN AU–751, part 4, 1971.

(with I. Ryhming & P. LUfgren) Nonlinear effects on sonic boom intensity. Proc. 3rd conf. on sor.ic boom, NASA SP–255, p. 3, 1971.

(with I. Ryhming, H. Sorensen & C. Drougge) A new method for determining sonic boom strength from near field measurements. Proc. 3rd conf. on sonic boom, NASA SP–255, p. 285, 1971.

Performance analysis of simple gas centrifuges with two countercurrents. FFA TN AU–751, part 9, 1972.

(with L. Plobeck) Maximum separation efficiency for gas centrifuges with simple countercurrent profiles. FFA TN AU–751, part 10, 1973.

Drag reduction by polymer addition. Proc. XIIIth IUTAM conf., Moscow, 1972 (eds E. Becker & G.K. Mikhailov), p. 177, Springer, 1973.

Wave mechanics of breakown. J. Fluid Mech., 56, p. 775, 1972.

(with F.H. Bark) Application of a two-scale boundary layer turbulence model to drag reduction. Presented at int colloq. on polymers and lubrication, Brest, France, 20–23 May, 1974. CNRS, 233, p. 249, 1974.

Wave mechanics of boundary layer turbulence and noise. Acous. Soc. Am., 57, p. 824, 1975.

Wave breakdown and turbulence. SIAM J Appl. Math., 28, p. 775, 1975.

(with F.H. Bark & E.J Hinch) Drag reduction in turbulent flow due to additives – a report on EUROMECH 52. J. Fluid Mech , 68, p. 129, 1975.

Some development in unsteady transonic flow research. Presented at IUTAM symp. transsonicum II, Guttingen, 1975. Symp. transsonicum II (eds. K. Oswatitsch and D. Rues), Springer, 1976.

Diffusion in a long countercurrent gas centrifuge as a perturbation problem. Proc. Euromech 80. Universität (TH) Karlsruhe, Heft 22, 1976.

Numerical modelling of blunt-body flows – problems and prospects. Aerodynamic drag mechanisms of bluff bodies and road vehicles, General Motors Research Laboratories, Plenum, 1976.

Recent developments in the modelling of turbulence in boundary layers. Proc. of the Theodorsen colloquim 1976 (ed. L.N. Persen), Det Konglige Norske Videnskabers Velskap, 1977.

(with W.O. Criminale) Wave breakdown in stratified shear flows. J. Fluid Mech., 79, p. 481, 1977.

Dynamics of boundary layer turbulence and the mechanism of drag reduction. Presented at IUTAM symp on turbulence structure and drag reduction, Washington D.C., 1976. Phys. Fluids 20, p S55, 1977.

Boundary layers and shear layers in a rapidly rotating gas (invited opening lecture). Proc. second workshop on gases in strong rotation, Cadarache, France (ed. Soubbaramayer), C.E.N.S., Gif-sur-Yvette, France, 1977.

Recent developments in turbulence research (invited opening lecture, presented at 2nd int. IAHR symp. on stochastic hydraulics, Lund 1976). Hydraulic problems solved by stochastic methods, p 1.1. Water Resources Publ., Fort Collins, 1977.

Course lectures on turbulence. Summer study program in geophysical fluid dynamics at the Woods Hole Oceanographic Institution, 1977.

(with S. Widnall & L. Hultgren) An interaction mechanism between large and small scales for wind-generated water waves. 12th symp. on naval hydrodynamics, 1978.

Modelling of coherent structure in boundary layer turbulence (invited paper). Proc. AFOSR workshop on coherent structures of turbulent boundary layers (eds. D. Abbott & C. Smith), p. 340, Lehigh University, 1978.

The structure of wall turbulence (invited opening lecture). Int. symp. on ship viscous resistance, 1978, Gothenbourg (ed. L. Larsson), p. 1.1, SSPA, 1978.

Momentum theory analysis of unconventional wind energy extraction schemes. FFA Report No. Au–1499, part 10, 1979.

Effects of additives on turbulent bursting dynamics (invited paper). Progr. Aero. and Astro., 72, p. 300, 1980.

A note on an algebraic instability of inviscid parallel shear flow. J. Fluid Mech., 98, p. 243, 1980.

Mathematical modelling in fluid mechanics (presented at GAMM-Tagung, Berlin). ZAMM, 61, p. T9, 1981.

Analysis of some four-pole centrifuge arrangements. Presented at 4th Workshop on gases in strong rotation, 1981.

A theoretical model for coherent structures in wall turbulence (invited paper). Proc. of IUTAM/ICHMT symp. on heat and mass transfer and the structure of turbulence, Dubrovnik (ed. Z. Zaric), Hemisphere Publ. Corp., 1981.

Roll-up model for rotor wake vortices. MIT FDRL Rep. No. 81-1, 1981.

The application of kinematic wave theory for wave trains and packets with small dissipation. Phys. Fluids, 25, p. 1512, 1982.

Theoretical modelling of coherent structures in wall bounded shear flows (invited paper). 8th biennial symp. in turbulence, University of Missouri-Rolla, Rolla, 1983.

On the dynamics of large eddies in the wall region of a turbulent boundary layer (invited paper, IUTAM symp. on turbulence and chaotic phenomena in fluids, Kyoto, 1983). Turbulence and chaotic phenomena in fluids (ed. T. Tatsumi), p. 467, Elsevier, 1984.

(with J.M. Russel) The evolution of a flat eddy near the wall in an inviscid shear flow. Phys. Fluids, 27, p. 557, 1984.

Coherent structures in turbulence and Prandtl's mixing length theory (invited paper, presented at the 27th Ludwig Prandtl memorial lecture, Regensburg, Germany, 1984). Z. Flugwiss. Weltraumforsch., 8, p. 233, 1984.

The growth of instability waves in a slightly nonuniform medium (invited paper, presented at 2nd IUTAM symp. on transition to turbulence, Novosibirsk, 1984). Laminar turbulent transition (ed. V.V. Kozlov), p. 133, Springer, 1985.

The effect of short waves on the transfer of wind momentum to long water waves (invited paper presented at Symp. on wave breaking, turbulent mixing and radio probing of the ocean surface, Sendai, Japan, 1984). The ocean surface, wave breaking, turbulent mixing and radio probing (eds Y. Toba & H. Mitsayasu), D. Reidel Publ. Comp., 1985.

Flat-eddy model for coherent structures in boundary layer turbulence (invited paper, presented at ICASE workshop on theoretical approaches to turbulence, Virginia Beach, 1984).

Shear flow instability and breakdown (invited paper presented at Workshop on instabilities in continuous media, Venice, 1982). Instabilities in continuous media (ed. L. Knopoff), Basel Birkheuser, 1984.

(with H. Ashley) Aerodynamics of wings and bodies. Dover, 1985.

(with D. Henningson) The effects of drag reduction measures on boundary layer turbulence structure – implications of an inviscid model (invited paper, presented at AIAA shear flow control conf., Boulder). AIAA-85-0570, 1985.

(with E. Mollo-Christensen) Turbulence and random phenomena in fluid mechanics. Cambridge University Press, 1986.

(with J.A. Smith and S.E. Widnall) The interaction between long and short wind-generated waves (invited paper, presented at IUCRM symp. on wave dynamics and radio probing of the ocean surface, Miami Beach, 1981). Wave dynamics and probing of the ocean surface (eds O.M. Philips & K. Hasselmann), Plenum, 1986.

Ordered and disordered structures in shear flow. Lecture notes (invited principal lecturer at the 1986 Geophysical fluid dynamics summer program, Woods Hole), 1986.

Unsteady transonic flow. Classic Science Series, Cambridge University Press 1987.

Linear and nonlinear mechanisms in boundary layer turbulence (invited paper presented at the 5th int. conf. on numerical methods in laminar and turbulent flow, Montreal, 1987). Numerical methods

in laminar and turbulent flow: Proc. 5th int. conf. (eds C. Taylor, W.G. Habashi & M.M. Hafez), Piner:dge, 1987.

(with J. Kim & P. Spalart) Active-layer model for wall-bounded turbulence. Proc. 1987 summer program, Center for Turbulence Research, CTR–S87, NASA/Stanford University, 1987.

(with D. Henningson & J. Kim) Wave-growth associated with turbulent spots in plane Poiseuille flow. Proc. 1987 summer program, Center for Turbulence Research, CTR–S87, NASA/Stanford University, 1987.

(with K. Breuer & J. Kim) The simulation of coherent structures in a laminar boundary layer. Proc. 1987 summer program, Center for Turbulence Research, CTR–S87, NASA/Stanford University, 1987.

(with E. Murman, K. Powell & A. Goodsell) Leading-edge vortex solutions with large total pressure losses. AIAA–87–0039, 1987.

Boundary layer turbulence regarded as a driven linear system. Presented at 8th ann. int. conf. of the center for nonlinear studies, Los Alamos, 1988. Advances in fluid turbulence, Physica D, 37, p. 11, 1989.

Theoretical model for VITA-educed coherent structures in the wall region of a turbulent boundary layer. Proc. 1988 summer program, Center for Turbulence Research, CTR–S88, NASA/Stanford University, 1988.

(with K.S. Breuer & J.H. Haritonidis) The control of transient disturbances in a flat plate boundary layer through active wall motion Phys. Fluids A, 1, p. 574, 1989.

Hydrodynamic instability and coherent structures in turbulence. 2nd IUTAM symp. on turbulence structure and drag reduction, ETH, Zürich, 1989.

On sublayer streaks. J. Fluid Mech., 212, p 593, 1990.

Waves in turbulence (invited opening lecture, presented at 3rd European turbulence conf., Stockholm, 1990) Advances in Turbulence 3 (eds A.V. Johansson & P.H. Alfredsson), p. 67, Springer 1991.

(with K.S Breuer) The evolution of a localized disturbance in a laminar boundary layer. Part 2. Strong disturbances. J. Fluid Mech., 220, p 595, 1990.

Model for the wall-layer structure of a turbulent shear flow. Eur. J. Mech., B/Fluids, 12, p. 85, 1993

Near-wall model for boundary layer turbulence Appl. Sci. Res., 51, p. 435, 1993.

There are also several internal company reports which are not included in this list. In cases where internal reports were followed by journal publication only the latter has been included.

Convection in Electrochemical Systems

FRITZ H. BARK
Department of Mechanics, Royal Institute of Technology, Stockholm, S 100 44 Sweden

and

FARID ALAVYOON
Government Industrial Research Institute, Sendai 983, Japan, Present address: Vattenfall Utveckling AB, Älvkarleby, S 810 71 Sweden

Abstract. Some theoretical and experimental results for the concentration and velocity fields that appear during unsteady electrolysis in small electrochemical cells are given. Two systems are considered: $|Cu|CuSO_4(aq)|Cu|$ and $|PbO_2, PbSO_4|H_2SO_4(aq)|Pb, PbSO_4|$. For the former system, in which the electrodes are solid, both linear and nonlinear electrode kinetics are considered. For the more complicated latter system, where the electrodes are porous, attention is restricted to linear kinetics. Theoretical results are obtained by using both perturbation methods and numerical analysis. Experimental results are obtained by Laser Doppler Velocimetry and Image Laser Holography. It is shown that the evolution of the concentration and velocity fields is controlled by stratification of the electrolyte. The boundary layer structure is similar to that appearing during nonlinear spin up of a homogeneous fluid. Theoretical and experimental results are in good agreement.

1. Introduction

In the late sixties and seventies, the Swedish government initiated a national research program for theoretical and experimental studies of the fluid mechanics of centrifugation of gaseous UF_6-isotopes. The aim of the program was to establish sufficient technological knowledge within the country in order to build an enrichment facility for fuel supply to the Swedish nuclear energy program, possibly in cooperation with some other European country. Mårten Landahl was one of the chief architects of this program and made several important contributions, in particular on the gas dynamics and the principal design of gas centrifuges. Much of the research was carried out under Mårten Landahl's supervision in the Department of Mechanics at the Royal Institute of Technology. During the summers, several of his colleagues at M.I.T., Roger Gans, Louis Howard, Willem Malkus and Sherwin Maslowe, visited Sweden for participation in the program. During this period, Mårten Landahl and his colleague Sune Berndt at KTH started a series of biannual international workshops on uranium enrichment by centrifugation. These workshops, with regularly participating researchers from France, Great Britain, Italy, Japan, The Netherlands, Sweden, U.S.A., West Germany and later also the Peoples Republic of China, remained very active until the middle of the eighties when, in most countries, including Sweden, research in this area was closed down. There were several reasons for this, the public opinion, the maturity of the tech-

nology and the excess of enriched uranium available at low price on the world market. However, the most important reason was probably that considerably more successful alternative technologies emerged. As for the Swedish program, it was characterized by Mårten Landahl as "... one of those technically and scientifically very interesting programs that never led anywhere ...".

The first of the present authors had the pleasure of participating in the aforementioned research. It was a period of great enthusiasm. The field was one of both scientfic and industrial interest where progress could be and was made by using analytic perturbation methods in parallel with large scale numerical computations. Also some very interesting experimental work was carried out.

Several years after the Swedish project on uranium enrichment was aborted, the first of the present authors, by mere incidence, entered another field where the physical phenomena are quite similar to those that appear in rapidly rotating flows, namely free convection in electrochemical systems. This area of research, which is a combination of electrochemistry and fluid mechanics, was rather active until the late fifties when, in spite of its significant technical importance, it simply started to fade away. The main reason for the decreased activity was probably that researchers in electrochemistry and fluid mechanics, respectively, tended to be successively more encapsulated in their own specialties as the steadily growing complexity of the two fields made simultaneous research in the two areas increasingly difficult.

The literature on the interaction between electrochemical phenomena and fluid motion is consequently quite small. The classical treatment of the subject is the book by Levich (1962). The standard reference from the electrochemical point of view is the book by Newman (1991). Some interesting recent contributions, in which fluid mechanical phenomena are of primary importance, are summarized by Probstein (1990) in a recent book.

In this paper, which addresses researchers in fluid mechanics, we give an outline of some of the basic mass transfer phenomena that are encountered in electrochemistry. Some published and some yet unpublished results, which have been obtained in collaboration with researchers in the Department of Technical Electrochemistry and Corrosion Science at the Royal Institute of Technology, are presented. The analogy with similar phenomena in the theory of rotating flows is discussed in some detail.

Some technical applications where interaction between fluid motion and electrochemical reactions are of primary importance should be mentioned. In materials science, combinations of electrochemical and fluid mechanical phenomena appear in electroplating, electrorefining and electrowinning of metals. Similar phenomena are of importance in various parts of energy technology such as charging and discharging of batteries and the operation of fuel cells. In electrolytic production of chemicals, effects of fluid motion are, in many cases, of primary importance. Another field of application is electrolytic purification of waste water and desalination of sea water. From a scientific point of view, an interesting application was pointed out by Ward III and LeBlanc (1984), who noted that experimental stud-

ies of thermal Benard convection in geophysical applications are, in certain cases, more readily carried out in electrochemical model systems than in thermally driven model systems.

In the present paper, attention is focussed on effects of stratification on laminar flows in electrochemical systems. In a lead acid battery, stratification of the electrolyte, with a larger concentration of sulphuric acid at the bottom of the battery than at the top, is known to significantly decrease the life time of the battery. The reason is that the loading of the electrodes, due to stratification, is nonuniform. The larger conductivity in the lower parts of the battery causes a larger part of the electric current to flow in this region compared to the upper parts. This means that the electrodes are more rapidly worn out than would be the case with a uniform distribution of the electric current density. Also in commercial refining of copper, which is carried out in large cells where the motion of the electrolyte is turbulent, effects of stratification are most likely of importance although the consequences are in this case less clear. Effects of stratification in small cells for refining of copper are in this paper taken up in order to elucidate some of the basic mechanisms that are present in the considerably more complicated lead acid batteries.

This paper is organised as follows: Section 2 gives a discussion of different transport mechanisms in a liquid electrolyte and the basic physical laws are stated. During electrolysis of a liquid electrolyte, chemical reactions take place at the electrolyte-electrode interfaces. These reactions lead to a nonhomogeneous composition of the electrolyte, which, in many cases, sets up a convective motion. The kinetics of the interface reactions are outlined in Section 3 and some general properties of the ensuing fluid motion are taken up in Section 4. Some results for electrolysis of a copper sulphate in a small electrochemical cell are given in Section 4. In Section 5, some phenomena encountered in charging of lead acid batteries are discussed. Section 6 is a summary of relevant problems to be investigated in the future. Throughout the paper, mathematical and experimental details are omitted.

2. Transport in liquid electrolytes

In metallic conductors, e.g. in a copper electrode, electric charge is carried by moving electrons. In liquid electrolytes, on the other hand, such as aqueous solutions of $CuSO_4$, $AgNO_3$ or H_2SO_4, electric current is due to moving ions. There are three mechanisms for such transport:
1. Diffusion,
2. Migration in the electric field,
3. Advection by the motion of the electrolyte.

For a dilute electrolyte that contains M ionic species, these transport mechanisms are quantified by the following formula for the mass flux vector $\overline{N}_j$, whose dimension is $moles/s \cdot m^2$, of species $j (j = 1, \ldots, M)$

$$\overline{N}_j = -\mathcal{D}_j \nabla c_j - \frac{z_j F \mathcal{D}_j}{RT} c_j \nabla \phi + c_j \overline{v}. \tag{1}$$

Here c_j is the concentration of species j, ϕ is the electric potential and $\overline{v}$ is the local velocity of the electrolyte. As attention is restricted to dilute electrolytes, the velocity field $\overline{v}$ may be taken as the velocity of the solvent. The constants z_j and $\mathcal{D}_j$ are the charge number and diffusion coefficient, respectively, for species j. In this paper, the diffusivities $\mathcal{D}_j$ are assumed to be constants. The quantities F, R and T are Faraday's constant, the gas constant and the absolute temperature. The temperature is henceforth assumed to be constant. Formula (1) is sometimes in the literature referred to as the *Planck-Nernst* law. The diffusive and advective modes of transport are well known but the migrative transport may be worth a comment. The second term in formula (1) may be split into three factors of different physical meaning: i. $z_j \nabla \phi$, which is proportional to the electrostatic force on the ionic species j, ii. The concentration c_j of that species and iii. A mobility factor $F\mathcal{D}_j/RT$ that determines the velocity relative to that of the electrolyte of the individual ions per unit electrostatic force on the ions. This mobility factor was originally computed by Nernst (1988).

Conservation of each ionic species in the electrolyte gives that

$$\frac{\partial c_j}{\partial t} = -\nabla \cdot \overline{\mathcal{N}}_j, j = 1, \dots, M, \tag{2}$$

which defines a set of M coupled partial differential equations to be solved. It should be noted that these equations are, of course, not sufficient for the computation of the concentration fields c_j since the velocity field $\overline{v}$ and the electric potential ϕ have to be determined as well.

An equation for the electric potential ϕ can be derived by making use of the fact that electrolytes can usually, as a very accurate approximation, be regarded as electrically neutral. Thus, there is no net accumulation or depletion of charge anywhere, which implies that

$$\sum_{j=1}^{M} z_j c_j = 0. \tag{3}$$

Using formula (1) and equations (2–3), it is easy to show that

$$\sum_{j=1}^{M} \frac{z_2 F \mathcal{D}_j}{RT} \nabla \cdot (c_j \nabla \phi) + \sum_{j=1}^{M} z_j \mathcal{D}_j \nabla^2 c_j = 0. \tag{4}$$

This equation has a simple physical interpretation. Let us for the moment neglect advective transport, which will not affect the following discussion. Since, in general, the diffusivities $\mathcal{D}_j$ are different, diffusion would, in the absence of migration, set up concentration fields that are incompatible with the constraint of electroneutrality. The role of the electric potential is thus to balance, by migration, the diffusive transport so that electroneutrality is maintained. This balance is quantified by equation (4). It should be noted that the advective transport has no effect

on this process as, in the limit case of a dilute electrolyte, all ions are advected by the same velocity field. From a mathematical point of view, one is here faced with the problem of solving the nonlinear elliptic equation (4) simultaneously with the other field equations, i.e. with the conservation equations (2) and the hydrodynamic equations. The situation is thus more complicated than in the case of a solid conductor, where the electric potential ϕ is to be computed from the linear Laplace equation. As expected, equation (4) reduces to Lapalce equation if the concentration fields are uniform.

An important special case, in which significant simplication appears, is that of a binary electrolyte, an electrolyte that contains just two ionic species. In this case, according to equation (3), the two concentration fields are proportional to each other, which implies that only one concentration variable is needed. For cases such that $z_1 = -z_2 > 0$, it turns out to be convenient to take

$$c = z_1 c_1 = -z_2 c_2.$$

Since the mass flux vectors $\overline{N}_j$ are linear in the gradient of the electric field, $\nabla \phi$, one can eliminate the electric field from the (two) equations (2), whereby one obtains the following equation for c:

$$\frac{\partial c}{\partial t} + \overline{v} \cdot \nabla c = \mathcal{D} \nabla^2 c. \tag{5}$$

The diffusion coefficient $\mathcal{D}$, which appears in this equation, is in the literature called the salt diffusivity and is defined by the expression

$$\mathcal{D} = \frac{(z_1 - z_2)\mathcal{D}_1 \mathcal{D}_2}{(z_1)\mathcal{D}_1 - z_2 \mathcal{D}_2)} > 0.$$

Thus, in the special case of a binary electrolyte, species *appear* to be transported by diffusion and advection only. This happens to be so because, as is readily shown from equations (2–3), the transport due to migration is proportional to that due to diffusion. The form of equation (5) indicates that the electric potential ϕ has been eliminated from the problem. However, as we will see later on, ϕ usually reappears in the boundary conditions.

A quantity of primary interest in electrochemistry is the electric current density $\overline{i}(A/m^2)$, which is given by *Faraday's law*

$$\overline{i} = F \sum_{j=1}^{M} z_j \overline{N}_j. \tag{6}$$

It follows from formula (1) and equation (3) for electroneutrality that the electric current does not seem to depend explicitly on the velocity field $\overline{v}$. However, as will be seen later, $\overline{i}$ depends indirectly on the velocity field, which is related to the concentration fields due to buoyancy.

3. Interface kinetics

In this section, the mass fluxes into the electrolyte from the electrode-electrolyte interfaces will be quantified in terms of the local values of the concentration fields c_j and the electric potential ϕ. Such formulae are needed as boundary conditions for the solutions of equations (2) and (4) in the previous section. The reader is once again reminded of the fact that these equations, in general, must be solved simultaneously with the hydrodynamic equations for the velocity field $\bar{v}$. However, in order to simplify the discussion, $\bar{v}$ is, for the moment, assumed to be known. A brief outline of the hydrodynamic problem is given in the next section.

Consider electrolysis of a solution of a metallic salt such as an aqueous solution of $CuSO_4$, which is a binary electrolyte. The positive ions of the salt are henceforth labelled as species 1. In many cases, e.g. in industrial refining of copper, the electrodes are made of a metallic material Me, say, and the positive ions of the dissolved salt are Me^{z_1+}. Attention will in what follows be restricted to such electrochemical systems.

At the interface between the positive electrode, i.e. the anode, and the electrolyte, the passage of electric current through the cell implies that there is a transfer of (positive) charge from the anode to the electrolyte. This transfer of charge drives the following reaction at the interface

$$Me \rightarrow Me^{z_1+} + z_1 e^-, \tag{7}$$

which says that metal atoms from the solid anode are dissolved as ions into the electrolyte. It should be noted that the reaction specified by this formula is irreversible and requires power. Thus, the interface between the anode and the electrolyte has a finite surface resistivity, whose magnitude is *a priori* unknown and has to be computed as part of the mathematical problem. Since the normal component of the electric current is continuous across the interface, there will be a jump, of unknown magnitude, in the electric potential across the interface, see Fig. 1. The magnitude of this discontinuity is called the *charge transfer potential*.

At the negative electrode, i.e. the cathode, where metal ions enter the crystal lattice of the solid metal Me, a reaction in the opposite direction to that specified by formula (7) will take place. Also this reaction is irreversible and requires power, which, in general, is different from that consumed at the positive electrode. For high electric current densities, bubbles, made up by gaseous hydrogen, may be released at the cathode. In the present work, it is assumed that conditions are such that no release of hydrogen bubbles takes place.

To be specific, let us consider a two-dimensional, closed rectangular electrochemical cell of width $2h$ and height $2H$ and use a Cartesian coordinate (system) (x, z) as shown in Fig. 2. The anode (cathode) is at $x = -h, |z| \leq H (x = h, |z| \leq H)$ and the boundaries $z \pm H, |x| \leq h$ are taken to be insulated.

Kinetic estimates of the rate of the reaction given by formula (7) can be used to derive a semi-empirical relation between the normal component of the electric
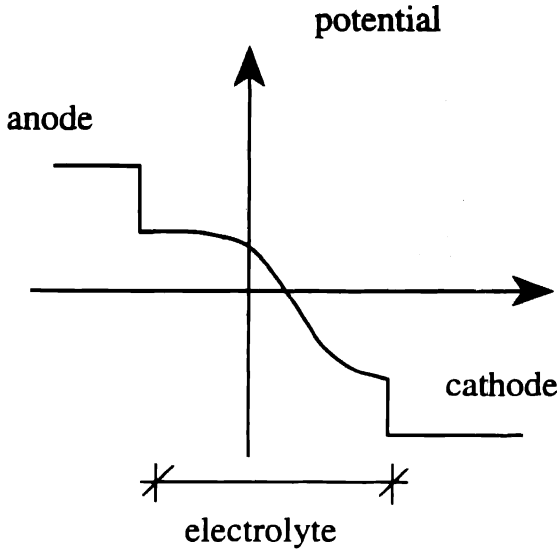
Fig. 1. Sketch of the horizontal variation of the electric potential in an electrochemical cell with vertical electrodes.
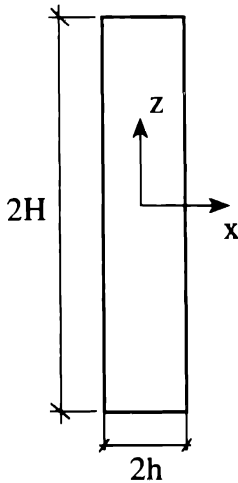
Fig. 2. Geometry of the electrochemical cell considered in the text and definition of coordinate system.

current at the anode, i.e. $\bar{e}_x \cdot \bar{i}$, the local values of $c(= z_1 c_1 = -z_2 c_2)$, ϕ and the prescribed constant electric potential V_a of the anode, see e.g. Newman (1991). For binary electrolytes and metallic electrodes, such relations are often of the form

$$\overline{e}_x \cdot \overline{\imath} = \imath_0 [e^{\beta z_1 F(V_a - \phi)/RT} - \left(\frac{c}{c_0}\right) e^{(1-\beta)z_1 F(\phi - V_a)/RT}],$$
$$x = -h, |z| \le H \, (anode), \tag{8}$$

where the quantities $\imath_0$, the exchange current density, and β, the symmetry factor, are experimentally determined constants. c_0 is a reference concentration, which, in the present case, is taken as the homogeneous initial concentration that is assumed to prevail before the electrolysis starts.[*] β is often very close to $\frac{1}{2}$. Expressions of this kind are called *Butler-Volmer* laws. The first (positive) term on the r.h.s. of this formula is called the anodic current and the second (negative) term is called the cathodic current. We note that, at equilibrium, i.e. $c = c_0$ and $V_a = \phi = 0$, the anodic and cathodic currents are non-zero but of equal magnitude $\imath_0$ and there is consequently no *net* current from the anode. It should be pointed out that the (unknown) charge transfer potential, i.e. $V_a - \phi$, in general depends on space and time in cases of nonequilibrium.

From formulas (1) and (6) in the previous section, we find that expression (8) gives *one* boundary condition at the anode for the *two* unknowns c and ϕ. The remaining boundary condition is obtained from the fact that, in the case under consideration, the nonmetallic (negative) ions of the dissolved salt do not participate in the reactions at the interfaces. If the negative ions are labelled species 2, we must thus require that

$$\overline{\mathcal{N}}_2 \cdot \overline{e}_x = 0, x = -h, |z| \le H \, (anode). \tag{9}$$

At the cathode, one has the similar boundary conditions

$$\overline{e}_x \cdot \overline{\imath} = \imath_0 [\left(\frac{c}{c_0}\right) e^{(1-\beta)z_1 F(\phi - V_c)/RT} - e^{\beta z_1 F(V_c - \phi)/RT}],$$
$$x = h, |z| \le H \, (cathode), \tag{10}$$

$$\overline{\mathcal{N}}_2 \cdot \overline{e}_x = 0, x = h, |z| \le H \, (cathode), \tag{11}$$

where V_c is the prescribed electric potential of the cathode.

At the insulated horizontal boundaries $z = \pm H$, the absence of transfer of mass and charge implies that

$$\overline{e}_z \cdot \nabla c = 0, \overline{e}_z \cdot \nabla \phi = 0, z = \pm H, |x| \le h. \tag{12}$$

---

[*] The magnitude of the exchange current density depends on the local concentration In formula (8), $\imath_0$ is the exchange current density at the reference concentration c_0.

Finally, because equation (2) contains a first derivative of c with respect to time t, an initial condition for c has to be specified. If the electrolysis starts from an initially uniform electrolyte, the initial condition is

$$c = c_0, t = 0, |x| \leq h, |z| \leq H \tag{13}$$

For a known velocity field $\bar{v}$, the electrochemical part of the mathematical problem for electrolysis of a binary electrolyte thus amounts to the solution of two non-linearly coupled partial differential equations, the parabolic equation (2) and the elliptic equation (4) subject to the boundary and initial conditions that are specified above.

The nonlinear boundary conditions (8) and (10) are quite difficult to deal with from a numerical point of view and even more so when analytic methods are used. Fortunately, some simplication results if the nondimensional difference in voltage between anode and cathode, i.e. $F(V_a - V_c)/RT$, is small. For such cases, it can be shown analytically, and demonstrated experimentally, that the normal component of the electric current density on the electrodes is approximately constant. Thus, expressions (8) and (10) can be replaced by the simpler expressions

$$\bar{e}_x \cdot \bar{i} = \mathcal{J} = const., x = \pm h, |z| \leq H. \tag{14}$$

In cases where these simplified boundary conditions are applicable and the current density $\mathcal{J}$ on the surfaces of the electrodes is known, the electric potential ϕ does not have to be considered in the computation of the concentration field c. ϕ and the charge transfer potentials can be computed afterwards in terms of the concentration field. The simplified model of the electrode kinetics that is given by formula (14) will henceforth be referred to as *linear kinetics*. For large current densities, where the kinetics is described by the more elaborate formulas (8) and (10), the electrode reactions are said to be controlled by *nonlinear kinetics*.

In the problem formulation that has been outlined above, the electric potentials V_a and V_c of the anode and cathode, respectively, have been prescribed. This case is called *potentiostatic* electrolysis. In many applications, however, the net electric current $\mathcal{I}$, say, passing through the cell rather than $V_{a,c}$ is prescribed. Such cases are referred to as *galvanostatic* electrolysis. In general, cases of the latter kind are more difficult to deal with mathematically and numerically.

4. Fluid motion and nondimensional parameters

This section gives the mathematical statement of the problem for the motion of the electrolyte, the nondimensional parameters entering the complete problem of electrolysis and a brief qualitative discussion of free convection in a closed electrochemical system.

The equations for the velocity field $\bar{v}$ and pressure field p in a dilute electrolyte are the Navier-Stokes equations in the Boussinesq approximation, which, in a general case with M species, read

$$\rho_0 \left(\frac{\partial \bar{v}}{\partial t} + \bar{v} \cdot \nabla \bar{v} \right) = -\nabla p + \mu \nabla^2 \bar{v} + \rho_0 \sum_{j=1}^{M} \alpha_j (c_j - c_{0j}) \bar{g} \tag{15}$$

and the equation of continuity

$$\nabla \cdot \bar{v} = 0. \tag{16}$$

Here ρ_0 is a reference density, which is preferrably taken as the density in the state of equilibrium, μ the dynamic viscosity and c_{0j} reference concentrations of species j. $\bar{g}$ is the acceleration of gravity. The quantities c_{0j} are usually chosen as the equilibrium concentrations. The constant quantities α_j are the densification coefficients, which measure the change in volume of the electrolyte for a unit change in concentration of species j relative to the reference concentration, i.e. $c_j - c_{0j}$. In general, α_j can be either positive or negative. A local surplus of e.g. light H^+ ions will tend to decrease the density of an aqueous solution whereas a surplus of heavy Cu^{++} or SO_4^{--} ions will have the opposite effect. It should be noted that the condition of electroneutrality, see equation (3) in Section 2, implies that, in the case of a binary electrolyte, the buoyancy term in equation (15) can be expressed in terms of one concentration variable only, which means that only one densification coefficient is needed. Unless otherwise explicitly stated, we will in what follows only discuss the case of a binary electrolyte, whose densification coefficient will be called α. Also, in order to avoid unnecessary notational complexity, we will henceforth choose the values $z_{1,2} = \pm 2$ for the charge numbers. These are the values for e.g. an aqueous solution of $CuSO_4$, a system for which some experimental results will be quoted later.

When the equations (15) and (16) for the velocity and pressure fields are supplemented with appropriate boundary and initial conditions, which need not be stated here, the mathematical problem for electrolysis is complete. Whether solutions exist or not appears to be an open question even though several analytic and numerical solutions have been reported in the literature.

In the case of galvanostatic electrolysis of a binary electrolyte at low current densities, the following nondimensional parameters will appear:

$$Ra = \frac{\alpha \rho_0 g \mathcal{J} h^4}{2F \mu D}, \text{ Rayleigh number,}$$

$$Sc = \frac{\nu}{D}, \text{ Schmidt number,}$$

$$\Gamma = \frac{2(D_1 + D_2)}{D_1 - D_2}, \kappa = \frac{\mathcal{J} h}{2c_0 F D_1}, \mathcal{H} = \frac{H}{h}.$$

In al' applications, the Rayleigh number is a large quantity, typical values are in the range $10^4 - 10^8$. It should be noted that the Rayleigh number is here based on the half-width of the cell rather than on its height. This is in contrast to the standard procedure in e.g. heat transfer problems where the length over which the forcing is applied is chosen as the reference length. The present, somewhat unusual, definition, which is perhaps not *a priori* obvious, will be commented upon later. As is always the case in mass transfer problems, the Schmidt number is a large quantity, typically of order 10^3. The number Γ is a measure of the ratio of the contributions from migration and diffusion to the electric current density. κ is a measure of the strength of the concentration field and $\mathcal{H}$ is the aspect ratio of the electrochemical cell. In the present work, large values of $\mathcal{H}$ will be considered whereas Γ and κ are assumed to be of order unity. For high current densities, where the elaborate boundary conditions (8) and (10) have to be used, the Rayleigh number must be defined in a different and somewhat more complicated way. For lead acid cells, additional nondimensional parameters are needed to specify, among other things, the effective coefficients of diffusion in the electrodes and geometries and porosities of the electrodes, respectively.

Next, we consider the general nature of electrolysis of a binary electrolyte, starting from a state of equilibrium with a constant concentration. In this paper, only closed electrochemical cells will be considered. As the current is switched on, the electrode reaction (7) starts at the anode. This means that, due to dissolution of metal ions at the interface between anode and electrolyte, the concentration field c will locally increase in the neighbourhood of the interface. In this region, the electrolyte will thus be heavier than that in the bulk and will start to sink downwards. At the cathode, where the reverse reaction takes place, the electrolyte will locally be lighter than in the bulk and will thus start to flow upwards.

We may now, depending on the time scale and cell geometry under consideration, distinguish different kinds of motion. The heavy electrolyte moving down and the light electrolyte moving up will eventually set up a density stratification in the cell. If the cell is small, this stratification appears quite rapidly and will soon exert significant control of the motion. For large cells, on the other hand, the build up time for the stratification will be very long and the motion near the electrodes will, during a significant period of time. have the same general character as the boundary layer flow near a cooled (heated) vertical plate immersed in a homogeneous fluid. It can be shown that, if a significant stratification prevails, the motion is practically inertialess whereas this is in general not so if there is no stratification. In the present paper, attention will be restricted to the former kind of motion, which, as will be discussed later, is akin to the motion of a rapidly rotating fluid.

5. Electrolysis driven by linear kinetics in small cells

Measurements of the concentration field by Eklund et al. (1991) and the velocity field by Karlsson et al. (1990) in an aqueous solution of copper sulphate during
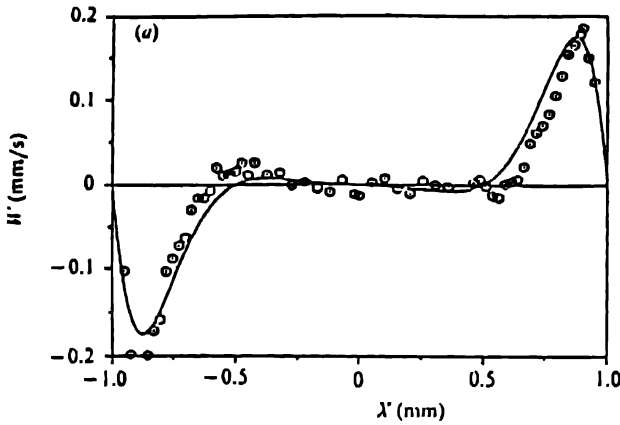
Fig. 3. The vertical velocity component in a horizontal section at midheight in a small copper sulphate cell under conditions of linear kinetics. $c_0 = 0.3 moles/litre, II = 16mm, h = 2mm. Ra = 3.08 \cdot 10^5, Sc = 1.28 \cdot 10^3, \Gamma = -10.3, \kappa = 1.10 \cdot 10^{-4}, \tau = 0.09$. The length of the cell is 20 mm. Hexagons: Measurements from Karlsson et al. (1990). Solid curve: Asymptotic theory from Bark et al. (1992).

electrolysis at low current densities in a small ($2 \times 32mm$) cell show conclusively that, after initial transients have decayed, a strong stratification appears and that the motion has boundary layer character. Some of these experimental results are shown in Figs 3 and 4.

Relying on a theoretical model, formulated by Prandtl (1952), for steady mountain winds in a stratified atmosphere, Bark et al. (1992) deduced the asymptotic structure of the concentration and velocity fields in a stratified electrolyte as the Rayleigh number Ra approaches infinity. Those authors showed that, in the steady state, the strength of the stratification outside the boundary layers is given by the estimate

$$|\frac{\partial c}{\partial z}| \sim Ra^{-1/9} \frac{\mathcal{I}}{FD_1}. \tag{17}$$

where $\mathcal{I}$ is the prescribed current density on the electrodes. The resulting boundary layer structure is shown in Fig. 5. It was shown by Bark et al. (1992) that, even though the evolution of the interior stratification is governed by nonlinear phenomena, the buoyancy layers are inertialess. The similarity between the boundary layer structure in Fig. 5 and that in a rotating fluid at small Ekman number E is striking. For $E \sim Ra^{-4/9}$, the thicknesses of the vertical buoyancy layers and the horizontal boundary layers in the electrochemical cell are the same as those of the Ekman and Stewartson $E^{1/3}$ and $E^{1/4}$ layers in a rotating fluid that is contained in a vessel of height $2h$. Outside the boundary layers shown in Fig. 5, the electrolyte is, in the steady state, stagnant but vertical diffusion of mass is significant due to the
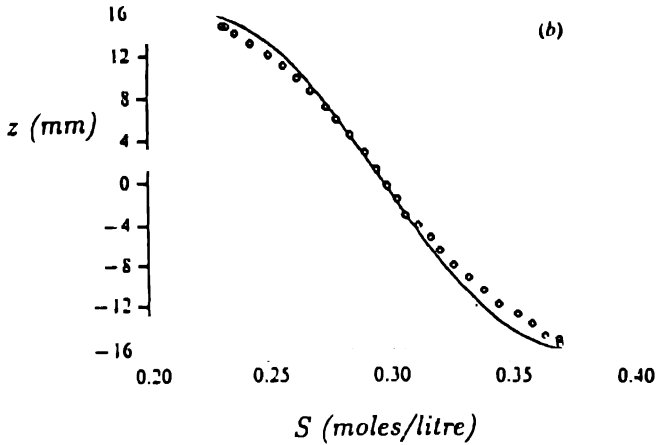
Fig. 4 The vertical variation of the concentration field in the midsection of a small copper cell under conditions of linear kinetics. The parameter values are the same as for the case shown in Fig. 3. Squares: Experimental results from Eklund et al. (1991). Solid curve: Asymptotic theory from Bark et al (1992).

presence of the stratification. The estimate (17) was deduced under the assumption that the vertical diffusive transport of mass in the interior is approximately balanced by the advective transport of mass in the vertical buoyancy layers.

The evolution time scale T, say, for the interior concentration field can be deduced under the assumption that there is a stratification of the order of magnitude given by the estimate (17) and that the major mechanisms for vertical transport of mass are those mentioned above, i.e. diffusion in the interior and advection in the buoyancy layers. Equating the local rate of change of the interior concentration to the divergence of the difference between the two aforementioned fluxes, one finds that

$$T \sim Ra^{-2/9} \frac{h^2}{D}.$$

(18)

For the deviation of the concentration field outside the boundary layers from the equilibrium value, nondimensionalized with $\frac{Jh}{FD_1}$ and denoted by $-S$, one can derive the following evolution equation for S

$$\frac{\partial S}{\partial \tau} = [1 + \frac{5\sqrt{2}}{16} \left(\frac{\partial S}{\partial \zeta} \right)^{-9/4}] \frac{\partial^2 S}{\partial \zeta^2}$$

(19)

where the independent variables are defined as $\tau = t/T$ and $\zeta = Ra^{-1/9} z/h$. In this equation, vertical mass transport due to diffusion in the interior is quantified
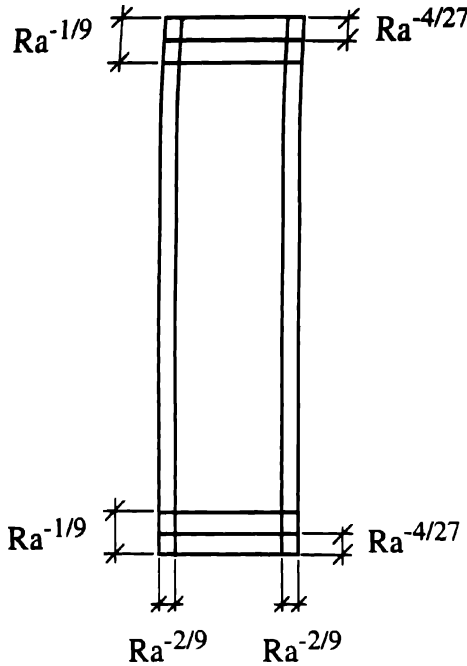
Fig. 5. Boundary layer structure of the concentration and velocity fields during electrolysis
in a small copper sulphate cell.

by the first term in the r.h.s. whereas the second term signifies advective transport
of mass in the vertical buoyancy layers.

It is well known that, for the kind of transient motion that is considered here,
the physical role of stratification is often analogous to that of rotation in rapidly
rotating flows, see e.g. Veronis (1969). The stiffening of isopycnic surfaces by
stratification in the former case is akin to the stiffening of vertical vortex lines
due to conservation of vorticity in the latter case. However, the parabolic equation
(19) for S is significantly different from the hyperbolic equation for nonlinear
spin up of a homogeneous fluid due to a suddenly increased rate of rotation of
the container, see e.g. Greenspan (1990). In physical terms, this difference reflects
the fact that, in the present case, diffusion (of mass) in the interior is significant
whereas (viscous) diffusion in the interior is negligible during spin up at small
Ekman numbers. Interior diffusion in the electrochemical case is of importance to
lowest order because the control of the motion in the interior by the buoyancy layers
is weaker than that of the Ekman layers in the case of spin up. This is so because
the motion is driven by a given flux of mass rather than a given concentration
at the vertical boundaries. If the latter kind of forcing was at hand, the physical
mechanisms for the evolution of the stratification in the electrochemical case and

evolution of the interior swirl velocity in the case of spin up would be in complete analogy and the equations, in the linear limit, would be the same.

It may be of some interest to briefly digress on what kind of spin up mechanism would be analogous to the present problem. In case of spin up due to an increased rotation rate of the container from Ω to $\Omega + \Delta\Omega$, the nondimensional order of magnitude of the forcing and of the swirl velocity is given by the Rossby number $\epsilon = \Delta\Omega/\Omega$. The order of magnitude of the inviscid interior meridional velocity field, which is driven by the Ekman suction, is $\epsilon E^{1/2}$. Viscous corrections of the interior motion are of order ϵE. Thus, transport in the Ekman layers is stronger (relative to diffusive transport in the interior) than the transport in the buoyancy layers in the electrochemical case. Orders of magnitude that correspond to those in the present problem would result for spin up in a (ficticious) container where the motion is driven by the shear stress rather than the velocity at the walls. For a shear stress of order ϵ, the order of magnitude of the Ekman suction velocity would be reduced to ϵE, which means that viscous effects would be of importance in the interior. The dimensional spin up time scale would change from the usual $E^{-1/2}\Omega^{-1}$ to $E^{-1}\Omega^{-1}$. It should be pointed out, however, that the analogy between rotation and stratification in such a case carries over only as far as orders of magnitudes of physical mechanisms are concerned.

The close analogy with the case of a rotating fluid makes the choice of length scale clear. The linearity of the buoyancy layers means that the length scale H, over which the forcing takes place, is irrelevant. Instead, the nature of the motion is determined by the thickness of the buoyancy layers compared with the distance $2h$ between the electrodes.

The boundary conditions for equation (19) can be derived by assuming that there is no net transport of mass from the interior and the vertical buoyancy layers into the horizontal boundary layers. One then finds that

$$\frac{\partial S}{\partial \zeta} = 2^{-2/3}, \zeta = \pm\mathcal{L}, \tag{20}$$

where $\mathcal{L} = Ra^{-1/9}H$ is taken to be of order unity for consistency of the perturbation scheme. Thus, attention is restricted to slender cells. We find immediately that the steady solution of equation (19) is a straight line with a slope that is given by the boundary conditions (20). In the steady state, the buoyancy layers are nondivergent and there is consequently no motion in the interior. The net diffusive flux of mass upwards in the interior is balanced by the net advective transport of mass downwards in the buoyancy layers. In this respect, it should be noted that, near the cathode, the fluid that is moving *upwards* carries a deficit in concentration, which means that there is a *downward* flux of mass as there is near the anode.

The formulation of an initial condition for equation (19) on the basis of perturbation theory is an extremely difficult task and has not yet been carried out. However, there is a very fortunate circumstance at hand here. The effective diffusivity in the equation, i.e. the coefficient of $S_{\zeta\zeta}$, is large for small values of S_ζ. Such values

are expected for small values of τ, i.e. before a significant stratification has been built up. But the solution of a parabolic partial differential equation with a large diffusivity will rapidly "forget" the details of its initial condition. Thus, one may start the integration of equation (19) for a small but arbitrary value of $\tau = \tau_0$, say, and prescribing practically any reasonable initial distribution of S with S_ζ being small and positive. The results obtained by using this *ad hoc* procedure compare very well with experiments, see Figs 3 and 4, as well as results from numerical computations of the complete set of partial differential equations, even for quite small values of $\tau > \tau_0$. The perturbation parameter in the present problem is, as is obvious from expressions (17–18), $Ra^{-1/9}$, which is about 0.25 in Figs 3 and 4. It should be noted that, even though the vertical variation of the interior concentration field has been shown to be weak ($\sim Ra^{-1/9}$), the motion of the electrolyte is still completely controlled by stratification. In fact, it can be shown that the motion outside the end regions will be essentially confined to buoyancy layers for much weaker stratifications than that in the present case.

The presence of an initially large diffusivity in equation (19) has a simple physical interpretation. As has already been pointed out, the term $\sim S_\zeta^{-9/4}$ quantifies vertical advective transport of mass in the buyoancy layers. When S_ζ is small for small values of τ, the motion in the buoyancy layers is strong as the blocking effect of the stratification then is weak. This means that the transport of mass in the vertical buoyancy layers is large compared to the diffusive transport in the interior. As the stratification builds up, the advective transport in the buoyancy layers decreases and the diffusive transport in the interior increases until there is a balance between these two modes of transport for large values of τ. It should be pointed out that, for $\tau \sim 1$, the buoyancy layers are divergent, i.e. there is a weak advective horizontal transport of mass due to inviscid motion in the interior, akin to the Ekman suction during spin up.

As soon as a dynamically significant stratification has been established, which, according to the previous discussion, is a rapid process,[*] the electric current outside the end regions is mainly carried by migration in the horizontal direction. The electric current lines are slightly deflected from the horizontal due to weak vertical diffusion. Thus, even though the resistivity of the electrolyte, which depends on the concentration, varies significantly in the vertical direction, the uniform distribution of the electric current density on the electrodes forces the electric current lines outside the end regions to be essentially horizontal. It deserves to be pointed out that, in the case under consideration, the mechanisms for transport of charge and mass are different. Transport of charge is essentially horizontal and due to migration. Transport of mass, on the other hand, takes place due to convection in the vertical and horizontal boundary layers and due to weak vertical diffusion in the interior.

---

[*] Rapid as measured on the diffusive time scale h^2/D.

The convective motion that is considered in this section is, in some sense, similar to that taking place at large Rayleigh numbers in a vertical slot with thermally conducting vertical walls, one of which is hotter than the other, see e.g. Gill (1966). In the steady state of that configuration, there are also boundary layers on the walls and a stratified interior. However, there are significant differences compared to the present case. The most important ones are that, in the thermal case, the steady stratification is strongly nonlinear and inertia is of primary importance for the motion in the vertical boundary layers. However, if the boundary condition for the temperature at the vertical walls of the slot are replaced by prescribing constant fluxes of heat, a problem investigated by Kimura & Bejan (1984), results are in complete analogy with those discussed in the present section. In the study by Kimura & Bejan (1984), though, only the steady state was investigated.

6. Electrolysis driven by nonlinear kinetics in small cells

At high current densities, the charge transfer potentials at the electrodes have to be accounted for and the analysis becomes considerably more complicated than in the linear case discussed in the previous section, both from a physical and from a mathematical point of view. However, it turns out that some analytic progress can be made for steady electrolysis with nonlinear kinetics. But before an asymptotic solution is given, some general properties of the physical process will be discussed.

For the same reasons as in the previous case, it is very reasonable to expect that a stratification will be set up in the cell. It also appears sensible to suppose that the general boundary layer structure of the concentration, electric potential and velocity fields will be the same as in the case of linear kinetics. There is no reason whatsoever, though, to expect that the stratification in the steady state will be linear. The presence of a stratification means that the resistivity of the electrolyte will be lowest near the bottom of the cell and increase vertically upwards. In the case of nonlinear electrolysis, the distribution of electric current density on the electrodes is determined by the electrolysis itself. Therefore, it seems natural to expect that the density of electric current lines would be highest where the resistivity of the electrolyte is lowest, i.e. near the bottom of the cell. But a locally large electric current density near the bottom would enhance the mass transfer there, which, in turn, would imply an additional local increase in concentration. The physical mechanism that limits the growth of concentration near the bottom is the fact that the *cathodic current at the anode* is proportional to the concentration, see formula (8). There is a similar limiting mechanism at the cathode, where the anodic current is proportional to the concentration.

It is in principle a straightforward but technically a somewhat tedious task to derive the analogue of equation (19) in the case of nonlinear kinetics. Details of the derivation and the approximations involved will be published elsewhere (Bark & Alavyoon, 1993). For steady electrolysis, an asymptotic solution of reasonably simple form can be derived for large values of the nondimensional difference in

electric potential between anode and cathode, i.e. $\mathcal{V} = F(V_a - V_c)/2RT$, where the factor 1/2 has been inserted for algebraic convenience. In practical cases, one has typically that $\mathcal{V} \sim 10$ or somewhat smaller. It turns out to be expedient to introduce the notations

$$\alpha = \frac{\Gamma}{\kappa(\Gamma + 2)}, \beta = 2^{-2/9} \left(\frac{\Gamma}{\Gamma + 2}\right)^{4/9} \mathcal{V}^{8/9} \tag{21}$$

and the stretched coordinate

$$\xi = \beta\zeta, |\xi| \leq \mathcal{L} = \beta\mathcal{H}. \tag{22}$$

For the special case of $\mathcal{L} = 9 \cdot 10^{1/9}/2$ one finds the following approximate expression for $\mathcal{S}$

$$= 1 - \frac{1}{9^9}(\mathcal{L} - \xi)^9 + \frac{2}{9^8\mathcal{V}}\{\frac{10^{10/9}}{25}[ln(\alpha\mathcal{V}) + \frac{1}{2}ln40 - \frac{9}{20}] -$$

$$\frac{4}{9}\int_{-\mathcal{L}}^{\xi} arcsinh(\alpha\mathcal{V}[\frac{\mathcal{L} - \xi'}{9}]^{9/2})d\xi'\}(\mathcal{L} - \xi)^8 + \ldots \tag{23}$$

This expression agrees very well with results from numerical integration of the full system of partial differential equations, which is, indeed, a very time consuming computation even on very fast computers. For details of the numerical computations, see Alavyoon & Bark (1993).

Formula (23) shows that, apart from a correction that is of order $\frac{1}{\mathcal{V}}ln\alpha\mathcal{V}$, the interior concentration field is zero at the top of the cell and that its variation is given by a ninth order polynomial with zero slope at the top. Thus, the stratification is much stronger than in the case of linear electrode kinetics, which quantifies the arguments given in the beginning of this section.

Figure 6 shows measurements by Kim et al. (1992) of the steady distribution of the interior concentration field of an aqueous solution of $CuSO_4$ during electrolysis with solid copper electrodes at high current densities. It can be seen from this graph that almost all of the copper sulphate is collected near the bottom of the cell. However, the shape of the distribution is only in qualitative agreement with formula (23). The reason for the discrepancy is that the correction term in formula (23) is not small due to the fact that the exchange current density i_0 is very small for the system considered, which gives a very large value of the constant α. A more suitable system for experimental validation of formula (23) is $|Ag(s)|AgNO_3(aq)|Ag(s)|$. Such experiments will be carried out in the near future.

7. Charging lead acid batteries

During charging of a lead acid cell, e.g. a car battery, the concentration of sulphuric acid in the electrolyte, which is an aqueous solution of sulphuric acid, is increased

S *(moles/litre)*
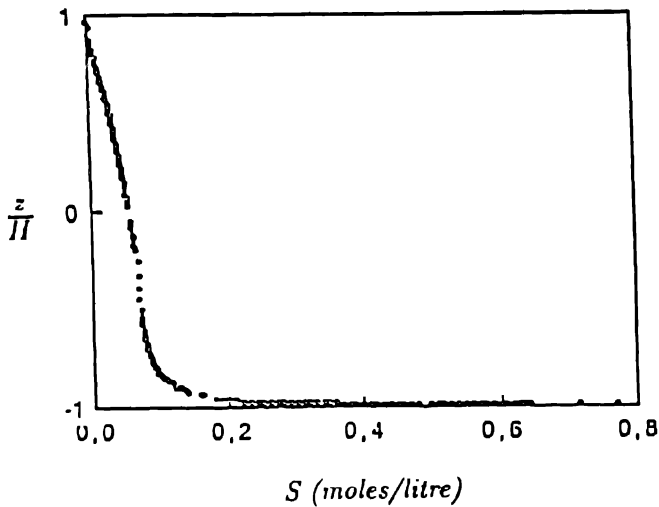
Fig. 6. Measurements of the vertical variation of the concentration field in the midsection of a small copper cell under conditions of nonlinear electrode kinetics. The size of the cell and the values of c_0, Sc and Γ are the same as that in Fig. 3. $Ra = 2.90 \cdot 10^9$, $\kappa = 1.04 \cdot 10^{-3}$, $\tau = 4.0$. From Kim et al. (1992).

by the electrode reactions. The chemical energy of the system is then increased. The additional energy is converted to electric energy by connecting the electrodes of the charged battery via an external circuit.

In contrast to the electrodes considered in the previous sections, the electrodes in a lead acid battery are not solid metal but porous, see Fig. 7. The reason for using porous electrodes is that one can thereby increase the effective area of the electrodes, and hence the energy stored in the battery, by several orders of magnitude. Lead acid battery electrodes are made from small grains of lead or lead dioxide. A typical grain size is 10 μm, which means that the pores in the electrodes are very narrow. The permeability of the electrodes is thus very low. As the pressure differences in the free electrolyte, which are associated with the mass transfer driven convective motion during charge or discharge, are rather small, the electrolyte in the electrodes is practically stagnant. This means that, within the electrodes, transport of mass takes place due to diffusion and migration only. In the free electrolyte, on the other hand, there is, of course, also advective transport.

As the pH of the electrolyte is neither small nor large, one may assume that the sulphuric acid dissociates into the two ionic species H^+ and HSO_4^- only. This approximation is quite accurate and the electrolyte can therefore be regarded as binary. Thus, as discussed at the end of Section 2, migration is proportional to diffusion and the electric potential ϕ can be eliminated from the field equations.

Anode (+)   +H   Cathode (-)

Free
electrolyte

-h   +h

z

-L-h   +L+h

x

-H
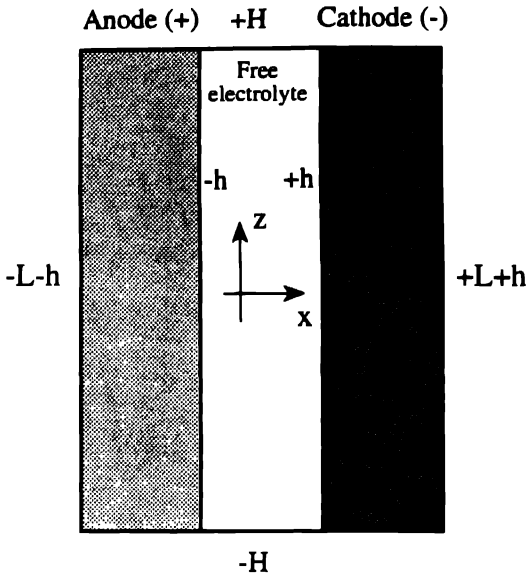
Fig. 7.   Sketch of a lead acid cell.

The only material constant that is needed in order to model transport within the electrodes is thus the effective salt diffusivity, which is a measurable quantity.

Because the grains that make up the electrodes in a lead acid battery are very small, one can use continuum theory to describe the transport in the electrodes. The transfer of charge from the electrodes to the electrolyte can thus, from a macroscopic point of view, be considered as due to volume sources in contrast to the surface sources considered in the previous sections. For reasons that space does not allow us to touch upon here, it turns out that, in the case of charging, one may assume that the strength of the volume source of charge is constant. The mathematics will then be similar to the case of linear kinetics that was discussed in Section 5. For the case of discharge, however, one is forced to use more elaborate models that account for effects of the charge transfer potential. No theoretical work on free convection in lead acid batteries during discharge has so far appeared in the literature.

The formulae for the electrode reactions during charge are

$$PbSO_4 + 2H_2O \rightarrow PbO_2 + HSO_4^- + 3H^+ + 2e^- (anode), \qquad (24)$$

$$PbSO_4 + H^+ + 2e^- \rightarrow Pb + HSO_4^- (cathode), \qquad (25)$$
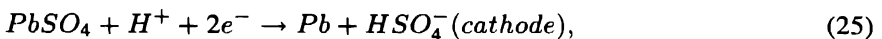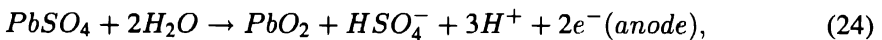
which gives the following overall reaction in the cell

$$2PbSO_4 + 2H_2O \rightarrow PbO_2 + 2H_2SO_4 + Pb.$$
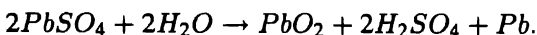
In comparison with electrolysis of a metal salt, a simple example of which was dealt with in Sections 5 and 6, these formulae show that the reactions in a lead acid battery are different in two important respects. Firstly, there is production of sulphuric acid in both electrodes, which means that there is a net increase of mass during the reaction. Secondly, there is a lack of symmetry in the reactions as the rate of production of sulphuric acid in anode and cathode are different. Nevertheless, it turns out that the nature of the ensuing free convection is similar to the case that was discussed in Section 5. Before the discussion of some theoretical and experimental results, we give a brief qualitative discussion terms of the mass transfer and free convection.

After the current has been switched on, a spatially homogeneous production of sulphuric acid is set up in the porous electrodes. The strength of the production in anode and cathode are, however, different as can be seen from formulas (24) and (25). The sulphuric acid starts to diffuse from the electrodes into the free electrolyte. This process will, as in the cases considered in the previous sections, make the electrolyte heavier near the surfaces of the electrodes than in the bulk and a convective motion ensue. In the present case, however, there will be a downward motion of heavy electrolyte near both anode and cathode. However, a stratification will still result and buoyancy layers will be formed on the surfaces of the electrodes.

As the motion in both buoyancy layers is directed downwards, there will, due to continuity of volume, be a weak inviscid motion in the opposite direction between the buoyancy layers. In contrast to the case of electrolysis of a metallic salt, though, a steady state does not exist as there is a net production in both electrodes. However, for large times, the system approaches an asymptotic state, which is reminiscent of the steady case that was discussed in Section 5. One finds that, outside the vertical and horizontal boundary layers, the (dimensional) concentration field is given by an approximate expression of the following simple form

$$c = c_0 + \mathcal{A}t - \mathcal{B}z,$$

where the positive constants $\mathcal{A}$ and $\mathcal{B}$ are somewhat complicated expressions that involve the physical parameters of the electrolysis, see Alavyoon et al. (1991).

Measurements of the evolution of the velocity and concentration fields in a small lead acid cell were made by Alavyoon et al. (1991). These experiments[*] were carried out with sulphuric acid of concentration $c_0 = 2$ *moles/litre* at a current density of 94.3 A/m^2. The values of H and h were the same as in the experiments with copper cells that were described in the previous sections. The length of the cell was 20 *mm*. Experimental results for the velocity field are compared with theoretical results in Fig. 8. It can be seen from this graph that the motion in the buoyancy layer on the anode, which is located to the left, is significantly stronger than the motion in the layer on the cathode. This is a consequence of the fact that the

---

[*] The nondimensionalization of the lead acid cell case is a bit tedious. Therefore, only the most important data are given in this paper. For details, the reader is referred to the original paper.
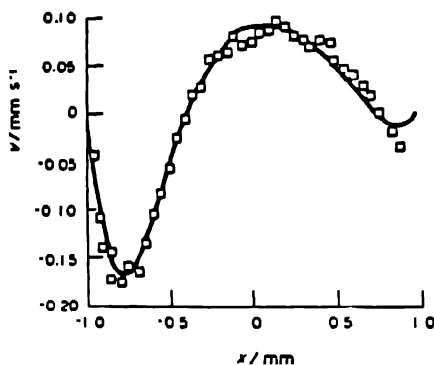
Fig. 8.   The vertical velocity component in a horizontal section at midheight in a small lead acid cell after 30 minutes under conditions of linar kinetics (charging) at $Ra = 5\ 64 \cdot 10^4$ The square symbols are experimental results and the solid curve is the prediction from numerical solution of the complete hydrodynamical problem. From Alavyoon et al. (1991).

production of sulphuric acid is more intense in the anode than in the cathode. In this case, the Rayleigh number is not sufficiently large for the boundary layers and the interior region of inviscid flow to be asymptotically distinct. The theoretical results that are shown in Fig. 8 were obtained by numerical integration of the full system of partial differential equations under the assumption that the kinetics is linear. In view of the unusually large number of physical assumptions and parameters that enter the problem, the agreement between theory and experiment must be regarded as satisfactory. In Fig. 9, comparisons between computed and measured concentration fields are shown. The agreement is satisfactory though not for large times. The discrepancy for large times can be attributed to the gradual expansion of the pores in the electrodes, which causes a change of the effective value of the coefficient of diffusion. This effect is not accounted for in the mathematical model but will be included as proposed by Simonsson (1973) in future studies.

It turns out to be possible to develop an asymptotic theory, of the kind that was outlined in Section 5 for electrolysis in a small copper sulphate cell, also for a lead acid battery. However, the algebraic expressions that enter the equation that corresponds to equation (19) are quite complicated and the equation is therefore not given here. The predictions are something like 10–15% less accurate than those for the copper sulphate cell, which, however, may well be sufficient for engineering applications, where costly numerical computations are not always feasible.

8. Outlook

The phenomena that have been discussed in the previous sections do all take place in binary electrolytes in closed elecrochemical cells of small dimensions. There are a number of technically very relevant and scientifically interesting extensions of

$t = 15$ min $t = 30$ min $t = 60$ min

y/mm

16
12
8
4
0
-4
-8
-12
-16

2 0   2.2   2 4   2 6   2 8

c / M
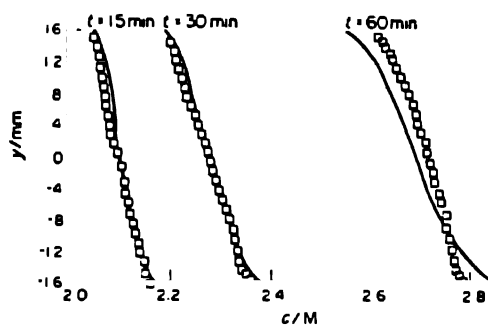
Fig. 9. The vertical variation, at different times, of the concentration field in the midsection of a small lead acid cell The cell data are the same as for the case shown in Fig. 8. The square symbols are experimental results and the solid curve is the prediction from numerical solution of the complete hydrodynamical problem. From Alavyoon et al. (1991).

these studies that have so far not been touched upon. It may here be worth pointing out that the main purpose of the studies made so far and those that are planned is not only to examine the fluid motion as such in electrochemical cells but rather to understand and to be able to predict the overall performance of the cell from an electrochemical point of view. As should be obvious from the examples given, this involves nonlinear interaction between electrochemical and fluid mechanical phenomena.

The most obvious continuation of the work carried out hitherto is free convection in a small lead acid cell with nonlinear kinetics, e.g. a car battery during discharge. The numerical solution of the full mathematical problem in this case turns out to be extremely time consuming. This calls for new perturbation schemes and physical modeling. Results from such studies would provide battery manufacturers with a working design tool, which has so far been lacking.

Another natural extension of the studies discussed in this paper is to nonbinary electrolytes, i.e. electrolytes that contain more than two ions. Effects of additional ions are of importance in industrial refining of copper, where one adds sulphuric acid to the electrolyte, which is an aqueous solution of copper sulphate, in order to increase its conductivity and thereby reduce ohmic losses. Some results for nonbinary electrolytes are at hand (Bark, 1989, Alavyoon, 1992a, and Eklund et al. 1992).

A problem of canonical nature is free convection in a large electrochemical cell with nonlinear electrode kinetics, where effects of stratification are unimportant. Somewhat surprisingly, it turns out that this problem is more difficult than the case with stratification, both from an analytic and from a numerical point of view.

Thermal effects due to ohmic heating are of primary importance in many electrochemical systems, e.g. in lead acid batteries that are made up of very large stacks

of electrodes. A simplified model of such phenomena has led to unexpected and very interesting results (Alavyoon, 1992b).

In many electrochemical systems, gas bubbles are formed at the electrodes. In some applications, e.g. production of gaseous chlorine, this is a desirable effect. In others, however, the presence of gas bubbles is often disadvantageous. An example of the latter case is industrial refining of copper. The large variety of effects of gas bubbles on the operation of electrochemical systems has so far been investigated only by very crude empirical models.

There are several other important phenomena in electrochemical cells that have so far not been mentioned, the most prominent one being turbulence, which occurs in a very large number of applications. Only a small number of studies, all of which using empirical correlations, of effects of turbulence on the operation of electro-chemical systems can be found in the literature. Another intriguing phenomenon of great practical importance is the morphological instability of the interface between electrodes and electrolyte that occurs for large values of the electric current density. This instability, about which very little is known, may lead to formation of den-drites on the surfaces of the electrodes. Both turbulence and formation of dendrites are first order effects in e.g. commercial electrolytic refining of raw copper.

References

Alavyoon, F., Eklund, A., Bark, F.H., Karlsson, R.I. and Simonsson, D., *Electrochimica Acta* 36 (1991) 2153.

Alavyoon, F., *Electrochimica Acta* 37 (1992a) 333.

Alavyoon, F., *Proc. 2nd JSME - KSME Therm. Eng. Conf.* 3 (1992b) 165.

Alavyoon, F. and Bark, F.H., *Proc. of the 183rd Meeting of the Electrochem. Soc.* (in press)

Bark, F.H., *Electrochimica Acta* 34 (1991) 307.

Bark, F.H., Alavyoon, F. and Dahlkild, A.A., *J. Fluid Mech.* 235 (1992) 665.

Bark, F.H. and Alavyoon, F., 1993. Submitted to *J. Fluid Mech.*

Eklund, A., Alavyoon, F., Simonsson, D., Karlsson, R.I. and Bark, F.H., *Electrochimica Acta* 36 (1991) 1345.

Eklund, A., Alavyoon, F. and Karlsson, R.I., *Electrochimica Acta* 37 (1992) 695.

Gill, A.E., *J. Fluid Mech.* 26 (1966) 515.

Greenspan, H.P., *The Theory of Rotating Fluids*. Breukelen Press (1990).

Karlsson, R.I., Alavyoon, F. and Eklund, A., *Laser Anemometry, Advances and Applications* p. 329. BHRA/Springer Verlag (1990).

Kim, J.W., Lim, M.-S. and Bark, F.H. (1992) *Proc. 2nd JSME-KSME Thermal Eng. Conf.* (1992) p. 205.

Kimura, S. and Bejan, A., *Trans. ASME J. Heat Transfer* 106 (1984) 99.

Levich, V.G., *Physicochemical Hydrodynamics* Prentice-Hall Inc. (1962).

Newman, J.S., *Electrochemical Systems* 2nd edn. Prentice-Hall Inc. (1991).

Nernst, W., *Zeitschr. Phys. Chem.* 2 (1888) 613.

Prandtl, L., *Essentials of Fluid Dynamics* Blackie & Son (1952).

Probstein, R.F., *Physicochemical Hydrodynamics*. Butterworths (1989).

Simonsson, D., *J. Appl. Electrochem.* 3 (1973) 261.

Ward III, W.J. and LeBlanc, O.H., *Science* 225 (1973) 1471.

Veronis, G., *Ann. Rev. Fluid Mech.* 2 (1969) 37.

Pressure Drop for Flow in Channels Subjected to Strong System Rotation

LEONARD BORGSTRÖM, CLAES-GÖRAN CARLSSON, CLAES INGE, TORGNY LAGERSTEDT and HANS MOBERG
Alfa-Laval Separation AB, S-14780 Tumba, Sweden

Abstract. A disc stack centrifuge is an industrial example of a fluid machine in which all the internal flow takes place in a rapidly rotating frame. The present report gives a survey of the experimental and theoretical work performed at Alfa-Laval in order to estimate the pressure drops in the different internal passages in the centrifuge, including both laminar and turbulent flow.

For the laminar flow between the discs, a theory has been developed using the concept of a rotating Hele Shaw cell and conformal mapping. The theory is valid in the limit of very small Rossby numbers. For moderately large Rossby numbers, this model overestimates the pressure drop. The linear theory was extended by introducing advecting vortices in a computer model. The vortices cause vertical fluid transport between the Ekman and geostrophic layers by Ekman pumping, an effect which decreases the pressure drop in the disc stack. The linear model and the enhanced model have both been confirmed by experiments.

The flow is turbulent in most parts of the centrifuge, except in the disc stack. The theoretical or numerical modelling for rotating turbulent flows is very difficult and no reliable models exist so far. We therefore have to rely on measurements, which show that the pressure is significantly influenced by rotation for Rossby numbers below unity.

1. Introduction

Industrial fluid dynamics is mainly concerned about integral parameters such as pressure drop or efficiency numbers, and detailed information on the flow field is often given a lower priority. For simple flow systems estimates of the pressure drops are readily assessed from tables or from actual measurements. Although, it may be noted that data on pressure drops given in tables usually have an empirical background.

The situation for a rotating flow system is more complicated as there is a lack of reliable data, and measurements on pressure drops in rotating systems are few. Also, numerical simulations of rotating flows are scarce, especially for turbulent flow. Studies of rotating flows have mostly been dealing with our most common rotating system which is the earth. The mathematics used in the study of geophysical flows may be used when studying the flow in rotating machines. But, the number of experimental data that can be used in the design of rotating machines are limited. However, to be able to design rotating flow machines, estimates of the pressure

drop in different internal channels have to be produced. Examples of industrial rotating systems are centrifugal pumps and centrifugal separators.

Alfa-Laval has been producing centrifugal separators (centrifuges) for about 100 years. The centrifuge is considered to have attained a state of maturity and operates fairly well in its main applications. However, knowledge of the flow inside the centrifuge has been limited which has hindered further development of the machine. To remedy this, Alfa-Laval has set up a long term research program in order to study the flow inside the centrifuge. The present report gives a survey of the experimental and theoretical work performed at Alfa-Laval in order to estimate the pressure drop in the internal flow passages in a centrifuge.

2. Description of a centrifuge

High speed centrifugal separation is used to enhance the separation efficiency when separating phases of different densities. "The centrifuge" was invented in 1878 for the separation of cream from milk. Today the centrifuge has many applications, a major one of which is the cleaning of lube oil and fuel oil on ships. Other applications are found in, for instance, breweries, wineries and chemical industries.

The rotating system comprises the fast rotating bowl shown in Fig. 1 in which the separation takes place. The speed of rotation is about $100rev/s$. The incoming liquid (feed) enters the centrifuge via the inlet (a) where it is spun up to the speed of the centrifuge. The feed is thereafter led radially outward in the distributor (b) and is distributed via the distribution holes (c) to the disc stack (d). The disc stack consists of closely spaced conical discs made of stainless steel. In order to have an efficient centrifuge a large surface area is needed and about two hundred discs are used in the disc stack. The spacing between the discs is about 0.5 mm and the diameter of a disc is typically 300 mm.

The actual process of separation takes place between the discs and the purpose of the centrifuge is to utilize the high G forces combined with the short separation distance between the discs to obtain an efficient separation of particles or liquid drops from a fluid. The drops may be heavy such as water drops in oil and migrate outward towards the disc surface. In other applications the drops may be light such as fat globules in milk and migrate inward towards the disc surface.

Figure 1 shows a centrifuge intended for the separation of heavy particles from a light liquid phase. The heavy particles after being separated accumulates in the sludge space in the periphery and the clarified fluid is led to a paring disc device (e) where it exits the centrifuge. The efficiency of the machine is high and a medium sized machine may replace a sedimentation basin having a surface area of $10000m^2$. For a general reference on centrifugal separation consult Sokolov (1971), Alfa-Laval (1983).
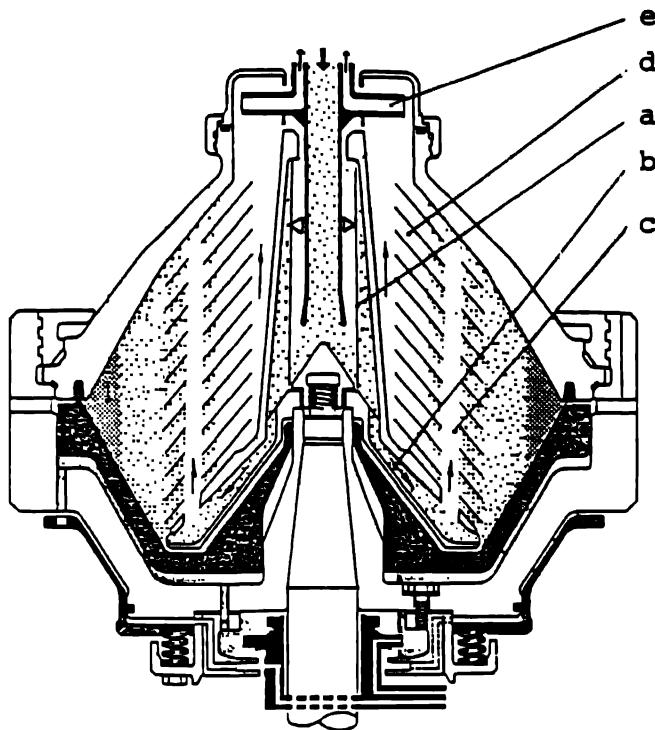
Fig. 1. Cross-section of a centrifuge. (a) inlet, (b) distributor, (c) distribution holes, (d) disc stack, (e) outlet.

3. General features of rotating flows

Characteristic for rotating flows are the strong Coriolis forces. If the advective terms are small, geostrophic regions are formed outside the boundary layers near the walls. The main force balance in these regions is between the Coriolis force and the reduced pressure gradient. The flow direction is parallel to the isobars. This is the cause of the wind circulation around zones of high or low pressure, as seen on weather maps.

The following non-dimensional parameters are commonly used to characterize flows in rotating systems:

Ekman number,

$$E = \frac{\nu}{\Omega L^2} \tag{1}$$

Rossby number,

$$Ro = \frac{U}{\Omega L} \tag{2}$$

where Ω is the angular velocity of the rotating system, L is a typical length, U a typical velocity and ν is the kinematic viscosity of the fluid. The typical features of rotating flows occur when E and Ro are small.

Close to solid walls, Ekman boundary layers arise. The viscous force is added to the pressure balance and this gives rise to a velocity component in the direction of the negative pressure gradient. Ekman layers have a thickness proportional to $E^{1/2}$. The boundary layers near vertical walls (i. e. with normals perpendicular to the axis of rotation) have a different structure. These vertical layers are denoted Stewartson layers. Their mathematical description is quite intricate and it can be shown that they consist of two overlapped layers of the thicknesses $E^{1/3}$ and $E^{1/4}$. The former of these transports fluid between Ekman layers and the interior, and the latter smooths out discontinuities in the tangential velocity.

A comprehensive discussion of rotating flows can be found in Greenspan (1968).

The concepts of geostrophic regions and Ekman and Stewartson layers have their origin in the areas of meteorology and oceanography. In the centrifuge, these types of flows are encountered in the disc stack, where Ro is particularly small and the flow is laminar.

4. Inlet

By inlet we here mean the open chamber (a) shown in figure 1, corotating with the centrifuge, in which non-rotating liquid is received, set into rotation and passed on to the distributor channels. Usually some kind of wings bring the liquid into rotation, although a set of concentric discs is sometimes used and even empty inlets exist.

In most inlets, the liquid forms a cylindrical interface parallel and concentric with the axis of rotation. The pressure set up by the difference between this level and the outlet level forces the liquid through the centrifuge. The inlet level adjusts itself so that the solid body rotation pressure between the inlet level and the fixed outlet level exactly equals the pressure drop in the liquid filled part of the centrifuge.

An important parameter which has influenced our definition of pressure drop in rotating systems, such as the centrifuge, is the increase in internal energy as the liquid flows through the centrifuge. The reason for our interest in internal energy is that it is caused by the work of viscous forces which may disrupt dispersed drops or particles rendering them impossible to separate. If the static pressure at the outlet and inlet is the same it can be shown that work on the liquid is divided equally between internal and kinetic energy of the liquid leaving the rotating system. The increase in internal energy is thus given solely by the outlet level and will eventually manifest itself as an increased temperature.

By defining the pressure drop between any two points in the centrifuge as the deviation from the corresponding solid body rotation pressure between the same points, the increase in internal energy will everywhere be given by the work of the pressure drop. The pressure drop from the centre and out to the inlet liquid

level equals the solid body rotation pressure at that level. The further out the inlet level is, the larger the work on the liquid becomes. As the non-rotating liquid hits the liquid level this work is transformed into intense local turbulence which may damage the feed.

Since the total increase in internal energy as the liquid passes the whole centrifuge is given by the outlet level, the total pressure drop is independent of the flow rate. At an increased flow rate, the liquid level is pushed inwards to meet the increased pressure drop in the liquid filled sections of the machine. This decreases the turbulence created by the incoming liquid and may be interpreted as a reduction of the pressure drop in the unfilled section of the inlet.

The purpose of the disc inlet is to minimise drop splitting. This is done by decreasing the pressure drop in the unfilled section to zero by bringing the inlet level all the way in to the centre by increasing the pressure drop in the liquid filled part of the separator. The dissipation is spread out into a larger volume, the turbulence is less intense and the feed becomes less damaged. A set of concentric discs, see Fig. 2, is used to bring the liquid into rotation. If the flow rate is low only a few discs will be active. When the flow rate increases and the pressure drop in the rest of the centrifuge increases, the pressure drop in the inlet will automatically decrease by the use of more discs, see Fig. 2. When the presently active discs are not enough, there will be an overflow to previously not active discs.

The flow rate between two discs is usually small and the flow close to linear. A weakly non-linear theory for the flow between two rotating discs, (Peube & Kreith, 1966), is used to calculate the pressure drop in a disc inlet.

The flow in wing inlets is highly non-linear and turbulent, and the pressure drop has to be estimated empirically. Experiments with different wings and vanes and even empty inlets have shown a universal dependence of the pressure drop in the liquid filled part of the inlet on the ratio of the flow rate and the angular velocity. This suggests a Rossby number dependence. The pressure drop in the liquid filled part of the inlet normalised with the solid body rotation pressure was found to be proportional to the Rossby number raised to 1/3. The constant of proportionality depends on the type of wings.

5. Distributor channels

The distributor channels lead the fluid from the inlet to the distribution holes in the stack. The channels are either straight channels of constant cross section or pie shaped sections divided by radial wings. The flow rate in the distributor channels is high and the flow therefore non-linear and turbulent.

The Coriolis force in a rotating channel is directed towards one side wall, the so called pressure side, of the channel and deflects the velocity profile against this wall, see Khesgi (1985). The flow close to the pressure side has been shown to be stabilized by the rotation, while the flow on the other side is destabilized, Johnston et al. (1972).
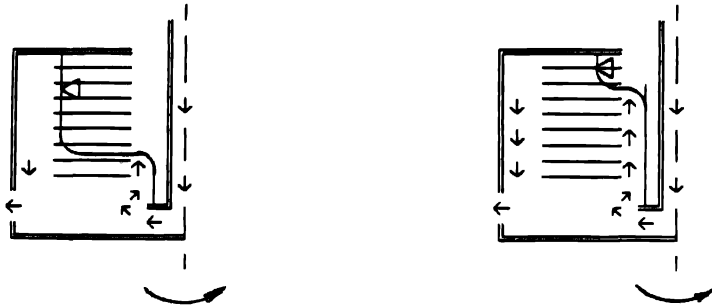
Fig. 2   Disc inlet at low and high flow rate. Flow direction and interface between liquid and air are shown.

The distribution hole is much smaller than the distance between the wings and centred between two wings in the pie shaped channels. Visual observations in model rigs have shown a strong flow on the pressure side of the wings. The flow follows the wing until it ends and if the wings extend beyond the hole, the flow has a considerable angular momentum relative to the hole as it leaves the wing. Since the flow is non-linear the transport to the hole has to take place in the inviscid interior, which results in a potential vortex with a considerable pressure drop. Measurements show that the pressure drop as function of the extension of the wing has a minimum when the wing extends just to the hole. Then the flow follows the wing radially outwards until it ends and then proceeds azimuthally to the hole without the formation of a vortex.

The pressure drop in a pie shaped channel with the wings extending out to the holes is rather small, although it is usually even smaller in a straight channel. It has been shown experimentally for both channels of circular and rectangular cross section as well as for pie shaped channels, that the pressure drop is essentially unaffected by rotation if the Rossby number is high and proportional to the inverse Rossby number when it is low.

Figure 3 shows measurements with three different square channels. The length scale of the Rossby number is the width of the channel. This can make the pressure drop in a rotating system rather insensitive to the width of the channel since a narrow channel has a high pressure drop when not in rotation and is not very much affected by rotation, while a wide channel has a low pressure drop which is considerably increased by rotation. This agrees with the hypothesis of a concentration of the flow to the pressure side of the channel.

6. Distribution holes

The holes in the disc stack form vertical channels from which fluid is withdrawn into the disc stack. The upward flow in this channel is complicated and affected by several mechanisms. It is also very hard to measure and study experimentally.
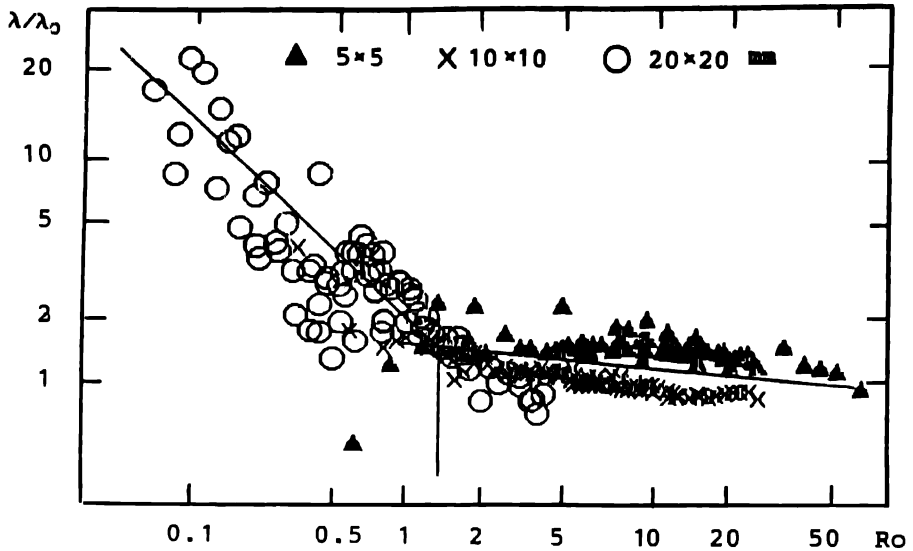
Fig. 3   Ratio of friction coefficients (rotating/non-rotating) as function of the Rossby number for a quadratic channel

The flow is turbulent, vortical and sometimes non-stationary. Another phenomenon that probably affects the flow is vortex breakdown, i.e. a sudden expansion of a swirling axial flow.

The parameters are often such that vortex breakdown should have occurred in a corresponding channel without withdrawal of fluid and the radial flow, caused by the withdrawal, most certainly increases the probability of vortex breakdown. The unpredictability is unfortunate since a pressure variation along the channel may give an uneven distribution of flow between the discs, resulting in poor separation.

If the channel did not rotate one would expect two competing effects to determine the pressure. The pressure would increase along the channel since the axial velocity decreases due to the withdrawal of fluid into the disc stack. On the other hand it would decrease due to the effect of boundary layer suction. If the latter is similar to the boundary layer suction along a flat plate, both effects will be of the same order of magnitude.

When rotation is considered the situation becomes more complicated. First the rotation of the liquid in the column will affect the pressure in the periphery. Since the flow is directed outward from the centre of the channel, the rotation will decrease with the height in the channel. This makes the pressure at the periphery of the holes decrease along the channel.
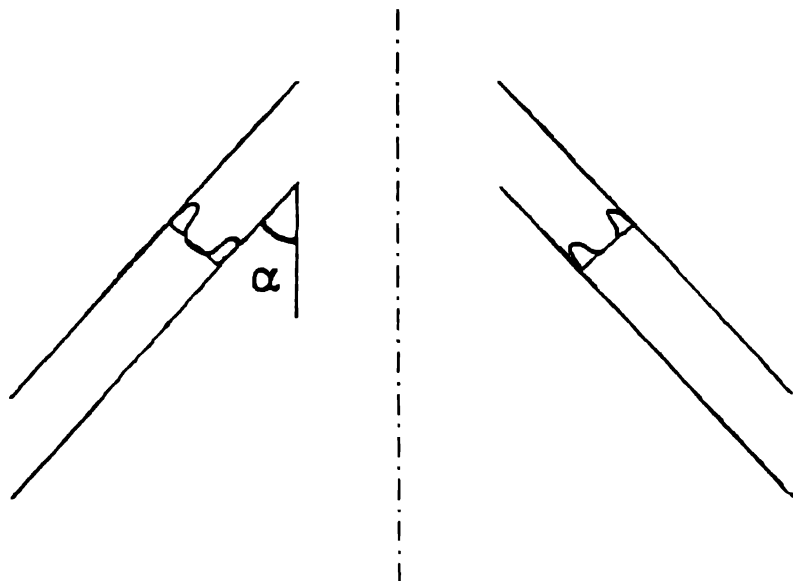
Fig 4   Schematic of two discs in the disc stack

7. Disc stack

7.1. AXISYMMETRIC FLOW

Centrifuge discs have a conical form, with the half cone angle α defined according to Fig. 4. The axis of rotation is vertical. For model purposes, when one-phase flow is studied, plane geometries with $\alpha = 90$ are often used.

Consider the flow between two plane, rotating discs with a small gap in between. The geometry has axial symmetry and the flow is driven by a radial pressure gradient. For low Ekman numbers, Ekman layers are formed close to the upper and the lower discs. Between the Ekman layers, a geostrophic layer is located.

Calculated velocity profiles for this situation is shown in Fig. 5. The u velocity is in the direction of the pressure gradient, and v is perpendicular to u and to the normal of the discs. When axial symmetry prevails, u is the radial flow and v is the tangential flow. The thickness of the Ekman layers are proportional to $E^{1/2}$. In this case, $E = 1/100$.

A striking feature of this flow is that the flow direction is a function of the distance from the lower disc. The only net transport of fluid takes place in the Ekman layers, and the geostrophic flow goes in circles around the centre.

For small Ro, the advective terms can be neglected in the Navier-Stokes equations. Analytical solutions for the flow and pressure fields can be found for simple
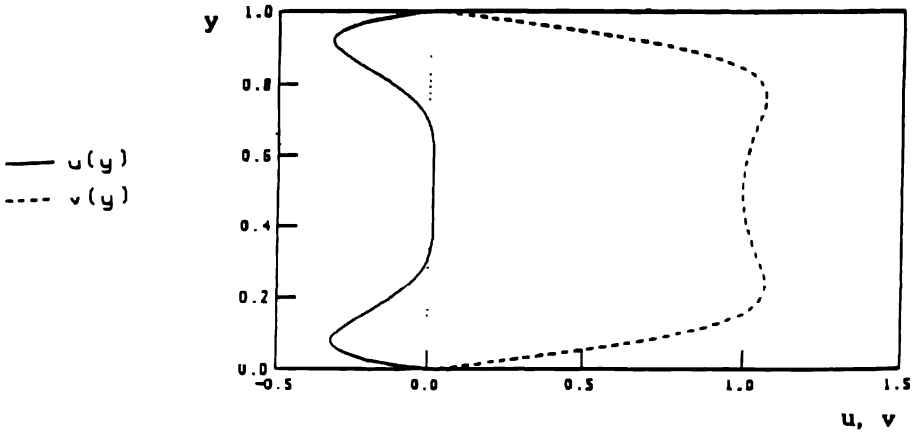
Fig 5   Tangential and radial velocity profiles for the flow between discs in the disc stack. y is the coordinate normal to the disc surface

geometries. The pressure drop between two radii, r_A and r_B, for plane axisymmetrical discs is given by

$$\Delta p = p'r_B) - p(r_A) = \phi(\lambda)\frac{Q\rho\ln(r_B/r_A)\Omega^{3/2}}{\nu^{1/2}\pi} \tag{3}$$

where Q is the volume flow rate, ρ the density and

$$\phi(\lambda) = \frac{\cosh\lambda + \cos\lambda}{\sinh\lambda - \sin\lambda} \tag{4}$$

with $\lambda = 1/E^{1/2}$. For small E. $\phi(\lambda) \approx 1$.

This expression for the pressure drop has been confirmed to be valid at low flow rates by measurements in a model test rig shown in Fig. 6. The test rig is further described in Lagerstedt and Nåbo (1986). At high flow rates, the measured pressure drop is below that given in the equation above. A theoretical study Gusev & Bark (1980) shows that the stability depends on the Ekman number and a Reynolds number defined as

$$Re = \frac{Q}{2\pi R\nu} \tag{5}$$

For E below $2 \cdot 10^{-3}$, the theoretical stability limit is 55 for plane discs. The value is somewhat lower for larger E or conical discs, with a minimum of about 30, Moberg (1989). Experiments by Pater et al. (1974) show that instabilities occur at Re above 110, and turbulence above $Re \approx 240$. Measurements in the test rig show that at higher Re, the pressure drop goes asymptotically to about 70 % of the theoretical value for inward flow.
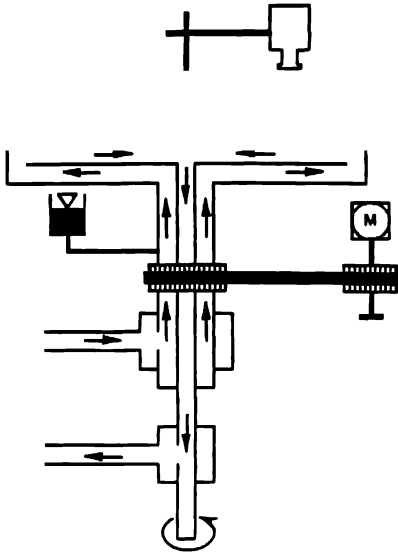
Fig 6   Test rig used in visualization and pressure drop measurements in the flow between discs in a disc stack
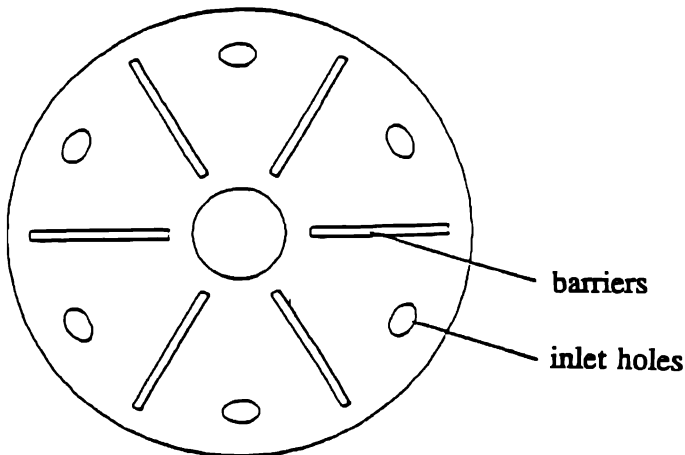
Fig 7   Typical disc geometry with barriers

7 2   FLOW WITH BARRIERS AND CHANGE IN DEPTH

The analysis of the axisymmetrical flow can be extended to several classes of non-axisymmetrical flows by classical methods utilizing complex functions and conformal mapping A typical example of a disc geometry is shown in Fig 7

The flow enters the gap between the discs through the inlet holes The flow is transported radially inwards between the discs This transport mainly takes place in
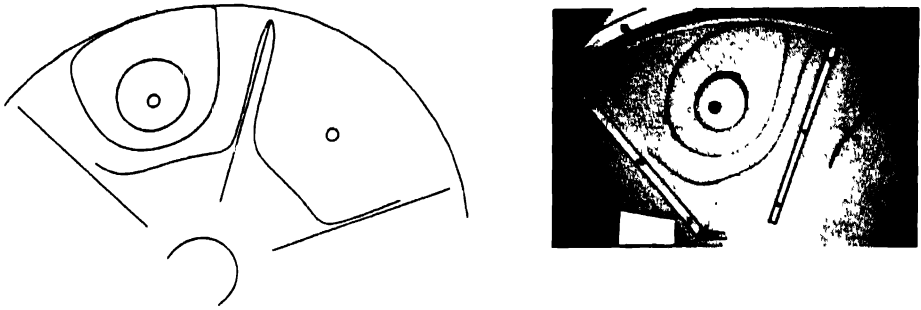
Fig. 8   Calculated and visualized streamlines for the flow between discs with barriers.

the Ekman layers. The presence of the long barriers shown in the figure also causes some net transport of fluid in the geostrophic layer.

The flow between the discs can be described by an analytical mathematical source-sink model. The small Rossby number and the small gap between the discs allows for the use of a linear two-dimensional model. A complex valued velocity potential can be used in the same way as for non-rotating Hele Shaw cells. The boundary conditions are, however, more complicated due to the system rotation and the interaction between the flow in the main region and the Stewartson layers, see Bark & Sundström (1981).

For very low Rossby numbers, the measured pressure drop with barriers is well in accordance with the theory. The calculated and visualised streamlines do also compare well, see Fig. 8. However, even moderately small Rossby numbers give rise to discrepancies between the theory and the experimental values. These discrepancies have their origins in the boundary layer separation at the barrier ends. Vortices and wakes are formed, which contribute to the transport of fluid between the Ekman layers and the geostrophic layer. When the wakes dominate the flow field, the pressure drop is considerably reduced.

An extension of the mathematical model takes these wake effects into account. The wakes are represented by discrete vortices, born near the barrier ends and advected with the flow. The vertical fluid transport in the vortices cause them to spin down. The spin down time scale is $E^{-1/2}/\Omega$, see Greenspan (1968). Figure 9 shows a comparison between the experimentally measured pressure drop, the linear theory and the enhanced theory.

The model rig (Fig. 6) has also been used to study the effects of a varying disc distance. The phenomenon has been studied mathematically as well, with a vortex sheet representing the edge of a shallow sector. The distance between the discs was reduced by 5% in this sector and this affects the flow field significantly. Comparisons between experimental and computed streamlines are seen in Fig. 10.
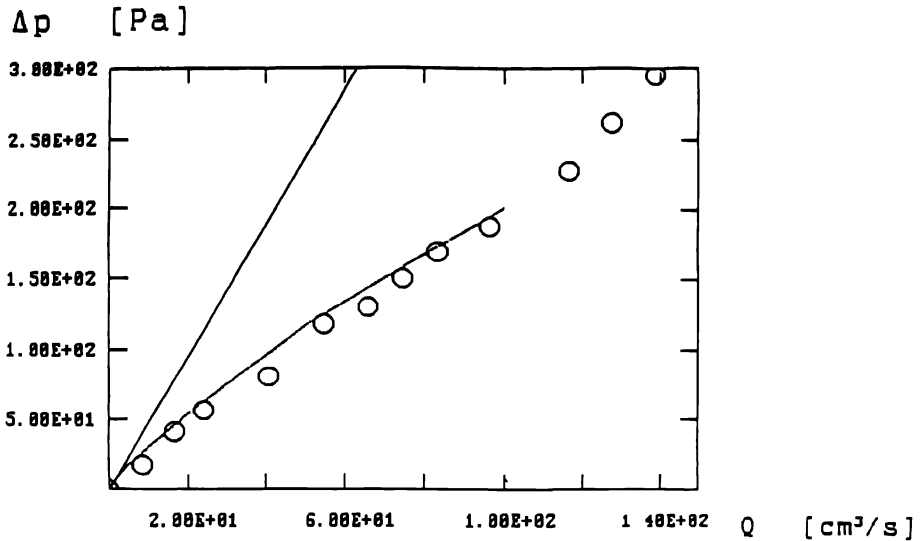
Fig 9   Example of computed and measured pressure drop versus flow rate between two radii for flow between disc with barriers Upper solid line Linear theory Lower solid line Numerical calculations with vortices Circles Experiments
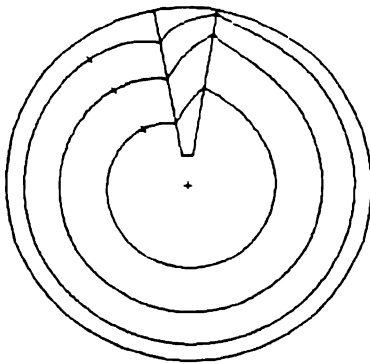
Fig 10   Computed and visualized streamlines for flow between axisymmetric discs with a shallow sector

Experimentally, it has been found that any deviation from perfect axial symmetry with a constant distance between the discs causes a lower pressure drop

7 3   ROUGH SURFACE

The fluid transport through the axisymmetric disc stack is confined to thin boundary layers The velocity in these layers is high The friction drag on separated particles or on a thin film of a second liquid phase may drag this second phase the wrong
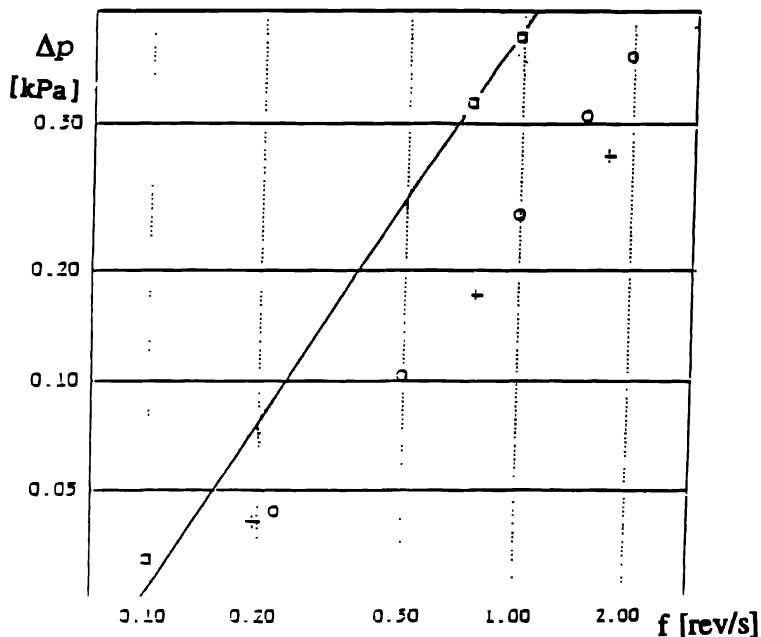
Fig. 11. Pressure drop as a function of rotational speed. Solid line: Theory. Squares: Measurements with two smooth surfaces. Circles: Measurements of one smooth and one rough surface. Crosses: Numerical calculations, one smooth and one rough surface.

way even though it has separated to the disc surface. One way to reduce this effect is to manipulate the surface. The side where the second phase is collecting is kept smooth while the other is made rough, with a roughness height equal or bigger than the Ekman layer thickness. The flow is distributed so that a minor part is transported by the Ekman layer of the smooth surface and the main part is flowing between the roughness elements in a widened boundary layer of the rough side. The drag at the smooth side is reduced. This does also cause a reduction of the pressure drop, Nåbo and Borgström (1989). Figure 11 shows measurements and calculations of pressure drop in the slowly rotating rig with one smooth and one radially rifled surface.

A number of numerical calculations has been used to calculate $\partial p / \partial r$ as a function of Rossby and Ekman numbers. Later this has been used to integrate the pressure drop.

8. Level ring, flow over a weir

The level ring is a small disc used to control the radial level of the free surface (see Fig. 12). The actual level over the level ring depends of the flow rate, the level ring radius and the speed of rotation. The problem to decide the level is analogous to the
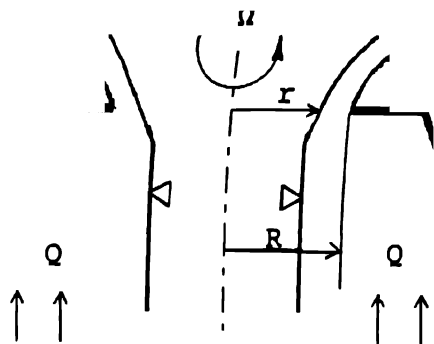
Fig. 12   Schematic of the flow over a weir in a rotating system.

classical weir flow problems encountered in hydraulics. However, factors like the conservation of the liquid's angular momentum complicate the situation compared to the classical case.

The flow passes axially. At radii greater than the level ring radius R, the liquid is assumed to have solid body rotation due to the presence of wings.

The problem has been studied theoretically and experimentally. A theoretical analysis depends upon to what extent the angular momentum is conserved when a liquid element changes radius. Two simple models are
  – solid body rotation even inside R
  – conservation of the angular momentum at radii smaller than R.

The difference between the models in predicted pressure contribution from the level ring is small for the full scale case. The former model gives a liquid level over the level ring.

$$\sqrt{R^2 - \left(\frac{\sqrt{2}Q}{\pi\Omega}\right)^{2/3}} \tag{6}$$

From this, the following expression for the pressure contribution of the level ring can be derived:

$$\Delta p = \frac{3\rho\Omega^{4/3}}{2}\left(\frac{Q}{2\pi}\right)^{2/3} \tag{7}$$

9. Concluding remarks

In this paper we have presented a survey of the pressure drop in different parts of an industrial centrifuge. For obvious reasons we are concerned with pressure drops in order to be able to properly design the centrifuge. Thus, we have tried to view and express the flow in a pressure drop frame of mind. However, the pressure

drop impacts the efficiency of the centrifuge differently in different parts of the centrifuge.

For the inlet, Section 4, the pressure drop or the increase in internal energy may cause particle disruption and thus a lowered separation efficiency. In order to obtain an improvement it is important to understand the destruction process and the forces causing disruption.

Section 5, 6, and 7 are concerned with the pressure drop and flow pattern in different internal channels in the centrifuge. Section 5 presents measurements of the pressure drop in the distribution channels. The experimental work will continue with more complicated geometries. Also, comparisons with numerical results will be made. For the distribution holes, Section 6, a detailed estimate of the pressure drop gives an uneven distribution of the flow in the disc stack. In the section we present a general description of the factors affecting the pressure in the distribution holes. At present this is pursued further both theoretically and experimentally. Section 7 describes the flow in the disc stack in which the actual process of separation takes place. Thus an explicit knowledge of the flow is needed not only in order to calculate the pressure drop but also to be able to make calculations on the actual process of separation. The length of Section 7 also reflects the amount of work done in order to understand the flow between the discs.

Section 8 deals with the flow over a weir. The flow over a weir is a common problem that is solved in textbooks in which the liquid level is calculated as a function of flow rate showing that the flow rate can be measured by measuring the liquid level. Here we have extended the problem to a rotating system and the level has both been calculated and measured.

Acknowledgements

References

1. Alfa-Laval, Laboratory Separation LAPX 202 user's guide. Can be ordered from Alfa-Laval (1983).
2. Bark, F.H., and Sundström, O , A note on rotating Hele Shaw cells. *J. Fluid Mech.* 111 (1981), 271–281.
3. Gusev, A. and Bark, F.H., Stability of rotation-modified plane Poiseuille flow. *Phys. Fluids* 23 (11) (1980), 2171–2177.
4. Greenspan, H. P., The theory of rotating fluids. Cambridge University Press (1968).

5. Johnston, J.P., Halleen, R.M. and Lezius, D.K., Effects of spanwise rotation on the structure of 2-D turbulent channel flow. *J. Fluid Mech.* 56 (1972), 533–542.
6. Khesgi, H. S. and Scrivan, L. E., Viscous flow through a rotating square channel. *Phys. Fluids* 28 (10) (1985), 2968–2979.
7. Lagerstedt, T. and Nåbo, O., Flow visualization in high speed centrifugal separators. Flow visualization IV, ed. C: Veret, Hemisphere, Washington D.C., pp. 603–608 (1986).
8. Moberg, H., Licentiate thesis, Dept. of Hydromechanics, Royal Institute of Technology, Stockholm (1989).
9. Nåbo, O. and Borgström, L., Enhanced separation with rough disc upper surfaces. Proceedings from the Filtech Conference, Karlsruhe, pp. 376–383 (1989).
10. Pater, L., Crowther, E. and Rice, W., Flow regime definition for flow between corotating discs. *J. Fluids Eng.* 96 (1974), 29–34.
11. Peube, J.-L. and Kreith, F., Ecoulement permanent d'un fluide visqueux incompressible entre deux disques paralleles en rotation. *J. Mec.* 5 (1966), 261–286.
12. Sokolov, W. J., *Moderne Industrizentrifugen*, VEB Verlag Technik, Berlin (1971).

Localized Disturbances in Parallel Shear Flows

DAN S. HENNINGSON
Department of Mathematics, Massachusetts Institute of Technology, Cambridge, MA 02139, USA
(Present address: FFA, Box 11021, S-16111 Bromma, Sweden)

L. HÅKAN GUSTAVSSON
Division of Fluid Mechanics, Department of Mechanical Engineering, Luleå University of Technology, S-95187 Luleå, Sweden

and

KENNETH S. BREUER
Department of Aeronautics and Astronautics, Massachusetts Institute of Technology, Cambridge, MA 02139, USA

Contents

Abstract. The development of localized disturbances in parallel shear flows is reviewed. The inviscid case is considered, first for a general velocity profile and then in the special case of plane Couette flow so as to bring out the key asymptotic results in an explicit form. In this context, the distinctive differences between the wave-packet associated with the asymptotic behavior of eigenmodes and the non-dispersive (inviscid) continuous spectrum is highlighted. The largest growth is found for three-dimensional disturbances and occurs in the normal vorticity component. It is due to an algebraic instability associated with the lift-up effect. Comparison is also made between the analytical results and some numerical calculations.

Next the viscous case is treated, where the complete solution to the initial value problem is presented for bounded flows using eigenfunction expansions. The asymptotic, wave-packet type behaviour is analyzed using the method of steepest descent and kinematic wave theory. For short times, on the other hand, transient growth can be large, particularly for three-dimensional disturbances. This growth is associated with cancelation of non-orthogonal modes and is the viscous equivalent of the algebraic instability. The maximum transient growth possible to obtain from this mechanism is also presented, the so called optimal growth.

Lastly the application of the dynamics of three dimensional disturbances in modeling of coherent structures in turbulent flows is discussed.

1. Introduction

Parallel and near-parallel shear flows form a group of technologically very important flows found in e.g. pipes, channels and in boundary layers. Their properties are readily calculated if the flows are laminar but if they become turbulent, as is usually the case, empirical data is required to estimate quantities such as pressure losses, drag and heat transfer. To complicate matters, laminar and turbulent flows often appear together in the same flow configuration with the former generally preceding the latter. Therefore, it is of primary concern to be able to predict the location of the transition between the two types of flows so as to obtain the overall performance of a given flow. Methods to delay, prevent or force the transition have also become of great practical interest and have in many cases been quite successful. However, for further progress to be made in this area it has been recognized that more fundamental insights are required about the underlying flow mechanisms.

After the classical contributions of Rayleigh (1880), Orr (1907) and Sommerfeld (1908) the question of the stability of laminar flows became focused on the exponential growth of disturbances. The study of exponential growth is motivated by the time derivative that appears in the governing equations. This suggests an $\exp(-i\omega t)$ factor in the solutions for the perturbation quantities and depending on the sign of the imaginary part of ω, a perturbation may become unstable, stable or neutral. As the stability calculations generally have offered analytical difficulties, results that could limit the scope of the studies were naturally welcome. One such result is Squire's theorem, which states that the stability of a plane wave moving oblique to the mean flow (in planar flows) is equivalent to a wave moving in the mean flow direction, but at a lower Reynolds number. Thus, the lowest Reynolds number at which a perturbation can become unstable is obtained by considering only two-dimensional waves.

However, as data have accumulated, it has become evident that the ability of the *linear* theory to account for observed transitional Reynolds numbers in parallel

shear flows is quite limited. Only in the case of Blasius flow is the agreement reasonable between theory and experiments, whereas other flows show various degrees of discord. The discrepancy is particularly serious for pipe and Couette flows which are stable according to the theory but still may become turbulent. Various schemes have therefore been devised to account for the disagreement and an obvious first candidate to consider is non-linear effects, not accounted for in the linear theory but certainly of importance at transition to turbulence. The most developed non-linear scenario is the one where the stability of a large amplitude two-dimensional wave (moving in the mean flow direction) to small three-dimensional disturbances is considered. This *secondary instability* mechanism has been quite successful in explaining many details of well-controlled vibrating ribbon experiments, in particular the generation on intense shear layers (spikes) and so-called Λ-structures (see Herbert 1988 for a summary of the main results). It is today considered the main road to the laminar-turbulent transition, in fact, to the extent that transition which does not exhibit the presence of large scale 2-D waves is denoted *by-pass* transition (Morkovin 1969).

Bypass mechanisms are inherently three-dimensional and would operate in many naturally occurring situations such as when surface roughness is present or when the background field contains 3-D disturbance. They are also generally thought to involve non-linear processes.

Within linear stability theory studies of three-dimensional disturbances have played but a minor role, mostly because of Squire's theorem. It was however also noted by Squire (1933) that there are three-dimensional disturbances in the flow with no motion normal to the wall. These are described by the so called Squire modes, which were found to be damped and thus further discouraged studies of three-dimensional disturbances with linear theory.

When the three-dimensional problem is treated, two equations must be solved where the solution to one (the Orr-Sommerfeld equation in viscous flows and the Rayleigh equation in inviscid) appears as an inhomogeneous term in the other (the Squire equation). A characteristic of the three-dimensional forcing was derived by Landahl (1975) who showed that for inviscid disturbances the forcing will eventually lead to a *permanent scar* in the streamwise velocity. In the special case when disturbances have no streamwise variation, Ellingsen & Palm (1975) showed that there is an algebraic growth of the streamwise velocity component, provided there is a spanwise structure. This mechanism was further studied by Landahl (1980) who showed that if the net normal momentum is non-zero, algebraic growth occurs in a localized disturbance. Further results pertaining to the inviscid case were obtained by Gustavsson (1978) and Henningson (1988) who worked out the solutions to the initial value problem in piecewise approximations to boundary layer and channel flow, respectively.

When viscosity is included, the algebraic growth can be deduced from the solution of the initial value problem for the normal vorticity (Henningson 1991) and will occur even if the participating eigenmodes are damped. Despite the damping,

large energy amplification is possible before the eventual decay sets in (Gustavsson 1991). Together with the results obtained for inviscid flows, these recent findings for viscous flow show that the development of three-dimensional disturbances may be quite subtle even in the linear case.

Since the results obtained thus far have appeared in various contexts it is the purpose of the present article to summarize the main findings into a more coherent picture. The approach taken is basically analytical since we consider it particularly important today, when so much interest is focused on numerical simulations, to maintain and develop the analytical foundation of the subject.

The paper is organized in the following manner: In Section 2 the equations governing the development of small three-dimensional disturbances are presented from the perspective of the initial value problem. In Section 3 the inviscid case is considered, first for a general velocity profile and then in the special case of plane Couette flow so as to bring out the key asymptotic results in an explicit form. In this context, the distinctive differences between the asymptotic behavior of waves and the (inviscid) continuous spectrum is presented. Also, comparison is made between the analytical results and some numerical calculations. The viscous case is treated in Section 4, where the complete solution to the initial value problem is presented for bounded flows. Since the eigenmode structure is intimately related to this solution, the eigenvalue spectrum is also considered in detail and their asymptotic behavior for large Reynolds number is summarized. Also the viscous continuous spectrum is discussed. The asymptotic behavior of wave disturbances is then also treated and compared to the kinematic wave theory. This section is concluded with a presentation of the more general vector eigenfunction approach and the idea of optimal disturbances. In Section 5 the application of the dynamics of three dimensional disturbances in turbulence modeling is briefly reviewed. Finally a brief discussion of the results as well as the main conclusions are given in Section 6.

2. Governing equations

The non-dimensional equations of motion for an incompressible fluid are given by the Navier-Stokes equations,

$$\frac{\partial u_i}{\partial t} + u_j \frac{\partial u_i}{\partial x_j} = -\frac{\partial p}{\partial x_i} + \frac{1}{R}\nabla^2 u_i, \tag{1}$$

and the equation of continuity,

$$\frac{\partial u_i}{\partial x_i} = 0 \tag{2}$$

where u_i denotes the velocity field, p the pressure and R the Reynolds number based on some appropriate length and velocity scale. In the present work, we

consider a Cartesian geometry with coordinates (x, y, z) denoting the streamwise, wall-normal and spanwise directions, respectively. The steady mean flow is in the x-direction, varies with y, and is denoted by $U(y)$.

The equations for small perturbations (u, v, w) and p on this mean flow are given by the linearized Navier-Stokes equations:

$$\frac{\partial u}{\partial t} + U\frac{\partial u}{\partial x} + vU' = -\frac{\partial p}{\partial x} + \frac{1}{R}\nabla^2 u \tag{3a}$$

$$\frac{\partial v}{\partial v} + U\frac{\partial v}{\partial t} = -\frac{\partial p}{\partial y} + \frac{1}{R}\nabla^2 v \tag{3b}$$

$$\frac{\partial w}{\partial t} + U\frac{\partial w}{\partial x} = -\frac{\partial p}{\partial z} + \frac{1}{R}\nabla^2 w \tag{3c}$$

and continuity,

$$\frac{\partial u}{\partial x} + \frac{\partial v}{\partial y} + \frac{\partial w}{\partial z} = 0. \tag{3d}$$

Here, a prime $(')$ denotes a y-derivative. Taking the divergence of the linearized momentum equations (3a–c), and using continuity (3d) yields an equation for the perturbation pressure:

$$\nabla^2 p = -2U'\frac{\partial v}{\partial v}. \tag{4}$$

This may be used together with equation (3b) to eliminate p, resulting in an equation for the normal velocity, v:

$$\left[(\frac{\partial}{\partial t} + U\frac{\partial}{\partial x})\nabla^2 - U''\frac{\partial}{\partial x} - \frac{1}{R}\nabla^4 \right] v = 0. \tag{5}$$

In order to describe the complete flow field, a second equation is also needed. This is most conveniently the equation for the normal vorticity,

$$\eta = \frac{\partial u}{\partial z} - \frac{\partial w}{\partial x} \tag{6}$$

where η satisfies

$$\left(\frac{\partial}{\partial t} + U\frac{\partial}{\partial x})\nabla^2 - \frac{1}{R}\nabla^2 \right] \eta = -U'\frac{\partial v}{\partial z}. \tag{7}$$

This pair of equations, together with the boundary conditions:

$$v = v' = \eta = 0; \quad \text{at a solid wall,} \tag{8a}$$

v, v', η bounded in the far field   (8b)

and the initial conditions

$$v|_{t=0} = v_0(x, y, z) \tag{9a}$$

$$\eta|_{t=0} = \eta_0(x, y, z) \tag{9b}$$

form a complete description of the evolution of an arbitrary disturbance in both space and time.

Since the coordinates x and z in this problem are homogeneous and the system is linear, it is possible to work in wave number space and consider the behavior of single Fourier-modes. Taking the Fourier transform in the horizontal directions results in the following pair of equations for $\hat{v}$ and $\hat{\eta}$

$$\left[(\frac{\partial}{\partial t} + i\alpha U)(D^2 - k^2) - i\alpha U'' - \frac{1}{R}(D^2 - k^2)^2 \right] \hat{v} = 0, \tag{10}$$

$$\left[(\frac{\partial}{\partial t} + i\alpha U) - \frac{1}{R}(D^2 - k^2) \right] \hat{\eta} = -i\beta U'\hat{v}. \tag{11}$$

Here a caret ^ represents a Fourier-transformed variable $D ='$ denotes a y-derivative, α and β are the components of the wavenumber vector in the streamwise and spanwise directions, respectively, and $k = \sqrt{a^2 + \beta^2}$ is its modulus. Once $\hat{v}$ and $\hat{\eta}$ are known, the horizontal velocities, $\hat{u}$ and $\hat{w}$ may be obtained from

$$\hat{u} = \frac{i}{k^2}(\alpha D\hat{v} - \beta\hat{\eta}) \tag{12a}$$

$$\hat{w} = \frac{i}{k^2}(\beta D\hat{v} + \alpha\hat{\eta}). \tag{12b}$$

The natural measure of the size of a perturbation is its kinetic energy. Using the Fourier transformed variables this can be written in a particularly simple form. Using Parseval's theorem, (12a) and (12b), the kinetic energy density, integrated over the normal direction can be written (Gustavsson 1986)

$$E = \frac{1}{2k^2} \int_{-1}^{1} \left(|D\hat{v}|^2 + k^2|\hat{v}|^2 + |\hat{\eta}|^2 \right) dy. \tag{13}$$

From the structure of equations (10) and (11), it follows that there is a fundamental difference between the normal velocity and the normal vorticity. The evolution of v is described by the homogeneous equation (10) with homogeneous boundary conditions, and can thus be determined if the initial data are given. In contrast, the equation for η is inhomogeneous, where the spanwise variation of v and the mean shear combine in the forcing term. Since (11) is the linearized form of the vorticity equation for normal vorticity, and the forcing term emanate from the linearized vortex tilting term, it may be appropriate to denote the forcing mechanism by vortex tilting. It will be given another kinematic interpretation in the next chapter, in connection with the treatment of the inviscid problem.

3. The inviscid analysis

3.1. GENERAL RESULTS

We first consider the inviscid analysis which reveals several key features of the problem. When the viscous terms are dropped, (10) becomes the time-dependent Rayleigh equation, giving the normal velocity. For a two-dimensional disturbance $(\beta = 0)$ the solution for v governs the complete problem since the streamwise velocity is given by two-dimensional continuity, see equation (12a).

When $\beta \neq 0$ the disturbance is three-dimensional, and we must also consider the normal vorticity. Equation (11) can, in the inviscid case, be integrated to yield

$$\hat{\eta} = \hat{\eta}_0 e^{-\imath \alpha U t} - \imath \beta U' e^{-\imath \alpha U t} \int_0^t \hat{v}(y, t') e^{\imath \alpha U t'} dt'. \tag{14}$$

The first term represents the advection of the initial normal vorticity field by the mean field, while the second term represents the integrated effect of the normal velocity, the so-called *lift-up* effect (Landahl 1975). This term represents the *generation* of horizontal velocity perturbations by the lifting-up of fluid elements in the presence of the mean shear. If a single Fourier component is considered this process can be illustrated as follows. Make a coordinate transformation such that one axis, x_1, is aligned with the wavenumber vector $\mathbf{k}$, see Fig. 1a. The other axis, z_1, will then be perpendicular to the wavenumber vector. The mean flow along the new coordinate axis will be denoted U_1 and W_1, respectively, and is easily found to be

$$U_1 = \frac{\alpha}{k} U \tag{15a}$$

$$W_1 = -\frac{\beta}{k} U \tag{15b}$$

Using equations (12a) and (12b) the disturbance velocities along the same axis become

$$\hat{u}_1 = \frac{\imath}{k} D\hat{v} \tag{16a}$$

$$\hat{w}_1 = \frac{\imath}{k} \hat{\eta} \tag{16b}$$

It is interesting to note that the velocity along the wavenumber vector is given by two-dimensional continuity in that direction, while the velocity perpendicular to the wavenumber vector is determined by the normal vorticity component. The lift-up process can now be easily visualized by considering the change in the $\hat{w}_1$ velocity during a short time Δt. Equations (14), (15b) and (16b) give

$$\Delta w_1 = -W_1' \hat{v} \Delta t \tag{17}$$
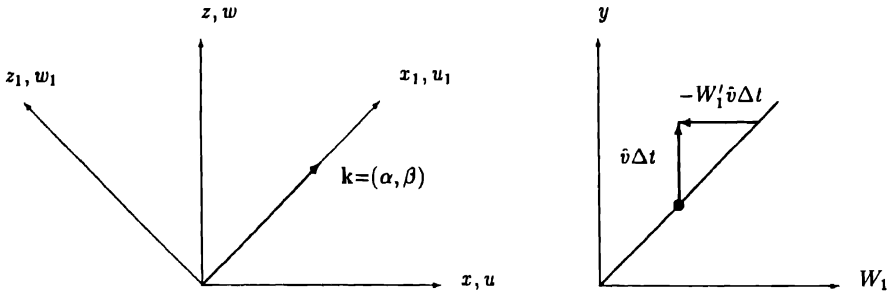
Fig. 1. Illustration of the *lift-up* effect. (a) Definition of the coordinate system aligned with the wavenumber vector. (b) Creation of a horizontal velocity defect in the z_1-direction by the lift-up of a fluid element that conserves its horizontal momentum in that direction.

where terms of $\mathcal{O}(\Delta t^2)$ have been neglected and it is assumed that the observer is moving with the wave. The derived expression for Δw_1 is readily identified as the induced horizontal velocity disturbance resulting from the lift-up of a fluid particle by the normal velocity such that the horizontal momentum in the direction perpendicular to the wavenumber vector is conserved. This is illustrated in Fig. 1b. Even if the normal velocity decays this process can give rise to large amplitude perturbations in the horizontal velocity components.

For Fourier components with $\alpha = 0$ the growth may be calculated explicitly. For that case the Rayleigh equation implies that $\hat{v}$ is not a function of time, while (14) gives

$$\hat{\eta} = \hat{\eta}_0 - i\beta U'\hat{v}_0 t \qquad (18)$$

We will refer to this growth as an *algebraic instability* (see also Ellingsen & Palm 1975).

3.2. SOLUTION OF THE NORMAL VELOCITY

Insight into the mathematical properties of the solutions of the Rayleigh equation can be found using the method of Laplace transforms. We Laplace transform the inviscid part of equation (10) and obtain

$$(D^2 - k^2)\hat{v} - \frac{U''\hat{v}}{U - c} \qquad \frac{\hat{\phi}_0}{i\alpha(U - c)} \qquad (19)$$

where the Laplace transform variable $s = -\alpha c$ have been used and where $\hat{\phi}_0 = (D^2 - k^2)\hat{v}_0$. The solution to this inhomogeneous problem can be found by the

method of variation of parameters and written in terms of a Green's function, we have

$$\tilde{v} = \int_{-1}^{1} G(y, y')\hat{\phi}_0 dy' \tag{20}$$

The Green's function is defined

$$
\begin{aligned}
G(y, y') &= \frac{\hat{v}_2(y)\hat{v}_1(y')}{i\alpha[U(y') - c]W(c)} y' < y \\
&- \frac{\hat{v}_1(y)\hat{v}_2(y')}{i\alpha[U(y') - c]W(c)} y' > y
\end{aligned}
\tag{21}
$$

where $\hat{v}_1$ and $\hat{v}_2$ are solutions to the homogeneous part of (19) satisfying $\hat{v}_1(-1) = 0$ and $\hat{v}_2(1) = 0$, and $W(c) = \hat{v}_1 D\hat{v}_2 - \hat{v}_2 D\hat{v}_1$ is the associated Wronskian. When the Laplace transformation solution is inverted each pole in the Green's function will give a contribution to the full solution. The first type of poles are zeros of the Wronskian. These correspond to discrete eigenvalues of the Rayleigh equation since $\hat{v}_1$ and $\hat{v}_2$ will not be linearly independent if c is an eigenvalue of the homogeneous part of (19), thus producing a zero in the Wronskian. The second type of pole consists of values of c such that $U(y') = c$, i.e. a continuous spectrum for which the phase velocity is equal to the local mean velocity.

The discrete spectrum

First we will consider the discrete eigenvalues of the Rayleigh equation. For a general velocity profile the eigenvalue problem constituted by the homogeneous part of (19) is not tractable analytically. However, some general results for the eigenvalues can be obtained. By taking the complex conjugate of the equation one can easily prove that if c is an eigenvalue, so is its complex conjugate. Another powerful result derived by Rayleigh (1880) is found by multiplying the Rayleigh equation by the complex conjugate of the solution and integrating over the interval. The imaginary part of the resulting expression becomes

$$\int_{-1}^{1} \frac{U''}{|U - c|^2}|\hat{v}|^2 dy = 0 \tag{22}$$

from which it follows that a necessary condition for instability $(c_i > 0)$ is that the mean velocity has an inflection point $(U'' = 0)$ somewhere in the y-domain.

The dispersive effects of the normal modes can be found by looking at the group velocity. The group velocity is found from derivatives of the dispersion relation which for the Rayleigh equation takes the form $\omega = \alpha c(k)$. The concept of group velocity is further discussed in Section 4.2.

Since c is in general a complicated function of k, a perturbation described by the discrete eigenmodes will gradually change its shape due to dispersive effects. These effects can be determined by applying the method of stationary phase to the solution of the initial value problem. For a homogeneous media the wavenumbers are found to be constant along group velocity rays, given by

$$\frac{x}{t} \quad \frac{\partial \omega}{\partial \alpha} = c + \frac{\alpha^2}{k} c' \tag{23a}$$

$$\frac{z}{t} \quad \frac{\partial \omega}{\partial \beta} \quad \frac{\alpha\beta}{k} c' \tag{23b}$$

where $c' = dc/dk$ and $\omega = \alpha c(k)$. By eliminating the explicit appearance of α and β, Gustavsson (1978) derived the relationship

$$\left(\frac{x}{t} - c - \frac{kc'}{2}\right)^2 + \left(\frac{z}{t}\right)^2 = \left(\frac{kc'}{2}\right)^2 \tag{24}$$

Equation (24) is the expression for a circle with center at $(c + kc'/2, 0)$ and with radius $kc'/2$. By varying k, all such circles will be generated and the area covered by them is the region where the dispersive waves may be found. For the simplified boundary layer profile of

$$U = \begin{cases} y & 0 < y < 1 \\ 1 & 1 \le y \end{cases} \tag{25}$$

the eigenvalue becomes $c(k) = 1 - e^{-k} \sinh k/k$ and the stationary wave area resulting from this relation can be seen in Fig. 2. An interesting feature of the wave-area is its opening angle at the origin. Since $k \to 0$ in this region, half this angle becomes

$$\lim_{k \to 0} \sin^{-} \left(\frac{kc'/2}{c + kc'/2}\right) \quad \sin \quad \sigma + 2 \tag{26}$$

if $c \sim k^\sigma$ for small values of k. In the particular example, $\sigma = 1$ and the angle becomes $\sim 19.47°$.

The continuous spectrum

When the Rayleigh equation is solved for the velocity profile of plane Couette flow $(U = y)$ no dispersive solution is obtained. Thus, only the continuous spectrum exists for that case, as first found by Case (1960). Taking the inverse Laplace transform of (19) we obtain the following simple expression for Couette flow

$$(D^2 - k^2)\hat{v} = \hat{\phi}_0 e^{-i\alpha y t} \tag{27}$$
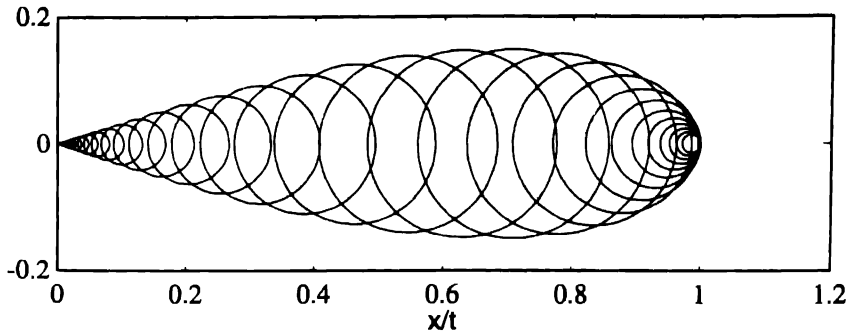
Fig. 2   Area where waves are found from the dispersive effects of an inviscid piecewise linear boundary layer The circles are found by use of equation (24).

or

$$\nabla^2 v = \phi_0(x - \alpha y t, y, z, t) \tag{28}$$

which shows that the continuous spectrum corresponds to a solution advecting with the local mean velocity. It may therefore also be termed a convective solution (Gustavsson 1978). Thus the continuous spectrum does not propagagte with a phase coherence in the y-direction, nor does it spread out in the spanwise direction, as the dispersive waves, instead it spreads only in the streamwise direction with velocities dependent on the y-position. For a velocity profile with curvature, the solution for $\hat{v}$ will contain both the dispersive and the convective parts.

Limitations of Rayleigh's theorem

On first sight, Rayleigh's inflection point criterion seems to exclude purely damped solutions for profiles without inflection points, since the eigenvalues to the Reyleigh equation come in complex conjugate pairs. This would prohibit a dispersive solution in inviscid Poiseuille and boundary layer flows, for example. The fact that such solutions exist has in the past generated some controversy, making it worthwhile to consider that question here.

Using the Frobenius method it is straightforward to show that the homogeneous solutions v_1 and v_2 in (20) are linear combinations of the Tollmien solutions (see Drazin & Reid (1981) eqs. 22.25, 22.26). The most important feature of these functions is the logarithm that appears in one of them. The solutions are otherwise analytical functions of y. The logarithm has a branch point at $U(y) = c$ and the branch can be specified by considering the inviscid solutions as a limit of the viscous ones (Lin 1955). When the initial value problem is considered one need

not resort to viscosity, however, to be able to find the correct branch. Applying the inverse Laplace transform to (20) a typical term has the form

$$\hat{v} = \frac{1}{2\pi i} \int_{-1}^{1} \int_{-\infty+\imath\gamma}^{\infty=\imath\gamma} f(y,y') \frac{(y'-y_c)\ln(y'-y_c)e^{-\imath\alpha ct}}{[U(y')-c]W(c)} dcdy' \qquad (29)$$

where $f(y,y')$ represents the remaining part of the Green's function. When the integral in the c-plane is evaluated the contour has to be closed in the lower half plane in order for the solution to remain bounded for $t > 0$. Thus when the argument of the logarithm is considered as a function of c the branch cut has to be made in the lower part of the c-plane so that the solution is analytic in the upper half. Now, consider the implication of this to the location of the branch cut in the y-plane. If $c_\imath \approx 0$ the behavior around the real y-axis can be found by Taylor expanding the mean flow around y_{cr} and we find

$$U(y_c) = U(y_{cr}) + U'(y_{cr}) + U'(y_{cr})\imath y_{c\imath} + \ldots = c_r + \imath c_\imath \qquad (30)$$

Thus, close to the real axis the argument of the logarithm can be written

$$\ln(y-y_c) \approx \ln\left[y_r + \imath y_\imath - y_{cr} - \frac{\imath c_\imath}{U'(y_{cr})}\right] \qquad (31)$$

The analyticity of the solution in the upper half of the c-plane implies that the logarithm has to be defined for positive values of $c_\imath$. Thus when (29) is integrated over y' we have to choose a path around the singularity such that $y_\imath$ has the same sign as when $c_\imath > 0$. This implies that the branch cut in the complex y-plane has the following location,

$$U'(y_{cr}) > 0 \Rightarrow y_\imath < 0 \quad \text{analytic} \Rightarrow \text{branch cut } above \text{ singularity}$$

$$U'(y_{cr}) < 0 \Rightarrow y_\imath > 0 \quad \text{analytic} \Rightarrow \text{branch cut } below \text{ singularity}$$

Away from the real y-axis we choose the direction of the branch cut in the same manner in order to ensure that all solutions use the same branch of the logarithm. The argument presented here essentially follows that of Dikii (1960).

As an example consider a parabolic mean profile ($U = 1 - y^2$) for which Rayleigh's inflection point criterion prohibits exponential growth. Figure 3 shows the location of the singularities and branch cuts for that case. Note that the branch cuts cross the real y-axis, resulting in a detour into the complex plane of the paths along which the solution is defined. Henningson (1988) has shown that it is possible to find two dispersive solutions for the parabolic mean flow using the indicated integration paths. This does not violate point criterion since the relation (22) no longer holds when y is allowed to take on complex values.
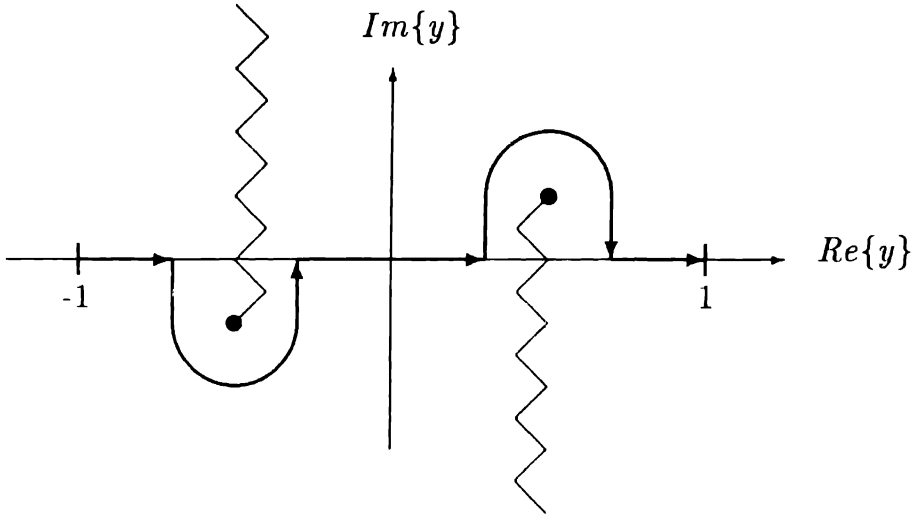
Fig 3.   Singularities and branch cuts for inviscid Poiseulle flow. The singularities are located at $(y_{cr}, -c_i/2y_{cr})$, where $2y_{cr}^2 = 1 - c_r + [(1 - c_r)^2 + c_i^2]^{1/2}$ and $c_i < 0$.

3.3. THREE-DIMENSIONAL DISTURBANCES IN PLANE COUETTE FLOW

In order to illustrate the non-dispersive aspects of the inviscid solution we will consider inviscid Couette flow. The solution to (27) for $U = y$ is readily obtained and can conveniently be written (Case 1960) as

$$\hat{v}(y) = \int_{-1}^{1} G(y, y')\hat{\phi}_0(y')e^{-i\alpha y'}dy' \tag{32}$$

where

$$G(y, y') = \frac{-\sinh k(1 - y)\sinh k(1 + y)'}{k \sinh k}; y' < y \tag{33}$$
$$\frac{-\sinh k(1 + y)\sinh k(1 - y')}{k \sinh k}; y' > y$$

The above Green's function can also be found from the general expression (21) by applying the inverse Laplace transform in the special case of plane Couette flow and introducing the explicit expression for the homogeneous solutions valid for that case.

With $\hat{v}$ determined, the solution for $\hat{\eta}$ is readily obtained from the inviscid version of (11). The solution for $\hat{\eta}$ becomes

$$\hat{\eta} = \hat{\eta}_0 e^{-i\alpha ty} + i\beta \int_{-1}^{1} G(y, y')\hat{\phi}_0 \frac{e^{-i\alpha yt} - e^{-i\alpha y't}}{i\alpha(y - y')}dy' \tag{34}$$
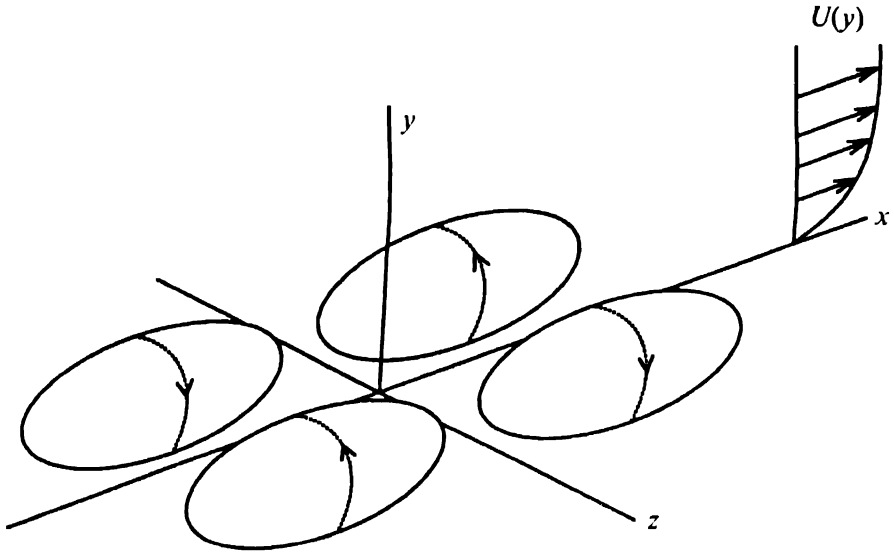
Fig. 4.   Schematic of the initial velocity field for a localized disturbances consisting of two pairs of counter rotating vortex pairs. From Breuer & Haritonidis (1990).

where $\hat{\eta}_0$ is the initial value of $\hat{\eta}$.

Of particular interest for these solutions is their small and large time behavior. To leading order in αt, (32) is found to recover $\hat{v}_0$ whereas for large αt partial integrations shows that the leading order term in $\hat{v}$ is $O(1/(\alpha t)^2)$. Thus, v is expected to decay in time. For $\hat{\eta}$, however, the temporal behavior is different.

For small times, a Taylor expansion shows that

$$\frac{e^{-i\alpha t y'} - e^{-i\alpha t y}}{i\alpha(y - y')} \sim t[1 + \frac{i\alpha t}{2}(y + y') + \cdots] \tag{35}$$

which reduces (34) to

$$\hat{\eta}_0 e^{-i\alpha t y} - i\beta\hat{v}_0 t - \frac{i\alpha\beta t^2}{2} \left| y\hat{v}_0(y) + \int_{-1}^{1} \frac{\delta G}{\delta y'}\hat{v}_0 dy' \tag{36}$$

This shows that $\hat{\eta}$, aside from the convected initial value, contains an induced term growing linearly for short times and which is due to the spanwise variation of $\hat{v}_0$. This is the previously mentioned lift-up effect present for three-dimensional disturbances.

The algebraic growth is moderated for large times as can be recognized by evaluating the integrals in (34) when $\alpha t \to \infty$. It is then noticed that the main

contribution to the integral in (34) comes from the region around $y' = y$. An expansion around this point gives the following result to leading order

$$\tilde{\eta} \sim \tilde{\eta}_0 e^{-\imath\alpha yt} \qquad \imath\pi\frac{\beta}{\alpha}\frac{\sinh k(1+y)\sinh k(1-y)}{k\sinh k}\tilde{\phi}_0 e^{-\imath\alpha ty} \qquad (37)$$

which shows that the forcing by the normal velocity leads to a *permanent scar* convecting downstream with the local mean velocity. This result is originally due to Landahl (1975), derived for a more general case. It was also derived for the piecewise linear boundary layer profile by Gustavsson (1978).

Note that the expression (37) is infinite for $\alpha = 0$. This is in agreement with the explicit expression for the normal vorticity obtained earlier. Equation (18) shows that $\tilde{\eta} \to \infty$ as $t \to \infty$. Thus a disturbance that has wavenumber components with $\alpha = 0$ excited will have a different asymptotic behavior than those without any such excitation. Landahl (1980) showed that a localized disturbance with energy along the spanwise wavenumber axis will experience a growth of the energy that is at least proportional to t. He further showed that this will manifest itself as an elongation of the disturbance in the streamwise direction.

3.4. NUMERICAL SOLUTIONS

The distinction between the dispersive and advective components that emerge in the solution of the inviscid problem may best be seen in the numerical results of Henningson (1988), who considered the evolution of an initial disturbance in a plane Poiseuille flow in which the mean profile was approximated by a three-part piecewise linear profile, and by Breuer & Haritonidis (1990) who used the Blasius boundary layer profile for their base flow. In both cases, the initial disturbance had the form of two pairs of counter-rotating eddies, schematically shown in Fig. 4. Note that the initial streamwise velocity perturbation is here zero.

Figures 5a,b are taken from Breuer & Haritonidis's boundary layer calculations and show contours of v and u, plotted in the $x - y$-plane. The normal velocity resembles the initial conditions, although the amplitude has decayed by about 50%, and the entire structure has moved downstream with an approximate velocity equal to $0.4U_\infty$, which corresponds to a typical wave-speed in the boundary layer. In sharp contrast to this, the streamwise velocity is dominated by the lift-up effect which creates a perturbation in the form of an inclined shear layer. This shear layer intensifies with time due to the convective nature of the disturbance and the absence of viscosity to moderate the sharp velocity gradients that develop.

The cross-stream structure of the disturbance, and the distinction between the convective and dispersive aspects of the inviscid disturbance are illustrated in Figs 6a,b which show v and u at time $t = 10$ plotted in the $x - z$-plane (taken from Henningson's 1988, piecewise linear results). The normal-component reflects the dispersive nature of the Rayleigh equation, and shows a wave-packet emerging with wave-crests swept back at 45°. The amplitude of v decreases as the disturbance
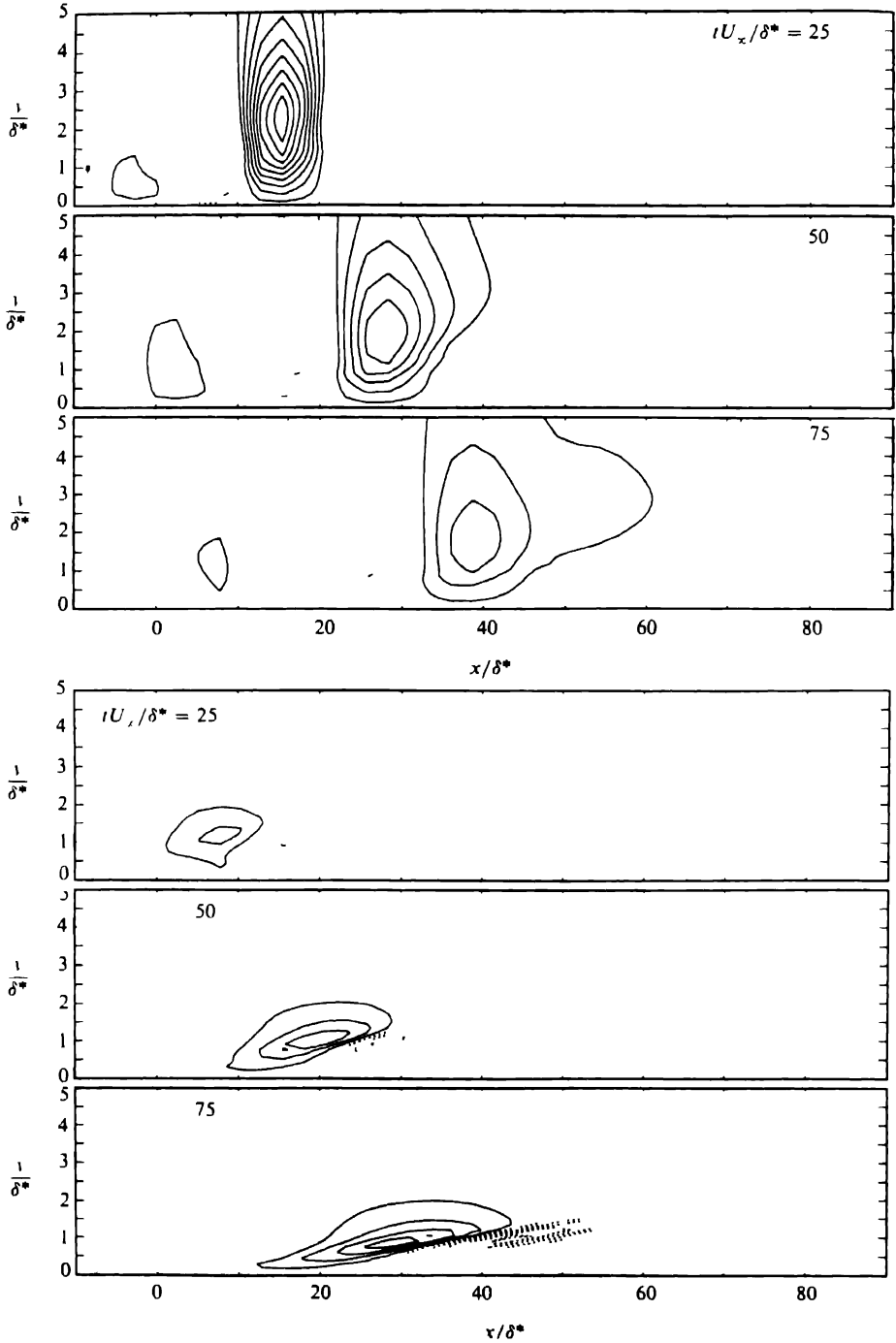
Fig 5   Inviscid boundary-layer results at $t = 25, 50, 75$ (a) Contours of normal velocity
at $z = 0$ (b) Contours of streamwise velocity at $z = 0$ The quantities are scaled with the
free-stream velocity and the displacement thickness From Breuer & Haritonidis (1990)
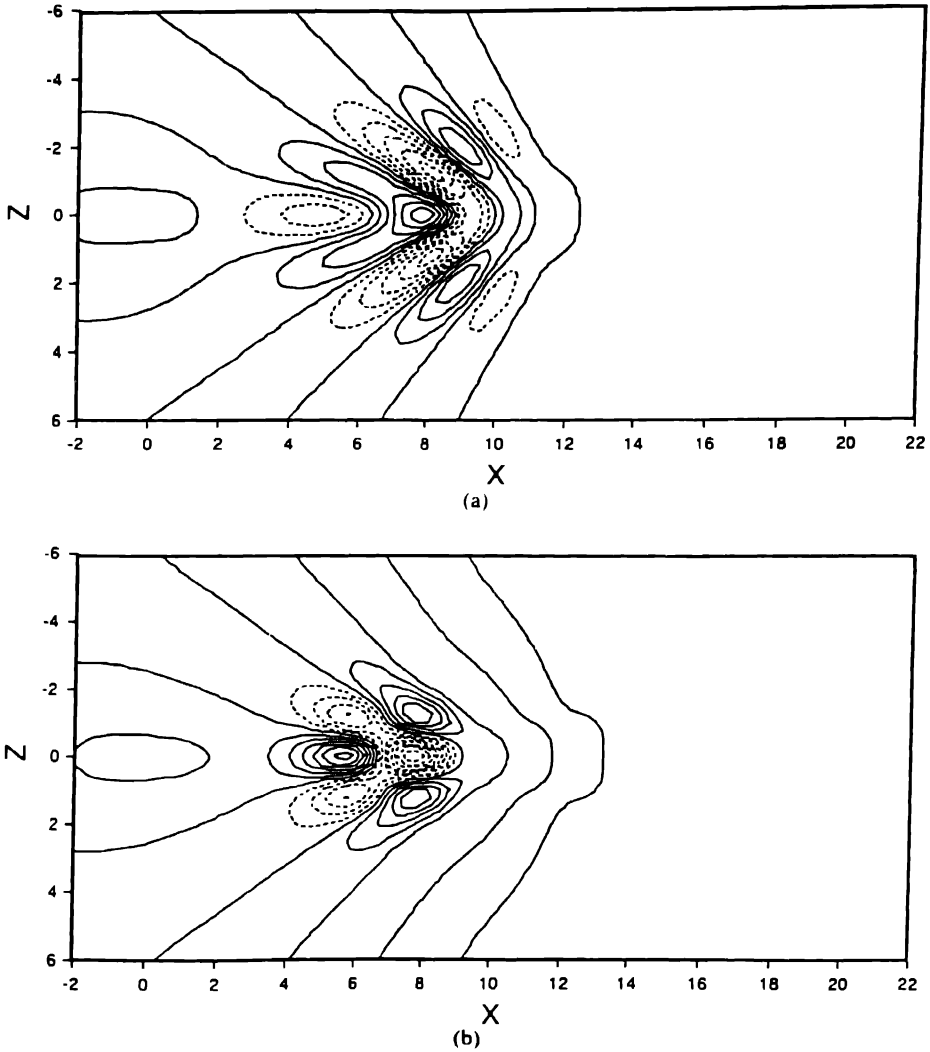
Fig. 6.   Inviscid piecewise linear Poiseuille results at $t = 10$. (a) Contours of normal velocity at $y = 0.44$. (b) Contours of streamwise velocity at $y = 0.44$. The quantities are scaled with the centerline velocity and the channel half-height. From Henningson (1988).

spreads in the horizontal plane such that its amplitude at $t = 10$ is only one-half its initial amplitude. The streamwise component, however, has attained an amplitude over 12 times that of v and is dominated, not by the wavepacket, but by the shear leayer, seen here as a strong peak and depression at the center of the structure.

We should note that, despite the obvious differences between the plane Poiseuille flow and the Blasius boundary layer, the numerical results are essentially inter-

changeable and that the formation of the shear layer and the wavepacket are not sensitive to the particular details of the mean flow.* The success of the piecewise linear approximation should also be noted. Both the dispersive and convective aspects of the evolving disturbance are captured, a result which is particularly gratifying since the solution is in closed-form, whereas the use of a continuous mean velocity profile requires a numerical integration of the Rayleigh equation.

4. The viscous problem

4.1. THE EIGENVALUE SPECTRA

The key ingredients in the solution to equation (10) and (11) are the eigenmodes of their respective homogeneous operators. The operator governing the normal velocity is the Orr-Sommerfeld (OS) operator and the operator governing the normal vorticity will be referred to as the Squire (SQ) operator. The respective eigenvalue problems are then, for the OS eigenvalues

$$\left[(-\lambda + i\alpha RU)(-D^2 + k^2) + i\alpha RU'' + (-D^2 + k^2)^2\right] \tilde{v} = 0 \tag{38}$$

with boundary conditions $\tilde{v} = D\tilde{v} = 0$ on solid walls and $\tilde{v} \to 0$ in the free stream, and for the SQ eigenvalues

$$\left[-\sigma + i\alpha RU + (-D^2 + k^2)\right] \tilde{\eta} = 0 \tag{39}$$

with boundary conditions $\tilde{\eta} = 0$ on solid walls and $\tilde{\eta} \to 0$ in the free stream. The eigenvalue λ is related to the more frequently used phase speed, c, and the frequency, ω, through

$$\lambda = i\omega R = i\alpha cR. \tag{40}$$

and for σ similar relations hold. From the above equations it is seen that the eigenvalues will depend on the two parameters $(k, \alpha R)$. However, it is noticed that the explicit k-dependence can be removed from the Squire equation by the transformation $\sigma' = \sigma - k^2$. The eigenvalues (and eigenfunctions) are today most easily obtained through numerical methods, but some general properties can be obtained by analytical treatment of the equations. Since the eigenvalue spectra for bounded and unbounded flows show distinct differences, they will be treated separately. Also, since we are concerned with the initial value problem, for which the temporal stability is most appropriate, the wave numbers are assumed to be real, and the eigenfunction and the eigenvalues are complex.

---

* An exception to this is plane Couette flow which does not admit any dispersive solutions.

Bounded flows

Bounds on the eigenvalues for the OS and the SQ operators can be obtained by multiplying the equations with the complex conjugate of their respective eigenfunctions, integrating over the y-interval, identifying real and imaginary parts, and using variational inequalities. For the Squire modes Davey & Reid (1977) obtained

$$U_{min} < c_r < U_{max} \tag{41a}$$

$$< c_i - (\pi^2/4 + k^2)/\alpha R \tag{41b}$$

These modes are thus always damped, as also noted by Squire (1933). For the OS eigenvalues the following bounds were obtained by Joseph (1968)

$$U_{min} + \frac{U''_{min}}{2(\pi^2 + k^2)} < c_r < U_{max} \qquad if \qquad U''_{max} < 0, \tag{42a}$$

$$c_i < U'_{max}/2\alpha - (\pi^2 + k^k)/\alpha R \tag{42b}$$

For the other possibilities of U'', the reader is referred to the original paper. These estimates were sharpened in Joseph (1969). The propagation speeds of small disturbances are thus essentially restricted to the range set by the mean flow, whereas the growth rate is always bounded from above.

It is interesting to note that these bounds do not only bound the eigenvalues but also the *numerical range* of the OS and SQ operators. For the SQ operator the numerical range is the set of all complex values in the c-plane such that

$$c = \int_{-1}^{1} \tilde{\eta} * [U + \frac{1}{i\alpha R}(-D^2 + k^2)]\tilde{\eta} \, dy \tag{43}$$

under the conditions that $\int_{-1}^{1} \tilde{\eta} * \tilde{\eta} \, dy = 1$ and $\tilde{\eta}(\pm 1) = 0$. Note that $\tilde{\eta}$ does not need to be an eigenfunction and that the bounds (41a) and (41b) are readily derived from (43). For the OS operator a similar relation holds. It can be shown that the eigenvalues of an operator is found within the numerical range and that the numerical range can be used to give a precise condition for no transient growth. *The energy of all initial disturbances decay monotonically if and only if the numerical range of the governing operator is confined to the lower half of the c-plane.* Thus (41b) shows that solutions governed by the SQ operator alone not only decay asymptotically as $t \to \infty$ but decay monotonically. This is a much stronger condition, which has often been overlooked. For further discussion of the numerical range of the OS and SQ operators see Reddy, Schmid & Henningson (1993).

As an example of the spectra, Fig. 7 shows the location in the complex c-plane of the SQ and the OS eigenvalues in plane Poiseuille flow ($k = 1.481, \alpha R = 3141.6$).
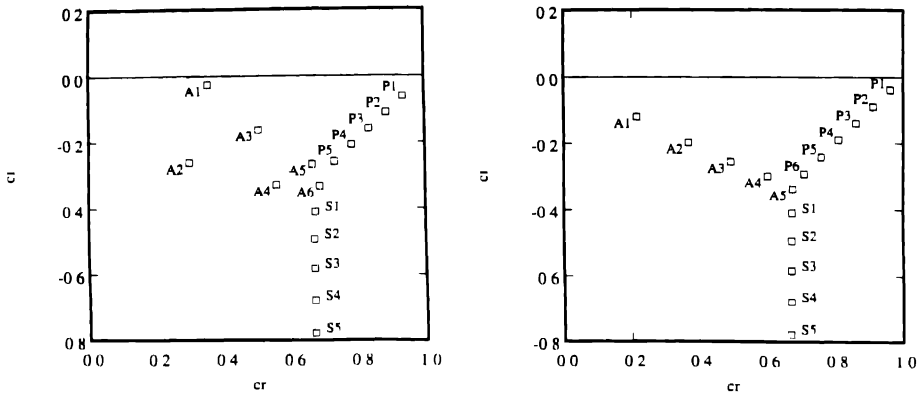
Fig. 7. a) Orr-Sommerfeld and b) Squire eigenvalues for plane Poiseuille flow with $\alpha = \beta = 1.0472$ and $R = 3000$

The eigenvalues are seen to be located on three main branches which for the OS eigenvalues were denoted as $A(c_r \rightarrow 0), P(c_r \rightarrow 1)$ and $S(c_r \approx 2/3)$ by Mack (1976). It is appropriate to adopt this notation also for the SQ modes since they have the same overall feature. The number of eigenvalues along the respective branches depends on the parameter αR.

The asymptotic behavior of the eigenvalues on the A-branch is governed by $(\alpha R)^{-1/3}$ and the eigenvalues are related to the zeroes of the (generalized) Airy function. The eigenfunctions will have large amplitudes close to the wall and are therefore generally called wall-modes. On the P-branch the asymptotics of the eigenvalues is governed by $(\alpha R)^{-1/2}$ and the real and imaginary parts of c are, to leading order, connected by

$$c_r - c_i = 1 + \mathcal{O}(\alpha R)^{-1/2}. \tag{44}$$

The eigenfunctions are related to the parabolic cylinder function (Abramowitz & Stegun 1965) and have large amplitudes close to the centerline and are therefore called center modes. In contrast to the other branches the number of eigenvalues on the S-branch is infinite and has been shown to be governed by $(\alpha R)^{-1}$ asymptotically. These are the main asymptotic behaviors for the eigenvalues of the OS and the SQ modes in plane Poiseuille flow. For plane Couette flow the structure is changed such that only the A and the S branches are present and for the Blasius boundary layer only the A branch exists (see the discussion about unbounded flows). For the techniques used to obtain the asymptotic expressions for the eigenvalues see Drazin & Reid (1981).

For bounded flows it has been shown that the modes of the OS operator form a complete set (DiPrima & Habetler 1969 and Schensted 1961). This also applies to

the SQ modes. Thus, a general three-dimensional disturbance can be expressed in terms of these discrete modes.

In calculations of OS eigenvalues for plane Poiseuille and plane Couette flows located in the region where the branches merge it is found that the eigenvalues are sensitive to perturbations, such as round-off errors in numerical computations or small variations of the parameters k and αR. Reddy, Schmid & Henningson (1993) showed that the sensitivity of these eigenvalues increased exponentially with the Reynolds number and that it is related to the near linear dependence of the eigenfunctions corresponding to eigenvalues close to the junction of the branches. In addition to making accurate numerical computations of these eigenvalues difficult it implies that expansions using the sensitive eigenfunctions will be numerically ill-conditioned. An $\mathcal{O}(1)$ disturbance may need orders of magnitude larger expansion coefficients due to cancellation effects when the non-orthogonal eigenfunctions are summed. The inner product used to define orthogonality is here the one associated with the energy norm, i.e. equation (13). Recall that orthogonality is dependent of the inner product used. In addition to these results Reddy et al. (1993) showed that the non-orthogonality of the eigenfunctions, which is related to the non-normality of the OS-operator, implies that there is a potential for transient growth. This growth can in some cases be large and is related to the algebraic instability found in the inviscid case. This is further discussed in the section dealing with optimal disturbances.

Unbounded flows

For the Blasius boundary layer Mack (1976) has shown that the number of eigenmodes is *finite* and only corresponding to the A-branch for plane Poiseuille flow. This means that the discrete modes cannot describe an arbitrary disturbance and hence the spectrum must be complemented. On basis of numerical experimentation, Mack suggested the complement to be a continuous spectrum located at $c_r = 1$ and $c_i < -\alpha/R$. Such a spectrum was derived by Grosch & Salwen (1978) from the assumption that the amplitude of the eigenfunctions of the OS equation is *bounded* as $y \to \infty$ as opposed to *decaying* which is assumed when determining the discrete modes. In particular, this allows the eigenfunctions to be oscillatory as $y \to \infty$. Solving the OS equation in the far field where $U \approx 1$ and $U'' \approx 0$, leads to $\phi = C_1 e^{-ky} + C_2 e^{-\mu y} + C_3^{\mu y}$ where $\mu^2 = k^2 + i\alpha R(1 - c)$. Thus, if $\mu = i\sigma$ with σ real, the oscillatory behavior is obtained. The condition for an imaginary μ thus gives the location of the continuous spectrum at

$$c = 1 - i(\sigma^2 + k^2)/\alpha R. \tag{45}$$

A similar analysis for the Squire equation shows that also this equation has a continuous spectrum. Gustavsson (1979) considered the initial value problem using Laplace transform techniques and showed that the continuous spectrum appears as a branch cut in the Laplace transform plane in that formulation. A given initial

disturbance may then be described in terms of both the discrete modes and the continuous spectrum. It is important to realize that the continuous spectrum for viscous unbounded flows is completely different from the inviscid continuous spectrum previously discussed. When viscosity is present the governing stability equations are regular and the continuous spectrum is due to the unbounded domain. This is mathematically similar to the need for continuously varying frequencies when a Fourier transform is used. In the inviscid case the governing stability equation is singular resulting in a continuous spectrum even for bounded flows.

The continuous spectrum has some noteworthy features relevant to the theme of the present paper. In the limit as $\alpha R \to 0$, no discrete modes exist and the continuous spectrum is the only component that can describe a disturbance. Hultgren & Gustavsson (1981) showed that the eigenfunctions of the continuous spectrum for $\alpha = 0$ have substantial amplitude within the boundary layer and, since the phase velocity is unity, that it represents fast moving disturbances. They further found that large transient growth in the normal vorticity component is possible due to the forcing of the continuous SQ modes by the continuous OS modes. This is the viscous version of the algebraic instability in the boundary layer geometry. Due to the added complexity resulting from the continuous eigenmodes we have chosen to discuss the details of the transient growth for viscous flows only in bounded domains. The majority of the remaining paper will be devoted to that topic.

4.2. SQUIRE'S TRANSFORMATION

The three-dimensional effects emphasized in this paper may have to a large extent been overlooked due to what is known as Squire's theorem. Squire (1933) noted that, by employing the following substitution of variables:

$$\alpha_1 R_1 = \alpha R \tag{46a}$$

$$\alpha_1 = k \tag{46b}$$

the three-dimensional Orr-Sommerfeld equation (38) may be reduced to an equivalent two-dimensional equation:

$$\left[(-\lambda + i\alpha_1 R_1 U)(-D^2 + \alpha_1^2) + i\alpha_1 R_1 U'' + (-D^2 + \alpha_1^2)^2\right] \tilde{v} = 0. \tag{47}$$

One result which is obtained from this transformation is that the first wave to become exponentially unstable (as the Reynolds number increases from zero) is two-dimensional. On the basis of this, together with the fact that he proved that the additional eigenmodes representing purely horizontal modes are always damped, Squire concluded that "For the study of the stability of flow between parallel walls it is sufficient to confine attention to disturbances of two-dimensional type." This is certainly correct if only exponential growth is of interest but if one considers growth in general it puts a severe limitation on the cases worthy of study. If one is

concerned with the development of an intrinsically three-dimensional disturbance, as in this paper, one needs to consider other possibilities of growth which are present because of the additional mechanisms operating for such disturbances. While these other mechanisms will asymptotically be overtaken by exponential decay, no matter how slight, we emphasize that the transient effects will in many cases dominate for finite times. In fact the behavior suggested by the eigenvalues can often be misleading.

4.3. ASYMPTOTIC RESULTS

As in the inviscid case analyzed above the discrete eigenmodes will represent dispersion. It can most easily be analyzed by using the method of steepest descent. This method can also be used for inviscid flows and can be used to justify the introduction of the group velocity in relations (23a,b). In addition, some approximations and extensions of the steepest descent solutions will be discussed in this section.

The method of steepest descent

For large times, one can assume that all higher eigenmodes of the Orr-Sommerfeld equation are exponentially small in comparison to the least-stable mode, in which case, the form of v (in physical space) is given by the Fourier inversion integral:

$$v(x, y, z, t) = \frac{1}{4\pi^2} \int_\alpha \int_\beta \tilde{v}(y; \alpha, \beta) e^{\Psi t} d\alpha d\beta \tag{48}$$

where the phase is defined

$$\Psi t = i(\alpha \frac{x}{t} + \beta \frac{z}{t} - \omega)t, \tag{49}$$

$\tilde{v}$ is the least-stable eigenmode of the OS equation for each value of (α, β) and $\omega = \omega(\alpha, \beta)$ is the dispersion relation. The first asymptotic evaluation of this integral in a hydrodynamic stability context was done by Benjamin (1961) for wave packets on a free-surface, although here we will instead follow the later work by Gaster (1968).

We can evaluate this integral using the method of steepest descents in which we expand the integrand about the stationary point of Ψ, defined by the two conditions

$$c_{gx} = \frac{\partial \omega^S}{\partial \alpha} = \frac{x}{t}, \tag{50a}$$

$$c_{gz} = \frac{\partial \omega^S}{\partial \beta} = \frac{\bar{z}}{t}. \tag{50b}$$

Here, c_{gx} and c_{gz} are the components of the group velocity in the x and z directions respectively and a superscript ^{S} denotes evaluation at the stationary point (α^S, β^S). Note that α^S and β^S may be complex valued and are defined by the above relations such that the group velocity is real. The interpretation of this result is that an observer moving along the rays defined by the group velocity will follow waves with a wavenumber vector which is the real part of (α^S, β^S).

Expanding Ψ about the stationary point and evaluating the integral (48) along the path of steepest descent gives the following result (see Gaster 1968):

$$v = \frac{\tilde{v}(y; \alpha^S, \beta^S)\exp(\Psi^S t)}{2\pi t\sqrt{\left|\frac{\delta^2 \omega^S}{\delta\alpha^2}\frac{\delta^2 \omega^S}{\delta\beta^2} - \left(\frac{\delta^2 \omega^S}{\delta\alpha\delta\beta}\right)^2\right|}}. \tag{51}$$

where

$$\Psi^S t = i(\alpha^S \frac{x}{t + \beta^S}\frac{z}{t} - \omega^S)t. \tag{52}$$

This result is valid along the corresponding group velocity ray and describes a three-dimensional wave packet that propagate in both the streamwise and spanwise directions. The exponential growth of the disturbance is given by the imaginary part of the phase, $\Psi_i^S t$, and has the form

$$\Psi_i^S t = \omega_i^S t - \alpha_i^S x - \beta_i^S z = (\omega_i^S - \alpha_i^S c_{gx} - \beta_i^S c_{gz})t \tag{53}$$

which may be interpreted as a combination of both spatial and temporal growth. The qualitative behavior of this solution is that already seen for the inviscid solutions in figure 6, although that figure was obtained by direct summation using FFTs.

Another general result pertaining to the spanwise spreading of the waves can be derived from (50b) by using the fact that the phase speed of the OS modes depends only on k and αR. Then the spanwise group velocity c_{gz} becomes

$$c_{gz} = \frac{\partial}{\partial\beta}[\alpha c(k, \alpha R)] = \alpha\frac{\partial c\partial k}{\partial k\partial\beta} = \frac{\alpha\beta}{k}\frac{\partial c}{\partial k} = k\frac{\sin 2\theta}{2}\frac{\partial c}{\partial k} \tag{54}$$

where the polar representation, $\alpha = k\cos\theta$, $\beta = k\sin\theta$, has been introduced. For a given k and under the assumption that $\partial c/\partial k$ varies only moderately with αR, it follows that the largest value of c_{gz} is obtained for $\theta = \pi/4$ (Landahl, private communication). In fact, waves with this orientation do exist on the outer edges of laminar wavepackets in boundary layers (Gaster & Grant 1975) and they have also been found behind turbulent spots in that geometry (Wygnanski, Haritonidis & Kaplan 1979). In Poiseuille flow, Henningson (1991) has also found that the waves at the wingtip of localized disturbances are inclined at 45°. Note that in inviscid flow $c = c(k)$, implying that the prediction that the waves with the largest spanwise group velocity are inclined 45° becomes exact.

Real-axis approximation

If the stationary opint (α^S, β^S) has small imaginary parts one may approximate the steepest descent solution by expanding the phase around a nearby point with a real wavenumber vector, (α^R, β^R) say. This will make the group velocity as it is defined in (50a,b) complex valued. In the real axis approximation one neglects the imaginary part of the group velocity, instead using the definition

$$c_{gx} = \frac{\partial \omega_r^R}{\partial \alpha} = \frac{x}{t} \tag{55a}$$

$$c_{gz} = \frac{\partial \omega_r^R}{\partial \beta} = \frac{z}{t}. \tag{55b}$$

where ω_r is the real part of the dispersion relation. Using this definition the phase at the new stationary point is denoted

$$\Psi^R t = i(\alpha^R \frac{x}{t} + \beta^R \frac{z}{t} - \omega^R)t \tag{56}$$

where the superscript ^{R} denotes evaluation at (α^R, β^R). One may proceed to evaluate the integral (48) by the method of stationary phase. The result is similar to (51) except for the fact that all quantities are evaluated at the approximate stationary point (α^R, β^R).

To find the error which is made in the real axis approximation we let ϵ be a small parameter and assume that the following holds

$$\alpha^R - \alpha^R = \mathcal{O}(\epsilon) \quad \beta^S - \beta^R = \mathcal{O}(\epsilon) \tag{57}$$

which implies that the stationary point is close to the real axis. If we further assume that the group velocity is the same for the two cases it is straigh forward to show that error in the pase using the real axis approximation is $\mathcal{O}(\epsilon^2)$, i.e.

$$\Psi^S t = [\Psi^R + \mathcal{O}(\epsilon^2)]t \tag{58}$$

Thus if $t = \mathcal{O}(1/\epsilon)$ or smaller the error in the above approximation is negligible and the real axis approximation may be used. One has to be careful, however, since the solution (51) is an asymptotic result and formally valid only as $t \to \infty$. The quantitative usefulness of the approximate solution for finite values of t and ϵ must thus be experimentally verified, as is the case with all asymptotic results. Gaster (1982) showed that the errors may indeed be large in the real axis approximation whtn t exceeds $\mathcal{O}(1/\epsilon)$.

Relation to kinematic wave theory

The asymptotic expansion resulting in the wave packet can be formally associated with results provided by kinematic wave theory (e.g. Whitham 1974). Kinematic wave theory describes the evolution of a wave train of the form

$$ae^{\imath\theta} \quad \theta = \Psi t = \alpha x + \beta z - \omega t \tag{59}$$

Note that the time variable is now included in the definition of θ. This is done in order to be able to define the wavenumbers and frequency in the following, more general manner:

$$\alpha = \frac{\partial \theta}{\partial x}; \quad \beta = \frac{\partial \theta}{\partial z}; \quad \omega = \frac{\partial \theta}{\partial x}. \tag{60}$$

This anticipates the application of the theory to inhomogeneous media where the wave properties are allowed to vary slowly in space and time. Equations relating the wavenumbers and the frequency can be found by taking cross derivatives of the definitions (60). These equations can be put in characteristic form using the total time derivative along rays defined by the group velocity, i.e.

$$\frac{d}{dt} = \frac{\partial}{\partial t} + c_{gx}\frac{\partial}{\partial x} + c_{gz}\frac{\partial}{\partial z}. \tag{61}$$

Here the components of the group velocity are equivalent to the ones defined by equations (50a,b). For a homogeneous media, the final equations can be put into the form (see Whitham 1974)

$$\frac{d\alpha}{dt} = 0, \quad \frac{d\beta}{dt} = 0 \tag{62}$$

along the rays

$$\frac{dx}{dt} = c_{gx}, \quad \frac{dz}{dt} = c_{gz} \tag{63}$$

These equations readily give the same results as found in the steepest descent case, namely that the wave numbers are constant along the group velocity rays.

In addition to the wavenumbers we need an equation for the amplitude. For dissipative media, where the phase θ is allowed to be complex, an equation for the amplitude squared was derived independently by Jimenez & Whitham (1976) and Chin (1976). Here we will use a slightly modified form (Landahl 1982)

$$\frac{da^2}{dt} = -a^2\frac{\partial}{\partial x}c_{gx} - a^2\frac{\partial}{\partial z}c_{gz} - 2a^2\theta_i \tag{64}$$

This equation is valid along the group velocity rays and θ_i denotes the imaginary value of θ. Note that the group velocity is real since we have used the definition

originating from the steepest descent solution, and that this in general implies that the wavenumbers will take on complex values.

It is straight forward to show that the steepest descent solution derived earlier satisfies the kinematic wave equations exactly. The solution to (64) gives the same exponential growth term as well as the $1/t$ dependence. The latter originates from the divergence of the group velocity rays, all of which start at the origin. The kinematic wave equations allow more general solutions, however, such as ones with initial conditions located outside of the origin. For such initial conditions the rays may also converge giving rise to wave energy focusing and growing solutions.

In many cases an approximation of the kinematic wave equations, corresponding to the real axis approximation, have been used. One simply assumes that the wavenumbers are real and neglects the resulting imaginary part of the group velocity. In analogy with the real axis approximation, this is associated with $\mathcal{O}(1)$ errors if one is interested in solutions for times that are larger then $\mathcal{O}(1/\epsilon)$. The approximation has often been applied in the case of an inhomogeneous background. To take the inhomogeneity into account, spatial derivatives of the dispersion relation, ω, need to be added to the right hand sides of equations (62). If the background variations are on a scale which is $\mathcal{O}(1/\epsilon)$ compared to the wavelength of a typical wave, Chin (1976) has shown that the extended theory has the same region of validity as the real axis approximation. This extended theory has been used among others by Landahl (1972) in a study of the breakdown of Tollmien-Schlichting waves, and by Henningson (1989) to study the propagation of the wave packet outside the wingtip of a turbulent spot in plane Poiseuille flow. In both of these studies the wave train was already formed when the equations were applied, thus limiting the time of interest to the region of validity of the approximate theory. Viewed in this light the criticism of Landahl's work by Stewartson (1974), who essentially attacked the real-axis approximation, seems somewhat misdirected.

4.4. THE FORCED PROBLEM AND TRANSIENT GROWTH

In addition to the dispersive effects discussed in the previous section, the viscous initial value problem allows for the possibility for initial transient growth which, in many cases, overshadow the asymptotic behavior predicted by the eigenmodes. The most striking example is the viscous counterpart of the inviscid algebraic instability. For simplicity we assume that only the l:th OS-mode is excited initially. Thus we have the following solution for the normal velocity:

$$\hat{v} = \tilde{v}_l e^{-\lambda_l t/R} \tag{65}$$

Having the solution to the normal velocity we solve the equation for the normal vorticity (11) using (65) in the right hand side. The solution consists of a homogeneous and a particular solution, which we can write in the following form:

$$\hat{\eta} = \hat{\eta}_{hom} + \tilde{\eta}_l^p e^{-\lambda_l t/R} \tag{66}$$

where the time dependence of the particular solution has been extracted. In order to solve for $\hat{\eta}_{hom}$ and $\bar{\eta}_l^p$ we assume that both can be expanded in the eigenmodes of the homogeneous part of the normal vorticity equation, i.e. in Squire modes. For the homogeneous part we have the expansion

$$\hat{\eta}_{hom} = \sum_{j=1} B_j \tilde{\eta}_j e^{-\sigma_j t/R} \tag{67}$$

where B_j are the expansion coefficients and $\bar{\eta}_j$ are the Squire modes corresponding to the eigenvalues of the Squire equation, σ_j. For the particular part we assume a similar expansion without the time dependence. When these expansions are substituted into equation (11) the following expression for the normal vorticity results

$$\hat{\eta} = \sum_{j=1} C_j \tilde{\eta}_j e^{-\sigma_j t/R} + \sum_{j=1} D_{jl} \frac{e^{-\lambda_l t/R} - e^{-\sigma t/R}}{\lambda_l - \sigma_j} \tag{68}$$

where the expansion coefficients are

$$C_j = \int_{-1}^{1} \hat{\eta}_0 \tilde{\eta}_j dy \tag{69}$$

$$D_{jl} = i\beta R \int_{-1}^{1} U' \tilde{v}_l \tilde{\eta}_j dy \tag{70}$$

This expression was originally derived by Henningson (1991) and a related version was used by Gustavsson (1991) in his calculation of transient growth. Gustavsson also showed that this form of the solution is equivalent to the solution he derived using the Laplace transform technique.

    In order to see the nature of the transient growth possible in the normal vorticity solution we will proceed to Taylor expand (68) assuming the quantity t/R is small. The first term in the expansion becomes

$$= \sum_{j=1}^{J} C_j \bar{\eta}_j \left[1 - \sigma_j \frac{t}{R} + O\left(\frac{t^2}{R^2}\right) \right]$$

$$- \sum_{j=1}^{J} D_{jl} \bar{\eta}_j \left[\frac{t}{R} - (\lambda_l + \sigma_J) \frac{t^2}{2R^2} + O\left(\frac{t^3}{R^3}\right) \right] \tag{71}$$

where the growth can be expected to be largest for the second term since the coefficient D_{jl} is proportional to R.

    To see the equivalence with the inviscid case we can consider finite times and assume that the Reynolds number approaches infinity. When this limit is taken in

the above expansion one has to be careful since the definition of the eigenvalues includes a factor R, which together with the factor of R in the coefficient D_{jl} makes all of the terms in the series of the same order. For $\alpha \to 0$, however, it is possible to show that the eigenvalues are not proportional to R. We find instead that

$$\lambda_l = i\omega_l^{OS} = \mathcal{O}(1) \tag{72a}$$

$$\sigma_j = i\omega_j^{SQ} R = \mathcal{O}(1) \tag{72b}$$

along the spanwise wavenumber axis. This implies that the angular frequencies for these waves are inversely proportional to the Reynolds number and that they coalesce as the Reynolds number approaches infinity. This can be interpreted as a near degeneracy between the viscous modes for large R. The $\mathcal{O}(1)$ terms in the series (71) can now be summed, we find

$$\hat{\eta} = \hat{\eta}_0 - i\beta U' \hat{v}_0 t + O(\frac{t}{R}) \tag{73}$$

which shows that the limit of the viscous solution for $\alpha = 0$ is identical to what was found in the inviscid analysis. Thus the inviscid algebraic instability is in the viscous case related to a near-degeneracy between the viscous modes along the spanwise wavenumber axis.

Gustavsson (1991) calculated the growth obtained from an initial condition for the normal velocity consisting of the least stable OS-mode, normalized to unit energy. He assumed that the initial normal vorticity was zero and solved for its subsequent time dependence using equation (68). Figure 8 shows the energy density of the normal vorticity and it can be seen that, even at this rather low Reynolds number, large transient growth is still possible.

4.5. GENERALIZED EIGENFUNCTION EXPANSION

A more general method for solving the complete problem is to utilize a formal eigenfunction expansion in the linear eigenmodes. We assume that the normal velocity and the normal velocity can be written

$$\begin{bmatrix} \hat{v} \\ \hat{\eta} \end{bmatrix} \sim \begin{bmatrix} \tilde{v} \\ \tilde{\eta} \end{bmatrix} e^{-\lambda t/R} \tag{74}$$

and introduce that into equations (10) and (11) to find the *system* of equations

$$-\lambda \begin{bmatrix} k^2 - D^2 & 0 \\ 0 & 1 \end{bmatrix} \begin{bmatrix} \tilde{v} \\ \tilde{\eta} \end{bmatrix} +$$

$$\begin{bmatrix} i\alpha RU(K^2 - D^2) + i\alpha RU'' + (k^2 - D^2)^2 & 0 \\ i\beta RU' & i\alpha RU + k^2 - D^2 \end{bmatrix} \begin{bmatrix} \tilde{v} \\ \tilde{\eta} \end{bmatrix} = 0 \tag{75}$$
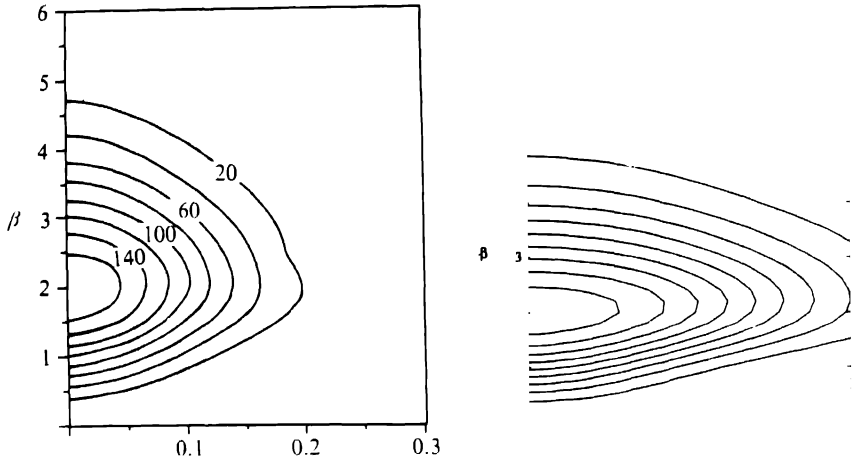
Fig. 8.   Contour curves in the (α, β)-plane for growth of energy density at $t/R = 0.08$ and $R = 1000$. (a) Using one OS modes as an initial condition. (From Gustavsson 1991). (b) Using the optimal combination of OS Modes. Contour spacing is 20.

here written in matrix form. Recall that with this definition of the eigenvalue the homogeneous operators above are only dependent on the two parameters $(k, \alpha R)$. Since the off-diagonal term in the second matrix operator contains the factor βR, however, the particular solution to that equation will depend on that third parameter, unless the normal vorticity itself is re-scaled.

The solution to the system (75), together with the boundary conditions $\tilde{v} = D\tilde{v} = \eta = 0$ at solid walls, gives the eigenmodes of the system. These can be divided into the two families previously discussed. The first are the OS-modes which consist of eigensolutions to the normal velocity equation, the first component of (75), *together* with its associated normal vorticity, solutions of the second component of (75). The second are the SQ-modes which are eigensolutions to the system when the normal velocity is zero. Although both the OS and the SQ eigenvalues are modes of the same system we will for clarity, and to conform with the previous notation, denote them λ_l and σ_j, respectively. The corresponding eigenmodes will be represented as

$$\left.\begin{array}{c} \tilde{v}_l \\ \tilde{\eta}_l^p \end{array}\right] \quad \text{OS-modes;} \qquad \text{SQ-modes} \qquad\qquad (76)$$

We use the symbol η_l^p for the normal dependence of the normal vorticity component of the OS-mode to emphasize that it is equivalent to the particular normal vorticity used in the previous section. Since the OS and SQ eigenmodes for a bounded

flow form a complete system and can be used to express a formal solution for the three-dimensional initial value problem. The solutions to the system (75) can be written

$$
\hat{v} \atop \hat{\eta} \Big] = \sum_{l=1}^{L} k_l \left[\begin{matrix} \tilde{v}_l \\ \tilde{\eta}_l^p \end{matrix} \right] e^{-\lambda_l t/R} + \sum_{j=1}^{J} B_j \quad \begin{matrix} 0 \\ \tilde{\eta}_j \end{matrix} \Big] e^{-\sigma_j t/R} \tag{77}
$$

Henninson & Schmid (1992) showed that the normal vorticity part of (77) is equivalent to the expression (68). This can be seen if the particular adjoint normal velocity and the particular normal vorticity are expanded in eigenmodes of their respective homogeneous operators.

The expansion coefficients K_l and B_j can be calculated at $t = 0$, using the initial values and the solutions of the system adjoint to (75). Henningson & Schmid (1992) derived the following adjoint system

$$
-\lambda \left| \begin{matrix} k^2 - D^2 & 0 \\ 0 & 1 \end{matrix} \right] \left[\begin{matrix} \tilde{v}^+ \\ \end{matrix} \right| +
$$

$$
\left. \begin{matrix} -\imath \alpha RU(k^2 - D^2) + \imath \alpha RU'D + (k^2 - D^2)^2 & \imath \beta RU' \\ 0 & -\imath \alpha RU + k^2 - D^2 \end{matrix} \right] \left[\begin{matrix} \tilde{v}^+ \\ \eta^+ \end{matrix} \right] = 0 \tag{78}
$$

The adjoint system is subject to the same boundary conditions as the previous one, and the eigenvalues can also be shown to be complex conjugates. It is interesting to note that the off diagonal term has moved to the adjoint normal velocity equation implying that the adjoint modes have the form

$$
\begin{matrix} \tilde{v}^+ \\ 0 \end{matrix} \quad \text{Adj. OS-modes,} \qquad \begin{matrix} \tilde{v}^{p+} \\ \tilde{\eta}_j^+ \end{matrix} \quad \text{Adj. SQ-modes.} \tag{79}
$$

The adjoint modes satisfy bi-orghogonality conditions with the regular OS and SQ modes. These can be used to derive the expressions for the expansion coefficients in the solution to the initial value problem, we find

$$
K_l = \int_{-1}^{1} \tilde{v}_l^+ * (-D^2 + k^2) \hat{v}_0 dy \tag{80}
$$

$$
B_j = \int_{-1}^{1} \left[\tilde{v}_j^{p+*} (-D^2 + k^2) \hat{v}_0 + \tilde{\eta}_j^{+*} \hat{\eta}_0 \right] dy \tag{81}
$$

Note that the coefficient for the SQ modes are dependent on the initial normal velocity. This is a consequence of the forcing term in equation (11) and represents
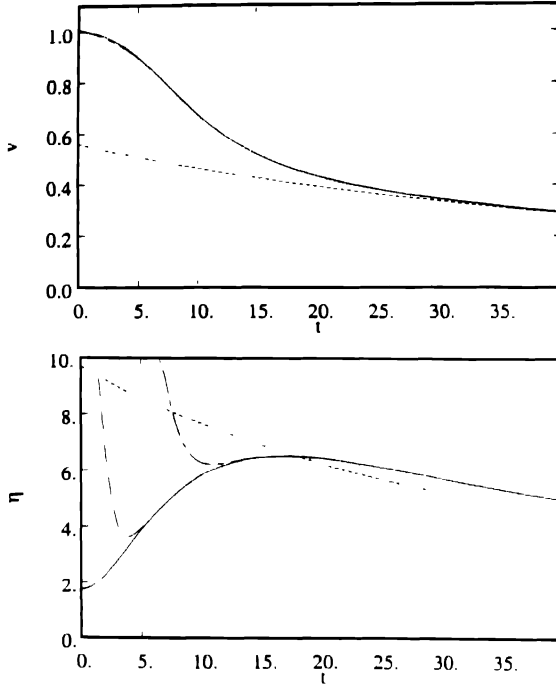
Fig. 9.   Time evolution of the integrated *rms* values for (a) the normal velocity and (b) the normal vorticity for a localized disturbance at $R = 300$. Solid curves represent an exact solution obtained from numerical simulations, while the dashed, dotted, chain-dashed and chain-dotted curves represent the eigenfunction expansions using $L = J = 1, 4, 10$ and 15 respectively. The curves for $L = J = 20$ are also included but cannot be distinguished from the numerical simulation results. From Henningson, Lundbladh & Johansson (1993).

the lift-up effect in terms of the modal decomposition. The potential for growth can be seen directly from equation (77). Suppose that we expand an initial condition with zero normal vorticity. This will excite a number of OS modes, in order to represent the normal velocity. Each OS mode has an associated particular normal vorticity η_l^p, which now needs to be canceled out by an appropriate combination of SQ modes. Thus both OS and SQ modes are excited by an initial condition of zero normal vorticity. As the disturbance evolves downstream each mode propagates with the characteristics given by its eigenvalue. Since the phase speeds and decay rates are different the modes will propagate apart and the cancellation that occurred initially will not persist. Thus the disturbance will experience transient growth in the normal vorticity component. It should be noted that the particular normal vorticity in an OS mode is typically orders of magnitude larger than the normal velocity, as can be seen from the large off-diagonal term (proportional to βR) in the second component of the system (75), thus giving rise to the cancellation effects even if the disturbance has a moderate initial normal vorticity.

The cancellation effects described are only possible because of the non-orthogonality of the eigenmodes and are mathematically a result of the non-normality of the operators governing the above systems (an operator is normal if it commutes with its adjoint). Solutions to problems governed by non-normal operators may only show the behavior predicted by the associated eigenvalues as $t \to \infty$. Initially they are not necessarily mode-like and have the possibility of large transient growth although all eigenvalues predict decay. This behavior has been seen in a number of different applications, including the analysis of the stability of numerical discretization schemes, the analysis of iterative methods in linear algebra as well as in the area of hydrodynamic stability. Most of the work is recent and is further discussed in Reddy (1991) and Trefethen (1992). Hydrodynamic stability results can also be found in Farrell (1988), Butler & Farrell (1992), Reddy, Schmid & Henningson (1993), Reddy & Henningson (1993) and Trefethen, Trefethen, Reddy & Driscoll (1993).

As an example of the properties of the eigenfunction expansion discussed we will consider an application to the development of a localized disturbance. Henningson, Lundlbadh & Johansson (1993) used the expansion (77) with an initial condition similar to that given in Fig. 4. Note that a number of streamwise and spanwise Fourier components have to be included to capture the streamwise and spanwise variation of the localized disturbance. For each such wavenumber a number of normal modes have to be used. Figure 9 shows the time evolution of the *rms* values of the normal velocity and the normal vorticity (for the complete development of the localized disturbance see Section 4.7). One, four, ten, fifteen and twenty of the least stable modes are used in the eigenfunction approximations. Four modes capture the behavior of the normal velocity after $t = 20$ whereas one mode is sufficient after $t = 30$. The cases with a larger number of modes fall on top of the exact solution found from a numerical simulation. The convergence of the expansion for the normal vorticity is not as regular. We have to increase the number of modes to a total of 40 (20 OS and 20 SQ modes) to be able to capture the initial transient growth phase. The 15 least stable eigenvalues of each type from the peak of the initial energy spectrum is shown in Fig. 7. There is large initial cancellation between non-orthogonal modes causing the transient growth. After the peak there is a mode like behavior as the least stable eigenvalues governs the decay. The fact that the expansions with insufficient number of modes overshoots initially for the normal vorticity component is again a result of the non-orthogonality of the modes. If the modes were orthogonal all partial sums would have a smaller energy than the exact solution. This gives an example of typical behavior of an initial value problem governed by a non-normal operator.

4.6. OPTIMAL DISTURBANCES

In the sections above we have found that large transient growth is possible for certain initial conditions. The question of optimizing this growth with respect

to the initial condition naturally arises. This can easily be answered using the eigenfunction expansion presented in Section 4.5. For this purpose it is instructive to write the solution (77) in the following more compact form

$$\hat{q} = \sum_{n=1}^{N} \kappa_n^0 \tilde{q}_n e^{-\lambda_n t/R} \tag{82}$$

where

$$\tilde{q}_n \quad \begin{matrix} v_n \\ \tilde{\eta}_n \end{matrix} \tag{83}$$

now denotes both the OS and the SQ-modes, depending on the index n, λ_n their respective eigenvalues and κ_n^0 the expansion coefficients for the initial condition. Here we have restricted the solution to the space spanned by the first N eigenmodes with maximal real parts. A natural set of basis vectors for this space is the eigenfunctions, implying that the solution is expressed in terms of an N-vector of expansion coefficients. Let $\kappa_0 = (\kappa_1^0, \ldots, \kappa_N^0)^T$ be the vector expressing the initial condition. Equation (82) this implies that the solution for subsequent times can be written

$$\kappa = \quad \begin{matrix} e^{-\lambda_1 t/R} \\ \\ e^{-\lambda_N t/R} \end{matrix} \quad \kappa_0 \equiv e^{-\Lambda t/R} \kappa_0 \tag{84}$$

where κ is the vector of expansion coefficients of the disturbance at time t and Λ is a matrix with the eigenvalues on the diagonal. We have here used the matrix exponential to simplify the notation, which for a diagonal matrix take the simple form shown above.[*]

We will measure the optimum in terms of the largest energy growth, given unit initial energy. To find the energy of disturbance we use equation (13). If the expansion (82), together with the definition of κ is used in (13) we can write the energy as the following quadratic form:

$$E = \kappa^H A \kappa \tag{85}$$

where the superscript ^{H} denotes the complex conjugate transpose operation and a component of the matrix A takes the form

$$A_{nm} = \frac{1}{2k^2} \int_{-1}^{1} (D\tilde{v} *_m D\tilde{v}_n + k^2 \tilde{v} *_m \tilde{v}_n + \tilde{\eta} *_m \tilde{\eta}_n) dy \tag{86}$$

[*] For a definition of the matrix exponential of a general matrix see Golub & van Loan (1983).

Note that A is not diagonal since the modes are not orthogonal. If the Hermitian matrix A is decomposed into $A = F^H F$, we find that the energy can be written

$$E = \kappa^H F^H F \kappa \equiv \|F\kappa\|_2^2 = \|\kappa\|_E^2 \qquad (87)$$

The energy of the perturbation is here written as a weighted 2-norm of the expansion coefficients. This energy norm is denoted by $\| \cdot \|_E$.

To find the optimal growth possible one need only take the energy norm of the matrix exponential, using the ususal definition of a matrix norm (Golub & van Loan 1983). We find

$$E_{max}^{1/2}(t) = \sup_{\|\kappa_0\| \neq 0} \frac{\|e^{-\Lambda t/R}\kappa_0\|_E}{\|\kappa_0\|_E} =$$

$$\sup_{\|F\kappa_0\| \neq 0} \frac{\|Fe^{-\Lambda t/R}F^{-1}F\kappa_0\|_2}{\|F\kappa_0\|_2} = \|Fe^{-\Lambda t/R}F^{-1}\|_2 \qquad (88)$$

where we have transformed to a weighted 2-norm to simplify the calculation. $E_{max}(t)$ is the envelope of maximum growth, implying that there is a particular disturbance which will attain that growth at a given time. The maximum of the curve thus gives the global maximum for the particular Fourier component considered. The initial condition giving the maximum growth as well as the calculation of the weighted 2-norm can easily be done using singular value decomposition.

A similar method to the one presented here has been used by Farrell (1988) to calculate optimal growth for two-dimensional disburbances. He found that even in that case growth of almost two orders of magnitude in energy was possible. Similar results were found by Reddy, Schmid & Henningson (1993). In the three-dimensional case, however, the growth can be much larger as seen from the results in the sections above. Recent results, adapted from Reddy & Henningson (1993), are seen in Fig. 8 where it can be noted that the energy growth can be increased compared to that obtained from choosing a single OS-mode as the initial condition, particularly away from the spanwise wavenumber axis. Optimal disturbances and growth for the three-dimensional case has also been calculated by Buter & Farrell (1992). They considered Couette, Poiseuille and Blasius boundary layer flows, where similar results were found. The paper by Trefethen, Trefethen, Reddy & Driscoll (1993) also considers optimal growth of initial perturbations in shear flow, in addition to other forms of optimal excitation.

4.7. NUMERICAL SOLUTIONS

The transient growth analyzed for specific wavenumber combinations may also result in growth of localized disturbances if they have initial energy in the regions of wavenumber space associated with the growth. In this section we give an example of such a disturbance. Henningson, Lundlbadh & Johansson (1993) calculated
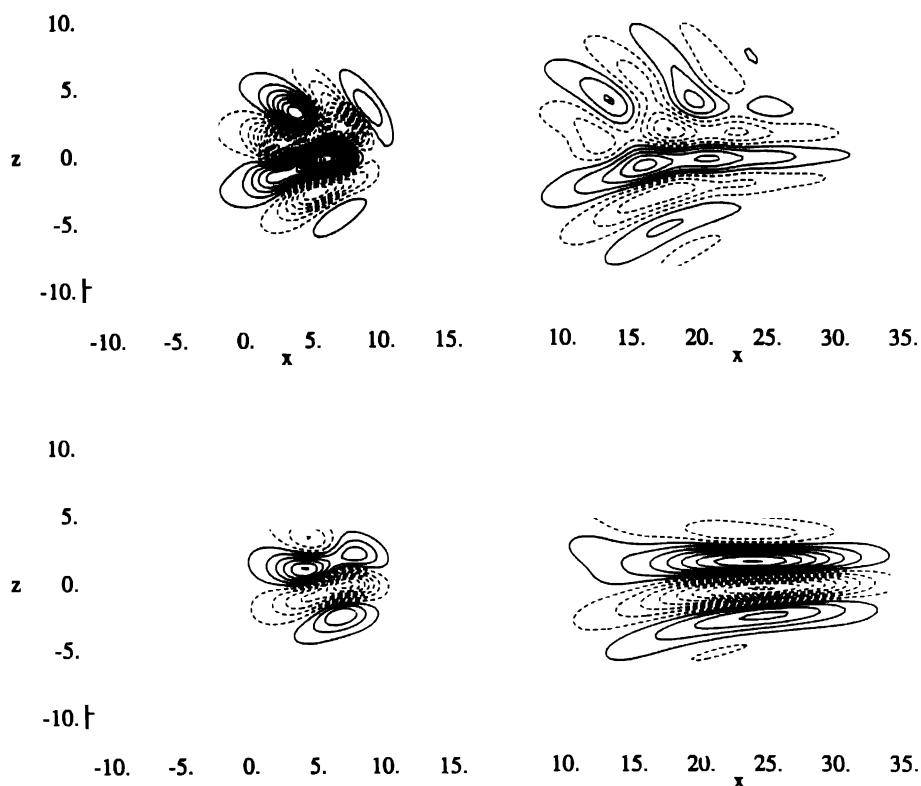
Fig. 10. Contours of velocity at $y = -0.56$ for a $\theta = 20°$ disturbance. (a) Normal velocity at $t = 10$. (b) Normal velocity at $t = 40$. (c) Streamwise velocity at $t = 10$. (d) Streamwise velocity at $t = 40$. The contour spacing of the streamwise velocity is 20 times that of the normal velocity. From Henningson, Lundbladh & Johansson (1993).

the development of the localized disturbances seen in Fig. 4. Figure 10 shows the streamwise and normal velocity for times $t = 10$ and $t = 40$. The normal velocity shows the typical decaying wavepacket while the streamwise velocity shows relatively large amplitude streaky structures. Note that although the initial streamwise and normal velocity were of the same order the amplitude of the streamwise velocity is about 30 times that of the normal velocity at $t = 40$. This is due to the lift-up effect and mostly associated with the normal vorticity component.

When the initial disturbance seen in Fig. 4 is turned around the normal symmetry axis the distribution of energy in wavenumber space also changes. For $\theta = 0$ there is no energy along the spanwise wavenumber axis while increasing the angle up to $\theta = 45°$ centers a large amount of the initial energy around that axis. Thus one would expect to increase the amount of transient growth by increasing θ. Figure

11 shows that this is the case and that the total energy of a subcritical localized disturbance can indeed grow substantially from linear effects alone.

5. Modeling of coherent structures in turbulent flows

Much of the ideas developed in the preceding sections have some counterpart in the modeling of coherent structures in fully developed turbulent shear flows. It is now well established (see, for example, Kim, Kline & Reynolds 1971; Blackwelder & Kaplan 1976; Johansson Alfredsson & Kim 1991) that the near-wall region of a turbulent boundary layer is characterized by well-defined flow structures which, once formed, retain their coherence over considerable distances and for times much longer than the statistical correlation time for a typical turbulent flow. These structures are typically characterized by elongated "streaks" of high- and low-speed fluid, spaced at approximately 100 wall units.[*] In the wall-normal direction, the coherent structures are characterized by three-dimensional, localized shear layers, inclined at an angle to the wall propagating at an average velocity of about $11u_*$. In the flow visualization experiments of Kim et al. (1971) the shear layers appear to break down rather rapidly, in a process which has been called *bursting*. Using a conditional sampling technique to isolate the bursts Blackwelder & Kaplah (1976) found that they were associated with inflectional velocity profiles and that a majority of the turbulence production occurred with these structures. Johansson et al. (1991) studied the three-dimensional nature of the coherent structures using numerically simulated velocity fields. They did not find the violent breakup described in the flow visualization experiments, but rather slowly meandering low and high velocity streaks. Again the shear layers associated with the streaks were found to be associated with most of the turbulence production, although the events only occupied a small portion of the near wall region.

The qualitative resemblance between these shear-layer structures in turbulent flows and those found to result from localized disturbances in laminar flows (e.g. Fig. 5) suggests that the dynamics of near-wall turbulence may be modeled by localized disturbance theory. The idea that near-wall turbulence structure might be described using linear theory was first proposed by Landahl (1968) and subsequently elaborated upon by Bark (1975). In this approach, the velocity field is first decomposed in the standard Reynolds-averaged manner into a mean and fluctuating component, $U(y)\delta_{1i} + u_i$, where U is the ensemble-averaged mean turublent velocity profile. The fluctuating component is further divided into a conditionally averaged velocity field and a random reminder, $u_i = \tilde{u}_i + u'_i$. If this decomposi-

---

[*] "Wall" variables, are quantities non-dimensionalized using the kinematic viscosity v and the friction velocity u_*, where $u_* = \sqrt{\tau_w/\rho}$, τ_w is the shear stress at the wall and ρ is the fluid density.
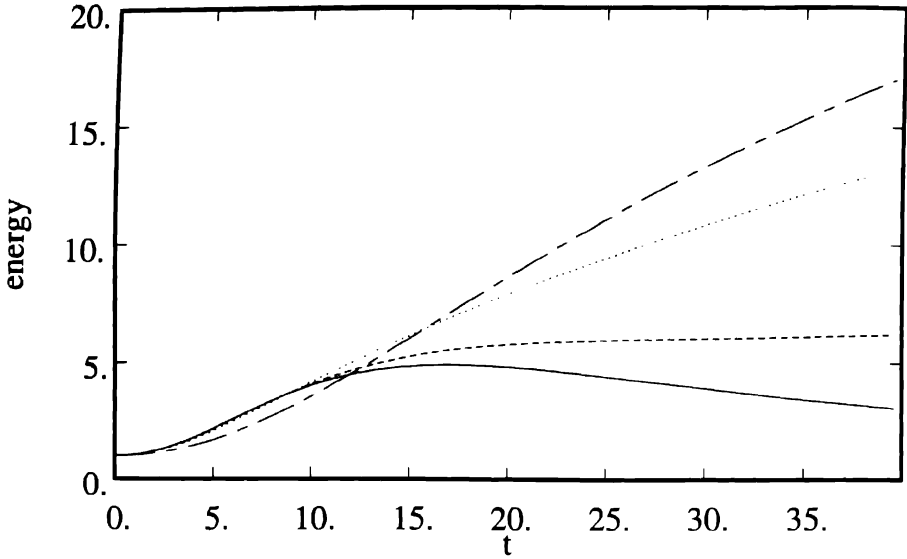
Fig. 11.   Energy for the small amplitude disturbances. Solid: $\theta = 0$; dash: $\theta = 10°$, dot: $\theta = 20°$, chain-dash: $\theta = 45°$, normalized by initial energy. From Henningson, Lundbladh & Johansson (1993).

tion is substituted into the Navier-Stokes equations (1) and the ensemble averaged equations are subtracted from the conditionally averaged equations we obtain

$$\frac{\tilde{D}}{Dt}(\tilde{u}_i + U\partial_{1i}) = -\frac{\partial \tilde{p}}{\partial x_i} + \frac{1}{R}\nabla^2 \tilde{u}_i + \frac{\partial \tilde{\tau}_{ij}}{\partial x_j} \tag{89}$$

where

$$\frac{\tilde{D}}{Dt} = \frac{\partial}{\partial t} + (\tilde{u}_j + U\partial_{1j})\frac{\partial}{\partial x_j} \tag{90a}$$

$$\tau_{ij} = \overline{u_i u_j} - \overline{u'_i u'_j} \tag{90b}$$

The overbar in the definition of the Reynolds stress signifies the ensemble average operation.

The above equations is the starting point for most of Landahl's models of coherent structures and bursting. He has developed the model in a series of papers (Landahl 1967, 1975, 1978, 1983, 1990) during the last 25 years. We will not attempt to present a comprehensive review of this work, but rather try to extract some of the basic features of the models.

There are three key assumptions that form the basis for much of Landahl's work in this area. The first is that the Reynold stresses at bursting act instantaneously to

create a modified flow field. The second is that the flow features of the evolving disturbance are representative of the coherent structures seen in turbulence. The third is that the evolution of the coherent structure is associated with some type of instability or breakdown to create a new burst. This closes the circle and would explain how the flow is able to maintain the bursting process. Landahl uses both linear and non-linear theory to investigate the development of the initial condition set up by the burst.

5.1. LAGRANGIAN SOLUTION TO THE INITIAL VALUE PROBLEM

Although a number of the ideas of Landahl parallels what has already been presented in this paper we will still discuss the methods he uses to solve and approximate the initial value problem posed in equation (89), since he uses a different solution technique. Assuming that the viscous terms are negligible the equations for the streamwise and spanwise momentum can be integrated following along a fluid particle

$$\tilde{u} + U = \tilde{u}_0(\xi, \eta, \zeta) + U(\eta) + \int_0^t \left(-\frac{\partial \tilde{p}}{\partial x} + \frac{\partial \tilde{\tau}_{1j}}{\partial x_j} \right) Dt \tag{91a}$$

$$x = \xi + \tilde{u}_0 t + U(\eta)t \int_0^t (t - t_1) \quad \cdot \frac{\partial \tilde{p}}{\partial x} + \frac{\partial \tilde{\tau}_{1j}}{\partial x_j} \tag{91b}$$

and

$$\tilde{w} = \tilde{w}_0 t(\xi, \eta, \zeta) + \int_0^t \left(-\frac{\partial \tilde{p}}{\partial z} + \frac{\partial \tilde{\tau}_{3j}}{\partial x_j} \right) Dt \tag{92a}$$

$$z = \xi + \tilde{w}_0 t \int_0^t (t - t_1) \left(-\frac{\partial \tilde{p}}{\partial z} + \frac{\partial \tilde{\tau}_{3j}}{\partial x_j} \quad Dt_1 \right) \tag{92b}$$

The Lagrangian coordinates (ξ, η, ζ) of a fulid particle are here defined to equal their position in Eulerian coordinates at $t = 0$. The relation between the Lagrangian and Eulerian coordinates at later times are found from the Jacobian of their coordinate transformation,

$$J = \frac{\partial(x, y, z)}{\partial(\xi, \eta, \zeta)} = 1 \tag{93}$$

where we have used the fact that the Jacobian equals unity in an incompressible flow. If the Jacobian is evaluated one may solve the equation $J = 1$ using the methods of characteristics. Along lines normal to the wall, the following system governs the relation between the two coordinate pairs

$$\frac{d\xi}{dy} = x_\zeta z_\eta - x_\eta z_\zeta \tag{94a}$$

$$\frac{d\eta}{dy} = x_\xi z_\zeta - x_\zeta z_\xi \tag{94b}$$

$$\frac{d\zeta}{dy} = x_\eta z_\xi - x_\xi z_\eta \tag{94c}$$

These equations form the starting point of most of the investigations made by Landahl into the evolution of coherent structures in turbulence. They cannot be solved without some additional assumptions about the pressure or without knowledge about the Reynolds stress terms. We will discuss those issues below.

5.2. MODELING OF THE FLOW STRUCTURE AFTER A TURBULENT BURST

A key element in the model is the assumption that a concentrated peak in the Reynolds stress, $\tilde{\tau}_{ij}$, acts impulsively to initiate a localized disturbance or coherent structure. This assumption is justified by the assumed infectional nature of the instability causing the burst. Such an instability would take place on a time scale which is much smaller than a typical convection time for the disturbance. Landahl further assumes that the Reynolds stresses due to the non-coherent fluctuations are much larger than the mean Reynolds stresses. The Reynolds stresses are thus assumed to satisfy

$$\frac{\partial \tilde{\tau}_{1j}}{\partial x_j} \qquad -u_1' u_j' = -F_{1y}\delta t \tag{95a}$$

$$\frac{\partial \tilde{\tau}_{3j}}{\partial x_j} \qquad -u_3' \overline{u_j'} = -F_{3y}\delta t \tag{95b}$$

Using these expressions in equations (91a) and (92a) we see that they can be used to specify new initial conditions for the initial value problem. We may define

$$\tilde{u}^i = \tilde{u}_0 - F_{1y} \tag{96a}$$

$$\tilde{v}^i = \tilde{v}_0 - F_{1x} - F_{3z} \tag{96b}$$

$$\tilde{w}^i = \tilde{w}_0 - F_{3y} \tag{96c}$$

where it has been assured that the new initial conditions satisfy continuity. The modeling of the stresses are now done as follows:

1. $F_{1y} = \tilde{u}_0$ since the inflectional instability tends to remove the disturbance that caused the inflection.
2. $F_1 = f(x)g(y)h(z)$, i.e. F_1 is assumed separable, and $F_3 = 0$.
3. $f(x) = \exp(-x^2/l_1^2)$ since averages over many statistically independent events tend to be Gaussian.

4. $g(y) = Cy^3/\delta^3 \exp(-y^2/\delta^2)$ which is obtained from the normal dependence of the Reynolds stress during bursting (Bark 1975).

5. $h(z) = 1 - 2z^2/l_3)\exp) - z^2/l_3^2)$ to obtain the correct symmetry properties on $\tilde{w}_0$ once $\tilde{v}_0$ has been assumed to vanish. Note that $\tilde{w}_{0z} = -\tilde{u}_{0x} = F_{1yx}$ from continuity.

The new initial condition is the counter rotating vortex pair seen in Fig. 4 and used in the numerical examples of localized disturbances above. The final form is

$$\tilde{u}^i = 0 \tag{97a}$$

$$\tilde{v}^i = g(y)x/l_1(1 - 2z^2/l_3)e^{-(x/l_1)^2-(z/l_3)^2} \tag{97b}$$

$$\tilde{w}^i = g'(y)xz/l_1 e^{-(x/l_1)^2-(z/l_3)^2} \tag{97c}$$

Here l_1, δ and l_3 are characteristic scales of the bursting event in the respective coordinate direction.

5.3. THE DEVELOPMENT OF A FLAT EDDY

If one assumes that $l_1 \gg \delta$ and $l_3 \gg \delta$, i.e. that the horizontal length scales are much greater than the normal one, the horizontal pressure gradients can be neglected in (91b) and (92b). Landahl argued that this is the case for a typical coherent structure observed in a turbulent flow. If this assumption in addition to the initial condition derived above is used in equations (94a–c) we obtain

$$\frac{d\xi}{dy} = -U_\eta(1 + \tilde{w}_\zeta^i t)t \tag{98a}$$

$$\frac{d\eta}{dy} = 1 + \tilde{w}_\zeta^i t \tag{98b}$$

$$\frac{d\zeta}{dy} = -\tilde{w}_\eta^i t + U_\eta \tilde{w}_\xi^i t^2 \tag{98c}$$

These equations can be integrated to find the positions of the fluid particles at a given time. The Lagrangian coordinates associated with the position of the fluid particles can then be used in equations refeq:u-lag and (92a) to find the new velocity field at the specified time. Note that this model assumes that the horizontal momentum is constant and that the fluid particles evolve under the constraint of continuity. Thus one is essentially considering a flow where lift-up is the sole effect determining its evolution.

One of the most striking aspects of the solution to these equations is the singularity that develops in finite time. It can easily be seen to occur if (98b) is solved by direct integration. We obtain

$$l_m = y - \eta = \int_0^\eta \frac{\bar{w}_\zeta^i t\, d\eta}{1 + \bar{w}_\zeta^i t} \tag{99}$$

where the mixing length l_m has here been defined in analogy with Prandtl's (1925) model. The integral approaches infinity as $t \to -1/\bar{w}_\zeta^i$, implying that the fluid particles approach infinity. Russell & Landahl (1984) argued that the behavior close to the singularity may describe the flow field at bursting. Henningson (1985) further showed that a trace of the particle positions as the singularity was approached compared favorably with the bubble wire experiments of Kim et al. (1971). In both investigations fluid particles were seen to rapidly move normal to the wall as a low speed fluid were lifted up. Although the influence of the pressure can no longer be neglected in the vicinity of the singularity the simple model may still capture an essential part of the bursting process.

The singularity discussed is inherently non-linear. To see the resulting development for small amplitude disturbances and to better be able to compare Landahl's model with the linear evolution of localized disturbances presented in this article, we may linearize the equations in the following manner. If we assume that $|\bar{v}_\eta^i t| = |\bar{w}_\zeta^i t| \ll 1$ the integrand of (99) may be expanded and the integral solved. We find

$$y - \eta = l_m \approx \tilde{v}^i t \tag{100a}$$

$$U(y) - U(\eta) = U'(y)l_m + \ldots \approx U'(y)\tilde{v}^i t \tag{100b}$$

where the dots signify higher terms in the Taylor expansion of the mean flow around the normal position y. Equation (100b) can readily be identified with the lift-up effect discussed in previous sections. Thus the mechanism generating the shear layers is the same for the localized disturbances analyzed in the linear regime and the coherent structures analyzed in Landahl's model.

We have seen two effects that will cause the coherent structure to break down and cause a burst. The first was the creation of shear layers which may be expected to be associated with unstable inflection points. This shear layer instability could cause a rapid breakdown of the coherent structure as well. If the velocity field produced by the burst would indeed resemble the one assumed in the model we have closed the model and explained the regeneration mechanism of the bursts needed to sustain a turbulent flow. Landahl (1983) further compared the velocity signal found form the evolution of his initial condition to the ones extracted using conditional sampling of the bursting process. He found that they were in good agreement.

Landahl has improved upon this model in various of his papers. Russell & Landahl (1984) for example took the pressure into account in an approximate manner and found that the singular behavior was moderated. Landahl (1990) discussed the generation of streaks based on what is a slightly modified model. There he argued that the disturbance should be turned in order to include asymmetric disturbances.

Finally we may address the difference between the results of the Lagrangian description of the flow and the Eulerian one used for example in numerical solutions. With the first description fluid particles were found to move rapidly away from the wall, giving the appearance of a violent bursting phenomenon. In the analysis of numerical simulation results Johansson et al. (1987), on the other hand, it was found that the shear layers themselves did not break up in a violent manner but only meandered slowly. Those two observations are consistent with the idea of considering the structures as wave phenomena that propagate in the flow. The coherent structures are not associated with the fluid particles that are rapidly transported out from the wall in a violent manner. Instead they are associated with a propagating structure in the Eulerian description of the fluid velocity.

6. Concluding remarks

In the hundred years since Reynolds first defined the problem of transition to turbulence, considerable progress has been made in understanding the problem. However, the legacy of Squire's theorem has been to define a narrow approach to the stability problem – namely to assume that the first manifestation of transition will be the appearance and subsequent growth of two-dimensional Tollmien-Schlichting waves. With this as the initial condition, the growth and decay of such wave trains, and the subsequent onset of three-dimensional secondary instability are nowe well understood both theoretically and experimentally.

However, it is by no means clear that two-dimensional T-S waves are in fact the first stage in the *natural* transition of a shear flow. In particular, flows characterized by localized surface roughness or other inhomogeneities are known to undergo transition to turbulence earlier than would be predicted by standard T-S wave growth analyses (cf. Corke, Bar-Sever & Morkovin, 1986). In such flows, it seems equally plausible that the onset of transition will be due to the three-dimensional transient growth mechanisms that we have discussed in this article. These transient mechanisms, which are ignored in the traditional normal-mode approach to stability theory, can result in rapid energy growth on a time scale *much* faster than those associated with Tollmien-Schlichting waves. This may result in an initially low-amplitude disturbance entering a regime where nonlinear effects can take over, driving the flow to turbulence. In such a scenario, the transition process occurs too fast for the effects of T-S waves to be observed – *bypass* transition.

The transient growth is not only important in the process of causing small amplitude perturbations to grow over a non-linear threshold, it may also be triggered non-linearly. Schmid & Henningson (1992) showed that for an initial condition

starting with two small but finite amplitude oblique waves, the main cause of the growth was the non-linear excitation of transient growth of modes along the spanwise wavenumber axis. Similar results were found by Henningson et al. (1993) for finite amplitude localized disturbances. In both investigations it was pointed out that the growth of the total disturbance energy must, in a subcritical flow, be due to the linear effects discussed in the present paper. Non-linearities will distribute the energy among the scales or wavenumbers in the flow but not add to the total disturbance energy.

It is worthwhile mentioning that the transient growth mechanisms are very closely related to the traditional secondary instability process. Both approaches examine the evolution of three-dimensional disturbances in a shear flow. The difference lies in the fact that the secondary instability approach requires a two-dimensional T-S wave to reach sufficient amplitude such that 3-D waves become unstable, while the transient growth approach simply assumes that a 3-D disturbance is present as an initial condition. Once three-dimensionality is present, the dynamics of the flow are similar and both approaches lead to the formation of internal shear layers (the "spike" stage in the language of secondary instability theory), lambda-vortices, etc.

Much more work remains to be completed before a full understanding of the behavior of localized disturbances is achieved. In particular, the nonlinear growth mechanisms must be further investigaetd to determine under what conditions a linear disturbance will exhibit sufficient transient growth such that nonlinear mechanisms can take over and drive the flow to transition. Recent work addressing this issue are Kreiss, Lundbladh & Henningson (1993) and Lundbladh, Henningson & Reddy (1993). In addition, it is still not clear exactly what kinds of flow perturbations are actually created by physical disturbances such as localized roughness elements, wall motion, blowing and suction, etc. Initial experiments (e.g. Breuer & Haritonidis 1990; Klingmann 1992) have begun to address this question but much more work remains. Nevertheless, it seems clear that the consideration of the dynamics of three-dimensional disturbances in shear flows reveals a wide spectrum of flow physics which has been thus far largely overlooked in transition (and turbulence) research, but which may provide important tools in the better understanding and modeling of these phenomena.

Acknowledgments

References

Abramowitz, M. and Stegun, I.A., *Handbook of Mathematical Functions*. Dover (1965).

Bark, F., On the wave structure of the wall region of a turbulent boundary layer. *J. Fluid Mech.* 70 (1975) 229–250.

Benjamin, T.B., The development of three-dimensional disturbances in an unstable film of liquid flowing down an inclined plane. *J. Fluid Mech.* 10 (1961) 401–419.

Blackwelder, R.F. and Kaplan, R.E., On the wall structure of the turbulent boundary layer. *J. Fluid Mech.* 76 (1976) 89–112.

Breuer, K.S. and Haritonidis, J.H., The evolution of a localized disturbance in a laminar boundary layer. Part I: Weak disturbances. *J. Fluid Mech.* 220 (1990) 569–594.

Butler, K.M. and Farrell, B.F., Three-dimensional optimal perturbations in viscous shear flow. *Phys. Fluids A.* 4 (1992) 1637–1650.

Case, K.M., Stability of inviscid plane Couette flow. *Phys. Fluids* 3 (1960) 143–148.

Chin, W.C., *Physics of slowly varying wavetrains in continuous systems.* PhD thesis, Massachusetss Institute of Technology, Department of Aeronautics and Astronautics, Cambridge, Mass. (1976).

Corke, T.C., Bar-Sever, A. and Morkovin, M.V., Experiments on transition enhancement by distributed roughness. *Phys. Fluids* 29 (1986) 3199–3213.

Davis, S.H. and Reid, W.J., On the stability of stratified viscous plane Couette flow. *J. Fluid Mech.* 80 (1977) 50.

Dikii, L.A., The stability of plane-parallel flows of an ideal fluid. *Sov. Phys. Doc.* 135 (1960) 1179–1182.

DiPrima, R.C. and Habetler, G.J., A completeness theorem for non-selfadjoint eigenvalue problems in hydrodynamic stability. *Arch. Rat. Mech. Anal.* 32 (1969) 218–227.

Drazin, P.G. and Reid, W.H., *Hydrodynamic Stability.* Cambridge University Press (1981).

Ellingsen, T. and Palm, E., Stability of linear flow. *Phys. Fluids.* 18 (1975) 487–488.

Farrell, B.F., Optimal excitation of perturbations in viscous shear flow. *Phys. Fluids.* 31 (1988) 2093–2102.

Gaster, M. 1968, The development of three-dimensional wave packets in a boundary layer. *J. Fluid Mech.* 32 (1968) 173–184.

Gaster, M., Estimates of the errors incurred in various asymptotic representations of wave packets. *J. Fluid Mech.* 121 (1982) 365–377.

Gaster, M. and Grant, I., An experimental investigation of the formation and development of a wave packet in a laminar boundary layer. *Proc. Roy. Soc. Lond. Ser. A.* 347 (1975) 253–269.

Golub, G.H. and van Loan, C.F., *Matrix Computations.* Johns Hopkins University Press (1983).

Grosch, C.E. and Salwen, H., The continuous spectrum of the Orr-Sommerfeld equation. Part 1. The spectrum and the eigenfunctions. *J. Fluid Mech.* 87 (1978) 33–54.

Gustavsson, L.H., *On the evolution of disturbances in boundary layer flows.* PhD thesis, Royal Institute of Technology, Stockholm, Sweden (TRITA-MEK 78–02) (1978).

Gustavsson, L.H., Excitation of direct resonances in plane Poiseuille flow. *Stud. Appl. Math.* 75 (1986) 227–248.

Gustavsson, L.H. 1991. Energy growth of three-dimensional disturbances in plane Poiseuille flow. *J. Fluid Mech.* 224 (1991) 241–260.

Henningson, D.S., Solution of the three-dimensional Euler equations for the development of a flat eddy in a boundary layer. Master's thesis, Department of Aeronautics and Astronautics, Massachusetts Institute of Technology, Cambridge, MA (1985).

Henningson, D.S., The inviscid initial value problem for a piecewise linear mean flow. *Stu. Appl. Math.* 78 (1988) 31–56.

Henningson, D.S., Wave growth and spreading of a turbulent spot in plane Poiseuille flow. *Phys. Fluids A.* 1 (1989) 1876–1882.

Henningson, D.S., An eigenfunction expansion of localized disturbances. In Johansson, A.V. and Alfredsson, P.H. (eds.), *Advances in Turbulence 3.* Stockholm: Springer-Verlag (1991) pp. 162–169.

Henningson, D.S., Lundbladh, A. and Johansson, A.V., A mechanism for bypass transition from localized disturbances in wall bounded shear flows. *J. Fluid Mech.* 250 (1993) 169–207.

Henningson, D.S. and Schmid, P.J., Vector eigenfunction expansions for plane channel flows. *Stud. Appl. Math* 87 (1992) 15–43.

Herbert, T., Secondary instability of boundary layers. *Ann. Rev. Fluid Mech.* 20 (1988) 487–526.

Hultgren, L.S. and Gustavsson, L.H., Algebraic growth of disturbances in a laminar boundary layer. *Phys. Fluids* 24 (1981) 1000–1004.

Jimenez, J. and Whitham, G.B., An averaged Lagrangian method for dissipative wavetrains. *Proc. Roy. Soc.Lond. Ser. A* 349 (1976) 277–287.

Johansson, A.V., Alfredsson, P.H. and Kim, J., Shear layer structure in near wall turbulence. In *Proceedings of the 1987 summer program*, pp. 237–251. NASA / Stanford Center for turbulence research (1987).

Johansson, A.V., Alfredsson, P.H. and Kim, J., Evolution and dynamics of shear-layer structures in near-wall turbulence. *J. Fluid Mech.* 224 (1991) 579–599.

Joseph, D.D., Eigenvalue bounds for the Orr-Sommerfeld equation. *J. Fluid Mech* 33 (1968) 617–621.

Joseph, D.D., Eigenvalue bounds for the Orr-Sommerfeld equation. Part 2. *J. Fluid Mech.* 36 (1969) 721–734.

Kim, H.T., Kline, S.J. and Reynolds, W.C., The production of turbulence near a smooth wall in a turbulent boundary layer. *J. Fluid Mech.* 50 (1971) 133.

Klingmann, B.G.B., On transition due to three-dimensional disturbances in plane Poiseuille flow. *J. Fluid Mech.* 240 (1992) 167–195.

Kreiss, G., Lundbladh, A. and Henningson, D.S., Bounds for threshold amplitudes in subcritical shear flows. TRITA-NA 9307, Royal Institute of Technology, Stockholm, Sweden (1993).

Landahl, M.T., A wave-guide model for turbulent shear flow. *J. Fluid Mech.* 29 (1967) 441–459.

Landahl, M.T., Wave mechanics of breakdown. *J. Fluid Mech.* 56 (1972) 775–802.

Landahl, M.T., Wave breakdown and turbulence. *SIAM J. Appl. Math.* 28 (1975) 735–756.

Landahl, M.T., Modeling of coherent structures in boundary layer turbulence.Workshop on coherent structure of turbulent boundary layers, Lehigh University (1979).

Landahl, M.T., A note on an algebraic instability of inviscid parallel shear flows. *J. Fluid Mech.* 98 (1980) 243–251.

Landahl, M.T., The application of kinematic wave theory to wave trains and packets with small dissipation. *Phys. Fluids* 25 (1982) 1512–1516.

Landahl, M.T., Theoretical modeling of coherent structures in wall bounded shear flows. Eighth Biennial Symposium on Turbulence, University of Missouri-Rolla (1983).

Landahl, M.T., On sublayer streaks. *J. Fluid Mech.* 212 (1990) 593–614.

Lin, C.C., *Theory of Hydrodynamic Stability*. Cambridge University Press (1955).

Lundbladh, A., Henningson, D.S. and Reddy, S.C., Threshold amplitudes for transition in channel flows. Proceedings from the 1993 ICASE/NASA Langley Workshop on the Transition to Turbulence (1993).

Mack, L.M., A numerical study of the temporal eigenvalue spectrum of the Blasius boundary layer. *J. Fluid Mech.* 73 (1976) 497–520.

Morkovin, M.V., The many faces of transition. In Wells, C.S. (ed.), *Viscous Drag Reduction*, Plenum Press (1969).

Orr, W.M.F., The stability or instability of the steady motions of a perfect liquid and of a viscous liquid. Part I: A perfect liquid. Part II: A viscous liquid. *Proc. R. Irish Acad. A* 27 (1907) 9–138.

Prandtl, L., Bericht über Untersuchungen zur ausgebildeten Turbulenz., *Zeitschrift für Angewandte Mathematik und Mechanik* 5 (1925) 136.

Rayleigh, J.W.S., On the stability, or instability, of certain fluid motions. *Proc. Math. Soc. Lond.* 11 (1880) 57–70.

Reddy, S.C., *Pseudospectra of operators and discretization matrices and an application to the method of liens*. PhD thesis, Massachusetts Institute of Technology, Cambridge (1991).

Reddy, S.C. and Henningson, D.S., Energy growth in viscous channel flows. *J. Fluid Mech.* 252 (1993) 209–238.

Reddy, S.C., Schmid, P.J. and Henningson, D.S., Pseudospectra of the Orr-Sommerfeld operator. *SIAM J. Appl. Math.* 53 (1993) 15–47.

Russell, J.M. and Landahl, M.T., The evolution of a flat eddy near a wall in an inviscid shear flow. *Phys. Fluids* 27 (1984) 557–570.

Schensted, I.V., *Contribution to the theory of hydrodynamic stability*. PhD thesis, University of Michigan, Ann Arbor (1961).

Schmid, P.J. and Henningson, D.S., A new mechanism for rapid transition involving a pair of oblique waves. *Phys. Fluids A* 4 (1992) 1986–1989.

Sommerfeld, A., Ein Beitrag zur hydrodynamischen Erklärung der turbulenten Flüssigkeitbewegungen. In *Atti. del 4. Congr. Internat. dei Mat. III* pp. 116–124, Roma (1908).

Squire, H.B., On the stability for three-dimensional disturbances of viscous fluid flow between parallel walls. *Proc. Roy. Soc. London Ser. A.* 142 (1933) 621–628.

Stewartson, K., Some aspects of nonlinear stability theory. *Fluid Dyn. Trans.* 7 (1974) 101–128.

Trefethen, L.N., Pseudospectra of matrices. In *Numerical Analysis 1991* (1992) pp. 234–266. Longman.

Trefethen, L.N., Trefethen, A.E., Reddy, S.C. and Driscoll, T.A., Hydrodynamic stability without eigenvalues. *Science* 261 (1993) 578–584.

Whitham, G.B., *Linear and Nonlinear waves.* Wiley-Interscience (1974).

Wygnanski, I., Haritonidis, J.H. and Kaplan, R.E., On a Tollmien-Schlichting wave packet produced by a turbulent spot. *J. Fluid Mech.* 92 (1979) 505–528

Nonlinear Shear-layer Instability Waves *

LENNART S. HULTGREN
National Aeronautics and Space Administration Lewis Research Center, Cleveland, Ohio 44135, USA

Abstract. The effects of critical-layer nonlinearity on spatially growing instability waves on shear layers between parallel streams are discussed. In the two-dimensional incompressible case, the flow in the critical layer is governed by a nonequilibrium ('unsteady') nonlinear vorticity equation. The initial exponential growth of the instability wave is converted into algebraic growth during the streamwise 'aging' of the critical layer into a quasi-equilibrium state. A uniformly valid composite formula for the instability wave amplitude, accounting for both nonparallel and nonlinear effects, is shown to be in good agreement with available experimental results. Nonlinear effects occur at smaller amplitudes for the three-dimensional and supersonic cases than in the two-dimensional incompressible case. The instability-wave amplitude evolution is then described by one integro-differential equation with a cubic-type nonlinearity, whose inviscid solution always end in a singularity at finite downstream distance.

1. Introduction

Considerable progress in the understanding of nonlinear phenomena in shear-layer transition has been made by using a combination of (high-Reynolds-number) asymptotic and numerical methods. Two important novel aspects of the analysis are that the disturbances evolve from strictly linear, finite-growth-rate instability waves on weakly nonparallel mean flows so that the proper upstream conditions are applied in the nonlinear streamwise region and, second, the question of proper outflow boundary conditions, which is still an issue of research for direct numerical simulations (DNS) of convectively unstable shear flows, does not arise since the asymptotic formulations lead to parabolic problems. Composite expansion techniques are used to obtain solutions that account for both mean-flow-evolution and nonlinear effects. For an incompressible mixing layer, the amplitude evolution of a two-dimensional instability wave is completely controlled by a nonlinear critical-layer vorticity equation. Although the solution of this parabolic partial differential equation requires supercomputer resources, it is sufficiently simpler than a direct numerical simulation using the Navier-Stokes equations so that grid-resolution problems can be avoided. Good agreement with available experimental data for the first nonlinear saturation stage for a plane-jet shear layer [1], a circular-jet shear layer [2], and a mixing layer behind a splitter plate [3] has been demonstrated [4].

---

* The US Government has the right to retain a nonexclusive royalty-free license in and to any copyright covering this paper.

Low-level external harmonic forcing of free shear layers between parallel streams produces spatially growing instability waves that are initially governed by linear dynamics. The local (linear) growth rate will ultimately be reduced due to the slow viscous spreading of the mean shear layer, and nonlinear effects eventually (may) become important. Huerre [5] has pointed out that for a Landau-Stuart-Watson type of nonlinearity to be effective in a shear-layer situation two mutually exclusive constraints must hold, and consequently, that, to use a Landau-Stuart-Watson type theory, an artificial body force must be introduced to keep the flow parallel. This effectively rules out the matching of a Landau-Stuart-Watson type nonlinear solution with an upstream finite-growth-rate linear instability wave on a weakly nonparallel mean flow. Since this upstream matching is a key requirement for a first-principles theory, one therefore is led to assume that the nonlinear effects first become important in the critical layer. In this situation, the perturbation flow outside the critical layer is essentially linear, but with the external instability-wave amplitude completely controlled by the critical-layer dynamics.

The most rapidly growing disturbances on an incompressible shear layer are two-dimensional according to linear stability theory, and the discussion will be concentrated on such disturbances in that case. The most rapidly growing instability wave can be three dimensional in supersonic shear layers and three-dimensional effects dramatically change the nonlinear behavior, which enters at much smaller amplitudes than in the two-dimensional case. There are, in a sense, two generic cases involving three-dimensional waves that need to be considered, namely that of a single mode growing in its propagation direction and that of a pair of oblique waves with the same frequency and streamwise wave number and spanwise wave numbers of equal magnitude but opposite sign, thus representing a disturbance with a fixed spanwise pattern growing in the streamwise direction.

2. The two-dimensional incompressible case

Consider a two-dimensional, incompressible and almost inviscid shear layer between two parallel streams with nominally uniform velocities $U_{1*} > U_{2*}$ (the star is used to denote dimensional quantities). In particular, consider the streamwise region where nonlinear effects have become important, cf. Fig. 1. The streamwise and transverse coordinates x and y, the time t, and all velocities are nondimensionalized by L_{v*}, L_{v*}/U_{A*}, and U_{A*}, respectively, where $2L_{v*} = (U_{1*} - U_{2*})/(\partial U_*/\partial y_*)_{max}$ is the vorticity thickness of the unexcited shear layer at a typical streamwise location, say $x = 0$, just upstream of the nonlinear region, and $U_{A*} = \frac{1}{2}(U_{1*} + U_{2*})$ is the average velocity of the streams. The origin of the y coordinate is taken to be at the inflexion point of the undisturbed mean flow at $x = 0$.

The mean-flow Reynolds number, $R = L_{v*}U_{A*}/\nu$, where ν is the kinematic viscosity, is assumed large enough so that the mean flow is nearly parallel and the
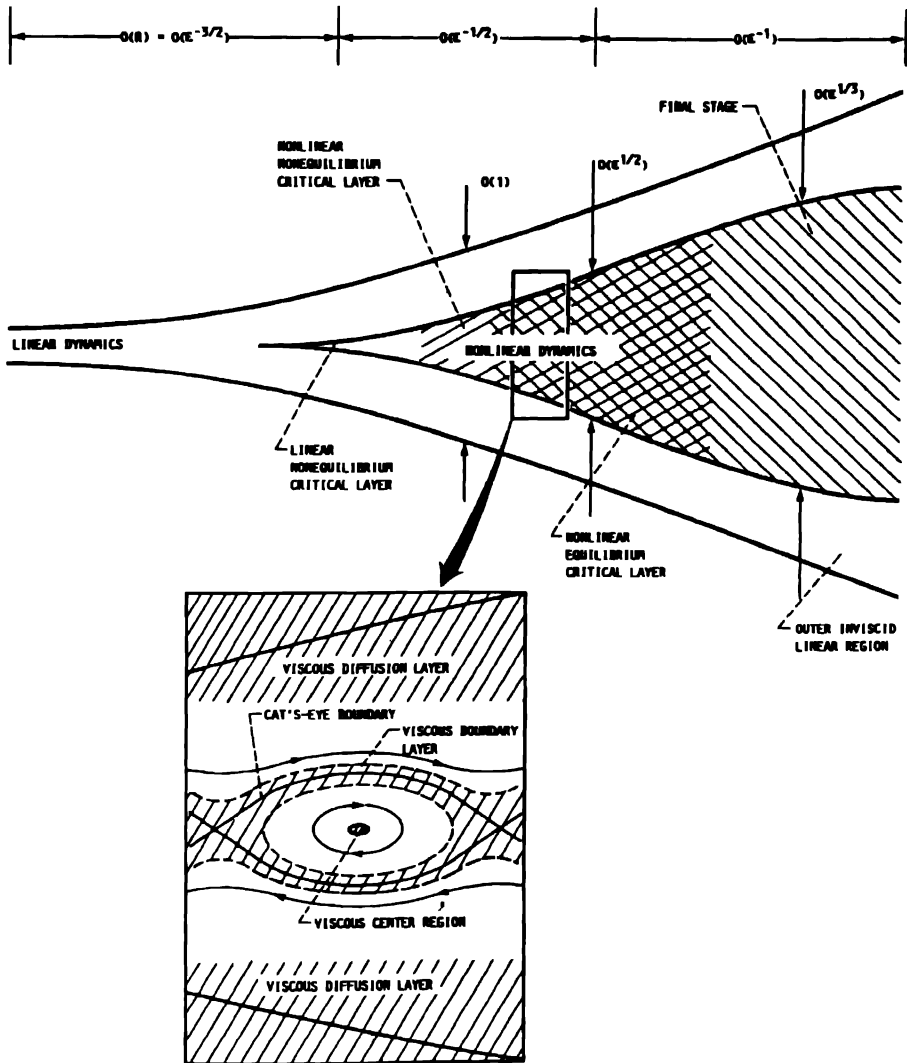
Fig. 1. Flow structure

shear layer width (at least initially) increases only slowly over the long viscous scale

$$x_3 = x/R. \qquad (1)$$

Upstream of the nonlinear region, the mean flow is essentially unaffected by the linear instability wave and its streamwise evolution can be determined from the laminar boundary-layer equation. In the same region, the instability wave can be

described by inviscid, weakly nonparallel, linear stability theory and, assuming that it remains sufficiently small, its amplitude grows in the streamwise direction until, due to the viscous mean-flow spreading, neutral stability is approached. As the local linear growth rate tends to zero, the leading-order inviscid stability problem becomes singular at the critical level, i.e., at the transverse location where the phase velocity of the instability wave equals the mean flow. This is indicative of a nonuniformity in the perturbation vorticity and that now the dynamics essentially is determined in a small transverse region. In this critical layer, the linear mean-flow convection of the perturbation vorticity can be balanced by spatial evolution (growth), viscous, or nonlinear effects, or a combination thereof. By themselves, these three possibilities would lead to an inviscid linear nonequilibrium critical layer with a thickness of the order of the small but nonzero growth rate, a viscous linear equilibrium critical layer of thickness $O(R^{-1/3})$, or an inviscid nonlinear equilibrium critical layer of thickness $O(\epsilon^{1/2})$, respectively, where ϵ is a measure of the local instability-wave amplitude.

As first shown in Goldstein & Leib [6], the requirement that the near-neutral nonlinear solution matches onto the upstream strictly linear, finite-growth-rate instability wave implies that the linear growth rate at the beginning of the nonlinear region must be $O(\epsilon^{1/2})$ and, consequently, that

$$S = \alpha_0 U_c + \epsilon^{1/2} S_1, \; S_1 < 0, \; S_1 = O(1). \tag{2}$$

$S = \omega_{e*} L_{v*}/U_{A*}$ is the local Strouhal number, $S_0 = \alpha_0 U_c$ is its local neutral value based on linear inviscid parallel flow stability theory, ω_{e*} is the excitation angular frequency, α_0 is the local neutral wave number, and U_c is the velocity at the inflexion point of the undisturbed mean flow at $x = 0$. S_0 and S_1 are taken to be constant when analyzing the nonlinear streamwise region, but will be allowed to vary on the long viscous scale x_3 when the streamwise composite solution is introduced. Goldstein & Leib [6] showed that the critical-layer effects cause changes in the flow on the scale of the slow streamwise variable

$$x_1 = \epsilon^{1/2} x \tag{3}$$

and that the critical layer becomes a linear-growth critical layer as $x_1 \to -\infty$, i.e., (in the matched asymptotic sense) its solution matches onto an upstream finite-growth-rate linear instability wave. Thus, this scaling represents a distinguished limit that allows both spatial evolution and nonlinear effects to enter the critical-layer vorticity balance and has a linear nonequilibrium critical-layer region (cf. figure 1) as an overlap domain between the upstream finite-growth-rate linear region and the near-neutral nonlinear region. The presence of the spatial-evolution term in this balance means that the critical layer is an 'unsteady' one but with a slow streamwise coordinate in place of time. It is commonly referred to as a nonequilibrium critical layer, however, in order to avoid any connotation of temporal evolution. Goldstein & Leib [6] assumed the local Reynolds number R

to be large enough so that viscous effects, including mean-flow spreading, could be ignored in the nonlinear (streamwise) region.

Goldstein & Hultgren [7] incorporated a small amount of viscosity into the analysis of Goldstein & Leib [6] by assuming the local Reynolds number R to be $O(\epsilon^{-3/2})$. The relative importance of viscous to nonlinear effects in the critical-layer vorticity balance is then determined by the $O(1)$ parameter,

$$\lambda = 1/\epsilon^{3/2}R, \tag{4}$$

while viscous effects are purely passive in the main part of the shear layer. They [7] also showed that it is sufficient to use a Taylor series expansion of the basic-flow velocity for the purpose of studying its changes on the nonlinear critical-layer streamwise length scale (3). The nonlinear critical-layer analysis need only be uniformly valid on the faster scale x_1 but not on the slower scale x_3, cf. figure 1. Variations on this latter scale are accounted for by the outer weakly nonparallel solution. An important feature of this matched-asymptotics approach is that it does not require any artificial body force to remain internally consistent, cf. [5].

Both Goldstein & Leib [6] and Goldstein & Hultgren [7] considered only the case where the mean flow is initially given by a hyperbolic-tangent profile. This restriction was removed by Hultgren [4] who also formed a composite solution that accounts for both mean-flow spreading and nonlinear critical-layer effects. A very brief description of the analysis for a general velocity profile will be given here – for a complete description of the derivations see Hultgren [4].

The solution in the nonlinear streamwise region is expanded separately outside and inside the critical layer. Matching (in the transverse direction) of these expansions, which also involves equating the so-called velocity jump across the critical layer as given by the two expansions, will then lead to a nonlinear nonequilibrium critical-layer problem which completely determines the external instability-wave amplitude.

The stream function outside the critical layer, i.e., for $y = O(1)$, is expanded as

$$\psi = \psi_0(y) + \epsilon \left\{ 2\lambda x_1 G(y) + \mathrm{Re}\left[A^\dagger(x_1)\hat{\phi}_1(y)e^{i\alpha_0\zeta} \right] \right\}$$
$$+ \ldots + \epsilon^{n/2} \left\{ \mathrm{Re}\left[\sum_{m=0}^{+\infty} \Phi_{n/2}^{(m)}(y, x_1)e^{im\alpha_0\zeta} \right] \right\} + \ldots , \tag{5}$$

where $\psi_0(y)$ is the zeroth-order term in the Taylor-series expansion of the mean flow, which is determined by the imposed upstream profile and by the previous slow development of the mean flow on the long viscous scale $x_3 = x/R$. The $O(\epsilon)$ term in the expansion (5) is the sum of the second term in the mean-flow Taylor series expansion and the (neutral) linear instability wave solution, where the mean-flow change term $G(y)$ and the slowly varying amplitude function $A^\dagger$ are ultimately determined by the second and third order problems, and $\zeta = x - St/\alpha_0$ is the streamwise coordinate in a reference frame moving with the actual phase velocity of the linear instability wave.

Substitution of (5) into the governing equations leads to a sequence of equations, of which the first one for the fundamental component is the Rayleigh equation for a neutral disturbance, $\hat{\phi}_1$. Since the shear-layer mean profile is inflexional, the linear neutral eigenfunction $\hat{\phi}_1$ is regular at the critical level, i.e., at $y = 0$. However, the next-order correction to the fundamental, $\hat{\Phi}_{3/2}^{(1)}$, which is governed by an inhomogeneous neutral Rayleigh equation with the nonhomogeneous terms involving the product of $\hat{\phi}_1$ with $A^\dagger$ and $dA^\dagger/dx_1$, has the following behavior for small values of y, i.e., as the critical layer is approached:

$$\Phi_{3/2}^{(1)\pm} = a_{3/2}^{(1)} + b_{3/2}^{(1)\pm} y + \frac{iU_c'''}{\alpha_0 U_c'^2} \left(U_c \frac{dA^\dagger}{dx_1} - iS_1 A^\dagger \right) y \ln y + O(y^2), \qquad (6)$$

where the $\pm$ superscript indicates different values for $y \gtrless 0$. A solvability condition for the $\hat{\Phi}_{3/2}^{(1)}$ problem can be constructed, cf. Hultgren [4], which yields the following relationship between $b_{3/2}^{(1)+}$ and $b_{3/2}^{(1)-}$:

$$b_{3/2}^{(1)+} - b_{3/2}^{(1)-} = 2i\alpha_0 \frac{dA^\dagger}{dx_1} J_1 - i\alpha_0 \left(U_c \frac{dA^\dagger}{dx_1} - iS_1 A^\dagger \right) J_2, \qquad (7)$$

where

$$= \int_{-}^{+\infty} \hat{\phi}_1^2 dy, \quad J_2 = \frac{1}{\alpha_0^2} \int_{-\infty}^{+\infty} U''(U - U_c)^{-2} \hat{\phi}_1^2 dy,$$

with the latter integral being a Cauchy principal value. Note that $J_2 = 0$ for antisymmetric mean velocity profiles, e.g. the hyperbolic-tangent profile considered in Goldstein & Leib [6] and Goldstein & Hultgren [7]. Equation (7) gives the so-called velocity jump across the critical layer as (formally) computed from the outer solution.

In the critical layer, i.e., for $y = O(\epsilon^{1/2})$, the stream-function is expanded as

$$\Psi = \epsilon^{1/2} U_c Y + \epsilon \left[\Psi_0(\zeta, Y, x_1) + \epsilon^{1/2} \Psi_{1/2} + \epsilon \ln \epsilon^{1/2} \Psi_{1L} + \epsilon \Psi_1 + \ldots \right], (8)$$

where $Y = y/\epsilon^{1/2}$ is a stretched transverse variable and the Ψ_n's are functions of ζ, Y, and x_1 only. Ψ_0 to Ψ_{1L} are given by the corresponding terms in the inner limit of the outer solution and Ψ_1, the first nontrivial term in (8), is determined by a viscous critical-layer vorticity equation that can be expressed [4] in terms of

$$Q^\dagger = \frac{\partial^2 \Psi_1}{\partial Y^2} - U_c''' \left(\frac{Y^2}{U_c} + \frac{\lambda x_1}{U_c} \right) - \left(\alpha_0^2 + \frac{U_c'''}{U_c'} \right) \text{Re} \left(A^\dagger e^{i\alpha_0 \zeta} \right) \qquad (9)$$

which is (minus) the part of the $O(\epsilon)$ critical-layer vorticity that vanishes as $Y \to \pm\infty$. Integration of that critical-layer vorticity equation gives an expression for the velocity jump $b_{3/2}^{(1)+} - b_{3/2}^{(1)-}$ as (formally) computed from the critical-layer solution

[4]. Equating the expressions for the velocity jump involving the inner and outer solutions, respectively, leads to a matching condition that, together with the initial condition that the solution approaches that of a linear growth critical layer as $x_1 \to -\infty$, completes the formulation of critical-layer problem. On rescaled form, the critical-layer vorticity equation reads [4]

$$\frac{\partial}{\partial \bar{x}} + \eta \frac{\partial}{\partial X} - \mathrm{Re}\left(i A e^{iX}\right)\frac{\partial}{\partial \eta} - \bar{\lambda}\frac{\partial^2}{\partial \eta^2}\ Q = \mathrm{Re}\left[\left(\frac{\bar{U}}{2}\frac{dA}{d\bar{x}} + iA\right) e^{iX}\right] \quad (10)$$

which is to be solved subject to the initial, boundary, and jump conditions

$$A \to \exp\left(\int_0^{\bar{x}} \sigma d\bar{x}\right) \quad \text{as } \bar{x} \quad -\infty, \quad (11)$$

$$Q \to 0 \quad \text{as } \eta \to \pm\infty, \quad (12)$$

$$\int_{-\infty}^{+\infty}\int_0^{2\pi} Q e^{-iX} dX d\eta = i\pi\left(\chi\frac{dA}{d\bar{x}} - i\mu A\right), \quad (13)$$

where $\bar{x}$, X, η, A, and Q are simply rescaled (and shifted) variables corresponding to x_1, ζ, Y, A^1, and $Q^\dagger$, respectively; and $\bar{\lambda} = (\alpha_0 U_c')^2 \lambda/(-\frac{1}{2}\bar{U}S_1)^3$, $\bar{U} = \gamma U_c$, $\sigma \equiv \sigma_r + i\sigma_i = (\pi + i\mu)/(\chi + \frac{1}{2}i\pi\bar{U})$, $\chi = 1 - \frac{1}{2}\mu\bar{U}$, $\mu = J_2/(\gamma J_1)$, and $\gamma = -U_c'''/(\alpha_0^2 U_c'|U_c'|J_1)$. Strictly speaking, the integrand in (11) is constant on the streamwise scale $\bar{x}$ considered here, but it is advantageous to write the upstream conditions for the nonlinear solution in the form (11) for the later introduction of a streamwise composite solution, however.

The nonlinear nonequilibrium critical-layer problem (10) - (13) depends on the three independent parameters $\bar{U}$, $\bar{\lambda}$, and μ. $\bar{U}$ is a scaled average mean-flow velocity in the critical layer (measured in the laboratory frame of reference); $\bar{\lambda}$ is a rescaled λ which in view of (2) and (4) could be thought of as based on the detuning from the local neutral conditions rather than the amplitude; and μ is π times the ratio of the real and imaginary parts of the derivative of the wave number with respect to the phase velocity (both from linear inviscid theory) evaluated at the neutral point, vanishes for antisymmetric mean profiles such as the one used in [6] and [7], and can be interpreted as a mean-flow symmetry parameter.

Goldstein & Hultgren's [7] computations showed the vorticity roll-up to be initially similar to the inviscid calculations of [6]. However, even very weak viscous effects eventually become important as a result of the continued roll-up of vorticity. They found that viscosity keeps the nonlinear effects from driving the critical-layer phase jump, and thereby the local growth rate, to zero and hence allows the instability wave to continue its growth asymptotically far downstream, cf. Fig. 2. This produces an unbounded increase of the nonlinear terms in the critical-layer vorticity equation so that a new dominant critical-layer balance between linear and nonlinear convection terms is eventually achieved. Thus, no matter what size of
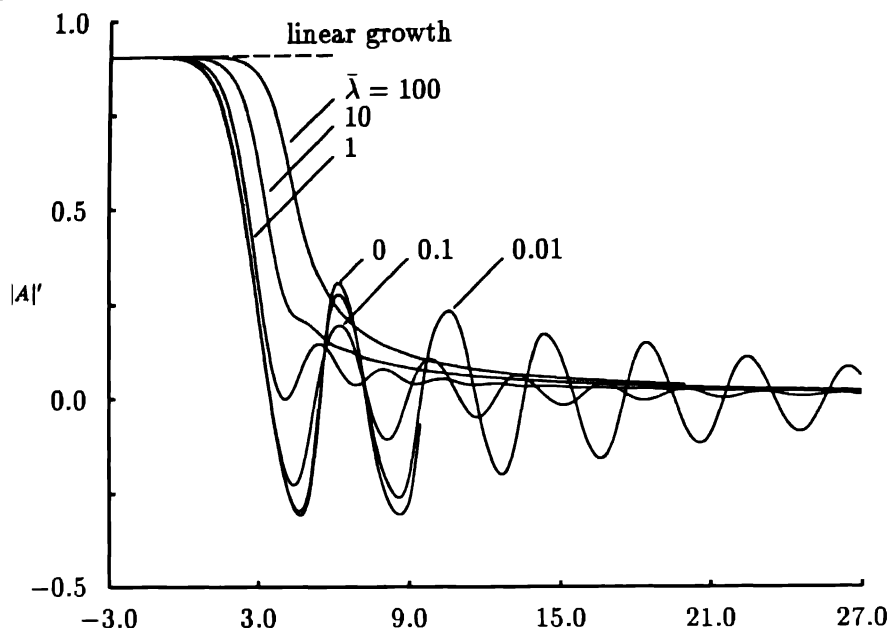
Fig. 2.   Local scaled growth rate of the fundamental instability wave as a function of the scaled slow streamwise distance for $\bar{U} = 1$, $\mu = 0$, and various values of $\bar{\lambda}$.

the parameter $\bar{\lambda}$, a primarily inviscid quasi-equilibrium critical layer eventually emerges, cf. Fig. 3. It may at first seem surprising that also no matter how large $\bar{\lambda}$ the problem in [7] becomes nonlinear sufficiently far downstream. This can be understood by realizing that the initial linear growth rate in the critical layer is independent of $\bar{\lambda}$ and that the growth rate is then rapidly reduced by nonlinear effects. A larger value of $\bar{\lambda}$ simply means that the growth rate is not reduced quite as fast because the relatively stronger viscous effects in a sense keep the problem linear for a longer streamwise distance. The instability wave can therefore, through continued growth, achieve the larger amplitude necessary for nonlinear effects now to come into play.

The quasi-equilibrium critical-layer problem is analogous to the situation that was analyzed by Benney & Bergeron [8], but the specific asymptotic solution in [7] turned out to be somewhat different and, in particular, has variable vorticity in the closed streamline region within the cat's-eye boundary. The asymptotic solution [7] shows that the initial exponential growth of the disturbance is converted into an algebraic one and that further downstream the disturbance is simultaneously affected by mean-flow-divergence and nonlinear critical-layer effects before the instability wave achieves an $O(1)$ amplitude. The analysis [7] of this next stage of evolution, which occurs on the streamwise scale $x_2 = \epsilon^{1/2}x_1 = \epsilon x = \epsilon^{-1/2}x_3/\lambda = O(1)$, shows that the instability-wave growth is eventually converted to decay. The asymptotic results obtained by Goldstein & Hultgren [7] are also valid in the
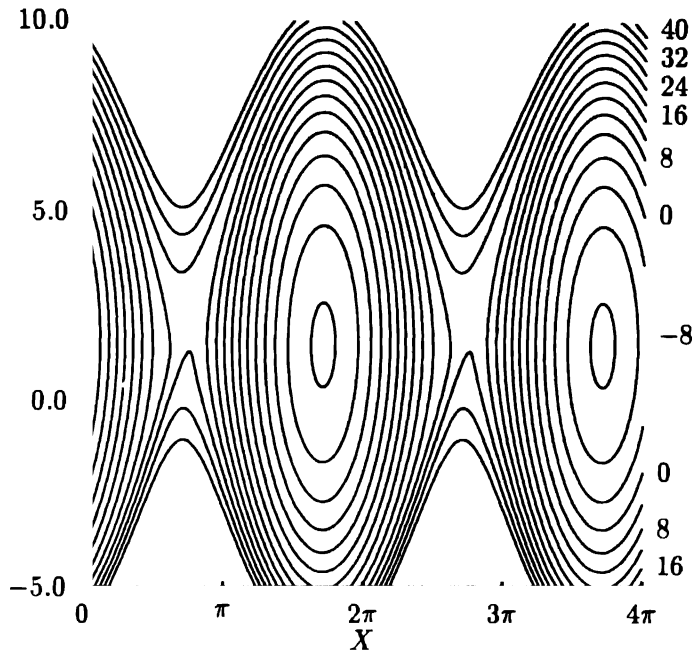
Fig. 3.   Vorticity contours in the (X, η)-plane for $\bar{U} = \bar{\lambda} = 1$ and $\bar{r} = 10$.

general case analyzed by Hultgren [4]. The different flow regions are illustrated in Fig. 1

The (streamwise) composite solution introduced in Goldstein & Leib [6] was generalized to include viscosity and extended to a general velocity profile in Hultgren [4]. The upstream linear unsteady flow can be determined by using weakly nonparallel stability theory and the resulting solution $\psi^{(o)}$, uniformly valid on the slow viscous spreading scale $x_3 = O(1)$, can easily be shown to match onto the inner nonlinear solution $\psi^{(i)}$ given by the unsteady part of the second term on the right-hand side of (5). A uniformly valid multiplicative composite solution can then be constructed by using the formula $\psi^{(c)} = \psi^{(o)}\psi^{(i)}/\psi^{(o/i)}$, where $\psi^{(o/i)}$ denotes the solution in the overlap domain. Upon substitution of the different solutions, the composite solution becomes

$$\psi^{(c)} = A(\bar{x}) \exp\left(-\int_0^{\bar{x}} \sigma d\bar{x}\right) A^{(o)}(x_3) \, \hat{\phi}_1^{(o)}(y, x_3)$$
$$\exp\left[i\left(\int_{x_e}^x \alpha(x_3)dx - St\right)\right], \tag{14}$$

where $\hat{\phi}_1^{(o)}(y, x_3)$ denotes the spatially growing eigensolution to the Rayleigh stability problem based on the streamwise mean-flow velocity at the location x_3,

$\alpha = \alpha_r + i\alpha_i$ is the corresponding complex eigenvalue, $A^{(o)}(x_3)$ is the slowly varying amplitude function due to the (weak) nonparallel effects, and x_e is the excitation (or a reference) position. $A(\bar{x})\exp\left(-\int_0^{\bar{x}} \sigma d\bar{x}\right)$ can be interpreted as a universal nonlinear correction factor, which depends only on $\bar{U}$, $\bar{\lambda}$, μ and the shifted coordinate $\bar{x}$. The the latter coordinate is given in terms of the coordinate x_3, cf. Hultgren [4], by the implicit relationship

$$\int_0^{\bar{x}} \sigma_r d\bar{x} = \ln \frac{\alpha_0^2 U_c' |A^{(o)}(x_3)\exp\left(i\int_{x_e}^{x} \alpha(x_3)dx\right)}{\left(-\frac{1}{2}\bar{U}S_1\right)^i} \tag{15}$$

where the parameters now also are allowed to vary with the slow streamwise coordinate x_3. The streamwise location of the inner nonlinear region is automatically set by the linear instability-wave growth when $\bar{x}$ is determined using (15). If the argument of the natural logarithm in (15), which can be interpreted as the ratio of the instability-wave amplitude and the square of a measure of the detuning from the local neutral conditions, remains much less than unity in the streamwise region of interest, then nonlinear effects are not important in that region. Hultgren [4] found that the composite solution also applies in the next stage of evolution, i.e., the streamwise region where $x_2 = \epsilon^{1/2}x_1 = \epsilon x = O(1)$ and nonparallel effects are again important.

The asymptotic theory accounts for the instability-wave nonlinearity as well as the viscous spreading of the basic flow. Among the requirements for the experiments used to test the resulting uniformly valid composite solution are that the shear layer initially is laminar and, in particular, that sufficient details are available about the early development of both the instability wave and the mean flow so that a first principle comparison can be assured. In this respect, it is necessary that there is an initial streamwise region where the flow can be treated as a superposition of a linear instability wave and an undisturbed mean flow. An excellent discussion of relevant experimental literature, as well as other topics of interest, can be found in the review paper by Ho & Huerre [9]. Comparisons were made with experimental data for a plane-jet shear-layer [1], a circular-jet shear layer [2], and a mixing layer behind a splitter plate [3] by Hultgren [4] and the procedure or strategy used to ensure a first-principle comparison between theory and experiment is described in detail in that paper. It is important to point out here, however, that the mean streamwise velocity profile was fitted by an analytical expression at *only one* streamwise measuring station – located sufficiently far upstream to ensure that the instability wave had small enough an amplitude so that the local mean flow was unaffected by its presence. The downstream evolution of the undisturbed mean flow was then computed and the amplitude evolution of the linear instability wave was determined numerically based on the computed local mean-flow velocity profiles. Finally, the nonlinear correction factor in (14) was evaluated by solving the nonlinear nonequilibrium critical-layer problem (10) - (13) with slowly varying parameters.

The Thomas & Chu [1] experiment involves a plane jet issuing from a two-dimensional nozzle. Although the mean-flow configuration is that of a submerged plane jet, the initial shear layers are completely noninteracting for the streamwise region of interest here (at most one and a half slot-width downstream of the plane-jet orifice) and can therefore be treated independently. They used a relatively low-level single-frequency acoustic excitation to somewhat organize the disturbance flow and to provide a phase reference. Figure 4 shows a comparison of the composite-solution and the experimental results for the energy associated with the streamwise velocity component u_* of the instability wave, $E_1 = \int_{-\infty}^{+\infty} \overline{u_*^2} dy_* / (2L_\omega U_{A*}^2) = \frac{1}{2} S \int_{-\infty}^{+\infty} \overline{\left[\mathrm{Re}\left(\partial \psi^{(c)} / \partial y \right) \right]^2} dy$, where the overbar stands for a period average and $\psi^{(c)}$ is given by (14). While the theory does not predict the last data point very well, Thomas & Chu's [1] figure 11 shows the flow to be dominated by subharmonics of the sum and difference frequencies of the forcing frequency of $750Hz$ and the so called jet-column frequency of $125Hz$ at that streamwise station and hence that the assumptions of the theory are probably violated there. Note that one of the inherent assumptions of the theory is that the disturbance flow is dominated by the forcing frequency outside of the critical layer. However, all harmonics are generated and are on equal footing inside the critical layer since the flow is strongly nonlinear there. The less drastic amplitude reduction predicted by the composite solution once the peak value is passed is also reminiscent of the experimental results obtained by Freymuth [2], see below. This figure also shows that there is an initial streamwise region where the disturbance is well described by weakly nonparallel linear theory based on undisturbed mean-flow profiles, which as pointed out above, is an essential part of assuring that a first-principle comparison is being carried out. As pointed out by Thomas & Chu [1] and as can be seen clearly from the present figure, the nonlinear instability wave saturates well upstream of the linear neutral stability point for the undisturbed mean flow. The effective saturation in the composite solution is associated with the first of the local amplitude maxima caused by oscillations in the growth rate, eg. [6] and [7]. The predicted instability-wave evolution and saturation is in excellent agreement with the experiment in the streamwise region where the experimental disturbance flow is dominated by the forced frequency, i.e., within the expected range of validity of the theory.

Figure 5 shows a comparison of the composite solution with Freymuth's [2, figure 10] circular-jet shear-layer amplitude-evolution data for four different excitation levels. Freymuth [2] used the transverse maximum of the r.m.s. value of the streamwise velocity component of the instability wave as a measure of the disturbance amplitude, i.e., u'_{max}, where $u'^2 = \overline{u_*^2}/U_{A*}^2 = \overline{\left[\mathrm{Re}\left(\partial \psi^{(c)} / \partial y \right) \right]^2}$, and $\psi^{(c)}$ is given by (14). This figure confirms that there is an initial streamwise region where the disturbance is well described by weakly nonparallel linear stability theory based on the undisturbed mean flow and that, of course, this region becomes shorter with increasing initial amplitude. The composite solution is in good agreement with the experimental data corresponding to the lowest excitation level except for what
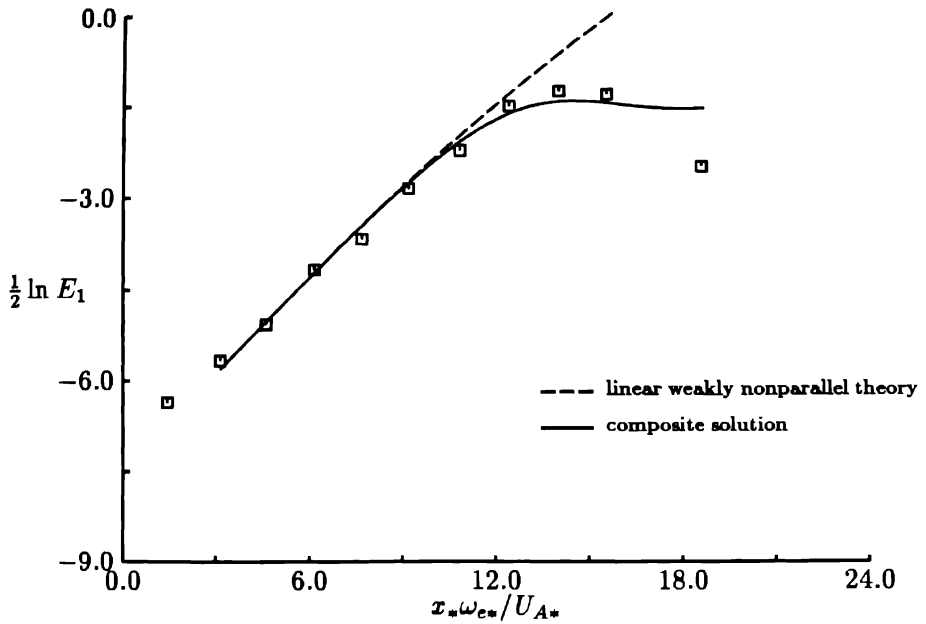
Fig. 4. Comparison of composite solution accounting for both nonlinear critical-layer effects and viscous mean-flow spreading with instability-wave energy data from Thomas & Chu's [1] plane-jet shear-layer experiment.

appears to be a local minimum in the experimental data just past the first nonlinear saturation. This discrepancy could be caused by an interaction with naturally occurring 'subharmonic' disturbances that are not accounted for in the present theory, as in the comparison above with the Thomas & Chu [1] experiment, but unfortunately Freymuth [2] does not provide any information about such disturbances. The agreement between theory and experiment is very good at the the next higher level of initial amplitude, however. This gives some further circumstantial evidence for the conjecture above since the naturally occurring 'subharmonic' disturbances probably have not reached a sufficient amplitude to ultimately influence the fundamental disturbance in any but the least excited case where the saturation occurs the furthest downstream. For the highest two excitation levels, the nonlinear effects come into play upstream of the streamwise location where ω_{e*} corresponds to the peak in the local linear growth-rate curve. Since the relative importance of the linear effects are then overestimated in the nonlinear theory, the composite solution, as can be seen in Fig. 5, will increasingly underestimate the deviation from the weakly nonparallel linear theory with increasing excitation level. The composite solution yields a qualitative correct result for the highest two levels of excitation here, however.
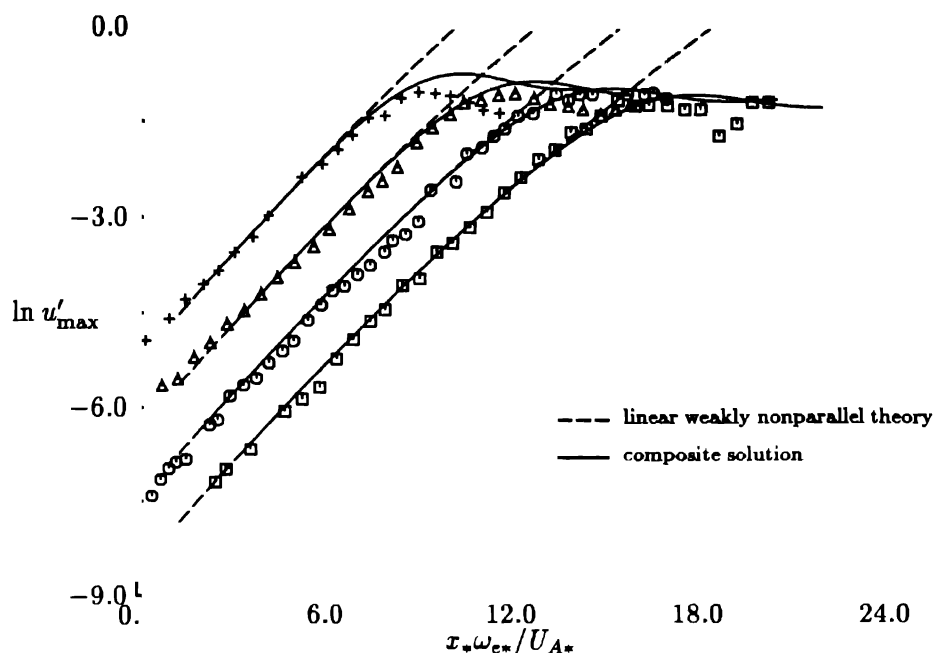
Fig. 5. Comparison of composite solution accounting for both nonlinear critical-layer effects and viscous mean-flow spreading with instability-wave amplitude data from Freymuth's [2] circular-jet shear-layer experiment.

The third experiment used for comparison consists of unpublished data kindly supplied by Ho & Zohar [3] for a mixing layer behind a splitter plate. A relatively low-level forcing at the so-called natural shear-layer frequency (here $355Hz$) was used to excite the shear layer, but data was also supplied for the corresponding unforced case. The shear-layer facility is the same as used in Huang & Ho [10] and further information about the windtunnel can be found in that paper. Figure 6 shows a comparison of the experimental data for the streamwise evolution of the instability-wave energy and the composite solution. This figure shows that there is an initial streamwise region where the instability wave is well described by weakly nonparallel linear stability theory based on the undisturbed mean-flow computation. The agreement between the composite instability-wave energy and the experimental data is good also in this case. The main effects of the wake component on the local linear stability properties are an increase in the maximum value of the growth rate and a reduction in the unstable frequency range. However, the undisturbed shear layer spreads less over the streamwise region of interest in this case compared to the experiments discussed above. Consequently, the local Strouhal number of the instability wave, initially being just slightly less than the one corresponding to the maximum growth rate, remains close to the peak value at all streamwise stations. This, as noted above, leads to an overestimation of the
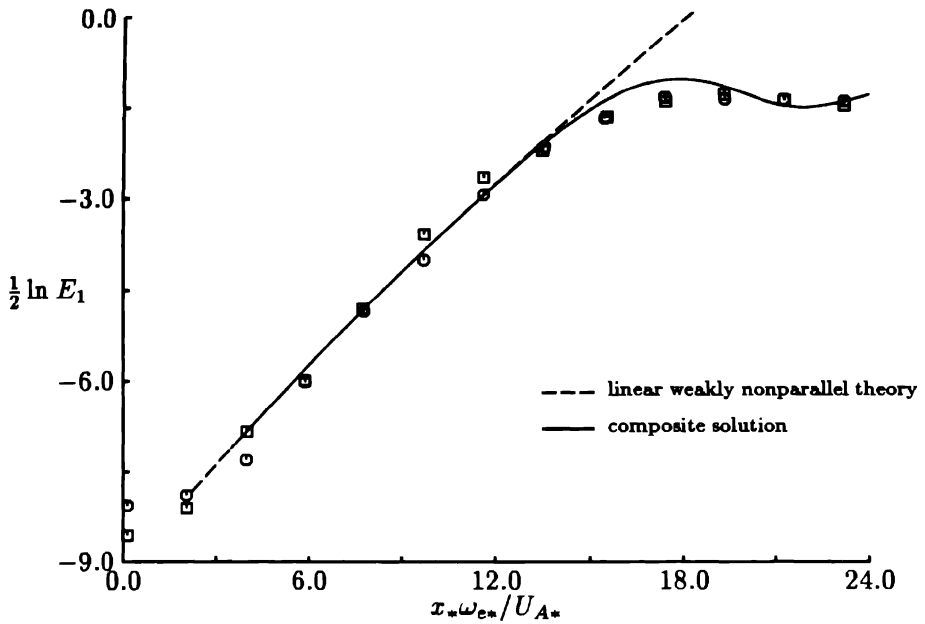
Fig. 6   Comparison of composite solution accounting for both nonlinear critical-layer effects and viscous mean-flow spreading with instability-wave energy data from Ho & Zohar's [3] mixing-layer experiment. □: low-level forcing, ○: unforced case.

relative importance of linear effects in the nonlinear theory and, hence, is the most likely cause for the small overshoot in the composite instability-wave energy.

3. The supersonic case

Consider a nearly inviscid compressible shear flow of an ideal gas between two parallel streams with nominally uniform temperatures T_1, T_2, and velocities $U_1 > U_2$. The upstream flow consists of oblique spatially growing time-harmonic linear instability waves on the steady two-dimensional shear layer that forms between the two streams. The flow parameters in the high-speed stream are generally used as reference quantities and a reference length scale δ can be taken as, say, half the vorticity thickness of the shear layer at some suitable streamwise location. The steady flow is then characterized by the Mach number $M = U_1/\sqrt{k\Re T_1}$ and the Reynolds number $R = \delta U_1/\nu_1$, where k is the isentropic exponent of the gas, $\Re$ is the gas constant and ν_1 is the kinematic viscosity of the high-speed stream. The Reynolds number is assumed large enough so that the mean pressure is constant across the shear layer and the mean flow is nearly parallel over many wavelengths of the instability wave.

Consider first a single three-dimensional instability wave growing in its propagation direction. When nonlinear effects do not first intervene, the slow viscous spreading of the mean shear layer again causes the spatial growth rate of the linear instability wave to gradually decrease until the neutral stability condition is reached. The Strouhal number and streamwise and spanwise wave numbers at the neutral stability point are denoted by S_0, α_0, and β_0, respectively. The analysis of Goldstein & Leib [11] and Leib [12] shows that the critical layer nonlinearity behaves quite differently for nonisothermal flows – primarily because the temperature fluctuations have an algebraic singularity at the critical layer in the linear theory (Reshotko [13]) and therefore become very large compared to the perturbation velocity components in the plane of the wave. Nonlinearity now becomes important when the spatial growth rate is $O(\epsilon^{2/5})$. The local Strouhal number in this region can be expressed as

$$S = S_0 + \epsilon^{2/5} S_1, \ S_1 < 0, \ S_1 = O(1). \tag{16}$$

and the relevant slow coordinate on which nonlinear effects take place is now

$$\bar{x}_1 = \epsilon^{2/5}(x \cos \theta + z \sin \theta), \tag{17}$$

where $\theta = \arctan \frac{\beta_0}{\alpha_0}$ is the angle of propagation.

The unsteady flow outside of the critical layer is, to leading order, governed by the compressible Rayleigh equation in terms of the perturbation pressure for a neutral disturbance, and a sequence of higher problems can be constructed in the manner described by Goldstein & Leib [11]. For Mach numbers less than about seven, it turns out that the neutral wave corresponding to a wave in the direction leading to maximum growth has a phase velocity that is subsonic relative to both streams. According to Lees & Lin ([14]), it thus has a critical level at the generalized inflexion point (or points) defined by $(U'/T)' = 0$, where U and T are the local mean streamwise velocity and temperature and the prime denotes differentiation with respect to y. Goldstein & Leib [11] restricted their analysis to this case where the critical level corresponds to a generalized inflexion point. As a consequence, the leading-order pressure perturbation is regular at the critical level which without loss of generality can be assumed to be at $y = 0$. As already pointed out, the leading-order temperature fluctuation is algebraically singular at $y = 0$, however.

The change in scaling relative to the incompressible two-dimensional case produces a corresponding change in the critical layer structure. The critical layer flow is now described by the scaled transverse coordinate $Y = y/\epsilon^{2/5}$, and is governed by linear dynamics to lowest order of approximation with nonlinearity entering only through inhomogeneous terms in the higher-order problems. Goldstein & Leib [11] analyzed the case where the viscous parameter $\lambda = 1/Re\epsilon^{6/5} = O(1)$ with the additional assumptions that the viscosity variation with temperature is linear (Chapman's Law) and that the Prandtl number is unity. With this restriction on the viscous parameter λ, viscous effects play a passive role outside the critical

layer but enter the critical-layer dynamics at the same order as the nonlinear effects. By equating the phase jump across the critical level as formally computed from the outer and critical-layer solutions, Goldstein & Leib [11] found that the instability growth rate is still completely controlled by the nonlinear critical-layer effects and that the instability evolution now can be calculated from the following equation:

$$\frac{dA}{d\bar{x}} = \bar{\kappa}A + \bar{\kappa}\gamma \int_{-\infty}^{\bar{x}} \int_{-\infty}^{\tilde{x}} K\left(\bar{x}|\hat{x},\tilde{x}\right) A(\hat{x})A(\tilde{x})A^*(\tilde{\bar{x}} + \hat{x} - \bar{x})d\tilde{x}d\hat{x}, \quad (18)$$

where

$$K\left(\bar{x}|\hat{x},\tilde{x}\right) = (\bar{x} - \hat{x})^2 \exp\left\{-\bar{\lambda}(\bar{x} - \hat{x})^2 \left[\bar{x} - \tilde{\bar{x}} - (\bar{x} - \hat{x})/3\right]\right\}, \quad (19)$$

$\bar{x}$ is a renormalization of the slow variable $\bar{x}_1$, A is a scaled and normalized instability wave amplitude, the star denotes complex conjugation, $\bar{\lambda}$ is a scaled parameter corresponding to λ, and $\bar{\kappa}$ and γ are two complex parameters that can be calculated from the outer linear solution. [Note that γ here corresponds to $-1/\gamma$ in the notation of Goldstein & Leib [11]]. $\bar{\kappa}$ can be thought of as the scaled (complex) growth rate of the linear instability wave entering the nonlinear region whereas γ is directly proportional to the mean temperature gradient at the critical level. Leib [12] has recently removed the restrictions to the regular neutral case and unit Prandtl number, generalized the viscosity-temperature law, and shown that the amplitude evolution equation is also of the form (18) when the critical level is no longer a generalized inflexion point.

Goldstein & Leib [11] found that the calculated instability wave amplitudes initially follow the prescribed linear growth, but soon begin to either saturate or increase their growth as nonlinear effects come into play. Cumulative history effects eventually overpower these trends causing a rapid increase in amplitude which ends in a singularity at a finite downstream distance in the inviscid case. An equilibrium solution exists for certain parameter ranges in the viscous case, however. Figure 7 shows examples of this behavior. Goldstein & Leib [11] obtained asymptotic solutions for both the equilibrium and singular cases. The latter solution suggests that the flow will become fully nonlinear everywhere in the shear layer and, hence, that the motion must be governed by the full three-dimensional Euler equations in the vicinity and downstream of the singularity.

Consider now the case where the initial three-dimensional instability wave grows in the streamwise direction. It is then appropriate to suppose that there are two oblique modes with the same frequency and streamwise wave number and with (real) spanwise wave numbers of equal magnitude but opposite sign in order to represent a fixed spanwise structure. Goldstein & Choi [15] realized that the cross-flow velocity fluctuations, which have the same algebraic singularity as the temperature fluctuations as the critical level is approached, now become coupled to the velocity fluctuations in the plane of the wave. This nonlinear oblique-mode interaction causes the critical-layer nonlinearity to become important when the instability-wave growth rate is $O(\epsilon^{1/3})$, which corresponds to yet smaller
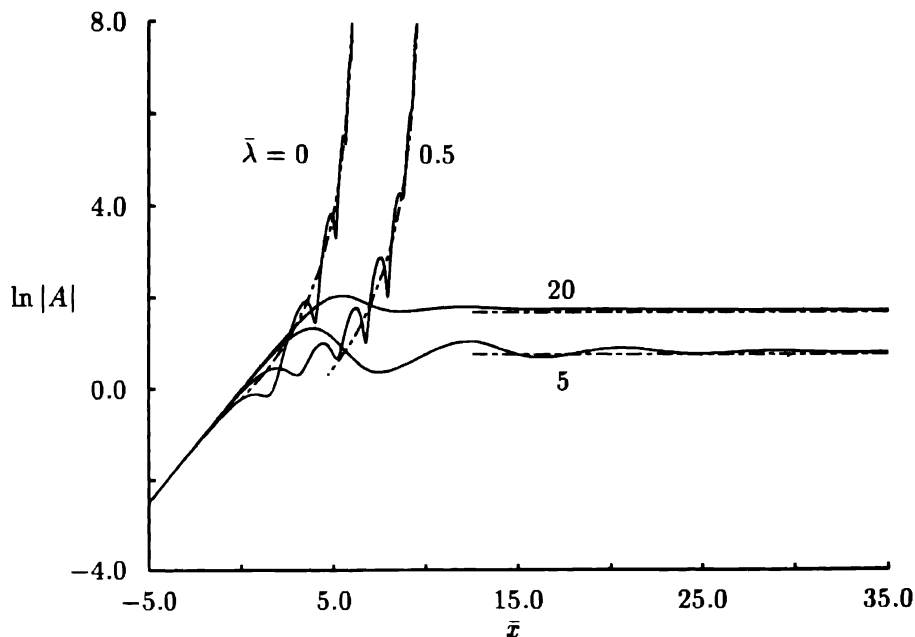
Fig. 7.   Three-dimensional instability-wave amplitude versus streamwise distance for a compressible shear layer for $\arg \bar{\kappa} = -\frac{\pi}{3}$, $\arg \gamma = -\frac{\pi}{2}$, and various values of $\bar{\lambda}$. The broken lines are asymptotic solutions.

amplitudes than the previously described case. In the nonlinear region, the local Strouhal number can now be expressed as

$$S = S_0 + \epsilon^{1/3} S_1, \; S_1 < 0, S_1 = O(1), \tag{20}$$

and the critical-layer nonlinearity now alters the flow on the slow streamwise scale

$$x_1 = \epsilon^{1/3} x. \tag{21}$$

and the critical layer itself is characterized by the scaled transverse coordinate $Y = y/\epsilon^{1/3}$.

The general solution procedure, although more complex, is in many respects similar to the one in Goldstein & Leib [11] and also leads to an integro-differential equation for the instability wave amplitude. While the phenomenon is of most importance in supersonic shear layers, Goldstein & Choi [15] restricted their derivations to the inviscid incompressible case for simplicity of exposition because compressibility effects do not affect the nonlinear critical-layer dynamics. Their final amplitude equation is also valid for the compressible case, however. It is of the form (18) but now with K given by

$$K\left(\bar{x}|\hat{x},\tilde{x}\right) = -\tfrac{1}{2}\tan^2 \theta \cos 2\theta \, (\bar{x} - \hat{x}) \left[(\bar{x} - \hat{x})^2 + (\bar{x} - \tilde{x})^2\right.$$

$$- \cos 2\theta \; (\bar{x} - \bar{\bar{x}})(\tilde{x} - \tilde{\bar{x}}) \Big] \; ; \qquad\qquad (22)$$

$\bar{r}$, A, θ, and $\bar{\kappa}$ have meanings similar to the corresponding quantities in the previous case and γ is a complex parameter that (as well as $\bar{\kappa}$) can be calculated from the outer solution.

The calculated instability wave amplitudes again initially follow the prescribed linear growth, then, in an intermediate region where the nonlinear effects begin to come in, the detailed behavior depends somewhat on the parameters of the problem, and finally the cumulative history effects lead to a rapid growth of the amplitude, again ending in a singularity at a finite downstream position. The local asymptotic solution valid in the vicinity of the singularity obtained by Goldstein & Choi [15] showed that the motion downstream of the singularity also here will be governed by the full tree-dimensional Euler equations.

4. Discussion

The nonlinear critical-layer behavior dynamics are quite different in each of the previous two sections. In the two-dimensional incompressible case, the critical-layer nonlinearity produces a redistribution of vorticity which rapidly reduces the instability-wave growth rate from its linear value. In the two cases discussed in the last section, the temperature nonuniformities acts as a vorticity source in the first and the three-dimensional effects allow for vortex stretching in the second with both effects completely counteracting the redistribution effect and thus producing explosive growth. This phenomenon is probably masked at subsonic speeds due to the fact that the linear growth rates of three-dimensional waves are much smaller than that of a two-dimensional wave. The presence of the latter wave can also alter the critical-layer structure of the oblique waves and thereby possibly remove the singular behavior.

References

1. Thomas, F. O. and Chu, H. C., An experimental investigation of the transition of a planar jet: subharmonic suppression and upstream feedback, *Physics of Fluids* A 1 (1989) 1566–1587.
2. Freymuth, P. J., On transition in a separated laminar boundary layer, *Journal of Fluid Mechanics* 25 (1966) 683–704.
3. Ho, C.-M. and Zohar, Y., Private Communication, Dept. Aerosp. Eng., Univ. South. Calif., Los Angeles, CA (1989).
4. Hultgren, L. S., Nonlinear spatial equilibration of an externally excited instability wave in a free shear layer, *Journal of Fluid Mechanics* 236 (1992) 635–664.
5. Huerre, P., The nonlinear stability of a free shear layer in the viscous critical layer regime, *Philosophical Transactions Royal Society London* A 293 (1980) 643–672.
6. Goldstein, M. E. and Leib, S. J., Nonlinear roll-up of externally excited free shear layers, *Journal of Fluid Mechanics* 197 (1988) 481–515.
7. Goldstein, M. E. and Hultgren, L. S., Nonlinear spatial evolution of an externally excited instability wave in a free shear layer, *Journal of Fluid Mechanics* 197 (1988) 295–330.
8. Benney, D. J. and Bergeron, R. F., A new class of non-linear waves in parallel flows, *Studies in Applied Mathematics* 48 (1969) 181–204.

9. Ho, C.-M. and Huerre, P., Perturbed free shear layers, *Annual Review of Fluid Mechanics* 16 (1984) 365-424.
10. Huang, L.-S. and Ho, C.-M., Small-scale transition in a planar mixing layer, *Journal of Fluid Mechanics* 210 (1990) 475–500.
11. Goldstein, M. E. and Leib, S. J., Nonlinear evolution of oblique waves on compressible shear layers, *Journal of Fluid Mechanics* 207 (1989) 73–96.
12. Leib, S. J., Nonlinear evolution of subsonic disturbances in a compressible free shear layer, *Journal of Fluid Mechanics* 224 (1991) 551–578.
13. Reshotko, E., Stability of the Compressible Laminar Boundary Layer, CALCIT Memo No 52. Calif. Inst. Tech, Pasadena, CA (1960).
14. Lees, L. and Lin, C. C., Investigations of the Stability of the Laminar Boundary Layer in a Compressible Fluid, NACA TN-1115 (1946).
15. Goldstein, M. E. and Choi, S.-W., Nonlinear evolution of interacting oblique waves on two-dimensional shear layers, *Journal of Fluid Mechanics* 207 (1989) 97–120. Errata, *Journal of Fluid Mechanics* 216 (1990) 659–663.

Modelling of Rapid Pressure-Strain in Reynolds Stress Closures – Difficulties Associated with Rotational Mean Flows

ARNE V. JOHANSSON, MAGNUS HALLBÄCK and ERIK LINDBORG
Department of Mechanics, Royal Institute of Technology
10044 Stockholm, Sweden

Abstract. Intercomponent energy transfer within the context of Reynolds stress closures is studied. Attention is focussed on the rapid limit of homogeneous flow situations where this energy transfer is caused solely by the rapid pressure strain rate. We present and analyze the performance of the recently proposed rapid pressure strain rate model of Johansson & Hallbäck (J Fluid Mech. 1994) in various homogeneous (rapid) flow situations, and compare with results obtained with other models from the literature and rapid distortion solutions. The prediction difficulties associated with rotational mean flows are analyzed. A generally formulated test case, which as special cases comprises, e.g. plane strain and homogeneous shear flow, is used to illustrate the modelling difficulties associated with rotational mean flows. An axisymmetric case is used to demonstrate that parts of the spectrum with anti-reflectional symmetry, which are instrumental for the dynamics when rotational effects are present, are totally missed in classical Reynolds stress closures. A closer prediction in cases with strong influence of rotation would require introduction of other transported quantities.

1. Introduction

There is a general trend in today's turbulence modelling efforts to aim for increased generality and better handling of complex flow situations where, e.g., effects of strong streamline curvature or system rotation may be important. Since the kinetic energy equation is unaffected by, e.g., system rotation, the lowest level of single-point closure at which such effects enter explicitly is that in which transport equations are formulated for the individual Reynolds stress components. In these, the Coriolis force gives rise to terms that directly will influence the intercomponent transfer. Launder, Tselepidakis and Younis (1987) showed that even with relatively simple modelling of the terms involved, a Reynolds stress model is capable of capturing the main effects of system rotation on a plane turbulent channel flow. The tendency to develop a distinctly asymmetric velocity profile cannot be predicted with, e.g., a standard $k - \varepsilon$ model, but was here clearly shown to result from the inherent dynamics of the Reynolds stress transport equations.

We will refer to closure schemes with transport equations for the velocity correlations, $\overline{u_i u_j}$, and the total dissipation rate, ε, as *classical* Reynolds stress models. For more background information the reader is referred to, e.g., the review of Launder (1989). Instead of using $\overline{u_i u_j}$ as the quantities for which transport

equations should be solved one may perhaps more conveniently formulate model equations for the kinetic energy, $k = \overline{u_i u_i}/2$, and the Reynolds stress anisotropy tensor

$$a_{ij} = \frac{\overline{u_i u_j}}{k} - \frac{2}{3}\delta_{ij},$$

where δ_{ij} is the Kronecker delta.

In homogeneous turbulence there is no spatial redistribution of energy and the transport equations for the stress anisotropies can symbolically be written

$$\frac{da_{ij}}{dt} = P_{ij}^{(a)} + \frac{1}{k}\Gamma^{(r)} + \frac{1}{k}\Pi_{ij}^{(s)} - \frac{\varepsilon}{k}(e_{ij} - a_{ij}) \tag{1}$$

where the production term $P_{ij}^{(a)}$ is explicit in a_{ij} and hence needs no modelling. e_{ij} denotes the dissipation rate anisotropy tensor

$$e_{ij} = \frac{\varepsilon_{ij}}{\varepsilon} - \frac{2}{3}\delta_{ij}$$

The pressure strain rate correlation term, which has zero trace, has in eq. (1) been divided into a rapid ($\Pi_{ij}^{(r)}$) and a slow term ($\Pi_{ij}^{(s)}$) in the traditional manner.

Our attention is here restricted to homogeneous turbulent flows, and there only the rapid part (a recent investigation, based on direct numerical simulations, of the slow part can be found in Hallbäck, Sjögren & Johansson 1993). For homogeneous flows the rapid pressure strain rate can be written in terms of a fourth rank tensor

$$\Pi_{ij}^{(r)} = 4kU_{p,q}(M_{iqpj} + M_{jqpi} \tag{2}$$

in which $U_{i,j}$ is the mean velocity gradient tensor and

$$M_{ijpq} = \frac{1}{2k}\int \frac{\kappa_p \kappa_q}{\kappa_m \kappa_n} \, \Phi_{ij} \, d\kappa = -\frac{\cdot}{8\pi k}\int \frac{\partial^2 \overline{u_i u_j'}}{\partial r_p \partial r_q} \, dx' \qquad x' = x + r \tag{3}$$

where κ is the wave number vector and Φ_{ij} is the spectrum tensor. The expression (3) comes from the formal solution of the Poisson equation for the pressure field.

A natural approach to the modelling of the rapid pressure strain is to express the M-tensor in terms of the dimensionless Reynolds stress anisotropy tensor. Actually, this is the only reasonable choice within the context of *classical* RST-modelling. The above expressions show that the M-tensor is not immediately affected by a sudden change in the mean strain field. This suggests that the modelled M-tensor should not explicitly depend on $U_{i,j}$. Furthermore, the M-tensor is dimensionless and can therefore not depend explicitly on k (or ε), except through a possible dependence on the turbulence Reynolds number. One may also note that the normalized Reynolds stress tensor is retrieved upon contraction of the two last indices in the M-tensor, which yields one exact relation between the M-tensor and the anisotropy tensor

$$M_{ijpp} = \frac{1}{2}a_{ij} + \frac{1}{3}\delta_{ij} \tag{4}$$

As a consequence, practically all existing models can be seen as expansions of M to first or higher order in a_{ij}.

Reynolds (1987) (see also Lee & Reynolds 1985) showed that the most general expansion of the M-tensor in terms of a_{ij}, that satisfies correct index symmetry properties, can be written with the aid of 15 undetermined scalar functions and contains terms up to fourth order in a_{ij}. A complete ansatz for a linear model can be written in terms of 5 model parameters. The determination of model constants have been done by use of basic constraints and often by use of comparisons with data from physical or numerical experiments. Also rapid distortion theory (RDT) has proven to be a powerful tool in the determination of the model constants (see Johansson & Hallbäck 1994).

Shih, Reynolds & Mansour (1990) presented a model for the spectrum tensor parametrized (to first order) in the Reynolds stress anisotropy tensor. It bears a close resemblance to the parametrization of the spectrum tensor in spectral anisotropy described by Cambon, Jeandel & Mathieu (1981). Shih *et al.* showed that the resulting pressure strain rate is equivalent to a linear model of the Launder, Reece & Rodi (1975) form. They found the range of validity of the spectrum model and thereby of linear $\Pi_{ij}^{(r)}$ models to be quite small in terms of the magnitude of the anisotropy It is clear from their results that in general accurate predictions require a model that is nonlinear in the stresses, or equivalently, the anisotropy tensor. In fact, already 1972 Hanjalić & Launder proposed a nonlinear model, quadratic in the stresses, on the grounds of lack of agreement between linear models and experimental data. One may also readily show (see, e.g., Lumley 1978) that linear models cannot satisfy the condition of ensuring realizable solutions under all flow conditions. Violation of this condition may under extreme conditions lead to prediction of negative energies (see Schumann 1977, Lumley 1978 and Pope 1985).

Speziale, Sarkar & Gatski (1991) analyzed the modelling of the two parts of the pressure strain, compared various existing models and proposed a new nonlinear model. They found an improved performance over linear models and recognized remaining difficulties in cases with rotational mean flows. Shih & Lumley (1993) studied the performance of various pressure-strain-rate models, partly by use of direct numerical simulation data. Efforts to generalize the concept of RST-models have been discussed in the literature. Mansour, Shih & Reynolds (1991) studied the effects of rapid rotation on initially anisotropic homogeneous turbulence with the aid of RDT and DNS, and discussed briefly some possibilities of extending the Reynolds stress closure concept in order to improve the treatment of effects of rotation. Also, Cambon, Jacquin & Lubrano (1992) analyzed a generalized approach with the aim of improving the description of effects of rotation. Some first steps were taken, and the great difficulty involved was recognized.

In the present study we present and analyze the performance of the recently proposed model of Johansson & Hallbäck (1994) in various homogeneous (rapid) flow situations, and compare with results obtained with other models from the

literature. Our attention is here focussed on the analysis of prediction difficulties associated with rotational mean flows, and illustrations of situations with varying degree of rotational influence.

2. The new $\Pi_{ij}^{(r)}$ model

The most general ansatz for a model of the M-tensor in terms of an expansion in a_{ij} (that satisfies the index symmetry properties of M_{ijpq}) may be written in terms of 15 tensorially independent groups including products up to fourth order in a_{ij}. The fact that fifth (and higher) order terms do not give rise to further independent terms can be shown with the aid of the Cayley-Hamilton theorem. The complete expression is given in Johansson & Hallbäck (1994) (hereafter referred to as JH, see also Reynolds 1987). Each of the groups is multiplied by a scalar function that may depend on the invariants of a_{ij}

$$II_a = a_{ij}a_{ji} \qquad III_a = a_{ij}a_{jk}a_{ki} \tag{5}$$

and other scalar flow parameters such as the turbulence Reynolds number Re_T and possibly the strain rate parameter S^*.

$$Re_T = \frac{4k^2}{\nu\varepsilon} \qquad S^* = 2(S_{ij}S_{ij}/2)^{1/2}\frac{k}{\varepsilon} \tag{6}$$

where $S_{ij} = (U_{i,j} + U_{j,i})/2$ is the strain rate tensor. In the following analysis the mean velocity gradient tensor will be replaced by the sum of S_{ij} and the rotation tensor $\Omega_{ij} = (U_{i,j} - U_{j,i})/2$. Direct numerical simulations (see JH) showed that the influence of Re_T and S^* is of minor importance and may be neglected for the present modelling purposes.

Insertion of the ansatz for the M-tensor in (2) leads, after some algebra and use of the extended Cayley-Hamilton theorem (see Spencer & Rivlin 1958) to an expression for the $\Pi_{ij}^{(r)}$ containing 11 tensorially independent groups. The continuity condition, which is equivalent to requiring $\Pi_{ij}^{(r)}$ to be traceless, is readily applied and further reduces the number of scalar functions to 9, and we get

$$
\begin{aligned}
\frac{1}{k}\Pi_{ij}^{(r)} = S_{pq} \ [\ & Q_1\delta_{ip}\delta_{jq} + Q_2(a_{ip}\delta_{jq} + a_{jp}\delta_{iq} - \frac{2}{3}\iota \\
+ \ & Q_3 a_{pq}a_{ij} + Q_4(a_{iq}a_{jp} - \frac{1}{3}a_{pk}a_{kq}\delta_{ij}) \\
+ \ & Q_5 a_{pl}a_{lq}a_{ij} + (Q_5 a_{pq} + Q_6 a_{pl}a_{lq})(a_{ik}a_{kj} - \frac{1}{3}II_a\delta_{ij})] \\
+ \Omega_{pq} \ [\ & Q_7(a_{ip}\delta_{jq} + a_{jp}\delta_{iq}) \\
+ \ & Q_8 a_{pk}(a_{jk}\delta_{iq} + a_{ik}\delta_{jq}) + Q_9 a_{pk}(a_{jk}a_{iq} + a_{ik}a_{jq})] \quad (7)
\end{aligned}
$$

where the scalar functions $Q_\alpha, \alpha = 1 - 9$, may depend on the invariants of a_{ij} and in principle on the scalar flow parameters (see (5, 6)).

The fact that the most general ansatz for $\Pi_{ij}^{(r)}$ can be written in terms of only 9 scalar functions (or 11 before application of the continuity condition) was first shown in JH. The expression (7) constitutes the ultimate form for the model of $\Pi_{ij}^{(r)}$ (for homogeneous flows) within the context of Reynolds stress closures, in which transport equations are used for $\overline{u_i u_j}$ and ε (or equivalently a_{ij}, k, ε). Hence, all existing models based on the concept of expansion of the M-tensor in terms of the stress anisotropy tensor, can be expressed as subsets of (7). For instance the general linear model (Launder et al. 1975) comprises the terms multiplied by Q_1–Q_2 and Q_7. The model of Lee (1990) is derived by use of rapid distortion theory for irrotational strain fields, and, hence, only contains the first six groups. Other models that will be discussed in the following are those of Speziale, Sarkar & Gatski (1991) (comprising Q_1–Q_3, Q_7), Fu, Launder & Tselepidakis (1987) (with Q_1–Q_4, Q_7–Q_9) and Shih & Lumley (1985) (with Q_1–Q_4, Q_7–Q_8).

The M-tensor index symmetry conditions and continuity is implicitly satisfied by the final form (7) for $\Pi_{ij}^{(r)}$. A further condition is obtained by the fact that $1 / |\mathbf{r}|$ is the Green's function of the Laplace operator, so that the normalized Reynolds stress is retrieved when the two last indices of the M-tensor are contracted. This condition (eq. 4) further reduces the number of unknown scalar functions to seven, B_α, say (the complete model is given in the appendix). Six of the scalar functions appear in the part associated with the irrotational part of the flow (S_{ij}).

The general form (7) for $\Pi_{ij}^{(r)}$ (with Q's as given in the appendix, eqs. 19a-i) ensures a correct response to first order in time for the anisotropy tensor in suddenly, rapidly distorted, initially isotropic turbulence, for arbitrary irrotational as well as rotational mean strain fields. This is true regardless of the specifics of the scalar functions $B_1 - B_7$.

It follows from the definitions (2,3) that $\Pi_{\lambda\lambda}^{(r)}$ (no summation) vanishes in the limit of two-component turbulence where $u_\lambda \equiv 0$. The condition that this property should be conserved by the model is equivalent to the strong realizability principle (Pope 1985). In the case of modelling the rapid pressure strain rate one may impose a somewhat more general condition,

$$M_{\lambda j p q} = 0 \tag{8}$$

which follows directly from the definition (3) of the M-tensor.

The model ansatz for the M-tensor is an expansion in the Reynolds stress anisotropy tensor a_{ij}. It is, hence, natural to form the final model as a truncation of the expression at a chosen power of $\|a_{ij}\|$. To obtain such a consistent truncation we need to expand the scalar functions B_α, (α =1–7) in terms of the invariants II_a and III_a. A natural approach is to use a Taylor expansion in these quantities.

$$B_1 = \alpha_1 + \alpha_4 II_a + \alpha_7 III_a \tag{9}$$

and similarly for the other B_α:s (see appendix). It is implicitly assumed that the expansions are well behaved within the complete invariant map (see Fig. 1).
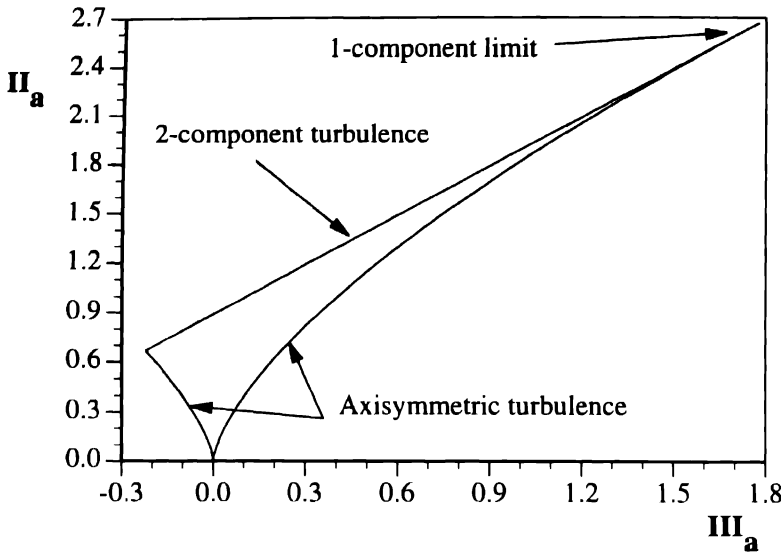
Fig. 1.   The a_{ij} invariant map

A consistent truncation at fourth order would include all tensorially independent terms in the model expression for the M-tensor, and contains 11 model parameters that may depend on Re_T and S^*, but not on the invariants of a_{ij}. Truncations at third, second or first order would involve six, three and one model parameter, respectively.

The importance of satisfying basic conditions and constraints is obvious for the possibility of obtaining a model of reasonable generality. The strong realizability condition plays a special role in ensuring a sound behaviour near extreme states. In strongly strained or sheared flows the component(s) of vanishing energy will then be reasonably well predicted regardless of the details of model. For the fourth order truncation six of the eleven parameters will be determined by the generalized realizability condition (8) (see appendix). Five parameters remain, one of which, however, does not appear in the expressions for Q_α. Hence, four parameters determine the complete fourth order model for $\Pi_{ij}^{(r)}$. In the following we will denote these by $\gamma_1, \gamma_2, \gamma_3$ and γ_4, respectively (see appendix). The latter has no influence for irrotational cases where a_{ij} is diagonal in the coordinate system where the axes coincide with the principal axes of the mean strain rate tensor.

2.1. MODEL PARAMETER VALUES

Since the simulation results in JH indicated that the relation between the M-tensor and the anisotropy tensor is practically independent of Reynolds number and little

influenced by the variations in energy distributions in wave-number space that may be caused by different mean strain rates, it appears sufficient to restrict the comparisons to the rapid limit. Here the results may be obtained by use of rapid distortion theory (RDT) and we may write the evolution equations for the stress anisotropies

$$\frac{da_{ij}}{dt} = P_{ij}^{(a)} + \frac{1}{k}\Pi_{ij}^{(r)}$$ (10)

where the a_{ij}-production term is explicit in the anisotropy tensor (a quadratic form) and linear in S_{ij} and Ω_{ij} (see e.g. JH).

The model parameters were in JH determined from comparisons between RDT solutions and model predictions for small times, where we may expand

$$a_{ij} = ta_{ij}^{(1)} + t^2 a_{ij}^{(2)} + t^3 a_{ij}^{(3)} + \cdots$$ (11)

for the case of initially isotropic turbulence.

The general $\Pi_{ij}^{(r)}$ model form (7) inserted into (10) gives a correct behaviour of a_{ij} to first order in time (t) for initially isotropic, suddenly distorted turbulence, regardless of degree of truncation. With $\gamma_1 = -1/7$ the model will also give correct results to second order in time (i.e. $a_{ij}^{(2)}$ correctly predicted) for arbitrary irrotational or rotational mean strain fields, and regardless of the values of the other model parameters.

No choice of model parameter values (for the fourth order model) will ensure correct predictions to third order in time for arbitrary mean flows, but it was shown in JH that if $\gamma_3 = \frac{9}{196} - \frac{16}{5}\gamma_2$ (and $\gamma_1 = -1/7$) correct predictions will also be obtained of $a_{ij}^{(3)}$ for arbitrary irrotational mean flows.

The last parameter influencing the irrotationally strained initially isotropic cases was determined in JH by requiring the model to correctly predict the behaviour to fourth order in time for the case of a rapid plane strain. The final parameter γ_4 was chosen to give the best possible prediction of the oscillation period (for the anisotropy components) in the case of a rapid pure rotation of initially anisotropic turbulence. The initial field was chosen as $(a_{11o}, a_{22o}, a_{33o}) = (1/3, -1/3, 0)$. The set of calibrated parameter values for the fourth order model becomes

$$\gamma_1 = -1/7, \quad \gamma_2 = \frac{148179}{5027792} \approx 0.0295,$$
$$\gamma_3 = \frac{9}{196} - \frac{16}{5}\gamma_2 \approx -0.0484, \quad \gamma_4 = 0.1$$

3. A test case with variable degree of influence of rotation

We will here investigate the performance of the fourth order model for cases with varying degree of influence of rotational effects. The cases studied here are

restricted to represent the rapid limit only and can all be described in terms of the following velocity gradient tensor

$$[U_{i,j}] = \begin{array}{ccc} 0 & \sigma + \Omega & 0 \\ \sigma - \Omega & 0 & 0 \\ 0 & 0 & 0 \end{array} \tag{12}$$

When appropriate, comparisons will be made with other models published in the literature. The cases represented by eq. (12) comprise, in order of increasing effect of rotation, plane strain ($\Omega = 0$), homogeneous shear flow ($\Omega = \sigma$) and pure rotation ($\sigma = 0$), as well as intermediate cases. The situations studied are chosen to illustrate the capability of the fourth order model and to focus on remaining modelling difficulties associated with rotational effects.

By choosing Ω greater than σ we obtain flow situations where the material elements following the mean flow are deformed periodically, returning to their initial shape with a period of $\sqrt{\Omega^2 - \sigma^2}$. This type of flow is sometimes referred to as elliptic due to fact that the streamlines constitute a family of similar ellipses. Linear (rapid distortion) analysis has been applied by a number of investigators in order to study the three-dimensional instability of this type of flow, see e.g. Bayly, Orszag & Herbert (1988).

As was shown in detail in JH the fourth order model gives a very accurate description of all irrotational cases as is illustrated in Fig. 2 for the situation of a rapid plane strain ($\Omega = 0$) applied to initially isotropic turbulence. The model predictions are shown both as function of total reference strain $c = \exp\left((S_{ij}S_{ij}/2)^{1/2}t\right)$ and as function of normalized time, and are compared with the corresponding RDT results.

The DNS results of JH also showed that for irrotational cases the (fourth order) $\Pi_{ij}^{(r)}$ model is valid far outside the RDT regime, even down to nondimensional mean strain rates of order unity.

3.1. RAPID HOMOGENEOUS SHEAR FLOW

In homogeneous shear flow the irrotational and rotational parts of the strain may be said to be of equally strong influence. Despite its apparent simplicity it is a challenging test case for turbulence models. It is a situation where there is a misalignment between the principal axes of the anisotropy and strain-rate tensors. This misalignment cannot be predicted by simple models, e.g., of eddy-viscosity type.

Model predictions for the stress anisotropies are compared with RDT-results in Fig. 3. The corresponding comparison for the kinetic energy in figure 4 are complemented with predictions by other models published in the literature.

The results for the fourth order model are reasonably close to the RDT results, although one should note that all details of the anisotropy state are not well captured
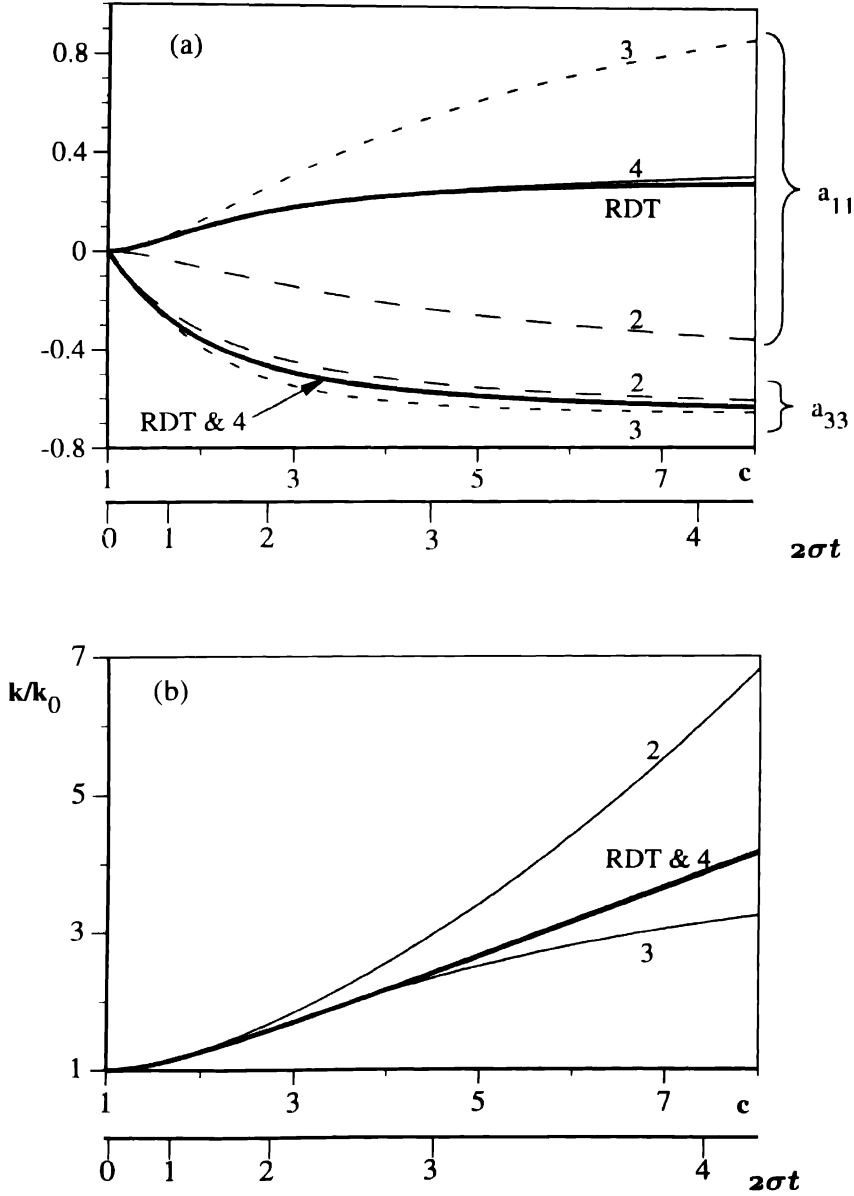
Fig. 2.   The Reynolds stress anisotropies (a) and kinetic energy (b) as function of total reference strain (and normalized time) in a (rapid) plane strain flow. The numbers 2 – 4 label the predictions with 2:nd 3:rd and 4:th order models.
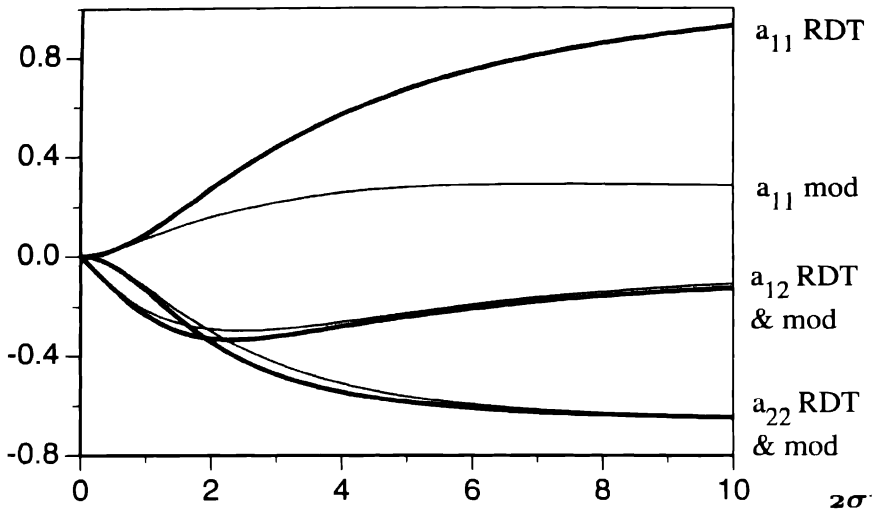
Fig. 3.   RDT and fourth order model predictions of the Reynolds stress anisotropies as function of nondimensional time in a (rapid) homogeneous shear flow (note that $2\sigma = U_{1,2}$)
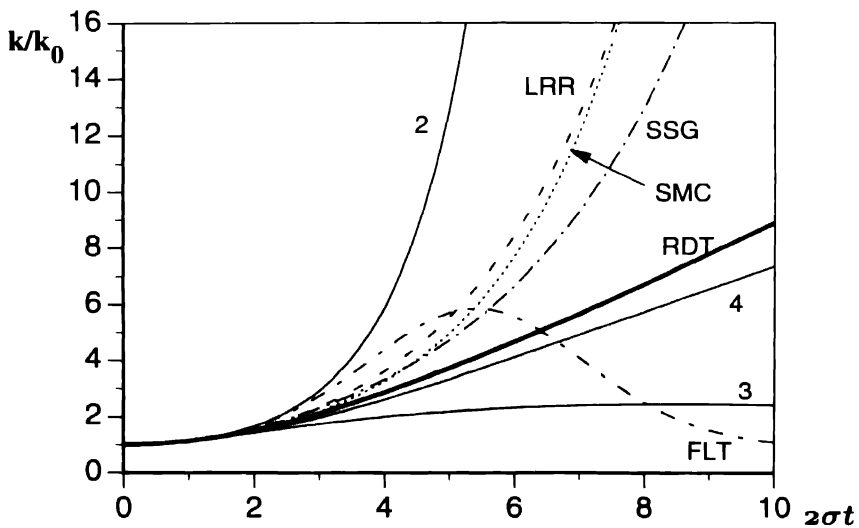

Fig. 4.   RDT and fourth order model predictions of the kinetic energy as function of nondimensional time in a (rapid) homogeneous shear flow. Included are also results obtained with the models of Launder et al. (1975), Fu et al. (1987), Speziale et al. (1991) and Shih et al. (1987).

here. The models referred to earlier in this paper, included in figure 4 give sub-
stantially worse results. For instance, the model of Shih, Mansour & Chen (1987)
predicts an energy that is off by a factor of about 3.5 for $2\sigma t = 8$. The present
fourth order model exhibits a nice behaviour of k for large times with a slowly
diminishing rate of increase. The third order model on the other hand predicts a
periodic behaviour qualitatively similar to that predicted by the Fu *et al.* model. The
second order model, as well as the LRR, SMC and SSG models give an unphysical
explosive growth of the kinetic energy.

Fifth or higher order truncations do not improve the situation significantly over
that of the present fourth order model. No truncation of this kind gives uniformly
correct results in accordance with RDT for arbitrary mean velocity gradient fields
(i.e. with non-zero Ω_{ij}). The reasons will be discussed in more detail later.

3.2. INTERMEDIATE CASES

The increasing prediction difficulties with increasing influence of rotation can be
well illustrated by studying intermediate cases with degrees of rotation influence
smaller and larger than that for homogeneous shear flow. For all cases with less
influence of rotation than that for homogeneous shear flow the fourth order model
behaves well and the predictions become increasingly better as we approach the
plane strain case.

The prediction difficulties increase rapidly as we increase the degree of rotation
above that for a homogeneous shear flow. To illustrate this fact the model results
for a case with $\Omega = 1.25, \sigma = 1$ (cf. $\Omega = \sigma = 1$ for homogeneous shear flow)
are compared with RDT in figure 5. Note that for all cases with $\Omega > \sigma$ the fluid
elements are stretched in a manner so that they return periodically to their initial
shape.

The RDT solutions show an oscillatory behaviour of the anisotropy components
around non-zero levels. Also the kinetic energy exhibits oscillations around the
approximately exponential growth curve. It is obvious from Fig. 5 that the model
here performs distinctly worse as compared to the homogeneous shear flow. For
instance, in the present intermediate case the model prediction of the kinetic energy
is only accurate for relatively small times. For large times the predictions exhibit
a periodic character, in contrast to the RDT solution. The situation is similar for
the anisotropy components and must be ascribed to the fact that some of the
fundamental features of rotationally influenced turbulence are not captured by the
transported quantities (a_{ij}, k) involved in *classical* Reynolds stress or lower level
closures. To analyze this matter in some detail we will study the case of pure rapid
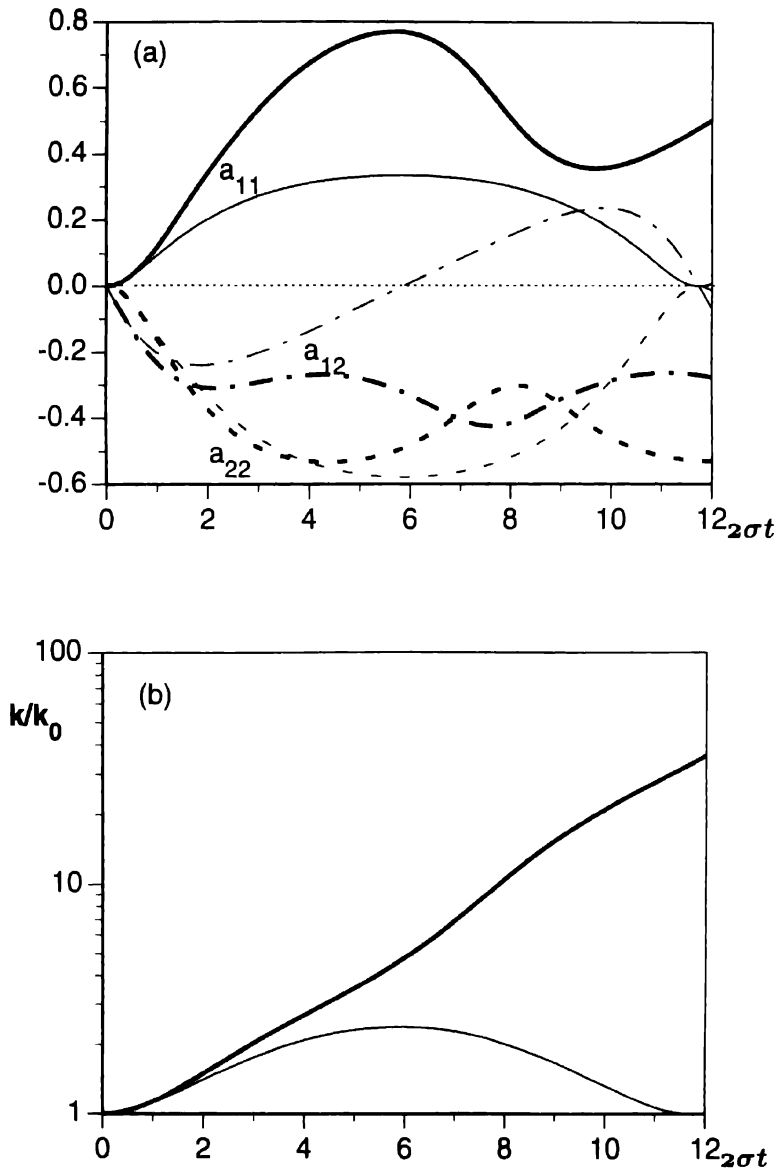rotation.

1

Fig. 5. The Reynolds stress anisotropies (a) and kinetic energy (b) as function of normalized time for an intermediate case ($\Omega = 1.25$, $\sigma = 1$). Comparison between RDT (thick lines) and model predictions (thin).

4. Turbulence submitted to rapid rotation

Straightforward rapid distortion analysis (see e.g. Cambon & Jacquin 1989 or Mansour, Shih & Reynolds 1991) shows that initial isotropy is preserved by rapid rotation, whereas for an initially anisotropic turbulence, the anisotropy components will exhibit damped oscillations. The asymptotic state will depend on the initial distribution of energy in wave number space, and the damping may be interpreted as a phase scrambling effect caused by internal waves. Cambon *et al.* (1992) studied the effects of rotation by dividing the spectrum tensor, after neglection of an imaginary (helicity related) part, into three parts

$$\Phi_{ij}(\kappa) = \underbrace{\frac{E(\kappa)}{4\pi\kappa^2}\Delta_{ij}}_{\Phi_{ij}^{\mathrm{ISO}}} + \underbrace{\left(\frac{1}{2}\Phi_{kk}(\kappa) - \frac{E(\kappa)}{4\pi\kappa^2}\right)\Delta_{ij}}_{\Phi_{..}^{\mathrm{e}}} + \underbrace{\Phi_{ij}(\kappa) - \frac{1}{2}\Phi_{kk}(\kappa)\Delta_{ij}}_{\Phi_{ij}^{Z}}$$

where $\Delta_{ij} \equiv \delta_{ij} - \frac{\kappa_i\kappa_j}{\kappa^2}$, and $E(\kappa)$ is the threedimensional energy spectrum. Only the first part has a non-zero trace after integration over spectral space, and thereby contributes to the kinetic energy. The two latter parts contribute to the anisotropy tensor $a_{ij} = a_{ij}^{\mathrm{e}} + a_{ij}^{Z}$. From the linearized dynamic equations, that are valid in the limit of rapid rotation, follows that only Φ_{ij}^{Z} is affected by pure rotation. This implies that a_{ij}^{e} is constant under rapid rotations whereas a_{ij}^{Z} vanishes as a result of phase scrambling caused by internal waves. We may note that $a_{ij}^{\mathrm{e}} = -y_{ij}$ where y_{ij} is the structure anisotropy tensor used by Reynolds (1989) (see also Mansour et al. 1991).

For the class of *classical* Reynolds stress closures we may note that a consequence of the assumption that the M-tensor is expandable in a_{ij} alone is that all model predictions based on this concept will give constant values of the anisotropy invariants for rapid rotation, as can be seen from the general form (7) with $S_{ij} = 0$

$$\frac{DII_a}{Dt} \quad 2a_i \quad {}_{ij}^{(a)} + \frac{1}{k}\Pi_{ij}^{(r)}\Big) \equiv 0 \tag{13a}$$

$$\frac{DIII_a}{Dt} = 3a_{ik}a_{kj} \quad P_{ij}^{(a)} + \frac{1}{k}\Pi_{ij}^{(r)}\Big) \equiv 0 \tag{13b}$$

The equations (13a,b) hold independent of the specifics of the scalar functions Q_α. The predicted individual anisotropy components may still vary in time, which indeed normally is the case, but not in a way as to reproduce the tendency towards the asymptotic RDT anisotropy state

$$II_a \quad II_a^{\mathrm{e}} \quad \text{and} \quad III_a \quad III_a^{\mathrm{e}}$$

Thus, the most one can hope for within the concept of *classical* Reynolds stress models is to predict a reasonable period of oscillation. With the present fourth order model this is achieved with $\gamma_4 \approx 0.1$ (in fact, the optimal value may vary somewhat with the specifics of the initial conditions).

As an example of the short-coming of this type of modelling one may mention that initially axisymmetric turbulence subjected to rotation around the symmetry axis will be predicted to remain unaffected by rotation. This can be understood from the fact that in axisymmetry there is only one independent anisotropy measure (for instance the anisotropy component in the direction of symmetry) and that it must be constant according to (13a,b). In reality, oscillations of the anisotropy measure will occur also here, and will be damped by phase scrambling.

4.1. ROTATING AXISYMMETRIC TURBULENCE - AN ILLUSTRATIVE EXAMPLE

In turbulence that is axially symmetric with respect to a direction given by a unit vector λ the second order spectrum tensor may be (see e.g. Craya 1958 or Hallbäck 1993) expressed as

$$\Phi_{ij}(\kappa) = N_1(\kappa,\mu)\beta_i\beta_j + N_2(\kappa,\mu)\gamma_i\gamma_j + S^r(\kappa,\mu)(\beta_i\gamma_j + \beta_j\gamma_i) \tag{14}$$

where N_1, N_2 and S^r are real-valued scalars and β_i and γ_i are unit-vectors orthogonal to κ defined as

$$\gamma = \frac{\kappa \times \lambda}{|\kappa \times \lambda|} \qquad \text{and} \qquad \beta = \frac{\kappa \times \gamma}{|\kappa \times \gamma|}$$

and μ is the cosine of the angle between λ and κ. If the further constraint is imposed that the turbulence is invariant under reflections with respect to planes parallel to the axis of symmetry then S^r must vanish. Equation (14) is the most general expression for axisymmetric turbulence except for an imaginary anti-reflectional part which has been omitted here for brevity. This part which describes helicity contributes neither to the Reynolds stress tensor nor to the rapid pressure-strain-rate correlation.

Our aim here is to derive expressions valid in axisymmetric turbulence for the Reynolds stress tensor and the rapid pressure-strain-rate-correlation tensor in terms of the scalar functions appearing in equation (14). For this purpose we will also need the expression for a general axisymmetric mean velocity gradient tensor

$$U_{p,q} = \frac{1}{2}\sigma(3\lambda_p\lambda_q - \delta_{pq}) - \omega\epsilon_{kpq}\lambda_k \tag{15}$$

where σ is the rate of strain along the direction of symmetry and ω is the rate of rotation about the symmetry axis. The relation between the pressure-strain rate correlation and the spectrum tensor is given by equations (2) and (3). Due to the axisymmetry property, and provided that the axis of symmetry is known, the stress tensor is uniquely determined by two scalars, for example

$$k = \frac{1}{2}\overline{u_i u_i} \qquad \text{and} \qquad u_\lambda^2 = \lambda_i\lambda_j\overline{u_i u_j}$$

and the rapid pressure-strain-rate tensor may be quantified by the single scalar

$$\Pi_{\lambda\lambda}^{(r)} = \lambda_i\lambda_j\Pi_{ij}^{(r)}$$

With the aid of (14) these quantities may be written

$$k = \pi \int_0^\infty \int_{-1}^1 (N_1(\kappa,\mu) + N_2(\kappa,\mu))\kappa^2 d\kappa d\mu \tag{16a}$$

$$u_\lambda^2 = 2\pi \int_0^\infty \int_{-1}^1 N_1(\kappa,\mu)(1-\mu^2)\kappa^2 d\kappa d\mu \tag{16b}$$

$$\Pi_{\lambda\lambda}^{(r)} = 12\pi\sigma \int_0^\infty \int_{-1}^1 N_1(\kappa,\mu)\mu^2(1-\mu^2)\kappa^2 d\kappa d\mu$$

$$- 8\pi\omega \int_0^\infty \int_{-1}^1 S^r(\kappa,\mu)\mu(1-\mu^2)\kappa^2 d\kappa d\mu \tag{16c}$$

The integral containing S^r does not integrate to zero since S^r is an odd function with respect to μ, which may be deduced from the homogeneity condition $\Phi_{ij}(\kappa) = \Phi_{ji}(-\kappa)$ keeping in mind that β is even and γ is odd in κ.

Equations (16b) and (16c) suggest that an expansion of $\Pi_{ij}^{(r)}$ in terms of the Reynolds stress tensor may capture the effects that are associated with the irrotational straining motion whereas those associated with the rotational part of mean velocity field will be completely missed since this latter part is determined by the anti-reflectionally symmetric part (S^r) of the spectrum tensor and this part does not enter the stress tensor variables.

One may also note that in the case of rotating axisymmetric turbulence S^r will be of significant influence even if it is initially zero. This fact is readily seen from the dynamical equations for $\Phi_{ij}(\kappa)$ which in the case of rapid pure rotation read

$$\begin{cases} \dot{N}_1 = -4\omega\mu\, S^r \\ \dot{N}_2 = 4\omega\mu\, S^r \\ \dot{S}^r = 2\omega\mu\,(N_1 - N_2) \end{cases} \tag{17}$$

Unless the turbulence is initially isotropic, i.e. $N_1 = N_2$ and $S^r = 0$, it is clear that the imposed rotation will induce a non-zero S^r. In the pure rotation case the solution for N_1, N_2 and S^r exhibit undamped oscillations with S^r being 90° out of phase with the two N-scalars. The phase varies in time and space as $4\omega t\mu$ so that for large ωt the integrands in (16b) and (16c) oscillate rapidly in wavenumber space leading to cancellation. By partial integration we may obtain the asymptotic form of (16b) and (16c) in the case of pure rotation, with S^r initially zero,

$$u_\lambda^2 = 2\pi \int_0^\infty \int_{-1}^1 \frac{1}{2}(N_1 + N_2)\big|_{t=0}(1-\mu^2)\kappa^2 d\kappa d\mu$$

$$+ 2\pi \frac{4\sin(4\omega t)}{(4\omega t)^3} \int_0^\infty \kappa^2 \frac{\partial(N_1 - N_2)}{\partial\mu}\bigg|_{\substack{t=0}} d\kappa + \mathcal{O}((\omega t)^{-4}) \tag{18a}$$

$$\Pi_{\lambda\lambda}^{(r)} = 8\pi\omega \, \frac{4\cos(4\omega t)}{(4\omega t)^3} \int_0^\infty \kappa^2 \left. \frac{\partial(N_1 - N_2)}{\partial\mu} \right|_{\substack{\mu=1\\t=0}} d\kappa + \mathcal{O}((\omega t)^{-4}) \quad (18b)$$

Here we have used the fact that N_1 and N_2 must be even in μ and that N_1 is equal to N_2 when κ is on the axis of rotation since the turbulence is locally isotropic there. As seen from (18a) and (18b) the one-point quantities exhibit damped oscillations towards asymptotic states, where the amplitude of the oscillations is determined by the initial derivative of the anisotropy $(N_1 - N_2)$ on the axis of rotation. The asymptotic value of u_λ^2 is determined by the initial distribution of energy $(N_1 + N_2)$ in wavenumber space. It appears difficult to capture the character of the damping in (18a,b) by any reasonable one-point modelling approach.

This example of axisymmetric turbulence illustrates one of the main modelling difficulties of rotational mean flows and it also suggests that in order to more closely capture the rotational effects in a turbulence closure new quantities must be introduced. Ideas along this line of thinking have been suggested recently, for instance by Reynolds (1989) who introduced the second rank structure tensor Y_{ij}. For homogeneous turbulence the structure tensor is given by

$$Y_{ij} = \int \frac{\kappa_i \kappa_j}{\kappa^2} \Phi_{kk} d^3\kappa$$

It is however clear that this tensor does not contain any information about the part of the spectrum associated with S^r since $\Phi_{ii} = N_1 + N_2$. An even more general approach is to extend the set of variables in the closure from $\overline{u_i u_j}$ (and possibly Y_{ij}) to the fourth rank M-tensor itself. A closure for rapidly strained turbulence based on the transport equations for the M-tensor involving linear modelling of the occurring source terms has been investigated (details of that work will be given elsewhere). In the axisymmetric case such a closure predicts an oscillatory, however undamped, behaviour of the M-variables in contrast to *classical* RST closures which reproduce no response at all to rotation in the axisymmetric case. The tendency towards an asymptotic state is not captured unless the damped behaviour is accounted for in an *ad hoc* manner, for instance by simply adding linear damping terms to the system as was suggested by Cambon *et al.* (1992).

5. Summary and conclusions

The recently proposed model of Johansson & Hallbäck (1994) (JH) for the rapid pressure strain-rate in Reynolds stress turbulence models is here presented and analyzed in terms of performance for mean flows with different degrees of rotational influence. Previously presented models for the rapid pressure strain rate can be seen as subsets of the JH model. Practically all models for this term are based, directly or indirectly, on an expansion of the fourth rank M-tensor in terms of the Reynolds stress anisotropy tensor. The JH model contains all tensorially independent terms in such an expansion.

Model predictions are here compared with RDT solutions, and predictions by other models, for various homogeneous (rapid) flow situations, all of which can be described by a generic mean velocity gradient tensor containing one variable strain rate parameter and one variable rotation rate parameter.

The JH model gives very accurate descriptions of all irrotational cases, and performs significantly better in (rapid) homogeneous shear flow than the other models from the literature used here for comparisons.

In homogeneous shear flow the pure strain and rotation can be said to be of equal strength. For cases where the rotational effects are stronger the prediction difficulties become quite severe for all Reynolds stress closures. The reasons for this were analyzed and found to be associated with parts of the spectrum that are averaged out in the transported quantities in *classical* Reynolds stress closures. In axisymmetric cases this is particularly clear and the 'missing' parts can be seen to be those with anti-reflectional symmetry as related to the axis of symmetry (which also is the axis of rotation). A closer prediction in cases with strong influence of rotation would require introduction of other transported quantities.

Acknowledgements

Appendix

A. Model functions and parameters

The complete fourth order $\Pi_{ij}^{(r)}$ model is defined by the expression (7) with

$$Q_1 = \frac{4}{5} - \frac{2}{5}(4B_2 + 15B_3)II_a - \frac{2}{5}B_5III_a - $$
$$- \frac{1}{220}(19B_6 - 120B_7)II_a^2 \tag{19a}$$

$$Q_2 = -12B_1 - \frac{1}{2}B_5II_a - \frac{1}{2}(B_6 - 8B_7)III_a \tag{19b}$$

$$Q_3 = -8B_2 + 36B_3 + \frac{1}{22}(7B_6 - 72B_7)II_a \tag{19c}$$

$$Q_4 = 96B_2 - 36B_3 - \frac{1}{22}(7B_6 - 72B_7)II_a \tag{19d}$$

$$Q_5 = B_5 \tag{19e}$$

$$Q_6 = B_6 \tag{19f}$$

$$Q_7 = -\frac{4}{3} - \frac{28}{3}B_1 + \frac{1}{6}(2B_4 - B_5)II_a - \frac{1}{18}(3B_6 - 56B_7)III_a \tag{19g}$$

$$Q_8 = -16B_2 + 28B_3 + \frac{1}{22}(3B_6 - 56B_7)II_a \tag{19h}$$

$$Q_9 = B_4 \tag{19i}$$

where the B:s are Taylor series expanded as

$$B_1 = \alpha_1 + \alpha_4 II_a + \alpha_7 III_a \tag{20a}$$

$$B_2 = \alpha_2 + \alpha_8 II_a \qquad\qquad B_3 = \alpha_3 + \alpha_9 II_a \tag{20b}$$

$$B_4 = \alpha_5 \qquad B_5 = \alpha_6 \qquad\qquad B_6 = \alpha_{10} \qquad B_7 = \alpha_{11} \tag{20c}$$

After application of the generalized realizability condition we get

$$\alpha_4 = -\frac{3}{160}(3 + 60\alpha_1 + 48\alpha_2 - 40\alpha_3) \tag{21a}$$

$$\alpha_5 = -\frac{3}{2} - 132\alpha_2 + 96\alpha_{10} \tag{21b}$$

$$\alpha_6 = \frac{3}{32} + \frac{15}{4}(\alpha_2 + \alpha_3) \tag{21c}$$

$$\alpha_7 = \frac{9}{8}\alpha_1 - \frac{9}{4}(\alpha_2 + \alpha_3) + \frac{1}{3}\alpha_{11} \tag{21d}$$

$$\alpha_8 = -\frac{3}{88}\left(\frac{3}{8} + 21\alpha_2 + 10\alpha_3 + 8\alpha_{10}\right) \tag{21e}$$

$$\alpha_9 = -\frac{9}{220}\left(\frac{3}{8} + 21\alpha_2 + 10\alpha_3\right) + \frac{1}{11}\alpha_{11} \tag{21f}$$

The parameters $(\alpha_1, \alpha_2, \alpha_3, \alpha_{10})$ are denoted by $(\gamma_1, \gamma_2, \gamma_3, \gamma_4)$ (α_{11} will not appear in the final expression for $\Pi_{ij}^{(r)}$). The optimized values of these parameters are

$$\gamma_1 = -1/7 \qquad \gamma_2 = 0.0295 \qquad \gamma_3 = -0.0484 \qquad \gamma_4 = 0.1 \tag{22}$$

The corresponding third order model is simply obtained from the fourth order model by setting

$$\gamma_2 = -\frac{3}{88} + \frac{21}{22}\gamma_1 \qquad \gamma_3 = -\frac{3}{88} - \frac{5}{11}\gamma_1 \qquad \gamma_4 = 0 \tag{23}$$

which, hence, has only one undetermined model parameter. The optimal value of γ_1 is $-1/7$. The corresponding second order model is found by setting

$$\gamma_1 = -\frac{1}{20} \qquad \gamma_2 = -\frac{1}{88} \qquad \gamma_3 = -\frac{3}{220} \qquad \gamma_4 = 0 \tag{24}$$

References

Bayly, B.J., Orszag, S.A. and Herbert, T.: 1988, 'Instability mechanisms in shear-flow transition', *Ann. Rev. Fluid Mech.* **20**, 359

Cambon, C. and Jacquin, L.: 1989, 'Spectral approach to nonisotropic turbulence subjected to rotation', *J. Fluid Mech.* **202**, 295

Cambon, C., Jacquin, L. and Lubrano, J.L.: 1992, 'Toward a new Reynolds stress model for rotating turbulent flows', *Phys. Fluids A* **4**, 812

Cambon, C., Jeandel, D. and Mathieu, J.: 1981, 'Spectral modelling of homogeneous non-isotropic turbulence', *J. Fluid Mech.* **104**, 247

Craya, A.: 1958, 'Contribution a l'analyse de la turbulence associée a des vitesses moyennes', No. 345, Publications Scientific et Techniques du Ministère de l'air, Paris, France.

Fu, S., Launder, B.E. and Tselepidakis, D.P.: 1987, 'Accommodating the effects of high strain rates in modelling the pressure-strain correlations', *UMIST Mech. Engng Dept Rep.* TFD/87/5.

Hallbäck, M.: 1993, 'Development of Reynolds stress closures of homogeneous turbulence through physical and numerical experiments', Doctoral thesis, Royal Institute of Technology, Stockholm.

Hallbäck, M., Sjögren, T. and Johansson, A.V.: 1993, 'Modeling of intercomponent transfer in Reynolds stress closures of homogeneous turbulence', Accepted for publication in Turbulent Shear Flows IX, eds F Durst, N. Kasagi, B.E. Launder, F.W. Schmidt and J.H. Whitelaw, Springer Verlag.

Hanjalić, K. and Launder, B.E.: 1972, 'A Reynolds stress model of turbulence and its application to thin shear flows', *J. Fluid Mech.* **52**, 609

Johansson, A.V. and Hallbäck, M.: 1994, 'Modelling of rapid pressure-strain in Reynolds stress closures', Accepted for publication in *J. Fluid Mech.*.

Launder, B.E.: 1989, 'Second-moment closure: present ... and future?', *Int. J. Heat and Fluid Flow* **10**, 282

Launder, B.E., Reece, G.J. and Rodi, W.: 1975, 'Progress in the development of a Reynolds stress turbulence closure', *J. Fluid Mech.* **68**, 537

Launder, B.E., Tselepidakis, D.P. and Younis, B.A.: 1987, 'A second moment closure study of rotating channel flow', *J. Fluid Mech.* **183**, 63

Lee, M.J.: 1990, 'A contribution toward rational modeling of the pressure-strain-rate correlation', *Phys. Fluids A* **2**, 630

Lee, M.J. and Reynolds, W.C.: 1985, 'Numerical experiments on the structure of homogeneous turbulence', *Stanford Univ. Tech. Rep.* TF-24.

Lumley, J.L.: 1978, 'Computational modeling of turbulent flows', *Adv. in Appl Mech.* **18**, 123

Mansour, N.N., Shih, T.-H. and Reynolds, W.C.: 1991, 'The effects of rotation on initially anisotropic homogeneous flows', *Phys. Fluids A* **3**, 2421

Pope, S.B.: 1985, 'PDF methods for turbulent reactive flows', *Prog. Energy Combustion Sci.* **11**, 119

Reynolds, W.C.: 1987, 'Fundamentals of turbulence for turbulence modelling and simulation', *Lecture Notes for Von Karman Institute*, AGARD-CP-93. NATO.

Reynolds, W.C.: 1989, 'Effects of rotation on homogeneous turbulence', *Proc. of the 10th Australasian Fluid Mechanics Conference*, Melbourne, December 1989, paper KS-2.

Schumann, U.: 1977, 'Realizability of Reynolds-stress models', *Phys. Fluids* **20**, 721

Shih, T.-H. and Lumley, J.L.: 1985, 'Modeling of pressure correlation terms in Reynolds stress and scalar flux equations', *Tech. Rep.* FDA-85-3. Cornell University.

Shih, T.-H. and Lumley, J.L.: 1993, 'Critical comparison of second-order closures with direct numerical simulations of homogeneous turbulence', *AIAA Journal* **31**, 663

Shih, T.-H., Mansour, N.N. and Chen, J.Y.: 1987, ''Reynolds stress models of homogeneous turbulence', in Proc. 1987 Summer Program, Center for Turbulence Research, NASA Ames - Stanford University.

Shih, T.-H., Reynolds, W.C. and Mansour, N.N.: 1990, 'A spectrum model for weakly anisotropic turbulence', *Phys. Fluids A* **2**, 1500

Spencer, A.J.M. and Rivlin, R.S.: 1958, *Arch. Rat. Mech. Anal.* **2**, 309

Speziale, C.G., Sarkar, S. and Gatski, T.B.: 1991, 'Modelling the pressure-strain correlation of turbulence: an invariant dynamical systems approach', *J. Fluid Mech.* **227**, 245

Near-wall Turbulence Models for 3D Boundary Layers

PER ÅKE LINDBERG
*Aeronautical Engineering, Department of Vehicle Engineering, Royal Institute of Technology,
S-10044 Stockholm, Sweden*

Abstract. Calculations of the three-dimensional boundary layer in an S shaped duct are performed
with various $k - \epsilon$ models. Three different near-wall models are used for the $k - \epsilon$ model, of which
one is using a new set of near-wall damping functions deduced from direct numerical simulations
of turbulent channel flow available in the literature The results show that it is possible to obtain
damping functions giving better agreement, especially for k and ϵ, with direct simulation data and
experiments than with damping functions deduced from trial and error.

1. Introduction

As new and more powerful computers become available, the need for turbulence
models applicable to flows in complex geometries increase. Such flows are common
in many technical applications, e.g. three-dimensional boundary layers on aircraft
wings, in pumps and turbines etc. For boundary layers adequate resolution of the
flow close to solid boundaries is essential, especially if the temperature equation
is solved simultaneously. This had lead to a number of modifications of existing
high Reynolds number models, such as the original $k - \epsilon$, with the introduction of
new terms accounting for low Reynolds number effects. The development of such
turbulence models needs reliable experimental data for calibrating the empirical
constants of these models and validating the results.

A basic assumption in the derivation of the original $k - \epsilon$ model is that the flow
under consideration is at high Reynolds number, thus restricting its applicability
to flows far from the influence of boundaries, but later extensions have been
introduced to allow for wall proximity effects. A number of $k - \epsilon$ variants are now
in use and some of them are reviewed in Patel, Rodi & Scheuerer (1985), Pollars
& Martinuzzi (1989) and Rodi (1990).

Finding suitable extensions of the $k - \epsilon$ model that will be valid in the vicinity
of boundaries requires information about their influence on the turbulence field.
Although there exist a number of careful experiments on aspects of the flow field
near boundaries, the information that is available is far from complete and affected
to an unknown degree by measurement errors that become increasingly significant
as the measuring instruments approach the boundaries. Complete information about
the flow field near boundaries is now available through the use of direct numerical
simulation (DNS) of turbulent flows, which can be used to test the modeling of

any term in the model equations. DNS is, however, limited to very low Reynolds number flows and simple geometries but this does not diminish their usefulness for the part of the flow field very close to the boundaries. DNS data is now available in plane channels from Kim, Moin & Moser (1987) (which will be referred as KMM hereinafter), in a boundary layer Spalart (1988), and in a fully developed flow through a square duct Gavrilakis (1992) (for a short review see Mansour 1991). Use of DNS data to study the behavior of the $k - \epsilon$ model have been made, among others, by Mansour, Kim & Moin (1988) (MKM), Rodi & Mansour (1993). The purpose of the present work is to continue the exploitation of DNS data which presently is focused on the wall damping functions commonly used with the $k - \epsilon$ model.

The models described above were employed in calculations of a boundary layer that develops at the top wall of an S-shaped duct. In this boundary layer, a pressure gradient develops that gives rise to a mean cross-flow. The cross-flow changes sign when the flow is deflected at the second turn of the S-bend. This flow field produces highly anisotropic Reynolds stresses where the difference in the angle between the Reynolds stresses and the mean velocity gradient is as much as 40°. The angle also changes sign across the boundary layer.

The present results are obtained with an anisotropic eddy viscosity model where a transport equation is solved for the direction of the Reynolds stress in the plane parallel to the wall. The model used here is described in Lindberg (1992). However, the model is giving Reynolds stress directions close to the direction of the gradient of the mean velocity, i.e. close to the standard Boussinesq approximation. The results indicate that this is a promising approach, but the model equations need some refinement. As the results are similar to the ones obtained with an isotropic model the reader is referred to the Lindberg (1992) for a description. A new set of damping functions are used with the $k - \epsilon$ model. These functions are obtained from DNS data and from physical arguments. It is shown that it is possible to obtain results very close to those obtained from the Lam & Bremhorst (1981) model (L&B). With a model that is less grid dependent than the L&B model. The main advantage of the present model is that the rapidly changing damping functions used in the Lam & Bremhorst model are avoided.

2. Theory

2.1. THE $k - \epsilon$ MODEL

The $k - \epsilon$ model has become the standard method for calculating turbulent flows. However, despite research over a number of years, no standard near-wall modifications have emerged. Different approaches can be found in the reviews by Patel, Rodi & Scheuerer (1985), Pollard & Martinuzzi (1989), Rodi (1990) and others.

In the present study three different near-wall models are used. They are the ones proposed by Lam & Bremhorst (1981) (L&B), by Chen & Patel (1988) (C&P),

and one new developed by the author (here referred as the P-AL model). The P-AL model is developed by using the results from the asymptotic behavior of the different turbulence quantities close to the wall and results from DNS of turbulent channel flow.

All three models solve the transport equations in the whole flow field, and do not use the law of the wall. The three different models differ in the definitions of the damping functions and the boundary condition for the dissipation. C&P is a two layer model which uses a one-equation model close to the wall. Their similarity and differences will be discussed below.

In a Cartesian coordinate system the k and ϵ equations become, in boundary layer approximation,

$$U\frac{\partial k}{\partial x} + V\frac{\partial k}{\partial y} + W\frac{\partial k}{\partial z} = P - \epsilon + \frac{\partial}{\partial y}\left((\nu + \frac{\nu_t}{\sigma_k})\frac{\partial k}{\partial y}\right) \tag{1}$$

$$U\frac{\partial \epsilon}{\partial x} + V\frac{\partial \epsilon}{\partial y} + W\frac{\partial \epsilon}{\partial z} = f_1 C_{\epsilon 1}\frac{\epsilon}{k}P - f_2 C_{\epsilon 2}\frac{\epsilon^2}{k} + \frac{\partial}{\partial y}\left((\nu + \frac{\nu_t}{\sigma_\epsilon})\frac{\partial \epsilon}{\partial y}\right) \tag{2}$$

where f_1 and f_2 are wall damping functions, discussed below, and P is the production term,

$$P = -\overline{uv}\frac{\partial U}{\partial y} - \overline{vw}\frac{\partial W}{\partial y} \tag{3}$$

The boundary conditions for k are the same for all models, namely,

$$k(y = 0) = 0. \quad \frac{\partial k}{\partial y}(y \to \infty) = 0 \tag{4}$$

For ϵ the boundary condition at the wall differs for the different models. At the outer edge of the boundary layer the same condition as for k is used, i.e.,

$$\frac{\partial \epsilon}{\partial y}(y \quad \infty) = 0 \tag{5}$$

It may be more appropriate to impose $k, \epsilon = 0$ at "infinity", however, in some situations this introduced some oscillations of k. For all calculations made with the boundary condition (4) k decreased to almost zero at the outer edge of the boundary layer. The constants used are the standard values used by e.g. Chen & Patel (1988)

$$C_\mu = 0.09 \quad C_{\epsilon 1} = 1.44 \quad C_{\epsilon 2} = 1.92 \quad \sigma_k = 1.0 \quad \sigma_\epsilon = 1.3$$

The eddy viscosity is obtained by

$$\nu_t = C_\mu f_\mu \frac{k^2}{\_} \tag{6}$$

where f_μ is a damping function, discussed below, analogous to the van Driest damping function used for algebraic eddy viscosity models.

2.2. REGION CLOSE TO THE WALL

Close to the wall, where the local Reynolds number is low, the original ϵ equation needs some modification. In this region the physical background to the approximations made for the high Reynolds number region are no longer valid. As a result of this the asymptotic behavior of the exact terms is different from their modeled counterparts. To account for the wall region it is therefore necessary to introduce the damping functions f_1 and f_2 in the ϵ-equation. Some of the physical background for the derivation of these functions are outlined below. The analysis is done for 2D flow, and comparison is made with DNS of turbulent channel flow. A drawback of this approach is that the Reynolds number of the DNS is low. The damping function f_μ derived from the DNS by MKM shows quite large Reynolds number dependence (Rodi & Mansour (1990 & 1993). It can therefore be expected that f_1 and f_2 also will show quite large Reynolds number dependence. However, for the present analysis only the DNS for channel flow with $Re = 180$ was available to the author.

The correct limiting behavior of the damping functions close to the wall may be obtained by a Taylor expansion of the turbulent quantities. If the fluctuating velocity components are expanded in a Taylor series and with the use of the continuity constraint one gets, see e.g. MKM,

$$u^+ = a_1^+ y^+ + a_2^+ y^{+2} + \ldots \quad v^+ = b_2^+ y^{+2} + b_3^+ y^{+3} + \ldots$$
$$w^+ = c_1^+ y^+ + c_2^+ y^{+2} + \ldots \tag{7}$$

where a_1 etc are functions of x, z and time, and + indicates scaling with wall units (a complete list of the limiting behavior of all terms involved in the $k - \epsilon$ equations can be found in e.g. MKM or Speziale, Abid & Anderson 1990). The results from the DNS of 2D channel flow by KMM show the following approximate values for the most important constants,

$$a_{1rms}^+ = 0.36 \quad c_{1rms}^+ = 0.19 \tag{8}$$

The value of a_1^+ has also been determined experimentally for higher Reynolds numbers by Alfredsson, Johansson, Haritonidis & Eckelmann (1988), they found $a_{1rms}^+ = 0.4$.

With use of the Taylor expansions of u, v and w it is possible to obtain the near wall behavior of the other turbulent quantitie as well.

$$k^+ = \frac{1}{2}\left(\overline{\left(a_1^{+2} + c_1^{+2}\right)}y^{+2} + 2\overline{\left(a_1^+ a_2^+ + c_1^+ c_2^+\right)}y^{+3} \ldots + \right) \tag{9}$$

$$\epsilon^+ = \overline{\left(\frac{\partial u^+}{\partial y^+}\right)^2} + \overline{\left(\frac{\partial w^+}{\partial y^+}\right)^2} = \overline{a_1^{+1} + c_1^{+2}} + 4\overline{\left(a_1^+ a_2^+ + c_1^+ c_2^+\right)}y^+ + \ldots \tag{10}$$

$$\overline{uv}^+ = \overline{a_1^+ b_2^+} y^+ + \overline{\left(a_1^+ b_3^+ + a_2^+ b_2^+\right)} y^{+4} + \dots \tag{11}$$

Close to the wall, where the mean velocity varies linearly, $U^+ = y^+$, equation (11) gives for the eddy viscosity,

$$\nu_t^+ = \frac{-\overline{uv}}{U_y^+} = -a_1^+ b_2^+ y^{+3} + \dots \quad U_y^+ = \frac{\partial U^+}{\partial y^+} \tag{12}$$

If the wall limiting behavior of ν_t, k and ϵ are inserted in (6) this gives the correct behavior of f_μ close to the wall, which is,

$$f_\mu \sim \frac{1}{y^+} \tag{13}$$

In analogy with the analysis made for f_μ the limiting behavior of the damping functions f_1 and f_2 may be obtained from the constraint that the modeled and the exact terms for the production of dissipation and destruction of dissipation terms ought to have the same asymptotic behavior. This gives (see Speziale, Abid & Anderson 1990),

$$f_1 = O(1) \tag{14}$$

$$f_2 \sim y^{+2} \tag{15}$$

close to the wall.

2.3. DIFFERENT NEAR WALL APPROACHES

2.3.1. *The model used by Chen & Patel*

This is a two layer model where only the k equation is solved close to the wall, see e.g. Chen & Patel (1988) and Norris & Reynolds (1975). In the wall region ϵ is calculated of the one and two equation models. The interface is situated at the location where the Reynolds number $R_y = 250$, below this point ϵ is obtained as

$$\epsilon(R_y \leq 250) = \frac{k^{3/2}}{l_\epsilon} \tag{16}$$

where l_ϵ is a length scale and

$$R_y = \frac{y\sqrt{k}}{\nu} = y^+ \sqrt{k^+} \tag{17}$$

The eddy viscosity, ν_t, is calculated using (6) when $R_y \geq 250$. For $R_y \leq 250$, ν_t is calculated using only k, i.e.

$$R_y \leq 250 : \nu_t = C_\mu l_\mu \sqrt{k} \quad R_y \geq 250 : \nu_t = C_\mu f_t \frac{k^2}{\epsilon} \tag{18}$$

The two length scales l_ϵ and l_μ and the damping function f_μ is not important for this model due to the fact that it is only used for $R_y \geq 250$. Instead it is the limiting behavior of l_ϵ and l_μ that may be important. To be consistent with the asymptotic behavior of ϵ and ν_t, equations (9–12) give the following requirements for l_ϵ and l_μ

$$l_\epsilon^+ = \frac{k^{+3/2}}{\epsilon^+} \sim y^{+3} \tag{19}$$

$$l_\mu^+ = \frac{\nu_t^+}{C_\mu \sqrt{k^+}} \sim y^{+2} \tag{20}$$

Chen & Patel (1988) suggest

$$l_\epsilon = C_1 y \left(1 - e^{-R_y/A_\epsilon} \right) \quad l_\mu = C_1 y \left(1 - e^{-R_y/A_\mu} \right) \tag{21}$$

where $A_\epsilon = 70.0 \quad C_1 = \kappa C_\mu^{-3/4} \quad A_\mu = 2C_1 = 5.0$

Close to the wall the length scales in (16) are equivalent to, (9) and (17) give $R_y \sim y^{+2}$

$$l_\epsilon^+ \approx \frac{C_1 y^+ R_y}{A_\epsilon} \sim y^{+3} \quad l_\mu^+ \approx \frac{C_1 y^+ R_y}{A_\mu} \sim y^{+3} \tag{22}$$

Hence, l_ϵ will have the correct asymptotic behavior, whereas l_μ will not. However, the limiting behavior close to the wall may not be critical for the overall behavior of the model, due to the fact that the eddy viscosity is small compared to the molecular viscosity close to the wall. It may be more important that the length scales used give the correct boundary conditions for the two equation part of the model. If the length scales are compared with the DNS data from MKM, (Figs 1 and 2), it is seen that l_μ follows the DNS data much closer than l_ϵ does. The length scales, l_μ and l_ϵ, are used for $R_y \leq 250$, in the figures the maximum R_y is about 120. In Rodi & Mansour (1990) a comparison between the length scales and DNS data for both channel flow and boundary layers can be found.

The damping functions, f_1, f_2 and f_μ will have an almost negligible influence on the results due to the fact that they are very close to 1.0 for $R_y \geq 250$. They are almost the same as the one suggested by L&B, with small changes in the various constants.

$$f_\mu = \left(1 - e^{-0.016R_y} \right)^2 \left(1 + \frac{19.5}{R_T} \right) \tag{23}$$
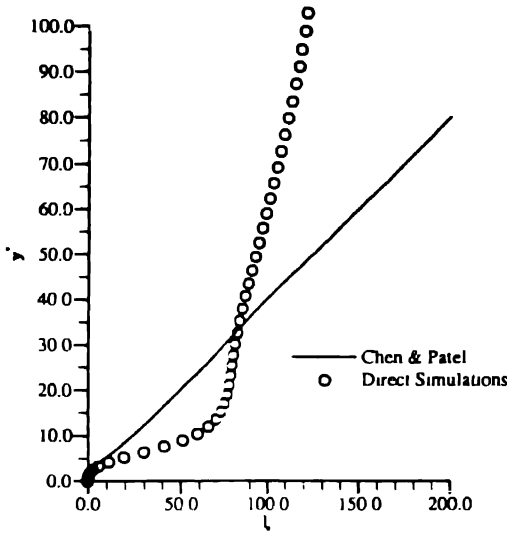
$$f_1 = 1 + \frac{0.06}{f_\mu} \tag{24}$$

Fig. 1. Comparison of l_ϵ used by C&P, and l_ϵ calculated from DNS by MKM
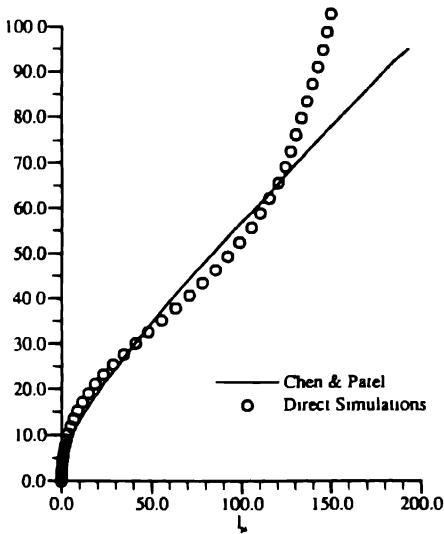

Fig. 2. Comparison of l_μ used by C&P and l_μ calculated from DNS by MKM.

$$f_2 = 1 - e^{-R_T^2} \tag{25}$$

where $R_T = k^2/\epsilon\nu = k^{+2}/e^+$

To obtain a continuous eddy viscosity at the interface f_μ has to be equal to l_μ/l_ϵ for $R_y = 250$. This is not the case, for $R_y = 250$ we have

$$l_\mu = 1.00 \quad l_\epsilon = 0.97 \quad \text{and} \quad f_\mu = 0.99.$$

2.3.2. *The Lam & Bremhorst model*

The model suggested by Lam & Bremhorst (1981) was one of those found best in the review by Patel, Rodi & Scheuerer (1985). It is here used in the variant named "LB1" by Patel et al. (1985) where it differs from the original by the boundary condition for ϵ, which is taken as

$$\frac{\partial \epsilon}{\partial y} = 0 \quad y = 0 \tag{26}$$

The damping functions were obtained from physical arguments and the constants were optimized by trial and error

$$f_\mu = \left(1 - e^{-0.0165R_y}\right)^2 \left(1 + \frac{20.5}{R_T}\right) \tag{27}$$

$$f_1 = 1 + \frac{0.05}{f_\mu} \tag{28}$$

$$f_2 = 1 - e^{-R_T^2} \tag{29}$$

If the asymptotic behavior of k and ϵ are used together with the numerical values given in (8), one obtains

$$f_\mu = O(1) \tag{30}$$

$$f_1 \sim 1 + \frac{1}{(0.2 + 0.004y^4)^3} \tag{31}$$

$$f_2 \sim y^{+8} \tag{32}$$

None of these functions have a correct asymptotic behavior close to the wall. Special attention should be given to f_1. If the Reynolds numbers are taken from DNS data it has a maximum value greater than 100, i.e. it gives a value about two orders of magnitude greater than the original equation without damping function. These functions are compared with the MKM data below.

2.3.3. *A new model based on direct numerical simulations data*

The new model follows the same approach as Lam & Bremhorst (1981), but it uses different expressions for the damping functions and has a different boundary condition for ϵ. Due to the fact that ϵ, or its derivatives, do not vanish at the wall, as k does, there is no simple way to obtain a boundary condition for ϵ. In the $k - \epsilon$ models reviewed by Patel et al. (1985) a number of different boundary conditions for ϵ, expressed in terms of k or its derivatives were used. None of these suggested boundary conditions were compatible with the Taylor expansions (9–11). Equation (10) may give a boundary condition for ϵ if the value of a_1^+ and c_1^+ can be found and can be treated as universal constants, in the same way as the additive constant in the log-law. As mentioned before, there seems to exist such a value which was obtained from the DNS by KMM and from the experiments (in air, water and oil) by Alfredsson, Johansson, Haritonidis & Eckelmann (1988). These references suggest that over a wide Reynolds number range, up to Reynolds number 28000 based on boundary layer thickness, the value of ϵ at the wall is

$$\epsilon^+ = a_1^{+2} + c_1^{+2} = 0.2 \tag{33}$$

Here the value obtained by KMM, $\epsilon^+ = 0.17$, is used as boundary condition for ϵ. This value may be too high when three-dimensional effects are important. In the DNS of channel flow with a transient spanwise pressure gradient Moin, Shih, Driver & Mansour (1990) found a value of ϵ at the wall which was slightly lower.

The damping functions f_1, f_2 and f_μ were obtained by fitting curves through the DNS data obtained by MKM. The exact terms for the production and destruction of ϵ calculated from the DNS data were compared with the modeled terms and the damping functions. In the notation of MKM the following expressions were used

$$f_1 = \frac{P_\epsilon^1 + P_\epsilon^2}{C_{\epsilon_1} \frac{\epsilon}{k} P} \tag{34}$$

$$f_2 = \frac{-P_\epsilon^4 + Y}{C_{\epsilon_2} \frac{\epsilon^2}{k}} \tag{35}$$

For f_μ the Reynolds stresses obtained from the DNS data were compared with the Reynolds stresses obtained from the eddy viscosity, see equations 6 and 12. The fitted curves were chosen so that the behavior close to the wall followed the Taylor expansions discussed previously,

$$f_\mu = \frac{tanh(0.00039y^{+2})}{tanh(0.0025y^{+3})} \tag{36}$$

$$f_1 = 1 + 2.05e^{-0.016(y^+ - 3)^2} - 0.6e^{-0.1y^2} \tag{37}$$

$$f_2 = 1.0 - e^{-0.02y^{+2}} + 0.2ye^{-0.1(y^+-7)^2} + 0.04ye^{-0.11(y^+-12)^2} \tag{38}$$

These three functions have almost the correct asymptotic behavior prescribed by equations (13–15) and all three approach unity for large y^+ ($y^+ > 50$). The maximum value of f_1 is less than 3.0. The expression for f_2 is not exactly proportional to y^{+2} near the wall, however the difference is very small.

Rodi & Mansour (1993) found from the DNS used in the present work that f_μ did not approach unity in the core region for $Re = 180$, but did so for their higher Reynolds number. For this reason the damping functions f_1, f_2 and f_μ are obtained from DNS data normalized with their value in the core region, so they all approach unity, before the curve-fitting is done. This proved to give better results than if the damping functions were fitted to the "unnormalized" DNS data. Calculations with different damping functions also showed that although f_μ etc are equal to unity for $y^+ \geq 50$, they influence the behavior of the model in the whole boundary layer.

2.4. DISCUSSION

The different models can be summarized in the following table where the equation numbers are given for the damping functions, eddy viscosity and boundary condition used for each model.

model	f_μ	f_1	f_2	B C for ϵ	ν_t
C&P	23	24	25	16	18
L&B	27	28	29	26	6
P-AL	36	37	38	33	6

The damping function f_μ is used to give an eddy viscosity that is not too large in the viscous sublayer, in analogy with the van Driest damping function. The asymptotic analysis gives that f_μ should be proportional to $1/y^+$. Figure 3 shows that the f_μ used by L&B and C&P are approximately constant for $y^+ \leq 5$, but follows approximately the DNS for $y^+ \geq 5$. However, they approach 1.0 significantly slower than the DNS.

The two other damping functions f_1 and f_2 (Figs 4 and 5) are also used by C&P but only for $R_y \geq 250$ where they will be approximately equal to 1.0. The function f_1 used by L&B has a very large amplitude around $y^+ = 5$, with a maximum value > 100, if the Reynolds numbers are calculated from DNS data, which is about two orders of magnitude larger than the direct simulation data shows. This large amplitude is an unphysical feature of the model used and can only be justified by the reliability of its results. The large amplitude is necessary for the correct behavior of this model. This has been established by test calculations in which f_1 was limited to 10, motivated by the fact that the high value of f_1 gave some numerical difficulties. However, with $f_1 \leq 10$ the results were totally different, and the model could
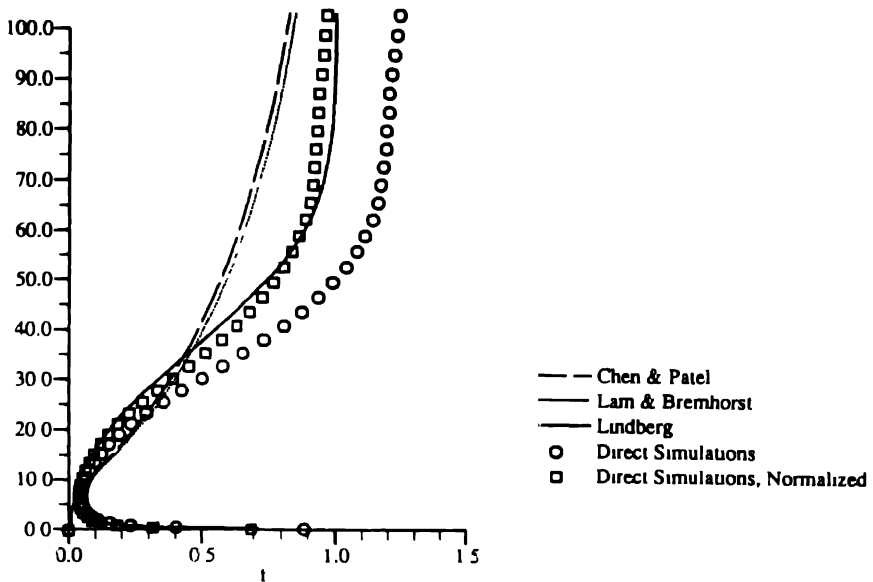
Fig 3   Comparison of f_μ used by L&B and P-AL and f_μ calculated from DNS and MKM

not calculate a $2D$ boundary layer correctly. Numerical difficulties, such as grid sensitivity, slow convergence etc., has also been reported by others, e.g. Chen & Patel (1988). The explanation for this grid dependence is probably the fact that the function f_1 varies between 1–100 where at most a few grid points are used.

The damping functions used by L&B and C&P use the turbulent kinetic energy, k, as a velocity scale instead of the friction velocity which is used in the P-AL model. The friction velocity is probably physically more correct, for flows where it is meaningful to define a friction velocity, since it is the velocity scale which is appropriate for the mean velocity and the turbulent fluctuations. However, for complicated flow fields, especially when recirculation occurs, the friction velocity calculated at the wall is not the correct velocity scale to use. In these cases the kinetic energy may be a better choice. The Reynolds number dependence shown by Rodi & Mansour (1993) may indicate that the Reynolds number also should be a parameter in the damping functions.

Apart from the many different expressions for the damping functions there also exist many suggesions of how the boundary condition for ϵ at the wall should be expressed. Two different approaches can be used, either a boundary condition for ϵ or for the variable $\bar\epsilon$, where $\bar\epsilon$ is equal to ϵ plus an extra term that vanishes away from the wall. The latter approach has the advantage that $\bar\epsilon$, can be set to zero at the wall, but no significant improvement of the results has been achieved (Patel et al. 1985).
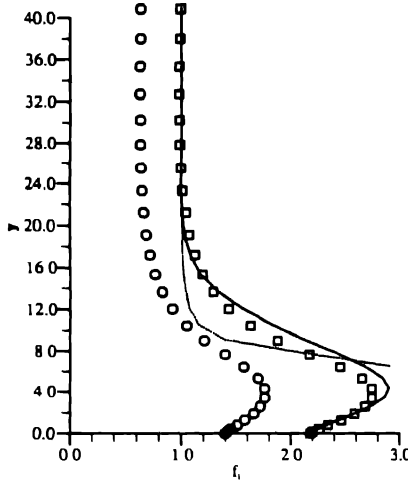
Fig. 4.   Comparison of f_1 used by L&B and P-AL and f_1 calculated from DNS by MKM. Note that the maximum value of $f_{1L\&B} > 100$.
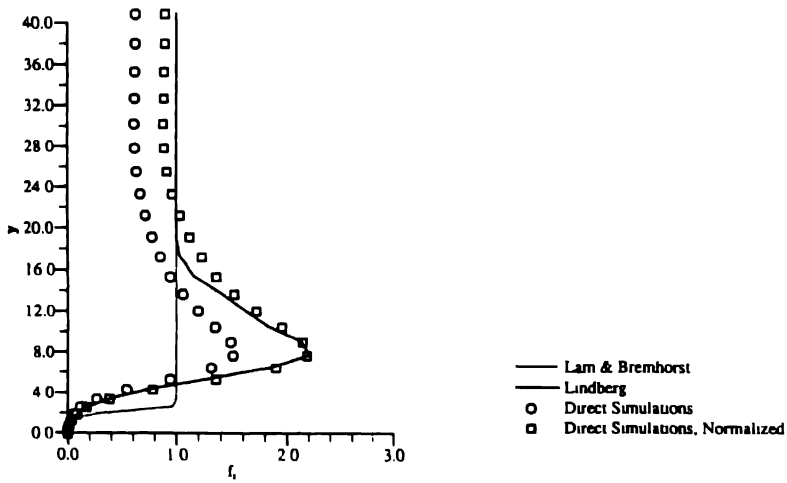
Fig. 5.   Comparison of f_2 used by L&B and P-AL and f_2 calculated from DNS by MKM.
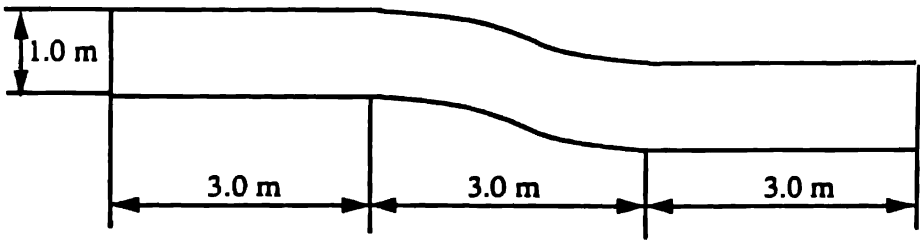
Fig 6   S-duct geometry

From equations (9 & 10) some of the conditions reviewed by Patel et al. (1985) can be examined. To set the derivative of ϵ to zero requires that $\overline{\left(a_1^+ a_1^+ + c_1^+ c_2^+\right)} = 0$.

This value may be small, which also is used in another suggestion where $\epsilon = \nu \partial^2 k / \partial x^2$ is used as boundary condition for ϵ. However, this condition has the disadvantage that a second derivative has to be calculated at the wall, which may cause numerical difficulties and thereby cause a solution with low convergence rate and/or a large grid dependence. The boundary condition used in the P-AL model is very convenient from the numerical aspect, although it has the disadvantage of being dependent of the assumption that the values of a_1^+ and c_1^+ can be treated as universal constants. Future direct simulations and experiments of different flow fields will show if this is an adequate boundary condition to be used for various three domensional flow fields.

3. Results

3.1. THE FLOW FIELD

Two different flow fields are used for the comparison of the different models. First a two-dimensional boundary layer is used where the calculated results are compared with the DNS data from MKM. For comparison with experimental results the detailed measurements of the flow field in an S duct, Truong & Brunet (1992), have been used. The duct in this experiment has a 3m long straight inlet section, a 3m S-haped section followed by a 3m straight section for flow relaxation (see Fig. 6). Careful measurements of all mean velocity components and all six Reynolds stress components at 21 stations at the inlet and at 24 stations in the curved part of the duct were made. These measurements were made in the boundary layer that develops at the top wall of the channel. The top wall is constructed by an aluminum plate equipped with about 1000 pressure taps. The experiments were made with $Re \approx 100000$, based on the external velocity and boundary layer thickness at the beginning of the curved part. A comparison of the outcome from several different turbulence models and solution techniques can be found in Ryhming, Truong & Lindber (1992).

The flow field in the S-duct serves as an excellent test case for turbulence models aimed for use in highly three dimensional flow fields. The geometry of the channel is simple which means that it is easy to obtain a suitable mesh for the calculations. However, the flow field is far from simple to model. In the core flow of the curved part of the channel there is a balance between the centrifugal acceleration and a spanwise pressure gradient. The pressure gradient is approximately constant through the boundary layer, whereas the velocity is smaller in the boundary layer. Hence, the balance between the pressure forces and the centrifugal forces is not sustained in the boundary layer. This imbalance is the cause of the three dimensionality in the boundary layer. A similar type of boundary layer may develop on three dimensional swept wings, on turbine blades etc. Furthermore the imbalance between the two forces changes sign in the double bend of the duct, which produces a cross-over velocity profile, i.e. the velocity component perpendicular to the external streamlines will change sign in the boundary layer.

3.2. NUMERICAL METHOD

The calculations were made with a boundary layer code. The external flow field was calculated from the Euler equations using the measured pressure distribution as input. In the first straight part of the duct is the pressure sparsely measured. This introduces an uncertainty in the stream line patterns which will influence the computed results.

The boundary layer equations are discretized using second order discretization schemes in all directions. The step length in the x-direction (stream wise direction) was chosen small enough to give stable solutions, which meant about 400–800 steps. In the z-direction (span wise direction) about 20 stream lines were used, and in the y-direction an uneven grid spacing has been used with 120 points across the boundary layer, for further details see Lindberg (1991).

As inlet conditions for the calculations, the measured velocity and turbulent kinetic energy profiles in the streamwise direction were used.

3.3. RESULTS FROM A 2D BOUNDARY LAYER

As a first test case for the various adoptions of the $k - \epsilon$ models a two dimensional boundary layer was calculated. The Reynolds number was the same as for the experiments in the S-duct, i.e. ~ 100000 and the equations were integrated long enough to give a solution independent of the stream wise direction, when scaled in wall units. The difference in Reynolds number between the present calculations and the DNS data is of course a drawback. It would also be more suitable to compare with DNS data from a boundary layer calculation, but the author did not have access to such data. However, close to the wall ($y^+ < 20 - 30$) the comparison is meaningful due to the fact that in this region different flow fields show small dependencies on the Reynolds number and flow geometry. In Fig. 7 the mean velocity, k and

ϵ are shown in wall coordinates. The mean velocity is best calculated with the C&P model, which is giving a mean velocity that follows the logarithmic profile very well. The L&B and the P-AL models are giving very similar results, with an additive constant somewhat smaller than the DNS. A smaller additive constant may be expected in these calculations though the Reynolds number in the present calculations is much higher than the one used in the DNS (Johansson & Alfredsson 1982).

Although the C&P model is best in calculating the mean velocity k and ϵ are best reproduced by the P-AL model. The mean velocity is of course the most important variable to calculate, but in many practical applications the value of k may also be of importance, for example in turbulent mixing, flows with chemical reactions etc. Further, a model that is able to reproduce the correct k-profile is more likely to give correct results for more complicated flows. It has also been pointed out by Lai & So (1990), who examined the near-wall behavior of the Reynolds stress equations, that a good representation of the dissipation rate is important for the result from the Reynolds stress equations.

3.4. RESULTS FROM THE S-DUCT

In the straight part of the S-duct, where the flow field is almost two-dimensional, it is possible to compare the three different $k - \epsilon$ models with the experiments and, very close to the wall, with the DNS data (Fig. 8). In this station the flow angle is about 4–5° This results in a diference between the magnitudes of the mean velocity in the x-direction and the total mean velocity of less than one percent. The experimental mean velocity has a well pronounced logarithmic part but the additive constant is smaller than what is found in a fully developed 2D boundary layer and the friction velocity obtained from the logarithmic part of the velocity profile ($u_\tau = 0.96m/s$) differs from the one obtained with the Preston tube and surface fence techniques ($u_\tau = 0.87m/s$). These differences from the fully developed mean velocity profile is uncertain. Note, that due to the large span in the measured friction velocity both the calculated and experimental data are normalized with value obtained from the calculations $u_\tau = 0.8m/s$.

The mean velocity obtained with the C&P model is in close agreement with the DNS, which predicts a larger velocity for small y^+ as compared with the experiments. The L&B and P-AL models are in better agreement with the experimental mean velocity. The difference between the C&P model and the other models may be due to the former using a one-equation model for $y+ \leq 200$. With just one equation in this region the result may be too dependent on the length scales used. These modeled length scales are best fitted for the fully developed profiles for which they were designed. However, the differences are small, and all models are giving results that are accurate enough for many applications.

The Reynolds stresss $\overline{uv}$ is captured very well by the three models, except that the C&P model does not give the correct shape very close to the wall. This is due
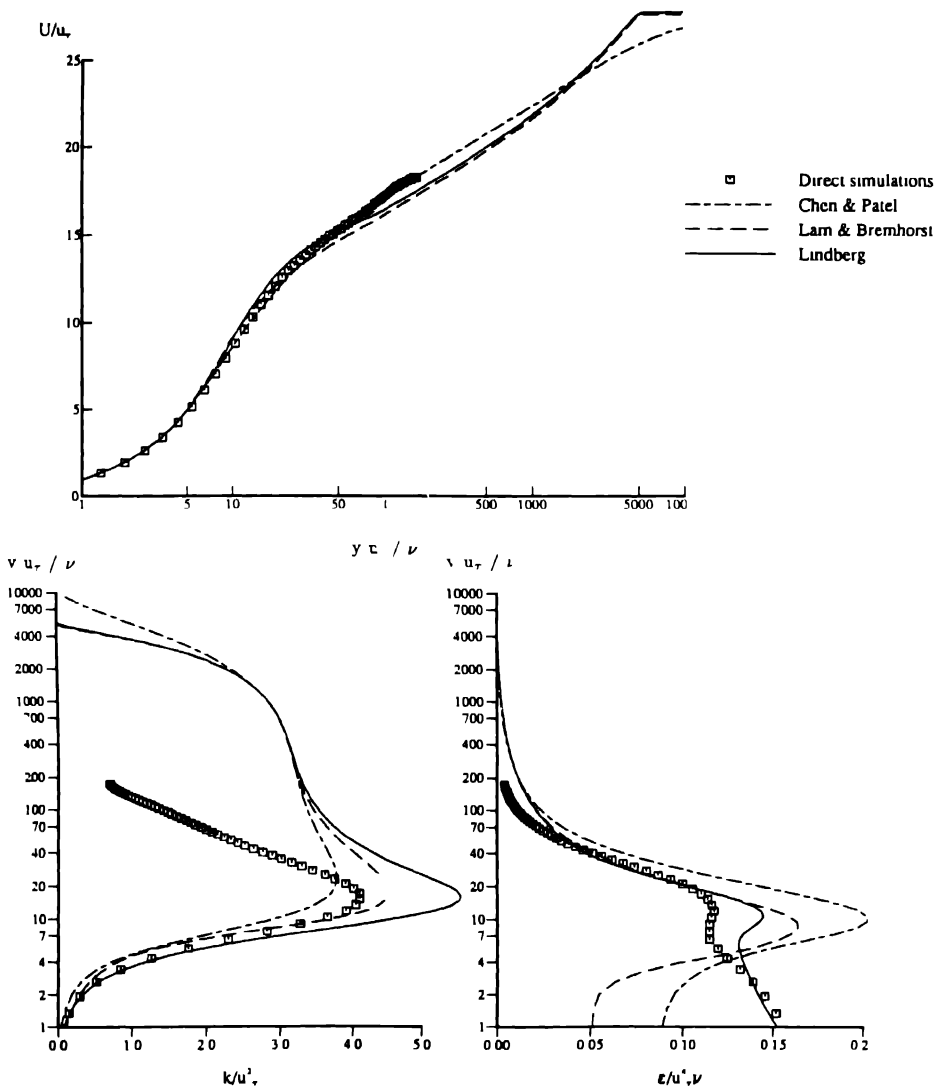
Fig 7   Calculation of a 2D boundary layer ($Re_\theta \sim 1000000$), L&B, C&P, P-AL and DNS by MKM $Re_\tau = 180$), all calculations are normalized with the respective friction velocity

to the length scale, l_μ, giving the eddy viscosity, which does not have the correct limiting behavior as was noted earlier

The predicted k profiles (Fig 9) show larger differences between the P-AL and the L&B models than the predicted mean velocities The only k profile that closely
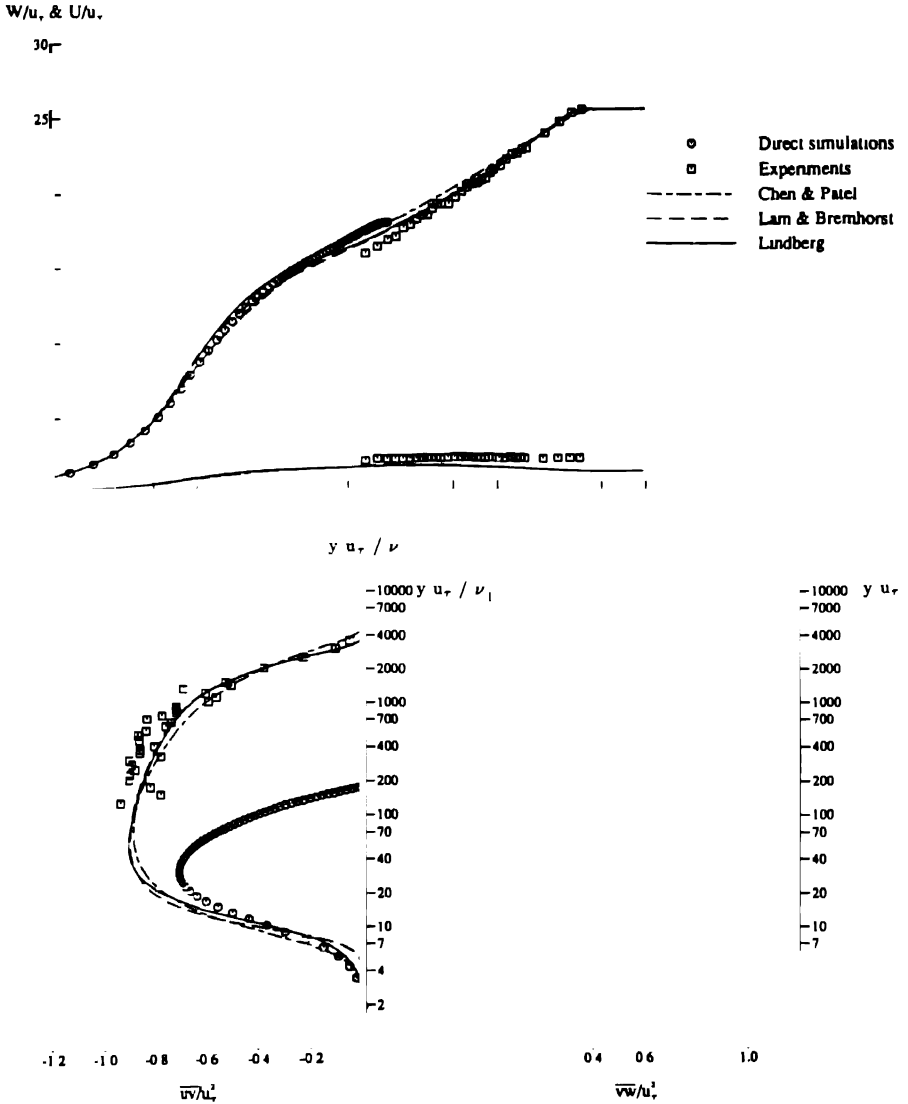
W/u, & U/u,

Fig. 8.   Comparison of experimental results, DNS by MKM and calculated results using the L&B, and C&P and P-AL near wall models in the S-duct. U^+, W^+, $\overline{uv}^+$ and $\overline{vw}^+$ in station $x = 2950\ mm$ $z = 500\ mm$. The friction velocity obtained from the experiments from the log-law is $0.955\ m/s$ and from the Preston tube measurements $0.886\ m/s$ and from the calculations $u_\tau P - AL = 0.7953\ m/s, u_{\tau L\&B} = 0.7957\ m/s, u_{\tau C\&P} = 0.7970\ m/s$, the experimental and calculated results are normalized with $u_\tau = 0.796\ m/s$.
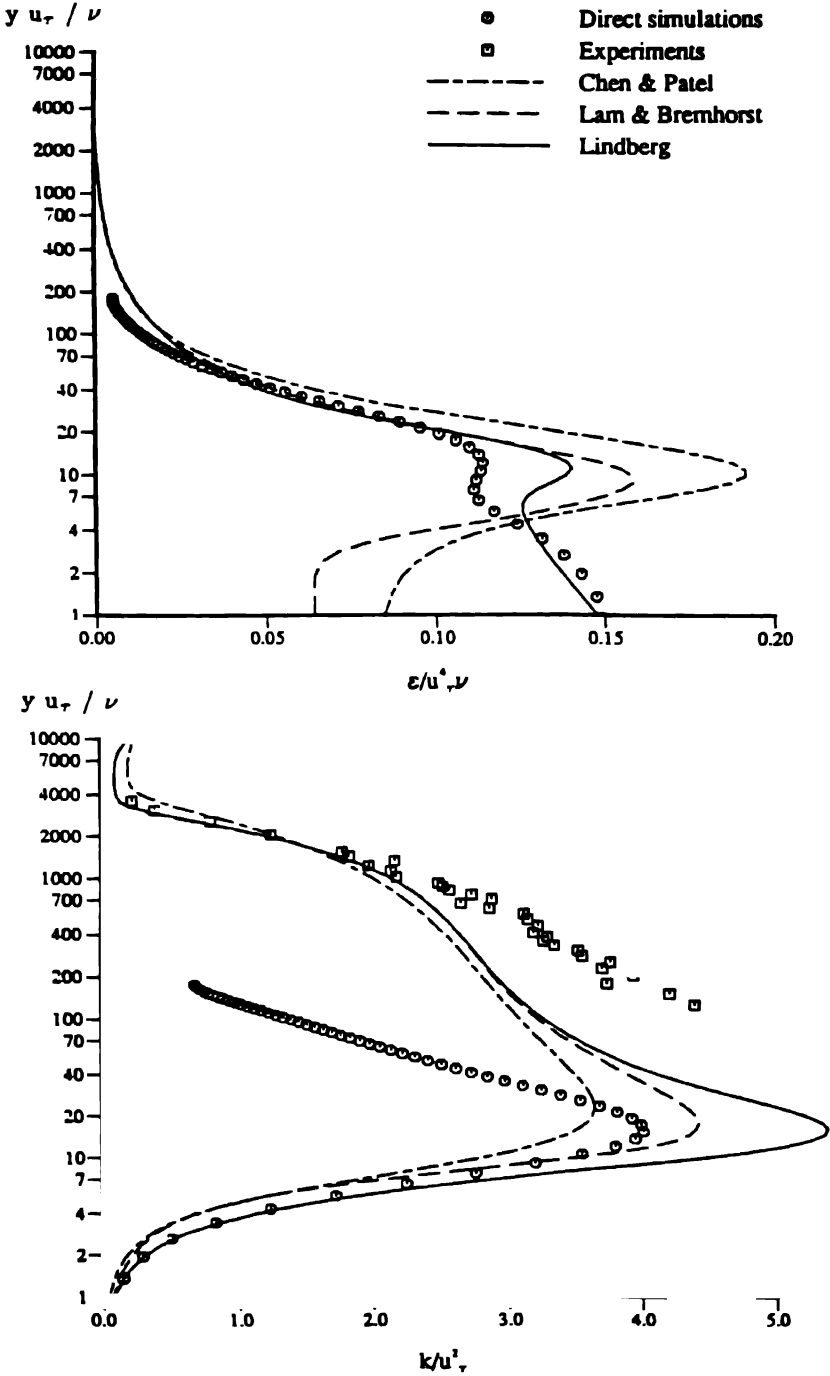
Fig 9   Comparison of experimental results, DNS by MKM and calculated results using the L&B, and C&P and P-AL near wall models in the S-duct k^+ and ϵ^+, in station $x = 2950\ mm$ & $z = 500\ mm$ The friction velocities obtained as in previous figure

follows the direct simulation data for small y^+, which is the only region where such comparison is meaningful in view of the difference in Reynolds number, is the results from the P-AL model. The P-AL and L&B models gives higher k^+ than the DNS results, whereas the C&P model gives a lower k^+. However, the maximum value of k in the experiments is probably larger than the DNS results closer to the wall (where no measurements are available). This can be judged from the fact that the maximum value of the measured k, when the friction velocity obtained from the Preston tube measurements are used, is $k^+ = 3.7$, whereas the maximum value of k^+ normally is between 4 and 5, (e.g. Patel et al. 1985). The calculations give a friction velocity which is lower ($u_{\tau acl} \approx 0.79 \ m/s$) than the Preston tube measurements ($u_{\tau Preston} = 0.89 \ m/s$).

There does not exist any measurements of the dissipation, so the only available data are those from the DNS. The boundary conditions for ϵ used in the L&B and C&P model are giving a value of ϵ^+ at the wall of about 0.05–0.10, which is quite different from the DNS by KMM that gives $\epsilon^+ = 0.17$ and the experiments by Alfredsson et al. (1988) giving $\epsilon^+ = 0.2$. The P-AL model is in quite good agreement with the direct simulation for $y^+ < 7$. The local maximum in ϵ around $y^+ \approx 15$ is overpredicted by all models, although less by the P-AL model. Although the agreement is very good for all models above this local maximum, a comparison may not be meaningful due to the difference in Reynolds number.

Further downstream in the S-bend the experimental velocity profile in the x-direction still has a pronounced logarithmic region (see Fig. 10), which is probably wider if the velocity was plotted in stream line coordinates. The results from the different models is about the same as found in Fig. 8. The C&P model gives a mean velocity profile which is quite close to the log-law profile and the mean velocity is therefore slightly overpredicted by this model than by the other models. The friction velocity obtained from the calculations ($u_{\tau P-AL} = 0.802 \ m/s$, $u_{\tau L\&B} = 0.804 \ m/s$ and $u_{\tau C\&P} = 0.766 \ m/s$) differ from the Preston tube measurements ($u_{\tau Preston} = 0.885 \ m/s$) also at this station. The underprediction of the friction velocity is about 10% which may be too large to be acceptable. Some, but not all, of this difference may be accounted by the overpredicted external velocity.

The difference between the L&B and P-AL models is not visible when the mean velocity is plotted in linear scales. In the S-bend (Fig. 11) the differences between the P-AL and the C&P model are quite small regarding the mean velocity, and the reason for the discrepancy is discussed ealier. The difference between the experimental and calculated results at the outer edge of the boundary layer is, as mentioned before, due to the inaccuracy of the external solution. The Reynolds shear stresses are slightly better predicted by the P-AL model than the C&P model, but the differences are not bigger than the scatter in the experimental data. For the station outside of the valid domain for the calculations (Fig. 12) the P-AL model captures the behavior close to the wall quite well whereas the C&P model is capturing the outer part well.
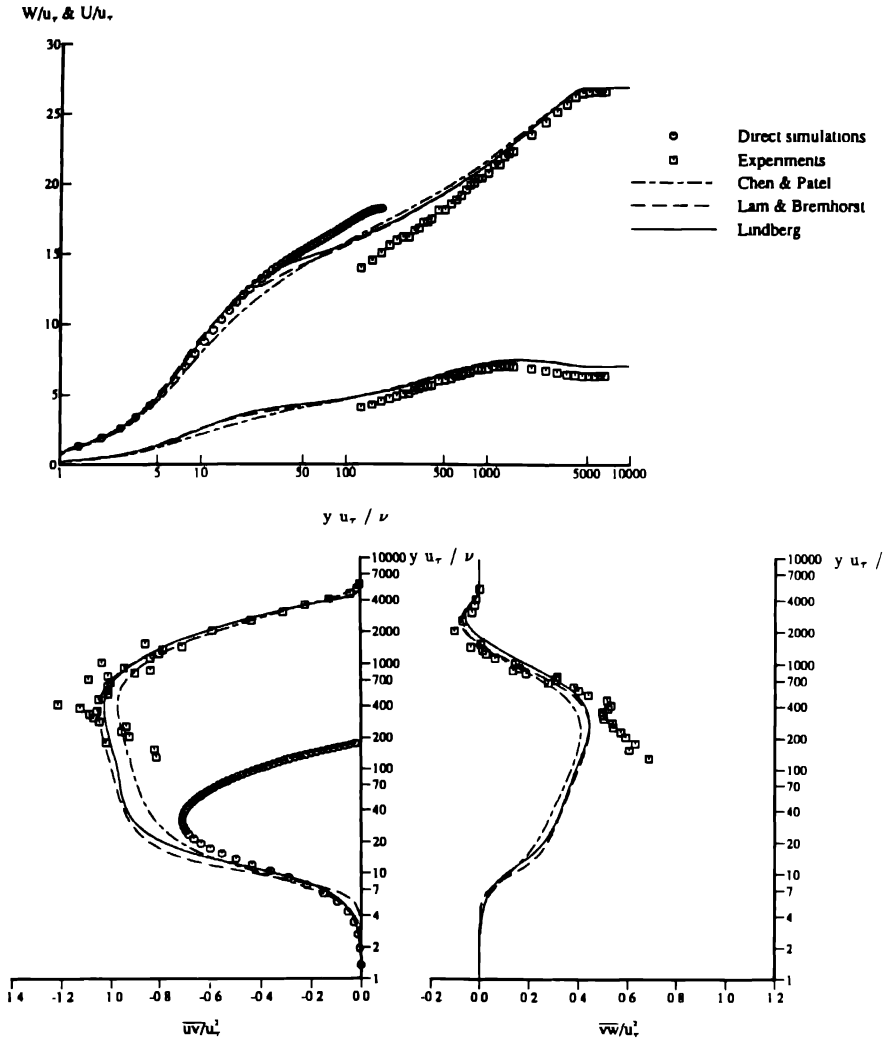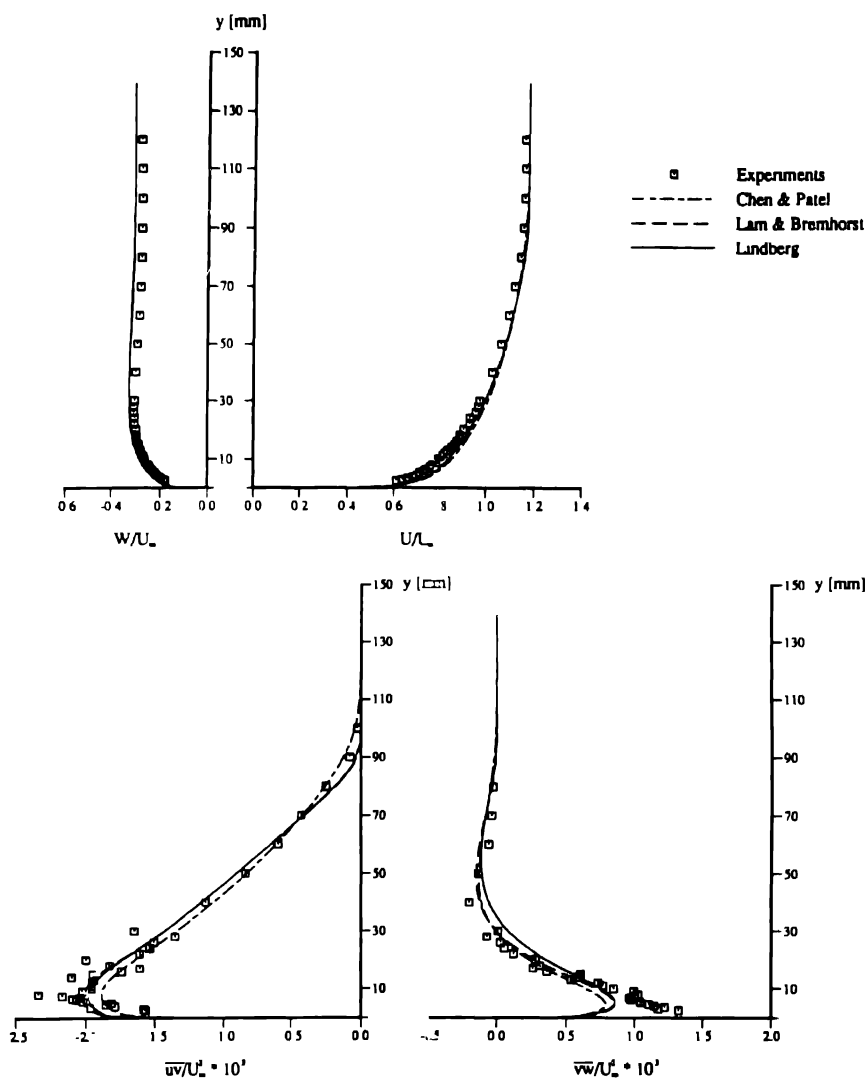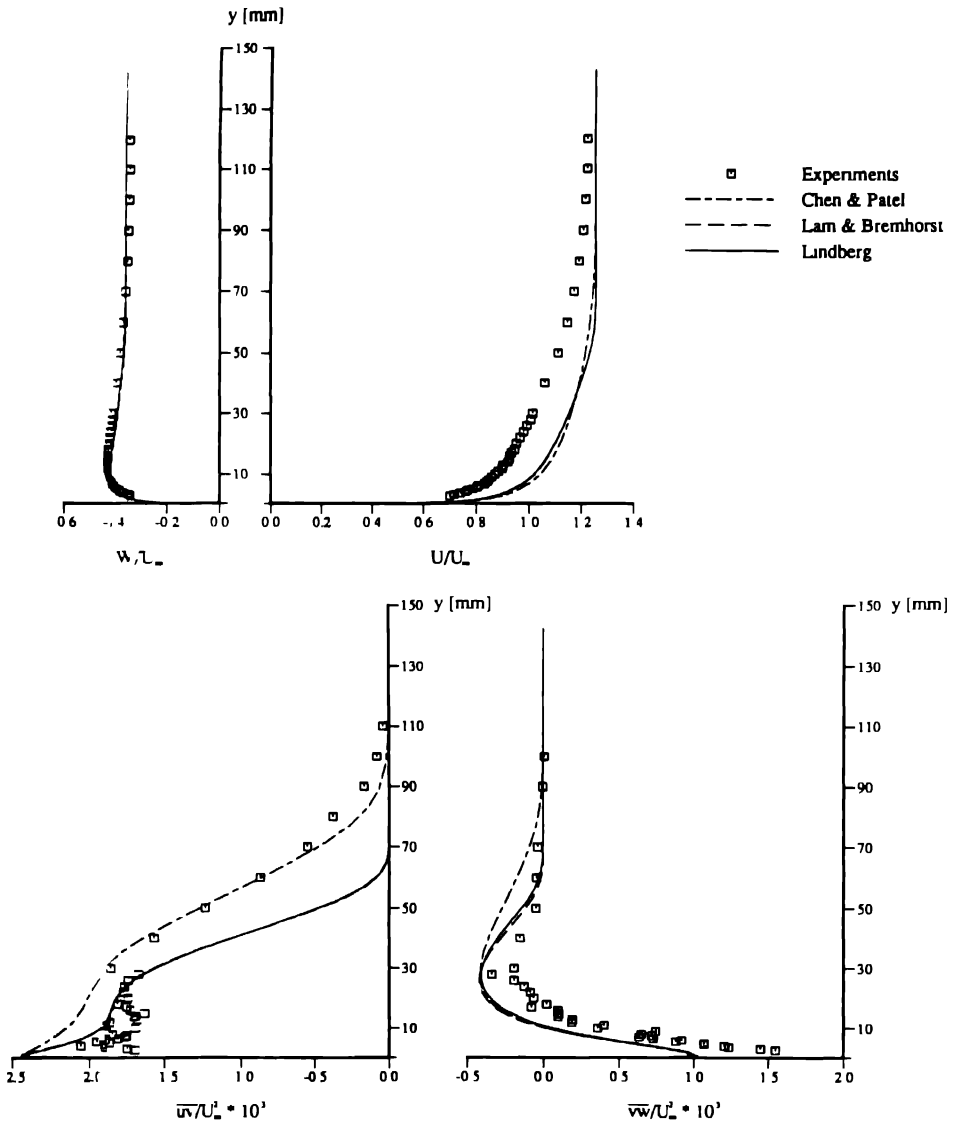
Fig. 10. Comparison of experimental results and calculated results using the L&B, C&P and P-AL near wall model in the S-duct. Showing $U^+, W^+, \overline{uv}^+, \overline{vw}^+$, in station $x = 5005\ mm$ & $z = 1150\ mm$ normalized with $u_\tau = 0.79\ m/s, u_{\tau P-AL} = 0.802\ m/s, u_{\tau L\&B} = 0.804\ m/s, u_{\tau C\&P} = 0.766\ m/s, u_{\tau Preston} = 0.885\ m/s$.

4. Conclusions

Calculations have been made of the three dimensional boundary layer in a S-shaped duct, where different turbulence models have been used.

The near wall behavior of three different $k - \epsilon$ models have been tested. The results show that it is possible to obtain as good results with the new model presented here as with the ones presented by Lam & Bremhorst (1981) and Chen & Patel

Fig. 11. Comparison of experimental results and calculated results using the L&B, C&P and P-AL near wall model in the S-duct. Showing U, W, uv and wv, $U_\infty = 18\ m/s$, in station $x = 4700\ mm\ \&\ z = 730\ mm$.

(1988). The numerical difficulties reported by Chen & Patel (1988) and others for the Lam & Bremhorst model is probably due to the large amplitude of the damping functions that are used, these problems are not present with the P-AL model. The P-AL is easier to implement than the C&P model as it is a one-layer model. In

Fig. 12.   Comparison of experimental results and calculated results using the L&B, C&P and P-AL near wall model in the S-duct Showing U, W, uv and $wv, U_\infty = 18\ m/s$, in station $x = 5005\ mm$ & $z = 1150\ mm$

comparison with the C&P model the P-AL model seems to be slightly better to predict flows which do not have a standard log profile. The damping functions are deduced from the DNS of Mansour, Kim & Moin (1988) with $Re^+ = 180$. The

behavior of the P-AL model can probably be improved by using DNS made with higher Reynolds number, such as the one used by Rodi & Mansour (1990 & 1993).

To further test the turbulence models the author suggests that the measurements in the S-duct be extended close to the wall. This is probably too difficult to do with multiple wire probe, but with a single wire it is probably possible to measure closer to the surface, which of course only can give the streamwise velocity. However, measurements of the streamwise mean and fluctuating velocity should help the further development of turbulence models. It may give a clue as to why the turbulence models give a friction velocity which is 10–15% too low. Finally, further improvement can be expected with a more representative external flow field.

Acknowledgments

References

Alfredsson, P.H., Johansson, A.V., Haritonidis, J.H. and Eckelmann, H., The fluctuating wall-shear stress and the velocity field in the viscous sublayer. *Physics of Fluids* 31 (1988) 1026–1033.

Brunet, M. and Truong, T.V Test case T1: Boundary layer in a "S"-shaped channel. In Pironneau, O., Rodi, W., Ryhming, I.L., Savill, A.M. and Truong, T.V. (eds), *Numerical Simulations of Unsteady Flows and Transition to Turbulence.* Cambridge University Press (1992).

Chen, H.C., and Patel, V.C., Near-wall turbulence models for complex flows including separation. *AIAA Journal* 26 (1988) 641–648.

Gavrilakis, S., Numerical simulation of low Reynolds number turbulent flow through a straight square duct. *Journal of Fluid Mechanics* 244 (1992) 101–129.

Johansson, A.V. and Alfredsson, P H., On the structure of turbulent channel flow. *Journal of Fluid Mechanics* 122 (1982) 295–314.

Kim, J., Moin, P. and Moser, R.. Turbulence statistics in fully developed channel flow at low Reynolds number. *Journal of Fluid Mechanics* 177 (1987) 133–166.

Lai, Y.G., an So, R.M.C., On near-wall turbulence *Journal of Fluid Mechanics* 221 (1990) 641–673.

Lam, C.K.G. and Bremhorst, K., A modified form of the k-e model for predicting wall turbulence. Transactions of the ASME, *Journal of Fluids Engineering* 103 (1981) 456–460.

Lindberg, P.-Å., Near-wall turbulence models for 3D boundary layers. Internal report no T-91-9, IMHEF-DME. Ecole Polytechnique Federale de Lausanne, CH-1015 Lausanne, Switzerland (1991).

Lindberg, P.-Å., An anisotropic eddy viscosity model, using the $k - \epsilon$ model or an extended Johnson & King model for solving the boundary layer equations. In Pironneau, O., Rodi, W., Ryhming, I.L., Savill, A.M. and Truong, T.V. (eds), *Numerical Simulations of Unsteady Flows and Transition to Turbulence.* Cambridge University Press (1992).

Mansour, N.N., The use of direct numerical simulation data in turbulence modeling. AIIA paper 91–0221 (1991).

Mansour, N.N., Kim, J. and Moin, P., Reynolds-stress and dissipation-rate budgets in a turbulent channel flow. *Journal of Fluid Mechanics* 194 (1988), 15–44.

Moin, P., Shih, T.-H., Driver, D. and Mansour, N.N., Direct numerical simulation of a three-dimensional turbulent boundary layer. *Physics of Fluids A* (1990) 1846–1853.

Norris, L.H. and Reynolds, W.C., Turbulent channel flow with a moving wavy boundary. Rept. No FM-10, Stanford University, Dept. Mech. Eng. (1975).

Patel, V.C., Rodi, W. and Scheuerer, G., Turbulence models for near-wall and low Reynolds number flows: A review. *AIAA Journal* 23 (1985) 1308–1319.

Pollard, A. and Martinuzzi, R., Comparative study of turbulence models in predicting turbulent pipe flow. Part II: Reynolds stress and $k - \epsilon$ models. *AIAA Journal* 27 (1989) 1714–1721.

Rodi, W., Some current approaches in turbulence modelling. AGARD Technical status review on "Appraisal of the suitability of turbulence models in flow calculations" (1990).

Rodi, W. and Mansour, N.N., One-equation near-wall turbulence modeling with the aid of direct simulation data. In *Proceedings of the Summer Program 1990*. Center for turbulence research, Stanford University (1990).

Rodi, W. and Mansour, N.N., Low Reynolds number $k - \epsilon$ modeling with the aid of direct simulation data. *Journal of Fluid Mechanics* 250 (1993) 509–519.

Ryhming, I.L., Truong , T.V., Lindberg, P.Å., Summary and conclusions for the test case T1. In Pironneau, O., Rodi, W., Ryhming, I.L., Savill, A.M. and Truong, T.V. (eds), *Numerical Simulations of Unsteady Flows and Transition to Turbulence*, Cambridge University Press (1992).

Spalart, P.R., Direct simulation of a turbulent boundary layer up to $R_\theta = 1410$. *Journal of Fluid Mechanics* 187 (1988) 61–98.

Speziale, C.G., Abid, R. and Anderson, E.C., A critical evaluation of two-equation models for near wall turbulence. ICASE Report No 90–46, ICASE, NASA Langley Research Center, Hampton, Virginia 23665–5225. USA (1990).

Truong, T.V., and Brunet, M., Test case T1: Boundary layer in an "S"-shaped channel. In Pironneau, O., Rodi, W., Ryhming, I.L., Savill, A.M. and Truong, T.V. (eds), *Numerical Simulations of Unsteady Flows and Transition to Turbulence*. Cambridge University Press (1992).

163

A Survey of Exact Solutions of Inviscid Field Equations in the Theory of Shear Flow Instabilty [*]

JOHN M. RUSSELL
*Department of Mechanical and Aerospace Engineering, Florida Institute of Technology,
Melbourne, Florida USA, 32901*

Abstract. This paper presents a survey of undisturbed flows that take one or another of the field equations of inviscid shear flow instability theory (e.g. the RAYLEIGH equation, TAYLOR-GOLDSTEIN-HAURWITZ equation or the KUO equation) to a differential equation satisfied by a *known* transcendental function for *arbitrary complex values of the parameters*. Some mean velocity profiles having this feature are well known. Thus, piecewise linear mean velocity profiles take the RAYLEIGH equations to a constant-coefficient differential equation and the exponential mean velocity profile takes the RAYLEIGH equation to the GAUSS hypergeometric equation. Less well known is the fact that a variety of mean velocity profiles take the RAYLEIGH equation to a differential equation due to KARL HEUN. These profiles include: (i) the sinusoidal profile; (ii) the hyperbolic tangent profile (an example pointed out by MILES (1963)); (iii) the profile in the form of the square of a hyperbolic secant (the BICKLEY jet); and, (iv) a skewed velocity profile in which each component has the form of a quadratic function of the variable $\exp(-z/l)$ (in which z is the cross-stream coordinate and l is a length scale). In all of these cases, one or another author has previously identified a *regular neutral mode* solution of the RAYLEIGH equation and has expressed that solution in the form of elementary functions. Such regular neutral modes apparently represent cases in which the solution of HEUN'S equation (which is normally an infinite series) truncates to a single term. The survey concludes by noting that the parabolic mean velocity profile takes the RAYLEIGH equation to the *differential equation of the spheroidal wave function*.

Key words: shear-flow instability, inflectional instability, stratified shear flow, barotropic zonal currents, exact solutions

1. Introduction

One standard method for analyzing the stability or instability of a shear flow is to begin by writing down both the set of equations of motion of the flow in some *reference state* and the corresponding set of equations of motion in some *disturbed state*. By subtracting the former set from the latter and linearizing for small disturbances, one obtains a set of linear partial differential equations in physical variables for the disturbance quantities. There may by a set of cartesian or curvilinear coordinates relative to which the velocity components of the undisturbed flow depend upon only one variable (the *cross-stream coordinate*), and are either nonvarying or slowly varying with respect to the other coordinates (the *propagation-space coor-*

---

dinates). In that case, one may seek solutions of the small disturbance equations by the method of separation of variables. Such solutions typically exhibit exponential travelling-wave character with respect to the propagation-space coordinates and more arbitrary character with respect to the cross-stream coordinate. If, as is usually the case, the travelling-wave character of the disturbances is manifested by a common exponential factor, then by cancelling this factor one obtains a linear homogenous set of ordinary differential equations for the unknown shape functions (one corresponding to each dependent variable), which collectively represent the cross-stream dependence of the disturbances. The term *field equations in the theory of shear flow instability*, as appears in the title of this paper, refers to such a set of ordinary differential equations.

In a typical instability problem, one seeks solutions of the classical field equations subject to a full set of homogeneous boundary conditions. Such boundary conditions may express the condition of impermeability of a wall, the condition of no slip at the interface between a viscous fluid and a solid wall, the condition that disturbances decay to zero in a remote free stream, or whatever other condition suits a particular physical situation. The homogeneous system of equations subject to the full set of homogeneous boundary boundary conditions has nontrivial solutions only if the parameters are related to each other in a particular way and the equation that relates those parameters is the *dispersion relation* or the *eigenvalue condition* of the problem.

A modern author who formulates a novel shear flow instability problem and develops the theory for it to the point of reporting a dispersion relation, will nearly always obtain that dispersion relation by numerical means. A novice to the subject, however, normally does well to work through a few simple problems in which one can obtain the dispersion relation analytically before attempting to program a computer to solve more ambitious problems. At that stage of learning, such a novice (and a professor who must find ways to teach the subject to novices) has a need for a catalog of solved cases, in particular a list of undisturbed flows for which one or another of the classical field equations of shear flow instability is solvable in terms of known transcendental functions *for arbitrary complex values of the parameters*. The object of this paper is to present such a list.

Exact solutions of the field equations of linear stability theory are of value in applications other than the teaching of the subject to novices*. Some perturbation methods for generating approximate solutions of nonlinear problems make use of an amplitude parameter whose value is presumed to be infinitesimal in the linear theory. The nonlinear problem is decomposed into a sequence of linear problems, the first of which is homogeneous and corresponds to the the equation for infinitesimal amplitude disturbances. To carry out the details of such a perturbation scheme, one must be able to solve the leading order problem, and must, therefore, have a solution of the linear equation at one's disposal. In this respect, a catalog

---

* I am indebted to a referee for calling my attention the main point of this paragraph

of solved cases of linear equations might be of interest to persons who apply such perturbation methods to solve weakly nonlinear problems.

Among the inferences one may draw from this survey are the following. First, there are very few examples of undisturbed flows for which the classical field equations for the disturbances are solvable in terms of known transcendental functions for arbitrary complex values of the parameters. Secondly, when the field equations for the disturbances *are* solvable, the transcendental functions that solve them are often unwieldy. Thirdly, if one is willing to put up with the unwieldiness of an exact solution, one can escape some of the limitations of numerical solutions.

2. Field equations in inviscid flow problems

In the case of inviscid flows, there are three classical field equations with so many mathematical features in common that one is led to discuss them as a group. First of these is the *Rayleigh stability equation* (RAYLEIGH, 1880) Suppose that the mass density of the fluid is uniform in space and constant in time. Suppose further that the undisturbed flow has straight streamlines, is steady in time, and that its velocity field **U** is everywhere parallel to a reference plane $\mathcal{P}$. Let (x, y, z) be cartesian coordinates oriented so that z is normal to $\mathcal{P}$. Then the cartesian components of the velocity field corresponding to the cartesian position components (x, y, z) are $(U(z), V(z), 0)$. One may arrange the equations of motion for the disturbance velocity into a single partial differential equation for the cross-stream velocity component w. In this partial differential equation, the coefficients depend only on the cross-stream coordinate z and one is led to seek solutions in the form of travelling waves, i.e.

$$w(x, y, z, t) = 2\Re\{\tilde{w}(\alpha, \beta, z, \omega)\exp[i(\alpha x + \beta y - \omega t)]\}. \tag{1}$$

If one substitutes (1) into the partial differential equation for w, one obtains the celebrated equation of RAYLEIGH (1880)

$$[kQ(z) - \omega]\left(\frac{d^2\tilde{w}}{dz^2} - k^2\tilde{w}\right) - k\frac{d^2Q}{dz^2}\tilde{w} = 0. \tag{2}$$

Here k is defined in terms of α and β by the definition $k^2 \equiv \alpha^2 + \beta^2$. The quantity $Q(z)$ is defined in terms of previously defined quantities by the equation $kQ(z) \equiv \alpha U(z) + \beta V(z)$.

One may rewrite the RAYLEIGH equation in several equivalent forms, one of which is

$$\frac{d}{dz}\left\{\rho[kQ(z) - \omega]^2\frac{d}{dz}\left(\frac{\tilde{w}}{kQ(z) - \omega}\right)\right\} - k^2\rho[kQ(z) - \omega]\tilde{w} = 0, \tag{3}$$

in which ρ is the mass density of the fluid. If one relaxes the assumption that the fluid is of uniform density and supposes that the cross stream coordinate z is

directed parallel to the gravitational vector and measured positive 'up', then the field equation one obtains as a generalization of (3) is

$$\frac{d}{dz}\left\{\bar{\rho}[kQ(z)-\omega]^2\frac{d}{dz}\left(\frac{\bar{w}}{kQ(z)-\omega}\right)\right\}-k^2\bar{\rho}[kQ(z)-\omega]\bar{w}$$
$$-g\frac{d\bar{\rho}}{dz}k^2\left(\frac{\bar{w}}{kQ(z)-\omega}\right)=0\,,\qquad(4)$$

in which $\bar{\rho}(z)$ represents the distribution of density versus height in the undisturbed flow. Equation (4) has the same meaning as equation (281) on page 499 of YIH (1969). The result is due to TAYLOR (1931), GOLDSTEIN (1931), and HAURWITZ (1931).

A flow instability problem that gives rise to a differential equation similar to the RAYLEIGH equation occurs in geophysical fluid dynamics. DRAZIN & HOWARD (1966, p 51) summarize the assumptions leading to this problem as follows (I have introduced minor variations of notation):

> For large-scale ($\approx 10^3$ km) motions of the earth's atmosphere or oceans, it is customary to neglect the kinematic effects of the earth's curvature and use rectangular CARTESIAN coordinates, but to retain the more important dynamic effects of the variation of the CORIOLIS parameter $f \equiv 2\Omega\sin\lambda$ with latitude λ. This is done in the beta-plane method of ROSSBY [cf. KUO (1949)]. With this approximation, it can be shown that the only modification to the stability of an eastward horizontal basic flow $\mathbf{U} = U(z)\hat{\imath}$ relative to the earth is the addition of $f\hat{\mathbf{k}}$ to the relative vorticity $U'(z)\hat{\mathbf{k}}$, the earth having angular velocity $\Omega(\cos\lambda\mathbf{j} + \sin\lambda\hat{\mathbf{k}})$. KUO (1949) has show that this leads to the stability equation
>
> $$[U(z)-c]\left(\frac{d^2\varphi}{dz^2}-\alpha^2\varphi\right)-\left(\frac{d^2U}{dz^2}-\bar{\beta}\right)\varphi=0 \qquad(5)$$
>
> by the usual methods for two-dimensional disturbances, where $\bar{\beta}\equiv df/dz$ is usually approximated by a constant and z by the product of the local value of λ and the radius of the earth.

Here $c \equiv \omega/\alpha$ is the complex frequency of the disturbance and φ is the shape factor in travelling-wave representation of the disturbance stream function. One must not confuse the derivative $\bar{\beta}$ of the Coriolis parameter f in (5) with the spanwise wavenumber parameter β as used elsewhere in this paper. Of course, (5) has a mathematical structure with many features in common with (2).

3. Mean flows that take one or another inviscid field equations to solvable form

3.1. MEAN FLOWS WITH PIECEWISE LINEAR VELOCITY DISTRIBUTIONS

The oldest exact solutions of field equations belonging to the family represented by equations (2), (4), and (5) are those obtained by KELVIN and RAYLEIGH in the last century under the assumption that the form of the velocity distribution in the undisturbed flow is *piecewise linear*. DRAZIN & HOWARD (1966) present a full

review of solutions of this kind with references to the earlier literature. These solutions remain the most instructive simple analytical models for the kinds of physical phenomena captured by the RAYLEIGH equation and its generalizations. Since these results are well known and frequently discussed, I will not discuss them further here.

3.2. TOLLMIEN'S SOLUTION OF THE RAYLEIGH EQUATION ABOUT AN ISOLATED CRITICAL POINT BY THE METHOD OF FROBENIUS

If the function $z \mapsto kQ(z) - \omega$ is analytic in z and has a simple zero at the point $z = z_c$, then that point is a regular singular point of the RAYLEIGH equation (2) and the method of FROBENIUS is at one's disposal for generating convergent series representations for a linearly independent pair of exact solutions in a neighborhood of that point. TOLLMIEN (1929, 1935) seems to have been the first to have studied these solutions in detail. One finds that the indicial exponents belonging to the singular point at $z = z_c$ equal zero and one. A general feature of the method of FROBENIUS is that if the indicial exponents are distinct, then one can always construct a linearly independent set of solutions such that each solution belongs to one and only one of the indicial exponents. In the case of the RAYLEIGH equation (2), the solution that belongs to the indicial exponent one is analytic at $z = z_c$ and has a first order zero there. Since the indicial exponents differ by an integer (in this case one), the possibility of a solution with a logarithmic branch point arises and if $Q''(z_c) \neq 0$ the solution belonging to the indicial exponent zero does indeed have such a branch point. TOLLMIEN applied these solutions in a number of ways. In his 1880 paper, RAYLEIGH had proved his celebrated *inflection-point theorem*, i.e. that a necessary condition for the existence of a temporally growing solution of the instability problem is that the second derivative of the undisturbed velocity distribution $Q(z)$ vanish somewhere between the boundaries. In his 1935 paper, TOLLMIEN applied his FROBENIUS series solutions to extend the scope of the RAYLEIGH inflection-point theorem. Thus, TOLLMIEN showed that if the regular singular point $z = z_c$ is real valued then the REYNOLDS stress associated with the disturbance is piecewise uniform on either side of that singular point. If, in particular, there is only one real root of the equation $kQ(z) - \omega = 0$, then this piecewise uniformity of the REYNOLDS stress is compatible with homogeneous boundary conditions for the disturbances only if the jump in REYNOLDS stress across the singular point vanishes. In the mean time, TOLLMIEN'S FROBENIUS-series solutions show that this jump in the REYNOLDS stress is directly proportional to $Q''(z_c)$ and to other factors that are nonzero if the solution is nontrivial. It follows that $Q''(z_c)$ must vanish, *i.e.* the mean velocity distribution must have an inflection point. In summary, an inflection point is necessary if there is to be a solution with a real valued singular point $z = z_c$. For such a mode, the complex phase velocity is real valued and if the wavenumber k is also real valued, the exponential amplification rate is zero. Modes with zero exponential amplification

rates are *neutral modes*. TOLLMIEN'S argument amounts to a demonstration that an inflection point in the mean velocity distribution is necessary not only for the existence of exponentially growing modes (as required by RAYLEIGH'S theorem) but for neutral modes as well.

TOLLMIEN also exploited his FROBENIUS solutions to derive approximate dispersion relations (relating ω to k) that hold in the limit of small wavenumbers. Many of the theorems TOLLMIEN derived from his FROBENIUS solutions make direct use of the logarithmic character of one of the solutions of the RAYLEIGH equation near $z = z_c$. The older solutions of the RAYLEIGH equation, *i.e.* the ones predicated on the assumption that the mean velocity disribution is piecewise linear, do not exhibit the logarithmic branch point. Thus, despite their success in representing some aspects of inertial instability, these older solutions in which the mean velocity profile is of broken-line type can never capture basic results of the sort derived by TOLLMIEN from the correct FROBENIUS solutions since the logarithmic branch point arises only in the case of a smooth mean velocity profile.

3.3. THE EXPONENTIAL BOUNDARY-LAYER PROFILE

If the flow domain over which one seeks a solution of the RAYLEIGH equation is semi-infinite (as in boundary-layer geometry) or doubly infinite (as in the case of jet, wake, or free shear layer geometry), then the point at infinity is an irregular singular point of the differential equation. The method of FROBENIUS is inapplicable at an irregular singular point, an observation that amounts to a practical limitation on the usefulness of TOLLMIEN'S series solutions. Another practical limitation is that the recursion relation for calculating the coefficient of the nth term in the series involves all of the coefficients in the series with lower index. An example of a solution of the RAYLEIGH equation that avoids both of these limitations was described by CHIARULLI & FREEMAN (1948), who cite an unpublished note by J.C. FREEMAN & C.C. LIN titled 'A note on the stability of the asymptotic suction profile' as the source. Their citation of this earlier note (on p 90 of their paper) attributes the result specifically to C.C. LIN. Suppose that the components $U(z)$ and $V(z)$ are both constant multiples of the factor $1 - \exp(-z/\delta)$, in which δ is a reference length. Then one can always orient the axes (x, y) such that these components have the form

$$U(z) = U_\infty[1 - \exp(-z/\delta)], \qquad V(z) = 0 , \tag{6}$$

in which U_∞ is a reference velocity. Under these assumptions, the RAYLEIGH equation (2) reduces to

$$[\alpha U(z) - \omega]\left(\frac{d^2\tilde{w}}{dz^2} - k^2\tilde{w}\right) - \alpha\frac{d^2U}{dz^2}\tilde{w} = 0. \tag{7}$$

The change of dependent variable $\tilde{w} \rightarrow W$ defined by $\tilde{w} \equiv e^{-kz}W$ followed by the second change of independent variable $z \rightarrow U$ takes (7) to

$$(\alpha U - \omega)\left\{(U_\infty - U)\frac{d^2W}{dU^2} - (2k\delta + 1)\frac{dW}{dU}\right\} + \alpha W = 0 \tag{8}$$

after some elementary manipulations. The second change of independent variable $U \rightarrow \zeta$ defined by

$$\zeta \equiv \frac{\alpha U - \alpha U_o}{\omega - \alpha U_\infty} \ , \tag{9}$$

after some more elementary manipulations, takes (8) to

$$\zeta(1 - \zeta)\frac{d^2W}{d\zeta^2} + (1 - \zeta)(2k\delta + 1)\frac{dW}{d\zeta} + W = 0 \ . \tag{10}$$

The special form of this equation that applies to the case of strictly two-dimensional flow (*i.e.* with $\beta = 0$) appears as equation (5.31) on page 92 of the paper by CHIARULLI & FREEMAN (1948) and as equation (2.6) on page 717 of HUGHES & REID (1965). The present version of the equation allows for nonparallelism between the wavenumber vector (α, β) and the velocity vector of the undisturbed flow. The differential equation satisfied by the GAUSS hypergeometric function $u = F(p, q, r; \zeta)$ is

$$\zeta(1 - \zeta)\frac{d^2u}{d\zeta^2} + [r - (p + q + 1)\zeta]\frac{du}{d\zeta} - pq\,u = 0 \ , \tag{11}$$

in which (p, q, r) are parameters. The correspondence between (10) and (11) is exact if one assigns the following values to these parameters:

$$p = k\delta + \sqrt{(k\delta)^2 + 1} \quad , \quad q = k\delta - \sqrt{(k\delta)^2 + 1}, \qquad r = 2k\delta + 1 \ . \tag{12}$$

From (6), (9), and some elementary manipulations, one may derive the identity

$$\exp(-kz) = \left(\frac{\alpha U_\infty - \omega}{\alpha U_\infty}\zeta\right)^{k\delta} \tag{13}$$

It follows that the definition $\tilde{w} \equiv \exp(-kz)W$ is equivalent to

$$\tilde{w} = \left(\frac{\alpha U_\infty - \omega}{\alpha U_\infty}\right)^{k\delta} \zeta^{k\delta}W \ . \tag{14}$$

According to the standard theory of the GAUSS hypergeometric equation (11), if the parameter r is not equal to an integer, then the two functions

$$u_1 = F(p, q, r; \zeta) \tag{15}$$

$$u_2 = \zeta^{1-r}F(p - r + 1, q - r + 1, 2 - r; \zeta) \tag{16}$$

form a linearly independent pair of solutions of (11) in the neighborhood of the singular point $\zeta = 0$. The solutions u_1 and u_2 belong to the indicial exponents 0 and $1 - r$, respectively. If p, q, r are replaced by the values given in (12) and if $2k\delta$ is not equal to an integer, then the corresponding forms of u_1 and u_2 represent a linearly independent pair of solutions of (10) for W. It follows from the definition (14) that one may represent the general solution of (8) by

$$\tilde{w} = A\zeta^{k\delta}F(k\delta + \sqrt{(k\delta)^2 + 1}, k\delta - \sqrt{(k\delta)^2 + 1}, 2k\delta + 1; \zeta)$$

$$+ B\zeta^{-k\delta}F(-k\delta + \sqrt{(k\delta)^2 + 1}, -k\delta - \sqrt{(k\delta)^2 + 1}, -2k\delta + 1; \zeta) \quad (17)$$

in which A and B are arbitrary constants. If $\Re\{k\} > 0$, then $\zeta^{k\delta} \to 0$ and $\zeta^{-k\delta} \to \infty$ as $\zeta \to 0$. The GAUSS hypergeometric series, moreover, equals unity at the origin. It follows that the right member of (17) becomes unbounded at the origin unless $B = 0$. If one recalls that the origin in the ζ-plane represents the remote free stream and imposes the boundary condition that $\tilde{w}$ remains bounded there, one concludes that the most general representation of $\tilde{w}$ consistent with these requirements is

$$\tilde{w} = A\zeta^{k\delta}F(k\delta + \sqrt{(k\delta)^2 + 1}, k\delta - \sqrt{(k\delta)^2 + 1}, 2k\delta + 1; \zeta) . \quad (18)$$

One may restore the original dependent variable z in the above result by repeated use of (13) to obtain

$$w = \tilde{A}e^{-kz}F\left((k\delta + \sqrt{(k\delta)^2 + 1}, k\delta - \sqrt{(k\delta)^2 + 1},\right.$$

$$\left. 2k\delta + 1; \frac{\alpha U_\infty e^{-z/\delta}}{\alpha U_\infty - \omega}\right), \quad (19)$$

in which $\tilde{A}$ is another arbitrary constant.

Inspection of (9) shows that the point $\zeta = 1$ corresponds to the critical point where $\alpha U - \omega = 0$. The GAUSS hypergeometric equation (11) has a regular singular point at $\zeta = 1$ and the indical exponents belonging to it are zero and $r - p - q$. According to the transformation of parameters (12), the corresponding indicial exponents of (10) belonging to the singular point $\zeta = 1$ are zero and one. The fact that these indicial exponents differ by an integer indicates there may be a logarithmic branch point in the solution $\tilde{w}$ there, and such a branch point does indeed occur. The problem of applying the solution (18) to instability problems reduces to the problem of finding the proper analytic continuations of the hypergeometric function appearing in the right member of (19) beyond the disk of convergence of the GAUSS hypergeometric series (*i.e.* the disk of radius unity centered on the origin in the ζ-plane). CHIARULLI & FREEMAN (1948) seem to be the first authors to have addressed this problem. HUGHES & REID (1965) present the details of these analytic continuations as well as some corrections to the original work.

This solution is the simplest exact solution of the RAYLEIGH equation for a smooth mean velocity profile. Since the mean profile lacks an inflection point, it cannot represent a temporally unstable flow. Now the proof of the RAYLEIGH inflection-point theorem presumes that the wavenumber components are real valued. The RAYLEIGH inflection point theorem as such does not, therefore, rule out instabilities of spatial type or of a type that involves complex values of both the wavenumber components and the frequency. A question that future investigators may wish to address is whether *superpositions* of solutions of the type (19), in which some or all of the parameters (α, β, ω) may be complex, may represent a *wave packet* disturbance in boundary-layer geometry. A disturbance in the form of a FOURIER integral may satisfy evanescent boundary conditions with respect to the propagation-space variables even if the individual FOURIER components that contribute to the integral do not. I know of no *a-priori* reason to exclude the possibility that such a wave packet may exhibit exponential amplification (when viewed, say, by an observer moving with the wave group) even if the mean velocity profile lacks an inflection point.

3.4. RAYLEIGH EQUATION WITH SINUSOIDAL MEAN VELOCITY PROFILE; FIRST APPEARANCE OF HEUN'S EQUATION

Suppose that the veocity components $U(z), V(z)$ of the undisturbed flow are of the form

$$U(z) = (U_0/2)[1 + \sin(z/l)], \qquad V(z) = 0 \tag{20}$$

in which U_0 and l are constants with the dimensions of velocity and length, respectively. Then the form (7) of the RAYLEIGH equation is applicable, and one may rewrite it in the familiar form

$$\frac{d^2\tilde{w}}{dz^2} - k^2\tilde{w} - \frac{1}{U(z) - c}\frac{d^2U}{dz^2}\tilde{w} = 0 , \tag{21}$$

in which $c \equiv \omega/\alpha$. It follows from (20) that

$$\frac{l}{U_0}\frac{dU}{dz} = \pm\frac{1}{l}\left(\frac{U}{U_0}\right)^{1/2}\left(1 - \frac{U}{U_0}\right)^{1/2} . \tag{22}$$

If one introduces the nondimensional variables $\tilde{U}, \tilde{c}, \tilde{z}, \tilde{k}$ defined by

$$\tilde{u} \equiv U/U_0 \quad , \quad \tilde{c} \equiv c/U_0 \quad , \quad \tilde{z} \equiv z/l \quad , \quad \tilde{k} \equiv kl \tag{23}$$

then (21) and (22) become

$$\frac{d^2\tilde{w}}{d\tilde{z}^2} - \tilde{k}^2\tilde{w} - \frac{1}{\tilde{U}(z) - \tilde{c}}\frac{d^2\tilde{U}}{d\tilde{z}^2}\tilde{w} = 0 , \tag{24}$$

and

$$\frac{d\tilde{U}}{d\tilde{z}} = \pm\tilde{U}^{1/2}(1 - \tilde{U})^{1/2} \,, \tag{25}$$

respectively. If one transforms (24) by means of the change of independent variable $\tilde{z} \rightarrow \tilde{U}$, it becomes, after elementary manipulations,

$$\frac{d^2\tilde{w}}{d\tilde{U}^2} + \left(\frac{1/2}{\tilde{U}} + \frac{1/2}{\tilde{U} - 1}\right)\frac{d\tilde{w}}{d\tilde{U}} + \frac{-(1 - \tilde{k}^2)\tilde{U} + (-\tilde{k}^2\tilde{c} + 1/2)}{\tilde{U}(\tilde{U} - 1)(\tilde{U} - \tilde{c})}\tilde{w} = 0. \tag{26}$$

The differential equation

$$\frac{d^2Y}{d\tilde{z}^2} + \left(\frac{\gamma}{\tilde{z}} + \frac{\delta}{\tilde{z} - 1} + \frac{\epsilon}{\tilde{z} - a}\right)\frac{dY}{d\tilde{z}} + \frac{\sigma\tau(\tilde{z} - q)}{\tilde{z}(\tilde{z} - 1)(\tilde{z} - a}\,Y = 0 \tag{27}$$

in which the parameters $\gamma, \delta, \epsilon, \sigma, \tau, a$ are subject to the constraint

$$\gamma + \delta + \epsilon = \sigma + \tau + 1 \tag{28}$$

but are otherwise arbitrary was studied by HEUN (1889a, p165).

   Equation (26) is a special case of (27) under the following correspondence of parameters:

$$\gamma = 1/2, \qquad \delta = 1/2, \qquad \epsilon = 0, \qquad a = \tilde{c},$$
$$\sigma = -\tau = (1 - \tilde{k}^2)^{1/2}, \qquad \sigma\tau q = \tilde{k}^2\tilde{c} - 1/2. \tag{29}$$

3.5. Heun's series and solutions of Heun's equation

HEUN (1889b) furnished a solution of (27) that is regular at the origin whenever γ is neither zero nor a negative integer. HEUN's representation of this solution is

$$F(a, q; \sigma, \tau, \gamma, \delta; \tilde{z}) = 1 + \sigma\tau\sum_{n=1}^{\infty}\frac{G^{(n)}(q)}{n!\gamma(\gamma + 1)\ldots(\gamma + n - 1)}\left(\frac{\tilde{z}}{a}\right)^n \,, \tag{30}$$

in which

$$G^{(1)}(q) = q \quad , \quad G^{(2)}(q) = \sigma\tau q^2 + \{\sigma + \tau - \delta + 1 + (\gamma + \delta)a\}q - a\gamma, \tag{31}$$

and for $n \in \{1, 2, 3, \ldots\}$,

$$G^{(n+1)}(q) = \{n[\sigma + \tau - \delta + n + (\gamma + \delta + n - 1)a] + \sigma\tau q\}G^{(n)}(q)$$
$$- (\sigma + n - 1)(\tau + n - 1)(\gamma + n - 1)naG^{(n-1)}(q) \tag{32}$$

[cf. HEUN (1889b, p181)]. HEUN (1889a, p165) points out that

For $a = 1$ and $q = 1 \ldots$ equation (27)...degenerates to the differential equation for the GAUSS hypergeometric function $F(\sigma, \tau, \gamma; \tilde{z})$. Alternatively, for $a = 0$, $q = 0$ it degenerates to [a differential equation satisfied by the GAUSS hypergeometric function $F(\sigma, \tau, \sigma + \tau - \delta + 1; \tilde{z})$].

Equation [(27)] may therefore be considered as a generalization of the hypergeometric differential equation.

There are many other features HEUN'S equation shares with the GAUSS hypergeometric equation. One feature is that, for each pair of indicial exponents belonging to one of the singularities of the differential equation in the finite plane of the independent variable, at least one member of that pair equals zero. Another feature is that three of the singular points are at standard locations, namely $\tilde{z} = 0$, $\tilde{z} = 1$, and $\tilde{z} = \infty$ (the fourth singular point of HEUN'S equation is at an arbitrary location). A third feature is that all of the singular points of the differential equation in the extended complex plane are regular-singular. A fourth feature is that there are numerous changes of variable (twenty-four in the case of the GAUSS hypergeometric equation and one hundred ninety-two in the case of HEUN'S equation) that take the differential equation with one set of parameters to the same differential equation but with a different set of parameters.

The usual normalization for the GAUSS hypergeometric function $F(A, B, C; z)$, taken as a function of the parameter C, has a simple pole at each of the negative integers. OLVER (1974, p 159) notes that function

$$\mathbf{F}(A, B, C; z) \equiv F(A, B, C; z)/\Gamma(A) \tag{33}$$

has no poles in the variable C and is thus more convenient in some situations. In the same spirit, one may introduce an OLVER-style modification of HEUN'S series defined by

$$Y_1 \equiv \mathbf{F}(a, q; \sigma, \tau, \gamma, \delta; \tilde{z}) \equiv \frac{F(a, q; \sigma, \tau, \gamma, \delta; \tilde{z})}{\Gamma(\gamma)}$$

$$\frac{1}{\Gamma(\gamma)} + \sigma\tau \sum_{n=1}^{\infty} \frac{G^{(n)}(q)}{n!\Gamma(\gamma + n)} \left(\frac{\tilde{z}}{-}\right)^n . \tag{34}$$

Since this renormalization amounts to multiplication by an overall constant, it does not affect the system of recursion relations (31) and (32). The function defined by the rightmost member of (34), unlike (30), has no poles with respect to the variable γ.

Now the indicial exponents of (27) belonging to the singular point $\tilde{z} = 0$ are zero and $1 - \gamma$. As one might expect, the change of dependent variable $Y \to Z$ defined by

$$Y = \tilde{z}^{1-\gamma} Z \tag{35}$$

takes HEUN'S equation (27) for Y to another form of HEUN'S equation for Z but with different values of the parameters. Such considerations lead to another putative solution of (27) of the form

$$Y_2 \equiv \tilde{z}^{1-\gamma} \mathbf{F}(a, q'; 1 - \gamma + \sigma, 1 - \gamma + \tau, 2 - \gamma, \delta; \tilde{z}) \tag{36}$$

in which

$$q' \equiv \frac{(\delta a + \epsilon)(1 - \gamma) + q}{(1 - \gamma + \sigma)(1 - \gamma + \tau)} .$$ (37)

The pair of solutions (Y_1, Y_2) of HEUN'S equation defined above are natural generalizations of the pair of solutions (u_1, u_2) of the GAUSS hypergeometric equation introduced in (15) and (16) above.

According to a well known identity due to ABEL, the logarithmic derivative of the WRONSKIAN of any two solutions of a second order linear homogeneous ordinary differential equation is determined in terms of the coefficients of that equation, and so the WRONSKIAN is known to within an arbitrary constant. If, as here, the two solutions are expressed in terms of infinite series in the neighborhood of a regular singular point, one may determine the constant in ABEL'S formula for the WRONSKIAN from the leading terms of those series. From considerations of this type, one may show that the WRONSKIAN of the solutions Y_1 and Y_2 above is given by

$$Y_1 \frac{dY_2}{d\tilde{z}} - Y_2 \frac{dY_1}{d\tilde{z}} = \frac{\sin[\pi(1 - \gamma)]a^\epsilon}{\pi \tilde{z}^\gamma (1 - \tilde{z})^\delta (a - \tilde{z})^\epsilon}$$ (38)

in which

$$\epsilon = \sigma + \tau + 1 - \gamma - \delta$$ (39)

by virtue of (28). This WRONSKIAN vanishes when γ equals an integer. Since the indicial exponents of (27) belonging to the singular point $\tilde{z} = 0$ are zero and $1 - \gamma$, one concludes that Y_1 and Y_2 lose their linear independence when the indicial exponents belonging to the singular point at the origin differ by an integer.

In the event that the indicial exponents belonging to the singular point at the origin differ by a nonzero integer, the solutions Y_1 and Y_2 are still nontrivial and well behaved. It so happens is that as γ approaches an integer, the coefficients of the leading terms of the solution belonging to the lesser of the two indicial exponents vanish and the exponent (of the variable $\tilde{z}$) in the lowest order surviving term equals the *higher* of the indicial exponents. Now in HEUN'S equation one of those indicial exponents is zero. It follows that the higher of the two indicial exponents belonging to the singular point at the origin is never less that zero. It then follows that if γ equals an integer, both Y_1 and Y_2 are regular at the origin.

If, for brevity, one writes $Y_1(\tilde{z})$ and $Y_2(\tilde{z})$ in place of full expressions in the right members of (34) and (36), then the expression

$$Y_2(0)Y_1(\tilde{z}) - Y_1(0)Y_2(\tilde{z})$$ (40)

must tend to zero as γ tends to an integer n. The following limit therefore generates a third solution of HEUN'S equation:

$$N(\tilde{z}) \equiv \lim_{\gamma \to n} \left\{ \frac{Y_2(0)Y_1(\tilde{z}) - Y_1(0)Y_2(\tilde{z})}{\gamma - n} \right.$$

$$= \lim_{\gamma \to n} \left\{ \frac{d}{d\gamma} \left(Y_2(0)Y_1(\tilde{z}) - Y_1(0)Y_2(\tilde{z}) \right) \right\} . \tag{41}$$

Since Y_2 contains a factor $\tilde{z}^{1-\gamma}$, its γ-derivative will contain the factor $\ln(\tilde{z})$.

Now a change of independent variable $\tilde{z} \to \xi$ defined by either $\xi \equiv \tilde{z} - 1$ or $\xi \equiv (\tilde{z} - a)/(-a)$ takes HEUN'S equation with one set of parameters to HEUN'S equation with another set of parameters. If one writes down a fundamental pair of solutions of HEUN'S equation about the singular point at the origin in the ξ-plane and transforms back to the original variable $\tilde{z}$, one obtains a fundamental pair of solutions about either the singular point $\tilde{z} = 1$ or the singular point $\tilde{z} = a$, depending on which transformation $\tilde{z} \to \xi$ one started with.

At this point, I have given the broad outlines of a method for generating a linearly independent pair of solutions of HEUN'S equation in the circle of convergence centered on any one of its singularities in the finite plane. The circles of convergence of these various series solutions overlap with each other and one may construct the analytic continuation of any definite solution defined in one circle of convergence into any other circle of convergence with which it overlaps.

To support this assertion, let D_1 and D_2 be two overlapping disks in the $\tilde{z}$-plane and let ϕ_1 and ϕ_2 be a linearly independent pair of solutions of HEUN'S equation represented by FROBENIUS series convergent in D_2. Let Φ be a given solution of HEUN'S equation represented as a FROBENIUS series convergent in D_1. In the region of overlap $D_1 \cap D_2$ of D_1 and D_2, there must exist constants A and B such that

$$\Phi(\tilde{z}) = A\phi_1(\tilde{z}) + B\phi_2(\tilde{z}) . \tag{42}$$

If one diffentiates this equation with respect to $\tilde{z}$, one obtains

$$\Phi'(\tilde{z}) = A\phi_1'(\tilde{z}) + B\phi_2'(\tilde{z}) . \tag{43}$$

If one views the last two equations as simultaneous linear equations for the A and B, one finds, by CRAMER'S rule, that

$$A = \frac{W[\Phi(\tilde{z}), \phi_2(\tilde{z})]}{W[\phi_1(\tilde{z}), \phi_2(\tilde{z})]}, \qquad B = \frac{W[\phi_1(\tilde{z}), \Phi(\tilde{z})]}{W[\phi_1(\tilde{z}), \phi_2(\tilde{z})]} , \tag{44}$$

in which, for any two functions $f(\tilde{z})$ and $g(\tilde{z})$, the symbol $W[f(\tilde{z}), g(\tilde{z})]$ denoted their WRONSKIAN, defined by

$$W[f(\tilde{z}), g(\tilde{z})] \equiv f(\tilde{z})g'(\tilde{z}) - f'(\tilde{z})g(\tilde{z}) . \tag{45}$$

From ABEL'S formula already mentioned, we know that the WRONSKIAN is determined from the coefficients of the differential equation up to an overall multiplicative constant. It follows that the *ratio* of two WRONSKIANS is indeed constant, as the above derivation implies.

Once one calculates the coefficients A and B at a convenient point in $D_1 \cap D_2$, one may proceed to use the same values of A and B to *define* the continuation of

the right member—and hence the left member–of (42) throughout all of D_2. This representation then defines the continuation of Φ (which was originally defined only in the initial disk D_1) into the overlapping disk D_2. One may, of course, continue Φ from D_2 into another overlapping disk D_3, and so on *ad infinitum* until the domain of definition of the continuation of Φ covers the whole complex $\tilde{z}$-plane (punctured, of course, by the singular points of the differential equation).

One may thus assert that the general solution of HEUN'S equation and its analytical continuations are *known in principle*. Having made that assertion, one must concede that this general solution is by no means *as well known* as are the various solutions of the GAUSS hypergeometric equation. The lack of convenient representations of solutions of HEUN'S equation such as integral representations—or even an explicit formula for the nth term in the MACLAURIN series of its regular solution about the origin—is at once a discouraging feature of the present state of knowledge in the theory of transcendental functions and a challenge to future investigators.

There is a great deal more one may write about the solutions of HEUN'S equation. Instead of writing it here, however, I will return to the subject of identifying undisturbed flows for which one or another of the classical field equations of shear flow instability are reducible to HEUN'S equation under a suitable change of variable.

3.6. RAYEIGH EQUATION WITH HYPERBOLIC TANGENT MEAN VELOCITY PROFILE

Consider the case in which

$$U(z) = \frac{U_0}{2}\left[1 + \tanh\left(\frac{z}{2l}\right)\right]. \tag{46}$$

If one writes (46) in terms of nondimensional variables as defined in (23) above, one obtains

$$\tilde{U} = (1/2)[1 + \tanh(\tilde{z}/2)] \tag{47}$$

from which it follows that

$$\frac{d\tilde{U}}{d\tilde{z}} = \tilde{U}(1 - \tilde{U}). \tag{48}$$

The change of dependent variable $\tilde{w} \to \tilde{W}$ defined by $\tilde{w} \equiv e^{-\tilde{k}\tilde{z}}\tilde{W}$ takes (24) to

$$\frac{d^2\tilde{W}}{d\tilde{z}^2} - 2\tilde{k}\frac{d\tilde{W}}{d\tilde{z}} - \frac{1}{\tilde{U} - \tilde{c}}\frac{d^2\tilde{U}}{d\tilde{z}^2}\tilde{W} \tag{49}$$

after some elementary manipulations. The change of independent variable $\tilde{z} \to \tilde{U}$, moreover, takes (49) to

$$\frac{d^2\tilde{W}}{d\tilde{U}^2} + \left(\frac{1 - 2\tilde{k}}{\tilde{U}} + \frac{1 + 2\tilde{k}}{\tilde{U} - 1}\right)\frac{d\tilde{W}}{d\tilde{U}} + \frac{(-2)\tilde{U} + 1}{\tilde{U}(\tilde{U} - 1)(\tilde{U} - \tilde{c})}\tilde{W} \tag{50}$$

after some more elementary manipulations. Equation (50) is a special form of HEUN'S equation (27) with the following parameter correspondence

$$\gamma = 1 - 2\tilde{k}, \qquad \delta = 1 + 2\tilde{k}, \qquad \epsilon = 0, \qquad a = \tilde{c},$$
$$\sigma = 2, \qquad \tau = -1, \qquad \sigma\tau q = -1. \tag{51}$$

The observation that the RAYLEIGH equation with a hyperbolic tangent velocity profile may be transformed to HEUN'S equation by means of a simple change of variable is a special case of a result do to JOHN W. MILES (MILES, 1963). In that paper, MILES showed that the TAYLOR-GOLDSTEIN-HAURWITZ equation (4), in the special case when the nondimensional mean velocity profile and the logarithm of the nondimensional mean density profile are both proportional to the hyperbolic tangent of the cross stream coordinate, may be transformed to HEUN'S equation. I will return to the discussion of this paper below. Suffice it to say, that this paper by MILES is the only one in the theory of shear flow instability that mentions HEUN'S equation in any context whatever.

3.7. RAYLEIGH EQUATION FOR THE BICKLEY JET

Consider the case in which

$$\frac{U(z)}{U_0} = \text{sech}^2 \left(\frac{z}{2l} \right) \tag{52}$$

If one writes (52) in terms of nondimensional variables as defined in (23), one obtains

$$\tilde{U} = \text{sech}^2(\tilde{z}/2) , \tag{53}$$

from which it follows that

$$\frac{d\tilde{U}}{d\tilde{z}} = \pm\tilde{U}(1 - \tilde{U})^{1/2} . \tag{54}$$

The change of independent variable $\tilde{z} \quad \tilde{U}$ with $d\tilde{U}/d\tilde{z}$ as given by (54) takes (24) to

$$\frac{d^2\tilde{w}}{d\tilde{U}^2} - \left(-\frac{1}{\tilde{U}} - \frac{1/2}{\tilde{U} - 1} \right) \frac{d\tilde{w}}{d\tilde{U}} \quad \frac{\tilde{k}^2}{\tilde{U}^2(1 - \tilde{U})}\tilde{w}$$
$$+ \left(\frac{1}{\tilde{U} - \tilde{c}} \right) \left(-\frac{1}{\tilde{U}} - \frac{1/2}{\tilde{U} - 1} \right) \tilde{w} = 0 . \tag{55}$$

This is not HEUN'S equation since the coefficient of the $\tilde{w}$ has a double pole at $\tilde{U} = 0$. In HEUN'S equation, only single poles in that coefficient may occur. One finds, however, that the change of dependent variable $\tilde{w} \rightarrow M$ defined by

$\tilde{w} = \tilde{U}^{\tilde{k}} M$, takes (55) to

$$\frac{d^2 M}{d\tilde{U}^2} + \left(\frac{1 + 2\tilde{k}}{\tilde{U}} + \frac{1/2}{\tilde{U} - 1} \right) \frac{dM}{dU}$$

$$+ \frac{(\tilde{k}^2 + \tilde{k}/2 - 3/2)\tilde{U} + (1 - \tilde{c}\tilde{k}(\tilde{k} + 1/2))}{\tilde{U}(\tilde{U} - 1)(\tilde{U} - \tilde{c})} M = 0 \tag{56}$$

after some elementary manipulations.

Equation (56) is a special form of HEUN'S equation (27) with the following parameter correspondence

$$\gamma = 1 + 2\tilde{k}, \qquad \delta = 1/2, \qquad \epsilon = 0, \qquad a = \tilde{c},$$

$$\sigma = \tilde{k} - 1, \qquad \tau = \tilde{k} + 3/2, \qquad \sigma\tau q = \tilde{c}\tilde{k}(\tilde{k} + 1/2) - 1. \tag{57}$$

3.8. RAYLEIGH EQUATION FOR A SKEWED MEAN VELOCITY PROFILE WHOSE COMPONENTS VARY QUADRATICALLY WITH RESPECT TO THE VARIABLE $\zeta = e^{-\tilde{z}}$

Recall equation (2) and recall in particular the definitions $k^2 \equiv \alpha^2 + \beta^2$ and $kQ \equiv \alpha U + \beta V$. Consider now a skewed mean velocity distribution whose velocity components are of the following form:

$$U(z) = U_0 + U_1 \exp(-z/l) + U_2 \exp(-2z/l)$$
$$V(z) = V_0 + V_1 \exp(-z/l) + V_2 \exp(-2z/l), \tag{58}$$

in which $U_0, U_1, U_2, V_0, V_1, V_2$ are constants with the dimensions of velocity.

If one introduces the definitions

$$kQ_0 \equiv \alpha U_0 + \beta V_0, \qquad kQ_1 \equiv \alpha U_1 + \beta V_1, \qquad kQ_2 \equiv \alpha U_2 + \beta V_2, \tag{59}$$

One concludes that

$$kQ = \alpha U + \beta V = kQ_0 + kQ_1 \exp(-z/l) + kQ_2 \exp(-2z/l). \tag{60}$$

The fluid speed in the remote free stream is $\sqrt{U_0^2 + V_0^2}$ in this flow. One is therefore led to introduce nondimensional variables defined as follows:

$$\tilde{z} \equiv z/l, \qquad \tilde{k} \equiv lk, \qquad \tilde{Q} \equiv \frac{Q}{\sqrt{U_0^2 + V_0^2}}, \qquad \tilde{\omega} \equiv \frac{l\omega}{\sqrt{U_0^2 + V_0^2}}. \tag{61}$$

The nondimensional form of (2) is therefore

$$[\tilde{k}\tilde{Q}(z) - \tilde{\omega}] \left(\frac{d^2\tilde{w}}{d\tilde{z}^2} - \tilde{k}^2\tilde{w} \right) - \tilde{k}\frac{d^2\tilde{Q}}{d\tilde{z}^2}\tilde{w} = 0. \tag{62}$$

If one divides by $\tilde{k}$ and introduces the definition

$$\tilde{c} \equiv \tilde{\omega}/\tilde{k} \tag{63}$$

equation (62) becomes

$$[\bar{Q}(z) - \bar{c}]\left(\frac{d^2\tilde{w}}{d\tilde{z}^2} - \bar{k}^2\tilde{w}\right) - \frac{d^2\bar{Q}}{d\tilde{z}^2}\tilde{w} = 0 \ . \tag{64}$$

The change of independent variable $\tilde{w} \rightarrow W$ defined by $\tilde{w} = e^{-\bar{k}\tilde{z}}W$ takes (64) to

$$[Q(\tilde{z}) - \bar{c}]\left(\frac{d^2W}{d\tilde{z}^2} - 2\bar{k}\frac{dW}{d\tilde{z}}\right) - \frac{d^2\bar{Q}}{d\tilde{z}^2}W = 0 \tag{65}$$

Let $\tilde{z} \rightarrow \zeta$ be the change of independent variable defined by $\zeta \equiv \exp(-\tilde{z})$. From (60), one concludes that $Q = Q_0 + Q_1\zeta + Q_2\zeta^2$ and one can always find constants ζ_{c1} and ζ_{c2} such that

$$\tilde{Q} - \bar{c} = \tilde{Q}_2(\zeta - \zeta_{c1})(\zeta - \zeta_{c2}) \ . \tag{66}$$

This change of independent variable takes (65) to

$$\frac{d^2W}{d\zeta^2} + \frac{2\bar{k} + 1}{\zeta}\frac{dW}{d\zeta} - \frac{(\tilde{Q}_1/\tilde{Q}_2) + 4\zeta}{\zeta(\zeta - \zeta_{c1})(\zeta - \zeta_{c2})}W = 0 \tag{67}$$

If one multiplies this equation by ζ_{c1}^2 and introduces the notation

$$\xi \equiv \zeta/\zeta_{c1}, \qquad \tilde{a} \equiv \zeta_{c2}/\zeta_{c1}, \qquad q'' \equiv \tilde{Q}_1/(\tilde{Q}_2\zeta_{c1}) \ , \tag{68}$$

one obtains

$$\frac{d^2W}{d\xi^2} + \frac{2\bar{k} + 1}{\xi}\frac{dW}{d\xi} + \frac{-4\xi - q''}{\xi(\xi - 1)(\xi - \tilde{a})}W = 0 \tag{69}$$

Equation (69) is a special form of HEUN'S equation (27) with the following parameter correspondence

$$\gamma = 2\bar{k} + 1, \qquad \delta = \epsilon = 0, \qquad a = \tilde{a}$$
$$\sigma = \bar{k} + \sqrt{\bar{k}^2 + 4}, \qquad \tau = \bar{k} - \sqrt{\bar{k}^2 + 4}, \qquad \sigma\tau q = q''. \tag{70}$$

STUART (1954) has modified KÁRMÁN'S well known formulation of the self similar boundary layer on a rotating disk to include the case of uniform suction through the disk. In one limit, namly the limit of large suction, STUART was able to solve the equations analytically and found that the velocity components in the directions parallel to the plate surface have a functional form that is a special case of (58) above, cf. STUART (1954, equations (3.3) and (3.4)). STUART (see GREGORY, STUART, & WALKER 1955, especially p. 187) considered the RAYLEIGH problem for this special velocity profile and found an exact represention (in terms of elementary functions) of the disturbance due to a regular neutral mode.

WEN-CHIN CHEN (1991) has computed dispersion curves for the solutions of the RAYLEIGH stability problem discussed in this subsection, including the effects of skewness of the mean velocity profile.

3.9. KUO EQUATION FOR THE HYPERBOLIC-TANGENT VELOCITY PROFILE

If the mean velocity distribution is of the hyperbolic tangent type as in (46), one may transform the KUO equation (5) to HEUN'S equation (27) as follows. Let $\tilde{U}$, $\tilde{c}$, $\tilde{\alpha}$, and $\hat{\beta}$ be nondimensional variables defined by

$$\tilde{U} \equiv U/U_0, \qquad \tilde{c} \equiv c/U_0, \qquad \tilde{z} \equiv z/l, \qquad \tilde{\alpha} \equiv \alpha l, \qquad \hat{\beta} \equiv \bar{\beta} l^2 / U_0 , \quad (71)$$

in which the parameter $\bar{\beta}$ was introduced in the paragraph containing equation (5) and the dimensional scales U_0 and l are the same as in equation (46). In terms of these nondimensional variables, the KUO equation becomes

$$[\tilde{U}(\tilde{z}) - \tilde{c}] \left(\frac{d^2\varphi}{d\tilde{z}^2} - \tilde{\alpha}^2 \varphi \right) - \left(\frac{d^2\tilde{U}}{d\tilde{z}^2} - \hat{\beta} \right) \varphi = 0 \qquad (72)$$

and the mean velocity distribution has the form (47). The change of independent variable $\tilde{z} \to \tilde{U}$ defined by (47) takes (72) to

$$\frac{d^2\varphi}{d\tilde{U}^2} + \left(\frac{1}{\tilde{U}} + \frac{1}{\tilde{U} - 1} \right) \frac{d\varphi}{d\tilde{U}} - \frac{\tilde{\alpha}^2}{\tilde{U}^2(\tilde{U} - 1)^2} \varphi$$
$$- \left\{ \frac{1}{\tilde{U} - \tilde{c}} \left(\frac{2\tilde{U} - 1}{\tilde{U}(\tilde{U} - 1)} \right) - \frac{\hat{\beta}}{\tilde{U} - \tilde{c}} \left(\frac{1}{\tilde{U}^2(\tilde{U} - 1)^2} \right) \right\} \varphi = 0 \qquad (73)$$

after some elementary manipulations. This equation has four singular points, all regular, situated at $\tilde{u} = 0$, $\tilde{u} = 1$, $\tilde{u} = \tilde{c}$, and $\tilde{u} = \infty$. The indicial exponents belonging to the singular point at $\tilde{u} = 0$ are $\pm\delta_0$, in which

$$\delta_0 \equiv \sqrt{\tilde{\alpha}^2 + \frac{\hat{\beta}}{\tilde{c}}} , \qquad (74)$$

the indicial exponents belonging to the singular point at $\tilde{u} = 1$ are $\pm\delta_1$, in which

$$\delta_1 \equiv \sqrt{\tilde{\alpha}^2 - \frac{\hat{\beta}}{1 - \tilde{c}}} , \qquad (75)$$

the indicial exponents belonging to the singular point at $\tilde{u} = \tilde{c}$ are 0 and 1, and indicial exponents belonging to the singular point at $\tilde{u} = \infty$ are -1 and 2. In HEUN'S equation, there are three singular points in the finite plane and the pair of indicial exponents belonging to each of them includes the number zero as at least one of the exponents. Since the singular points of (73) at $\tilde{u} = 0$ and $\tilde{u} = 1$ have

nonzero values for their indicial exponents, one is led to the consider the change of dependent variable $\varphi \rightarrow \Phi$ defined by

$$\varphi = \tilde{U}^{\delta_0}(\tilde{U} - 1)^{\delta_1} \Phi \ . \tag{76}$$

The transformation (76) takes (73) to

$$\frac{d^2\Phi}{d\tilde{U}^2} + \left(\frac{1 + 2\delta_0}{\tilde{U}} + \frac{1 + 2\delta_1}{\tilde{U} - 1}\right)\frac{d\Phi}{d\tilde{U}} + \left\{\frac{A\tilde{U} - B}{\tilde{U}(\tilde{U} - 1)(\tilde{U} - \tilde{c})}\right\}\Phi = 0 \ , \tag{77}$$

in which

$$A \equiv 2\delta_0\delta_1 + \delta_0 + \delta_1 + 2\tilde{\alpha}^2 + \frac{\tilde{\beta}}{\tilde{c}} - \frac{\tilde{\beta}}{1 - \tilde{c}} - 2 \ , \tag{78}$$

$$B \equiv (2\delta_0\delta_1 + \delta_0 + \delta_1 + 2\tilde{\alpha}^2)\tilde{c} + \frac{\tilde{\beta}}{\tilde{c}} - 1 + 2\hat{\beta} \ , \tag{79}$$

after a lengthy but straightforward calculation. Of course, equation (77) has the structure of HEUN'S equation (27). The foregoing derivation demonstrates that the KUO equation may be transformed to HEUN'S equation when the mean velocity profile is of hyperbolic-tangent type.

Experience with this example and others leads one to expect that the KUO equation, like the RAYLEIGH equation, is transformable to HEUN'S equation in the other standard cases, namely the case when the mean velocity profile has the form of a sine wave and the case when the mean velocity profile has the form of the square of a hyperbolic secant.

KUO (1973) presents a general review of the dynamics of quasigeostrophic flows and instability theory. Section VII of that work presents solutions of the KUO equation in the case when the mean velocity profile is of the form of a sine wave, the square of a hyperbolic secant, and a hyperbolic tangent. For all three profiles, there are neutrally stable solutions whose forms are expressible analytically. In the case of amplified waves, KUO reports results obtained by numerical solution of the differential equation. There is no indication that the differential equation may be transformed to HEUN'S equation or to any other canonical equation whose solutions are expressible analytically for arbitrary complex values of the parameters.

3.10. THE TAYLOR-GOLDSTEIN-HAURWITZ EQUATION FOR THE HYPERBOLIC-TANGENT VELOCITY PROFILE

Most authors who study the TAYLOR-GOLDSTIEN-HAURWITZ problem apply an approximation to it, which MILES (1963) summarizes as the neglect of 'the inertial effects of density stratification' This approximation allows one to move the mean density term $\bar{\rho}$ outside the derivative sign in the first term in the left member of (4) even while one keeps the bouyancy term in that equation. The resulting field equation is what most authors call the TAYLOR-GOLDSTEIN equation. As I

mentioned previously, MILES showed that this abbreviated equation reduces to HEUN'S equation if the mean velocity profile and the logarithm of the nondimensional mean density profile are both proportional to the hyperbolic tangent of the nondimensional elevation.

3.11. OTHER MEAN FLOWS FOR WHICH ONE OR MORE OF THE CLASSICAL FIELD EQUATIONS REDUCE TO HEUN'S EQUATION

One may remark in passing that if the mean velocity and density distributions are of the form

$$Q(\tilde{z}) = Q_0 + Q_1 \exp(-\tilde{z}) + Q_2 \exp(-2\tilde{z}) \tag{80}$$

$$\rho(\tilde{z}) = \rho_0 \exp(-C\tilde{z}) \tag{81}$$

(in which C is an arbitrary positive constant), then one may transform the full TAYLOR-GOLDSTIEN-HAURWITZ equation (4) to HEUN'S equation by changes of variable similar to those introduced section 3.10 above.

There are at least two other forms of mean velocity profile for which the RAYLEIGH equation reduces to HEUN'S equation. They are: (i) the hyperbolic-cotangent velocity profile; and (ii) the hyperbolic-cosine velocity profile. Since these velocity profiles seem to be of less physical interest than those discussed in detail above, I will not discuss them further here.

3.12. RAYLEIGH EQUATION FOR THE PARABOLIC VELOCITY PROFILE

Another example of a mean velocity profile that takes the RAYLEIGH equation to a standard form is the parabolic mean velocity profile. This profile takes the RAYLEIGH equation to the *differential equation of spheroidal wave functions*, as I will now show. If one divides equation (3) by ρk and introduces the notation $c \equiv \omega/k$, one obtains

$$\frac{d}{dz}\left[(Q-c)^2 \frac{d}{dz}\left(\frac{w}{Q-c}\right)\right] - k^2(Q-c)w = 0 . \tag{82}$$

DRAZIN & HOWARD (1966, p 18) point out that the change of dependent variable $w \to G$ defined by $G \equiv (Q-c)^{-1/2}w$ takes (82) to

$$\frac{d}{dz}\left[(Q-c)\frac{dG}{dz}\right] - \left(k^2(Q-c) + \frac{1}{2}\frac{d^2Q}{dz^2} + \frac{1}{4}\frac{(dQ/dz)^2}{Q-c}\right)G = 0 . \tag{83}$$

after some elementary manipulations. If the velocity profile $z \to Q(z)$ is of the form

$$Q = Q_M + \frac{Q''}{2}z^2 , \tag{84}$$

in which $Q'' < 0$ is a constant, then one can interpret Q_M as the maximum mean velocity in the flow. Let z_c be one of the two values of z at which $Q(z) - c$ vanishes. Then (84) takes the form

$$c = Q_M + \frac{Q''}{2} z_c^2 \tag{85}$$

at $z = c$. If one subtracts (85) from (84), one obtains

$$Q - c = \frac{Q''}{2}(z^2 - z_c^2) . \tag{86}$$

If one substitutes this identity into (83), one obtains

$$\frac{d}{dz}\left[\frac{Q''}{2}(z^2 - z_c^2)\frac{dG}{dz}\right]$$
$$- \left(k^2\frac{Q''}{2}(z^2 - z_c^2) + \frac{Q''}{2} + \frac{1}{4}\frac{(Q'')^2 z^2}{(Q''/2)(z^2 - z_c^2)}\right) G = 0 . \tag{87}$$

If one multiplies through by $-2/Q''$ and introduces the nondimensional independent variable $\eta \equiv z/z_c$, one obtains

$$-\frac{d}{d\eta}\left[(\eta^2 - 1)\frac{dG}{d\eta}\right] + \left((kz_c)^2(\eta^2 - 1) + 1 + \frac{\eta^2}{\eta^2 - 1}\right) G = 0 . \tag{88}$$

Writing $\eta^2 = (\eta^2 - 1) + 1$ in the numerator of the last quotient and rearranging, one obtains

$$\frac{d}{d\eta}\left[(1 - \eta^2)\frac{dG}{d\eta}\right] + \left(2 - (kz_c)^2(1 - \eta^2) - \frac{1}{1 - \eta^2}\right) G = 0 . \tag{89}$$

If the HELMHOLTZ wave equation is written in prolate spheroidal coordinates (cf. MORSE & FESHBACH (1953, p. 1502)) and one seeks solutions by the method of separation of variables, then two of the three equations that arise are identical and have the structure of the equation

$$\frac{d}{d\eta}\left[(1 - \eta^2)\frac{dV}{d\eta}\right] + \left(\lambda + \delta^2(1 - \eta^2) - \frac{\mu^2}{1 - \eta^2}\right) V = 0 , \tag{90}$$

in which $(\lambda, \delta^2, \mu^2)$ are separation constants. Here, η represents either a *colatitude* or a *radial* coordinate, depending on the range of values of that variable. A full treatment of the mathematical theory of solutions of (90) is given in the treatise by MEIXNER & SCHÄFKE (1954) and a shorter version appears in MEIXNER'S contribution to FLÜGGE'S *Encyclopedia of Physics* (1956, pp 171–172 and pp 214–216). Of course, equation (89) is a special case of (90) corresponding to the parameter choice

$$\lambda = 2 \quad , \quad \delta^2 = -(kz_c)^2 \quad , \quad \mu^2 = 1 . \tag{91}$$

The differential equation of spheroidal wave functions has three singular points in the extended complex plane of the independent variable. The point at infinity is an irregular singular point and the points $\eta = \pm 1$ are regular-singular. One may, of course, construct solutions in the neighborhood of either one of the regular singular points by the method of FROBENIUS. This proccess yields a linearly independent pair of solutions in each of two overlapping disks, the centers of which are separated by a distance equal to their radii. Here, as elsewhere, the advantage of the FROBENIUS method is that each series has a recognizable leading term and the exponents of successive terms in the series are strictly increasing. In this respect the index of summation—which is also the power of the independent variable in a generic term in the series representation of the solution—extends to infinity *in only one direction*.

Starting with NIVEN (1881), most of the authors who construct solutions of the differential equation of spheroidal wave functions make use of the fact that (90) reduces to a form of the associated LEGENDRE differential equation

$$\frac{d}{d\eta}\left[(1 - \eta^2)\frac{dM}{d\eta}\right] + \left(\nu(\nu + 1) - \frac{\mu^2}{1 - \eta^2}\right)M = 0\,, \tag{92}$$

when the parameter δ is equal to zero. One may construct solutions of (90) by seeking expansions of STURM-LIOUVILLE type in which the associated LEGENDRE functions are the eigenfunctions in the expansion. There is a completeness and expansion theorem available for the the associated LEGENDRE functions and MEIXNER & SCHÄFKE prove it rigorously. The coefficients of the STURM-LIOUVILLE series one generates in this way satisfy a three-term recurrence relation, but, unlike the FROBENIUS series discussed earlier, the summation index in the STURM-LIOUVILLE expansions *extends to infinity in both directions*. The STURM-LIOUVILLE series converges in an annulus in the η-plane centered on the origin of inner radius equal to one and outer radius equal to infinity. One is, so to speak, seeking solutions in the neighborhood of the point at infinity and since that point is an irregular singular point, one can not construct indicial exponents (or their appropriate generalizations) directly from the coefficients of the differential equation as one could if the point at infinity were a regular singular point. The problem does, however, give rise to *characteristic exponents* which replace the indicial exponents and, like them, depend only on the parameters of the equation and not on the independent variable. One way of defining the characteristic exponents is to regard the three-term recurrence relation for the coefficients of the STURM-LIOUVILLE expansion as an infinite set of simultaneous homogeneous linear algebraic equations with a tridiagonal coefficient matrix. Nontrivial solutions for the coefficients of the STURM-LIOUVILLE expansion are then possible only if the HILL determinant of the infinite-dimensional coefficient matrix is zero. In the formulation of the problem, the characteristic exponents appear as parameters in the three-term recurrence relation for the coefficients of the STURM-LIOUVILLE expansion, so the condition

for the vanishing of the HILL determinant associated with that recurrence relation amounts to an *eigenvalue condition* for the characteristic exponents.

There is another standard method for formulating the eigenvalue problem for the characteristic exponents, namely the *continued fraction method*. In that approach, one rewrites the three-term recurrence relation for the coefficients of the STURM-LIOUVILLE expansion as a two-term recurrence relation for the *ratio* of successive coefficients. One may write the solution of such a two-term recurrence relation as an infinite continued fraction in either of two ways, one of which involves increasing and the other decreasing the index of the coefficients of the original STURM-LIOUVILLE expansion. By calculating the ratio of any two consecutive terms in the STURM-LIOUVILLE series in each of these two ways and equating the results, one obtains a transcendental equation—or eigenvalue condition—for the characteristic exponents. I refer the reader to the primary sources for further details.

4. A remark on regular neutral modes

The focus of this survey, as I have already noted, is on solutions of one or another of the field equations of inviscid shear flow instability theory which hold for arbitrary complex values of the parameters. Several of these solutions are expressible in terms of solutions of HEUN'S equation. Of the four of these discussed in detail above, there are well known regular-neutral-mode solutions. Thus, for the RAYLEIGH equation with sinusoidal mean profile, TOLLMIEN (1935) found a regular neutral mode. Regular neutral modes for the hyperbolic tangent velocity profile and for the BICKLEY jet are described in DRAZIN & HOWARD (1966). Finally, STUART (1955) found a regular neutral mode for the velocity profile in the form of a quadratic function of $\zeta \equiv \exp(-\hat{z})$. In all these cases, it appears that the HEUN series (or related series generated by expanding solutions of HEUN'S equation) terminates after a single term.

Acknowledgement

References

Chen, Wen-Chin, Solution of the Rayleigh stability problem for a skewed mean velocity profile whose horizontal velocity components are quadratic in the variable $\eta = \exp(-z)$. Thesis submitted for the Master of Science degree, Department of Mechanical and Aerospace Engineering, Florida Institute of Technology, Spring (1991).

Chiarulli, P. and Freeman, J.C. (under the supervision of C.C. LIN), Stability of the boundary layer. Technical Report No. F-TR-1197-IA (GDAM A-9-M VI). Headquarters Air Materiel Command, Wright-Patterson Air Force Base, Dayton, Ohio (1948).

Drazin, P.G. and Howard, L.N., Hydrodynamic stability of parallel flow of inviscid fluid. *Advances in Applied Mechanics* 9 (1966) 1–89.

Goldstein, S., On the stability of superposed streams of fluids of different densities. *Proc. Roy. Soc. (Lond.) A* 132 (1931) 424–548.

Gregory, N., Stuart, J.T., and Walker, W.S., On the stability of three-dimensional boundary layers with application to the flow due to a rotating disk. *Phil. Trans. Roy. Soc. (Lond.) A* 248 (1955) 155–199.

Haurwitz, Bernard, Zur Theorie der Wellenbewegungen in Luft und Wasser. *Veröffentlichungen des Geophysikalischen Instituts der Universität Leipzig.* (herausgegeben von L. Weickmann). Zweite Serie: Spezialarbeiten aus dem Geophysikalischen Institut. 5(1), (i+106 ss) (1931).

Heun, Karl, Zur Theorie der Riemann'schen Funktionen zweiter Ordnung mit vier Verzweigungspunkten. *Mathematische Annalen* 33 (1889a) 161–179.

Heun, Karl, Beiträge zur Theorie der Lame'schen Funktionen. *Mathematische Annalen* 33 (1889b) 180–196.

Hughes, T.H. and Reid, W.H., On the stability of the asymptotic suction boundary layer. *The Journal of Fluid Mechanics* 23 (1965) 715–735.

Kuo, Hsiao-Lan, Dynamic instability of two-dimensional nondivergent flow in a barotropic atmosphere. *Journal of Meteorology* 6 (1949) 105–122.

Kuo, Hsiao-Lan, Dynamics of quasigeostrophic flows and instability theory. *Advances in Applied Mechanics* 13 (1973) 247–330.

Meixner, J., Spezielle Funktionen der mathematischen Physik. In *Encyclopedia of Physics.* 1 (1956) 117–217 (General editor S. Flügge).

Meixner, J. and Schäfke, F.W., *Mathieusche Funktionen und Sphäroidfunktionen. (Grudleheren der Mathematischen Wissenschaften in Einzeldarstellen.* Band 21, Springer-Verlag, Berlin (1954).

Miles, J.W., On the stability of heterogeneous shear flows. Part 2. *The Journal of Fluid Mechanics* 16 (1963) 209–227.

Morse, P.M. and Feshbach, H., *Methods of Theoretical Physics* (in two volumes), McGraw-Hill (1953).

Niven, C., On the conduction of heat in ellipsoids of revolution. *Phil. Trans. Roy. Soc. (A)* 171 (1881) 117–151.

Olver, F.W.J., *Asymptotics and Special Functions.* Academic Press (1974).

Rayleigh, Lord, On the stability, or instability, of certain fluid motions. *Proc. Lond. Math. Soc.* 11 (1880) 57–70. Also *Scientific Papers* 1 (1880) 474–487.

Stuart, J.T., On the effects of uniform suction on the steady flow due to a rotating disk. *Quarterly Journal of Mechanics and Applied Mechanics* 7 (1954) 446–457.

Taylor, G.I., Effect of variation in density on the stability of superposed streams of fluid. *Proc. Roy. Soc. (Lond.) A* 132 (1931) 499–523. Also *Scientific Papers* 2 (1931) 219–239. Cambridge University Press.

Tollmien, Walter, Über die Entstehung der Turbulenz. *Gesellschaft der Wissenschaft (Göttingen). Nachrichten. Mathematiche und Physische Klasse* (no volume number), ss 21–44. [Translated (by Dwight M. Miner as: The production of turbulence. *U.S. National Advisory Committee for Aeronautics,* Technical Memorandum TM-609, March 1931] (1929).

Tollmien, Walter, Ein allgemeines Kriterium der Instabilität laminarer Geschwindigkeitsverteilungen *Gesellschaft der Wissenschaft (Göttingen). Nachrichten. Mathematiche und Physische Klasse (Fachgruppe I),* Neue Folge 1, ss 79–114. [Translated (by J. Vanier) as: General instability criterion of laminar velocity distributions. *U.S. National Advisory Committee for Aeronautics. Technical Memorandum* TM-792, April 1936] (1935).

Yih, Chia-Shun, *Fluid Mechanics,* McGraw-Hill (1969).

On Rayleigh Instability in Decaying Plane Couette Flow

NILS TILLMARK and P. HENRIK ALFREDSSON
Department of Mechanics/Fluid physics, Royal Institute of Technology, S-100 44 Stockholm, Sweden

Abstract. The inflexion point criterion of Rayleigh is one of the most well-known results in hydro-dynamic stability theory but cannot easily be demonstrated experimentally in wall bounded flows. For plane Couette flow, where both walls move with equal speed in opposite directions, it is possible to establish a (time-dependent) inflectional velocity profile if both walls are brought momentarily to rest. If the Reynolds number is high enough a growing stationary instability develops. This situation is ideally suited for flow visualization of the instability. In this paper we show flow visualization experiments and stability calculations of the developing transverse roll cell instability in such a flow at low Reynolds numbers. Although the stability calculations are based on a quasi-stationary velocity profile, the measured and most amplified wave length obtained from the calculations are in excellent agreement.

1. Introduction

One of the first results in hydrodynamic stability theory was that of Rayleigh (1880) regarding the inviscid stability of inflectional velocity profiles. The effect of an inflexion point on the stability of boundary layer flows, is clearly observed in, e.g., adverse pressure gradient boundary layers. However, direct observations of such an instability in wall bounded flows in nature or in the laboratory are scarce. In this paper we show flow visualization results in a decaying plane Couette flow in which the inflectional instability is clearly observed.

Plane Couette flow may be viewed as a paradigm of wall bounded flows, conceptually one of the simplest non-trivial fluid dynamical systems. However, experimentally it turns out to be quite complicated to realize this flow and several different approaches have been taken to establish plane Couette flow. From the fluid dynamic point of view the best way is to use an apparatus with counter-moving walls. In such a set-up the net transport of fluid along the channel is zero and the fully developed state is only dependent on the diffusion of vorticity from the walls across the channel. This means that the pressure gradient can be zero along the full channel length (which is not the case with only one moving wall) and that the inlet regions at both ends of the channel are only a few channel widths.

The development of the velocity profile from rest towards the fully developed state, when the two walls are instantaneously brought from rest to the final velocity, can be calculated (see for instance Batchelor, 1967, p. 190 and Schlichting, 1979, p.
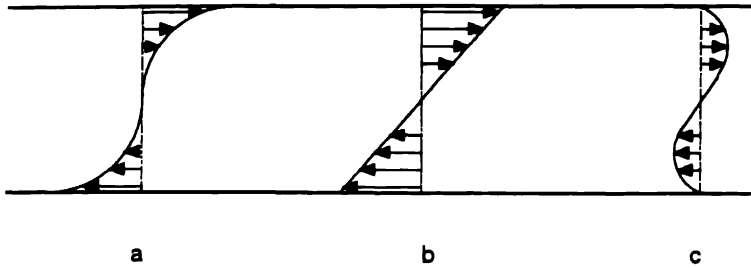
Fig. 1.   Velocity profiles in plane Couette flow. a) start up phase, b) fully developed flow, c) decaying flow

91). The velocity profile during this development is S-shaped and hence inflectional, but in this case the shear at the inflexion point is at a minimum and the Fjørtoft (1950) criterion for instability is not fulfilled (see Fig. 1a). However, these profiles may be susceptible to a viscous instability and this was investigated by Schlichting (1932). He indeed found that such an instability may develop, but only for high Reynolds numbers, $Re > 4800$ ($Re = hU_w/\nu$, where h is half the distance and U_w is half the the velocity difference between the walls).

The same class of solutions for the basic flow state can be used to analyse the developing flow set up by bringing the walls to rest instantaneously from the fully developed state (Fig. 1b), which we in the following will refer to as decaying Couette flow (Fig. 1c). For a system with two walls moving with equal speed but in opposite directions, a time-dependent inflectional velocity profile with maximum shear at the inflection point develops. This profile fulfils the Fjørtoft criterion and is hence susceptible to the Rayleigh instability mechanism. It is interesting to note that Rayleigh (1896, p. 389) investigated a piece-wise linear profile (consisting of three segments), resembling the decaying Couette profile and found that this profile was always unstable. Furthermore, we note that for the case of one moving and one stationary wall the instability conditions are not satisfied, when the moving wall is stopped.

In Section 2 we give the analysis for determining the velocity profile of decaying Couette flow, whereas Section 3 gives a description of the experimental set-up and results. In Section 4 we present linear stability results which are compared to the experiments.

2. Flow field development in decaying plane Couette flow

The velocity field associated with an impulsively started infinite plane wall bounding a semi-infinite domain of viscous fluid at rest is usually called "Stokes' first problem" and was solved more than one hundred years ago. For that case a similarity solution can be obtained, however for the case of two walls in relative motion the flow is not self-similar. In both cases the Navier-Stokes equation reduces to

$$\frac{\partial U}{\partial t} = \nu \frac{\partial^2 U}{\partial y^2} \tag{1}$$

where U is the velocity in the x-direction parallel to the walls, y is the coordinate normal to the walls and ν the kinematic viscosity. The boundary and initial conditions for a plane Couette flow with the walls moving in opposite directions, which are brought instantaneously to rest at $t = 0$ are

$$U = 0 \text{ at } y = \pm h \text{ for } t > 0$$

and

$$U = U_w \frac{y}{h} \text{ for } -h \le y \le h \text{ at } t = 0.$$

By introducing non-dimensional coordinates defined as $\xi = y/h$ and $\eta = \nu t/h^2$ and the non-dimensional velocity $u = U/U_w$, equation (1) becomes

$$\frac{\partial u}{\partial \eta} = \frac{\partial^2 u}{\partial \xi^2} \tag{2}$$

and the boundary and initial conditions reduce to

$$u = 0 \text{ at } \xi = \pm 1 \text{ for } \eta > 0. \tag{3a}$$

and

$$u = \xi \text{ for } -1 < \xi < 1 \text{ at } \eta = 0. \tag{3b}$$

The solution to the problem (2) and (3a,b) is given by

$$u = \frac{2}{\pi} \sum_{n=1}^{\infty} \frac{1}{n} \exp(-n^2\pi^2\eta) \sin n\pi(1-\xi), \quad -1 \le \xi \le 1, \quad \eta \ge 0.$$

The sum converges rapidly for η not too small. The evolution of the velocity profile is shown in Fig. 2. The non-dimensional time η runs from 0.001 to 0.3, covering the span from the almost linear profile to a flow where the maximum velocity is less than 5 % of the original wall velocity.

3. Experiments

3.1. EXPERIMENTAL APPARATUS AND PROCEDURE

The experiments were made in a flow apparatus previously used by us for studies of transition to turbulence in plane Couette flow (Tillmark & Alfredsson, 1992). A schematic of the design is shown in Fig. 3. The channel consisted of 2 vertical glass plates 1500 mm long, 400 mm high and 10 mm thick placed 10 mm apart,
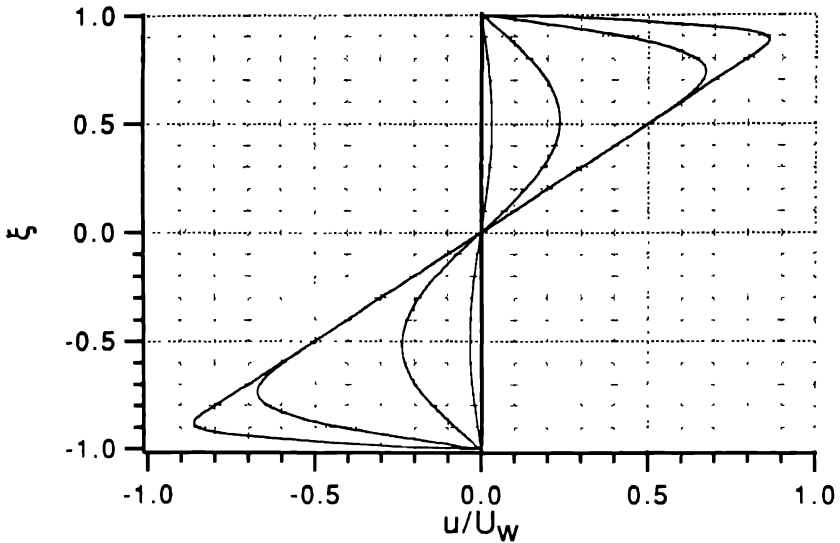
Fig 2   Velocity profiles of decaying plane Couette flow at $\eta = 0\,001, 0\,018, 0\,10, 0\,30$
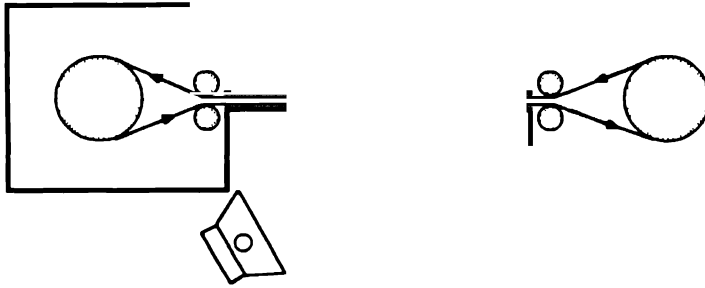
Fig 3   Experimental set-up

where the motion of the walls was accomplish by having a thin (0.1 mm thick, 360 mm wide) translucent plastic film, formed into a infinite belt, sliding along the inner glass surfaces of the channel. However it was also possible to change the configuration by letting half of the belt loop run outside of the narrow gap between the glass plates thus forming a plane Couette channel with a single moving wall. Outside each end of the channel the belt partly circumferenced a cylinder which positioned and drove the belt via friction. One of the cylinders was driven by a tachometer controlled DC motor.

The flow medium was water and to visualize the flow the fluid was seeded with small amounts of reflective flakes (Merck Irodin 120). The flakes were oriented by the flow and the reflected light clearly revealed changes from parallel flow. Two types of flow visualization were made. By viewing the xz-plane through

illumination of the channel with a slide projector from an angle of about 35° to the normal of the glass surfaces and taking photographs and video recordings of the flow normal to the surfaces an overall picture of the flow development was obtained. To get information about the internal structure of the instability a slit-light in the horizontal (xy) plane was applied and a series of photographs and video recordings were taken perpendicular to the illuminated plane through the upper, free water surface, side wall.

Ideally the experiment should start from a fully developed linear velocity profile. Due to disturbances that occur at the inlet regions of the channel turbulence is triggered and starts to move into the channel if the Reynolds number is above about 400. Therefore only a finite time can be used for the start up phase. Test runs in the channel gave an upper limit of about 8 seconds for the the start-up time period due to the disturbances that propagated into the channel from the inlets at the highest Reynolds numbers used. Using the same type of analysis as in section 2 it was possible to show that after 8 seconds, corresponding to a time equivalent to $\nu t/h^2 = 0.4$, the velocity profile deviated with at most 2% from the linear profile. Note that the development time is independent of Reynolds number.

3.2. RESULTS

In a series of preliminary experiments the stability of the start-up flow field both with single and double wall motion was visually checked in the Re interval from 500 to 1000 but as expected no traces of instabilities could be observed. The same result was found in the case of one moving and one stationary wall, when the moving wall was brought to an instant stop.

In the case of counter-moving walls which are brought to an instant stop a visually striking pattern was observed in the flow about two seconds after the stop ($\eta = 0.1$). The pattern was first seen as weak stationary bright and dark areas which developed into a periodic pattern of long, slightly wavy, spanwise stripes, gradually becoming irregular. Figure 4 shows the evolution of the instabilities at $Re = 700$ in a sequence of four pictures starting at $\eta = 0.1$ and at a time increment of $\Delta\eta = 0.015$. The pattern is not perfectly regular, a waviness as well as stripes that do not span the full channel width are observed.

If the belt motion was reversed to get opposite wall velocities the pattern after the stop had a somewhat different appearance. The distance between the stripes were the same but the bright and dark areas were changed slightly as the symmetry with respect to the illuminating light was changed.

In Fig. 5 a channel length of $20h$ is seen from above with the slit light approximately $3h$ below the free surface. The upper wall moved towards the left and lower towards the right before being stopped. The first picture was taken at $\eta = 0.092$ and the subsequent pictures were taken at an increment of $\Delta\eta = 0.008$. At the beginning only faint oblique dark lines in the central part of the flow are seen, which later became curved, more distinct and extended across the channel. At $\eta = 0.112$
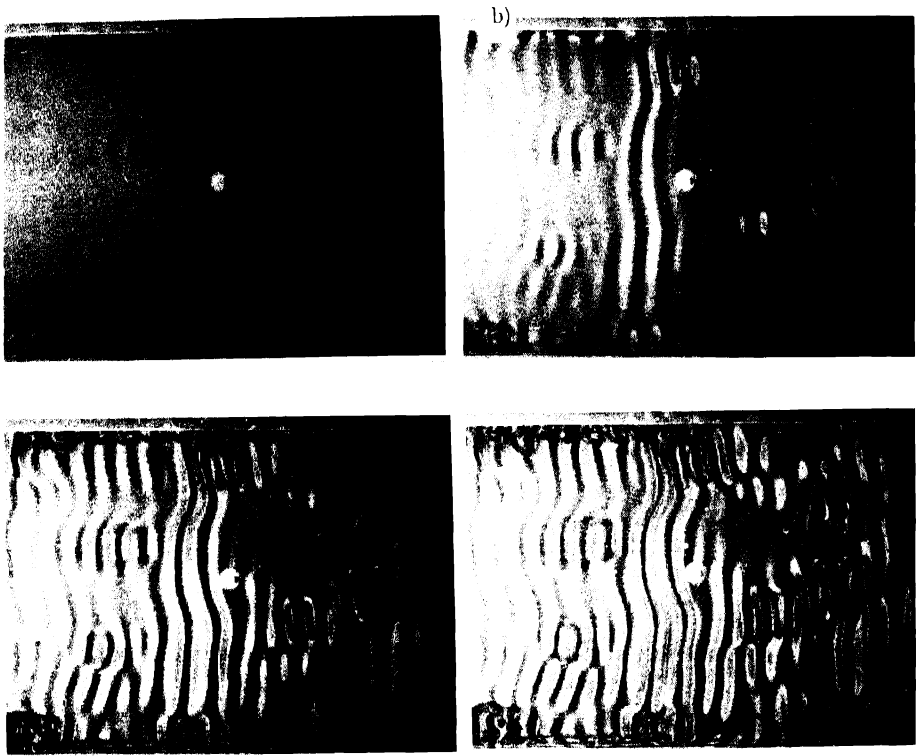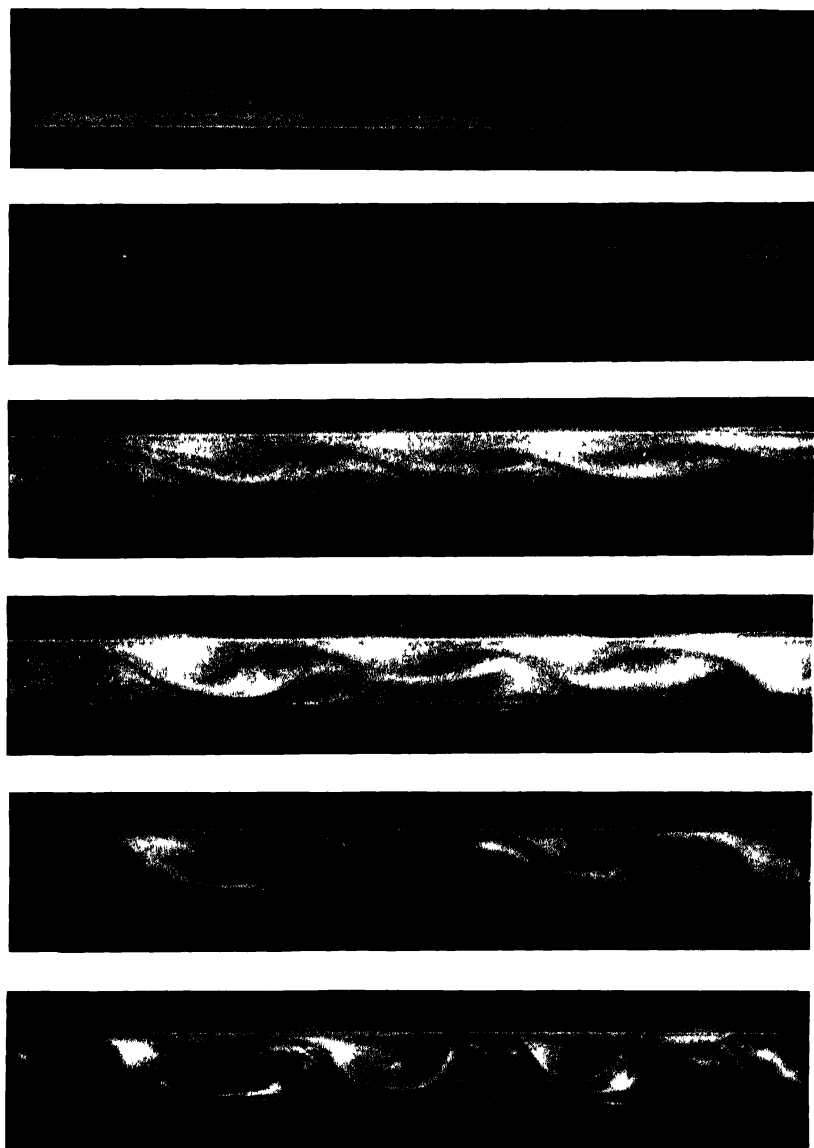
Fig. 4.   View of xz-plane of the developing instabilities in decaying plane Couette flow at $Re = 700$. Instantaneous stop of the two moving walls is at non-dimensional time $\eta = 0$. a) $\eta = 0.100$, b) $\eta = 0.115$, c) $\eta = 0.130$, d) $\eta = 0.145$.

the picture looked very much like the roll-up of a vortex sheet but it rapidly became deformed as the pattern wrinkled. The still photographs were complemented with video recordings which showed circular particle motions, and it was concluded that the instability gave rise to spanwise oriented stationary roll cells extending across the entire gap between the walls.

A systematic study was made to determine the wave number α ($= 2\pi h/\lambda$ where λ is the wave length) of the stripe pattern for various Re. Experiments were carried out for Re in the interval between 500 and 1000. The low Re was set by the weakness of the visual pattern and the high Re by the inlet disturbances. The wavelengths were determined from video recordings of the xz-plane. In most cases four or five consecutive stripes, taken from a region of regular cells, were used in the estimate. There were no significant wavelength changes in time. In Fig. 6 we have plotted the span of observed wave numbers as a function of Re. It shows

Fig 5   View of xy-plane of the developing instabilities in decaying plane Couette flow at $Re = 980$. Instantaneous stop of the two moving walls is at non-dimensional time $\eta = 0$ Time increment between subsequent photographs $\Delta\eta = 0.008$ First photograph taken at $\eta = 0\,092$
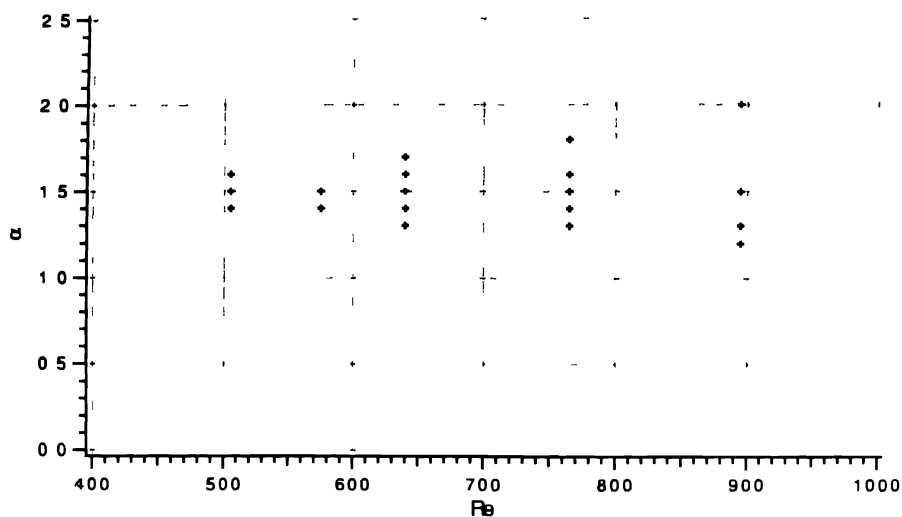
Fig 6   Experimentally determined streamwise wave number as a function of Reynolds number

an almost constant α of 1.5, corresponding to a wave length of about 21 mm, i e approximately two channel heights

4. Numerical results

The stability of the decaying flow was analyzed assuming that the mean flow could be regarded as quasi-stationary The disturbance was assumed to have the form

$$\exp i\alpha(x - ct), \quad \text{where} \quad c = c_r + ic_i$$

and α, x, c and t are normalized in the appropriate way by h and U_w For the disturbances observed in experiments $c_r = 0$ Using the linearized equations of motion this approach gives the Orr-Sommerfeld equation with a disturbance that either grows or decays in time. The resulting eigenvalue problem was then solved by a spectral collocation method using an expansion in Chebychev polynomials

Computations were carried out for velocity profiles at various η and Reynolds numbers. For small η only damped modes were observed and the least damped were non-stationary ($c_r \neq 0$). For larger η (and $Re > 112$) amplified modes were obtained These modes were stationary ($c_r = 0$) An example of the variation of the amplification factor (αc_i) with wave-number at various η are shown in Fig. 7 for $Re = 700$. In the interval between 0 018 and 0 3 the most amplified mode is stationary and has a positive amplification factor Above $\eta = 0.3$ all modes are again damped At η approximately 0.075, αc_i has a maximum corresponding to a wave number of 1.5 There is a strong variation in the spanwise wave number
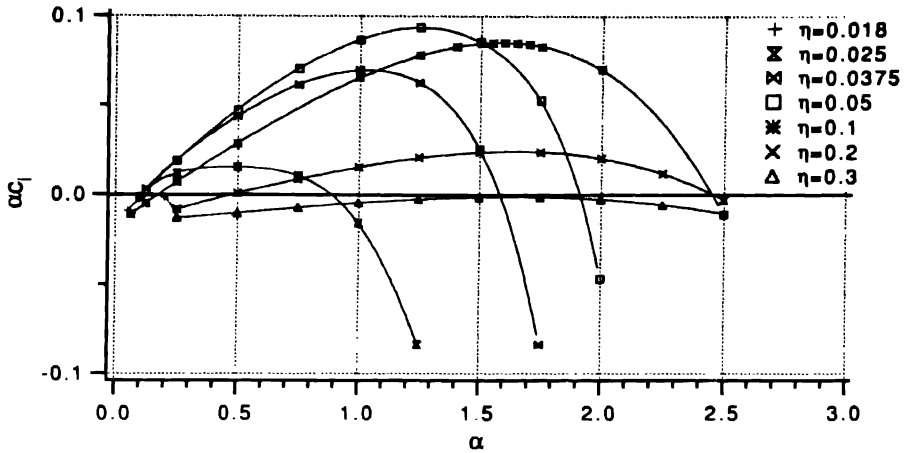
Fig. 7.   The amplification factor as a function of the streamwise wave number at $Re = 700$ for differnt η.

at which the local $(\alpha c_i)_{max}$ occurs for times less than 0.075 whereas it is almost constant (1.55) for profiles at times larger than 0.075 in this interval. The maximum amplification is fairly high, of the order of 0.1. From the data in Fig. 7 it is possible to approximately determine the wave number with maximum overall growth, and comes out close to $\alpha = 1.5$. The overall growth at this wave number is more than 3000 times.

The amplification of the most unstable mode increases with Re. In Figure 8 the maximum amplification for $\eta = 0.1$ is shown as function of Re. It is seen that the amplification tends towards a constant value at high Re, i.e. it approaches the inviscid limit. For this case instability is first observed above $Re = 112$.

To get a clearer view of the most amplified mode its velocity distribution in the xy-plane at a fixed time ($\eta = 0.1$) was calculated and plotted in Fig. 8. It shows a roll cell sheared by the mean flow, filling the full gap between the walls in agreement with the flow visualization results in figure 5.

Acknowledgement

References

1. Batchelor, G.K., *An Introduction to Fluid Dynamics*. Cambridge Univ. Press (1967).
2. Fjørtoft, R., Application of integral theorems in deriving criteria of stability for laminar flows and for the baroclinic circular vortex. *Geofys. Publ., Oslo* 17 (1950), No. 6, 1.
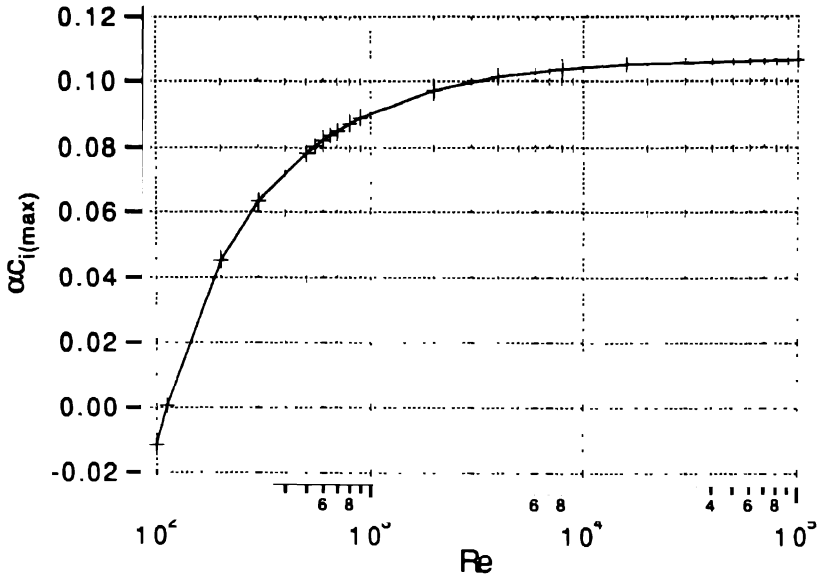
Fig 8   The maximum amplification factor as a function of Reynolds number for $\eta = 0.1$
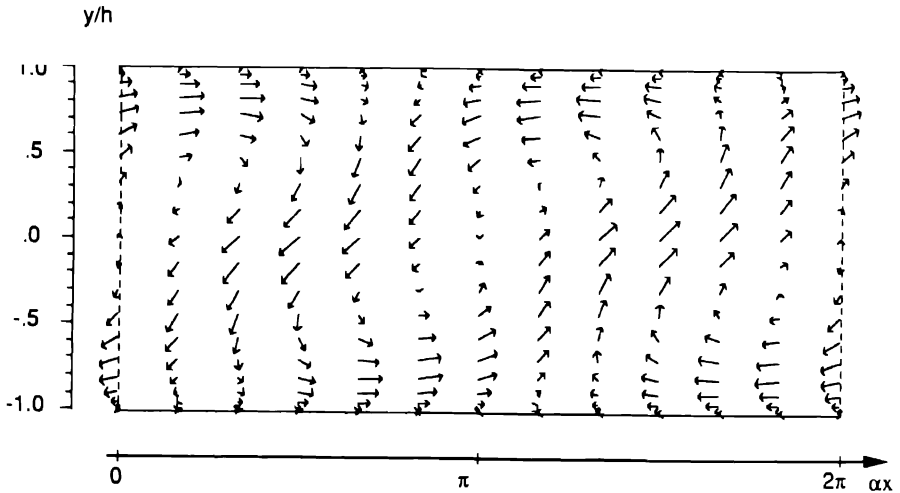
Fig 9   Velocity vector plot of one roll cell in the xy-plane for $\alpha = 1.55$, $\eta = 0.1$, $Re = 700$

3 Rayleigh, Lord, On the stability, or instability, of certain fluid motions *Proc London Math Soc*
   174 (1980), 57
4 Rayleigh, Lord, *The theory of sound* Reprinted by Dover, New York 1945 (1896)
5 Schlichting, H , Uber die Stabilität der Couetteströmung *Ann. Phys* 14 (1932), 905
6 Schlichting, H , *Boundary layer theory* McGrawHill, New York (1979)
7 Tillmark, N & Alfredsson, P H , Experiments on transition in plane Couette flow *J Fluid Mech*
   235 (1992), 89.

Euromech Meetings 1995

The EUROMECH Council has overall responsibility for EUROMECH Colloquia and EUROMECH Conferences. The latter comprise the European Solid Mechanics Conference, the European Fluid Mechanics Conference, the European Turbulence Conference and the European Nonlinear Oscillations Conference. Fifteen Colloquia, but no Conference, will take place in 1995.

EUROMECH Colloquia are informal meetings on specialized research topics. Participation is restricted to a small number of European research workers actively engaged in the field of each Colloquium. The organization of each Colloquium, including the selection of participants for invitation, is entrusted to a Chairman. Proceedings are not normally published. Those who are interested in taking part in a Colloquium should write to the appropriate Chairman. Number, Title, Chairman or Co-chairmen, Dates and Location for each Colloquium in 1995, and an advance notice for a Colloquium in 1996, are given below.

329. *Methods for nonlinear stochastic structural dynamics*
     Prof. G. I. Schueller, Institute of Engineering Mechanics, University of Innsbruck, Technikerstrasse 13, A-6020 Innsbruck, Austria
     13–17 March 1995, Innsbruck, Austria

330. *Laminar/turbulent transition of boundary layers influenced by free-stream disturbances*
     Dr P. Jonás, Institute of Thermomechanics, Academy of Sciences of the Czech Republic, Dolejskova 5, CZ-182 00 Praha 8, Czech Republic
     Prof. F. Pittaluga, Genova
     10–12 April 1995, Prague, Czech Republic

331. *Flows with phase transition*
     Prof. G. E. A. Meier, Institut für Strömungsmechanik der DLR, Bunsenstrasse 10, D-37073 Göttingen, Germany
     Prof. G. H. Schnerr and Prof. J. Zierep, Karlsruhe
     13–16 March 1995, Göttingen, Germany

332. *Drag reduction*
     Prof. P. Luchini, Dipartimento di Progettazione Aeronautica, Università di Napoli Federico II, P. le Tecchio, I-80125 Napoli, Italy

Dr D. Bechert, Berlin
19–20 April 1995, Ravello (near Naples), Italy

333. *Ground freezing: mathematical models and applications*
Prof. M. Primicerio, Dipartimento di Matematica "U. Dini", Viale Morgagni
67/a, I-50134 Firenze, Italy
Prof. M. Fremond, Paris
2–4 June 1995, Montecatini, Italy

334. *Textile composites and textile structure*
Prof. P. Hamelin, Laboratoire Mécanique et Matériaux, Université Lyon 1,
IUT A Génie Civil, 43, boulevard du 11 Novembre 1918, F-69622 Villeur-
banne Cédex, France
P. de Wilde, Brussels
15–17 May 1995, Lyon, France

335. *Image techniques and analysis in fluid dynamics*
Prof. A. Cenedese, Department of Mechanics and Aeronautics, University
"La Sapienza", Via Eudossiana 18, I-00184 Roma, Italy
Prof. F. T. M. Nieuwstadt, Delft
5–7 June 1995, Rome, Italy

336. *Flows dominated by centrifugal and Coriolis forces*
Prof. H. Andersson, Applied Mechanics, The Norwegian Institute of Tech-
nology, N-7034 Trondheim, Norway
21–23 June 1995, Trondheim, Norway

337. *Plastic flow instabilities at high rate of strain*
Prof. C. Fressengeas, L.P.M.M./I.S.G.M.P., Université de Metz, Ile du Saulcy,
F-57045 Metz Cédex 01, France
Dr B. Dodd, Reading
10–13 July 1995, Metz, France

338. *Atmospheric turbulence and dispersion in complex terrain*
Dr F. Tampieri, FISBAT CNR, Via Gobetti 101, I-40129 Bologna, Italy
4–6 September 1995, Bologna, Italy

339. *Internal waves, turbulence and mixing in stratified flows*
Dr C. Staquet, Ecole Normale Supérieure de Lyon, Laboratoire de Physique,
46, allée d'Italie, F-69364 Lyon Cédex 07, France
6–8 September 1995, Lyon, France

340. *Statistical properties of turbulent gaseous flames*
  Prof. D. Roekaerts, Heat Transfer Section, Faculty of Applied Physics, Delft
  University of Technology, Lorentzweg 1, NL-2628 CJ Delft, The Netherlands
  Dr Th. van der Meer, Delft
  30 August–1 September 1995, Delft, The Netherlands

341. *Smart structures and materials*
  Prof. J.-M. Crolet, Université de Franche-Comté, Laboratoire de Calcul Sci-
  entifique, 16, route de Gray, F-25030 Besançon Cédex, France
  Prof. A. Preumont, Brussels
  26–28 September 1995, Giens (near Toulon), France

342. *Aerodynamics*
  Dr G. Eitelberg, Aerothermodynamics Branch, Institute for Fluid Mechanics,
  DLR, Bunsenstrasse 10, D-37073 Göttingen, Germany
  Dr H. Legge, Göttingen, and Prof. R Brun, Marseille
  26–29 September 1995, Göttingen, Germany

343. *Computerized symbolic manipulation in mechanics*
  Prof. E.J. Kreuzer, Meerestechnik II, Technische Universität Hamburg-Har-
  burg, Eissendorfer Str. 42, D-21071 Hamburg, Germany
  Prof. M. Lesser, Stockholm
  9–13 October 1995, Hamburg, Germany

344. *Fluid–structure interactions in biomechanics* (advance notice)
  Prof. T. J. Pedley, Department of Applied Mathematical Studies, University
  of Leeds, Leeds LS2 9JT, England
  Prof. C. G. Caro, London
  April 1996, London, England

CALL FOR PAPERS
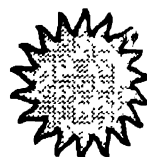
ITEC95

SECOND INTERNATIONAL THERMAL ENERGY CONGRESS

Morocco, June 5-9 1995

Objectives
- To provide a bridge between the north and south thermal energy technologies;
- To provide a forum and to encourage a realistic dialogue at all levels for the implementation of the R&D results;
- To accelerate the development, application and exchange of knowledge in thermal energy fields.

Topics
- Heat and Mass Transfer
- Energy Conservation
- Environment Protection
- Energy Systems
- Renewable Energies
- Hydrogen Economy
- Optimization and Control
- Experimental Techniques

Fees
The registration fee of the Congress is US$400. This fee covers a set of volumes of the Congress Proceedings, refreshments and receptions. Limited financial support will be available for young researchers.

Submission of Papers
Three copies of the papers, maximum 6 single-spaced pages should be submitted to the Congress Secretary prior to December 1, 1994 for review. Notification of acceptance will be mailed by January 15, 1995 Authors with papers accepted for presentation are requested to submit manuscript on mats by February 28, 1995 for inclusion in the Congress Proceedings, which will be available at the Congress.

For all correspondance
Brigitte Hayeur
Congress Secretary/ITEC95
Ecole Polytechnique
Department of Mechanical Engineering
Box 6079, "City Center"
Montreal, Qc, Canada, H3C 3A7
Tel· (514) 340-4399
Fax: (514) 340-4052
e-mail: brhaye@meca.polymtl.ca

Sponsored by: *École Polytechnique • University Cadi Ayyad • Faculty of Science Semlalia*
Hosted by: *University Ibnou Zohr • École Supérieure de Technologie*

Selected papers from a IUTAM Symposium held at Poitiers, France,
12–14 October 1992

Preface

Turbulent flows can be characterized by organized eddies, generally of large scale, embedded in a random field. These large scale structures are either directly or indirectly associated with the production of the turbulent stresses. An understanding of the generation and destruction mechanisms associated with these large eddies is an active topic of research at this time. This special double issue of *Applied Scientific Research* highlights some of the recent advances in this area and the methodologies used in identifying the underlying physical mechanisms.

The issue contains a collection of papers from the **IUTAM** Symposium entitled "Eddy Structure Identification in Free Turbulent Shear Flows" which was held at CEAT/LEA in Poitiers, France, October 12–14, 1992. The scope of this meeting was to display, discusss and compare structure identification methods and concepts. The topics covered were both experimental and numerical/theoretical – with several papers devoted to presentation, analysis and development of detection or identification methods, and others devoted to concepts or some fundamental aspects of coherent structure characteristics and behavior. Free shear flows are of primary interest in this issue. This allows for focus on methods which are shared in common with numerous groups, without the somewhat more complex variety of structure types – and associated detection methods – present in the case of wall-bounded flows. However, most of the methods developed for free turbulent shear flows which are presented here have direct applications in wall-bounded turbulent shear flows as well.

The papers selected for this issue of *ASR* are revised and updated versions of contributions that have already appeared in a volume entitled *Eddy Structure Identification in Free Turbulent Shear Flows* (J.P. Bonnet and M.N. Glauser, eds, 500 pages, 39 contributions, Kluwer Academic Publishers, 1993). These selections cover both reviews and the description of recent progress and developments of several detection methods. In addition, applications of several approaches are given for a variety of flows to illustrate the numerical and/or theoretical possibilities of several methods for educing and analyzing the eddy structure of turbulent flows.

This special issue provides the experimentalist and numerical analyst with a guide for chosing the appropriate detection method for extracting the organized large scale structures in turbulent shear flows.

JEAN-PAUL BONNET
MARK N. GLAUSER

Vorticity-Based Eduction of Large-Scale Structures in Turbulent Shear Flows

M. HAYAKAWA
Department of Mechanical Engineering II, Hokkaido University, N13 W8, Sapporo 060, Japan

Abstract. This paper is mainly concerned with a vorticity-based conditional sampling technique, which identifies large-scale vorticity-bearing flow events in turbulent shear flows using multiple X-wire probes. Basic ideas and procedures of the technique are described, and several examples of the results are presented Advantages and limitations of the technique are also discussed from an experimental point of view.

1. Introduction

1.1. BACKGROUND

While the discovery of spatially coherent, recurrent, large-scale flow events (often called "coherent structures") in turbulent shear flows mostly benefited from flow visualization studies, one has to rely upon a certain quantitative method in order to gain further insights into the detailed characteristics and dynamical roles of those structures ([1–4]). To date, various methods have been developed for this purpose (see Ref. [5], for example).

The technique of conditional sampling and averaging has been one of the most widely used methods in laboratory experiments. The general description and historical overview of the technique are provided by Kaplan [6], Van Atta [7] and Antonia [8], among others. In recent years, the technique is also utilized by numerical analysts, since the increasing computer power has made it possible to regard the results of direct numerical simulation as "data" analogous to the data from laboratory experiments ([9]).

What one obtains from the conditional sampling is a "conditional average", which is defined as an ensemble average taken over many events that satisfy a certain prescribed condition [10]. Implicit working rules in obtaining the conditional average are: (1) the existence of identifiable, recurrent flow events, (2) the selection of similar events through conditioning, and (3) the decomposition of any sampling signal f into an ensemble-averaged (i.e. "coherent") part $\langle f \rangle$ and the remained part f_r through averaging; $f = \langle f \rangle + f_r$.

In spite of its broad use, the conditional sampling involves two major problems. One is concerned with "subjectivity", which enters in the process of conditioning, i.e., in the choice of proper conditioning signals and the decision of suitable conditions. In general, the ensemble average $\langle f \rangle$ more or less depends on the detection

scheme used. Sato [1] noted that many patterns are hidden in a random field, and in the limit we can find any pattern [we like] in a perfectly random field. This is of course an extreme case, but such a dangerous aspect always resides in conditional sampling techniques.

The other problem is the so-called "jitter", which occurs in the process of sampling/averaging. This is caused by the fact that a signal sampling point and a detection (or "trigger") point are usually different, both in space and time. Consequently various random factors of individual flow events enter into the averaging process and lead to the loss of phase information, eventually causing a large degradation of the ensemble-averaged result ([10, [12], [13]). Since variations of individual events in their detail, movement and history arise from the inherent nature of turbulence, any conditional sampling technique cannot be entirely free from the jitter problem.

In a sense, the development of conditional sampling techniques has been a history of researchers' effort in settling the two difficult problems.

1.2. VORTICITY-BASED TECHNIQUE

To adapt a conditional sampling technique to the identification of organized structures, whose appearance is generally at best quasi-periodic, one has to choose a proper conditioning signal, which ought to be a characteristic flow property associated with the flow events under consideration.

In 1980, Hussain [14] proposed a definition of coherent structures: "a coherent structure is a connected turbulent fluid mass with 'instantaneously phase-correlated vorticity' ('coherent vorticity' in his terminology) over its spatial extent." This led him to believe that "vorticity" should be the best flow property to recognize coherent structures. While the usefulness of vorticity in the quantitative study of organized turbulence structures had been often suggested (e.g. [6], [15]) difficulty in high resolution measurements of vorticity even at a point, let alone at multiple points, in a flow prevented its practical use in the experimental studies. But the above operational definition by Hussain implied that coherent structures could be identified by measuring relatively low frequency vorticity components, rather than a sufficiently wide frequency range of vorticity fluctuations.

Motivated by Hussain's idea, Tso [16] employed, in his study of a far field round jet, a rake of seven X probes to measure the azimuthal component of (instantaneous) vorticity in a meridian plane, and extracted vortical structures by referring to the local peak of the filtered vorticity concentration. His method appeared insensitive to the effects of jitter, because structures were captured at their (approximate) centers without use of any auxiliary reference signal for trigger. Since then, this "vorticity-based conditional sampling technique" (hereinafter, referred to as "vorticity-based technique" for brevity) has been applied to other free shear flows and found to be a useful method for the investigation of coherent structures [3, 17].

In this paper, basic procedures involved in the vorticity-based technique are described first. Then, several results are presented and compared with those
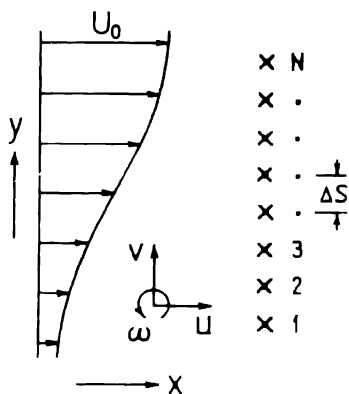
Fig 1   Definition sketch

obtained by other conditional sampling techniques. Discussion is mainly made in terms of instantaneous and ensemble-averaged vorticity fields, without entering into detailed turbulence mechanisms. Finally, the merit and demerit of the present technique and some related issues are discussed. Consideration is restricted to either two-dimensional or axisymmetric free shear flows.

2. Basic Procedures: Eduction Scheme

2.1. CALCULATION OF VORTICITY

For an illustrative purpose, let us consider an array with a number N of X probes with a relative separation Δs, aligned in the direction of the main shear of a plane shear layer (Figure 1). Coordinate axes are designated as x, y and z in the streamwise-, transverse- (main-shear-) and spanwise direction respectively, and the corresponding velocity components are u, v and w.

From a time series of simultaneous u and v signals at N y locations, the spanwise vorticity component ω_z is calculated with Taylor's hypothesis and a central difference approximation (Figure 2);

$$\omega_z = \frac{\partial v}{\partial x} - \frac{\partial u}{\partial y} \approx -\frac{1}{U_c}\frac{\Delta v}{\Delta t} - \frac{\Delta u}{\Delta s} .$$

Here U_c is the average convection velocity of structure centers in the x direction and Δt is the time step between successive data points. For instance, the vorticity at a point A in Figure 2 is estimated as follows, in an approximation to the instantaneous spanwise vorticity (in this section, ω will be used in place of ω_z, for brevity);

$$(\omega)_A \approx -\frac{1}{U_c \Delta t}\left\{\frac{v_{21}+v_{22}}{2} - \frac{v_{11}+v_{12}}{2}\right\} - \frac{1}{\Delta s}\left\{\frac{u_{12}+u_{22}}{2} - \frac{u_{11}+u_{21}}{2}\right\} .$$
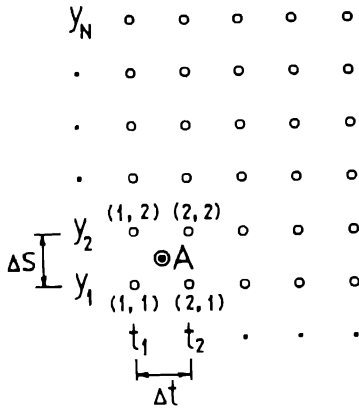
Fig. 2.   Vorticity computation grid.

Hence we have ω values at $(N-1)$ y locations.

2.2. RECOGNITION

Since our primary concern is in large-scale features, we take the moving, short-time average of vorticity signals to have simultaneous records of low-pass filtered vorticity $\bar{\omega}$ at $(N-1)$ y locations. The signal smoothing is not performed in the y direction, not only because a locally intense but small-scale vorticity patch would produce spurious bumps in $\bar{\omega}$ values over the neighboring y locations through the smoothing, but also because the calculation of vorticity has already contained a spatial filtering effect due to the probe spacing Δs.

Figures 3(a)–(d) show four examples of the iso-contour map of smoothed vorticity, obtained in three different flow configurations: a circular cylinder wake (a, b) a plane mixing layer (c) and a round jet (d). In these figures, if time t is converted to stream-wise distance x by $x = -U_c t$, the abscissa scale is compressed relative to the ordinate scale. The pseudo-instantaneous vorticity maps visualize the occurrence of vorticity concentrations, and help us to recognize the presence of vorticity-bearing organized events, more quantitatively than in flow visualization pictures.

2.3. TRANSVERSE DETECTION CENTER

As the events of interest usually occur with wide dispersion across the shear layer, it is preferable to determine first a transverse detection center. For an ordinary purpose, the detection center is determined so as to coincide with the most probable y location of advecting structure centers. This is done by counting the number of $\bar{\omega}$
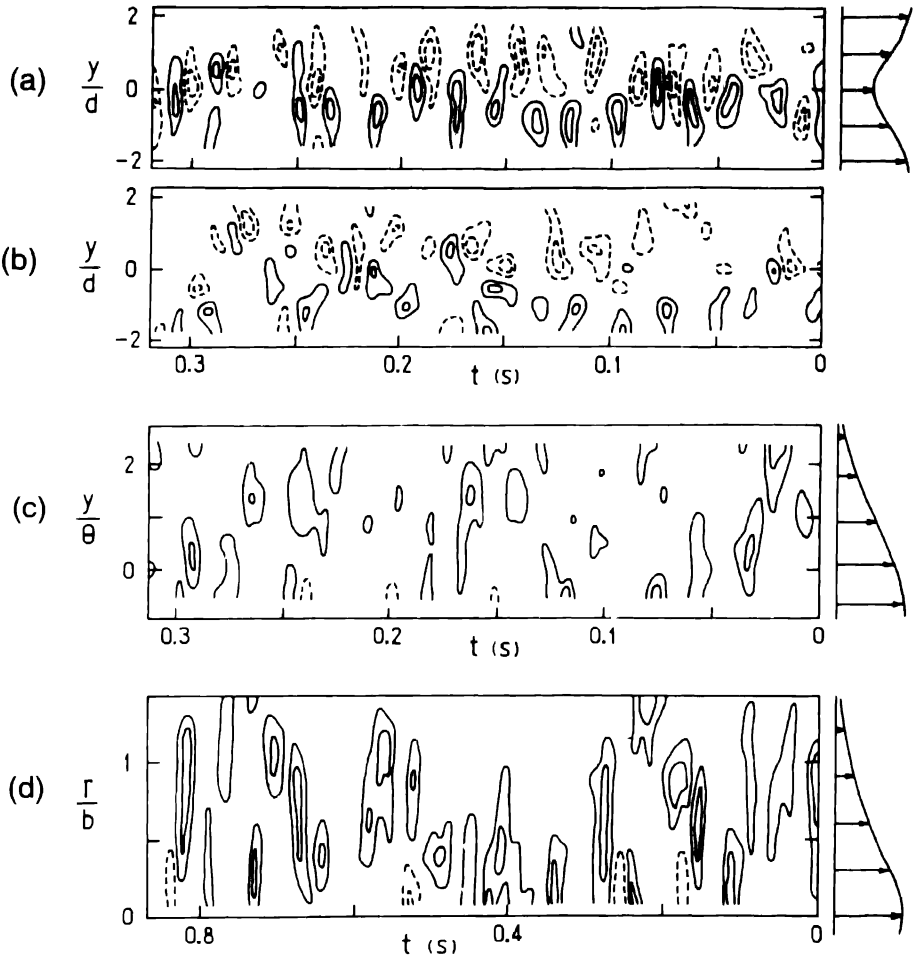
Fig 3   Pseudo-instantaneous $\bar{\omega}_z$ maps Circular cylinder wake at a) $x/d = 20$ and b) $x/d = 40$ (Ref [23]) c) Plane mixing layer at $x/\theta_e = 1000$ (Ref [32]) d) Circular jet at $x/D = 50$ (Ref [16])

peaks higher than a certain level, as a function of y (Figure 4). The detection center is assigned to the location y_c which gives the maximum probability. Then, the X-wire rake is relocated so that the middle location corresponds to y_c, as illustrated in Figure 4. This is the transverse detection center to be used in the following processes.

If the number of X probes is large enough for the probe spacing to be sufficiently narrow, this relocation is not essential. However, we have typically used eight X
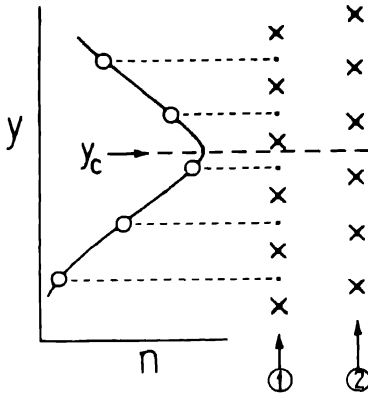
Fig. 4. Determination of the middle location of an ×-wire rake; n is the number of vorticity peaks.

probes only, the relocation is necessary for efficient use of information from the limited number of the probes.

2.4. DETECTION: CONDITIONING

In the present technique, the detection conditions are imposed on the "strength" and "size" of (smoothed) vorticity concentrations. The strength is discriminated by applying a threshold Th_1 to $\tilde{\omega}$ at y_c;

$$\text{I. } \tilde{\omega}_c > Th_1, \quad Th_1 = k_1 S_M; \quad S_M = \left(\frac{\partial u}{\partial y}\right)_{\max}$$

Here the local maximum mean shear S_M is used for fixing the threshold level. The middle point during the interval of $\tilde{\omega}(y_c)$ being higher than Th_1 is assigned to a trigger instant t_c. Also, we check $\tilde{\omega}(y_c)$ to be transversely maximum at t_c;

$$\text{II. } \tilde{\omega}(y_c, t_c) > \tilde{\omega}(y, t_c) \quad \text{for} \quad y \neq y_c.$$

The size criterion is applied to both the streamwise and transverse scales. The condition is such that $\tilde{\omega}$ values around a point (y_c, t_c) are simultaneously greater than another threshold Th_2 (Figure 5);

$$\text{III. } \tilde{\omega}(y_c \pm \Delta y, t_c) > Th_2 \quad \text{(transverse size), and}$$
$$\text{IV. } \tilde{\omega}(y_c, t_c \pm \Delta \tau) > Th_2 \quad \text{(streamwise size); } Th_2 = k_2 S_M.$$

Here $\Delta \tau$ is so chosen as $U_c \Delta \tau$ is nearly equal to Δy; that is, a common condition is imposed to both the streamwise and transverse sizes. In other words, we assume the cross-section of structures to be nearly circular. However, if the selected events have a preferential (say, elliptical) shape, such a feature can survive through the detection process because the above condition is moderately mild.
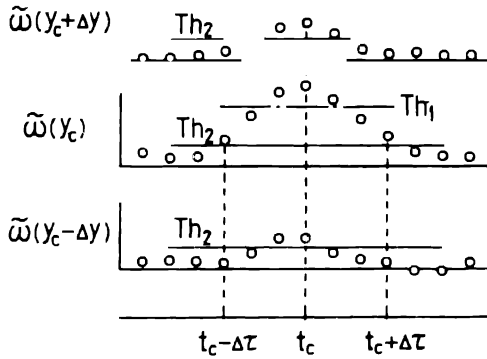
Fig 5   Illustration showing the criteria on streamwise and transverse scales of vorticity concentration

Large-scale events are accepted only when all the criteria above are satisfied, so that weaker, transversely-shifted, smaller-scale or highly distorted events are discarded.

2.5. EDUCTION: ENSEMBLE AVERAGE

Once the trigger instants $t_{c,i}$ ($i = 1, 2, ...$) are determined, the accepted realizations are relatively aligned with respect to each center (y_c, t_c), and the ensemble-averages of velocity components, $\langle u \rangle$ and $\langle v \rangle$, are calculated. Then, the coherent vorticity $\langle \omega \rangle$ distribution is obtained by using again the Taylor hypothesis and the central difference approximation. It may be important to note that the ensemble averages are computed from original, unsmoothed velocity signals; the smoothed signals have been used only as a means of selecting similar large-scale events. Otherwise, ensemble-averaged results should suffer from excessive filtering effects, and the departure from the ensemble average, $f_r (= f - \langle f \rangle)$, would have no specific physical meaning.

2.6. REALIGNMENT: SIGNAL ENHANCEMENT

While the essential procedure of the present technique has been outlined above, it is preferable to perform further alignment of individual structure centers, because smoothed vorticity peaks are usually not sharp enough to be identified clearly. For this purpose, we take the cross-correlation between the vorticity-signal segment $\tilde{\omega}(y_c)$ of each realization and the initial ensemble average $\langle \omega(y_c) \rangle$ (Figure 6). Each realization is then relatively shifted by the time delay of the peak correlation. In practice, the trigger instants $t_{c,i}$ which have been stored in a data file are revised to $t'_{c,i}$, as illustrated in Figure 6.
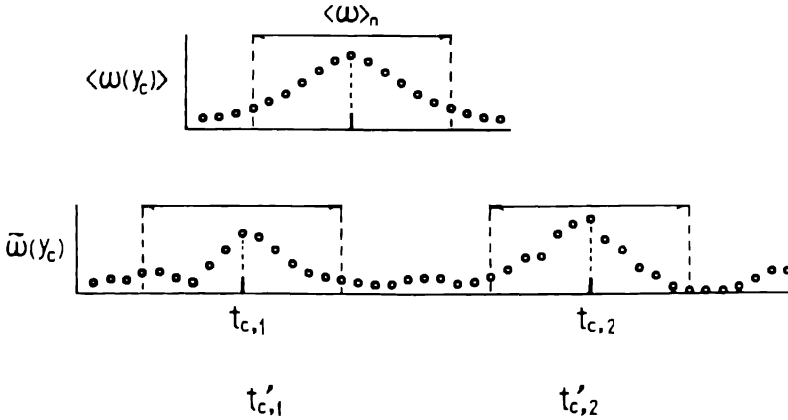
Fig 6   Illustration showing the realignment process.

3. Applications

The eduction scheme explained in the previous section has been applied to geometrically simple free shear flows by Hussain's group at Houston. Similar techniques based on the use of multiple X probes have been recently employed by Antonia's group at Newcastle and Bonnet's group at Poitiers. In this section, several results obtained by the present and similar vorticity-based techniques are presented, in comparison with the relevant results obtained by other techniques.

3.1. CIRCULAR JET

In order to check the present eduction scheme, we first applied it to the near field of a circular free jet using a rake of seven X probes ([18]). The jet flow was weakly excited at the jet preferred mode, $f_e D/U_0 \approx 0.3$. Here, f_e is the excitation frequency (= 44 Hz), D is the nozzle diameter (= 7.6 cm) and U_0 is the jet exit speed (= 11 m/s). Structures educed at $x/D = 3$ and 8 are shown in Figs. 7(a,b), where the locations of the probes are indicated by thick cross marks, and $\langle \omega \rangle$ values are made dimensionless with f_e. The number of finally accepted structures per second was $0.82 f_e$ at $x/D = 3$ and $0.40 f_e$ at $X/D = 8$.

For this particular case, detailed data by Hussain and Zaman [19] were available. They used local periodic u fluctuations on the jet axis as a trigger signal for phase-locked measurements. Phase-average flow properties were obtained using an X-wire probe moved to different (x, r) locations over the spatial extent of the preferred-mode structure, without use of Taylor's hypothesis. Figure 7(c) shows their result, when the reference probe for trigger was placed at $x/D = 3$.

In comparing the two data sets, caution must be made that Figs. 7(a,b) represent a selectively sampled, temporal picture at each x station, whereas Figure 7(c) shows a periodically sampled, spatial picture at a particular phase of excitation.
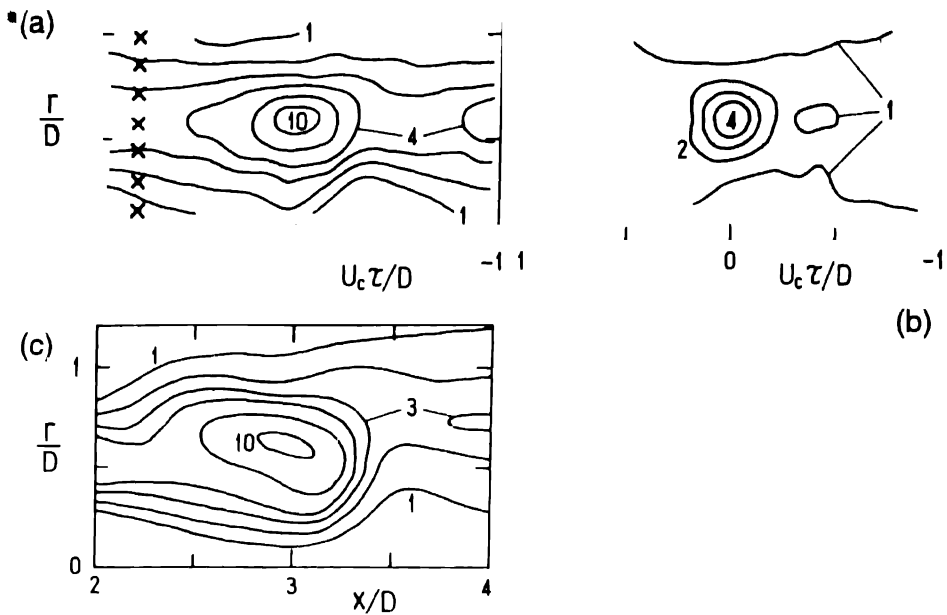
Fig. 7   Near field circular jet under the preferred mode excitation: $\langle\omega_z\rangle$-contours; a) x/D = 3 and b) x/D = 8 (Ref [18]), c) x/D = 3 (Ref. [19]).

Keeping this difference in mind, the agreement between Figs. 7(a) and 7(c) is fairly good. This indicates that the present eduction scheme works well and that Taylor hypothesis based on U_c yields a good approximation in this case, where the preferred mode excitation prevents the occurrence of vortex pairing ([19]).

Since the sharp signature of structure passage disappears beyond the potential core, the point trigger measurement did not reveal any clear structure for $x/D > 6$ ([19]). Figure 7(b) indicates, however, that at least 40 percent of the initially induced structures still retain their organization at $x/D = 8$. This example clearly shows a superior feature of our technique, which can detect structures without recourse to any external signal for trigger. Of course, because of the single radial plane measurement, it is not clear whether individual events are axisymmetric or spiral; the latter mode is known to be dominant in the region beyond the potential core ([20]).

Recently, Chua and Antonia [21] adapted a similar X-wire rake technique to the jet near-field and identified the opposing and alternating modes even at $x/D = 4$, on the basis of filtered vorticity signals on a diametral plane.

In the fully developed state of a circular jet, Tso [16] employed a rake of 7 X probes, coupled with two single-wire probes which were displaced azimuthally by $90°$ on either sides of the rake and used for the mode discrimination. He found that the helical modes ($m = \pm1$) predominate over the axisymmetric ($m = 0$) and
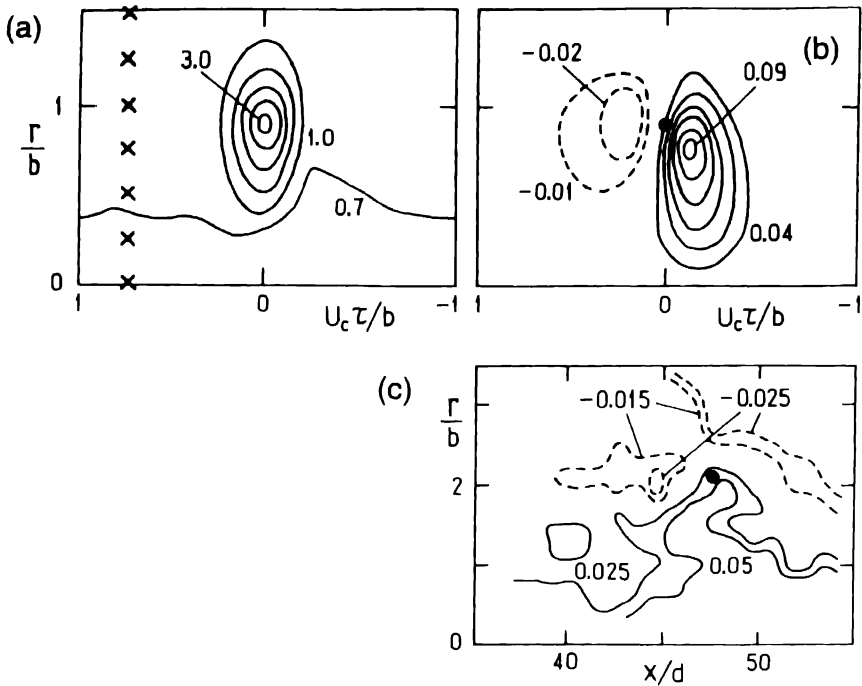
Fig. 8.   Far field circular jets: a) $\langle \omega_r \rangle / S_M$ and b) $\langle v \rangle / U_0$ (Ref. [16]); c) $\langle v \rangle / (U_0 - U_a)$ (Ref [22])

double-helical modes (m = ±2). Figures 8(a,b) show the ensemble averages of azimuthal vorticity and radial velocity component for a helical mode (m = +1) at $x/D = 50$. Since the helical structures intersect the jet diametral plane at an angle of roughly 60° ([16]), the cross-section sliced by an $x - r$ plane appears elongated more in the radial direction.

A comparable data set was reported by Komori and Ueda [22]. They made simultaneous measurements of the two velocity components (u and v) and temperature fluctuations in a slightly heated jet surrounded by a low speed (non-heated) co-flowing stream and adopted a pattern-averaging technique. The ensemble averages of the three quantities were obtained at 240 points around a trigger probe placed in the intermittent zone of the jet at $x/D = 47.5$. In spite of their elaborate technique (see [22] for detail), the iso-contours of $\langle v \rangle$ in Figure 8(c) look much more complicated than Figure 8(b). The reason may be that the events they captured contain structures of various sizes and different modes, and hence the ensemble-averaged result may have been smeared due to sizable effects of jitter.
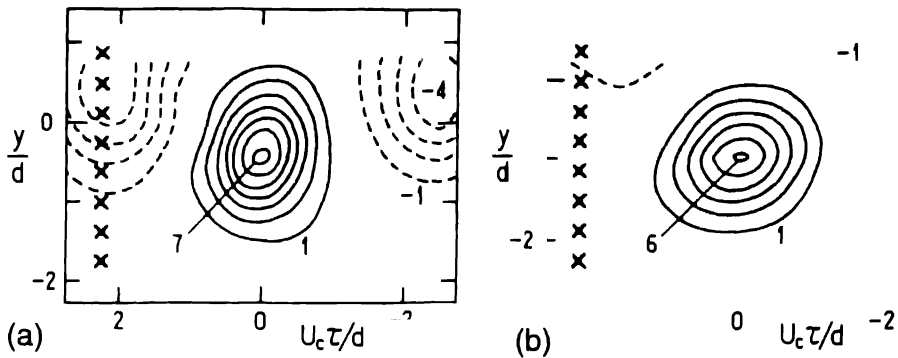
Fig 9.   Intermediate wake of a circular cylinder (Ref. [23]). $\langle \omega_z \rangle$-contours at a) $x/d = 10$ and b) $x/d = 40$

3.2. PLANE WAKE

Taking advantage of the fairly periodic motion of shed vortices, many investigators have studied organized structures in the near region of bluff-body wakes using periodic sampling techniques. Since the periodicity is progressively lost with increasing the downstream distance from the body however, such techniques are effective at best up to $x/l = 10$; here, l is the lateral dimension of the body. Therefore, for farther downstream regions, the situation becomes quite similar to the excited jet case (for $x/D > 6$) discussed in the previous sub-section.

The intermediate region of a circular cylinder wake was studied in some detail by us [23] using a rake of 8 X-probes. The Reynolds number based on the cylinder diameter ($d = 2.7$ cm) and the free-stream velocity ($U_0 = 7.0$ m/s) was about 13000. Measurements were made at $x/d = 10, 20, 30$ and 40, and most of the data were taken by the X-wire rake covering mainly one side of the wake in order to analyse the details of structures to be educed.

Ensemble-averaged spanwise vorticity contours obtained at $x/d = 10$ and 40 are compared in Figs 9(a,b). The detected and phase-aligned structures are depicted by solid lines and the opposite-signed vorticity contours corresponding to structures shed from the upper side of the cylinder are drawn by broken lines. Contour levels are non-dimensionalized by the local mean-flow variable, S_M, while coordinates are normalized by d (and U_c) for the sake of direct comparison of the structure scales between different x stations. The number of accepted events decreases from $0.37 f_s$ to $0.13 f_s$ between the two stations: here, f_s is the vortex shedding frequency corresponding to the Strouhal number of 0.21.

A comparison of the two structures at a same contour level (say, $\langle \omega_z \rangle / S_M = 1.0$) suggests that typical structures do not grow in size with increasing x but their size relative to the local wake width decreases downstream. It is also apparent that the

structure cross-section, which is initially somewhat elongated to the y direction (Figure 9a), becomes rounded and inclined as x increases (Figure 9b).

Since in the conditioning process, we have assumed the structure cross-section to be nearly circular and have not specified the upper bound scale of structures, the above observations should not be a consequence biased by the detection scheme used but reflect real features of the intermediate wake, where the (nominally) spanwise vortices shed from the cylinder are largely in a process of gradual decay. Such detailed features could not have been revealed, unless the detection method can capture the centers of individual events directly and align them adequately. If the detection point is distant away from the center of events, as is often so in periodic sampling measurement (e.g. [24]), then the ensemble average $\langle w_z \rangle$ would show a vaguer distribution.

In Figs 10(a)–(c), available data on bluff-body wakes obtained with different conditional sampling techniques ([24]–[29]) are compared, with regard to the streamwise variations of global structure properties: (a) the peak vorticity $\langle \omega_z \rangle_c$, (b) the convection velocity U_c, and (c) the average trajectory of structure centers y_c. The present data denoted by dark symbols are generally consistent with other data, except those of the D-shape cylinder ([24]) and normal plate ([28]) wakes, whose characteristics may be somewhat different from those of the circular cylinder wake. This comparison indicates that the present structure eduction, though being highly selective, properly identifies representative spanwise structures out of various events and provides a fairly objective result.

Bisset, Antonia and Browne [30] studied the far-field structure of a circular cylinder wake at $x/d = 420$ using a rake of 8 X probes, which covered both sides of the wake. They attempted at capturing the varicose and sinuous modes separately, the coexistence of which had been suggested by Wygnanski, Champagne and Marasli [31] on the basis of a linear stability analysis. Bisset et al. successfully educed the two modes by employing both the WAG (Window Averaged Gradient) detection applied to the filtered v fluctuations and the vorticity-based detection. Their result obtained by the latter technique is shown in Figs. 11(a,b), where coordinates are made dimensionless with the local wake half-width b. It is noticed that the educed structures contain two vorticity maxima, the resason for which remains unclear.

3.3. PLANE MIXING LAYER

We applied the present technique to the self-preserving region of a single-stream plane mixing layer initiated from a turbulent boundary layer [32]. Measurements were made at two x stations: $x/\theta_e = 1000$ and 2000; here, θ_e is the initial boundary layer momentum thickness. A rake of 8 X-probes covered the transverse extent of 60 percent of the (local) entire mixing-layer width B, because a preliminary test showed that large-scale vorticity-bearing events comparable in size with B were very rare.
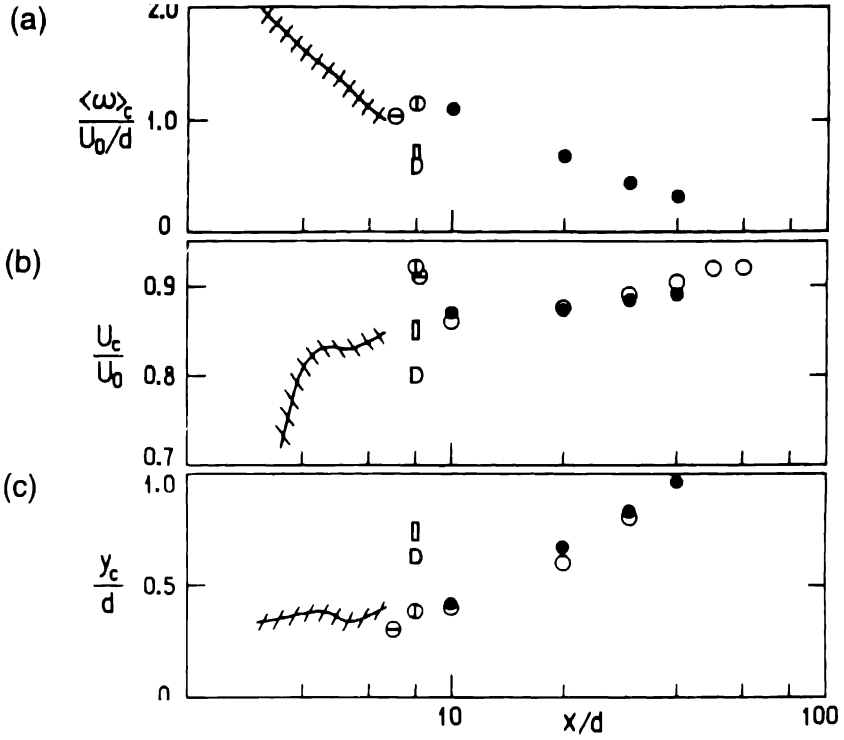
Fig. 10.   Comparison of various bluff-body wake data. a) Peak coherent vorticity. b) Convection velocity. c) Average location of structure centers. Symbols are: $///$: Cantwell and Coles (Re = 140000), $\oslash$: Kiya and Matsumura (16000), $\ominus$: Armstrong and Barnes (21500), $\bigcirc$: Zhuo and Antonia (5600), $\bullet$: Hussain and Hayakawa (13000). D: Davies (27000; D-shape cylinder), $\square$: Kiya and Matsumura (23000; normal plate).
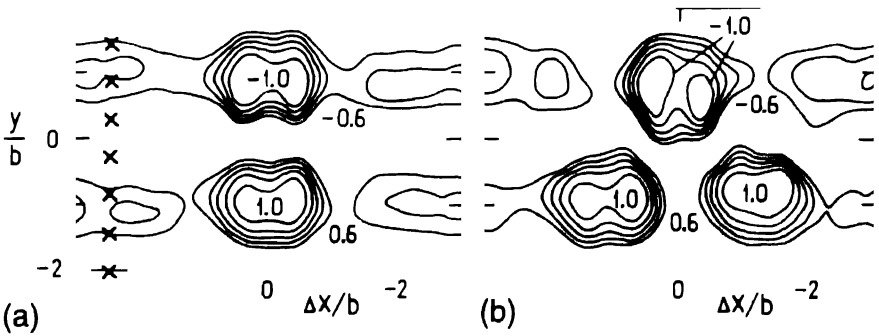

Fig. 11.   Far wake of a circular cylinder (Ref. [30]): $\langle \omega_z \rangle$-contours for a) varicose mode and b) sinuous mode.
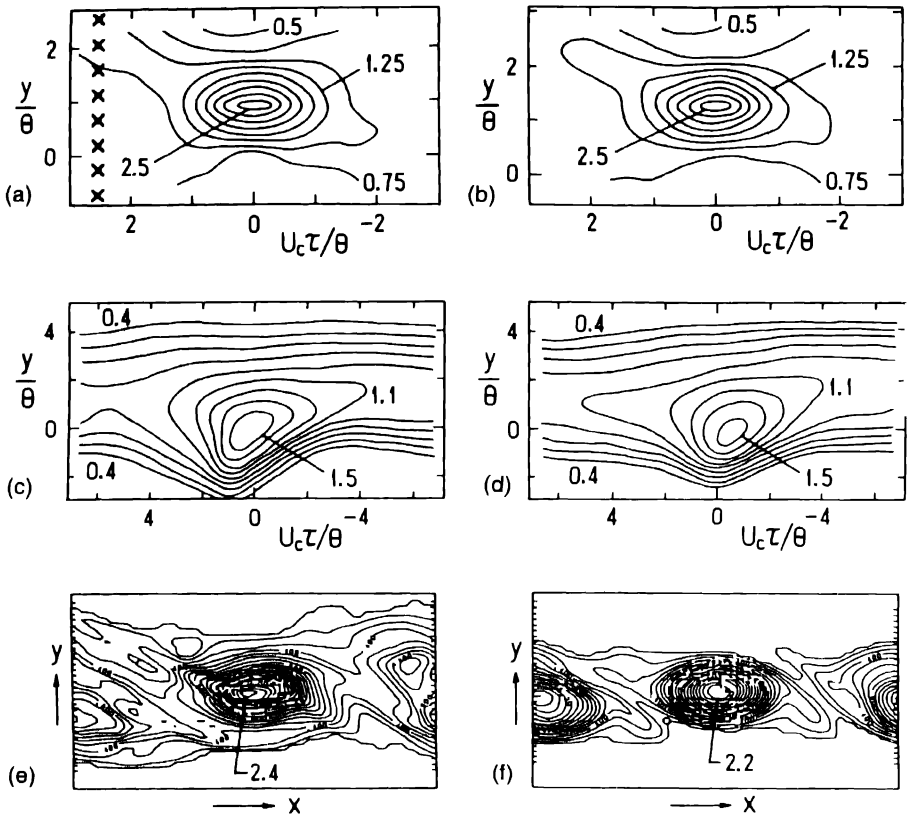
Fig. 12.   Plane mixing layers: $\langle \omega_z \rangle$-contours; a) $x/\theta_c = 1000$ and b) $x/\theta_e = 2000$ (vorticity-based detection; Ref. [32]); c) $x/\theta_e = 600$ and d) $x/\theta_e = 4800$ (point-trigger detection; Ref. [33]); e) naturally evolving case and f) weakly forced (direct numerical simulation; Ref. [32]).

The results are shown in Figs 12(a,b), where coordinates are made dimensionless with the local momentum thickness θ. The two $\langle \omega_z \rangle$ patterns are quite similar in both the geometry and the peak value, in accordance with the self-similar development of the mean velocity field. The structures have a streamwisely elongated shape with protrusions at the front and back portions. It is noted again that while the detection criteria were common to the two x stations (in terms of the local flow variables), the eduction scheme is capable to preserve different structure features if they were.

Under nearly the same experimental condition, Hussain and Zaman [33] educed coherent structures by using u fluctuations at the high-speed edge of the layer as a trigger signal. Their results are shown in Figs 12(c,d), which look apparently different from Figs (a,b). In particular, the $\langle \omega_z \rangle$ contours on the high-speed side show

a bulgy appearance. The reason may be that the detection made at a distance from the center of event tends to yield ensemble-averaged flow properties exaggerated toward the trigger location and to distort their real distributions.

Another relevant information was provided by Metcalfe and Menon [32]. They applied an eduction scheme similar to the present one to their 3D direct numerical simulation data of a mixing layer, which evolves in time from an initial condition with random fluctuations. The Reynolds number of the simulated flow is roughly two-order in magnitude lower than that of the laboratory data discussed above. Because of the limited flow range and periodic boundary condition in the x direction, the ensemble average was obtained by taking data at successive spanwise planes as separate realizations. Results thus obtained are shown in Figs 12(e,f): one for a naturally evolving case (e) and the other for a weakly excited case (f).

In spite of several differences existing between the experimental and simulated flow conditions, the vorticity contour patterns in Figs 12(e,f) remarkably resemble those of our experimental data (Figs 12a,b) in their peak value and geometry, including the protrusions at the front and back of structures. This good correspondence suggests a possibility that the cross-sectional shape of typical structures in the turbulent plane mixing layer does not depend on the local Reynolds number (see also Panides and Chevray [34]).

3.4. OTHER APPLICATIONS

For plane shear flows, the X-wire rake technique can be readily extended to measurements of the transverse vorticity component ω_y, by rotating X probes by 90° and aligning them in the spanwise direction. This probe arrangement has been employed in order to study three-dimensional aspects of the intermediate wake by us [35] and of the far wake by Antonia and Bisset [36].

The experimental condition in the former case was identical with that mentioned in §3.2, and the number of X-probes used was again eight. A pseudo-instantaneous $\tilde{\omega}_y$ map at $x/d = 20$ is shown in Figure 13. There are frequent occurrences of $\tilde{\omega}_y$ concentration, whose scale and strength are comparable with those of spanwise vorticity concentrations (see Fig. 3a). It is interesting to note that $\tilde{\omega}_y$ patches often exhibit a paired pattern with opposite-signed circulations, as marked by dotted lines in Figure 13. This vorticity map suggests the emergence of three-dimensional organized structures in the moderately near wake region. Similar $\tilde{\omega}_y$ distributions were also observed at $x/d = 40$ ([35]). In this connection, the pattern recognition analysis of Ferré and Giralt [37] revealed that "rollers eddies", which are known for the far wake ([38]–[40]), occur even at $x/d = 60$. This is qualitatively consistent with our observation.

From simultaneous records of ω_y at seven z locations, we educed three dimensional structures sliced by an x-z plane. The education procedure was basically the same as used for the identification of spanwise structures. The result showed that when $\tilde{\omega}_y$ peaks of one sign were detected at a fixed z location, the ω_y con-
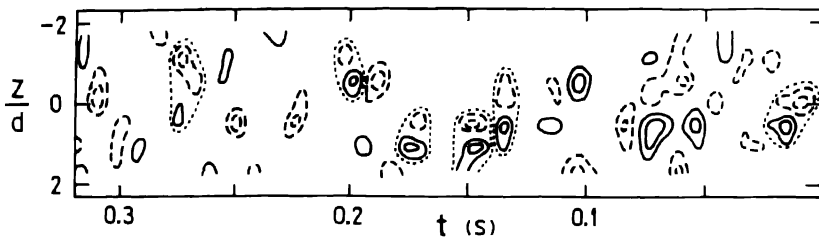
Fig. 13.   Pseudo-instantaneous $\tilde{\omega}_y$ maps in the intermediate wake of a circular cylinder at $x/d = 20$ (Ref. [35]).

centration of the opposite sign preferentially appeared on one side of the detected (i.e., aligned) structure ([35]), suggesting the presence of paired, counter-rotating vortices. However, the peak $\langle\omega_y\rangle$ value of the opposite-signed structure was only about 20 percent of the corresponding value of the detected structure. This indicates that while paired $\tilde{\omega}_y$ patterns are often observed instantaneously, the relative spatial distance between such a pair significantly varies from one realization to another in both the x and z directions, due to various random factors (see [35] for detailed discussion).

In order to gain a further insight into the highly three-dimensional structures, we attempted simultaneous two-plane vorticity measurements [35], in which two parallel rakes were used for measurements of either spanwise or transverse vorticity component at separated two planes (Figure 14a). Two-plane ω_z measurements for several spanwise separations between the rakes (by a probe arrangement A1 in Figure 14a) showed that the typical spanwise extent of nominally two-dimensional vortices at $x/d = 20$ and 40 was roughly $b \sim 2b$; here b is the wake half-width. Similarly, two-plane ω_y measurements were made with various combinations of two rakes spearated in the y direction (by a probe arrangement A2 in Figure 14a). The result showed that the transverse coherence of ω_y concentrations was identifiable over a y range comparable with b but was mainly confined within one side of the wake, and that the most probable orientation of transverse structures with respect to the y axis was about 30°.

As to measurements of three-dimensional structures using multiple hot-wire probes mention is to be made of two recent investigations for the far wake of a circular cylinder. Bisset, Antonia and Britz [41] employed two orthogonal rakes of X probes (coupled with a cold-wire probe in a slightly heated wake) and measured all three components of (large-scale) vorticity at a crossing point of the two rakes (Figure 14b). Ferré, Mumford, Savill and Giralt [42] applied the pattern-matched correlation technique, originally developed by Townsend [43], to velocity fluctuations taken by eight single-wire probes which were aligned either in the y or z direction. These studies shed more light on the relationship between double-roller
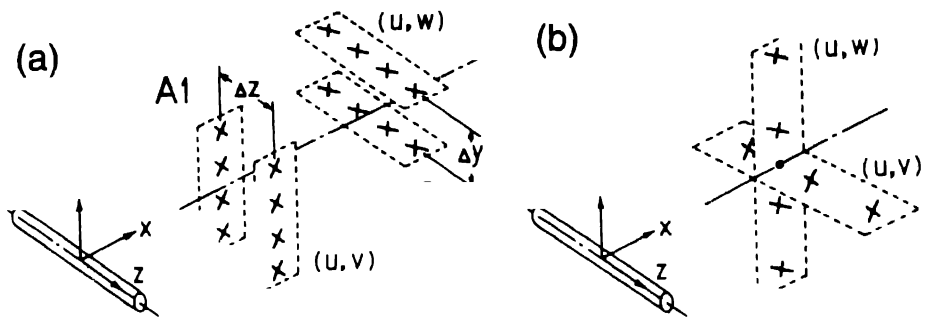
Fig 14   Examles of x-wire rake arrangement used in plane wake studies. a) Parallel rakes (Ref. [35]). b) Orthogonal rakes (Ref. [41]).

and spanwise entrainment structures, an issue that has been a long-pending one since the early studies of Townsend [38], Grant [39] and Payne and Lumley [44].

4. **Advantages and Limitations**

4.1. ADVANTAGES

Major advantageous features of the present technique are summarized below.

(1) The whole procedure involved in the technique relies on an intrinsic flow property (i.e., "vorticity") of organized turbulence structures, and hence it is conceptually self-consistent and objective, provided that those events are presumed to be characterized by spatially correlated vorticity.

(2) Low-pass filtered vorticity maps help us to have a physical perception of vorticity-bearing organized events in a flow more quantitatively than that obtained from conventional flow visualization pictures.

(3) The (approximate) center of each event is directly captured and is used as a phase reference for triggering the ensemble averaging operation. This feature serves the following important merits.

   (a) Effects of jitter are minimal at the educed structure center, affording a sharper decomposition of the ensemble-averaged part and the remained part. This feature is particularly important in order to clarify the relative spatial distributions of large-scale and smaller-scale motions and to infer the mechanisms of entrainment, production and mixing.

   (b) Vortical events can be captured at any transverse/spanwise location, as far as they occur within the extent covered by the X-wire rake. This feature is similar to that of "delocalized conditional sampling" by Bellin, Delville, Vincendeau, Garem and Bonnet [45].

(c) A condition on the sectional shape of structures can be included rather easily in the detection process (at the step III in §2.4), such as $\tilde{\omega}(y_c + \Delta y, t_c + \Delta\tau) > Th_2$ and $\tilde{\omega}(y_c - \Delta y, t_c - \Delta\tau) > Th_2$. Here, an optimum value of $\Delta\tau$ can be determined from the cross-correlation between $\tilde{\omega}(y_c)$ and $\tilde{\omega}(y_c \pm \Delta y, \tau)$. A similar procedure has been employed by Tso [16] for the mode discrimination in the far field jet, as mentioned earlier.

Some recent studies related to the advantages above need to be mentioned here. Instantaneous fields similar to our vorticity maps have been measured by other techniques. Agui and Jimenez [46] obtained the instantaneous spatial distribution of spanwise vorticity in a circular cylinder wake with the aid of a particle-tracking method. Delville, Bellin, Garem and Bonnet [47] visualized instantaneous high shear regions in a plane mixing layer using a rake of 24 single-wire probes coupled with a color-coded image processing technique, called "pseudo flow visualizations" (see also [45]).

Aside from direct numerical simulations, instantaneous 3D field data recently became measurable by novel experimental techniques. Let us mention here only two examples. Kasagi and Nishino [48] improved the 3D particle-tracking velocimetry system using three video cameras set at different viewing angles to a flow, and succeeded in fairly accurate measurements of the three-dimensional velocity field in a turbulent channel flow. Meng and Hussain [49] developed a holographic particle velocimetry for measurements of the velocity vector field in both 3D space and time, and demonstrated its promising capability in some vortical flows.

A good correspondence between low pressure regions and vortical structures has recently received attention both in theoretical and numerical studies (e.g. [50], [51]). Toyoda [52] developed a specially designed small pressure probe and obtained the ensemble average of static pressure in the near field of a circular jet excited at the vortex pairing mode. Vortices undergoing pairing were well identified as the evolution of low pressure regions (see also [53]). Therefore, static pressure can be also a good flow property to characterizing vortical structures. In laboratory experiments, however, multi-point measurements of static pressure, which ought to be required to capture structure centers unambiguously, may not be an easy task.

4.2. LIMITATIONS

Limitations of the present technique are primarily due to the coarse resolution in measurements and the use of Taylor's hypothesis.

(1) The spatial resolution depends on the number of X probes used and on their separation relative to the thickness of a shear layer.

   (a) Measurements of thin shear layers are difficult, unless specially designed miniature probes are available.

   (b) Vorticity concentrations smaller in size than the probe separation escape the measurement.

(c) The transverse scale of identifiable events must be larger than $2\Delta s$, because otherwise, the center of events cannot be detected properly, except in the case that the transverse location of the centers is well fixed, say, via artificial excitation.

(d) Calculated instantaneous vorticity values are crude approximation to the actual values. Vorticity estimated from a coarse resolution measurement (containing a spatial-filter function) may not be identical with filtered vorticity computed from the data of a finer resolution measurement.

(e) Use of a larger number of probes requires a large capacity of laboratory computer along with a sufficiently high speed A/D conversion system for the acquisition and analyses of data, and hence it costs much.

(2) The use of Taylor's hypothesis is unavoidable, since measurements are made at a fixed streamwise station. Note that the conversion of data from t to x, based on a constant convection velocity, is used in both the vorticity computation and the calculation of ensemble averages.

(a) Any information about the spatial evolution of structures is limited within a short duration around a given instant.

(b) Measurements in regions where structures are undergoing rapid evolution or interaction, such as vortex paring, may include significant error.

(c) The applicability of Taylor's hypothesis, based on the structure celerity, to smaller-scale motions may be questionable, but is generally hard to be evaluated.

(3) The process of conditioning involves subjectivity. Choice of thresholds in discriminating the strength and size of structures includes arbitrariness, and the number of selected events depends on the thresholds used.

With regard to the limitations listed above, some comments are necessary. Our experience, based on the use of a rake of 8 X-probes, has indicated that the spatial resolution is not necessarily a serious problem. Through a preliminary survey of instantaneous vorticity maps, we can choose a suitable probe arrangement to identify representative structures in the flow considered.

Vorticity fluctuations, whose scales are at least larger than the probe spacing, seem to be estimated reasonably well, as would be inferred from several examples presented in this paper. Moreover, velocity signals at N y locations contain spectral contents up to the Nyquist frequency of data sampling. Therefore the resolution of ensemble-averaged quantities through data interpolation is about a half the probe spacing, to the first-order approximation. For the time-to-space conversion of data, we have used the average streamwise celerity of structure centers, which was iteratively determined so as to be equal to the ensemble-averaged u component at the educed structure center. The pertinence of this choice for isolated structures was validated by Zaman and Hussain [54]. They warned, however, that when structure interactions like vortex pairing are involved, no convection velocity can be found

with which Taylor's hypothesis works well. In such a case, phase-locked spatial measurements without use of the hypothesis appear to be a better approach, as was done by many investigators (e.g. [55]–[58]).

Arbitrariness involved in the process of conditioning is a common problem in any conditional sampling techniques. In the present case, the arbitrariness corresponds to our judgement in selecting the events of 'similar' characteristics. Such subjectivity is unavoidable to some extent, as far as we try to extract dominant structures in turbulent shear flows.

Finally, it may be worth mentioning that the generic usefulness of the present eduction scheme has been confirmed in the numerical simulations of a plane mixing layer ([32]) and a thick flat plate wake ([59]), where there is no concern about the limitations due to the spatial resolution and Taylor's hypothesis.

5. Closing Remarks

The vorticity-based conditional sampling technique using a rake of multiple X-wire probes has been outlined, and its effectiveness has been demonstrated through several examples.

Since recent progress in the laboratory technology has made it easier to employ a larger number of the probes simultaneously ([60]–[62]), it is not currently difficult to perform the rake measurement which is more resolvable and accurate than the one presented in this paper. However the present approach may not be easily extended to the measurement of all three components of vorticity at multiple points in a flow, which is obviously desired to unveil the topology and dynamics of essentially three-dimensional organized structures in turbulence. While accurate measurements of three vorticity components at a point has become possible owing to the development of miniature vorticity probes (e.g. [63], [64]), the simultaneous use of the probes at many points in a flow is still beyond the current laboratory technology.

These problems in hot-wire probe measurements will be conquered by newly developing methods, such as 3D particle-tracking velocimetry ([49]), holographic particle velocimetry ([50]), NMR imaging velocimetry ([65]) and scalar imaging velocimetry ([66]); all these methods have an excellent capability in acquiring instantaneous 3D vector field data. However, even if a massive amount of 3D data are taken through the novel experimental techniques as well as direct numerical simulations, it is crucial how to focus on dynamically significant flow events in the flow considered and how to extract them with some least subjective means. It seems to us that "vorticity" should be a primarily important flow property to observe for that purpose. This has been a basic concept in the vorticity-based conditional sampling technique.

Acknowledgement

References

1. Roshko, A., Structure of turbulent shear flows: a new look. *AIAA J.* 14 (1976) 1349–1357.
2. Cantwell, B.J., Organized motion in turbulent flow. *Ann. Rev. Fluid Mech.* 13 (1981) 457–515.
3. Hussain, A.K.M.F., Coherent structures and turbulence. *J. Fluid Mech.* 173 (1986) 303–356.
4. Fiedler, H.E., Coherent structures. *Advances in Turbulence* I (ed. G. Comte-Bellot and J. Mathieu) (1987) 320–336.
5. Proc. IUTAM Symp., *Eddy Structure Identification in Fee Turbulent Shear Flows*. Poitiers (1992). See also, *Fluid Mechanics and Its Application* 21 (ed. J.P. Bonnet and M.N. Glauser). Kluwer Acad. Pub. (1993).
6. Kaplan, R.E., Conditioned sampling technique. *Turbulence in Liquids* (1973) 274–283. Univ. Missouri-Rolla.
7. Van Atta, C.W., Sampling techniques in turbulence measurements. *Ann. Rev. Fluid Mech.* 6 (1974) 75–91.
8. Antonia, R.A., Conditional sampling in turbulence measurement. *Ann. Rev. Fluid Mech.* 13 (1981) 131–156.
9. Hunt, J.C.R., Studying turbulence using direct numerical simulation: 1987 Center for Turbulence Research NASA Ames/Stanford Summer Programme. *J. Fluid Mech.* 190 (1988) 375–392.
10. Blackwelder, R.F., On the role of phase information in conditional sampling. *Phys. Fluids* 20 (1977) S232–S242.
11. Sato, H., Cognition and description of patterns in turbulent flows. *Proc. 2nd Asian Congr. Fluid Mech.* (ed. T. Deyan). Science Press, Beijing (1983).
12. Yule, A.J., Phase scrambling effects and turbulence data analysis. *Turb. Shear Flows* 2 (1979) 263–281.
13. Hussain, A.K.M.F., Coherent structures – reality and myth. *Phys. Fluids* 26 (1983) 2816–2850.
14. Hussain, A.K.M.F., Coherent structures and studies of perturbed and unperturbed jets. *Lecture Notes in Physics* 136 (1980) 252–291.
15. Laufer, J., New trends in experimental turbulence research. *Ann. Rev. Fluid Mech.* 7 (1975) 307–326.
16. Tso, J., Organized structures in the far field of a circular jet. Ph.D. Thesis. Johns Hopkins Univ., Baltimore (1983). See also, Tso, J. and Hussain F., Organized motions in a fully developed turbulent axisymmetric jet. *J. Fluid Mech.* 203 (1989) 425–448.
17. Hayakawa, M. and Hussain, A.K.M.F., Eduction of coherent structures in the turbulent plane wake. *Proc. 5th Symp. Turb. Shear Flows*, Cornell Univ. (1985) 4.33–4.37.
18. Hayakawa, M. and Hussain, A.K.M.F., 1984 (unpublished data).
19. Hussain, A.K.M.F. and Zaman, K.B.M.Q., The 'preferred mode' of the axisymmetric jet. *J. Fluid Mech.* 110 (1981) 39–71.
20. Batchelor, G.K. and Gill, A.E., Analysis of the stability of axisymmetric jets. *J. Fluid Mech.* 14 (1962) 529–551.
21. Chua, L.P. and Antonia, R.A., Spatial organization of large structures in the near-field of a circular jet. *Fluid Dyn. Res.* 9 (1992) 59–71.
22. Komori, S. and Ueda, H., The large-scale coherent structures in the intermittent region of the self-preserving round jet. *J. Fluid Mech.* 152 (1985) 337–359.

23. Hussain, A.K.M.F. and Hayakawa, M., Eduction of large-scale structures in a turbulent plane wake. *J. Fluid Mech.* 180 (1987) 193–229.
24. Davies, M.E., A comparison of the wake structure of a stationary and oscillating bluff body, using a conditional sampling technique. *J. Fluid Mech.* 75 (1976) 209–231.
25. Cantwell, B. and Coles, D., An experimental study of entrainment and transport in the turbulent near weke of a circular cylinder. *J. Fluid Mech.* 136 (1983) 321–374.
26. Kiya, M. and Matsumura, M., Turbulence structure in the intermediate wake of a circular cylinder. *Bull. JSME* 28 (1985) 2617–2624.
27. Armstrong, B.J. and Barnes, F.H., A comparison of the structure of the wake behind a circular cylinder in a steady flow with that in a perturbed flow. *Phys. Fluids* 30 (1987) 19–26.
28. Kiya, M. and Matsumura, M., Incoherent turbulence structure in the near wake of a normal plate. *J. Fluid Mech.* 190 (1988) 343–356.
29. Zhou, Y. and Antonia, R.A., Convection velocity measurements in a cylinder wake. *Exps. Fluids* 13 (1992) 63–70.
30. Bisset, D.K., Antonia, R.A. and Browne, L.W., Spatial organization of large structures in the turbulent far wake of a cylinder. *J. Fluid Mech.* 218 (1990) 439–461.
31. Wygnanski, I., Champagne, F. and Marasli, B., On the large-scale structures in two-dimensional, small-deficit, turbulent wakes. *J. Fluid Mech.* 168 (1986) 31–71.
32. Metcalfe, R.W., Hussain, A.K.M.F., Menon, S. and Hayakawa, M., Coherent structures in a turbulent plane mixing layer: a comparison between direct numerical simulations and experiments. *Turb. Shear Flows* 5 (1987) 110–123.
33. Hussain, A.K.M.F. and Zaman, K.B.M.Q., An experimental study of organized motions in the turbulent plane mixing layer. *J. Fluid Mech.* 159 (1985) 85–104.
34. Panides, E. and Chevray, R., Vortex dynamics in a plane, moderate-Reynolds-number shear layers. *J. Fluid Mech.* 214 (1990) 414–435.
35. Hayakawa, M. and Hussain, F., Three-dimensionality of organized structures in a plane turbulent wake. *J. Fluid Mech.* 206 (1989) 375–404.
36. Antonia, R.A. and Bisset, D.K., Three-dimensional aspects of the organized motion in a turbulent boundary layer. *Turbulence and Coherent Structures* (eds M. Lesieur and O. Metais), (1989) 1–17.
37. Ferré, J.A. and Giralt, F., Pattern-recognition analysis of the velocity field in plane turbulent wakes. *J. Fluid Mech.* 198 (1989) 27–64.
38. Townsend, A.A., The Structure of Turbulent Shear Flow. Cambridge Univ. Press. (1956).
39. Grant, H.L., The large eddies of turbulent motion. *J. Fluid Mech.* 4 (1958) 149–190.
40. Mumford, J.C., The structure of the large eddies in fully developed turbulent shear flows: Part 2 The plane wake. *J. Fluid Mech.* 137 (1983) 447–190
41. Bisset, D.K., Antonia, R.A. and Britz, D., Structure of large-scale vorticity in a turbulent far wake. *J. Fluid Mech.* 218 (1990) 463–482.
42. Ferré, J.A., Mumford, J C., Savill, A.M. and Giralt, F., Three-dimensional large-eddy motions and fine-scale activity in a plane turbulent wake. *J. Fluid Mech.* 210 (1990) 371–414.
43. Townsend, A.A., Flow patterns of large eddies in a wake and in a boundary layer. *J. Fluid Mech.* 95 (1979) 515–537.
44. Payne, F.R. and Lumley, J.L., Large eddy structure of the turbulent wake behind a circular cylinder. *Phys. Fluids* 10 (1967) S194–S196.
45. Bellin, S., Delville, J., Vincendeau, E., Garem, J.H. and Bonnet, J.P., Large scale structure characterization in a 2D mixing layer by pseudo-flow visualization and delocalized conditional sampling. In Ref. [5], (1992) V.2.1.–2.8.
46. Agui, J.C. and Jimenez, J., On the performance of particle tracking. *J. Fluid Mech.* 185 (1987) 447–468.
47. Delville, J., Bellin, S., Garem, J.H. and Bonnet, J.P., Analysis of structures in a turbulent, plane mixing layer by use of a pseudo flow visualization method based on hot-wire anemometry. *Advances in Turbulence* 2 (eds H.H. Fernholz and H.E. Fiedler) (1989) 251–256.
48. Kasagi, N. and Nishino, K., Probing turbulence with three-dimensional particle-tracking velocimetry. *Exp. Thermal Fluid Sci.* 4 (1991) 601–612.
49. Meng, H. and Hussain, F., Holographic particle velocimetry: a 3D measurement technique for vortex interactions, coherent structures and turbulence. *Fluid Dyn. Res.* 8 (1991) 33–52.

50. Larcheveque, M., Velocity field, vorticity field, pressure field and coherent structures. In Ref. [5] (1992) VII.11.1–11.5.
51. Sandham, N.D. and Reynolds, W.C., Three-dimensional simulations of large eddies in the compressible mixing layer. *J. Fluid Mech.* 224 (1991) 133–158.
52. Toyoda, K. and Hussain, F., Eduction of vortical structures in a circular jet by pressure measurements. *Proc. 5th Asian Congr. Fluid Mech.* 1 (1992) 587–591.
53. Toyoda, K. and Shirahama, Y., Eduction of vortical structures by pressure measurements in noncircular jets. In Ref. [5] (1992) VII.2.1–2.5.
54. Zaman, K.B.M.Q. and Hussain, A.K.M.F., Taylor hypothesis and large-scale coherent structures. *J. Fluid Mech.* 112 (1981) 379–396.
55. Browand, F.K. and Weidman, P.D., Large scales in the developing mixing layer. *J. Fluid Mech.* 76 (1976) 127–144.
56. Zaman, K.B.M.Q. and Hussain, A.K.M.F., Vortex pairing in a circular jet under controlled excitation. Part 1. General jet response. *J. Fluid Mech.* 101 (1980) 449–491.
57. Wygnanski, I. and Weisbrot, I., On the pairing process in an excited plane turbulent mixing layer. *J. Fluid Mech.* 195 (1988) 161–173.
58. Husain, H.S. and Hussain, F., Elliptic jets Part 2. Dynamics of coherent structure: pairing. *J. Fluid Mech.* 233 (1991) 439–482.
59. Jeong, J. and Grinstein, F.F., Eduction of coherent structures in a numerically simulated plane wake. In Ref. [5] (1992) V.4.1–4.5.
60. Delville, J., Characterization of the organization in shear layers via proper orthogonal decomposition. In Ref. [5] (1992) VI.1.1–1.8
61. Zhou, Y. and Antonia, R.A., A study of flow properties near critical points. In Ref. [5] (1992) IX.2 1–2.6.
62. Albanis, N., Husain, H.S. and Hussain, F., (private communication) (1992).
63. Vukoslavcevic, P., Wallace, J.M. and Balint, J.L., The velocity and vorticity vector fields of a turbulent boundary layer. Part 1. Simultaneous measurement by hotwire anemometry. *J. Fluid Mech.* 228 (1991) 25–51.
64. Tsinober, A., Kit, E. and Dracos, T., Experimental investigation of the field of velocity gradients in turbulent flows. *J. Fluid Mech.* 242 (1992) 169–192.
65. Kose, K., Instantaneous flow distribution measurements of the equilibrium puff in a circular pipe using NMR imaging. *Phys. Rev. A* 44 (1991) 2495–2504.
66. Dahm, W.J.A., Su, L.K. and Southerland, K.B., A scalar imaging velocimetry technique for fully resolved four-dimensional vector velocity field measurements in turbulent flows. *Phys. Fluids A* 4 (1992) 2191–2206.

Eduction of Coherent Structures in a Numerically Simulated Plane Wake

J. JEONG[1], F. F. GRINSTEIN[2] and F. HUSSAIN[1]
[1] *Department of Mechanical Engineering, University of Houston, TX 77204-4792, U.S.A.*
[2] *Naval Research Laboratory, Code 6410, Washington, D.C., U.S.A.*

Abstract. Coherent structures (CS) are educed using a conditional sampling technique involving alignment of vorticity patches of largest size and strength; hence we educe dominant CS. A numerically simulated spatially evolving wake of a thick flat plate is used as the database, and the inflow condition for the simulated wake includes random velocity perturbations which emulate turbulent conditions at a plate exit in the laboratory. In addition to previously educed properties such as coherent vorticity and production, and incoherent Reynolds stress and turbulence intensity, other measures such as coherent pressure and passive scalar distributions are also studied. In spite of the geometry difference, the near-wake dynamics of the plate seem quite similar to that of a cylinder. For example, turbulence is mostly produced by vortex stretching of the ribs at the saddle and then advected to the structure center, where it accumulates, and is balanced by incoherent dissipation. The distribution of coherent passive scalar indicates that mixing occurs in the saddle regions and that the mixed fluid is advected into the structure center.

1. Introduction

CS in a circular jet and the wake of a circular cylinder were educed previously in laboratory flows using a linear rake of X-wires, which provided spanwise vorticity distribution in a spanwise plane (see [1, 2], the latter referenced as HH). Despite the unavoidable crude transverse resolution of the experimental data, these studies provided significant insights into the geometry and dynamics of CS. In this paper, a database of a spatially evolving flow reported previously by Grinstein et al. [3] (references as GHB) is used to educe CS and evaluate CS properties in more detail as well as other measures, which are difficult to obtain experimentally. Detailed description of the basic flow configuration investigated, as well as the numerical model, gridding and boundary conditions can be found in GHB. The plane-wake system studied involves streams of air initially separated by a thick splitter plate, with free-stream Mach number, $M_\infty = 0.6$, at standard initial temperature and pressure conditions. Initial conditions for the simulated wakes included laminar regimes as in GHB, and wakes for which 3D random velocity perturbations (rms-level 2.5%) were added to the mean free-stream velocity U_∞ to emulate the upstream turbulence in the laboratory experiments.

The numerical model is based on the solution of the unsteady inviscid conservation equations for mass, momentum, and energy of an ideal gas, with appropriate inflow/outflow boundary conditions. A passive scalar c with unity Schmidt number S_c, is advected with the velocity field in order to explore mixing in the flow. It is

initialized by setting its free-stream values as $c = 1$ and $c = -1$ on the two sides of the wake. Characteristic Reynolds numbers (based on U_∞ and d) for the simulated flows in this work were $10^3 \lesssim \text{Re} \lesssim 4 \times 10^4$.

Monotonically-integrated large-eddy-simulation (MILES) approach [4] is used, involving a fourth-order phase-accurate FCT algorithm in conjunction with directional and timestep-splitting techniques on structured grids, in which the FCT nonlinear high-frequency filtering provides the minimal subgrid turbulence model. Relevant convergence studies of MILES scheme have been recently reported, involving FCT-based models in the simulation of 3D periodic round jet [4], and the Piecewise-Parabolic Method (PPM) in turbulence decay studies [5]. Although this numerical scheme solves the Euler equations instead of the full Navier–Stokes equations, numerical viscosity enables us to stimulate the Navier–Stokes equations up to the inertial range of spectrum; thus the small-scale eddies are resolved up to the inertial range. Since the most of energy of smaller scales than the large-scale structures is expected to be contained in the inertial range, the comparison of coherent and incoherent quantities with previous experimental data are justified.

2. Eduction of CS

2.1. EDUCTION PHILOSOPHY

Although our eduction approach in principle applies to the 3D vorticity field, limitation of experimental data forced us so far to use one vorticity component in a 2D plane, namely ω_z in the xy plane. Numerically, eduction of 3D structure based on the easily available 3D vorticity data is quite feasible except that it is computationally prohibitive to obtain 3D instantaneous data for long times. Therefore, in the present case, we educe the 2D structure in the xy plane considering statistical homogeneity in the z direction. The eduction process, in principle, consists of the following steps: (i) choose smoothed spanwise vorticity as a feature that denotes passage of large-scale structures, (ii) select the most dominant ones based on their vorticity magnitude and size, (iii) phase align the accepted structures and obtain their ensemble average, (iv) refine the phase average by an iterative procedure that is based on the cross-correlation of individual realizations (rejecting 'freak' structures) and their ensemble average, and then (v) compute by ensemble averaging relevant coherent and incoherent quantities that are important to the dynamics of the flow from the *unsmoothed* data. Thus, smoothing, used only for identification of structures in the random vorticity field, does not affect any of the educed quantities: coherent or incoherent.

One advantage of our eduction scheme over other eductions of CS, say using POD (proper orthogonal decomposition) or LSE (linear stochastic estimation) is the ability to address the dynamics of physically occurring CS in any flow. This is possible through a conditionally averaged equation derived from the Navier–Stokes equation after decomposing the instantaneous field into coherent and incoherent

parts (see [6]). Another advantage is that the educed incoherent quantities provide information about the dynamics of the small-scale motions, not totally possible in POD or LSE.

2.2. EDUCTION SCHEME

Compared to laboratory experiments, the instantaneous flow field in the simulation is free from limitations such as the effects of probe interference and the highly restrictive Taylor's hypothesis. The computations also have the advantage of being free from errors of hot wire measurements due to high turbulence levels and flow reversal (specially in the near-wake). On the other hand, numerical simulations have limitations as well. The relatively large number of realizations required for the statistical studies, the extremely long times needed for phase-space analysis of the flow variables, and computations of 3D flows at practical Reynolds numbers can become prohibitive [6]. An unavoidable compromise that we were forced to make here was to regard each spanwise section (xy plane) of a roll near the location $x/d = 10$ as a separate realization. This was also done in the eduction of CS in numerically simulated mixing layers by Metcalfe et al. [7].

Since our primary interest in large-scale events, the identification of structures was performed on the smoothed instantaneous spanwise vorticity data which were obtained by local spatial smoothing. In the present case, a nine point averaging (3×3 in an xy plane) was used; this amounts to 8% of the average interval between successive structures. This operation smooths out the fine-scale fluctuations, but retains the underlying large-scale vorticity. Once again, note that all structure properties are finally educed from the unsmoothed data.

The first condition employed by the present eduction scheme is for the structure strength. Based on that, realizations (i.e. vorticity maps in the streamwise-transverse plane) with maximum smoothed ω_z exceeding $2S_M$ (where S_M is the maximum mean shear at $x/d = 10$) are detected at each spanwise plane. The choice of the local S_M for specifying the threshold is justified by the fact that both S_M and the structure strength evolve in x. The second condition is for the structure size. In order to specify this, ω_z is required to be higher than $0.3S_M$ within a distance of $0.25d$ from its peak in the xy plane.

Each realization is then aligned with respect to the peak of ω_z and averaged to obtain the zeroth-order ensemble average. Each realization is then shifted in both x and y directions to maximize its cross-correlation with the zeroth-order ensemble average in order to obtain sharper structure boundaries. This process is iterated until convergence in structure shape is achieved. The purpose of the iteration is to find the underlying, true center of each realization necessary for its optimal alignment before its inclusion for the ensemble averaging. Note that the location of maximum spanwise vorticity can only give a local peak and not the center of the overall structure, which can be obtained from the location of maximum cross-correlation in this study. The domain selected for the cross-correlation is shown in

a)

b)
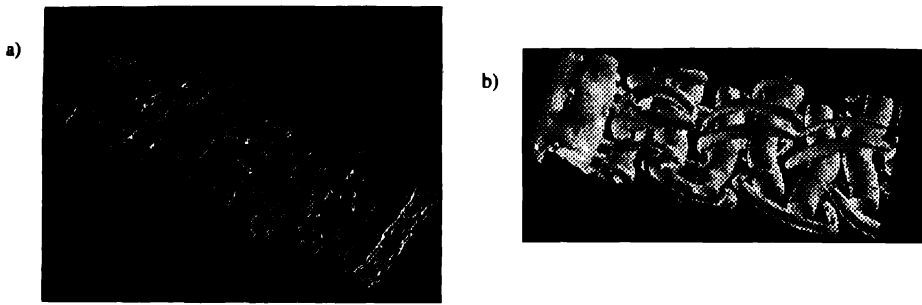
Fig. 1.   Instantaneous visualization of the plane wake perturbed with coherent (sinusoidal) spanwise-excitation; (a) superimposed isosurfaces of ω_z (grid) and ω_x (solid), (b) isosurfaces of Ω.

Fig. 5c. Realizations that produce weak cross-correlation coefficients, here below 0.8, or require shifts more than $0.5d$ were discarded because they are considered to be 'freak', i.e. significantly different from the ensemble-averaged structure. Note that this iteration process is similar to the pattern recognition technique, provided that the zeroth iteration ensemble-average is considered as the trial pattern. Here, the trial pattern is not guessed, but derived from signals themselves. After a new alignment of the realizations through the modified peak locations, the smoothed data are discarded and only the unsmoothed data are used to obtain the final ensemble average. Whatever survives the ensemble average is the coherent structure; the departure of each accepted realized from the average is the incoherent turbulence in that realization. Incoherent turbulence is then rms ensemble averaged to extract its statistical measures over the structure cross-section.

The data presented in this paper are spatial distributions of various phase-averaged quantities; velocities are normalized by the free-stream velocity U_∞, and vorticity and strain rate are normalized by the peak value of $\partial U/\partial y$ at the corresponding x station.

3. Instantaneous Flow Field

Figure 1a shows superimposed isosurfaces of spanwise (grid) and streamwise (solid) vorticity at a level 10% of the peak vorticity magnitude ($\Omega = (\omega_x^2 + \omega_y^2 + \omega_z^2)^{1/2}$) in the computational box; Fig. 1b shows isosurfaces of the vorticity magnitude at the same level as Fig. 1a, but as seen from the opposite side of the wake. The instantaneous visualization in Fig. 2 corresponds to a perspective view of Fig. 1, and shows isosurfaces for the passive scalar, c, associated with the particular values $c = 0$ (solid) and $c = \pm 0.5$ (grid), characterizing regions of large and moderate mixing between the two sides of the wake, respectively.

The vorticity introduced by the spanwise excitation in the transverse and stream-wise directions is deformed, stretched and concentrated in longitudinal ribs as a result of the high strain-rates between rolls. The ribs appear in counter-rotating
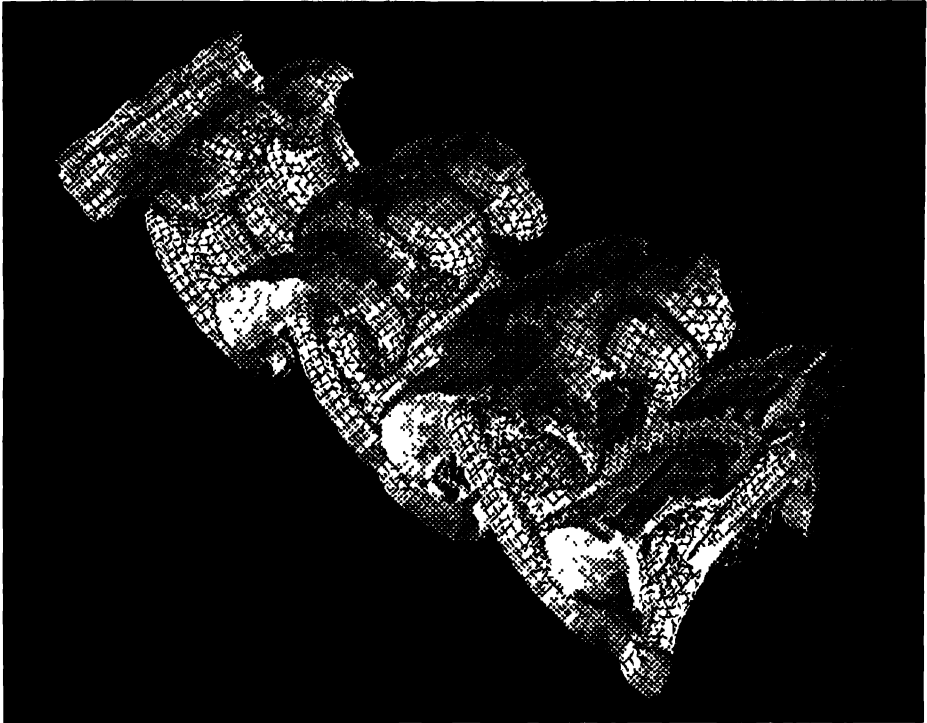
Fig 2   Isosurfaces of the passive scalar c for the structure shown in Fig 1

pairs distinctly superimposed on the rolls and can be initially interpreted as legs of horseshoe vortices

Eduction analysis of the simulated wake shows that when one mode of sinusoidal excitation is used at the inflow, one can find very good agreement with experimental results on the coherent quantities However, basic incoherent properties reported in HH, such as occurrence of peak incoherent turbulence intensity at the spanwise roll centre, are not observed In order to emulate the inflow background turbulence, we imposed random perturbations on the streamwise and cross-stream velocities with a rms-level of 2 5% of the free-stream velocity

A particularly relevant issue is that of the dependence of the flow properties on outflow boundary conditions in the simulation These conditions can trigger formation of rolls through feedback at the inflow boundary. They can also affect the evolution of the rolls directly, when the rolls are close to the outflow boundary. For the flows simulated in the present study, the feedback amplitude level is small compared to the imposed random perturbation level at the inflow boundary Direct effects of the outflow boundary conditions on the structure properties are minimized by choosing the detection location sufficiently far away from the outflow boundary.
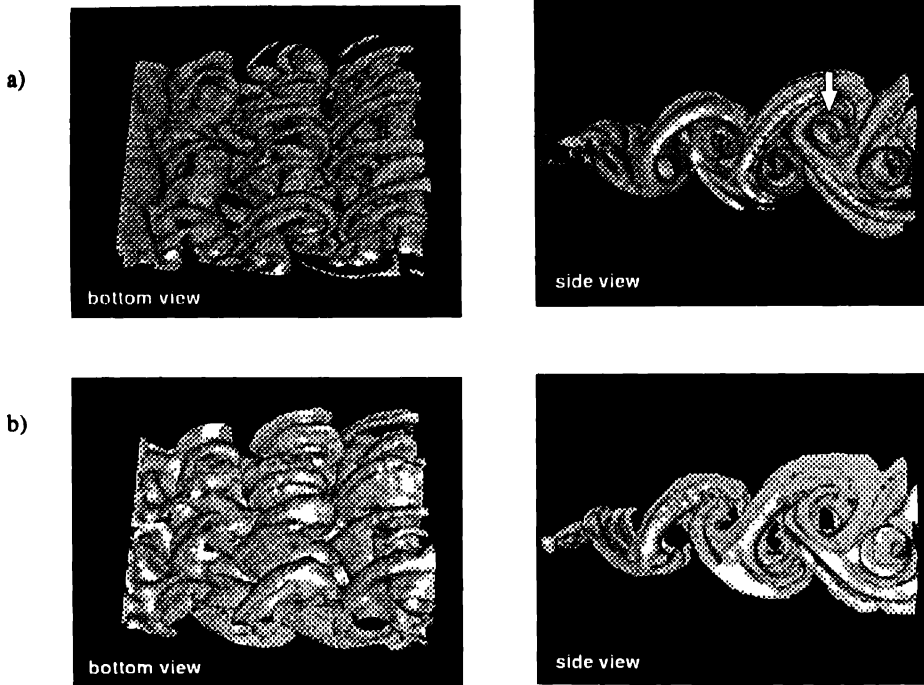
Fig. 3.   Instantaneous visualization of the plane wake perturbed with (incoherent) spanwise-excitation; (a) isosurfaces of Ω, (b) isosurfaces of the passive scalar c.

Figures 3a, b show isosurfaces of the vorticity magnitude and the passive scalar corresponding to the levels $0.1\Omega_{\text{peak}}$ and $c = 0$ for the flow with the inflow conditions discussed above. From these, it is clear that rolls and ribs become much more disorganized as a result of the inflow perturbations.

4. **Educed Flow Field**

To increase the number of realizations available in a typical roll (indicated by an arrow in Fig. 3a), we consider spanwise planes of five successive structures captured near $x/d = 10$. This yields about six hundred realizations. Of these, half were rejected during iterative selection process, and the remaining half were optimally aligned before final ensemble-averaging. Figure 4 shows $\langle u - U_c \rangle$, $\langle v \rangle$, $\langle \omega_z \rangle$, $\langle S_{xy} \rangle$ in the xy plane. In all the figures, the circle denoting the contour level at 10% of the peak $\langle \omega_z \rangle$ (Fig. 4c) serves as the common references. The corresponding results obtained using one mode of sinusoidal spanwise excitation (not shown), have distributions quite similar to those in Fig. 4, indicating that the selection of the perturbation has little effect on these quantities. The distributions of $\langle u - U_c \rangle$, $\langle v \rangle$, $\langle \omega_z \rangle$ and $\langle S_{ij} \rangle$ shown here are quite similar to those obtained by
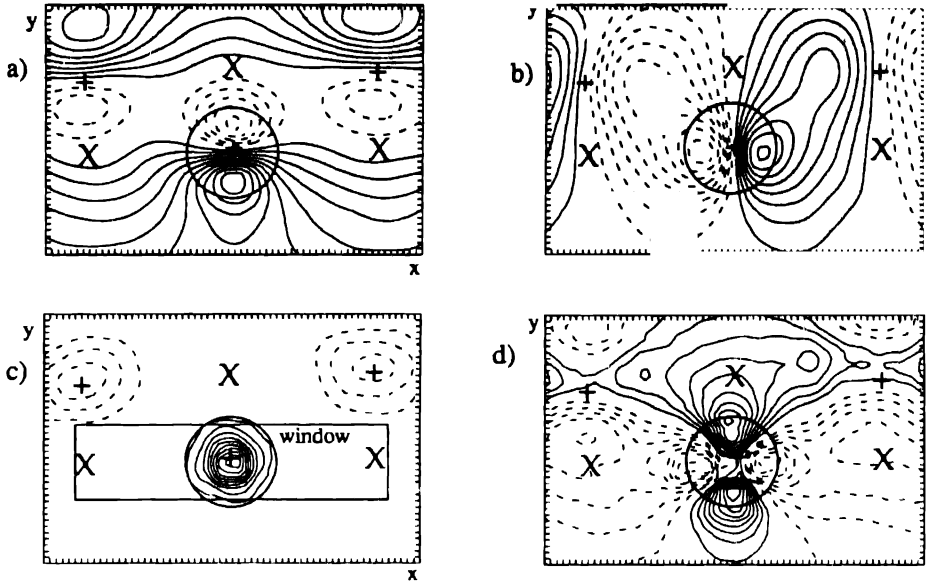
Fig 4   Educed structure properties, the structure boundary is indicated by a circle; (a) $\langle u - U_c \rangle$, (b) $\langle v \rangle$, (c) $\langle \omega_z \rangle$, (d) $\langle S_{xy} \rangle$

HH in a cylinder wake. For references, we marked the vortex center and the saddle by '+' and '×', respectively,

Due to the ribs, peaks of $\langle \omega_x^2 \rangle$ (Fig. 5a) occur in the saddle region and coincide with those of incoherent Reynolds stress (Fig. 5b). There is also significant $\langle \omega_z^2 \rangle$ at the center of the CS due to the undulation of the rolls. The ratio of $\langle \omega_x^2 \rangle$ to $\langle \omega_z \rangle^2$ is about 20%. There exists also significant incoherent ω_z at the center of CS (Fig. 5c) due to the presence of small scales within the core of CS. It can be argued that the incoherent Reynolds stress in Fig. 5b is produced by the induced motion of the ribs (intermediate-scale CS) as seen in Fig. 5d, and that ribs connect CS with opposite signs of ω_z (Fig. 5a). The coherent shear production also shows peaks near the saddle because of the large incoherent Reynolds stress and shear strain in those regions (Fig. 5d). Thus, the mechanisms of turbulence production in the wake of the flat plate is the same as that in the cylinder wake (HH), namely vortex stretching of ribs by the shear strain caused by adjacent rolls. The incoherent turbulence along the ribs is apparent in Fig. 5e; however, most of the incoherent turbulence occurs at the structure center, implying that incoherent turbulence produced at the saddle is transported to the center of the structure (see [2, 8]) and is accumulated there.

Coherent pressure $\langle p - p_0 \rangle$, where p_0 is the free-stream pressure, has a negative peak at the structure center and has positive value at the saddle, as expected (Fig. 5f). This suggests that the pressure signal can be used for the detection of the roll. The advantage of using the pressure signal is that it is invariant under
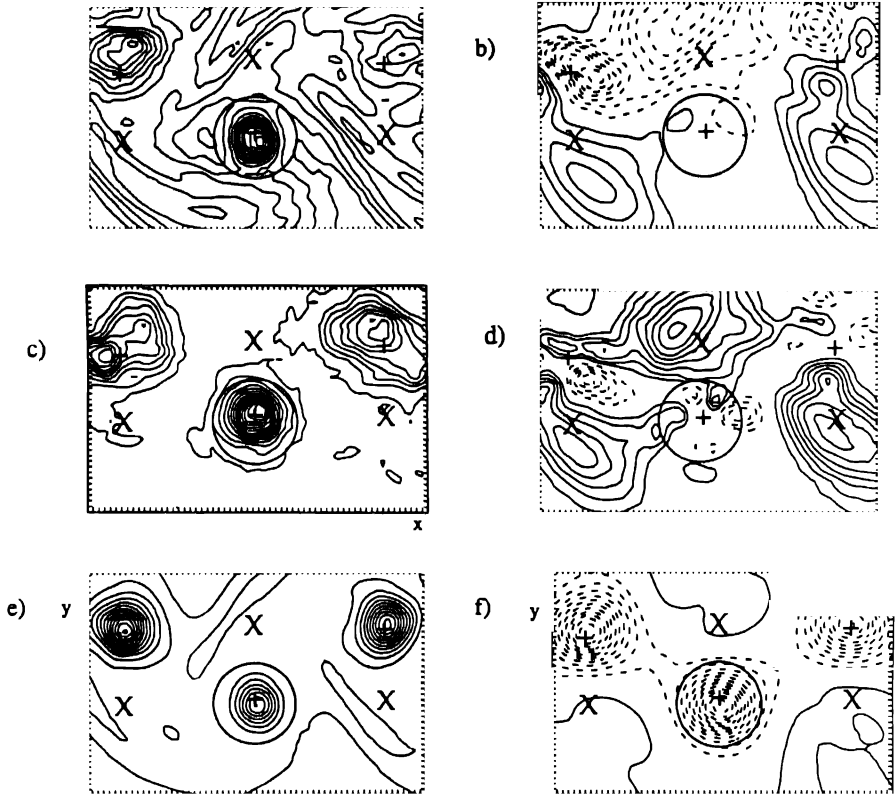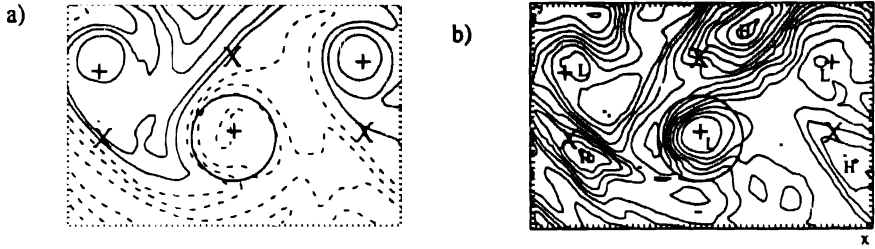
Fig. 5.   Educed structure properties; the structure boundary is indicated by a circle; (a) $\langle \omega_x^2 \rangle$, (b) incoherent Reynolds stress $\langle u_r v_r \rangle$, (c) $\langle \omega_z^2 \rangle$, (d) coherent shear production $P_s = -2\langle u_r v_r \rangle \langle S_{xy} \rangle$, (e) incoherent turbulent kinetic energy $\langle u_r^2 + v_r^2 \rangle$, (f) coherent pressure $\langle p - p_0 \rangle$.

any coordinate transformation, and that the negative peak pressure at the structure center is proportional to the circulation of the structure, so that one can directly detect the large-scale structure from it [9]. However, the pressure is high in the saddle region and locally drops in the ribs. Therefore, if the circulation of the ribs is not high enough, the pressure drop is not sufficient for their detection [10]. Note that the ribs can be easily detected using $(\omega_x^2 + \omega_y^2)$ even when they do not have circulation comparable to that of the rolls. Therefore, vorticity magnitude allows the identification of both CS and dynamically relevant ribs.

The coherent passive scalar level $\langle c \rangle$ (Fig. 6a) has large gradients in the neighborhood of the saddle region, reflecting that scalar mixing is the largest there. This is expected because passive scalars from the two sides of the wake are advected into the saddle region, and the interface between them is increased by rib-induced flow. Clearly, $|\langle c \rangle| = 0$ on the interface separating the two fluids on the two sides

a)

b)

x

Fig. 6   Educed structure properties; the structure boundary is indicated by a circle; (a) coherent passive scalar $\langle c \rangle$, (b) incoherent passive scalar $\langle c_r^2 \rangle$; 'L' and 'H' denote local minima and maxima respectively

primary mixing $\Longrightarrow$ advection of unmixed passive scalar

secondary mixing $\cdots\blacktriangleright$ advection of partially mixed passive scalar
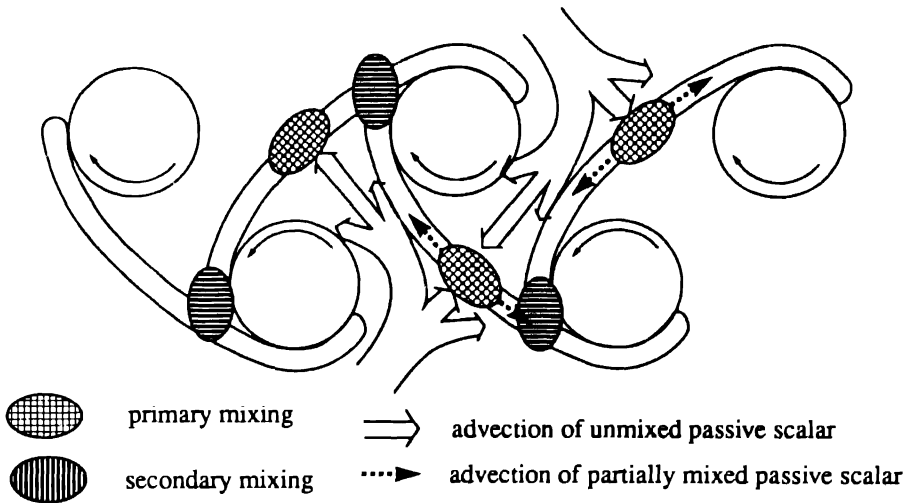
Fig. 7.   Conceptual model of turbulent mixing.

of the wake. However, a region of $|c| \ll 1$ would also indicate mixing by cross diffusion; while a region of $|\langle c \rangle| \ll 1$ may indicate both stirring and mixing, only $\langle c^2 \rangle$ would indicate a measure of mixing. Regions of local minimum of $|\langle c \rangle|$ are found to occur at the structure centers. Contours of incoherent passive scalar $\langle c_r^2 \rangle$ (Fig. 6b) have minimum values in the structure centers, showing that the core fluid is indeed mixed. Minimum coherent passive scalar occurs at the structure center essentially due to turbulent diffusion.

The above discussion on the passive scalar and turbulence properties suggests a conceptual model for turbulent mixing as shown in Fig. 7. Roll-induced motion advects the unmixed passive scalar from two sides of the wake into the saddle region as well as towards the rib-roll contact region. In the saddle region, mixing starts due to further stretching of the scalar interface by rib-induced motion; at the rib-roll interface, mixing starts due to interactions between ribs and rolls. The

partially mixed scalar is then advected to the structure center, where mixing is completed by the high turbulence there.

5. Conclusion

Random velocity fluctuations at the inflow boundary in the numerical simulation are necessary for the incoherent properties to be consistent with laboratory experimental data. The mechanism of turbulence production and the behavior of incoherent turbulence in a flat-plate wake is essentially the same as in a cylinder wake; i.e. turbulence is produced at the saddle and is advected into the structure center where it accumulates. However, the incoherent passive scalar shows a minimum at the structure center. Mixing of the passive scalar starts in the saddle region and the rib-roll contact region and is completed at the structure center by high level turbulence.

Acknowledgements

References

1. Tso, J. and Hussain, F., *J. Fluid Mech.* 203 (1989) 425.
2. Hussain, F. and Hayakawa, M., *J. Fluid Mech.* 180 (1987) 193.
3. Grinstein, F.F., Hussain, F. and Boris, J.P. In: A.V. Johansson and P.H. Alfredsson (eds), *Advances in Turbulence 3*. Berlin: Springer-Verlag (1991), pp. 34–41.
4. Boris, J.P., Grinstein, F.F., Oran, E.S. and Kolbe, R.J., *J. Fluid Dyn. Res.* 10 (1992) 199–228.
5. Porter, D.H., Pouquet, A. and Woodward, P.R., *Theoretical and Computational Fluid Dynamics* 4 (1992) 13–49.
6. Hussain, F., *Phys. Fluids* 26(10) (1983) 2816.
7. Metcalfe, R.W., Hussain, F., Menon, S. and Hayakawa, M. In: F. Durst et al. (eds), *Turbulent Shear Flows 5*. Berlin: Springer-Verlag (1985) pp. 110–123.
8. Hussain, F. and Zaman, K.B.M.Q., *J. Fluid Mech.* 110 (1981) 39.
9. Robinson, S.K., Ph.D. Dissertation (1991).
10. Jeong, J., Ph.D. Dissertation (1994).

Eduction of Vortical Structures by Pressure Measurements in Noncircular Jets

K. TOYODA, T. OKAMOTO and Y. SHIRAHAMA
Department of Mechanical Engineering, Hokkaido Institute of Technology, Sapporo 006, Japan

Abstract. Vortical structures in the noncircular jets excited at the interaction mode were educed by measuring fluctuating static pressure, and their characteristics were discussed in relation to the mixing mechanism of the noncircular jets. The contours of phase-average fluctuating pressure show clearly the vortical structures of the noncircular jets, which compare reasonably with those observed by the flow visualization experiments. The evolution of the vortical structures is characterized by partial merging, stretching and splitting to smaller vortices. The effects of the noncircular vortical structures on mixing were also discussed based on the quantitative measurements of the velocity fields, the results suggesting that the interactions of vortical structures in the noncircular jets are very effective to enhance mixing.

1. Introduction

The existence of coherent structures has been noted as a key feature of turbulent shear flows, and many research works have been done on the structures. In the experimental works, it is crucial to educe coherent structures; previous works suggest that vorticity is a useful measure to educe coherent structures which are closely related to vortex motions [1]. However, the educed results involve serious errors due to the structure 'jitter' and to the differential operation required in the vorticity measurements.

It is well known that the vortical structures are closely related to the pressure fluctuations, which show direct footprints of the vortical structures better than the velocity fluctuations [2]. Indeed the results of direct numerical simulation reveal that the low-pressure regions correspond to the vortical structures [3]. Thus the detailed pressure measurements in the turbulent shear flows are expected to give us useful information on the vortical structures. Moreover the pressure fluctuations are very important in view of the noise-generating mechanism related to the vortical structures [4]. Although a significance of the pressure fluctuations has been pointed out, there have been few works on the direct pressure measurements which are usually attended with serious errors due to disturbance by a pressure probe inserted in the flow. The authors have developed a probe to measure the fluctuating static pressure in the turbulent flows [5], and confirmed that the direct pressure measurements with the probe were very effective to educe the large-scale vortical structures in a circular jet [6].

Use of noncircular jets has been noted as a useful technique to control jet mixing. It is suggested that the mixing enhancement in noncircular jets is owing to the
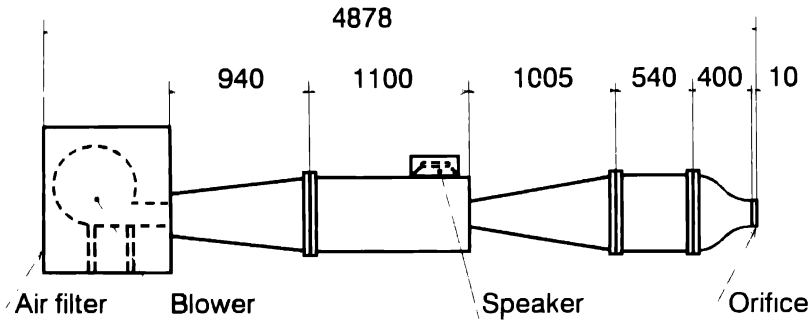
Fig. 1. Wind tunnel.
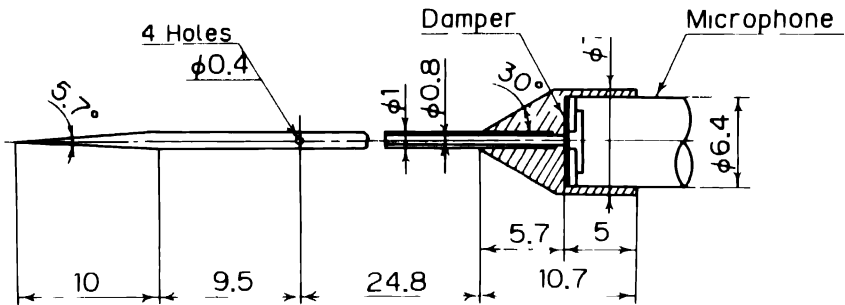
Fig. 2. Pressure probe.

motions of the noncircular vortical structures evolving in the jets [7, 8]. The vortical structures are three-dimensionally complicated, and except flow visualization [9] there has been no way to detect the structures. However the visualized results often have serious problems of misleading to incorrect physical perception different from the real structures, and we need other methods to detect the complicated vortical structures.

In the present study, the vortical structures in noncircular jets excited at the interaction mode were educed by measuring the phase-average fluctuating pressure, and compared with those observed by the low-Reynolds number visualization experiments, and the characteristics of the vortical structures were discussed in relation to the mixing mechanism of noncircular jets.

2. Experimental Apparatus and Procedures

The wind tunnel used in the experiments is shown in Fig. 1. The air issued from sharp-edged noncircular orifices attached at the end of the wind tunnel. In order to regulate the formation of vortical structures, the jets were excited by a loudspeaker at the side of settling chamber. The excitation frequency was a quarter of the natural frequency of the shear layer generated from the orifice edge, and the
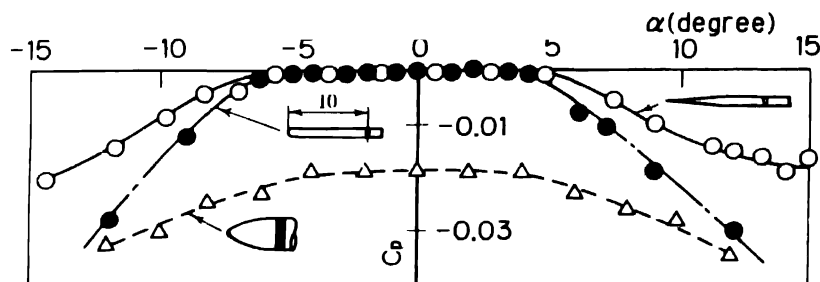
Fig. 3.   Errors of static pressure tubes in steady flow; $Cp = \Delta p / \frac{1}{2}\rho U_e^2$.

excitation intensity u′e/Ue (u′e, Ue: the r.m.s. value of fluctuating velocity and the mean velocity at the jet exit) was 3%. Under the excitation the stable interaction of vortical structures was evolved. The orifice shapes are triangular and rectangular of aspect ratios of 2 & 4. The equivalent diameter of each orifice De is 50 mm, Ue is 4 m/s and the Reynolds number Re (= UeDe/ν) is 1.3×10^4.

The pressure probe used in the experiments is shown in Fig. 2. The static pressure tube with four small holes is connected at the end to the condenser microphone. The structure and the dimension of the probe were determined so as to minimize errors in the measurements of fluctuating static pressure. In order to damp the organ pipe resonance in the tube, a thin nylon gauze was inserted in front of the diaphragm of microphone, and the probe had a nearly flat frequency response to 2.0 kHz. The cross-flow error of the static pressure tube was calibrated in the uniform flow by changing the flow attack angle to the tube. The result is shown in Fig. 3 in comparison with those of a standard static pressure tube and a nosecone tube. The cross-flow error is minimal in the present tube; lCpl is less than 0.02 within the attack angles of ± 15 degrees. It means that the tube is applicable to the flow with an equivalent turbulence level of 27% [9].

The dynamic calibration of the pressure probe was carried out in the wake of a circular cylinder by measuring pressure- and velocity-fluctuations simultaneously [11]. The true pressure was predicted with the measured velocity by the following equation [12]:

$$p_f = -\rho(u - u_c)u_f, \tag{1}$$

where p_f and u_f are the fluctuating pressure and velocity, ρ is the density, u is the mean velocity and u_c is the convection velocity of disturbance. Since equation (1) is deduced from the inviscid momentum equation, p_f and u_f should be measured in the potential flow region outside Karman vortices behind the circular cylinder. The fluctuations were measured by pressure and hot-wire probes as shown in Fig. 4, where an example of measured velocity and pressure signals are also shown. The cylinder diameters were 1–40 mm, the free-stream velocities were 8–25 m/s, and the frequencies of vortex shedding were 100–2000 Hz. The ratio of the measured
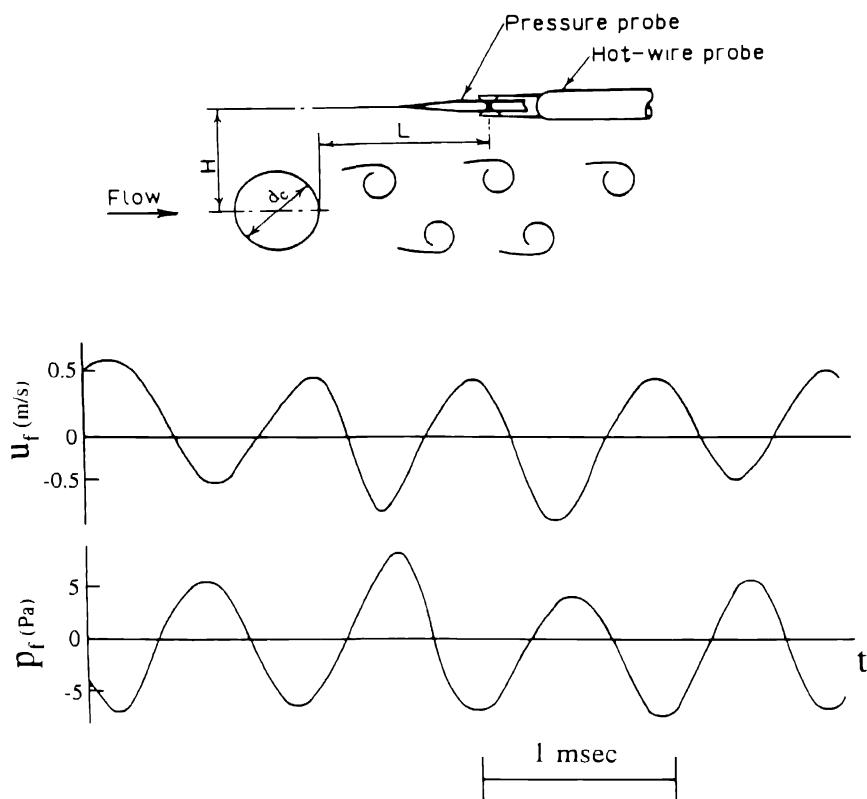
Fig. 4.   Calibration procedure of the pressure probe in fluctuating flow; $H/d_c = 1.25$–2.25, $L/d_c = 1.8$–3.3.

rms value $\hat{p}_{fm}$ to the predicted rms value $\hat{p}_{fth}$ is shown in Fig. 5, where the ratic is plotted against the nondimensionalized wave length λ/D (λ: wave length of disturbance). The result shows that the error in the measured values is less thar 18% of the true values.

The response of the pressure probe to the vortex motion was also calibrated by measuring pressure- and velocity-fluctuations in a turbulent vortex ring generatec by a single pulse jet. The fluctuation signals are shown in Fig. 6. The result show: that the pressure probe responds reasonably well to the pressure fluctuation of the vortex.

This type of pressure probe was also used to educe the vortical structures of a circular jet excited at the pairing mode [6], and the results were compared witl those of the vorticity measurements [13]. An example of the comparison is showr in Fig. 7, where the phase-average pressure contours at a certain phase of excitatior are compared with the phase-average vorticity contours nearly at the same phase.
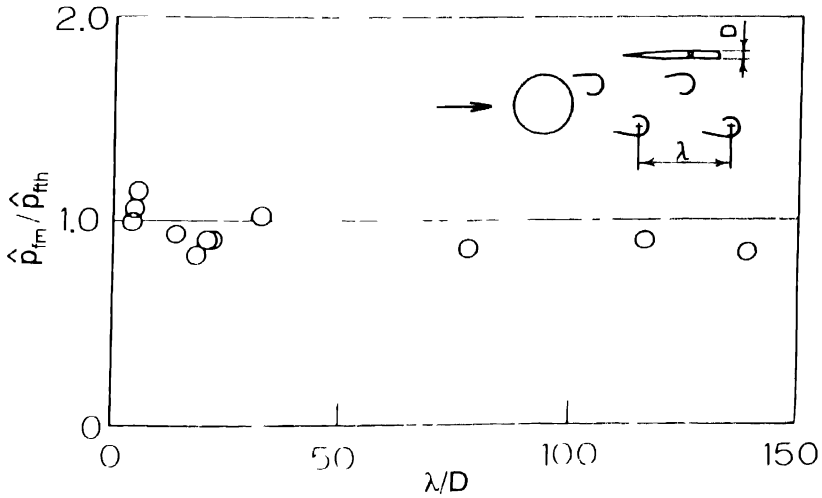
Fig 5   Calibration result of the pressure probe
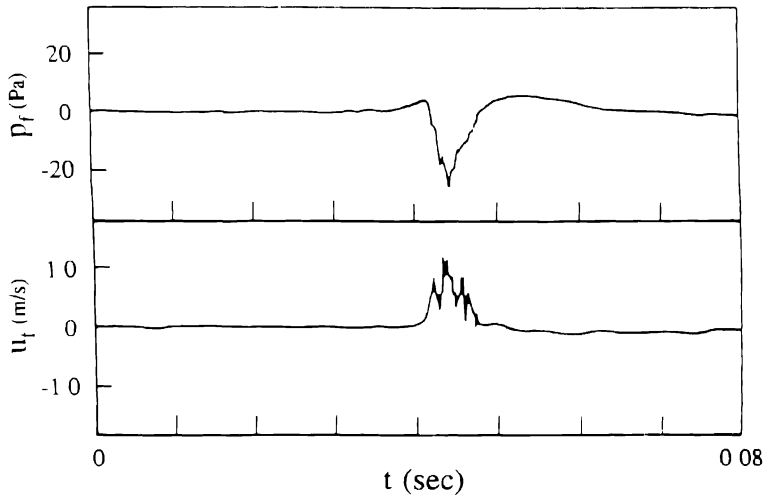
Fig 6   Response to vortex motion

The negative pressure region corresponds to the vorticity concentrated region, and the pressure minima locate at the vorticity maxima. The result suggests that the pressure measurements are very useful to detect the vortical structures in turbulent shear flows.

The arrangement of the probes for the present measurements is shown in Fig. 8. The reference velocity and the fluctuating pressure were measured respectively by a single hot-wire probe fixed near the jet center at $x/De = 0.8–1.0$ and by the
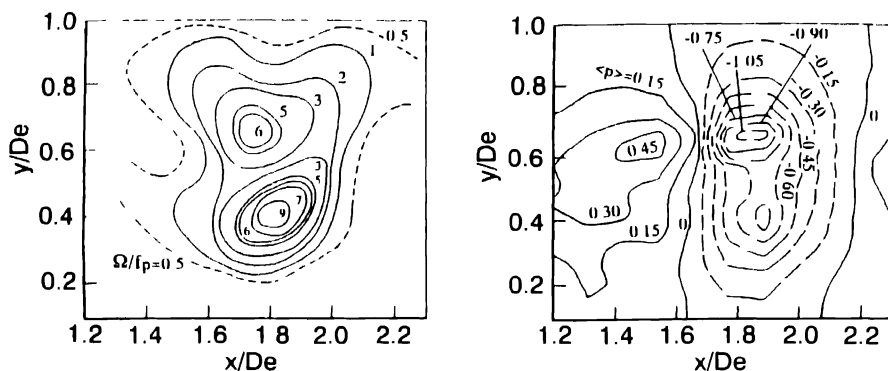
Fig. 7. Phase-average vorticity and pressure contours; Ω: vorticity, fp: excitation frequency; <p>: phase-average fluctuating pressure nondimensionalized by $\rho Ue^2/2$.
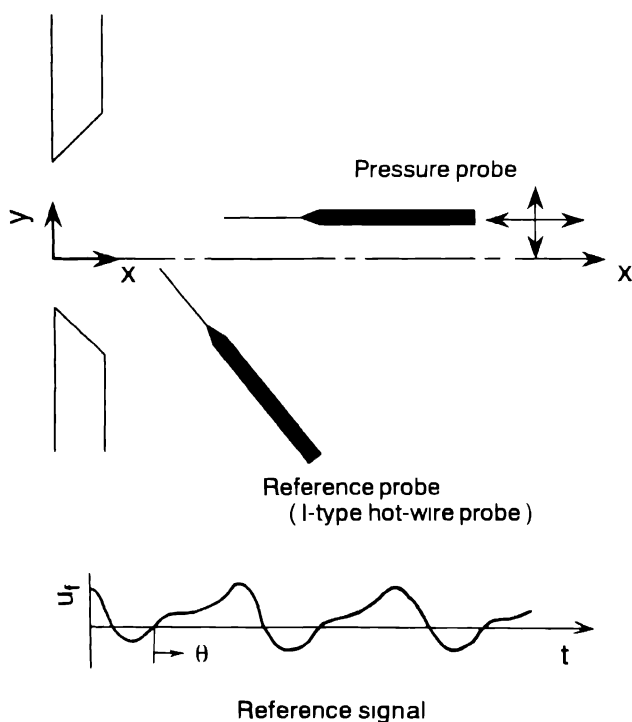
Fig. 8. Arrangement of the probes for the phase-average measurement.

pressure probe moved at about 500 locations over $0.8 < x/De < 3.0$ and $-1.2 < y/De < 1.2$. The phase-averaging was carried out at $\theta = 0$ (zero-cross point) and $\theta = \pi/2$ of the reference signal as shown in Fig. 8. The traversing of the pressure
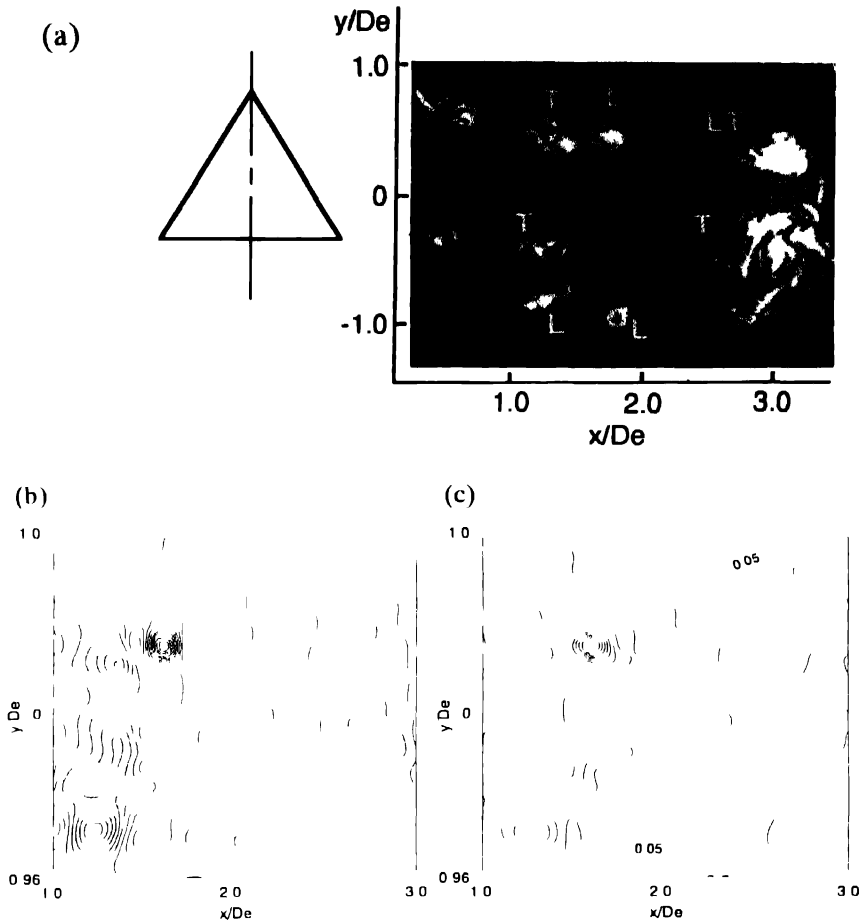
Fig 9   Triangular jet ($\theta = \pi/2$) (a) visualization, (b) <p> contours (dotted zone <p> <
-0 08, Δ<p> = 0 08), (c) <p'> contours (Δ<p'> = 0 05)

probe, the data acquisition and the data processing were automatically controlled
by the personal computer.

3. Results and Discussions

Figure 9 shows the results of triangular jet: a visualized picture, contours of phase-
average fluctuating pressure <p> and contours of incoherent fluctuating-pressure
intensity <p'>. The values of <p> and <p'> are nondimensionalized by the
dynamic pressure $\rho Ue^2/2$ at the jet exit. The visualized result was obtained in the
water jet experiments at Re = 1.5×10^3 [8]. Note that the Reynolds numbers of
the present and visualization experiments are different, and that the vortex motions
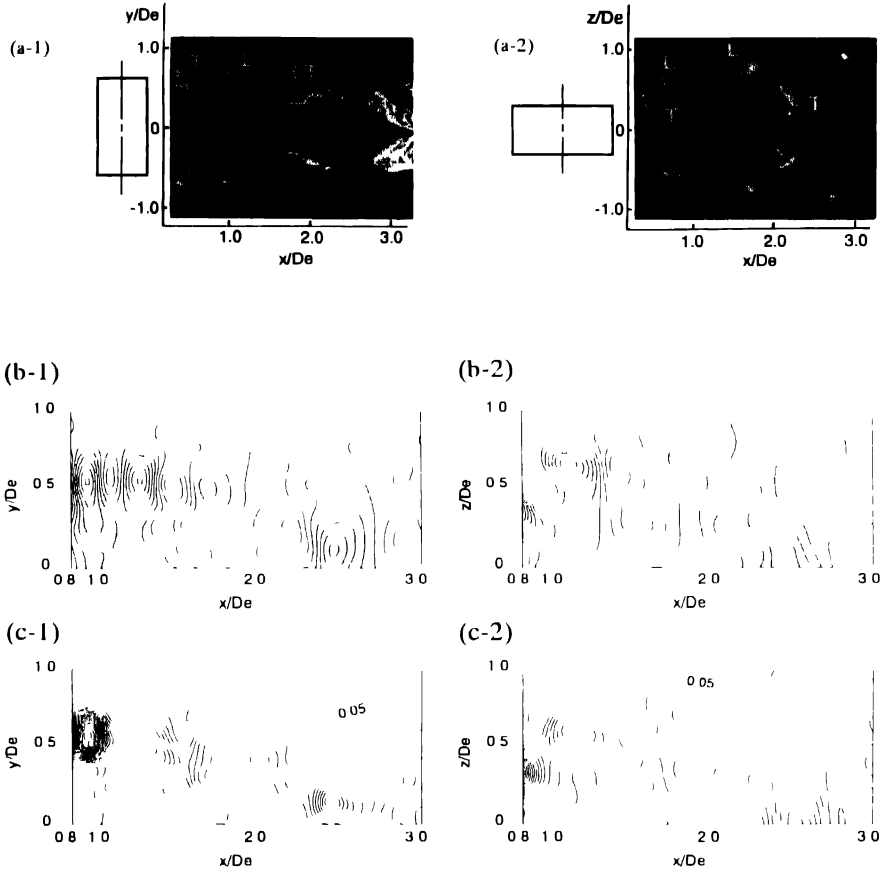
Fig. 10. Rectangular jet (AR = 2): (a-1) visualization in the major axis plane; (a-2) visualization in the minor axis plane; (b-1) $<p>$ contours in the major axis plane (dotted zone: $<p>$ < -0.08; $\Delta<p>$ = 0.08); (b-2) $<p>$ contours in the minor axis plane; (c-1) $<p'>$ contours in major axis plane ($\Delta<p'>$ = 0.025); (c-2) $<p'>$ contours in the minor axis plane.
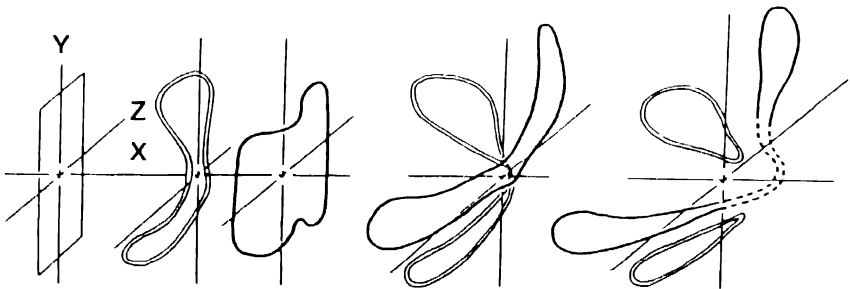
Fig. 11. Interaction of vortical structures in rectangular jet (AR = 4).
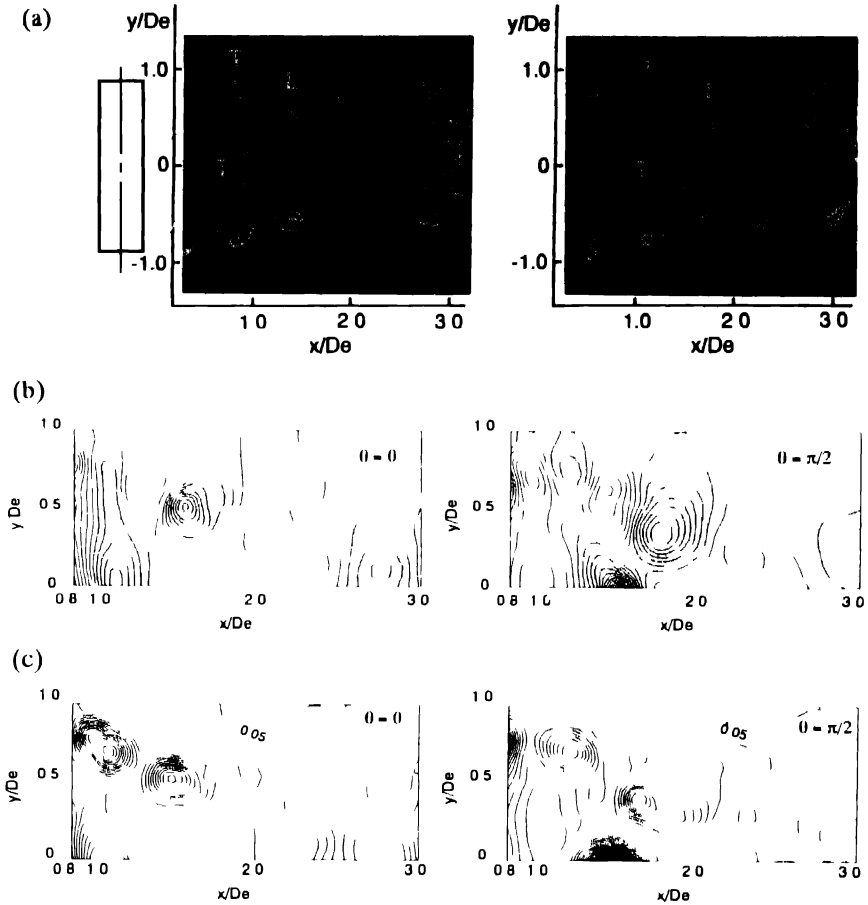
Fig 12 Major axis plane of rectangular jet (AR = 4) (a) visualization, (b) <p> contours (dotted zone <p> < −0 08; Δ<p> = 0 08), (c) <p'> contours (Δ<p'> = 0.025).

are dependent on the characteristics of vortices (core size, circulation, vorticity diffusion and so on) which are affected by Reynolds number. Thus the comparisons with the visualized results are restricted to qualitative aspects. The negative regions (<p> < −0.08) in the <p> distribution, shown by dotted zones, reveal characteristics of the vortical structures and agree well with the dye concentrated regions in the visualized result: the merging of leading (L) and trailing (T) vortices on the upper side, and the passing-through of trailing vortex into leading vortex on the lower side. The <p'> contours suggest that the maxima of <p'> locate at the centers of the vortical structures.

(a)

(b)

(c)
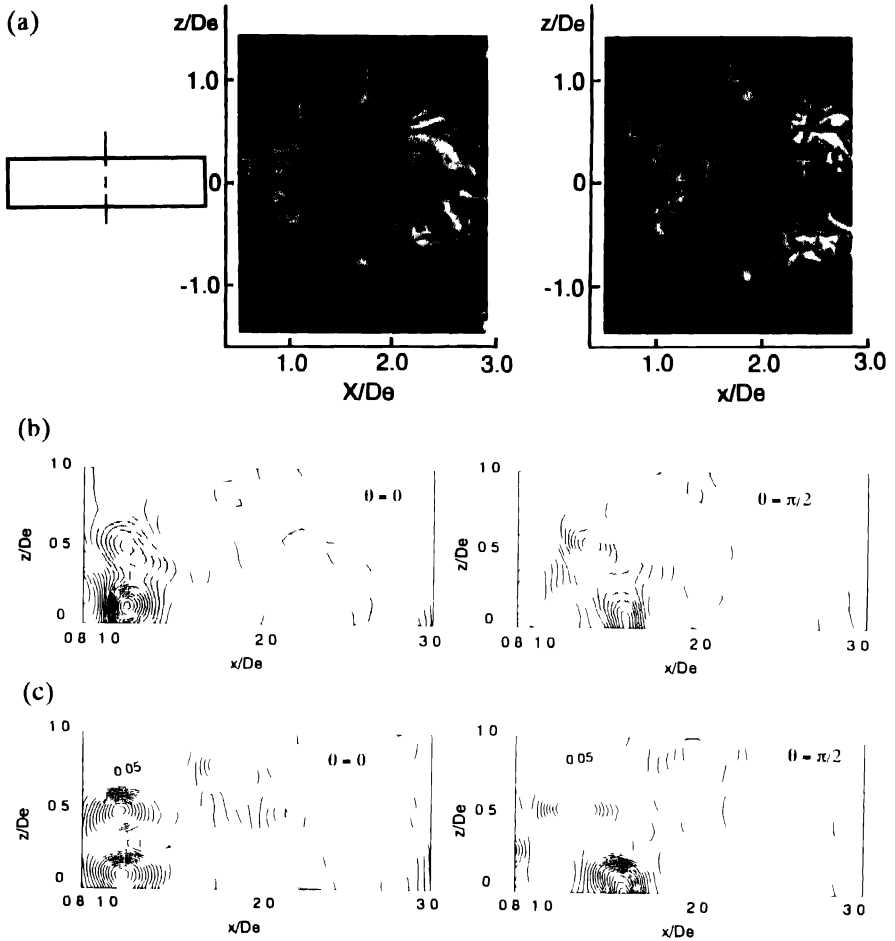
Fig 13   Minor axis plane of rectangular jet (AR = 4)   (a) visualization, (b) <p> contours (dotted zone <p> < −0 08, Δ<p> = 0 08), (c) <p'> contours (Δ<p'> = 0 025).

The results of rectangular jet (AR = 2) are shown in Fig. 10. The vortical structures identified with negative <p> contours on the major axis plane agree well with the visualized result which shows the merging of leading and trailing vortices. On the minor axis plane, the <p> contours show the passing-through of trailing vortex into leading vortex, as inferred also from the visualized result.

The vortical structures of the rectangular jet (AR = 4) are very complicated as shown in Fig. 11, which was obtained by the visualization experiments [8]. Thus the phase averaging was carried out at two phases ($\theta = 0$, $\pi/2$) to detect the sequence of the complicated vortical structures. Figure 12 shows <p> and <p'>

TABLE I. Flow rates (Q/Qc at x/De = 5)

Orifice shape	Unexcited jet	Excited jet
Circle	1.00	1.17
Triangle	1.07	1.21
Rectangle (AR = 2)	1.10	1.40
Rectangle (AR = 4)	0.99	1 35

contours at the two phases on the major axis plane together with the visualized result. The visualized result illustrates how the vortical structures on the major axis plane change in the streamwise direction. The vortical structures in the $<p>$ contour correspond to those in the visualization experiments. In Fig. 12(a), we can see clear dye lumps near the leading vortices. However there is no corresponding vortical structures in Fig. 12(b), (c). It suggests that the dye lumps do not reflect the real structures but indicate the remains of dye integrated by the upstream vortical structures. The results on the minor axis plane in Fig. 13 show that the vortical structures in the visualized result and in the $<p>$ contours agree very well. Figures 11–13 reveal that the interaction of vortices is three-dimensionally complicated. To educe the vortical structures by vorticity measurements, we need the detection of three vorticity components which is a very tough work. Compared with the vorticity measurements, since the pressure is scalar and closely related to vortex motions, the pressure measurements are easier and may be more effective to educe three-dimensionally complicated vortical structures.

To discuss entrainment and mixing in the noncircular jets, the local flow rates of the jets were calculated by the equation

$$Q = \int_{A_{0.2}} U\,dA, \tag{2}$$

where $A_{0.2}$ is defined as the jet cross-sectional area inside of the velocity ratio of 0.2. The flow rates at x/De = 5 are shown in Table 1, where Q is nondimensionalized by the corresponding flow rate of an unexcited circular jet Qc. The flow rate is significantly increased by excitation especially in the rectangular jets, suggesting that the intense stretching and the splitting of noncircular vortical structures are very effective to enhance entrainment and mixing.

4. Conclusions

The present study is concluded as follows:
  (1) The direct measurements of static pressure fluctuations are very useful to educe vortical structures in turbulent shear flows. In particular, since the pressure

is scalar, the pressure measurements can be used to detect three-dimensional vortical structures in turbulent shear flows.

(2) The contours of phase-average fluctuating pressure are effective to identify the vortical structures, and the incoherent fluctuating pressure intensity is maximum at the center of vortical structure.

(3) The interactions of vortical structures contribute to the enhanced mixing in the noncircular jets.

References

1. Hussain, A. K. M. F., *J. Fluid Mech.* 173 (1986) 303.
2. Bradshaw, P. and Koh, Y. M., *Phys. Fluids* 24 (1981) 777.
3. Gyr, A., Structure of turbulence and drag reduction, *IUTAM Symposium in Zurich* (1989) Springer-Verlag, 50.
4. Powell, A., *J. Acoust. Soc. America* 33 (1964) 177.
5. Toyoda, K. and Shirahama, Y., *Proc. 2nd Asian Congr. of Fluid Mech.* 148 (1983) 555.
6. Toyoda, K. and Hussain, F., *Proc. 5th Asian Congr. of Fluid Mech.* 1 (1992) 587.
7. Ho, C. M. and Gutmark, E., *J. Fluid Mech.* 179 (1987) 383.
8. Hussain, F. and Husain, H. S., *J. Fluid Mech.* 208 (1989) 257.
9. Toyoda, K. and Hussain, F., *Proc. 4th Asian Congr. of Fluid Mech.* (1989) 117.
10. George, W. K. *et al.*, *J. Fluid Mech.* 148 (1984) 155.
11. Maekawa, T. *et al.*, *Proc. 15th Japan Nat. Congr. Appl. Mech.* (1965) 159.
12. Fuchs, H. V., *J. Sound Vibr.* 22–3 (1972) 361.
13. Hussain, A. K. M. F. and Zaman, K. B. M. Q., *J. Fluid Mech.* 101–3 (1980) 493

A Study of Flow Properties near Critical Points in the Near Wake of a Circular Cylinder

Y. ZHOU and R.A. ANTONIA
Department of Mechanical Engineering, University of Newcastle, NSW 2308, Australia

Abstract. By applying the phase-plane technique to velocity data in the near-wake of a circular cylinder, three types of critical points are identified. Foci and saddle points occur most frequently, but a significant number of nodes is also found. Flow topology and properties associated with these points are examined in some detail. While foci and saddle points are associated with maxima of local vorticity and strain rate respectively, nodes are associated with a strong local divergence, indicating significant local three-dimensionality. The relative probability of time delay between critical points is also discussed.

1. Introduction

When complicated three-dimensional flow patterns are viewed in an appropriate frame of reference (e.g. relative to an observer translating at a suitable convection velocity), they reveal a number of critical points. These are points where the velocity components are zero and the streamline slope is therefore indeterminate. In their review, Perry and Chong (1987) showed how the identification of these points can aid in describing and understanding flow patterns. They also provided examples of how critical point concepts can be applied to the study of flow patterns. Critical point theory has been extended (Chong et al., 1988) to provide a classification of three-dimensional flow patterns. Three-dimensional critical point methodology has been applied to direct numerical simulation data in various flows (Hunt et al., 1988; Chen et al., 1989, 1990; Soria and Cantwell, 1992). The approach focuses on the invariants of the velocity gradient tensor.

With experimental data, a more restrictive approach is necessary since only incomplete information of the velocity gradient tensor is available. There is nevertheless interesting information that can be obtained in experiments, such as the one described here, where orthogonal arrays of X-probes provide instantaneous velocity data in two orthogonal planes ($u - v$ data in the (x, y) plane, $u - w$ data in the (x, z) plane). Such data allow critical points to be identified in both planes, thus permitting the interrelationship between these points to be examined with the possibility of gaining some insight into the three-dimensionality of the flow.

The present approach differs from previous experimental work in that the critical points are identified rigorously by application of the two-dimensional phase-plane technique on the computer. The main aim of this paper is to quantify flow properties in the vicinity of critical points and investigate the spatial relationship between

different types of critical points which are identified in the two planes. The identification of critical points is essentially one way of detecting the flow organisation; a comparison with other detection methods has been presented in another paper (Zhou and Antonia, 1994).

The flow considered here is the turbulent near-wake of a circular cylinder. It was chosen for several reasons. Firstly it has a high degree of organisation, and is therefore attractive for the purpose of clarifying the contribution of the organised motion to turbulent transfer processes. Secondly, a significant body of data is already available on the organisation of this flow. Additionally, the convection velocity of vortices for this particular flow has been estimated by Zhou and Antonia (1992); this knowledge is important in the present context since the flow field is viewed in a frame of reference translating with the vortices. Significant information has already been obtained on the organised motion of the flow (e.g. Cantwell and Coles, 1983; Kiya and Matsumura, 1985; Hussain and Hayakawa, 1987; Zhou and Antonia, 1993). Nevertheless, our knowledge of this flow, such as the quantification of flow kinematics in regions surrounding critical points, is far from complete; this provided the main incentive for the present work.

2. Experimental Details

Experiments were carried out in an open return low turbulence wind tunnel with a 2.4 m long working section (0.35×0.35 m). The bottom wall was tilted to obtain a zero streamwise pressure gradient. A circular brass cylinder ($d = 12.5$ mm) was installed in the mid-plane and spanned the full width of the working section, 20 cm from the exit plane of the contraction. This resulted in a blockage of about 3.6% and an aspect ratio of 28. Measurements were made at a constant free stream velocity ($U_0 = 6.7$ m/s) at a distance of 20 diameters behind the cylinder. The corresponding Reynolds number Re ($\equiv U_0 d/\nu$) was 5600. In the free stream the longitudinal and lateral turbulence intensities were about 0.05% and 0.08% respectively.

Using two orthogonal arrays, each comprising eight X-wires (Fig. 1), velocity fluctuations u, v in the (x, y) plane and u, w in the (x, z) plane were simultaneously obtained. The arrays were attached to separate transversing mechanisms and could be moved independently of each other. The eight X-wires in the (x, y) plane were fixed with the second X-wire (from the bottom) at the centreline so that they covered the transverse extent of vortices shed from the upper side of the cylinder, while the eight X-wires in the (x, z) plane could be displaced in the y direction and lay at $y/d \simeq 0.7$. The nominal spacing between X-wires in both planes was about 5 mm except for a relative large gap of 9.1 mm between the fourth and fifth X-wire in the (x, z) plane. The physical blockage caused by the two arrays, cables and supports was estimated to be about 3%. Several types of measurements indicated that the interference to the flow due to the two arrays was negligible (Zhou and Antonia, 1994).
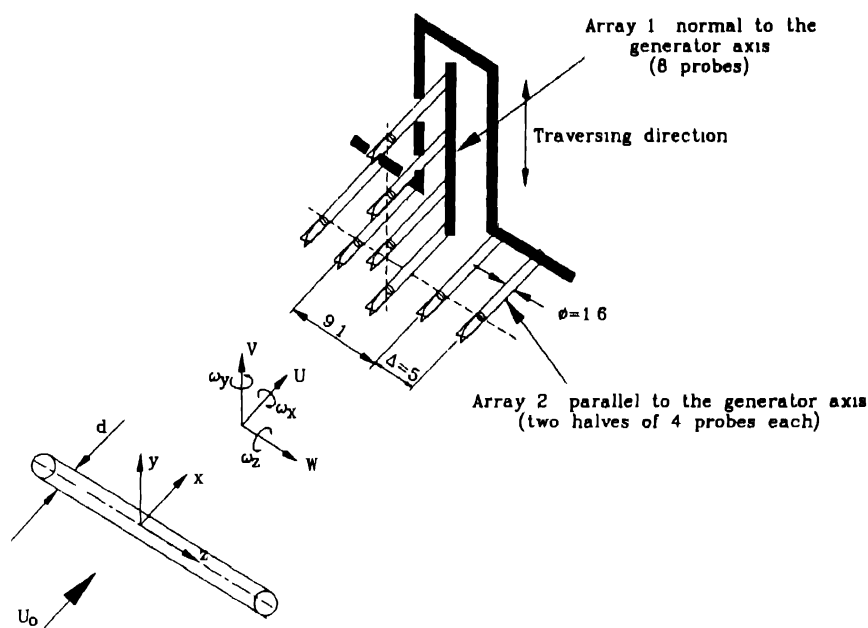
Fig 1   Experimental arrangement

The Wollaston (Pt-10% Rh) wires (dia. = 5 μm, length $\simeq$ 1 mm) were operated with constant temperature circuits. Signals from the circuits were offset, low pass filtered (cut-off frequency = 1.7 kHz), amplified and then digitised using two 16 channel, 12 bit RC A/D boards respectively into two personal computers (NEC 386) at a sampling frequency of 3.5 kHz per channel. Data acquisition by the two computers was synchronised using a common external trigger pulse (the configuration is shown in Krogstad et al., 1992). The wires were calibrated for velocity and yaw and continuously checked for drift. Using calibration data, signals proportional to u, v and w, together with the local mean velocities $\bar{U}$, $\bar{V}$ ($\simeq$ 0), $\bar{W}$ ($\simeq$ 0), were formed and stored on digital tapes. The duration of the digital records was about 38 sec. Subsequent data processing was carried out on a VAX 8550 computer.

3. Determination of Critical Points

The classification of critical points with the aid of a p–q chart is relatively well known (e.g. Kaplan, 1958; Perry and Chong, 1987). Although the following discussion is for the (x, y) plane, it is equally applicable to the (x, z) plane. With the origin of the co-ordinate system located at the critical point ($x_c = y_c = 0$), the velocity components U and V close to the origin can be approximated by first order Taylor series expansions

$$\begin{bmatrix} U \\ V \end{bmatrix} = \begin{bmatrix} a_{11} & a_{12} \\ a_{21} & a_{22} \end{bmatrix} \begin{bmatrix} x \\ y \end{bmatrix} = \underset{\sim}{A} \begin{bmatrix} x \\ y \end{bmatrix} \tag{1}$$

The eigenvalues which correspond to (1) are solutions of the characteristic equation

$$\lambda^2 - p\lambda + q = 0 \tag{2}$$

where $p = $ trace $\underset{\sim}{A} = (a_{11} + a_{22})$ and $q = $ det $\underset{\sim}{A} = (a_{11}a_{22} - a_{21}a_{12})$. The former may be referred to as the velocity divergence in the (x, y) plane. The three critical points of interest here are the saddle point ($q < 0$), node ($q > 0$, $\Delta < 0$) and focus ($\Delta < 0$), where Δ is the discriminant ($p^2 - 4q$) of Eq. (2). Note that the present convention is similar to that used in Kaplan (1958) and differs from Perry's (1984) in that the sign of p is inverted. In the present convention, streamlines spiral into or converge towards foci and nodes when p is negative; they spiral out of or emanate from these critical points when p is positive.

In a 2-D frame of reference which translates with a convection velocity U_c, the velocity components are now given by

$$\left. \begin{aligned} u_c &= U - U_c \\ v_c &= V \end{aligned} \right\} . \tag{3}$$

The instantaneous signals U and V were formed by adding the local mean velocity values $\bar{U}$ and $\bar{V}$ ($\simeq 0$) to the digital time series of u and v. The convection velocity U_c ($= 0.87U_0$) along the vortex path was used.

The size of the experimental data grid is given by $\Delta x = 1.7$ mm and $\Delta y = 5$ mm (nominal spacing between X-wires). The value of Δx was identified, using Taylor's hypothesis (see Zaman and Hussain, 1981, for justification), with the product $(-\Delta t U_c)$, where Δt is the time interval between samples ($\equiv 3500^{-1}$ s). In view of the disparity in the magnitude of Δx and Δy, data were added at two equispaced y locations between each pair of existing rows of data. These extra data were obtained by interpolation, based on least-square cubic spline fits to the original data.

The detection procedure used to detect the three types of critical points is summarised in Fig. 2. More details of this scheme are given in Zhou and Antonia (1994). An inspection of instantaneous sectional streamlines (Fig. 3) indicates that some critical points, e.g. foci at $(tU_c/d, y/d = (-3.8, 1.0), (1.0, 1.1)$ and saddle points at $(-2.1, 0.6), (3.8, 1.4)$, appear to be quasi-periodic events. Others, e.g. foci at $(tU_c/d, y/d) = (-1.5, 1.5), (2.4, 1.6)$ and a saddle point at $(2.2, 1.4)$, occur randomly and the inclusion of these points in detections would certainly smear conditional averages. Additional criteria were therefore introduced to exclude the latter events (see Fig. 2). For foci (with the same sign of vorticity $\omega \equiv a_{21} - a_{12}$), the minimum detection wavelength λ_d was applied. Initially, λ_d was assumed to be equal to the average shedding wavelength λ_s but, after inspecting instantaneous sectional streamlines, λ_d was reduced $0.6\lambda_s$. When several foci occurred within

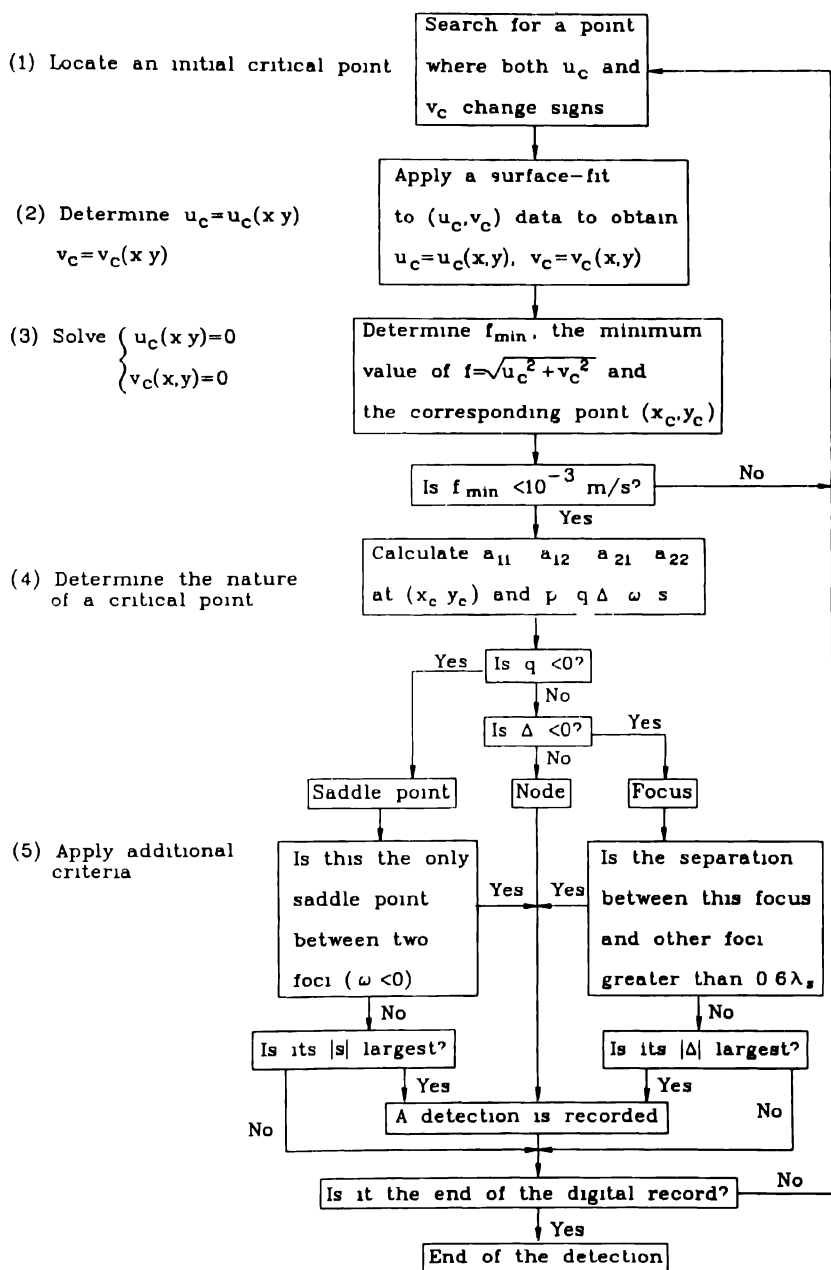(1) Locate an initial critical point — Search for a point where both u_c and v_c change signs

(2) Determine $u_c = u_c(x\ y)$
$v_c = v_c(x\ y)$ — Apply a surface−fit to (u_c, v_c) data to obtain $u_c = u_c(x,y)$, $v_c = v_c(x,y)$

(3) Solve $\begin{cases} u_c(x\ y) = 0 \\ v_c(x,y) = 0 \end{cases}$ — Determine f_{min}, the minimum value of $f = \sqrt{u_c^2 + v_c^2}$ and the corresponding point (x_c, y_c)

Is $f_{min} < 10^{-3}$ m/s? — No

Yes

(4) Determine the nature of a critical point — Calculate a_{11} a_{12} a_{21} a_{22} at $(x_c\ y_c)$ and p q Δ ω s

Yes — Is $q < 0$?

No

Is $\Delta < 0$? — Yes

No

Saddle point   Node   Focus

(5) Apply additional criteria — Is this the only saddle point between two foci ($\omega < 0$)   Yes   Yes   Is the separation between this focus and other foci greater than $0\ 6\lambda_s$

No   No

Is its $|s|$ largest?   Is its $|\Delta|$ largest?

Yes   Yes

A detection is recorded

No   No

Is it the end of the digital record? — No

Yes

End of the detection

Fig 2 Flow chart for the detection scheme
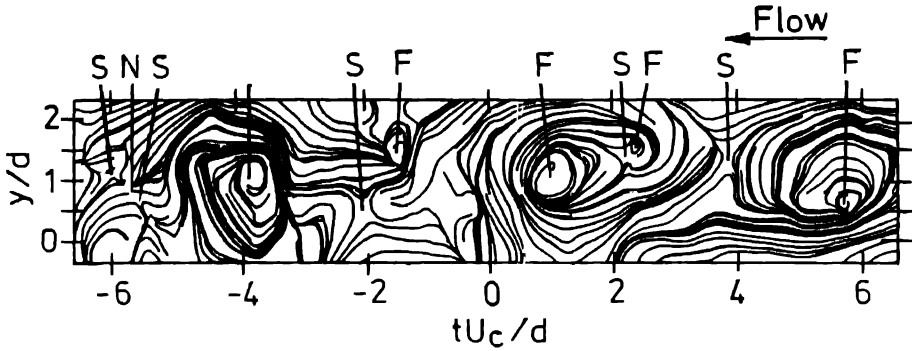
Fig. 3.   Instantaneous sectional streamlines in the (x, y) plane, $(U_c = 0.87U_0, t = 0$ is arbitrary). F denotes a focus, S a saddle point and N a node.

this distance, only the one associated with the largest magnitude of Δ (negative) was chosen. This choice was based on the observation that quasi-periodic foci usually have a larger $|\Delta|$ than randomly occurring ones. In fact, a focus with a large $|\Delta|$ is generally associated with a large $|\omega|$ (Zhou and Antonia, 1994). For a saddle point, only one detection with the largest magnitude of the strain rate $s \equiv a_{21} + a_{12}$ between two foci was retained. Approximately two-thirds of the number of original focus or saddle point detections survived these additional criteria. No additional condition was used for nodes since their occurrence is somewhat random.

Once critical points are detected, the conditional average of an instantaneous quantity F is given by

$$\langle F \rangle_\tau = \frac{1}{N} \sum_{m=1}^{N} F_{j_m + \tau} \tag{4}$$

where τ represents time (in samples, positive or negative) relative to the detection points j_m and N is the total number of detections.

4. General Properties of Critical Points

Since the location of a critical point ($u_c = v_c = 0$) is clearly affected by the choice of the convection velocity (see Eq. (3)), it was important to assess the sensitivity of this location to the variation of U_c. At $x/d = 20$, U_c increases from about $0.85U_0$ at the wake centreline to $0.92U_0$ near the edge of the wake (Zhou and Antonia, 1992). The effect of this variation on location of the critical points was found to be quite small (Zhou and Antonia, 1994). The effect was further minimised by using the value of U_c ($= 0.87U_0$) along the vortex path. Unless otherwise stated, results in both (x, y) and (x, z) planes are only presented for critical points associated with negative vorticity since critical points associated with positive vorticity exhibit essentially the same features.

TABLE 1. Averaged values of properties at critical points

	(x,y) Plane			$((x,z)$ Plane		
	Focus	Saddle	Node	Focus	Saddle	Node
N	3571	2774	767	3605	2862	1675
$(N/T)d/U_0$	0.18	0.13	0.04	0.18	0.13	0.08
$\langle y_c \rangle/d$	0.64	1.06	0.95			
$\langle |\omega| \rangle d/U_0$	1.78	0.25	0.31	1.44	0.25	0.29
$\langle |s| \rangle d/U_0$	0.42	0.92	0.36	0.41	0.81	0 31
$\langle |p| \rangle d/U_0$	0.35	0.25	0.88	0.31	0.23	0.83
$\langle \theta_1 \rangle$		48°			50°	
$\langle \theta_2 \rangle$		−51°			−50°	

The total numbers of critical points which remained following the application of the additional criteria are shown in Table I. Foci and saddle points make up most of the population, although the number of nodes is not small. There are almost twice as many nodes in the (x, z) plane as in the (x, y) plane. This is probably because the eight X-wires in the (x, z) plane covered a larger active area than those in the (x, y) plane. (Note that a few X-wires in the (x, y) plane were close to the free stream and thus detected fewer critical points than those close to the centreline. This was confirmed by examining the lateral distribution of detections (not shown here).) Not surprisingly, the normalised frequency $(N/T)d/U_0$ for detections of foci is close to the expected Strouhal number ($\simeq 0.2$, for the present Reynolds number). In the (x, y) plane, the average location of the saddle points ($y_c \simeq 1.06d$) is significantly larger than that of foci ($y_c \simeq 0.64d$); both values are in good agreement with those obtained by Hussain and Hayakawa (1987) at $x/d = 20$. Conditional averages, defined by Eq. (4), allows various flow properties to be examined in the vicinity of critical points. A few such properties, evaluated at $\tau = 0$, are given in Table I. As expected, the conditional vorticity is largest at foci while the conditional strain rate is greatest at saddle points. The values are larger – but only slightly – in the (x, y) plane than in the (x, z) plane. The magnitude of the divergence is largest at the nodes. The separatrix angles $\theta_{1,2} = \tan^{-1}[(\lambda_{1,2} - a_{11})/a_{12}]$ (Perry, 1984) have approximately the same magnitude ($\simeq 50°$) in both planes. For irrotational flow, the converging and diverging separatrices through the saddle point should be orthogonal (Perry, 1984). The fact that the value of $(\langle \theta_1 \rangle - \langle \theta_2 \rangle)$ is slightly greater than 90° is probably associated with the existence of weak vorticity at the saddle points.

5. Topology Based on Critical Points

Conditional sectional streamlines based on detected foci are shown in Fig. 4 (the same scale is used in the x and y directions in order to avoid any distortion of the physical space). These streamlines spiral in or out depending on the sign
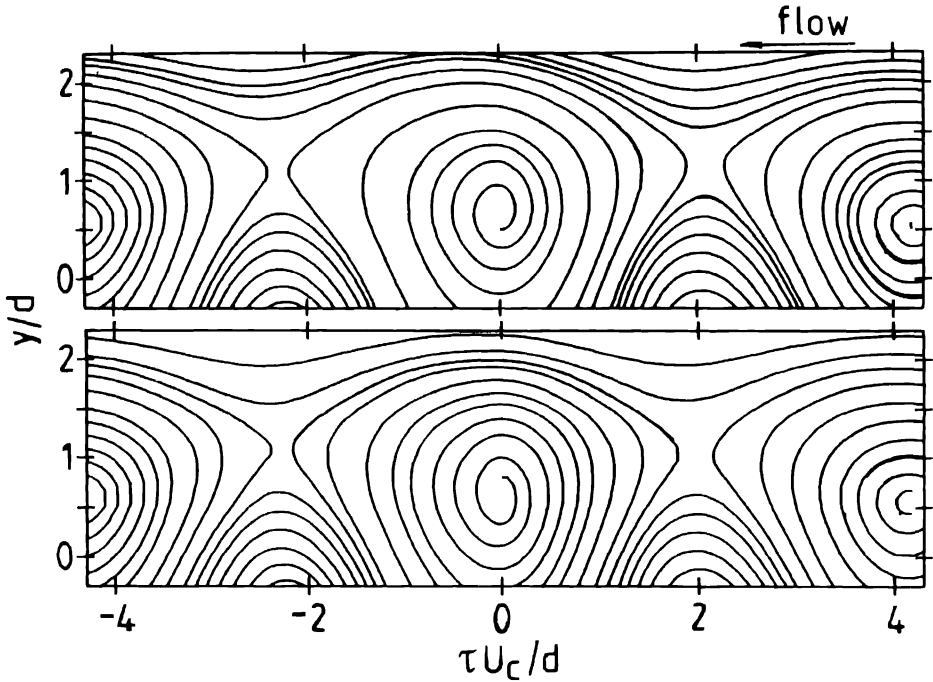
Fig. 4.   Conditional sectional streamlines based on foci. ($U_c = 0.87U_0$). (a) $p > 0$, (b) $p < 0$

of the velocity divergence at the focus and exhibit the familiar Kármán vortex street topology, in close similarity to those based on vorticity detections (Zhou and Antonia, 1993). Conditional sectional streamlines spiral out of foci for $p > 0$ (Fig. 4a) and into foci for $p < 0$ (Fig. 4b). For $p > 0$, the continuity equation $\partial u/\partial x + \partial v/\partial y + \partial w/\partial z = 0$ requires that $\partial w/\partial z$ is negative. Conversely, for $p < 0$, $\partial w/\partial z > 0$. The former situation may be consistent with vortices undergoing axial compression while, for the latter, the vortices are probably being stretched axially (Perry and Steiner, 1987). The flow is therefore three-dimensional when p is non-zero and locally two-dimensional when p is zero. The conditional vorticity contours corresponding to Fig. 4a (those corresponding to Fig. 4b are identical and therefore not shown) are shown in Fig. 5. Evidently foci coincide with the vorticity peak. The elongated contours near $\tau U_c/d = 0$ are due to the lateral dispersion of foci.

The conditional sectional streamlines (not shown) based on saddle points exhibit a topology similar to that of Fig. 4, except for a streamwise displacement. The corresponding contours of $\langle s \rangle d/U_0$ (not shown) show a maximum at the saddle point, as observed by Hussain and Hayakawa (1987).

Conditional sectional streamlines based on nodes detected in the region $0.9 \lesssim y/d \lesssim 1.3$ are shown in Figs 6a and 6b. The two saddle points and the node
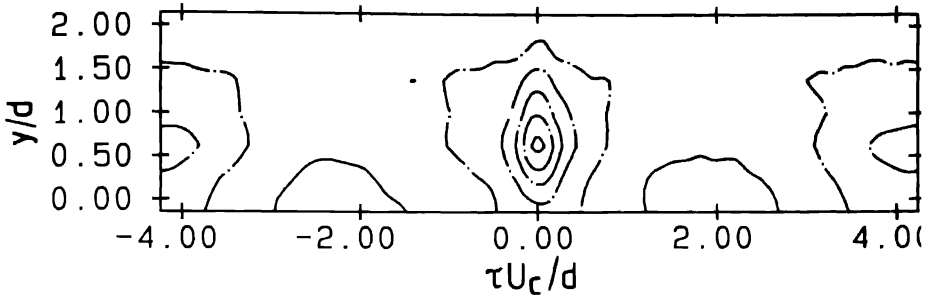
Fig. 5. Spanwise vorticity contours based on detections of foci. Solid and dashed lines represent positive and negative values of $\langle \omega \rangle d/U_0$ respectively; the values range from -0.9 to 0.1 with a step of 0.2.
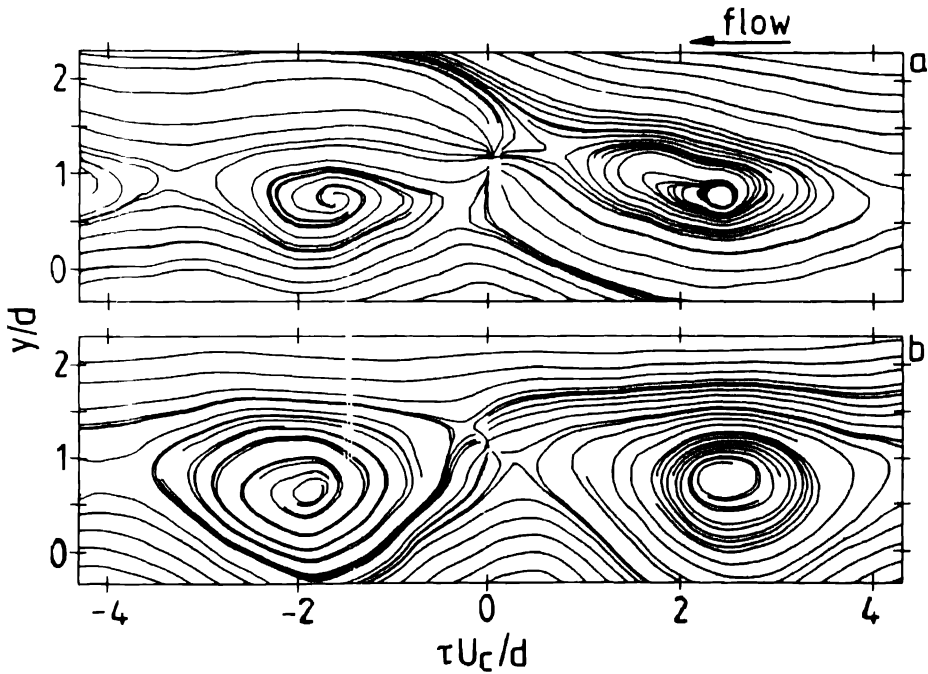
Fig. 6. Conditional sectional streamlines based on node detections. (a) $p > 0$; (b) $p < 0$.

near $\tau = 0$ seem to be aligned with the converging separatrix when $p > 0$ (Fig. 6a) and with the diverging separatrix when $p < 0$ (Fig. 6b). The patterns in Fig. 6 are also observed instantaneously, e.g. $tU_c/d \simeq -6.0 \sim -5.6$ and $y/d = 0.6 \sim 1.1$ in Fig. 3. Conditional contours (Fig. 7) of p corresponding to Fig. 6 show a maximum at $\tau = 0$. As previously noted non-zero p corresponds to a local three-dimensionality. The concentration of $\langle p \rangle$ near the origin therefore indicates a strong three-dimensionality near the node. Independently of the sign
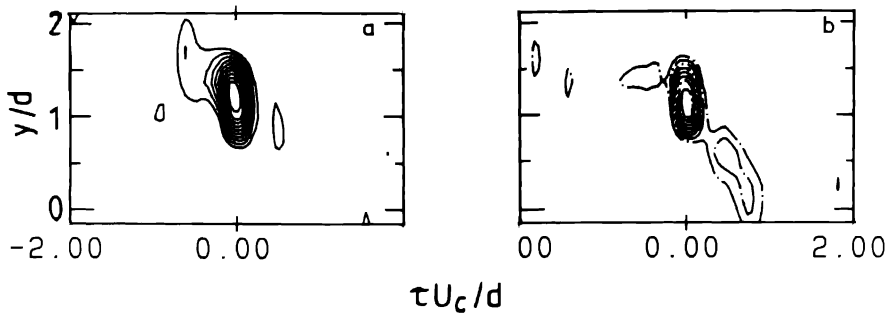
Fig. 7. Contours of the velocity divergence $\langle p \rangle d/U_0$ based on node detections. (a) 0.05 to 0.5; (b) -0.5 to -0.05 (step = 0.05).

of p, the contours in Fig. 7 tend to be aligned with the diverging separatrix (cf. Fig. 6). It has been suggested that ribs, or structures which lie in the (x, y) plane and have vorticity components in the x and y directions, are generally oriented along the diverging separatrix (e.g. Hayakawa and Hussain, 1989). This suggestion has been strengthened by Zhou and Antonia's (1994) observation that ribs tend to have an inclination to the x axis of about 55°, which is only marginally larger than the slope ($\simeq$ 50°) of the diverging separatrix through the saddle point. This near-coincidence in orientation suggests a possible connection between nodes and ribs, which is corroborated in the following section.

6. Interrelationship between Critical Points

Figure 8 presents the relative probabilities of the duration between critical points in the (x, y) plane and between saddle points in the (x, y) plane and foci in the (x, z) plane, where $\tau U_c/d = 0$ corresponds to the instant at which saddle points in the (x, y) plane are detected. These probabilities have been normalised to have a maximum value equal to 1. As expected, the peak probability for foci in the (x, y) plane occurs at $\tau U_c/d \simeq \pm 0.5\lambda_s$. For nodes the main peak appears near $\tau U_c/d = 0$, although two minor peaks are identifiable at $\tau U_c/d \simeq \pm 0.5\lambda_s$. Nodes are therefore more likely to occur at the same location as saddle points than at the focus location. Foci in the (x, z) plane occur with a relatively high probability near saddle points in the (x, y) plane. The foci corresponding to the peak probability can be interpreted in terms of rib-like structures (details are given in Zhou and Antonia (1994), where the three-dimensional aspects of the motion are discussed in greater detail) and their distribution (Fig. 9) relative to nodes in the (x, y) plane exhibits a relatively strong peak near $\tau U_c/d = 0$ (i.e. the instant at which the nodes are detected), indicating a tendency for nodes to occur at approximately the same instant as these foci. If it is assumed that ribs are associated with relatively intense vortex stretching, it is not unreasonable to expect them to be accompanied by strong three-dimensional activity, thus accounting for the presence of nodes. It

would appear that although the importance of foci and saddle points is relatively well established in the context of studying organised motions, the significance of nodes should not be underestimated.

7. Conclusions

The phase-plane technique was used to determine critical points from simultaneously sampled measurements in the (x, y) and (x, z) plane in the near-wake of a circular cylinder. Foci and saddle points occurred most frequently, but a significant number of nodes was detected. While foci and saddle points are associated with local maxima of vorticity and strain rate respectively, nodes correspond to the maximum of the velocity divergence, implying a total three-dimensional activity. The interrelationship between critical points indicates that nodes in the (x, y) plane are most likely to occur in the saddle region and be associated with rib-like structures.

Acknowledgement
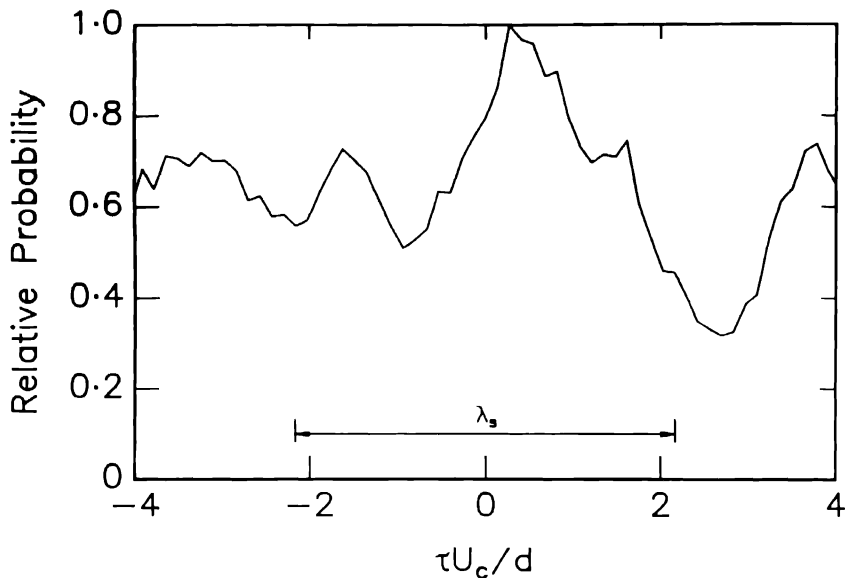
Fig. 9.   Relative probability (smoothed) of duration between nodes in the (x, y) plane and those foci in the (x, z) plane corresponding to the saddle region (window width $\simeq \pm 0.25\lambda_s$) in the (x, y) plane. ($\tau U_c/d = 0$ is the instant at which nodes are detected.)

References

Cantwell, B. and Coles, D., An experimental study of entrainment and transport in the turbulent near wake of a circular cylinder. *J. Fluid Mech.* 136 (1983) 321–374.

Chen, J., Cantwell, B. and Mansour, N.N., The topology and vorticity dynamics of a three-dimensional plane compressible wake. *Proc. Tenth Australasian Fluid Mechanics Conference*, Melbourne (1989), p. 5.1.

Chen, J.H., Chong, M.S., Soria, J., Sondergaard, R., Perry, A.E., Rogers, M., Moser, R. and Cantwell, B.J., A study of the topology of dissipating motions in direct numerical simulations of time-developing compressible and incompressible mixing layers. *CTR Proc. Summer Program 1990* (1990) pp. 139–141.

Chong, M.S., Perry, A.E. and Cantwell, B., A general classification of three-dimensional flow patterns. Stanford, SUDAAR 572 (1988).

Hayakawa, M. and Hussain, F., Three-dimensionality of organised structures in a plane turbulent wake. *J. Fluid Mech.* 206 (1989) 375–404.

Hunt, J.C.R., Wray, A.A. and Moin, P., Eddies, streams, and convergence zones in turbulent flows. *CTR Proc. Summer Program 1988.* Report CTR-S88 (1988) pp. 193–208.

Hussain, A.K.M.F. and Hayakawa, M., Eduction of large-scale organized structures in a turbulent plane wake. *J. Fluid Mech.* 180 (1987) 193–229.

Kaplan, W., *Ordinary Differential Equations.* Reading, Mass.: Addison-Wesley Publ. Co. (1958) pp. 414–423.

Kiya, M. and Matsumura, M., Turbulence structure in intermediate wake of a circular cylinder. *Bulletin of JSME* 28 (1985) 2617–2624.

Krogstad, P.-Å., Antonia, R.A. and Browne, L.W.B., Structure investigation in a turbulent boundary layer using orthogonal X-wire arrays. *Proc. Eleventh Australasian Fluid Mechanics Conf.*, Hobart (1992) pp. 251–254.

Perry, A.E., A study of degenerate and nondegenerate critical points in three-dimensional flow fields. *Forschungsbericht.* Institut für experimentelle Strömungsmechanik, Göttingen (1984) p. 63.

Perry, A.E. and Chong, M.S., A description of eddying motions and flow patterns using critical-point concepts. *Ann. Rev. Fluid Mech.* 19 (1987) 125–155.

Perry, A.E. and Steiner, T.R., Large-scale vortex structures in turbulent wakes behind bluff bodies. Part 1. Vortex formation process. *J. Fluid Mech.* 174 (1987) 233–270.

Soria, J. and Cantwell, B.J., The identification and classification of topological structures in free shear flows. *IUTAM Symposium "Eddy Structure Identification in Turbulent Shear Flows",* Poitiers (1992) pp. VII.12.1–VII.12.5.

Zaman, K.B.M.Q. and Hussain, A.K.M.F., Taylor hypothesis and large-scale coherent structures. *J. Fluid Mech.* 112 (1981) 379–396.

Zhou, Y. and Antonia, R.A., Convection velocity measurements in a cylinder wake. *Expts. in Fluids* 13 (1992) 63–70.

Zhou, Y. and Antonia, R.A., A study of turbulent vortices in the near-wake of a cylinder. *J. Fluid Mech.* 253 (1993) 643–661.

Zhou, Y. and Antonia, R.A., Critical points in a turbulent near-wake. *J. Fluid Mech.* 275 (1994) 59–81.

263

Characterization of the Organization in Shear Layers via the Proper Orthogonal Decomposition

JOËL DELVILLE
C.E.A.T., Laboratoire d'Etudes Aérodynamiques, URA CNRS 191, 43 route de l'Aérodrome, F-86036 Poitiers cedex, France

Abstract. Experiments are performed in an incompressible plane turbulent mixing layer, using various hot wire rake configurations. From these experiments, the Proper Orthogonal Decomposition is applied for kernels where the space-time correlation tensor is evaluated over different spatial meshes and velocity components configurations. The resulting decompositions are then discussed in terms of "characterization of the organization of the flow" for various scalar or vectorial approaches of the POD. An inertial range law is evidenced. The instantaneous contribution of the first modes of the POD to the organization of the flow is analyzed. A dynamical behavior for the organization of the flow is observed from the correlation between the first two modes contribution.

1. Introduction

A lot of attention has been given recently to the identification of the so-called Large Scale, Coherent, Dominant, Characteristic or Eddy structures which play a dominant role in the dynamical properties of the flow. The aim of the present paper is to specify, from an experimental investigation, what kind of information can be inferred from long time averaged stochastic quantities such as the space or space-time correlations. Two methods have become increasingly popular: the Proper Orthogonal Decomposition (POD) introduced by Lumley (1967) [15] and the Linear Stochastic Estimation (LSE), introduced by Adrian (1977) [1]. In the work presented here, only the POD is utilized.

In this paper, the POD is discussed in terms of "characterization of the organization of the flow". The POD is applied for various scalar or vectorial approaches. An analysis is then performed for the convergence efficiency, the turbulent energy representation and the modes/ scales relationship. Consideration of the instantaneous contribution of the first modes of the POD permits the determination on selected samples, of the contribution of these modes to the organization of the flow. Using a statistical approach based on these instantaneous contributions, the temporal coupling of the first two modes of the POD allows to introduce a dynamical behavior for the organization of the flow.

2. **Proper Orthogonal Decomposition**

The POD was proposed by Lumley [15] as an unbiased way to extract structures from turbulent flows. He proposed that the coherent structure is that which has the largest mean square projection on the velocity field. This maximization leads to a Fredholm integral value problem, where the kernel is the correlation tensor.

The POD is applied here for scalar configurations, involving only one component of the velocity as u (longitudinal), v (transverse) or w (spanwise). Vectorial applications are also considered where the instantaneous velocity vectors (u, v) or (u, w) are taken into account. The scalar applications of POD will be noted POD_u, POD_v and POD_w respectively, while the vectorial POD's will be noted POD_{uv} or POD_{uw}.

In the present study, only the spatial direction y (mean gradient, inhomogenous) and the time delay τ are considered. The flow being stationary, a Fourier transform has to be used in the time direction before applying the POD [15, 4]. Of course, this approach is limited by the fact that the three dimensional aspect of the flow cannot be assessed; only one slice of the flow is viewed here. Hence the full three dimensional behavior of the flow is not analyzed. However, useful information on the global organization of the flow can be outlined.

Following the approach of Lumley [15], the dominant structure of the flow can be determined from the following equation:

$$\sum^{n_c} \int \Psi_{ij}(y, y'; f) \tilde{\Phi}_j^{(n)}(y'; f) dy' = \lambda^{(n)}(f) \tilde{\Phi}_i^{(n)}(y; f),$$

where n_c is the number of velocity components on which POD is performed and where the cross-spectrum $\Psi_{ij}(f)$ is the temporal Fourier transform of the two-point space-time correlations $R_{ij}(y, y'; \tau) = \langle u_i'(y, t) u_j'(y', t + \tau) \rangle$. The averaging process involved $\langle \ \rangle$ is the conventional statistical average of different samples chosen at independent reference times t. Here, the number of components n_c is 1 or 2 depending on the scalar or vectorial approach used. The components of velocity effectively used can be either (u), (v), (w), (u, v) or (u, w) depending on the experiment under consideration.

This approach is not unique and is only one among the different ways POD may be performed. For example, POD can be derived directly from the spatial correlations, then no frequency dependence is involved [12], or from conditional measurements as in the work of Glezer et al. [11]. In this last case, the ensemble average $\langle \ \rangle$ would be based on phase locked events appearing at times $t = t_c$ where t_c corresponds to the occurrence of a given event or excitation.

From the POD, statistical quantities of the flow field can be rebuilt: energy, spectra, space-time correlations. Moreover, the use of rakes of probes, allows for reconstruction of the instantaneous contribution of each mode to the velocities [5]. Then the well known problem of the phase loss of the POD, intrinsic to the use of two-point correlations, can be overriden by the fact that, in this case, the

velocity field is known by the experimental process simultaneously over the whole inhomogeneous direction. This knowledge allows to project the instantaneous field on the eigenvectors. Hence the instantaneous contribution of each mode can be recovered.

Four main levels of POD can be introduced:
- For the one-dimensional scalar POD, only one quantity (e.g. u) is considered,
- The vectorial POD simultaneously takes into account two components. In these two cases only the inhomogeneous direction of the flow is considered.
- A third level could be to take into account the cross homogeneous direction of the flow (e.g. spanwise direction in the case of the mixing layer). In this case, the spanwise direction is included in the application of the POD (e.g. Delville & Ukeiley [6]).
- Lastly, the most general POD is to consider all the components of the velocity (e.g. Herzog [12], Moin & Moser [18] or Aubry et al. [2]).

A feature to keep in mind when applying the POD is that the first mode becomes more and more representative of the general behavior of the flow when the "complexity" of the POD is increased (i.e. when more degrees of freedom of the flow are taken into account: time, spanwise-direction, number of velocity components, ...). However, the notion of "representativity" is surely subjective, because it depends on what we consider to be efficient. For example a simple scalar slice POD (POD_u) based only on the u component of the velocity will be certainly more efficient in terms of the energy reconstruction of the u component of the velocity than more complicated PODs (i.e.: involving other components). But this POD does not take fully into account other degrees of freedom (in fact it takes into account the other spatial or temporal directions only by their integral contributions) and fully forgets the inter-component relationships. The resulting POD may then lead to a too simple unrealistic description of the flow organization. When increasing the degree of freedom, the "inter-relations" of the different parameters will bring new information about the flow features, providing a compromise between "energy representativity" and "morphological organization".

Hence, when POD is applied, several aspects remain to be specified: what is the meaning of the modes we get?, can the resulting first mode be directly linked to the "structure(s)"?, ...

In a way, the POD can be viewed as an extension of the Fourier transform where the direction for which it is performed is inhomogeneous. the modes of POD in case of homogeneity or periodicity are found to be simply the Fourier modes [16, 4]. Consequently, an analogy exists between modes of POD and modes of harmonic decompositions [7].

3. Experimental Apparatus and Flow Configuration

This study involves multi-probe (single or X-hot wires) measurements. Rakes of up to 48 single or 24 X-wires are used, providing a good resolution of the
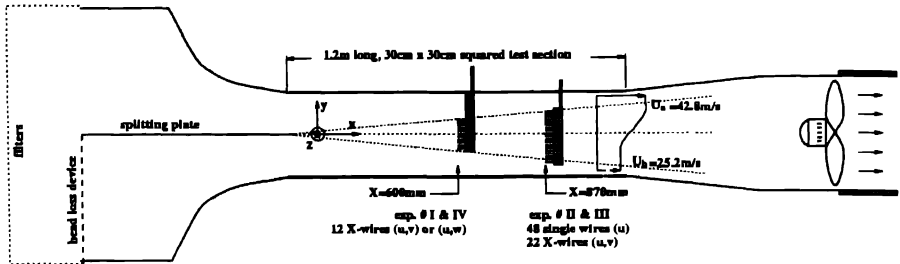
Fig. 1. Schematic of the experimental facility and of the rakes placement.

temporal-spatial behavior of the flow. The sub-minature probes are home made, with a squared cross section 1 mm × 1 mm and W-Pt wires (dia. 2.5μm, length 0.5 mm). The probe holder is also developed in our Lab from a printed circuit board. By comparing spectra, space time correlations and higher moments with the corresponding results obtained with conventional one or two single probes, it has been shown that the hot wire rake does not significantly perturb the flow at least for the abovementioned characteristics [3]. Constant Temperature Anemometers built from TSI 1750 are used; the entire hot wire rake is automatically calibrated in velocity yaw and temperature. The experimental procedure is fully automated (gain adjustment, antialiasing filtering) and the signals can be simultaneously sampled at rates of up to 100kHz. In the present study, the sampling rate is limited to 10kHz and a low-pass filtering at 5kHz is used. The number of independent samples used to estimate the cross-spectra used in this study is about 1000 samples of size 1024 instantaneous time steps per channel.

The experimental facility is an open wind tunnel (Fig. 1). The turbulent plane mixing layer is created by a flat plate splitting the streams. The velocity ratio between the two streams is controlled by different head loss devices located in the inlet section of the wind tunnel. The boundary layers on the plate are fully turbulent with a thickness of about 7 mm at the trailing edge of the plate. The test section is 1.2m long with a square section 300 mm × 300 mm. The velocity ratio between the streams is $r = U_b/U_a = 0.59$ with the high speed side and low speed side being respectively $U_a = 42.8$ and $U_b = 25.2$ m.s^{-1}. The frame of reference is Ox in the streamwise direction, Oy normal to the plate and Oz parallel to the trailing edge of the plate. The asymptotic part of the mixing layer starts from $X > 300$ mm from the trailing edge of the splitting plate.

Four independent experiments are performed at two downstream distances X from the trailing edge of the plate, in the asymptotic part of the mixing layer (see the following table). The hot wire rakes are oriented along the mean gradient direction Y. The rake extent L_y for each experiment is greater than twice the vorticity thickness δ_ω. The separation between probes Δ_Y ranges from half to twice the Taylor micro-scale λ_f measured on the mixing layer axis:

$$\lambda_f^2 = 2\bar{U}^2\overline{u'^2}\,\overline{(\partial u/\partial t)^2}^{-1}.$$

Exp #	Probes configuration	X mm	Δ_Y mm	L_y/δ_ω	δ_ω mm	λ_f mm	Re_θ $(U_a - U_b)\theta/\nu$
I	12 X wires (u, v)	600	6.0	2.2	27.6	3.6	$4.9 \, 10^5$
II	48 single wires (u)	870	1.8	2.4	35.8	4.0	$7.6 \, 10^5$
III	22 X wires (u, v)	870	3.6	2.1	35.8	4.0	$7.6 \, 10^5$
IV	12 X wires (u, w)	600	6.0	2.2	27.6	3.6	$4.9 \, 10^5$

In this study, the temporal evolutions will be related to spatial ones by use of a Taylor hypothesis by using a constant convection velocity for each scale. This convection velocity has not been estimated from the experiments and is chosen arbitrarily to be $U_c = (U_a + U_b)/2$. Of course other values could be considered for U_c. However this value gives a rough order of magnitude of the relation between temporal scales and spatial scales that can be sufficient for the following discussion. On the other hand, the use of the Taylor hypothesis to access longitudinal spatial scales from temporal ones can be discussed. The reader can refer to the papers of Zaman & Hussain [13] and Lumley [17] for the considerations that have to be taken into account when analyzing this kind of information.

4. POD Approach

SCALAR AND VECTORIAL POD

Figure 2 compares three applications of the POD performed on the same data set. The eigenvalue spectra $\lambda^{(n)}(f)$ are global and take into account the distribution of energy over the whole spatial extent of the experiment. They are representative of the occurrence of the given mode (n) in the flow realizations. Figures 2(a), (b) and (c) correspond to the scalar POD_u, POD_v and vectorial POD_{uv} respectively. The eigenvalues found from these PODs show quite different characteristics. In the case of the POD_u (Fig. 2a) the first mode is maximum for $f\delta_\omega/U_c \sim 0.15$, that is only half the value of the corresponding frequency found for the POD_v (Fig. 2b). In this flow, the typical Strouhal number found for the passage of structures (from spectral analysis at the edge of the mixing layer) is $S_w \simeq 0.3$. In this context of the scalar POD_u, the first mode seems then not to be directly related to the "structure concept".

The first mode of POD_u is in fact proportionally less representative than the one of POD_v, as proved by the significant level of energy remaining in the second mode, $\lambda_u^{(2)}$ when compared to $\lambda_v^{(2)}$. This behavior has to be related to the main organization of the flow: the passage of structures is translated onto the u component by phase oppositions of alternate signs in the external parts of the mixing layer, while the v component remains dominantly in phase over the whole y extent and presents then a simpler organization.
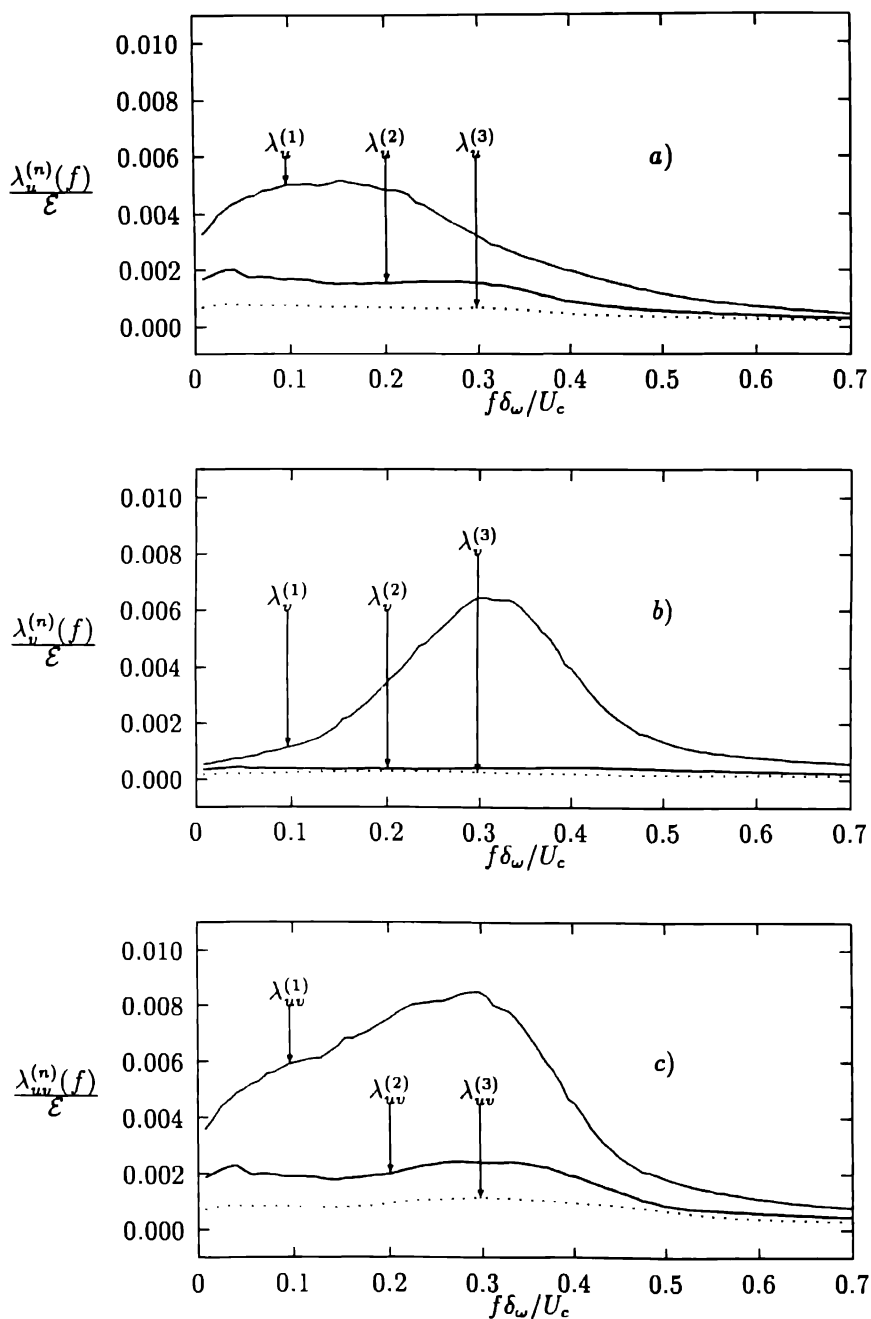
Fig. 2.   Eigenvalues distributions for a) u scalar POD, b) v scalar approach and c) vectorial u, v approach. Experiment I.
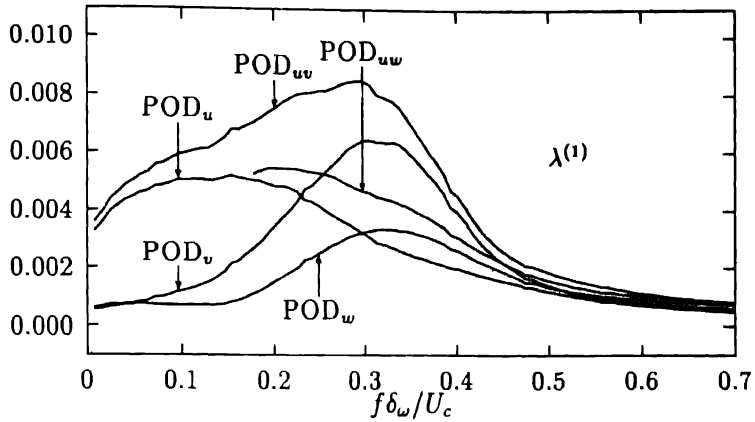
Fig. 3. Eigenvalues· First mode for various applications of the POD.

For the vectorial POD_{uv}, the first eigenvalues $\lambda_{uv}^{(1)}(f)$ correspond mainly to the envelope of the first two modes of the scalar PODs: for each frequency $\lambda_{uv}^{(1)}(f) \geq \max(\lambda_u^{(1)}(f), \lambda_v^{(1)}(f))$ This is clearly visible in Figure 3. In fact the $\lambda_{uv}^{(1)}(f)$ evolution can be split into two frequency ranges· for $f\delta_\omega/U_c < 0.2$, the u component dominates while for higher frequencies, the v component becomes dominant.

The same features can be found when the POD_{uw} is considered (Fig. 3). In the POD_{uw} the general shape and level of the eigenvalue remain close to that of the POD_u. This is due to the relative levels of $\lambda_u^{(1)}$ and $\lambda_w^{(1)}$: for each frequency, $\lambda_w^{(1)}(f)$ remains always less than $\lambda_u^{(1)}(f)$.

This overall behavior is in agreement with the definition of POD, which maximizes energy representation: for each range of frequency, the POD will "select" the corresponding more energetic component of the velocity. Moreover, because the vectorial POD_{uv} contains information on both u and v, it seems to be more effective than the scalar PODs for rendering the organization of the flow. This will be confirmed by the analysis of the space-time correlations reconstructed by the different PODs.

CONVERGENCE

The dominant POD mode, is by definition, the best representation of the turbulent energy in the flow. The energy contained in the first mode is generally found to be of the order of 40–50% [5, 8] for one-dimensional POD and up to more than 70% for higher levels of POD applications [18]. By analogy with the Fourier modes, one can expect that the degree of representativeness of one mode of the POD (i.e. the amount of energy caught by this mode) is directly linked to the number of spatial

points used. The convergence of the POD can be defined as the ratio between the energy contained in n modes and the global energy $\mathcal{E}$ contained within the flow:

$$c_n = \sum_{i=1}^{n} \mathcal{E}^{(i)} / \mathcal{E}.$$

Here $\mathcal{E}^{(i)} = \int \lambda^{(i)}(f) df$ is the energy contained in the whole field for mode (i), integrated over all frequencies. This criterion is drawn in Figure 4a for the scalar case POD_u. On this figure, the extent of the rake is kept constant while the number of probes Ny used in the rake decreases from 48 to 11 (here the number of modes one can obtain is simply Ny). For mesh sizes varying in a ratio of 4, the energy contained in the first mode remains quasi constant (about 42%). The level of representation of this mode is then a characteristic of the flow itself and is not dependent on the mesh size. However, one given mode becomes more and more biased as N decreases, as denoted by the increase of the convergence rate. For example, the energy contained in the first three modes is 0.7 for $N = 48$ and reaches 0.8 for $N = 11$.

The same kind of study can be performed in the vectorial case POD_{uv}. Similar results are obtained for the convergence of the global energy $\overline{u'^2 + v'^2}$. However in the vectorial case, one can determine the convergence of each term of the Reynolds stresses individually (fig. 4b). In this case, one can define the convergence as:

$$c_l = \int \overline{u_i'(y)u_j'(y)}^{(l)} dy \Big/ \int \overline{u_i'(y)u_j'(y)} dy$$

where

$$\overline{u_i'(y)u_j'(y)}^{(l)} = \int \lambda^{(l)}(f) \tilde{\Phi}_i^{(l)}(y, f) \tilde{\Phi}_j^{*(l)}(y, f) df.$$

The components $\overline{u'^2}$ and $\overline{v'^2}$ converge uniformly toward their asymptotic value. However the $\overline{u'v'}$ Reynolds stress starts to converge vergy quickly and then exhibits an overshoot from the third mode. This overshoot is associated with an underestimation of the $\overline{v'^2}$ component as indicated by the linear slope of the curve appearing between modes 3 and 10. This relatively quick convergence of $\overline{u'v'}$ is retrieved for a wide variety of flow configurations (e.g. Moin & Moser [18] in a channel flow or Herzog [12] in the near wall region of turbulent pipe flow or Glauser [8] in the axisymmetric jet mixing layer).

The number of modes obtained from an application of POD is $N = n_c \times Ny$ where Ny is the number of spatial nodes used. This number is always greater than the Nyquist number of the spatial mesh $(Ny/2)$ and one can ask about the significance of the extra number of modes obtained. Discussion on this Nyquist number effect can be found in the early work of Lumley [15] or more recently in Glauser and George [7, 9]. In order to clarify this point, the distribution of the relative energy $\mathcal{E}^{(n)}/\mathcal{E}$ contained in one mode is plotted in Figure 5 in a log-log representation. The convergence of POD seems to follow a quasi-universal
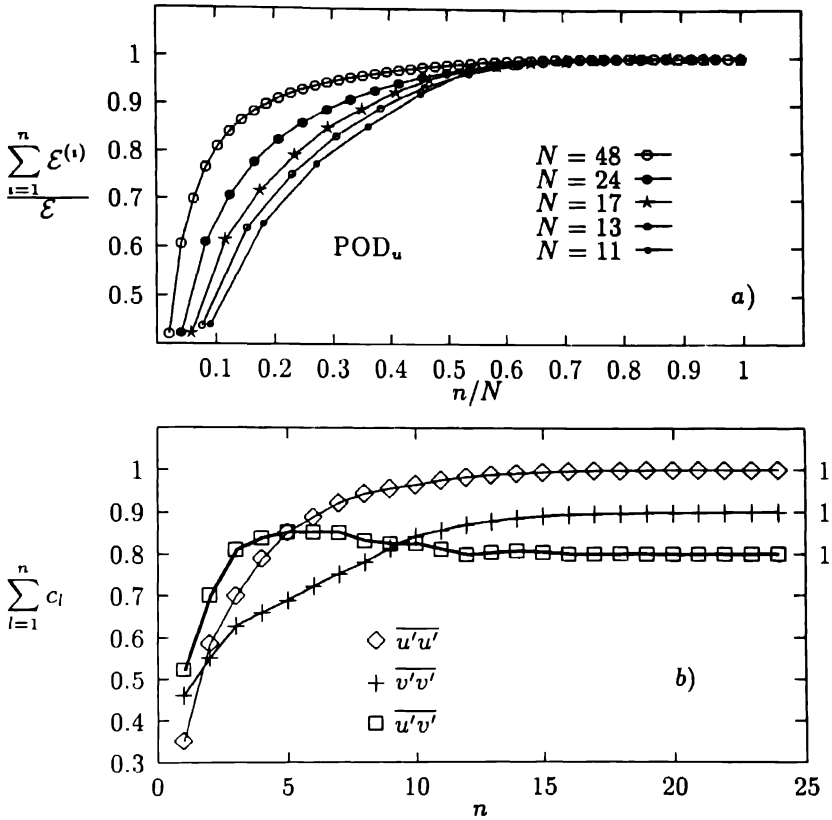
Fig 4   Convergence of POD a) Influence of number N of spatial nodes on POD convergence Scalar u POD Experiment II b) Convergence of $\langle u'_i u'_j \rangle$ Vectorial POD$_{uv}$ experiment 1

behavior. For the first modes, up to $n \sim N/2$, a first slope close to $-5/3$ is found. The higher modes follow another much higher slope ~ -12. Moreover, for the modes before $N/2$, an overshoot can be seen (Fig. 5a). The first slope can be related to a scale law and the overshoot, to an aliasing effect which is unavoidable for spatial measurements [7]. The second slope is more related to numerical effects.

The quasi-universality of this behavior is evident in Figure 5b. For different flow configurations (mixing layer, wake, axisymmetric jet), the corresponding distributions are plotted for various applications of POD (scalar or vectorial) where N is of the same order of magnitude. It can be noticed that the mode $N/2$ plays the same role of cut-off mode for the scalar PODs as well as for the vectorial ones. It should be recalled that in these last cases the number of modes obtained is twice the number of spatial nodes. Contradictorily, the cut-off mode then seems to be related to N rather than to Ny.
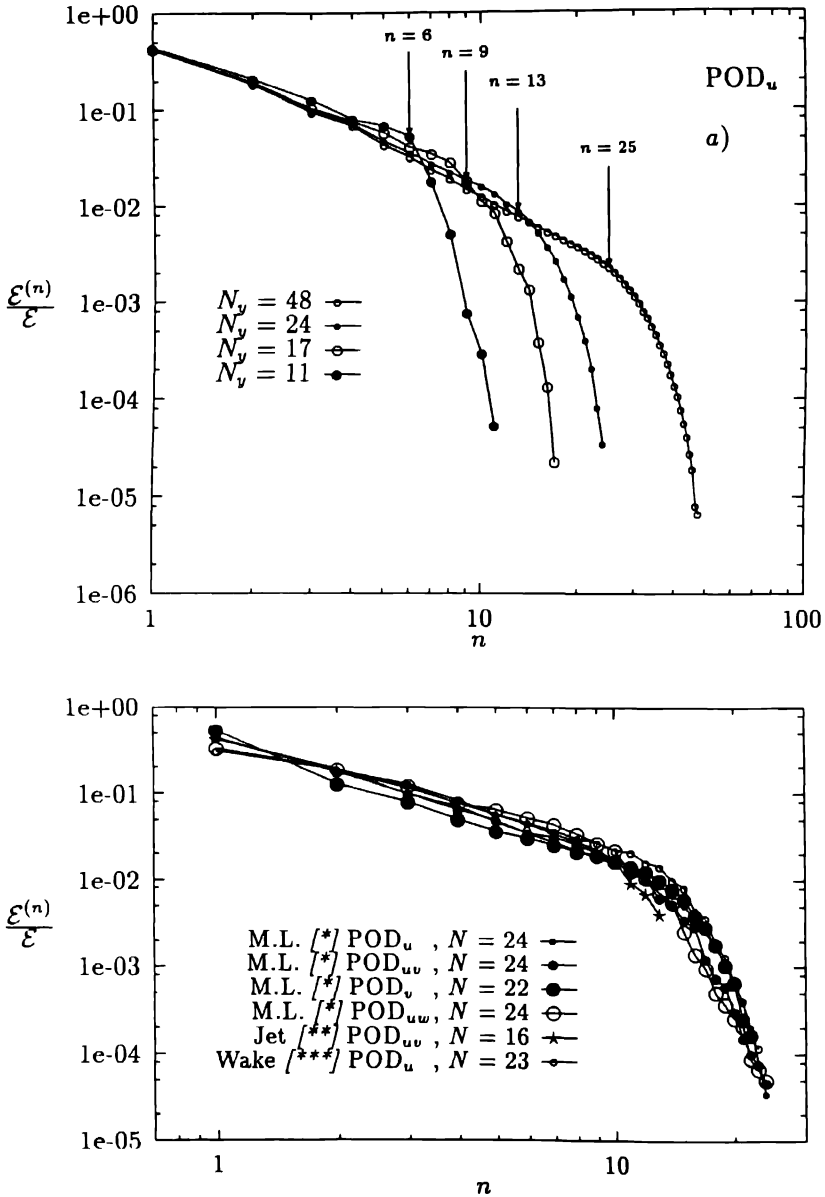
Fig. 5.   Distribution of relative energy (integrated over frequencies and space) for each mode of the POD. a) Experiment II. b) Same distribution for various applications of POD (scalar or vectorial) and for various flows: [*] present study, [**] from axisymmetric jet data [8], [***] far wake of a flat plate.

This behavior may be analyzed by analogy with the harmonic decomposition: the modes of POD can be compared with wave numbers or frequencies so that this kind of plot can be compared with a classical spectrum. In fact the relationship between the mode index n and an equivalent wave number is not trivial. For example Knight & Sirovich [14] propose that the mode index n can be related to an equivalent wave number k_n by $n \propto k_n^3$ while Moser [19] prefers to define an "effective" wave number as $k_n^2 \propto \epsilon_n$ where ϵ_n is the contribution to the dissipation of the mode n.

The slope of the POD spectrum has already been analyzed in other works: Knight & Sirovich [14], Moser [19]. This slope can be related to the existence of a Kolmogorov inertial range power-law: $E \propto \epsilon^{2/3} k^{-5/3}$. This law was established for homogeneous turbulent flows. In the case of inhomogeneous turbulent flows, both authors agree on the fact that the POD modes have to be used to characterize this inertial range. Through dimensional reasoning, Knight & Sirovich [14] argue that the existence of an inertial range is translated on the eigenvalues distribution by: $\lambda^{(n)} \propto n^{-11/9}$. The slope found in the present study is closer to $-5/3$ than to $-11/9$. In fact the distributions of relative energy plotted in Fig. 5 correspond to the summation of the eigenvalues over all the frequencies then they can be smeared by this integration. If the same plot is drawn for a POD where the frequency dependence is not taken into account i.e. corresponding to the following equation:

$$\sum_{j=1}^{n_c} \int R_{ij}(y, y') \tilde{\Phi}_j^{(n)}(y') dy' = \lambda_s^{(n)} \tilde{\Phi}_i^{(n)}(y),$$

where $R_{ij}(y, y')$ is the conventional two-point spatial correlation tensor, a different slope is found for the POD spectrum which value is closer to $-11/9$ (Fig. 6). Note that the two sets of eigenvalues cannot be directly compared for the two different PODs ($\lambda_s^{(n)} \neq \int \lambda^{(n)}(f) df$).

LOCAL SPECTRA RECONSTRUCTION

The link between the mode of the POD and the spatial scale which appears from the analysis of the convergence of the POD can be analyzed more precisely. For this purpose, the contribution of the modes to the conventional frequency spectrum is studied on the mixing layer axis:

$$E_u^{(l)}(y = 0, f) = \lambda^{(l)}(f) \tilde{\Phi}_1^{(l)}(y = 0, f) \tilde{\Phi}_1^{*(l)}(y = 0, f).$$

The contribution of the first three modes of the vectorial POD to the spectrum of the longitudinal component u is plotted in Fig. 7 for a probe lying near the mixing layer axis ($y = 0$). By using a $f.E_u(y, f)$ vs $\log(f)$ representation, the frequencies where the modes are dominant are more easily detected: the area under each curve remains then directly proportional to the energy in the frequency band considered (Fig. 7a). It is then obvious that the higher modes contribute to higher frequencies.
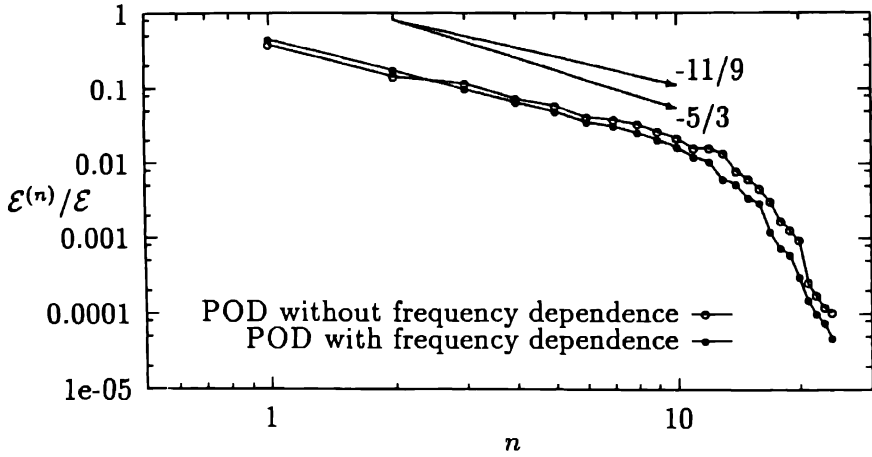
Fig. 6.   Comparison of the distribution of the relative energy for applications of the PODs with and without frequency dependence. Experiment II.

Thus, if the Taylor hypothesis is assumed they can be thought of as contributing to smaller spatial scales. The aim of this paper is not to discuss the validity of Taylor's hypothesis. However, some remarks may be drawn concerning the eventual link between modes index and spatial frequencies. One of the first problems that can be encountered with this assumption is that even if the Taylor hypothesis can be used for the full turbulent flow, applying this hypothesis for one given mode of the POD is not straightforward. On the other hand, it is well known that when the index of the mode number increases, the number of zero-crossings of the eigenfunctions also increases [18] and the eigenfunctions become locally sinusoidal [14]. A limitation to this link between spatial scales and mode of the POD can be illustrated when looking at the specific behavior of the first two modes plotted in Fig. 7. It appears that these modes are interlaced: as the frequency increases, the first mode is more dominant then the second one, then the first one again. It may then be difficult to relate one mode to only one range of scales.

In fact these modes toggle to preserve a continuous slope in the total spectrum (Fig. 7b). The resulting spectrum, obtained by keeping only these two modes, corresponds in fact to the one that can be obtained in the case of the POD_u. A typical slope (f^{-3}) is obtained [5] in this case.

SPACE-TIME CORRELATIONS

Space-time correlations (STC) rebuilt from different POD applications are plotted in Fig. 8. These STC are obtained from the eigenmodes by the inverse time Fourier Transform of $\Psi_{ij}^{(l)}(y, y', f)$ where:

$$\Psi_{ij}^{(l)}(y, y', f) = \lambda^{(l)}(f)\tilde{\Phi}_i^{(l)}(y, f)\tilde{\Phi}_j^{*(l)}(y, f).$$
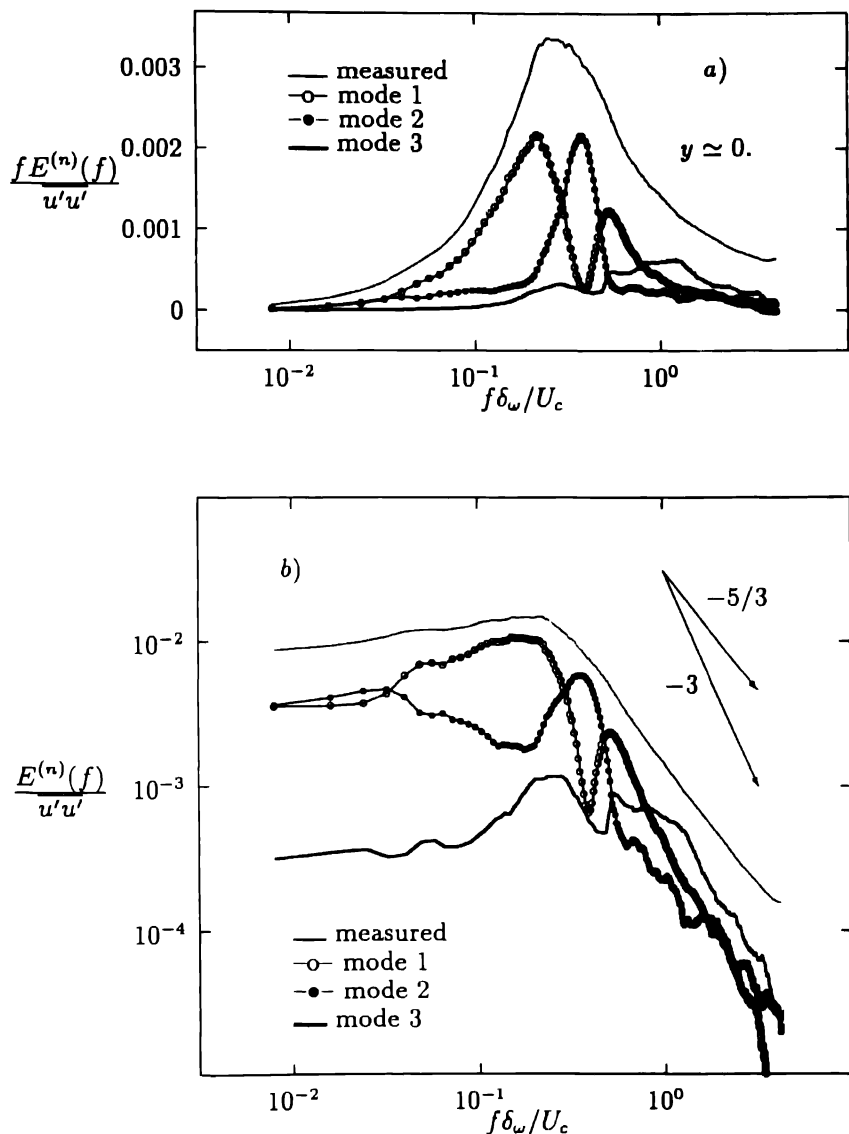
Fig. 7. Reconstruction on the mixing layer axis ($y = 0$) of the spectrum of the u component velocity. Vectorial POD experiment III. a) $f E_u(y = 0, f)$ vs $\log(f)$ representation b) log-log representation.

In each case of POD, the first mode always predicts the correlations quite well, when the reference probe is located near the mixing layer axis (Figs 8a,b,c and h to l). The prediction of R_{uu} obtained from POD_{uv} is less satisfactory than from
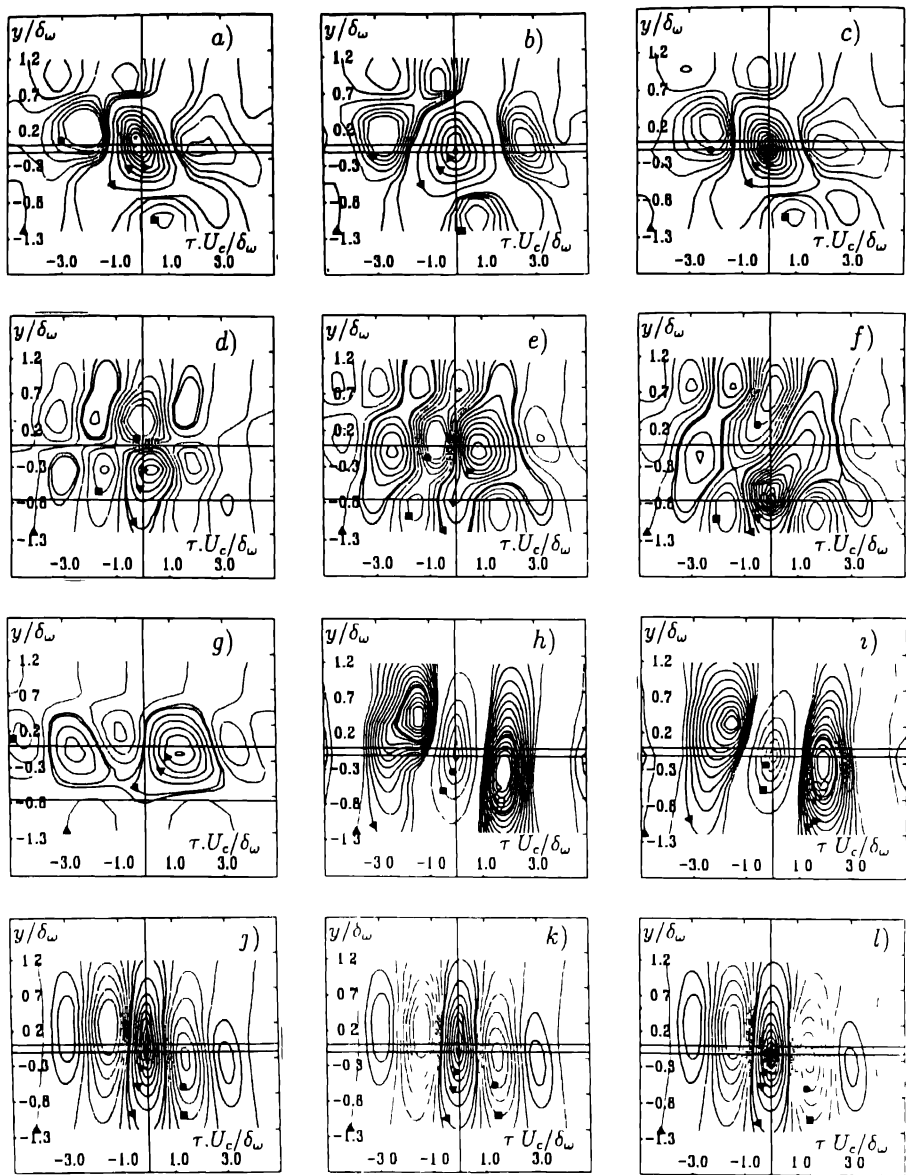
Fig 8.   Comparison of various POD reconstructions of the space time correlations in the mixing layer. (←: reference probe).

Fig.							f			j		l
R_{ij}	uu	uu	uu	uu	uu	uu	uu	uv	uv	vv	vv	vv
Y/δ_ω	0	0	0	-0 8	-0.8	-0.8	-0.8	0	0	0	0	0
POD	u	uv	orig	u	uv	orig	u	uv	orig	v	uv	orig
mode	l	l	l	2	l	l	l	l	l	l	l	l

POD$_u$, but the overall organization of the STC is preserved. This is due to the contribution of v (Fig. 8b). On the contrary, R_{vv} and even R_{uv}, predicted by the first mode of the various PODs are quite comparable (Figs 8h to l). In fact, this last characteristic can be observed, regardless of the location of the reference probe within the mixing layer.

When the reference probe is located near the external part of the mixing layer, the R_{uu} correlation is not correctly predicted by the first mode of the scalar POD$_u$ (Fig. 8f and g) and additional modes are required for a correct reconstruction (Fig. 8d). Particularly, the antisymmetric organization which is generally considered as being the trace of the passage of the structures cannot be retrieved from only the first mode. One can then question the significance of the first mode of POD$_u$ in terms of "conventional" structures. However the POD$_{uv}$ leads to a better representation (Fig. 8e) at this location. In this case, the spatial behavior of the scalar POD$_u$ is weighted by the contribution of the v component and consequently, the first mode is able to catch some new information such as the phase opposition between the external parts of the flow.

4.1. INSTANTANEOUS RECONSTRUCTION

When hot wire rakes are used, the velocity distribution is known simultaneously at each time step for the direction in which the POD is applied (y). The instantaneous velocity contribution of each mode can then be examined. The Fourier transform of the velocity can be retrieved from the eigenfunctions $\tilde{\Phi}_i$:

$$\tilde{u}_i(y, f) = \sum_{l=1}^{N} a_n(f)\tilde{\Phi}_i^{(l)}(y, f)$$

where $a_n(f)$ is found from:

$$a_n(f) = \int \tilde{u}_i(y, f)\tilde{\Phi}_i^{(l)}(y, f)dy.$$

In terms of structure identification, the participation of any mode to the instantaneous flow field can be considered. Figure 9 shows, for a selected sample, an example of the instantaneous velocity field plotted in a frame moving with the convective velocity U_c using a Taylor hypothesis based on U_c for the longitudinal direction. The sample size is $\tau U_c/\delta_\omega \simeq 18$, which corresponds to about 5.5 structure separations based on the typical Strouhal number $St_\omega = 0.3$. The organization which can be visually detected from the original velocities (Fig. 9a) is relatively well reconstructed by the first mode of the vectorial POD$_{uv}$ (Fig. 9b). However, the spatial extent of the events in the Y direction is generally underestimated, and other modes are needed to improve this spatial estimation (Fig. 9c).
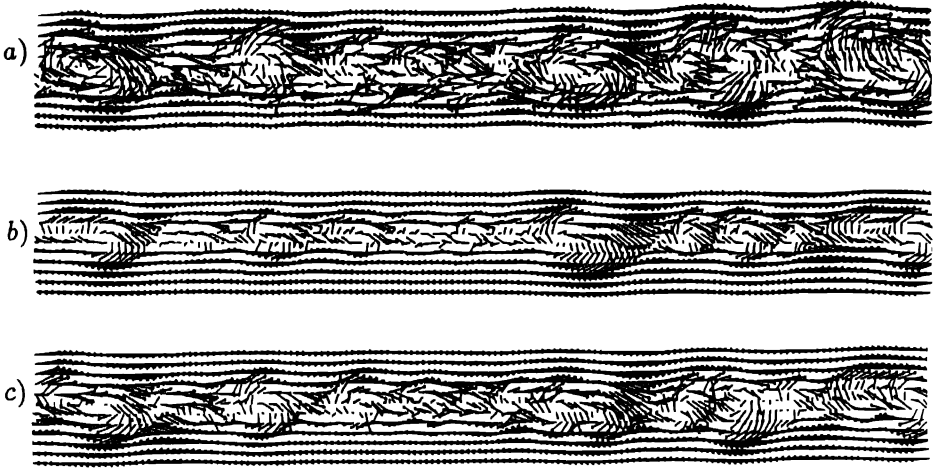
Fig. 9.   Instantaneous flow patterns in the mixing layer, experiment I: a) Original directly measured velocity field. b) Contribution of first mode of the POD_{uv}. c) Contribution of the first three modes.

4.2. COUPLING BETWEEN MODES

For each time step (or for each realization of the flow), according to the definition of the POD, each mode is statistically non-correlated with the other modes. However a *dynamic relationship* can be introduced by considering the "time correlation" between the contribution of the modes to the components of the velocity. As an example, the coupling between the modes (p) and (q) of the longitudinal component u_1 of the velocity can be written:

$$r^{p-q}(\tau) = \langle u_1^{(p)}(y,t).u_1^{(q)}(y,t+\tau)\rangle / \sqrt{\langle u_1^{(p)}(y,t)^2\rangle.\langle u_1^{(q)}(y,t)^2\rangle}.$$

In other words, a temporal coupling between modes can then be introduced and is plotted in Fig. 10. A typical resulting behavior is exhibited for r_{11}^{1-2} (Fig. 10a).

The correlation coefficient r_{11}^{1-2} is estimated only in the turbulent part of the flow ($|\,y\,| < 0.5\delta_\omega$) and for $y \neq 0$. As expected, for zero time-delay ($\tau = 0$), the correlation between the first two modes is found to be zero. Two extrema of correlation with opposite sign appear from part to part of $\tau = 0$. For the discussion, two optimal time delays are introduced: τ^+ and τ^- which correspond respectively to the maxima and minima of correlations. τ^+ is positive and τ^- is negative when $y < 0$ (low speed side) while τ^+ is negative and τ^- is positive when $y > 0$.

The temporal scale corresponding to the values of τ^+ and τ^- is one order of magnitude smaller than T_p, the one corresponding to the average time separation between structures (this last scale is of the order of $(St_\omega U_c/\delta_\omega).T_p = 1$). The characteristic delays τ^+ and τ^- seem then to represent the behavior of a process appearing within the structure itself, or to be related to a phenomenon not directly linked to the convection of the structure.
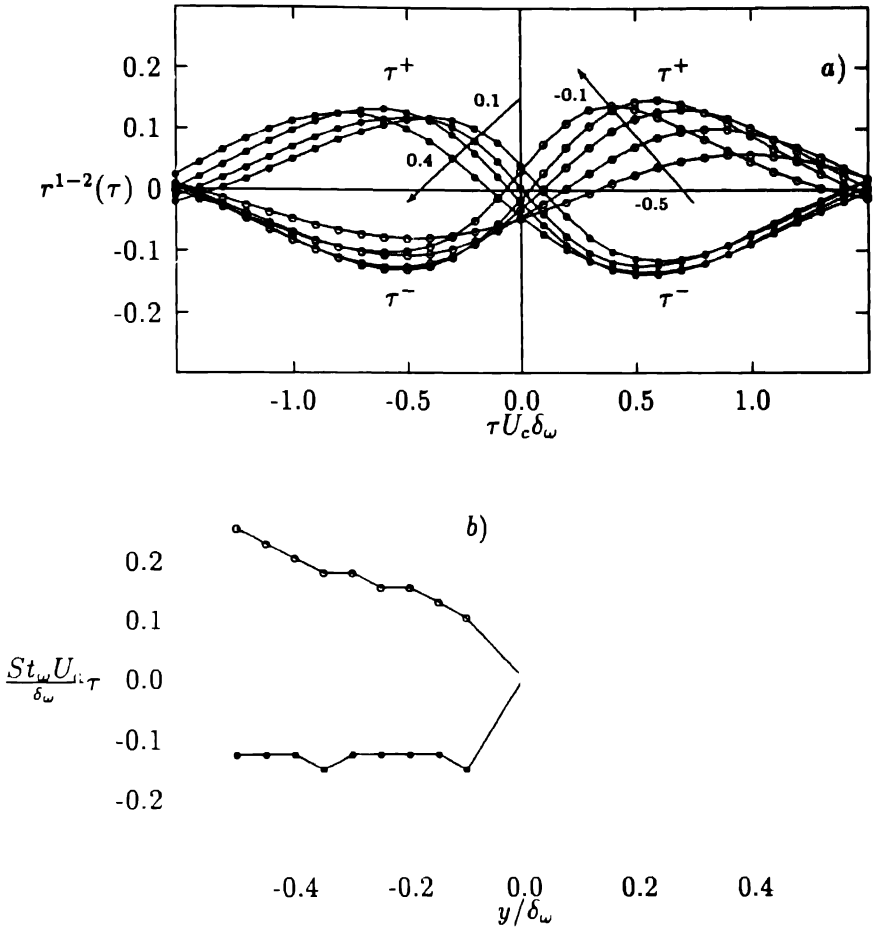
Fig. 10. Coupling between modes 1 and 2. Mixing layer, scalar u POD, experiment II. a) Evolution of the temporal correlation coefficient for $y/\delta_\omega = -0.5$ to -0.1 and 0.1 to 0.4. b) Corresponding evolution of the optimum correlation time delay.

A quite different behavior is found for the positive and negative correlations: For each y location, $(St_\omega U_c/\delta_\omega) \cdot \tau^-$ remains quasi-constant, of the order of $\pm 1/8$, while $(St_\omega U_c/\delta_\omega) \cdot \tau^+$ is quasi-proportional to y, the distance from the axis with a slope -0.5 (Fig. 10b).

These specific behaviors remain delicate to analyze, due to the nature of the signals under consideration. However an explanation can be attempted.

If the iso-correlation plots of the first two modes of the POD are considered (Figs 8a and d), it appears first that $R_{uu}^{(1)}$ presents a negative tilt. The optimum time delay of this correlation evolves proportionally to y (i.e. block rotation). Contrarily

for $R_{uu}^{(2)}$ the optimum time delay remains constant and close to zero (i.e. block translation).

It can be guessed that the correlation between the mode 1 and the mode 2 will present the same feature as the one of the first mode alone. This feature is clearly evidenced when τ^+ is considered. The relation $\tau^+/T_p \sim -0.5y/\delta_\omega$ is obtained experimentally.

The block rotation due to the mean shear can be expressed $\Delta U/\delta_\omega$, where $\Delta U = U_a - U_b = (1-r)/(1+r)U_c$ with $r = 0.6$; then in the present experiment $\Delta U \sim U_c/2$. The corresponding evolution with y of the optimum time delay is $\tau_{opt}/T_p = y/\delta_\omega[\delta_\omega/\Delta U] \sim 2yS_{t\omega}/\delta_\omega \sim 0.6y/\delta_\omega$.

The optimum time delay τ^+ between mode 1 and 2 is then very close to τ_{opt}, the time delay due to the mean shear, and the proportionality between τ^+ and y may be assumed to be related to this mean shear (or mean large scale vorticity) of the flow $(\Delta U/\delta_\omega)$. In fact for τ^+ the mean shear effect is dominant and probably smears other possible effects.

The fact that τ^- remains constant whatever the y location may be linked to a different coupling or a time triggering between the first two modes. The present results do not allow to clarify this possible coupling and other studies are needed in order to analyze more precisely what occurs. However, it has to be recalled that the dominant frequencies of the first two modes differ, the second mode appearing in average about twice when the first mode appears once (Fig. 7). Then if a triggering exists between these modes it will surely not be simple. Nevertheless a typical time delay between these two modes of the order of $T_p/8$ can be evidenced. The dynamic of these coupling remains to be explained. We can hope that studies based on dynamical system approaches such as the ones developed by Aubry et al. [2] in the near wall region, by Glauser et al. [10] in the jet or more recently by Ukeiley et al. [20] in the present flow will bring new information on this behavior.

5. Conclusion

The convergence of POD under different scalar or vectorial applications and for various flow configurations seems to follow a quasi-universal behavior. A power law can be introduced for the modes up to a Nyquist cut-off mode number. This feature, combined with the frequency contribution of the modes to the spectra on the mixing layer axis, show that the higher modes of POD can be related to smaller spatial scale characteristics. From the analysis of the reconstruction of space time correlations and of instantaneous velocity profiles, the vectorial POD is found to produce a better representation of the organization of the flow in terms of "structures" than more simple PODs. Lastly, the temporal coupling between the first two modes of POD exhibits an asymmetric behavior when in phase or opposite phase couplings are considered.

Acknowledgements

References

1. Adrian, R.J., On the role of conditional averages in turbulence theory. *Turbulence in Liquids*. Science Press, Princeton (1977) 323.
2. Aubry, N., Holmes, P., Lumley, J. & Stone, E., The dynamics of coherent structures in the wall region of a turbulent boundary layer. *J. Fluid Mech.* 192 (1988) 115–173.
3. Bellin, S., "Etude Expérimentale des Structures Cohérentes d'une Couche de Mélange Plane Turbulente de Fluide Incompressible". Thèse Université de Poitiers (1991).
4. Berkooz, G., Holmes, P. & Lumley, J., The proper orthogonal decomposition in the analysis of turbulent flows. *Annual Review of Fluid Mech.* 25 (1993) 539–575.
5. Delville, J., Bellin, S. & Bonnet, J -P., Use of the proper orthogonal decomposition a plane turbulent mixing layer. In O. Metais and M. Lesieur (eds), *Turbulence and Coherent Structures*. Kluwer Academic Publishers Dordrecht (1990), pp 75–90.
6. Delville, J. & Ukeiley, L., Vectorial proper orthogonal decomposition, including spanwise dependency, in a plane fully turbulent mixing layer. In *Proceedings of the Ninth Symposium on "Turbulent Shear Flows"*. Kyoto, Japan, August 16–18, 1993 16–3.
7. George, W. & Glauser, M., Flow structure identification from multi-point measurements. *Proceedings of the Second World Conference on Experimental Heat Transfer, Fluid Mechanics and Thermodynamics*. Dubrovnik, Yugoslavia, June 23–28, 1991.
8. Glauser, M., "Coherent structures in the axisymmetric turbulent jet mixing layer". PhD Dissertation, Buffalo University (1987).
9. Glauser, M. & George, W., Application of multipoint measurements for flow characterization. *Experimental Thermal and Fluid Sciences* 5 (1992) 617–632.
10. Glauser, M.N., Zheng, X. & Doering, C.R., The dynamics of organized structures in the axisymmetric jet mixing layer. In O. Metais and M. Lesieur (eds), *Turbulence and Coherent Structures*, Kluwer Academic Publishers, Dordrecht (1989), p. 253.
11. Glezer, A., Kadioglu, A.J. & Pearlstein, A.J., Development of an extended proper orthogonal decomposition and its application to a time periodically forced plane mixing layer. *Physics of Fluids A.* 1 (1989), p. 1363.
12. Herzog, S., The large Scale Structure in the Near-Wall of Turbulent Pipe Flow. PhD Dissertation, Cornell University (1986).
13. Zaman K.M.B.Q. & Hussain, A.K.M.F., Taylor hypothesis and large-scale coherent structures. *J. Fluid Mech.* 112 (1981) 379–396.
14. Knight, B. & Sirovich, L., Kolmogorov inertial range for inhomogeneous turbulent flows. *Phys. Review Letters* 65 (1990) 1356–1359.
15. Lumley, J.L. 1967 The structure of inhomogeneous turbulent flows. In *Atmospheric Turbulence and Radio Wave Propagation* (ed. A.M. Yaglom & V.I. Tatarski), pp. 166–178, Moscow: Nauka.
16. Lumley, J.L., *Stochastic Tools in Turbulence*. Academic Press, New York (1970).
17. Lumley, J.L., Interpretation of time spectra in high intensity shear flows. *Phys. of Fluids* 8 (1965) 1056–1062.
18. Moin, P. & Moser, R.D., Characteristics-eddy decomposition of turbulence in a channel. *J. Fluid Mech.* 200 (1989) 471–509.
19. Moser, R., Kolmogorov inertial range spectra for inhomogeneous turbulence. *Phys. of Fluids* 6 (1994) 794–801.
20. Ukeiley, L., Delville, J., Bonnet, J.P. & Glauser, M., "A Dynamical Systems Model for Large Scales in a Plane Turbulent Mixing Layer". *Proceedings of the 12th U.S. National Congress of Applied Mechanics*. Seattle, June 1994, 364.

The Application of Classical POD and Snapshot POD in a Turbulent Shear Layer with Periodic Structures[†]

D. HILBERG, W. LAZIK and H.E. FIEDLER*
*Hermann-Föttinger-Institut, Technische Universität Berlin, Germany (*author for correspondence)*

Abstract. The classical and snapshot proper-orthogonal-decomposition was applied to data taken in a one-stream mixing layer in a narrow channel. Due to this particular geometry the flow develops large periodic structures. POD-analysis of simultaneously measured velocity components in spanwise direction identify as largest mode not only their periodic fraction, but also higher Fourier modes of the two-dimensional fluctuation. The energy content of the plane motion reaches values of about 90%. The amplitude of small three-dimensional vortices embedded in higher POD modes is correlated with the phase of the large structures, which indicates their influence on the entire turbulent motion.
Application of scalar snapshot POD on phase averaged data of the entire flow field allows separation into modes. The eigenvalues and eigenvectors show identical distribution for the u'- and v'-component. Comparison of streakline plots of the reconstructed velocity field from different numbers of modes with flow visualization exhibits that the largest physical structure is described by only the first two modes. This is also supported by calculation of the vorticity component in z-direction. The total energy content of the largest structure is approximately 60%.

1. Introduction

The classical POD as introduced by Lumley (1967, 1981) and Sirovich (1989) and the snapshot POD suggested by Sirovich (1987) and Sirovich and Kirby (1987), both based on the Karhunen–Loeve expansion (Loeve, 1955), were applied to hot-wire measurements taken in the turbulent region of a one-stream mixing layer with small sidewall distances B, where B is typically less 1/10 of the test section of length L. Due to this geometry this flow develops periodic structures of large scale corresponding to the test section length. The periodicity is caused by the feedback of coherent acoustic waves originating at the trailing edges of the two sidewalls, when a dominating structure leaves the test section. These waves travel upstream, where they trigger a new wave at the trailing edge of the mixing layer. Accordingly, the Fourier spectrum shows a strong peak with a periodic fraction of about 30–45% of the total u'-value. Correlation measurements and flow visualization in spanwise direction exhibit the two-dimensionality of the periodic motion (Hilberg and Fiedler, 1989; Fiedler and Hilberg, 1992).

2. The Classical and Snapshot POD Method

The POD methods applied here are based on a scheme suggested by Glezer et al. (1989). Assuming u'-fluctuations to be measured simultaneously at M-positions in space and at N-points in time, the time series of the data is to be combined in a matrix A as columns $a^{(i)}$

$$A = u'_{ij} \qquad i = 1, 2, \ldots M; j = 1, 2, \ldots, N$$

$$a^{(i)} = (u'_{i1}, u'_{i2}, \ldots, u'_{iN}) \qquad i = 1, 2, \ldots, M.$$

For optimal representation of the time series an orthogonal basis Ξ is searched, for which the mean quadratic scalar-product

$$\xi^{(k)} = \sum_{i=1}^{M} (a^{(i)} \cdot \Xi^{(k)})^2 \qquad k = 1, 2, \ldots, M$$

is maximized. This leads to an eigenvalue problem

$$(A^T A)\Xi^{(k)} = \xi^{(k)}\Xi^{(k)} \qquad k = 1, 2, \ldots, M.$$

EISPACK routines were used for the numerical solution and decomposition of the signals into orthogonal POD modes of number M. The corresponding eigenvalues ξ denote the energy content. The flow field corresponding to a POD mode is calculated from

$$\langle u' \rangle^{(k)} = a_t^{(k)}\Xi^{(k)},$$
$$a_t^{(k)} = A\Xi^{(k)}, \qquad k = 1, 2, \ldots, M,$$

where the coefficients a_t are functions of time only. Summation over the flow-fields allows the reconstruction of the original velocity field.

This method is known as the classical POD. By exchanging rows and columns of the matrix A the snapshot POD is obtained, where one column corresponds to one instantaneous 'snapshot' of the flow field. In this case then, the eigenvectors Ξ are functions of time and the coefficients a_t are functions of space.

3. Application of Classical POD

The classical POD method was applied to u'-time series measured simultaneously with a rake of four hot-wires at different transverse positions, each 5 mm apart, in a narrow mixing layer with $B = 30$ mm and $L = 1200$ mm. The nozzle velocity was $U_0 = 8$ m/sec. The test section with adjustable sidewalls is shown in Fig. 1. Typical dimensions are displayed in the sketch. Rake measurements were done at the streamwise positions $x = 200, 400, 600, 800, 1000$ and 1200 mm and at 41 different lateral positions with a resolution of $\Delta y = 10$ mm.

U_o = 2 - 10m/sec
H = 175 - 300 mm
B = 20 - 300 mm
L = 1200 1450 mm
h = 650 mm
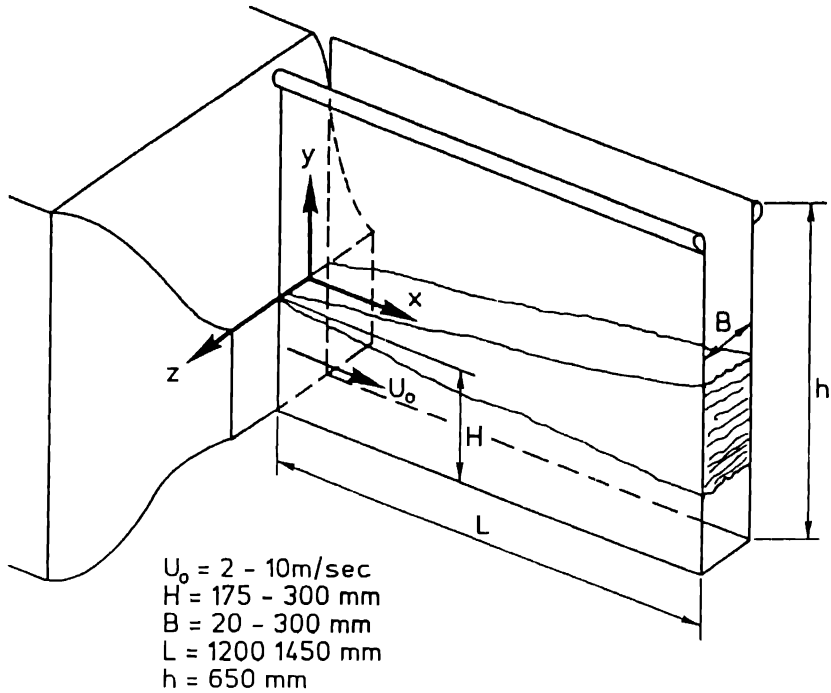
Fig.   Sketch of the test section

Figure 2 shows the distribution of four eigenvalues over the y-axis at different streamwise positions, where b denotes the local width of the shear layer. At all positions the normalized energy content of the first POD mode is significantly higher than that of the other modes, reaching maximum values of 65–90%. This indicates that more than just the periodic energy is captured in the first POD mode. The y-position of the maximum within the mixing layer is identical with the location of the largest periodic fraction.

At streamwise positions close to the splitterplate the first eigenvalue shows a second maximum outside the mixing layer at negative y-positions. Closer inspection shows that the corresponding eigenvectors differ from those within the shear-layer. At positions further downstream this behaviour is no longer observed. The calculated components of the eigenvectors Ξ within the mixing layer have nearly equal distribution for each vector at all streamwise and lateral positions. An example is shown in Fig. 3 for $x = 1000$ mm. Small differences of the components of respective eigenvectors at different lateral positions at $x < 400$ mm are vanishing further downstream, being independent of y. Particularly, the components of the first eigenvector are identical also in spanwise direction, which points at the two-dimensionality of the large structures depicted by the first POD mode. This is in agreement with correlation measurements of the periodic part of the turbulent
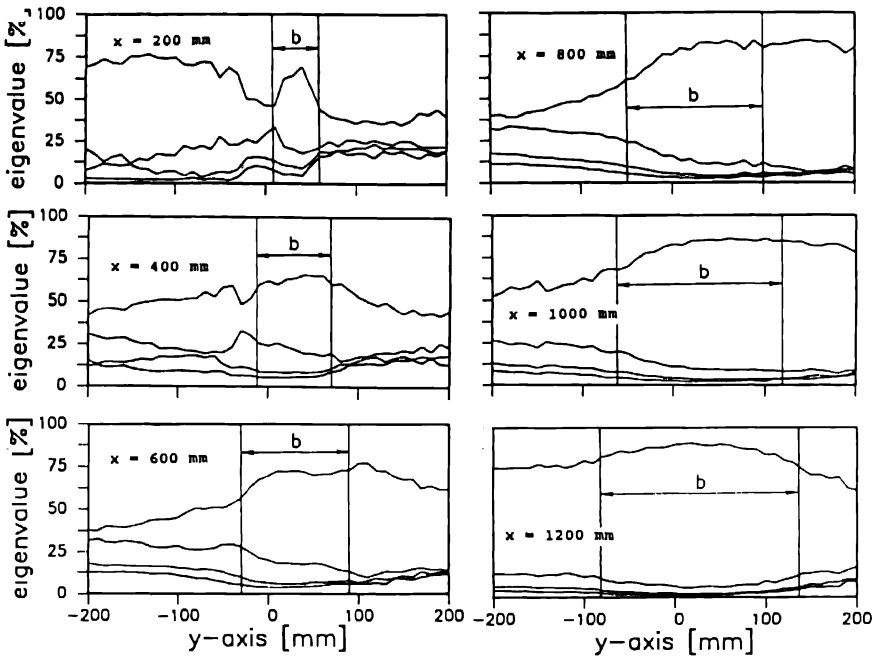
Fig. 2.   Eigenvalues at different x-positions as functions of y.
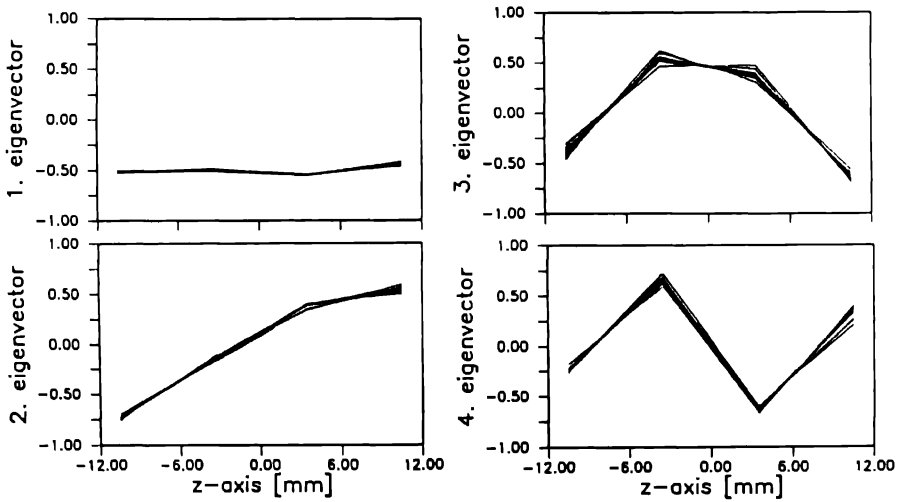
Fig. 3.   Eigenvectors at $x = 1000$ mm.
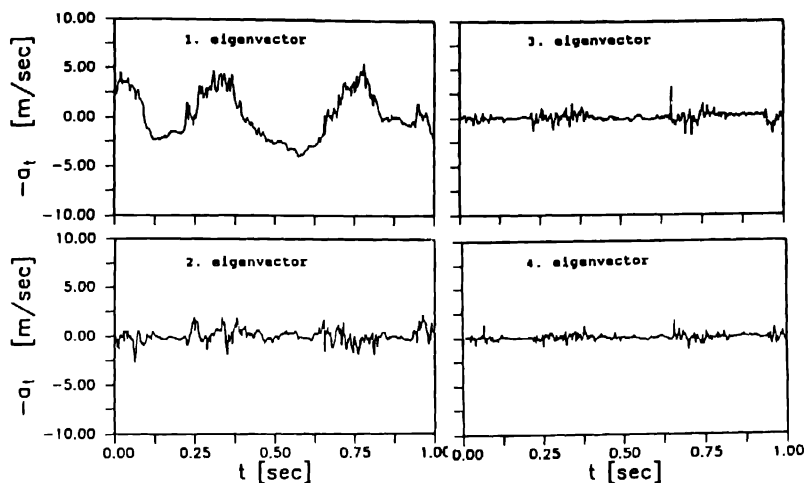
Fig. 4.   Coefficients at $x = 1000$ mm.

motion. In relation to the corresponding eigenvalues the two-dimensional fraction of the turbulent fluctuations describes most of the turbulent motion within the narrow shear-layer.

Figure 4 shows the coefficients a_i at $x = 1000$ mm and $y = 40$ mm, where the first eigenvalue has its maximum. The large periodic fraction is found only in the coefficient of the first mode. However, also higher Fourier modes are embedded in this mode, indicating a two-dimensionality of higher spectral fractions. Especially the small scale fluctuations near the maximum of the large scale motion suggest that the small three-dimensional vortices are partly stretched by the large structures, thereby becoming essentially two-dimensional.

The other POD modes include only higher Fourier modes. Obviously, there is a correlation between the phase of the large fluctuation and the amplitude of the motion captured by the higher modes. This is clearly seen in the third and fourth modes, showing the influence of larger structures on the entire turbulent motion. Due to this phenomenon the mixing process in the shear-layer may be different from that in more or less stochastic turbulence. The large vortex rolls up layers of potential fluid from both sides, where the mixing between those is generated by small scale vortices. This is supported by measurements of intermittency, which shows considerably smaller values than those obtained in the wide shear layer.

4. Application of Snapshot POD

For the application of snapshot POD phase-averaged u- and v-data were taken with an X-wire probe in a field of 451 lateral and streamwise positions in the centre
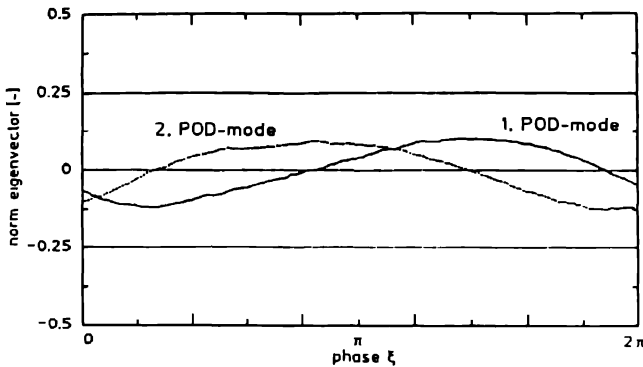
Fig. 5.   First and second eigenvector.
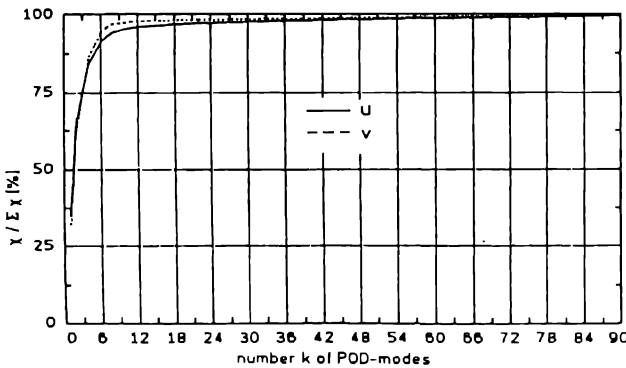
Fig. 6.   Eigenvalue distribution.

plane between the sidewalls. The inherent periodicity of the flow was stabilized by weak forcing to simplify the eduction of data.

A total of 180 snapshots at equidistant phase positions were calculated. The components of corresponding eigenvectors of the u'- and v'-data show strong similarity. The eigenvectors of the first and second mode show the same periodicity of one wavelength, however, with a phase shift of about 180 degrees (Fig. 5). Corresponding normalized eigenvalues reach vales of 30%. Higher modes have exponentially decreasing eigenvalues (Fig. 6) and the components of the eigenvectors exhibit smaller wavelengths, decreasing by integer fractions. The first four modes alone describe about 80% of the total energy. According to the previous results of the classical POD analysis, the energy containing modes of the snapshot POD should be two-dimensional. The application of the snapshot POD at other spanwise locations show, that the first four modes are independent of z.

Velocity and streakline plots were calculated from the reconstructed flow field with different numbers of modes. Thus, reconstruction from the first ten modes provides a reconstruction quality of 96%, according to a criterion by Sirovich
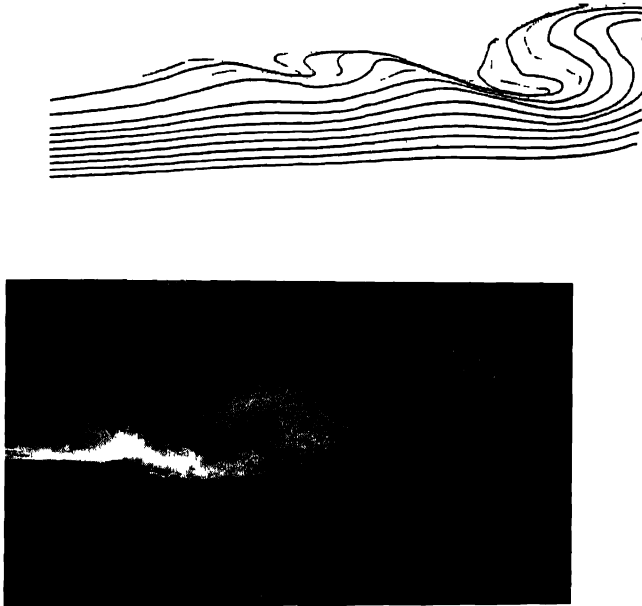
Fig. 7.   Streakline reconstruction and flow visualization.

and Kirby (1987). Comparison of streakline plots and flow visualization enables the identification and association of physical patterns to POD modes, showing in particular the largest physical structures to be contained in the first four modes (Fig. 7).

Calculation of the vorticity component $\omega_z \approx -\partial u/\partial y$ of the original and reconstructed velocity field by use of different number of POD modes ($k = 2, 4$ and 180) shows that only 2 of 180 modes contain the largest fraction of coherent vorticity (Fig. 8). Also streakline plots identify the largest visible structure to be represented by only the first two POD modes.

5. Conclusions

Both, classical and snapshot POD, were applied to data measured in a shear-layer with small sidewall distance. The classical POD showed that the major portion, up to 90%, of the turbulent energy within the shear-layer is typically of two-dimensional character. This fraction is described by the first POD mode. This mode includes, however, not only the periodic part of the fluctuation referring to the significant peak in Fourier spectra, but also higher Fourier modes. It was shown, that the coherent physical structures are described by only the first mode. In principle, those results may also be obtained by extracting coherent Fourier modes
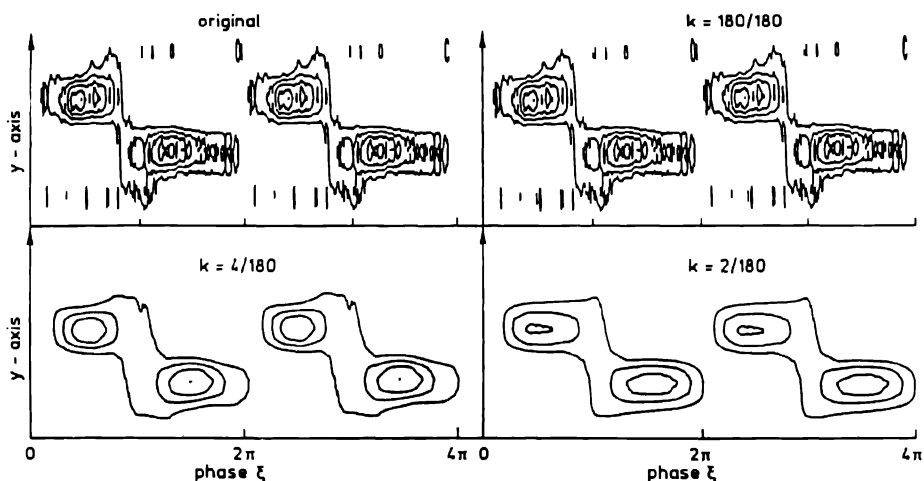
Fig. 8.   Comparison of vorticity component, ω_z of original and reconstructed velocity field at $x = L$ as function of phase (POD modes: $k = 2, 4$ and 180).

by correlation calculations. However, the POD does not require pre-information about the correlation functions, so that the computation time is reduced. In contrast to methods requiring a given base, POD is an objective analysis (Lumley, 1981).

Application of snapshot POD on phase-averaged data permits unambiguous separation of modes, which are related to physical patterns. The first four modes contain about 80% of the energy. The reconstructed velocity field from 10 modes out of 180 shows less than 4% overall deviation when compared to the original data. Comparison of streakline plots with flow visualization identifies the first four modes to be included in the typical structure.

References

Fiedler, H.E. and Hilberg, D., Control of turbulent shear flows via stationary boundary conditions. In *NATO Advances Research Workshop: The Global Geometry of Turbulence* (1992).

Glezer, A., Kadioglu, Z. and Pearlstein, A.J., Development of an extended proper orthogonal decomposition and its application to a time periodically forced mixing layer. *Physics of Fluids A* (1989) 1363–1373.

Hilberg, D. and Fiedler, H.E., The spanwise confined mixing layer. In Fernholz and Fiedler (eds), *Advances in Turbulence*, Vol. 2 (1989) pp. 443–448.

Loeve, M., *Probability Theory*. Van Nostrand (1955).

Lumley, J.L., The structure of inhomogeneous turbulent flows. In Yaglom and Tatarski (eds), *Atmospheric Turbulence and Radio Wave Propagation* (1967).

Lumley, J.L., Coherent structures in turbulence. In *Transition and Turbulence* (1981).

Sirovich, L., Turbulence and the dynamics of coherent structures, parts i–iii. *Quart. J. Appl. Math.* 45 (1987) 561–590.

Sirovich, L., Chaotic dynamics of coherent structures. *Physica D* 37 (1989) 126–145.

Sirovich, L. and Kirby, M., Low dimensional procedure for the characterization of human faces. *J. Opt. Soc. Am.* (1987) 519–525.

Stochastic Estimation of Conditional Structure: a Review

RONALD J. ADRIAN
University of Illinois, Department of Theoretical and Applied Mechanics, 216 Talbot Laboratory, 104 S. Wright Street, Urbana, IL 61801, U.S.A.

Abstract. Mean square estimation methods can be applied to the approximation of conditionally averaged turbulent fields to educe mean structure of the fields. The mathematical procedure is reviewed, and the results obtained by selecting events of increasing complexity are summarized.

1. Introduction

In a general sense, stochastic estimation is the approximation or estimation of a random variable in terms of some other random variables which are known. In the context of turbulent structure identification the estimated variable is typically the velocity field $\mathbf{u}' = \mathbf{u}(\mathbf{x}', \mathbf{t}')$ for some domain of positions and times, and the known variables are associated with the occurrence of certain events at one or more points in the field. Their totality is referred to as the *event data vector*, $\mathbf{E}$. We shall denote the estimate of $\mathbf{u}'$ by $\hat{\mathbf{u}}'$.

The best mean square estimate of $\mathbf{u}'$ given the data $\mathbf{E}$ is the conditional average of $\mathbf{u}'$ given $\mathbf{E}$, $\langle \mathbf{u}' \mid \mathbf{E} \rangle$. That is, of all possible estimates $\mathbf{u}' = \mathbf{F}(\mathbf{E})$, $\langle [u_i' - F_i(\mathbf{E})]^2 \rangle$ is a minimum when $F = \langle \mathbf{u}' \mid \mathbf{E} \rangle$. In general, $\langle \mathbf{u}' \mid \mathbf{E} \rangle$ is a non-linear function of $\mathbf{E}$, but under the condition that the elements of $\mathbf{u}'$ and $\mathbf{E}$ are joint normally distributed, it is well known that $\langle \mathbf{u}' \mid \mathbf{E} \rangle$ is a linear function of $\mathbf{E}$ (Papoulis, 1984). Often, this property is applied approximately to non-normal random variables by postulating an estimate of $\mathbf{u}'$ in the form of a linear combination of the event data. Then one speaks of *linear mean square estimation*. This is a well-known subject, thoroughly discussed in the literature of stochastic theory (Papoulis, 1984; Deutsch, 1965). The mean square error of the linear estimate must be greater than or equal to that of the conditional average.

The application of linear mean square estimation to a turbulent field $\mathbf{u}'$ raises certain objections, in part because the linear approximation seems unlikely to be able to describe a strongly non-linear phenomenon, and in part because the joint normal property has not enjoyed much success as an approximation in turbulence. Another objection is that any estimate of $\mathbf{u}'$ in terms of event data $\mathbf{E}$ must become erroneous as the location $\mathbf{x}'$ moves away from the location of the event data, because $\mathbf{u}'$ will become uncorrelated with the event data for large spatial (or

temporal) separations. However, this latter objection is easily answered because the conditional average $\langle u' \mid E \rangle$ also has this same property, and we traditionally accept its consequences.

Instead of estimating u' as a function of E, it is more straightforward conceptually to estimate $\langle u' \mid E \rangle$, which can always be interpreted as random variable since it is a function of E, and E is random. Then, it is natural to expand $\langle u' \mid E \rangle$ in a Taylor series about $E = 0$ and truncate at some level (Adrian, 1977, 1979). When the series contains only first order terms, we refer to this as the *linear stochastic estimation* (LSE) to distinguish it from linear mean square estimation. In fact, the linear stochastic estimate of $\langle u' \mid E \rangle$ and the linear mean square estimate of u' are numerically equal, so the principal difference is one of interpretation. In particular, while the mean square error of the linear estimate of u' must be large when u' is uncorrelated with E, due, for example, to a large separation between x' and the location of the event data, the error of the linear stochastic estimate of $\langle u' \mid E \rangle$ may be small because $\langle u' \mid E \rangle$ also vanishes as the separation becomes large.

The equations for *linear* stochastic estimations of the $\imath$th component of u' are

$$\hat{u}'_\imath = \text{linear estimate of } \langle u'_\imath \mid E \rangle = \sum_{J=1}^{M} L_{\imath J} E_J, \tag{1}$$

where M is the number of event data, and $L_{\imath J} = L_{\imath J}(\mathbf{x}, \mathbf{x}')$. The estimation coefficients $L_{\imath J}$ are chosen so that the mean square error

$$\left\langle [\langle u'_\imath \mid E \rangle - \sum_J L_{\imath J} E_J]^2 \right\rangle = \text{minimum}, \quad \imath = 1, 2, 3 \text{ and } \jmath = 1, \ldots, M. \tag{2}$$

A necessary condition for minimization is the *orthogonality principle* which states that the errors $\langle u'_\imath \mid E \rangle - \sum_J^M L_{\imath J} E_J$ are statistically orthogonal to the data:

$$\left\langle [\langle u'_\imath \mid E \rangle - \sum_J L_{\imath J} E_J] E_k \right\rangle = 0, \quad \imath = 1, 2, 3 \quad \jmath, k = 1, \ldots, M. \tag{3}$$

Simple manipulation leads to the *Yule–Walker* equations, an $M \times M$ system of linear algebraic equations for the coefficients $L_{\imath J}$ whose coefficients are the correlations between each event datum and every other event datum and the quantity being estimated,

$$\sum_{J=1}^{M} \langle E_J E_k \rangle L_{\imath J} = \langle E_k u'_\imath \rangle, \quad \jmath, k = 1, \ldots, M. \tag{4}$$

If the data consist of velocity vectors $\mathbf{u}_\alpha = \mathbf{u}(\mathbf{x}_\alpha, t_\alpha)$ at a set of space-time points $\{\mathbf{x}_\alpha, t_\alpha\}$, $\alpha = 1, \ldots, N$, then $\langle E_J E_k \rangle$ involves only the second-order, two-point space-time correlation $R_{Jk}(\mathbf{x}_\alpha, \mathbf{x}_\beta, t_\alpha, t_\beta)$ and $\langle E_k u'_\imath \rangle$ reduces to

$R_{ki}(\mathbf{x}_\alpha, \mathbf{x}', t_\alpha, t')$. Thus knowledge of $R_{jk}(\mathbf{x}_\alpha, \mathbf{x}', t_\alpha, t')$ suffices to fully determine any linear estimate in terms of velocity data. Likewise, if the event vector contains derivatives of the velocity fields, $(\partial u_i/\partial x_j)$ at points $\mathbf{x}_\alpha$, the resulting two-point correlations that appear in Eq. (4) contain correlations between velocities and derivatives, and derivatives and derivatives. Since each type of correlation can be expressed in terms of R_{ij}, it follows that knowledge of $R_{jk}(\mathbf{x}, \mathbf{x}', t, t')$ again suffices to determine fully the linear estimate of u' in terms of velocity data and derivatives of any order. This is a powerful result, as it states that very complicated conditional averages can be approximated once R_{ij} is known.

The accuracy of LSE has been evaluated by direct comparison to experimentally measured conditional averages in a number of flows, such as grid turbulence, axisymmetric jets, wakes, plane shear layers and pipe flow (Adrian et al., 1989). Usually the agreement is surprisingly good, even for large values of the event data. To improve accuracy, it has been suggested that (1) be generalized to include higher order terms in E (Adrian, 1977). Often, higher order terms have little effect for probable values of the events, but sometimes they improve accuracy (Pecseli and Trulsen, 1989; Brereton, 1992). Interestingly, Brereton (1992) has also suggested a Laurent-type expansion which contains negative powers of the event data, and he shows improved estimation for low amplitude events.

2. Conditional Eddies

The foregoing discussion shows how conditional averages can be linked to two-point correlation functions through the process of stochastic estimation. Thus, conditional averages and stochastic estimates can be considered to contain approximately the same information about the structure of the flow, and this information is given by a proper combination of the structure information contained in the two-point spatial correlation tensors and the event data. It is absolutely essential to distinguish conceptually between the structure of any particular conditional average and the structure of coherent elements of the flow, should they exist. There is no *a priori* guarantee that any conditional average (or indeed, the structure extracted by any other pattern recognition procedure that yields *average* or probable structures) *must* coincide with individual, random realizations of portions of the flow field. The conditional averages are well-defined mathematical quantities, and they should be treated the same as the mean or correlation, which exist for any flow. In contrast, while some flows contain readily recognized coherent patterns, in the sense that similar patterns occur repeatedly, we have no rational basis for asserting that all turbulence flows contain such structures (although we may suspect this to be true). To avoid confusing conditional averages with realizations of the random field (and to avoid the problem of defining 'coherent structure') the flow fields described by conditional averages have been referred to as 'conditional eddies'. There are many types of conditional eddies depending upon the conditional event. They always exist, and the same type of conditional eddy can be used to compare

the structures of different flows. However, the relationship between conditional eddies and random realizations of the flow can only be established by empirical comparison. Thus, the interpretation of the structure found in a conditional eddy should be done by performing 'calibration' experiments. (Methods such as proper orthogonal decomposition do form a representation that converges to a realization, but the representation through any partial sum of modes is a projection of a random realization onto a set of basis function, and is not therefore an averaged quantity.)

Conditional eddies are defined by the event. One of the simplest and best known events is the quadrant analysis method of Wallace et al. (1972) and Willmarth and Lu (1972) in which there are only four events corresponding to the four quadrants of the u–v plane. There are, however, infinitely many alternative choices. It seems clear that the definition of the conditional event for a particular application must be determined by the ultimate goals of the conditional structure analysis in that application. For example, it is well known that the equation governing the probability density function of the velocity at one point $f_1(\mathbf{v}, \mathbf{x}, t)$ contains terms which are two-point conditional averages given the velocity at the point $\mathbf{x} : \langle \mathbf{u}(\mathbf{x}', t) \mid \mathbf{v} \leq \mathbf{u}(\mathbf{x}, t) < \mathbf{v} + d\mathbf{v} \rangle$ (Adrian, 1977). Thus, if one is interested in closure approximations for the one-point pdf equation, it is natural to examine the structure of the one-point conditional eddies $\langle \mathbf{u}' \mid \mathbf{u} \rangle$. If closure approximations at the two-point level are of interest, the two-point conditional eddy $\langle \mathbf{u}' \mid \mathbf{u}_1, \mathbf{u}_2 \rangle$ is relevant, and so on. Obviously, the two-point conditional eddy will more faithfully reproduce the random field than the one-point eddy $\langle \mathbf{u}' \mid \mathbf{u} \rangle$ because of the additional information contained in the second velocity, but for the purposes of one-point closures, the governing equation for f_1 does not require this information.

This approach to the selection of events seems more rational than searching for a very likely non-existent magic condition that will extract the most faithful representation of the coherent structure. After all, the best representation of a particular structure is given by the event that describes that structure completely, e.g., the structure itself. It is clear that what we really want is a good representation of the structure subject to certain constraints, and one method of defining those constraints is by recourse to governing equations which define the amount of information that is just adequate to close the theory.

In addition to one- and two-point events, conditional eddies have also been studied for multi-point events (Cole et al., 1992; Bagwell et al., 1993) and for events involving the velocity $\mathbf{u}(\mathbf{x}, t)$ and the local deformation tensor $d_{ij}(\mathbf{x}, t) = \partial u_i(\mathbf{x}, t)/\partial x_j$ (Adrian and Moin, 1988; Ditter, 1987). The latter is referred to as a one-and-one-half point event in the sense that d_{ij} contains a subset of the information embedded in the behavior of the flow at two neighboring points.

3. Structures Found by Stochastic Estimation of Conditional Eddies

In isotropic turbulence the LSE of $\langle \mathbf{u}' \mid \mathbf{u} \rangle$ is a vortex ring oriented axisymmetrically about the given velocity, $\mathbf{u}(\mathbf{x}, t)$ (Adrian, 1979). Thus, specifying a vector
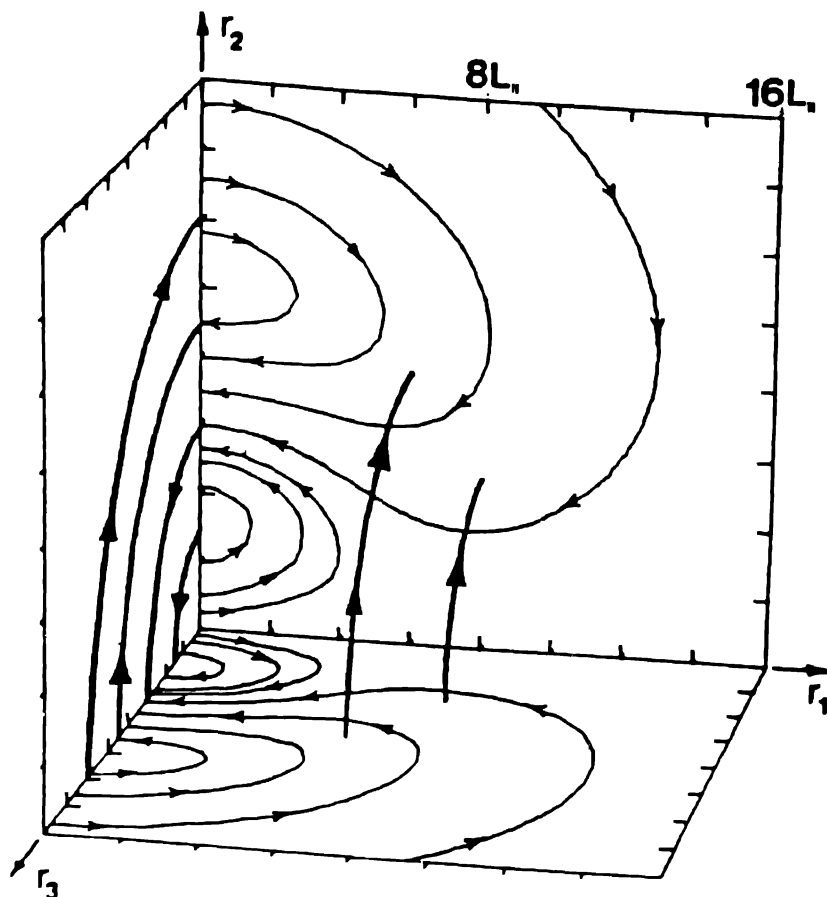
Fig. 1.   Conditional eddy given $\mathbf{u}(\mathbf{x}) = (u, 0, 0)$ in isotropic turbulence. Streamlines are shown in the light ink and vortex lines in heavy ink (Ditter, 1987).

direction in an isotropic field results in an axisymmetric field. Higher order estimates produce more complex ring structure, but do not significantly alter the basic structure for probable values of the velocity fluctuation (Tung and Adrian, 1980). Although the flow is a ring on a scale of order many integral scales, Fig. 1, most of the flow around the ring is very weak, except in the vicinity of the conditional vector where the flow more nearly resembles a jet of fluid. Thus, observations of random isotropic turbulence are not likely to be able to see the weak outer structure of the ring and one expects to see long, thin jets at locations where the velocity fluctuations are large. Axisymmetric structures have zero helicity, $\mathbf{u} \cdot \boldsymbol{\omega} \approx 0$, unless they are also spinning around their axis of symmetry. It is therefore of interest to impose the local deformation tensor as an additional condition. Ditter (1987) studied the conditional average $\langle \mathbf{u}' \mid \mathbf{u}, \mathbf{d} \rangle$ and in isotropic turbulence u found a

linear estimate of the form

$$\langle \mathbf{u}' \mid \mathbf{u}, \mathbf{d} \rangle = \hat{u}_i(\mathbf{x} + \mathbf{r})$$

$$= \frac{R_{ij}(\mathbf{r})}{u^2} u_j(\mathbf{x}) - \frac{2\lambda^2}{15u^2} \{R_{ki,j}(\mathbf{r}) + 4R_{ji,k}(\mathbf{r})\} d_{jk}(\mathbf{x}). \qquad (5)$$

The first term corresponds to the usual translation event, and the second gives the contribution of deformation. The Taylor microscale is λ and $u^2 = \langle u_i u_i \rangle / 3$.

Setting $u = 0$, implies that $\mathbf{x}$ is a critical point of the flow. The local structures at such a point can be found by the methods described in Perry and Chong (1987), since the linear estimate is a solenoidal vector field. If the flow at $\mathbf{x}$ is purely rotated about the x_3-axis (with no translation), the streamlines and vortex lines are as shown in Fig. 2. In the vicinity of $\mathbf{x}$ the flow field is essentially a long, thin vortex tube whose length is of order of several longitudinal integral scales, L_{11} and whose diameter is of the order of the Taylor microscale, λ. As before, the strength of the flow is small at larger distances from $\mathbf{x}$, making the total flow pattern difficult to observe when the eddy is immersed in an environment of random eddies. For example, the vorticity in the vortex tube at the origin is of order u/λ, whereas the vorticity of the large scale conditional vortex is of order u/L_{11}. The latter is, of course, substantially smaller at large Reynolds number. These considerations may explain the tendency of visualizations based on thresholded vorticity to observe long, thin vortex tubes, or 'worms', but fail to observe the much weaker large scale motions induced by the concentrated vorticity. It is also possible that the large scale motions of the conditional eddies are the average motion of many smaller vortices, e.g., a collective pattern.

The conditional average $\langle \mathbf{u}' \mid \mathbf{u}, \mathbf{d} \rangle$ has also been stochastically estimated for homogeneous shear flow using R_{ij} computed from direct numerical simulation (Adrian and Moin, 1988). In this case the conditional eddy has the form of a hairpin vortex inclined at 45° to the flow when the conditional vector corresponds to the value that contributes the largest amount to the mean Reynolds shear stress. If the mean shear flow is subtracted the hairpin vortex becomes a vortex ring.

Single-point conditional eddies have been estimated for turbulent channel flow using the two-point spatial correlation tensor computed from DNS simulations (Moin, Adrian and Kim, 1987; Adrian, Moin and Moser, 1987; Moser, 1990). The vector events were chosen to be the second- and fourth-quadrant $u-v$ event that contribute most to the mean Reynolds shear stress by minimizing the product $uvf_1(u, v)$. Consider the Q2 event. Very close to the wall the structure is a low speed streak under the given vector with two counter-rotating streamwise vortices on either side of the given vector. Farther above the wall a bridge of vorticity forms between the streaks, resulting in a hairpin geometry. Fig. 3 shows the contours of constant enstrophy of the LSE of $\langle \mathbf{u}' \mid \mathbf{u} \rangle$ for $y^+ = 103$. The legs of the hairpin lay back along the wall with spacing of approximately 100 viscous wall units. The conditional vector is positioned between the legs and just under the
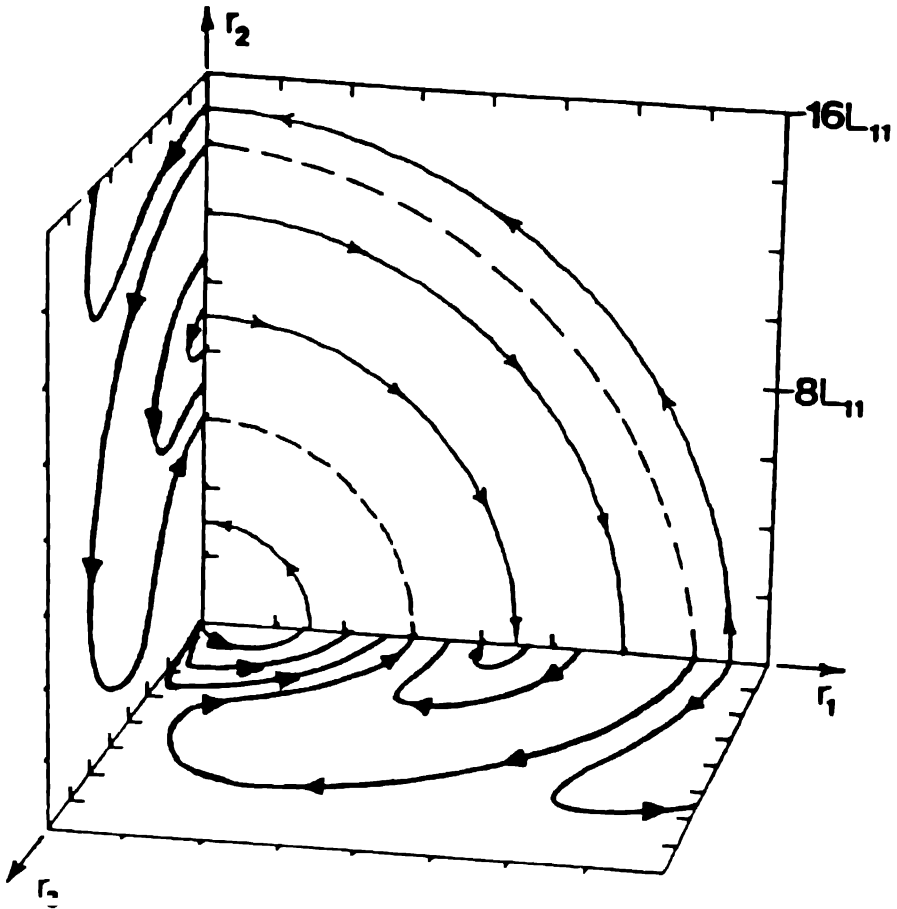
Fig. 2.   Conditional eddy given pure rotation about the r_3-axis. Streamlines in the r_1-r_2 plane and vortex lines in r_1-r_3 and r_2-r_3 planes demonstrate symmetry about the r_3-axis (Ditter, 1987).

head of the hairpin. Robinson et al. (1990) report observations of 'canes' or one-legged hairpins rather than symmetric hairpins. Such structures are obtained from stochastic estimation by letting the given velocity have a sufficiently strong w-component of velocity so that the streamwise vorticity associated with $\partial w/\partial y$ enhances the vorticity of one leg and cancels the vorticity of the other. Farther still from the wall, e.g., at the centerline of the channel, the one-point LSE becomes a vortex ring.

The one-point hairpins found by LSE possess many of the features observed in experiments and direct numerical simulations. However, they do not have the thin shear layer that has been observed in computations and experiments to lie above the space between the legs. The shear layer is believed to be the part of the flow that creates the VITA signature. To obtain this element, it is necessary to combine
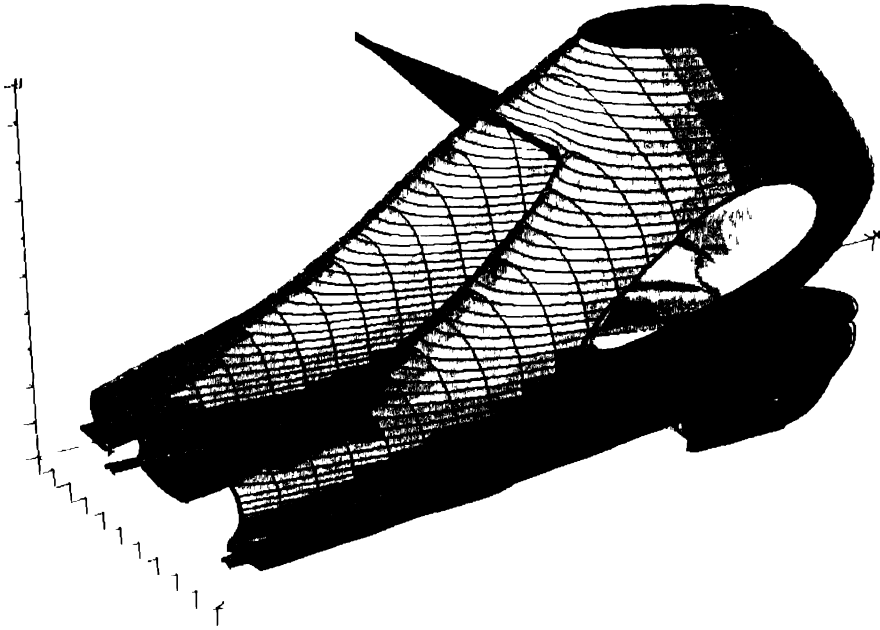
Fig 3   Hairpin structure resulting from a Q2 event specified at $y^+ = 103$ in turbulent channel flow at low Reynolds number. The index marks on the axes are in increments of 20 viscous wall units.

a downstream Q2 vector with an upstream Q4 vector in close proximity. The Q2 event creates a hairpin as in Fig. 3, and the Q4 event creates a fast downward flow that collides with the upward motion from the Q2 event. The result is a stagnation point flow on a thin strip above the hairpin's legs. The fact that two events are required to represent the shear layer suggests that it should be considered as arising from the interaction of two separate conditional eddies that are colliding. It also suggests that closure of the pdf equation at the two-point level may be intrinsically superior to closure of the one-point pdf, because conditions at two-points may be essential to represent important flow interactions.

Single-point estimation of the log-layer in the x–y plane of Re = 50,000 pipe flow yields cross-stream vortex patterns that are consistent with a large hairpin vortex (Adrian, 1990b).

Single-point estimation of a plane shear layer yields a cross-stream vortex, but not one that is particularly rich in detail. Multi-point estimation of the shear layer using points along a streamwise line yields relatively detailed vector fields (Cole et al., 1992). Guezennec (1989) has shown how one-point space-time estimates can be used to study evolution of the boundary layer.

Multi-point LSE of the form $\langle u' \mid u_1, u_2, \ldots, u_N \rangle$ is best viewed as a means of stochastic interpolation or extrapolation. If the locations $x_1, \ldots, x_N$ are grid points in a numerical algorithm, $\langle u' \mid u_1, \ldots, u_n \rangle$ can be interpreted as the best estimate

of the subgrid field given the resolved scale data (Adrian, 1977, 1990a). An effort is currently underway to use this approach to estimate the fluctuating pattern of subgrid wall shear stress in a large eddy simulation (Bagwell et al., 1993). The velocity vectors computed on the lowest grid plane are used to estimate the shear stress on the wall.

4. Detection of Structures in Random Realizations by Stochastic Estimation

The greatest single virtue of LSE is that it makes it easy to estimate conditional averages for complex events. Even a relatively simple event like $\{u, d\}$ constitutes a twelve-dimensional space in which it would be almost impossible experimentally to find a reasonable number of realizations that satisfy the condition by conditional sampling. Once the LSE coefficients are found for a given flow and given type of event, the event can be changed quantitatively to cover the full range of probable values without re-calculating the coefficients or re-sampling the data. This flexibility places more emphasis on the selection and definition of the events than is encountered in conditional averaging, where the events must be constrained to have simple forms for the sake of feasibility. We have seen that certain events are indicated naturally by the theory, and it has been argued that the fidelity with which they represent the structure should be considered enough for the purpose of that particular theory. In this sense the problem of event definition is solved.

However, suppose we consider the classical coherent structure detection problem in which one attempts to find events which serve as accurate *detectors* of the presence of a coherent structure. How well can LSE address this problem? First, it should be pointed out that the simple one-point event $\{u(x, t)\}$ is already significantly more specific than the quadrant detection methods which have been used extensively. Even so, it may not be good enough if the flow contains structures that have the same velocity vector at several points in their volume. Then, the conditional average will average over all of these events indiscriminately. A simple example is the conditional average $\langle u(t') \mid u(t) \rangle$ where $u(t) = \sin \omega t$. If $-1 \leq v \leq 1$ is the prescribed sampling level, $u(t) = v$ at two different times during any cycle, one with positive slope and one with negative slope. The conditional average averages over these two different events and predicts a cosine wave, e.g., a sine wave whose phase is the average of the two events. To define one event uniquely, more information must be specified. This can be done by adding the slope as an event, analogous to specifying d.

In principle, a sufficiently detailed list of events will define a structure uniquely. The list is *sufficient* if the addition of more events results in negligible reduction of the mean square error. An example of this process is that of estimating $u(x')$ from uniformly spaced events $u(\Delta x)$, $u(2\Delta x)$, $u(3\Delta x)$. ... It can be shown that as the sample spacing decreases the mean square error decreases until it vanishes at the Nyquist sampling limit. In this case the linear estimation functions become the sinc function of the Nyquist sampling theorem.
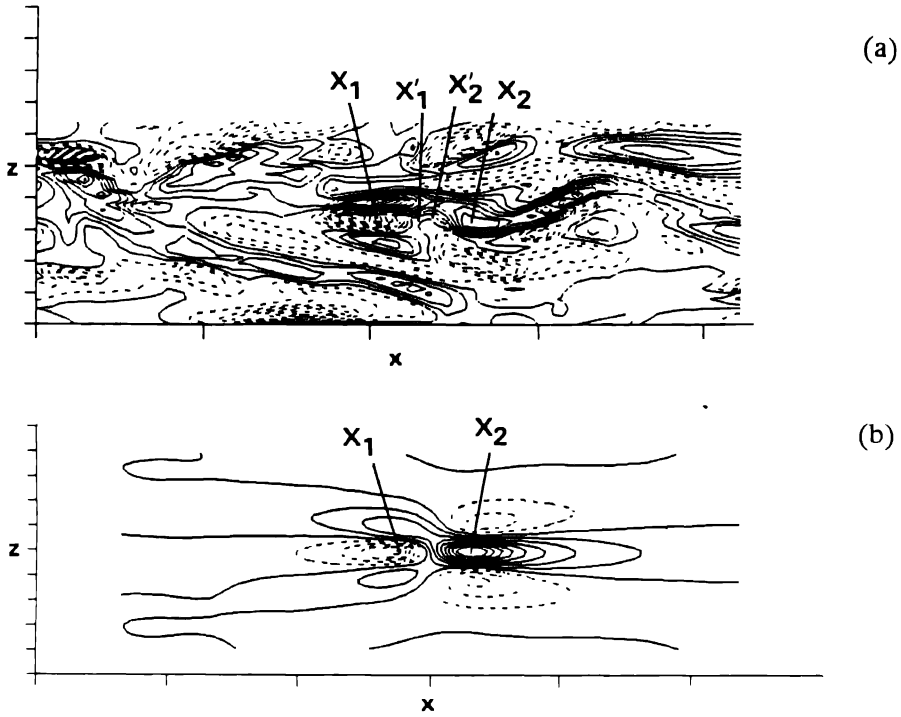
Fig. 4.   (a) Contours of the instantaneous v-component in the $x-z$ plane passing through x_1 at $y^+ = 30$ in turbulent channel flow. (b) Linear estimate of v-component in the $x-y$ plane passing through x_1 given the Q4 event at x_1 and the Q2 event at x_2. Note how the pattern of alternating positive and negative velocities is made apparent (Adrian, Moin and Moser, 1987).

Clearly, Nyquist sampling is too detailed for eddy structure identification, so we must constrain the set of given data by another principle. One approach which has been investigated to a limited extent is to identify points of interest in a random field and use the actual random values of the flow variables at those points as data for the LSE. The result is a smooth structure that is free from random background noise, and represents the average structure that is present when those events occur. Figure 4 illustrates the procedure. Two points x_1 and x_2 were located by searching for the location of maximum in the fluctuating Reynolds shear stress on a $y =$ constant plane of turbulent channel flow. The random field does not exhibit a readily recognized pattern, but the LSE using $u(x_1)$ and $u(x_2)$ shows a clear pattern of alternating signs in the v-component of velocity that corresponds to the average footprint of a Q4 event interacting with the back of a Q2 hairpin.

5. New Directions

Several new ways of using stochastic estimation have been proposed recently, or are under development. Balachandar and Adrian (1993) consider the use of adaptive events as a means of replacing *a priori* definition of events with algorithms that are iteratively adapted to give the best representation of the flow. An example is given from thermal convection between horizontal parallel plates in which it is known that the large scale motion is a roll-cell. By specifying a vertical velocity at one point on, say, the horizontal mid-plane, a roll cell is obtained from the linear stochastic estimate, but its horizontal width is incorrect. By specifying three vertical velocities, one down, one up, and one down, a clearer pair of roll-cells is predicted. If the spacing of the data is larger than the full width of the roll cell, the estimated cell has a smaller spacing, and vice versa. Thus, one can use the roll spacing to form new events and get an improved estimate. Iteration rapidly converges to a stable estimate which has the correct spacing.

Balachandar and Adrian (1993) also investigated the problem of determining structure when the turbulent field contains distinctly different types of vortices. The example chosen was again thermal convection between parallel plates. In addition to large roll cells, this flow contains smaller scale motions in the form of mushroom-shaped thermals. The latter are predicted by LSE when the event is very close to a thermal boundary where the thermals are stronger than the rolls. The rolls rapidly dominate the LSE as the location of the event (e.g., a vertical velocity) is moved away from the boundary. A non-linear filtering scheme is developed in which the roll cell predicted by the event located far from the boundary is subtracted from the total LSE based on an event near the boundary. The strength of the roll cell is found by projecting the combined estimate onto the estimate of the large scale motion. After subtracting the large scale roll cell, the smaller, weaker mushroom vortex is revealed very clearly.

Bonnet et al. (1994) have developed an interesting combined method in which LSE and proper orthogonal decomposition (POD) are used together to obtain very compact representations of the total velocity field. The idea is to project the linear estimate, using many event locations, onto the first few modes of the POD, which are known to contain most of the energy of the flow field.

Another idea for filtering the coherent structure out of a more random pattern is to specify deformation data at the critical points of the vector field. This appears promising because the spacing of critical points is of the order of the eddy size so that data at these locations identify different eddies and their interactions.

6. Summary

Linear stochastic estimation is essentially a method of approximating conditional averages in terms of correlations between the conditional data and the variable being averaged. When the given data are velocity vectors at several different locations,

and the estimated variable is the velocity field, the estimate is fully determined by the two-point spatial correlation tensor of the velocity field. This provides a means of interpreting velocity correlation tensors. The simplicity of the linear estimation procedure also makes possible the use of very complicated events.

Acknowledgement

References

Adrian, R.J., Stochastic estimation of sub-grid scale motions. *Appl. Mech. Rev.* 43 (1990a) S218.

Adrian, R.J., Linking correlations and structure: stochastic estimation and conditional averaging. In: S. Kline and N. Afgan (eds), *Near Wall Turbulence*. New York: Hemisphere Publ. (1990b) pp. 420–436.

Adrian, R.J., Conditional eddies in isotropic turbulence. *Phys. Fluids* 22 (1979) 2065–2070.

Adrian, R.J., On the role of conditional averages in turbulence theory. In: G. Patterson and J. Zakin (eds), *Turbulence in Liquids*. Princeton: Science Press (1977) pp. 322–332.

Adrian, R.J., Jones, B.G., Chung, M.K., Hassan, Y., Nithiandan, C.K., and Tung, A.T.C., Approximation of turbulent conditional averages by stochastic estimation. *Phys. Fluids A* 1 (1989) 992–998.

Adrian, R.J. and Moin, P., Stochastic estimation of organized turbulent structure: Homogeneous shear flow. *J. Fluid Mech.* 190 (1988) 531–559.

Adrian, R.J., Moin, P. and Moser, R.D., Stochastic estimation of conditional eddies in channel flow. *Report CTR-S87*, Center for Turbulence Research, NASA Ames/Stanford (1987).

Bagwell, T.G., Adrian, R.J., Moser, R.D. and Kim, J., Improved approximation of wall shear stress boundary conditions for large eddy simulations. In: R.M.C. So, C.G. Speziale and B.E. Launder (eds), *Near Wall Turbulent Flows*. Amsterdam: Elsevier (1993) pp. 265–275.

Balachandar, S. and Adrian, R.J., Structure extraction by stochastic estimation with adaptive events. *J. Theor. & Comp. Fluid. Dyn.* 5 (1993) 243–257.

Bonnet, J.P., Cole, D.R., Delville, J., Glauser, M.N. and Ukeiley, L.S., Stochastic estimation and proper orthogonal decomposition: Complementary techniques for identifying structure. *Exp. Fluids* (1994) (to appear).

Brereton, G.J., Stochastic estimation as a statistical tool for approximating turbulent conditional averages. *Phys. Fluids A* 4 (1992) 1046–2054.

Cole, D.R., Glauser, M.N. and Guezennec, Y.G., An application of the stochastic estimation to the jet mixing layer. *Phys. Fluids A* 4 (1992) 192.

Deutsch, R., *Estimation Theory*. New York: Prentice Hall (1965) 269 pp.

Ditter, J.L., *Stochastic Estimation of Eddies Conditioned on Local Kinematics*, M.S. Thesis, University of Illinois (1987).

Guezennec, Y.G., Stochastic estimation of coherent structure in turbulent boundary layers. *Phys. Fluids A* 1 (1989) 1054.

Moin, P., Adrian, R.J. and Kim, J., Stochastic estimation of organized structures in turbulent channel flow. *Proc. 6th Turbulent Shear Flow Symp.*, Toulouse (1987) pp. 16.9.1–16.9.8.

Moser, R.D., Statistical analysis of near-wall structures in turbulent channel flow. In: S. Kline and N. Afgan (eds), *Near Wall Turbulence*. New York: Hemisphere Publ. (1990) pp. 45–62.

Papoulis, A., *Probability, Random Variables and Stochastic Theory*, 2nd edn. New York: McGraw-Hill (1984).

Pecseli, H.L. and Trulsen, J., A statistical analysis of numerically simulated plasma turbulence. *Phys. Fluids B* 1 (1989) 1616–1636.

Perry, A.E. and Chong, M.S., A description of eddying motions and flow patterns using critical-point concepts. *Ann. Rev. Fluid Mech.* 19 (1987) 125–156.

Robinson, S.K., Kline, S.J. and Spalart, P.R., Quasi-coherent structures in the turbulent boundary layer· Part II. Verification and new information from a numerically simulated flat-plate layer. In: S. Kline and N. Afgan (eds), *Near Wall Turbulence*. New York: Hemisphere Publ. (1990) pp. 218–247.

Tung, T.C. and Adrian, R.J., Higher-order estimates of conditional eddies in isotropic turbulence. *Phys Fluids* 23 (1980) 1469–1470.

Wallace, J.M., Eckelmann, H. and Brodkey, R S., The wall region in turbulent shear flow. *J. Fluid Mech.* 54 (1972) 39.

Willmarth, W.W. and Lu, S.S., Structure of the Reynolds stress near the wall. *J. Fluid Mech.* 55 (1972) 65–92.

305

Stochastic Estimation of Multipoint Conditional Averages and their Spatio-Temporal Evolution[*]

T. J. GIESEKE[**] and Y. G. GUEZENNEC
The Ohio State University, Mechanical Engineering Department

Abstract. A novel application of the stochastic estimation procedure is used to examine the three-dimensional structure of the turbulent wake of a cylinder at $x/d = 100$ and $Re_D = 5000$. The basis for this method is the measurements of the full 3-D correlation tensor for all components across the width of the wake. Using this large data base, events contributing most to the Reynolds stress are identified and the most likely ensemble-averaged structures corresponding to these events are reconstructed using the stochastic estimation procedure. This powerful technique offers the distinct advantage that multi-point conditional averages can readily be estimated. An extension of this multi-point conditional average estimation is presented in this paper in the form of a pseudo-dynamic reconstruction of the flow field. To that effect, measured time sequences of "conditions" at several points in the wake are used to estimate the three-dimensional structures most likely associated with these events, hence providing a useful tool to reconstruct the evolution of the large-scale flow structures.

Identifying coherent structures in turbulent flows has been successfully accomplished in the past using several techniques. Among them are flow visualization, proper orthogonal decomposition (POD), conditional averaging, pattern recognition, and stochastic estimation. Each of these methods has advantages, but the stochastic estimation is exceptional in its flexibility, objective nature, and ease of validation. As an illustrative problem and application of the stochastic estimation, the turbulent wake of a cylinder at $Re_d = 5000$ is examined at $x/d = 100$. Single and multiple point conditionally averaged structures will be estimated and a quantitative three-dimensional flow-reconstruction technique will be used to study the flow dynamics.

Three-dimensional structures in the turbulent wake of a two-dimensional body wake were first identified by Townsend (1956) and Grant (1957). After noting the structure in the transverse velocity correlations measured by Townsend, Grant extended Townsend's measurements to include spanwise and normal velocity component correlations. Based on the structure of the space-time correlation tensor, Grant proposed that the far-wake contains pairs of counter-rotating eddies, rotating in the plane of the wake with axes inclined with the mean shear. Supporting evidence for the existence of double-rollers was found by Lumley (1965), Payne (1966), and Payne and Lumley (1967) by using the correlation data of Grant to

compute the first POD mode. The structure computed in this way was identical to that postulated by Grant with the exception that Payne and Lumley's eddies had a v component of velocity while Grant's original eddy model did not. To explain the absence of the normal velocity component in Grant's large eddies, Townsend (1970, 1978) proposed that along with the rollers, the wake contains jets that eject turbulent fluid into the mean flow. Using the stochastic estimation procedure, single and two point estimates of conditionally averaged structures can be computed to be compared to these jet and double-roller flow patterns. A similar comparison between estimated velocity fields and actual experimental instantaneous velocities can be found in Cole *et al.* (1992).

The description of far wake turbulence as a distribution of rollers and jets has been generally accepted as an accurate depiction. Many supporting studies have been conducted to determine more about the distribution of eddies and their role in the turbulent dynamics (Keffer, 1965; Barsoum *et al.*, 1978; Townsend, 1978; Wlezien, 1981; Mumford, 1983; Antonia *et al.*, 1987; Ferrè, Giralt, 1989; Ferrè *et al.*, 1990). Despite the extensive research in this field, no conclusive evidence has been found for a preferred distribution of eddies. Most studies indicate that they appear in groups and several have suggested that eddies causing entrainment of irrotational fluid are less important than those causing ejection of turbulent fluid.

The stochastic estimation procedure can be used to help answer questions about the distribution of large eddies and to estimate their temporal evolution. A technique called *pseudo-dynamic reconstruction* will be developed and used to reconstruct an estimate of the time evolution of turbulent velocity fields from experimental data. Structures can be identified in the estimated velocity fields by visualization of physical quantities which will aid in identifying preferred distributions of eddies in the wake. In addition, the dynamics of these eddies can be inferred from the fields because the fields are based on measured realizations of the actual evolution of the far-wake turbulence.

1. Description of Experiment

The experimental portion of this study was conducted in the subsonic wind-tunnel in the Department of Mechanical Engineering at The Ohio State University. The wind-tunnel is an open-return type, the inlet of which consists of a bellmouth followed by a plastic-tube honeycomb, three steel wire screens, and a settling chamber. A 9 to 1 contraction leads to the test section. The test section has the internal dimensions 0.46 m wide by 0.61 m high by 3.66 m long. A 0.635 cm diameter steel cylinder was mounted horizontally in the center of the test section and was fitted with end-plates near the tunnel walls with a 10° angle to the mean flow. With the end-plates, the model has an aspect ratio $L/d \simeq 55$. The coordinate system in the test section has its origin at the center of the cylindrical model. The

streamwise direction is x, the normal direction is y, and z is the spanwise direction completing the orthonormal set.

Two precision traversing mechanisms are mounted on tracks on the top of the test section. The traversing mechanisms are powered by computer controlled stepper motors. The first traversing mechanism has the capability of motion in all three coordinate directions. The second traversing system, mounted 21 cm downstream of the first, is capable of independent vertical motion only. The two mechanisms are mounted to the same carriage and therefore move together in the streamwise direction. Additional rigid probe supports are mounted through holes in the test section walls.

A Masscomp 55-S-05 computer with a 12 bit, 16 channel A/D interface and two D/A channels are used to control the traversing mechanisms and to acquire data from various instruments. Sampling of multiple channels was conducted in bursts at the maximum sampling rate of the A/D system. This sequential sampling resulted in a delay between channel samples of 3 micro-seconds. The resolution of both the A/D and the D/A systems was 4.88 mV per bit which compares to a typical r.m.s. of a fluctuating quantity being measured of roughly 0.24 V. Fourth order Butterworth analogue filters with a cut-off frequency tuned to 6.2 kHz are used as anti-aliasing filters for the data acquisition system. The cut-off frequency was selected slightly above the Nyquist frequency so as to improve the gain characteristics in the frequency pass range. The gain of these filters at the Nyquist frequency was 0.8 which is a slight improvement over a gain of 0.5 which would be the case for similar filters tuned to exactly the Nyquist frequency. By tuning the filters in this way, the filter gain in the frequency pass range is improved while also providing adequate removal of very high frequency noise well above the frequency range of interest.

Turbulence measurements were made using triple hot-wire probes connected to custom made constant temperature anemometers. Each anemometer has its own variable overheat setting, frequency compensation, and analogue linearizer. The two models of probes used were the TSI model 1295-20 and custom-made Auspex probes.

The experimental portion of this study was divided into two parts. The first part was designed to measure the space-time correlation tensor at $x/d = 100$ and $\mathrm{Re}_d = 5000$. Auspex triple-wire probes were mounted on each of the traversing mechanisms and they were traversed over a sampling grid, as shown in Figure 1. The grid was defined to span the width of the wake, $-3.52 \leq y/b \leq 3.52$, and an equivalent spanwise scale, $0.00 \leq z/b \leq 3.52$. Here b is the wake half-width, defined as the distance in the cross-wake direction from the wake centerline to the point where the mean streamwise velocity defect is half of its maximum value. The grid spacing was $0.44b$ which was sufficiently small to capture the spatial structure in the correlation function. The probes were positioned at each spatial separation on this grid. At each point, time histories of the anemometer signals were simultaneously recorded. A total of 65536 samples were collected at 10 kHz.
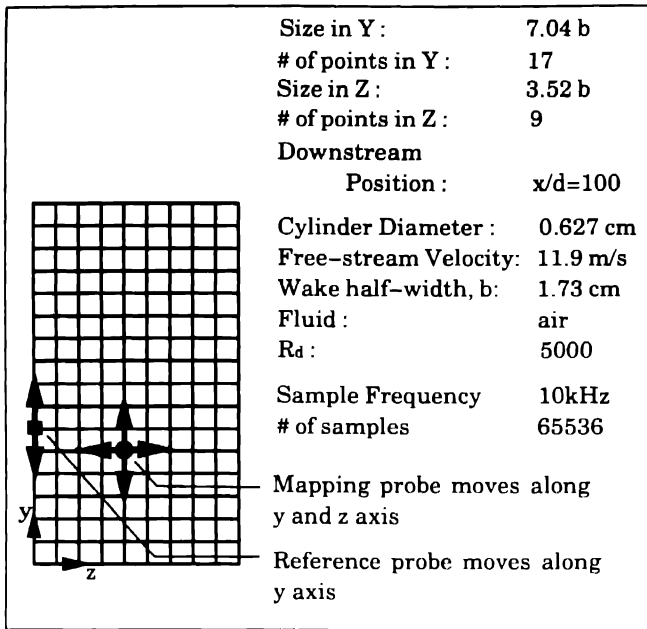
Size in Y :	7.04 b
# of points in Y :	17
Size in Z :	3.52 b
# of points in Z :	9
Downstream Position :	x/d=100
Cylinder Diameter :	0.627 cm
Free–stream Velocity:	11.9 m/s
Wake half–width, b:	1.73 cm
Fluid :	air
R_d :	5000
Sample Frequency	10kHz
# of samples	65536

Mapping probe moves along y and z axis

Reference probe moves along y axis

Fig. 1.   Illustration of the measurement grid and probe movement with a summary of the experimental parameters.

These parameters were selected based on the convergence and the curvature of the autocorrelation function. Periodically during the course of the experiment, the hot-wires were calibrated against the freestream velocity to provide a function relating the anemometer output to cooling velocity. Using this calibration data, the anemometer outputs were converted to cooling velocities which were corrected for drifts in the ambient temperature and mean velocity.

   To determine the three components of velocity based on cooling velocity measurements, the procedure given by Gieseke (1990) and Gieseke and Guezennec (1992) was used.

   For each probe separation, the temporal correlation between the velocity components was computed using an FFT approach. The original data was broken into 64 blocks of data which translates to calculating the correlation function at 1024 temporal separations. This significantly longer than the typical large scales which scale with b. Based on the free-stream velocity as an advection speed, 512 positive temporal offsets span approximately $35b$. Owing to the flow symmetries, a total of four redundancies exist in the spatial correlation measurements. Therefore the correlation functions represent the average of 256 separate 1024 point measurements. The wake mean statistics have been measured on a more finely resolved grid and are shown in Figure 2. Cross-wake symmetry has been used to smooth the curves and some scaling has been used to improve readability.
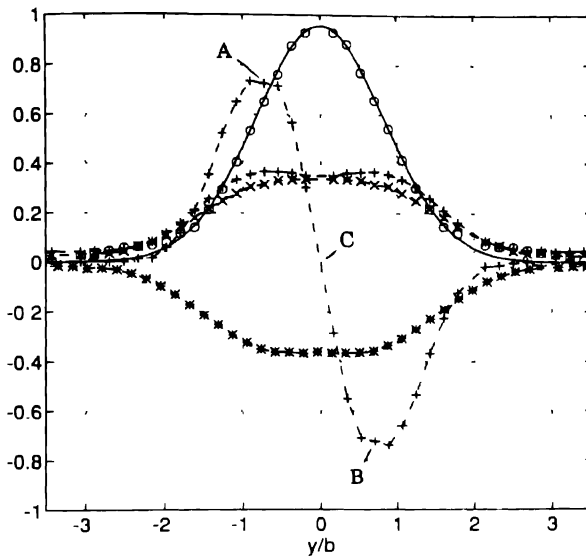
Fig 2.   Statistics at $x/d = 100$ and $Re_d = 5000$:
——— Gaussian profile, $\circ$ $(1 - U/U_\infty)(x/d)^{-1/2}$,
$+ - - - - +$ $(\sigma_u/U_\infty)(x/d)^{-1/2}$, $\times - - - - \times$ $(\sigma_v/U_\infty)(x/d)^{-1/2}$,
$* - - - - * -(\sigma_w/U_\infty)(x/d)^{-1/2}$, and $+ - \quad - \quad - + 20(\overline{uv}/U_\infty^2)(x/d)^{-1}$

The second part of the experiment was designed to measure time traces of the three velocity components at three physical locations simultaneously. One Auspex probe was positioned at y/b = 0.88 (point *B* in Figure 2), the other at y/b = 0.0 (point *C*), and the TSI triple-wire probe, at $y/b =-0.88$ (point *A*). All three probes were at the same z location. The velocity histories were recorded and stored for use in the pseudo-dynamic reconstruction technique.

Turbulent Events

In order to identify coherent turbulent structures, some quantities must be defined that is indicative of their presence. From an experimental standpoint, these must be a measurable quantities, the realization of which during the course of an experiment should indicate the occurrence of the coherent structure of interest. Such a realization is termed an *event*.

The quantity or quantities that constitute an event can be determined based on physical arguments and consideration of the statistical properties of the turbulence. The structures that contribute most to the Reynolds stress are those that contribute to turbulence transport. To associate events with these structures, specific detection
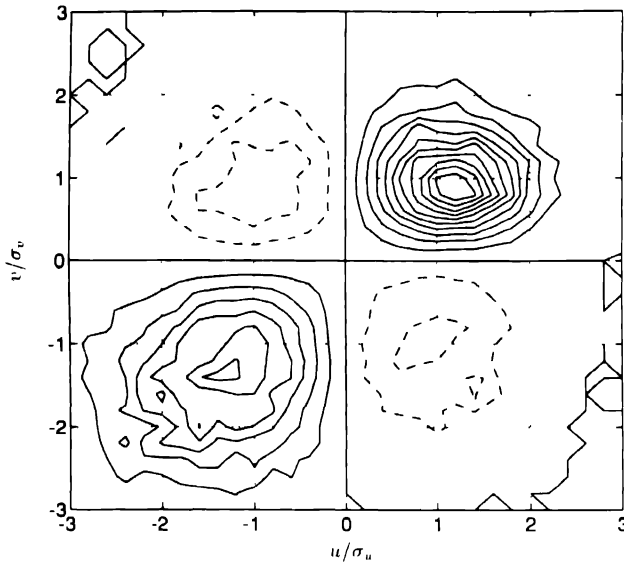
Fig. 3.   Joint probability density function of u and v weighted by the Reynolds stress $P(u, v)uv$. The contours are on a linear scale, have an arbitrary magnitude, are shown with solid lines when positive, and with dashed lines when negative.

points were chosen corresponding to peaks in the Reynolds stress profile. These points are labeled A, B, and C in Figure 2.

Following the *Quadrant* technique used by Wallace *et al.* (1972) and Willmarth and Lu (1973) in the turbulent boundary layer, the joint probability density functions (PDFs) of the velocity fluctuations were used to identify events at the points of interest. Figure 3 shows the joint PDF of u and v weighted by uv at point A. Two types of events can be clearly identified: a first quadrant event (which entrains irrotational fluid), and a third quadrant event (which ejects turbulent fluid away from the wake center). Similar events can be identified on the opposite side of the wake, where the entraining motions are found in the fourth quadrant and the ejecting motions are found in the second quadrant.

These events are based on very localized information and do not provide any information about the relative locations (in space or time) of various types of events. Events can also be defined by quantities simultaneously measured at two locations. To determine the importance of events that contribute to the Reynolds stress on both sides of the wake, a joint PDF of the velocity directions can be defined. Figure 4 shows the joint PDF of the flow angle defined by $\theta = \tan^{-1}(v/u)$ at points A and B weighted by the contributions to the Reynolds stress at each point. Peaks in the function $P(\theta_A, \theta_B)uv_A uv_B$ indicate what combinations of events are most likely to contribute to the Reynolds stress simultaneously on both sides of the
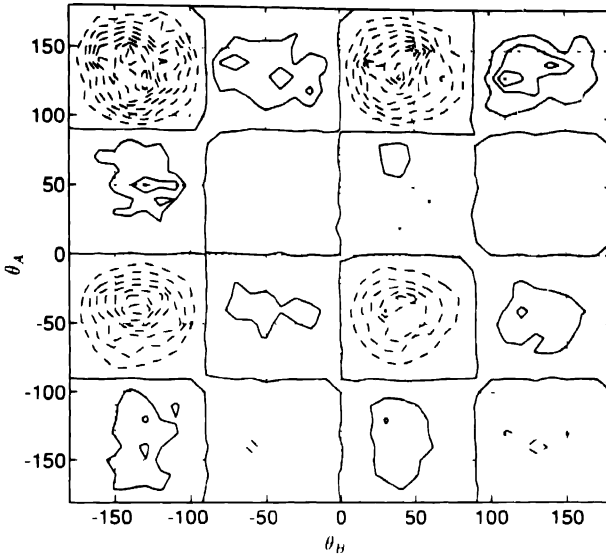
Fig. 4. Joint probability density function of the flow angles at points A and B weighted by the Reynolds stress at both points, $P(\theta_A, \theta_B)u_{vA}u_{vB}$ The contours are on a linear scale, have an arbitrary magnitude, are shown with solid lines when positive, and with dashed lines when negative.

wake. The cell associated with simultaneous ejection motions illustrates that these are important types of motions.

2. Stochastic Estimation of Coherent Structures

Conditional and phase averaging are the traditional approach to determining the flow structures associated with turbulent events. The stochastic estimation was originally proposed by Adrian (1976) as a way to estimate conditionally averaged structures without having to pre-select an averaging condition or event. This work was followed by many related studies testing and applying the theory (Adrian, 1979; Adrian *et al.*, 1987; Guezennec, 1989; and others).

The procedure can be summarized by the statement, *given velocities at some coarsely distributed points in space and/or time, the velocities at all other points in space and/or time can be estimated as functions of the known velocities.*

Single point conditionally averaged flow fields are computed with the stochastic estimation procedure by fixing the velocity at a single location and computing the velocities in a neighborhood around that point. The resulting field can be considered the most likely state of the field, in a least square error sense, given the prescribed condition. The corresponding conditionally averaged field is the average state of the

field given that the velocity at the condition location is within a small neighborhood of a prescribed value. Despite the difference in definition, fields computed using the two methods have been found to be qualitatively similar (Adrian, 1987). The stochastic estimation approach has two major advantages over the conditional average approach; it can be extended from the single condition estimate to a multi-condition estimate very easily and the conditions used for the field reconstruction need not be fixed before the required experiment is conducted.

The procedure is built from the premise that given a set of N_s realizations of $(N + P)$ stochastic variables, some of the variables $(\mathbf{y}^1, \cdots, \mathbf{y}^p)$ can be estimated by functions of the others $(\mathbf{x}_1, \cdots, \mathbf{x}_n)$ having the form

$$\mathbf{y}^l \approx F^l(\mathbf{x}_1, \cdots, \mathbf{x}_n) = a_j^l f_j^l(\mathbf{x}_1, \cdots, \mathbf{x}_n) . \tag{1}$$

The basis functions f_j^l and the number of them can be chosen arbitrarily. The constants a_j^l must be determined such that the function F^l predicts $\mathbf{y}^l$ as best as is possible based on the available statistical sample.

The error for a given variable $\mathbf{y}^l$ is defined as the sum of the square of the difference between F^l and $\mathbf{y}^l$,

$$\varepsilon_T^{l\,2} = \left\langle \left(y^l - a_j^l f_j^l \right)^2 \right\rangle , \tag{2}$$

where $\langle\ \rangle$ denotes averaging over all realizations. This error can be minimized with respect to each of the coefficients by taking the partial derivatives of ε_T^{l2} with respect to each a_j^l and setting the result equal to zero,

$$\frac{\partial \varepsilon_T^{l2}}{\partial a_j^l} = \left\langle \left(-2y^l f_j^l + 2a_k^l f_k^l f_j^l \right) \right\rangle = 0 . \tag{3}$$

Sets of simultaneous equations are generated that can be solved for the coefficients

$$a_k^l f_k^l f_j^l = y^l f_j^l . \tag{4}$$

The functions F^l can be expanded as polynomials, here limited to the linear terms,

$$F^l(\mathbf{x}_1, \cdots, \mathbf{x}_n) \approx a_0^l + a_1^l \mathbf{x}_1 + \cdots a_n^l \mathbf{x}_n . \tag{5}$$

Substituting these definitions for f_j into Equation (4) and defining correlation matrices $L_{jk} = \langle x_k x_j \rangle$ and $D_{jl} = \langle y^l x_j \rangle$, the simultaneous equations can be expressed as a matrix problem:

$$\mathbf{AL} = \mathbf{D} . \tag{6}$$

This problem can be solved for all of the coefficients **A** so that the variables **y** can be predicted based on values of the variables **x** using a matrix multiplication:

$$\mathbf{y} \approx \mathbf{A}\mathbf{x}. \tag{7}$$

The procedure can be used to estimate the coherent structures associated with the turbulent events defined in the preceding section by considering space and time dependent perturbation velocities $\mathbf{u}(\mathbf{r}, t)$ as the variables that are to be estimated. The perturbation velocities are defined as used in the Reynolds decomposition. The simplest application of the stochastic estimation is the estimated single-point conditional average. For this calculation, the three components of velocity are prescribed at a single point in space. This velocity vector is called the *condition* and noted $\mathbf{u}_c$. Near this condition, the estimated flow field $\mathbf{u}_e(\mathbf{r}, \tau)$ is the most likely state of the field given the condition. Here τ represents the time delay between the occurrence of the condition and the time when the velocities are to be estimated. The field can be considered the coherent structure associated with the condition and is reconstructed using the formulas

$$u_e(\mathbf{r}, \tau) = a_{11}(\mathbf{r}, \tau)u_c + a_{12}(\mathbf{r}, \tau)v_c + a_{13}(\mathbf{r}, \tau)w_c,$$
$$v_e(\mathbf{r}, \tau) = a_{21}(\mathbf{r}, \tau)u_c + a_{22}(\mathbf{r}, \tau)v_c + a_{23}(\mathbf{r}, \tau)w_c, \tag{8}$$
$$w_e(\mathbf{r}, \tau) = a_{31}(\mathbf{r}, \tau)u_c + a_{32}(\mathbf{r}, \tau)v_c + a_{33}(\mathbf{r}, \tau)w_c,$$

or more concisely by

$$\mathbf{u}_e(\mathbf{r}, \tau) = \mathbf{A}(\mathbf{r}, \tau)\mathbf{u}_c. \tag{9}$$

Here, the estimated variable vector is $\mathbf{y}(\mathbf{r}, \tau) = [u_e, v_e, w_e]^T(\mathbf{r}, \tau)$ and the conditions are $\mathbf{x} = [u_c, v_c, w_c]^T$. In these expressions, the regression coefficients have been presented as functions of spatial and temporal separation. This extension of the procedure simply requires that the regression analysis be conducted for each point in space and time offset where the reconstruction formulas are to be applied. To construct the matrix of coefficients $\mathbf{A}(\mathbf{r}, \tau)$, the two-point space-time correlation tensor is required between the velocities at the condition location and each location at which the reconstructed velocities are needed. These correlations are available for the turbulent wake as measured in the experimental portion of this study.

An example estimated perturbation velocity field associated with a third quadrant event at point A is shown in Figure 6. The velocities shown are the u and v components in the $x^* - y$ plane in which the event condition was fixed. Notice that the mean velocities have been removed. Using Taylor's hypothesis, an advection speed equal to the free-stream velocity has been used to relate the temporal development of the flow field to the streamwise structure. Taylor's hypothesis was validated by measuring space-time correlations for probes separated in the streamwise direction (with a small spanwise spacing). There was little decay in the peak
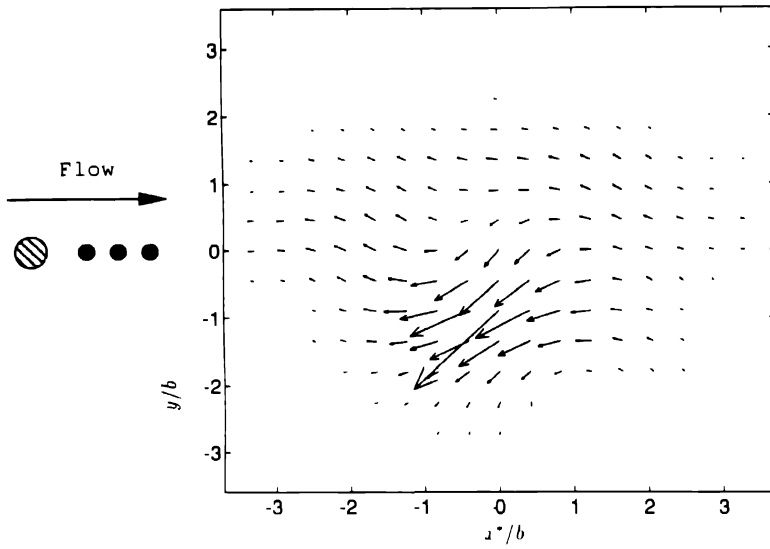
Fig. 5.   A two-dimensional slice in the $x - y$ plane of the estimated velocity field based on a Q3 event at point A.
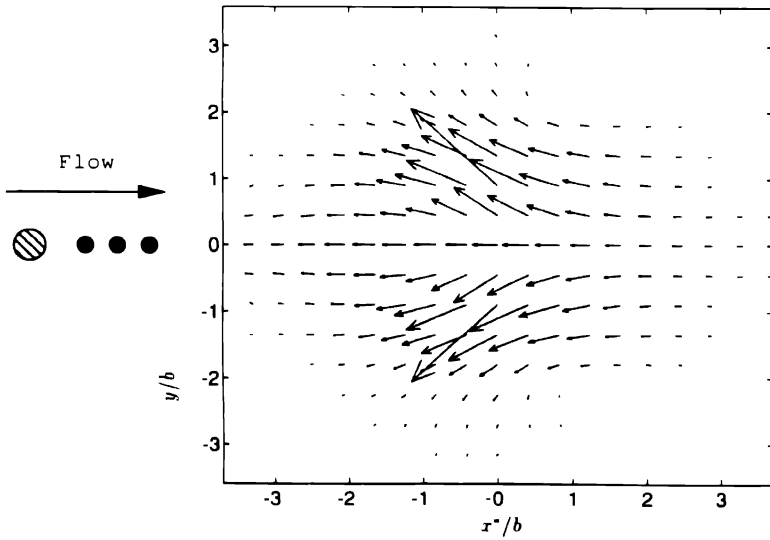

Fig. 6.   A two-dimensional slice in the $x - y$ plane of the estimated velocity field based on a simultaneous Q3 event at point A and a Q2 event at point B.
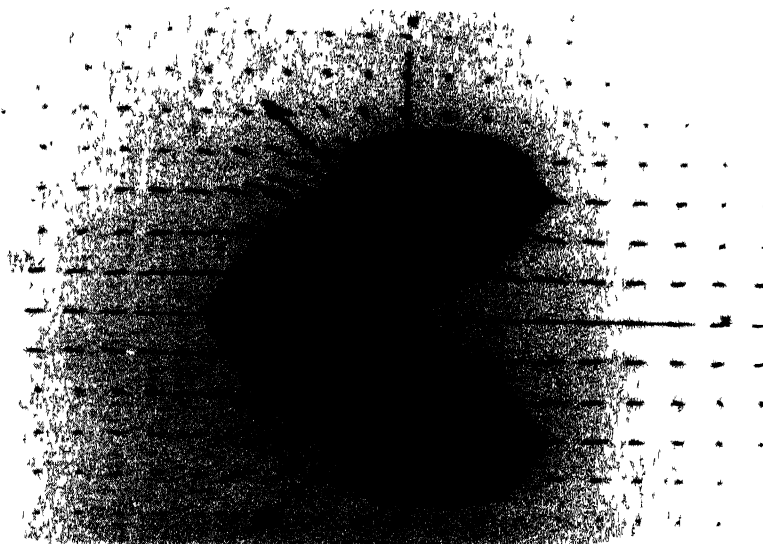
Fig. 7   A side view of a surface of constant enstrophy with a $x^* - y$ plane of velocity vectors for the Q2–Q3 event

in $\overline{u(x,t)u(x + \Delta x, t + \tau)}$ for Δx up to $4b$. The location of the peak indicated that the advection speed was very close to the free-stream velocity. A symbolic representation of the space-time relationship is given as $x^* = U_\infty \tau$. In the figures, the flow is from left to right. The information obtained from this single-point estimate is very localized, suggesting that multiple point estimates would be more informative.

Extending the reconstruction technique to estimate the most likely velocity field given the velocities at two or more points in space requires the redefinition of $\mathbf{u}_c$ and computation of the required coefficients. For a reconstruction based on conditions at points A and B, $\mathbf{u}_c$ is defined as

$$\mathbf{u}_c = [u_A, v_A, w_A, u_B, v_B, w_B]^T .$$ (10)

The matrix of coefficients can be computed from the space-time correlation tensor using Equation (6).

The estimated field for the event associated with simultaneous ejection on both sides of the wake is shown in Figures 7, 8, and 9. The two point estimation reconstructs the flow across the entire width of the wake much better than the single point estimation of Figure 6. The three-dimensional topology is illustrated in Figures 7b and 7c using an iso-surface of constant perturbation enstrophy, represented as a solid object, superposed on a selected planar cut through the field showing the velocity vectors. The structure suggested by this analysis is a pair of
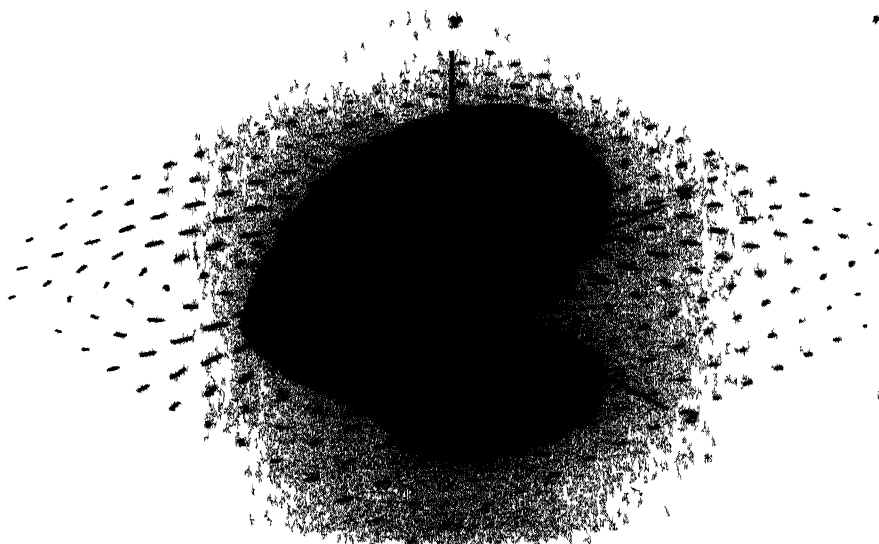
Fig 8   As above but viewed at an oblique view from above with an $x^* - z$ plane of vectors
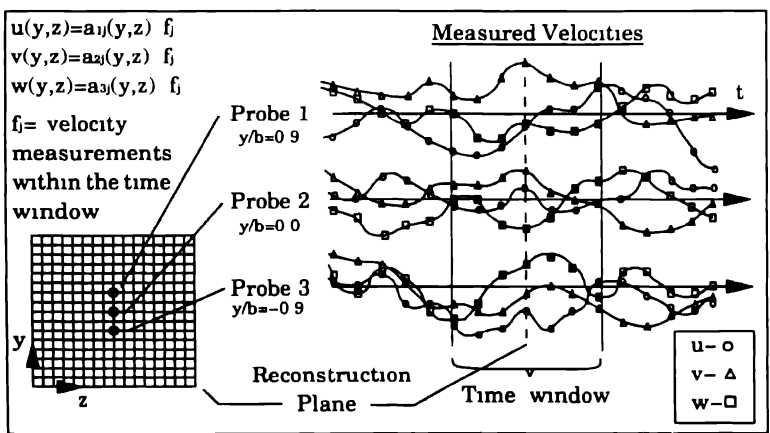
Fig 9   Illustration of the pseudo-dynamic reconstruction technique to reconstruct a single $y - z$ plane of velocity vectors The process is used to construct a three-dimensional velocity field by repeatedly advancing the time record one step and estimating additional planes of velocities
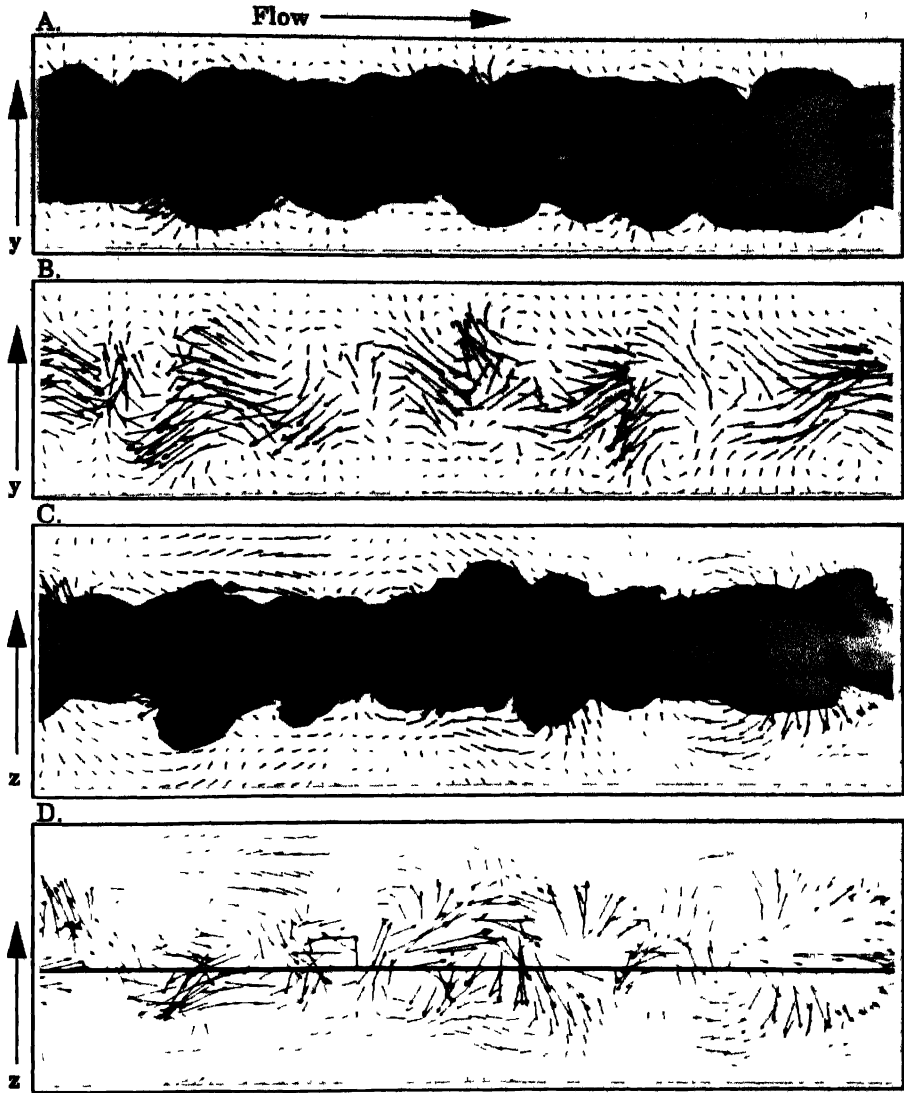
Fig. 10.   A short time history of a reconstructed field: A side view of an iso-surface of constant vorticity magnitude with velocity vectors. B. side view of the velocity vectors only. C. top view of the same reconstructed field, iso-surface and velocities. D. top view with only the velocities shown

counter-rotating eddies, inclined approximately 55° in the direction of the mean shear.

Pseudo-Dynamic Reconstruction

In an effort to estimate the dynamics of the turbulent motions and the interactions between neighboring events, the stochastic estimation procedure was extended to the pseudo-dynamic reconstruction technique. In this technique, time histories of conditions are measured using a coarsely distributed array of hot-wire probes. Within that history, short time series of simultaneously measured conditions are considered at each of the probe locations. The condition vector of Equation (9) is defined as

$$\mathbf{u}_c = [u_1, v_1, w_1, u_2, \cdots, u_3, \cdots]^T \; . \tag{11}$$

Each condition velocity in this vector is given at the location of one of the hot-wire probes and at some time within the short time segments. The velocity field in the $y - z$ plane is estimated based on these measured conditions, the regression equations of Equation (6), and the space-time correlation tensor (illustrated in Figure 5). The condition histories are then advanced in the time record thus defining a new set of conditions to estimate another plane of velocities. This process is repeated until a complete time history of reconstructed two-dimensional velocity fields is obtained. Using an optimization procedure, the best temporal spacing of conditions was found to be approximately 6 samples ($0.4b$). The accuracy of the estimated field increases with the number of conditions in time. In this case, 9 temporal conditions were considered at each probe location for a total of 27 conditions for each $y - z$ reconstruction plane. By panning a window several integral lengths long over the data set, the dynamics of the turbulence can be approximated. It should be noted that in this pseudo-dynamic reconstruction, the kinematics are provided by the stochastic estimation procedure, while the dynamics is measured in the actual flow.

Figure 10 contains views of one instant of a reconstruction made using simultaneously measured velocities at points A, B, and C. Flow is from left to right in the figures and the mean velocity has been removed. These figures illustrate the complex distribution of eddy structures. The streamwise direction is to the right so the sequence of events is from right to left. At the far right of the figures, a set of double roller eddies are observed which are nearly identical to those shown in Figure 7. They are strongly symmetric about the wake centerline, appear in relative isolation, and have a fairly large streamwise scale. Immediately to the left is an interaction between a symmetric entraining event and a strong ejection on the bottom of the wake. A similar combination of events is found slightly upstream on the opposite side of the wake. In contrast to the entraining motions, these front-like structures do not appear in symmetric configurations and are not clearly associated with rollers. Still further upstream, a combination of strong jet motions can be seen. No clear association with rollers is observed and the motions are anti-symmetric. Just off the left edge of the figure are wavy motions with strong spanwise components of velocity.

The sequence of events shown in these figures are specific to this selected time segment. However, the elements of this sequence are generic and representative of the remainder of the data.

There does not appear to be any single pattern of structure distribution, but some characteristics do appear to be repeated throughout the data. Entrainments tend to be symmetric across the wake center. In this sample, ejections appear isolated on one side of the wake or on both sides with a phase delay. It should be noted that in other sample data sets, strong symmetric ejection motions were found but the staggered configuration was found more repeatedly. In all of the data studied, the entrainment motions are associated with rollers while ejection motions generally are not. Jets tend to occur with very strong spanwise components of velocity and in more chaotic turbulent regions.

Conclusion

Coherent structures can be identified using the stochastic estimation technique as has been illustrated here and in many other studies. With those structures established, a new technique, the pseudo-dynamic reconstruction, was developed to estimate the *evolution of three-dimensional* velocity fields from experimental data. This new technique has several very useful properties. The most important is that three-dimensional velocity fields can be estimated from several point measurements. This data can then be analyzed using many techniques. The most direct is to visualize the data to look for flow structures and repeated flow patterns. The very strongly three-dimensional nature of turbulent motions is preserved by this type of reconstruction and visualization. In addition, this type of visualization overcomes the ambiguity found in normal flow visualization results as to what physical quantities are correlated with the concentration of smoke, dye, etc. Here the visualized quantities are relevant physical quantities so the observed structures can be interpreted literally and identifying structures is much more direct.

Using the pseudo-dynamic reconstruction to determine flow dynamics may be a useful application of the technique. However, the current approach of determining these dynamics through visualization does not appear to be a fruitful one. No clearly observable patterns were visualized in the data sets for the wake flow. If there is some identifiable dynamics pattern, it will be present in the reconstructed field as these fields are generated using experimental data. Extracting these patterns may require a more sophisticated numerical approach than the present visual analysis.

References

1. Adrian, R. J.: *Proceedings of the 4th Symposium on Turbulence*, Univ. of Missouri-Rolla (1976).
2. Adrian, R. J.: *Physics of Fluids*, 22 (1979) 2065–2070.

3. Adrian, R. J., Chung, M. K., Hassan, Yassin, Jones, B. G., Nithianandan, C. K., and Tung, A. T. C.: *Sixth Symposium on Turbulent Shear Flows*, Toulouse, France, Sept. 7–9, 1987.
4. Antonia, R. A., Browne, L. W. B., and Shah, D. A.: *J. Fluid Mech.*, 189 (1987) 349–365.
5. Cole, D. R., Glauser, M. N., and Guezennec, Y. G.: *Physics of Fluids A*, 4 (1992) 192–194.
6. Barsoum, M. L., Kawall, J. G., and Keffer, J. F.: *Physics of Fluids*, 21 (1978), 157–161.
7. Ferrè, J. A., Mumford, J. C., Savill, A. M., and Giralt, F.: *J. Fluid Mech.*, 210 (1990) 371–414.
8. Ferrè, J. A. and Giralt, F.: *J. Fluid Mech.*, 198 (1989) 65–78.
9. Ferrè, J. A. and Giralt, F.: *J. Fluid Mech.*, 198 (1989) 27–64.
10. Gieseke, T. J.: M.S. Thesis, The Ohio State Univ. (1990).
11. Gieseke, T. J. and Guezennec, Y. G.: accepted for publication in *Experiments in Fluids*.
12. Grant, H. L.: *J. Fluid Mech.*, 3 (1957) 149–190.
13. Guezennec, Y. G.: *Physics of Fluids*, 1 (1989) 1054–1060.
14. Keffer, J. F.: *J. Fluid Mech.*, 22 (1965) 135–159.
15. Lumley, J.: *Proc. Intern. Colloquium, Moscow* (1965).
16. Mumford, J. C.: *J. Fluid Mech.*, 137 (1983) 447–456.
17. Payne, F. R.: PhD. Thesis, Penn State Univ. (1966).
18. Payne, F. R. and Lumley, J. L.: *Physics of Fluids Supplement*, S194–S196 (1967).
19. Townsend, A. A.: *The Structure of Turbulent Shear Flow*, Cambridge Univ. Press. (1956).
20. Townsend, A. A.: *J. Fluid Mech.*, 41 (1970) 13–33.
21. Townsend, A. A.: *J. Fluid Mech.*, 95 (1978) 515–537.
22. Wallace, J. M., Eckelmann, H., and Brodkey, R. S.: *J. Fluid Mech.*, 54 (1972) 39–48.
23. Willmarth, W. W. and Lu, S. S.: *J. Fluid Mech.*, 50 (1972) 65–92.
24. Wlezien, R. W.: PhD. Thesis, I.I.T. (1981)

The Proper Orthogonal Decomposition, Wavelets and Modal Approaches to the Dynamics of Coherent Structures *

GAL BERKOOZ, JUAN ELEZGARAY, PHILIP HOLMES,
JOHN LUMLEY** and ANDREW POJE
*Cornell University, Sibley School of Mechanical and Aerospace Engineering, Ithaca, NY
14853-7501, U.S.A.*

Abstract. We present brief précis of three related investigations. Fuller accounts can be found elsewhere. The investigations bear on the identification and prediction of coherent structures in turbulent shear flows. A second unifying thread is the Proper Orthogonal Decomposition (POD), or Karhunen–Loève expansion, which appears in all three investigations described. The first investigation demonstrates a close connection between the coherent structures obtained using linear stochastic estimation, and those obtained from the POD. Linear stochastic estimation is often used for the identification of coherent structures. The second investigation explores the use (in homogeneous directions) of wavelets instead of Fourier modes, in the construction of dynamical models; the particular problem considered here is the Kuramoto–Sivashinsky equation. The POD eigenfunctions, of course, reduce to Fourier modes in homogeneous situations, and either can be shown to converge optimally fast; we address the question of how rapidly (by comparison) a wavelet representation converges, and how the wavelet-wavelet interactions can be handled to construct a simple model. The third investigation deals with the prediction of POD eigenfunctions in a turbulent shear flow. We show that energy-method stability theory, combined with an anisotropic eddy viscosity, and erosion of the mean velocity profile by the growing eigenfunctions, produces eigenfunctions very close to those of the POD, and the same eigenvalue spectrum at low wavenumbers.

1. Introduction

Coherent structures are observed in most turbulent flows. Their relative intensity depends on inflow and boundary conditions, flow geometry and streamwise position in the flow. It is tempting to think that they may represent instability modes either of a laminar precursor or of the turbulent flow, which have grown to non-linear maturity. Dynamical models can be constructed using these coherent structures, which can then be used for many purposes: prediction of transport or noise, active control of the flow, and so forth. Such possibilities raise several questions: how best to identify structures in experimental data; how to predict structures in flows

** Author for correspondence.

that have not been extensively documented; what mathematical choices to make in implementing such models.

The Proper Orthogonal Decomposition or Karhunen–Loève expansion has been used for the identification of coherent structures (Aubry et al., 1988). It has been shown in many respects to be optimum. However, other techniques have also been put forward, in particular linear stochastic estimation (Adrian, 1979). We would like to know what connections there may be between these two methods for identifying coherent structures. Below (in Section 2) we explore this.

Many flows are homogeneous in one or more directions. In a homogeneous direction, the POD reduces to a Fourier representation. Such a representation is optimum, in the sense that it converges no slower, and usually faster, than any other representation. However, a Fourier representation is not particularly well suited to phenomena in a turbulent flow. Fourier modes are of infinite spatial extent, while eddies in a turbulent flow are quite finite in their spatial extent. A much more attractive possibility would be the wavelet, since it also is of limited extent, but this is not optimum. Just how far from optimum is it? If we use wavelets, we will have wavelet-wavelet interactions in space, and we have to make a decision regarding appropriate truncations of these interactions. In Section 3 we examine these questions.

Obtaining the POD eigenfunctions for a given flow either requires extensive experimental measurements (Herzog, 1986), or extensive post-processing of data from direct numerical simulation of the flow. Either is expensive and time-consuming. We would like a simpler way of obtaining the eigenfunctions, particularly in flows for which neither DNS nor extensive measurement exist. In particular, we can implement our suspicion that the coherent structures may (at least in some circumstances) result from a disturbance of the turbulent profiles of mean velocity and stress, a disturbance which is unstable, and which grows non-linearly, leading the system to a new attractor, consisting of the flow plus coherent structures (Poje and Lumley, 1991; Leibovich, 1991). In this new stable state, we may hope that the coherent structures will resemble the non-linear growth phase of the instability mode. We pursue these questions in Section 4 below.

2. Linear Stochastic Estimation

In this section we comment on the connection between the POD and linear stochastic estimation, as applied by Adrian and coworkers in Adrian (1979), Adrian and Moin (1988), Adrian, Moin and Moser (1987) and Moin, Adrian and Kim (1987). Elaboration of this material can be found in Berkooz (1991). Suppose one wanted to find an estimate for $u(x)$ given $u(x')$ (at some other point), an estimate which would minimize the mean square difference between $u(x)$ and the estimate. For the sake of simplicity of exposition, we limit ourselves to complex scalar functions of a single variable. Suppose, moreover, that one seeks an estimate linear in $u(x')$; this is called a linear stochastic estimate. We are examining $V(x, x')$ such that

$V(x, x')u(x')$ will be the estimate for $u(x)$, and we want to search through the class $V(x, x')$ to find $A(x, x')$ such that:

$$\min_{V(x,x')} \langle |u(x) - V(x, x')u(x')|^2 \rangle = \langle |u(x) - A(x, x')u(x')|^2 \rangle \tag{1}$$

is achieved by $A(x, x')$. We indicate by $\langle \cdot \rangle$ an ensemble average. We use the classical calculus of variations (cf. Adrian, 1979), which leads directly to:

$$A(x, x') = \langle u(x)u^*(x') \rangle \cdot \langle u(x')u^*(x') \rangle^{-1}. \tag{2}$$

In (2) the two point correlation tensor $R(x, x') = \langle u(x)u^*(x') \rangle$ appears with a normalization. Using classical results for the POD, we can write (Berkooz, 1991)

$$A(x, x') = \frac{\sum_{i=1}^{\infty} \lambda_i \phi_i(x) \phi_i^*(x')}{\sum_{i=1}^{\infty} \lambda_i |\phi_i(x')|^2} = \sum_{i=1}^{\infty} \phi_i(x) f_i(x'), \tag{3}$$

where $f_i(x') = \lambda_i \phi_i^*(x') / \sum_{j=1}^{\infty} \lambda_j |\phi_j(x')|^2$. We may interpret $f_i(x')$ as the relative contribution of ϕ_i to $u(x')$ on the average.

It is remarkable, and is the point of this section, that we get exactly the same result from a simplified PDF model based on the POD. Here we assume that the coefficients a_i in a modal expansion $u(x, t) = \Sigma a_i(t)\phi_i(x)$ are jointly normal and independent, with zero mean and variance λ_i. Let us compute the estimator $\langle u(x) \mid u(x') \rangle$. Since we have an expression for the PDF (through our assumption on the a_i) we can compute this explicitly. Recall from probability theory that if the x_i are independent and normal with zero mean and variance σ_i^2 for $i = 1, \ldots, m$ then

$$x_i \sum_{j=1}^{m} x_j = C \quad \frac{\sigma_i^2 C}{\sum_{j=1}^{m} \sigma_j^2} \tag{4}$$

(See the formula for the conditional expectation of joint normal variables in Feller, 1957.) Using (4), we have

$$a_i \phi_i(x') \mid \sum_{j=1} a_j \phi_j(x') = u(x') \rangle = \frac{\lambda_i |\phi_i(x')|^2 u(x')}{\sum_{j=1}^{\infty} \lambda_j |\phi_j(x')|^2} \tag{5}$$

which gives (Berkooz, 1991)

$$\langle u(x) \mid u(x') \rangle = \frac{\sum_{i=1}^{\infty} \lambda_i |\phi_i(x')|^2 u(x') \phi_i(x)/\phi_i(x')}{\sum_{j=1}^{\infty} \lambda_j |\phi_i(x')|^2}$$

$$\frac{\sum_{i=1}^{\infty} \lambda_i \phi_i^*(x') \phi_i(x) u(x')}{\sum_{j=1}^{\infty} \lambda_j |\phi_j(x')|^2}. \tag{6}$$

This is exactly the same result obtained from linear stochastic estimation: (3).

This single result helps to place linear stochastic estimation in context: it is not a different animal altogether, but is just the POD with a simplifying assumption on the PDF of the coefficients. As long as we are not discussing transport (which probably requires non-zero third moments) the assumption on the coefficients is physically not unrealistic.

3. Wavelets

All the flows of interest to us have one or more homogeneous directions. We are accustomed to use in these directions the Fourier transform, which is the homogeneous equivalent of the POD. However, the Fourier transform is not nearly so appropriate in the homogeneous case as is the POD in the inhomogeneous case. This is because the Fourier modes are not confined to a neighborhood, but extend to infinity without attenuation. All disturbances in fluid, and coherent structures in particular, are localized. There is therefore considerable motivation to find another representation that is more appropriate.

In Tennekes and Lumley (1972) it was suggested that a more appropriate quantity would be the energy surrounding a wavenumber κ, say from κ/a to $a\kappa$, where $a = 1.62$. In physical space, this packet with appropriate phase relations is confined to a region, essentially dropping to zero in about $2\pi/\kappa$ from the origin. Tennekes and Lumley called these 'eddies', but the are an example of what are now called wavelets.

While wavelets appear to make more physical sense, we might worry because we would be discarding the optimality of the Fourier representation; would convergence be much slower, so that we would need many more terms, or would we lose considerable energy if we used the same number of terms? A main result of a recent paper (Berkooz et al., 1992) is that very little energy is lost when using a wavelet basis instead of a Fourier basis. Although wavelets are physically appealing, it would also be nice to have reassurance from calculations that physical behavior would be preserved in a wavelet representation in which interactions are truncated. To set our minds at rest on this point, Berkooz et al. (1992) also display a *relatively* low-dimensional wavelet model of the Kuramoto–Sivashinsky equation with truncated interactions that shows dynamical behavior similar to the full equation.

Without getting involved with mathematical details, an orthonormal wavelet basis is constructed by starting with a function, say $\Psi(x)$, similar to the eddy suggested by Tennekes and Lumley (1972). From this, construct a set $\Psi_{j,0}(x) = \Psi(x2^j)$, $j = 1, 2, \ldots$ Each of these is shrunk affinely, but is geometrically similar to the original function. Now consider the translates of $\Psi_{j,0}$: $\Psi_{j,k}(x) = \Psi_{j,0}(x - k2^j)$, $k = 1, 2, \ldots$

Berkooz et al. (1992) consider a periodic, homogeneous stochastic process. It is then obvious that the POD decomposition becomes identical to the Fourier decomposition. Now, if, for a given ε, we need $N(\varepsilon)$ POD modes in order to satisfy

$$\sum_{\iota < 1} \langle a_\iota(t)|^2 \rangle - \sum_{\iota=1}^{N(\varepsilon)} \langle |a_\iota(t)|^2 \rangle \leq \varepsilon \tag{7}$$

then, if the $\{b_i\}$ are the coefficients in a wavelet basis, they show that, for some
' constant C, depending only on the process (and not on ε):

$$\left| \sum_{i \geq 1} \langle |a_i(t)|^2 \rangle - \sum_{i=1}^{\mathcal{N}(\varepsilon)} |b_i(t)|^2 \rangle \right| \leq C\varepsilon \tag{8}$$

for some $\mathcal{N}(\varepsilon) > N(\varepsilon)$ only slightly bigger than $N(\varepsilon)$ (the precise statement is
given in Berkooz et al., 1992). This suggests that we will not be too much worse off
using a wavelet basis, but it would be reassuring to have numerical confirmation.

3.1. NUMERICAL RESULTS

Berkooz et al. (1992) wished to apply these ideas to a simple situation. The three-
dimensional, three component Navier–Stokes equations are too complicated for a
first effort.

The one-dimensional, scalar Kuramoto–Sivashinsky (K–S) equation appears in
a variety of contexts, such as quasi-planar fronts, chemical turbulence, etc. It shares
some properties with Burgers' equation and the Navier–Stokes equations, but is
much easier to deal with. Up to a rescaling, this equation can be written as:

$$u_t + u_{xx} + u_{xxxx} + u_x u = 0, \quad 0 \leq x \leq L \tag{9}$$

u periodic on $[0, L]$, where L, the length of the spatial domain, is the only free
parameter in the problem.

Although the dynamical behavior for small values of L is fairly well understood
(see Hymans and Nicolaenko, 1986 for an overview), many open questions remain
concerning the limit $L \to \infty$ (Zaleski, 1989; Pomeau et al., 1984). As can be seen
from the numerical simulations, for $L > 30$, a chaotic regime involving both space
and time disorder occurs (see Fig. 1, where we plot a space-time representation of
a typical solution, $L = 400, 0 \leq t \leq 100$; the grey scale represents the magnitude
of u).

In order to check the estimate (8), we compare the energy resolved by a given
number of modes using either a Fourier (POD) or wavelet basis. Note that, to
compare the Fourier and wavelet bases, all the translates in the wavelet basis
must be considered. Here are some results (see Fig. 2; the numbers indicate the
percentage of the mean of u^2 that is captured by the indicated number of modes):

Number of modes	wavelets ($m = 6$)	wavelets ($m = 8$)	Fourier
64 ($j = 6$)	70.84%	71.5%	72.2%
96 ($j = 6, 5$)	79.1%	79.43%	83.3%
127 ($0 \leq j \leq 6$)	84.1%	84.9%	89.7%
255 ($0 \leq j \leq 7$)	99.9%	99.9%	99.9%

Time
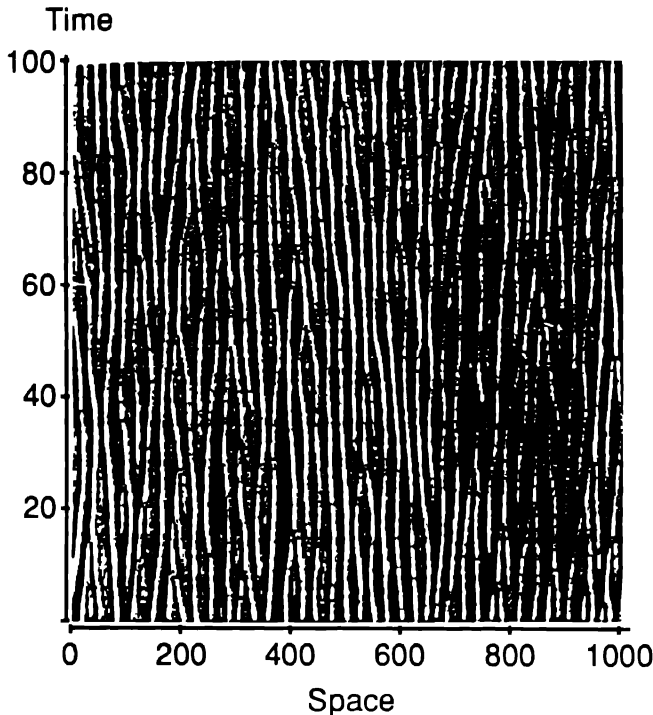
Fig. 1.   A typical solution of the periodic Kuramoto–Sivashinsky equation ($L = 400$).

The scale $j = 6$ which captures most of the energy on the average, corresponds to a characteristic length $2^{-6}L \approx q_m^{-1}$, which is also the length scale associated with the most unstable wavelength q_m. In agreement with the general shape of the energy spectrum, the scales $0 \leq j \leq 5$ are shown to capture more energy than the scales in the dissipative range ($j \geq 7$). The above figures show that (for sufficiently smooth splines) the wavelet projection captures almost the same amount of energy as the Fourier (= POD) decomposition (within 5%).

These results prompted Berkooz et al. (1992) to conclude that from an average energy point of view wavelets were a reasonable candidate for a modal decomposition of the K–S equation. The localized nature of the wavelets may give a unique view of the spatial attributes of the coherent structures. We outline their approach. They conjecture the existence of a dynamically relevant length scale L_C such that interactions between physical regions of distance greater than L_C are dynamically insignificant (a dynamical St. Venant principle). Determining the validity of this conjecture is part of their study. They use this conjecture to remove terms in a wavelet-Galerkin projection that correspond to interactions between regions of distance greater than L_C. To study whether the dynamics of coherent structures are indeed locally determined they construct truncations corresponding to a small box size L_B in the larger box of size L.

Partial traces
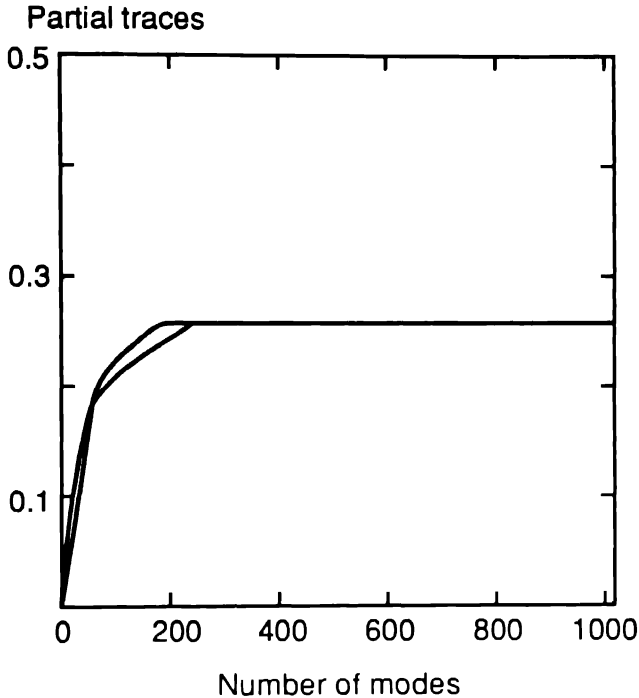
Fig. 2. The energy resolved by the Fourier (POD) basis (upper curve) and the wavelet basis (lower curve), as functions of the number of modes.

They need to address the role of unresolved physical space (i.e. modes located outside the box of size L_B). It is obvious that the Dirichlet type of boundary condition imposed will create a boundary layer which will affect the dynamics, especially in small boxes which are of interest to us. There are two plausible approaches to remove this effect. One approach uses a stochastic boundary condition (which is hard to implement numerically and treat analytically). The other approach appeals to the conjecture on the existence of L_C. One takes a box of size L_B greater than $2L_C$ so that one can periodize the small model using resolved relatively distant modes instead of unresolved ones. They opted for the second approach.

We present some preliminary results of the integration of one such model. They resolved a box of size $L_B = 50$ (this is 1/8 of the original box). Figure 3 shows the spatio-temporal evolution of the full system, with a Fourier basis. Figure 4 shows the spatio-temporal evolution of a (rescaled) model with $L_C = 50 \times 3/8$, which is in excellent qualitative agreement with the dynamics of the full system. As in Fig. 1, Figs 3 and 4 indicate by grey scale the magnitude of u. If L_C is too small, after a long initial transient, the system eventually settles down to a periodic oscillatory state, in which no interaction between the localized structures is observed. This can be avoided by an increase in L_C, which adds significant non-linear interactions
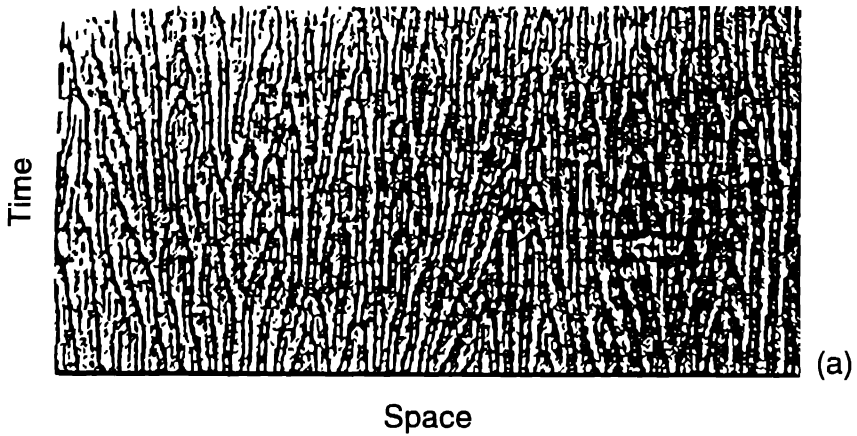
Fig 3   Full simulation of the Kuramoto–Sivashinsky equation (Fourier basis)
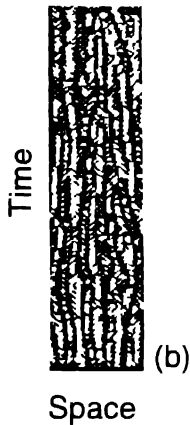
Fig 4   Wavelet simulation of the K–S equation (4 mode) with $L_B = 50$ (rescaled)

between relatively distant physical space locations. It might also be avoided by a stochastic boundary condition

Thus we see that. we do not lose any significant amount of energy by changing from a Fourier to a wavelet basis, and it is possible to use a wavelet basis with truncated spatial interaction to reproduce complex dynamical behavior reminiscent of that governed by the Navier–Stokes equations

4   Eduction of Coherent Structures

Ideally, one would like to apply the POD approach to a wide range of flows where coherent structures are known to play an important role in the dynamics The POD procedure, however, requires the two-point velocity autocorrelation tensor as

input, thus necessitating complete documentation of the flow before the analysis can proceed. For flows with very high Reynolds numbers or complicated geometries this can be prohibitively expensive given current computational and experimental capabilities. In this section we will describe an analytic procedure for extracting basis functions (structures) which approximate those given by the POD but which requires much less *a priori* statistical information about the flow.

The method presented here is based on energy stability considerations put forth by Lumley (1971). A fuller description can be found in Poje (1993); Poje and Lumley (1994). First, the instantaneous flow field is decomposed into three components in order to isolate the large scale structures. Evolution equations can then be written for the coherent velocity field and the coherent kinetic energy. A procedure can then be formalized to search for the structures which maximize the instantaneous growth rate of coherent energy, the rationale being that the structures which on average have the largest growth rates will compare well with the structures which contribute the most to the average turbulent kinetic energy (POD eigenfunctions).

As an example we consider turbulent channel flow assumed statistically homogeneous in both the downstream (x_1) and cross-stream (x_3) directions. In order to extract spatial structures from the total velocity field, we avoid traditional Reynolds averaging and instead decompose the instantaneous velocity field into three components: the spatial mean (U), the coherent field (v) and the incoherent background turbulence (u').

$$u_i(\mathbf{x}, t) = U(x_2) + v_i(\mathbf{x}, t) + u_i'(\mathbf{x}, t). \tag{10}$$

The spatial mean is an average over the x_1–x_3 plane; we will indicate it by $[\ldots]$. We introduce a second averaging procedure, denoted by $\langle \ldots \rangle$, which eliminates the small-scale turbulence while leaving the coherent field intact.

$$\langle u_i(\mathbf{x}, t) \rangle = U(x_2) + v_i(\mathbf{x}, t). \tag{11}$$

Practically this can be accomplished in several ways (Reynolds and Hussain, 1972; Liu, 1988; Brereton and Kodal, 1992; Berkooz, 1991). We will refer to this average as a phase average. For our purpose here it is sufficient that the phase average and space average commute, and that the cross-correlations be negligible.

$$\langle u_i'v_j \rangle = [u_i'v_j] = 0. \tag{12}$$

It is possible to devise various models to support Equation (12). Given these averaging procedures, we can manipulate the Navier–Stokes equations to arrive at evolution equations for the coherent velocity field.

$$Dv_i/Dt + v_j v_{i,j} = -\pi_{,i} + \nu v_{i,jj} + \tau_{ij,j} - S_{ij} v_j + [v_i v_j]_j \tag{13}$$

where D/Dt denotes the mean convective derivative, S_{ij} the mean rate of strain, and ν the kinematic viscosity, τ_{ij} represents the rectified effects of the small scale fluctuations on the coherent field and is defined by

$$= [u_i'u_i'] - \langle u_i'u_j' \rangle. \tag{14}$$

This can be thought of as a perturbed Reynolds stress, which is unknown and will ultimately require modeling. In the limit of a complete random turbulence containing no structure (i.e. $\langle \ldots \rangle = 0$) this quantity is equal to the usual Reynolds stress. In the case when the turbulence is completely structured so that $\langle \ldots \rangle = [\ldots]$, τ_{ij} is identically zero.

We now follow classical energy method stability analysis for the coherent field. First, the growth rate of the volume averaged coherent energy E is defined as a functional of the coherent velocity field.

$$\lambda(\mathbf{v}, U, \nu, \tau) = (1/2E) \, dE/dt. \tag{15}$$

Integration by parts and continuity are used to eliminate the non-linear convective and pressure terms. We seek the solenoidal velocity field which maximizes λ. Application of the calculus of variations then gives the Euler equations for the maximizing $\mathbf{v}$ field in the form of an eigenvalue relation.

$$\lambda v_i + S_{ij}v_j = -\pi_{,i} + \nu v_{i,jj} + \tau_{ij,j}$$

$$v_{i,i} = 0. \tag{16}$$

We consider coherent fields which are periodic in the homogeneous directions. This allows a decomposition into poloidal and toroidal components which satisfy continuity exactly (Joseph, 1973)

$$v_1 = \Psi_{,12} - v_{,3}; \quad v_2 = -(\Psi_{,11} + \Psi_{,33}); \quad v_3 = \Psi_{,23} + v_{,1}. \tag{17}$$

The two scalar functions are then expanded in normal modes in the streamwise and spanwise directions.

$$\Psi(\mathbf{x}) = \Psi(x_2)\exp\{\imath(k_1 x_1 + k_3 x_3)\}$$

$$v(\mathbf{x}) = v(x_2)\exp\{\imath(k_1 x_1 + k_3 x_3)\}. \tag{18}$$

Substituting the above into Equation (16) and eliminating the pressure π results in two coupled equations, forming a differential eigenvalue problem.

In order to proceed we need to specify a mean velocity field and a model for the unknown stress terms.

4.1. CLOSURE MODELS

We have investigated two different models for the unknown stress terms appearing in the eigenvalue relation. It should be noted that, modulo the modeled terms, Equation (16) is linear in the coherent velocities, providing an inexpensive means of determining basis functions. This linearity is an essential advantage of the method and for this reason we will constrain any stress model to be both linear and homogeneous in the $\mathbf{v}$ field insuring that the governing equation remains a regular eigenvalue problem. Tensorially this requires

$$\tau_{ij} - \tau_{kk}\delta_{ij}/3 = \Gamma_{ijkl}(v_{k,l} + v_{l,k}). \tag{19}$$
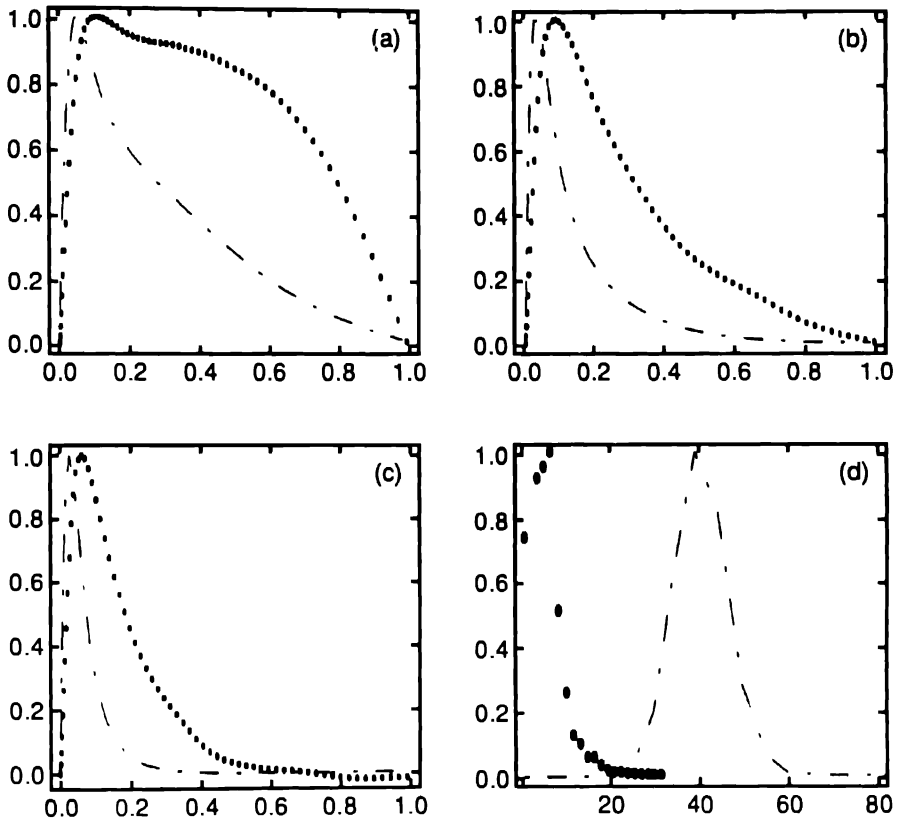
Fig. 5. Isotropic eddy viscosity model. ●●●● POD; —··——··—· isotropic model; (a) $k_1 = 3.00$, (b) $k_1 = 6.00$, (c) $k_1 = 12.00$, (d) spectrum.

The nature of the averaging procedure implies that the scales of the coherent field and the background turbulence are different. Assuming that the background turbulence evolves on much shorter time and length scales than the structures, it seems plausible that a Newtonian stress-strain relationship like that for the molecular stresses will provide the basis for a model. We set

$$\tau_{ij} - \tau_{kk}\delta_{ij}/3 = \nu_t(v_{i,j} + v_{j,i}). \tag{20}$$

Due to the inhomogeneity of the turbulence in the wall normal direction, we specify ν_t as a function of x_2 corresponding to experimentally determined values of the traditional eddy viscosity. We will refer to this basic model as the isotropic eddy viscosity model.

Using the basic stress model and an analytic expression for the fully turbulent mean profile (Reynolds and Tiederman, 1967) we have solved the resulting equations numerically. Figure 5 shows comparisons between the calculated first order eigenvectors and the POD results of Moin and Moser (1989) obtained from a

numerical data base; the results are shown as a function of distance from the wall, for three different values of the cross-stream wavenumbers (recall that the stream-wise wavenumber is zero). Figure 5d compares the first order eigenvalue spectrum obtained both ways, as a function of cross-stream wavenumber. Although there are qualitatively similarities in the shape of the structures, the modes predicted by the stability method fall off much more rapidly away from the wall than do the POD functions. The eigenvalue spectrum clearly shows that the stability analysis favors modes which have a much higher wavelength than the maximum energy modes of the POD.

Although there may be a number of reasons for this discrepancy, we choose to first examine more closely the closure model. We find that the isotropic eddy vis-cosity model creates no coupling between the different components of the coherent velocity. When there is no streamwise variation of the coherent field the only cou-pling terms in the equations are those multiplying the mean gradient. For realistic mean profiles, regions of high shear are confined to thin regions near the wall, and the structures predicted may be expected to fall off as quickly as the shear.

We now seek to develop a stress model that allows for some anisotropy in the eddy viscosity, and thus couples the component equations through the stress terms. We begin with the evolution equation for the Reynolds stresses, where we are obliged to model a number of terms to obtain a closed system. We use standard second-order turbulence models. We model the pressure-strain correlation by a return-to-isotropy term and an isotropization-of-production term (Naot et al., 1970); we use an isotropic dissipation. We assume the stresses are in local equilibrium: $D[u_i u_j]/Dt = 0$. This reduces the evolution equation for the Reynolds stress to an algebraic expression.

Now we set up a perturbation expansion in terms of mean field quantities, taking the coherent field as an order ε perturbation to the spatial mean. On physical grounds, we argue that the perturbed stress field is due entirely to the presence of the structures and consequently we restrict the model to include only production due directly to coherent velocity gradients. This is in agreement with a cascade analogy for the complete flow: the coherent structures are fed energy directly by the mean gradients while the small scale turbulence is in turn fed by gradients of the coherent field. If we identify the 0th order stresses with an eddy viscosity tensor, then the closure model can be written as

$$\tau_{ij} - \tau_{kk}\delta_{ij}/3 = -\nu_{ik}s_{kj} \tag{21}$$

where the tensor viscosity has the following structure in this specific case: $\nu_{13} = \nu_{23} = 0$, $\nu_{33} = \nu_{22}$.

Despite the absence of mean production terms, this model is still a major improvement over the isotropic eddy viscosity formulation. In the simple model the effects of the mean field have been neglected entirely. Here we have allowed for modulation of the perturbation stresses by the mean field through the 0th order stresses appearing in the production terms. Also we have unconstrained the model
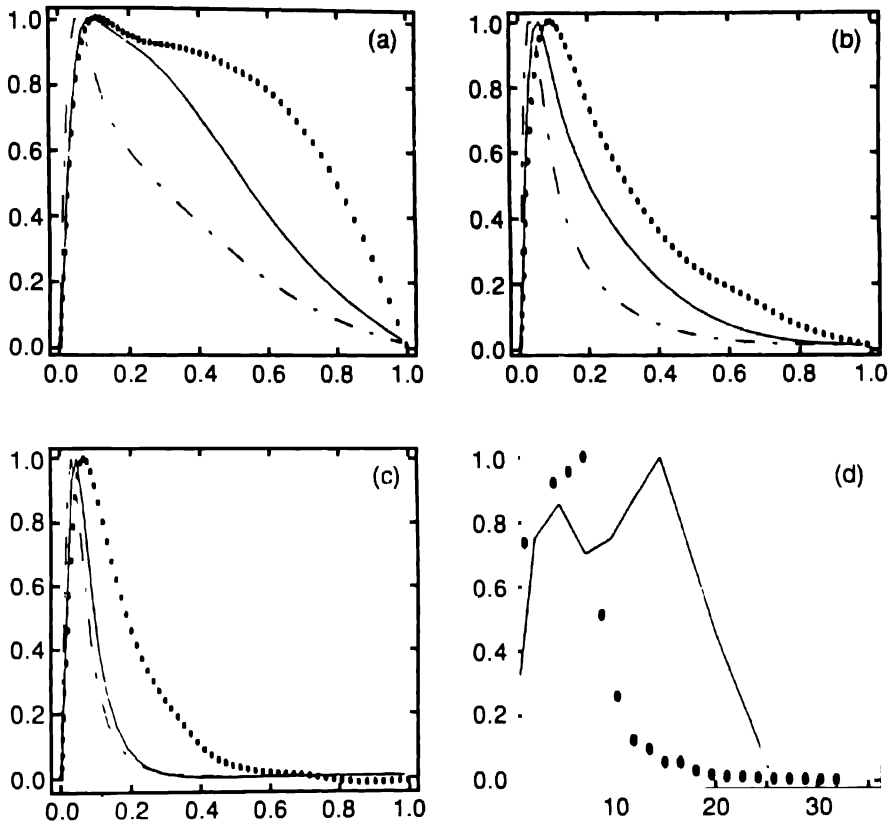
Fig. 6. Anisotropic eddy viscosity model: ●●●● POD; ——·——·—— isotropic model; ·
anisotropic model; (a) $k_3 = 3.00$, (b) $k_3 = 6.00$, (c) $k_3 = 12.00$, (d) spectrum.

in an important way since the tensorial form of the eddy viscosity allows the
principal axes of the stress tensor to be unaligned with the axes of the rate of strain.
This is more realistic considering the three-dimensionality of the coherent field.
This model leads to the expected cross-coupling of the equations through the stress
terms.

Figure 6 shows eigensolutions for several values of k_3 (see the description
of Fig. 5 for clarification). The results compare well with the POD eigenval-
ues, especially for wavenumbers at or below the peak in the POD spectrum. The
improvement with decreasing wavenumber is expected given the modeling con-
siderations. The separation of scales between the background turbulence and the
coherent structures increases as the wavenumber decreases adding to the expected
accuracy of the stress model. The comparison of the two models indicates signifi-
cant improvements in the results given by the anisotropic eddy viscosity form. The
energy method procedure with the more refined closure model appears capable of

extracting structures which closely approximate those given by the POD at least at the energy containing scales of motion.

Despite the general improvement, it is still clear that more needs to be done. From Figs 5 and 6, it is evident that the eigenspectrum produced by solution of Equation (10), while improved by the use of the anisotropic closure model, still predicts structures with maximum growth rate that are a factor of 2 smaller than those containing the most energy (as given by the POD). We next consider the effect on the spatial mean velocity field of the growing coherent perturbation.

4.2. INTERACTION WITH THE MEAN

At this point we consider the role of the mean velocity in the two methods. The POD structures are derived from solutions to the non-linear Navier–Stokes equations which allow for complicated interaction between the different scales of motion. The structures evolve in a mean velocity field that is changing due to the presence of the structures themselves. Conditionally averaged mean profiles clearly show the evolution of the local shear in the presence of coherent structures (see Fig. 7). It is clear from Fig. 8 that profiles with a larger region of high shear also have eigenfunctions which are non-negligible in a broader region. We see that structures, in the relatively long period before bursting, act to erode the shear that they see. The POD eigenfunctions are given by averages of contributions from different mean profiles.

The stability method on the other hand does not allow for any interaction between the mean and the coherent field. The mean flow is imposed and the resulting structures are calculated. The mean profiles we have used are time averages which mask any contribution from the coherent field. As such the stability analysis predicts that the highest growth modes are those which can best extract energy from the time averaged mean shear which is concentrated in the small near-wall region. Since the structures have an aspect ratio of about 1, the narrow region of high imposed shear leads to a peak in the eigenspectrum at a large wavenumber.

To allow the mean field to evolve under the influence of the coherent field, we follow Liu (1988) and write time evolution equations for the energy density of the coherent field. We allow the mean profile to depend on the coherent velocity as it does in reality. We expect that equilibrium solutions for the energy density as a function of cross-stream wavenumber will approximate the average energy content as given by the POD spectrum.

We assume that the coherent field is given by the eigenmodes of the stability problem, but we now allow them to vary in time

$$v_i(\mathbf{x}, t) = A(t)\Psi_i(\mathbf{x}) \tag{22}$$

$$\langle u_i u_j \rangle(\mathbf{x}, t) = E(t)B_{ij}(\mathbf{x}) \tag{23}$$

where $\Psi_1 = v \exp\{ikx_3\}$, $\Psi_2 = ik\Psi \exp\{ikx_3\}$, $\Psi_3 = -D\Psi \exp\{ikx_3\}$. By examining the evolution equation for $r_{ij} = \langle u_i u_j \rangle - [u_i u_j]$, the forcing terms are
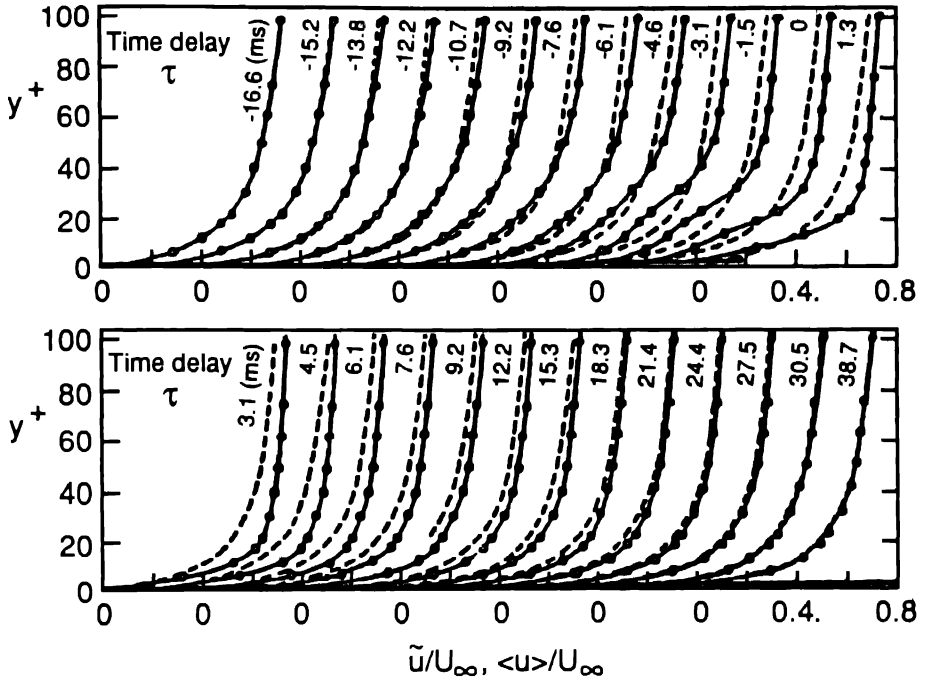
Fig. 7.   Conditionally averaged velocity profiles before and after a burst, showing the influence on the local shear of the coherent structures (Blackwelder and Kaplan, 1976).
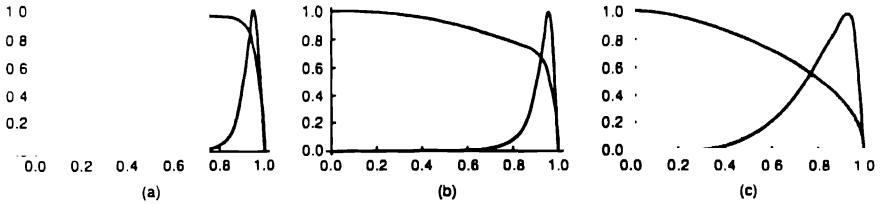

Fig. 8.   The eigenfunctions generated by the anisotropic eddy viscosity model with various mean velocity profiles.

of the form $\langle u_i u_j \rangle v_{i,j}$. Consequently, we assume the perturbation stresses also to be a product:

$$r_{ij}(\mathbf{x}, t) = A(t)E(t)R_{ij}(\mathbf{x}). \tag{24}$$

Since we have used an eddy viscosity in obtaining the coherent forms we further assume that:

$$R_{ij}(\mathbf{x}) = -\nu_{ik}(\Psi_{j,k} + \Psi_{k,j}) \tag{25}$$

where $\nu_{11} = \nu_{22} = \nu_{33} = \nu_\tau$, $\nu_{12} = \nu_{21} = \beta_\tau$, $\nu_{13} = \nu_{23} = 0$. All that remains is to model the mean profile. For this we adopt the quasi-steady model used in Aubry
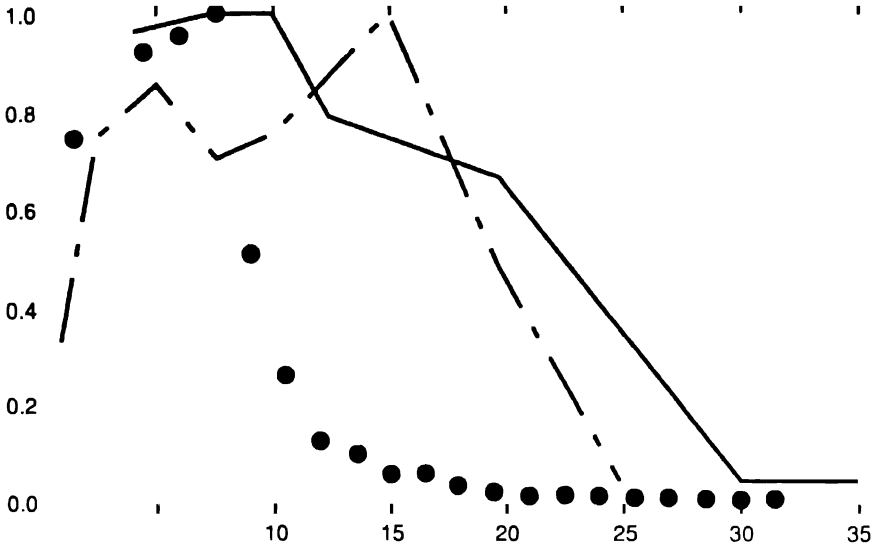
Fig. 9. ●●●● the POD eigenvalue spectrum; —·——·—·· the eigenvalue spectrum generated by the anisotropic model without mean flow interaction; —— the eigenvalue spectrum generated with mean flow interaction.

et al. (1988). This allows the mean to respond to growing structures providing the necessary feed-back to the evolving modes. Using the friction velocity, u_τ, and the channel half height, a, the scaled equation for the mean gradient is:

$$\partial U(x_2, t)/\partial x_2 = \mathrm{Re}_\tau\{\langle u_1 u_2 \rangle + \langle v_1 v_2 \rangle - x_2\}. \tag{26}$$

The rate of dissipation of turbulent energy is given by a simple model adopted from second order closure schemes.

$$D\varepsilon/Dt = c_1(\varepsilon/k)\langle u_i u_k \rangle U_{i,k} - c_2\varepsilon^2/k + \text{Transport}. \tag{27}$$

Substituting these various models into the energy equations results in a set of three coupled ODEs for the temporal evolution of the energies and dissipation.

In order to evaluate the integrals appearing in these equations, we need to assume the spatial form of the averaged turbulence quantities B_{ij} and the dissipation $D(x_2)$. For this simple model we have assumed that while the intensity of the turbulence varies its spatial dependence remains unchanged. We use experimental data for fully developed turbulent channel flow to determine both B and D. The coherent structures are found by energy stability analysis, as described above.

5. Conclusions

The POD has played a central role in identifying coherent structures in experimental or computational data, and in constructing low-dimensional models of turbulent

flows, models which resolve only the coherent structures and their interaction, and parameterize the smaller scale, less organized turbulence. However, use of the POD raises a number of questions: is it the best way to identify the coherent structures? When we construct low-dimensional models, are we tied to Fourier decompositions in homogeneous directions, or can we use wavelets, and get away from periodic boundary conditions and periodic arrays of structures? Can we find cheaper ways to obtain the forms of the POD eigenfunctions, the coherent structures?

We have shown here that linear stochastic estimation, the other popular method for identification of coherent structures in experimental or computational data, is equivalent to the POD with the assumption that the coefficients in the POD are jointly Gaussian. For many purposes (so long as only second order quantities are being considered) this is a physically realistic assumption.

When we construct low-dimensional models using the POD, if there are homogeneous directions we have been accustomed to use Fourier decomposition. This is awkward physically, since the Fourier modes are not confined to a neighborhood while the disturbances to the real flow are. Here we have shown in connection with a one-dimensional equation that wavelets can be used instead with a negligible sacrifice in efficiency; and that simple assumptions regarding spatial interaction of the wavelets permits a relative simple model that reproduces the dynamics. This suggests that similar things are probably true of the Navier–Stokes equations, and that we will be able to construct low dimensional models for real flows, like the wall region of the boundary layer, using the more realistic wavelet representations, with reasonable truncations of the spatial interactions, thus freeing ourselves from periodic boundary conditions, and periodic arrays of coherent structures; we will thus be able to consider soliton coherent structures, which are much more realistic.

In order to construct these low-dimensional models, it is necessary to have at hand the POD eigenfunctions. Up to the present, this required extensive statistical documentation of the flow, either experimental or computational. Clearly, the flow with coherent structures represents a new attractor for the flow. We do not know how to analyze this new attractor to find the coherent structures. The coherent structures are extracting energy from the mean velocity profile, modifying it, and giving up energy to the small scale turbulence, also modifying it. We have suggested simple models for both modifications, and have shown that, with these adjustments, the form of the instability in its non-linear growth phase is essentially the same as the POD eigenfunctions, and the peak of the eigenvalue spectrum is in the same place. The flow whose instability we consider, of course, is the real flow with the coherent structures already present – we do not know how to remove them before we have them. Fortunately, it does not seem to make any difference. We may hope that, in poorly documented flows, we will have the same luck, and will be able to extract the eigenfunctions by a similar, relatively cheap, procedure.

References

Adrian, R. J., Conditional eddies in isotropic turbulence. *Physics of Fluids* 22(11) (1979) 2065–2070.

Adrian, R. J. and Moin, P., Stochastic estimation of organized turbulent structure: homogeneous shear flow. *J. Fluid Mech.* 190 (1988) 531–559.

Adrian, R. J., Moin, P., and Moser, R. D., Stochastic estimation of conditional eddies in turbulent channel flow. In: P. Moin, W.C. Reynolds and J. Kim (eds), *CTR, Proceedings of the Summer Program 1987.* NASA Ames Research Center/Stanford University (1987).

Aubry, N., Holmes, P., Lumley, J. L., and Stone, E., The dynamics of coherent structures in the wall region of a turbulent boundary layer. *J. Fluid Mech.* 192 (1988) 115–173.

Berkooz, G., *Turbulence, Coherent Structures and Low Dimensional Models*, Ph.D. Thesis, Cornell University (1991).

Berkooz, G., Elezgaray, J., and Holmes, P., Coherent structures in random media and wavelets. *Physica D* 61 (1993) 47–58.

Berkooz, G., Holmes, P., and Lumley, J. L., Intermittent dynamics in simple models of the turbulent wall layer. *J. Fluid Mech* 230 (1991) 75–95.

Brereton, G. J. and Kodal, A., A frequency domain filtering technique for triple decomposition of unsteady turbulent flow. *J. Fluids Engineering* 114 (1992) 45–51.

Cantwell, B. J., Organized motions in turbulent flow. *Ann. Rev. Fluid Mech.* 13 (1981) 457–515.

Clavin, P., Dynamic behavior of premixed flame fronts in laminar and turbulent flows. *Prog. Energy Comb. Sci.* 11 (1985) 1–59.

Feller, W., *An Introduction to Probability Theory and Its Applications*. New York: John Wiley (1957).

Hyman, J. M. and Nicolaenko, B., The Kuramoto–Sivashinsky equation: a bridge between PDEs and dynamical systems. *Physica D* 18 (1986) 113–126.

Joseph, D. D., *Stability of Fluid Flow*. Berlin: Springer (1973).

Liu, J. T. C., Contributions to the understanding of large scale coherent structures in developing free turbulent shear flows. *Advances in Applied Mechanics* 26 (1988) 183–309.

Lumley, J. L., Some comments on the energy method. In: L. H. N. Lee and A H. Szewczyk (eds), *Developments in Mechanics 6*. Notre Dame, IN: N.D. Press (1971).

Moin, P. and Moser, R. D., Characteristic-eddy decomposition of turbulence in a channel. *J. Fluid Mech.* 200 (1989) 471–509.

Moin, P., Adrian, R. J., and Kim, J., Stochastic estimation of organized structures in turbulent channel flow. In: *6th Turbulence Shear Flow Symposium*, Toulouse, France (1987).

Poje, A., *An Energy Method Stability Model for Large Scale Structures in Turbulent Shear Flows*, Ph.D. Thesis, Ithaca, NY: Cornell (1993).

Poje, A. and Lumley, J. L., A model for large scale structures in turbulent shear flows. *J. Fluid Mechanics* (1994) (submitted).

Pomeau, Y., Pumir, A., and Pelce, P., Intrinsic stochasticity with many degrees of freedom. *J. Stat. Phys.* 37 (1984) 39–49.

Reynolds, W. C. and Hussain, A. K. M. F., The mechanics of an organized wave in turbulent shear flow. Part 3. Theoretical models and comparisons with experiment. *J. Fluid Mech.* 54 (1972) 263–287.

Reynolds, W. C. and Tiederman, W. G., Stability of turbulent channel flow with application to Malkus' theory. *J. Fluid Mech.* 27 (1967) 253–272.

Tennekes, H. and Lumley, J. L., *A First Course in Turbulence*. Cambridge, MA: The MIT Press (1972).

Zaleski, S., A stochastic model for the large scale dynamics for some fluctuating interfaces. *Physica D* 34 (1989) 427–438.

A Comparison of Different Analytical Techniques for Identifying Structures in Turbulence

N.K.-R. KEVLAHAN[1], J.C.R. HUNT[1,2] and J.C. VASSILICOS[1]

[1] *DAMTP, University of Cambridge, U.K.*
[2] *Meteorological Office, Bracknell, U.K.*

Abstract. Vortical structures play an important role in the kinematics and dynamics of turbulence, but in order to understand this role we require techniques to identify and classify them. Proper Orthogonal Decomposition (POD), conditional sampling with ensemble statistics, and conditional sampling with conditional statistics are applied to a simple test function and the results are compared to determine the strengths and weaknesses of each approach. The second method gives the closest approximation to the test signal and is the easiest to use, although it is sensitive to the choice of conditions. None of these techniques can give much insight into the dynamics of turbulence, or into the organisation of eddies with complex, fine-scale structure.

New methods for investigating complex (self-similar) structures based on fractal and wavelet analyses are presented. Methods of distinguishing between locally (accumulating) and globally (fractal) self-similar structures are suggested.

1. Introduction

There has been much interest recently in the identification of characteristic structures in turbulence as a way of understanding its dynamical properties such as intermittency, the transfer of energy between length scales and the dispersion of contaminants. Experiments and Direct Numerical Simulations (DNS) have provided evidence that turbulence is not random, but contains structures with complex internal organisation (Vincent and Meneguzzi, 1991). Statistical approaches to turbulence are capable of predicting some quantities averaged over many realisations of a turbulent flow, but they are not able to provide insight into dynamical quantities that are directly related to the flow structures of a given realisation. In order to be effective the structural approach requires mathematical tools capable of unambiguously identifying complex turbulence structures according to appropriate kinematical and dynamical criteria. Once different sorts of structures have been identified it is possible to determine which of them play important roles in the dynamics of turbulence.

Many mathematical techniques have been used to identify and describe structures, e.g. the Fourier transform, Karhunen–Loeve orthogonal decomposition (Lumley, 1967; Aubry et al., 1988), functional/pattern recognition (Mumford, 1982), non-functional conditional sampling (Hussain, 1986), kinematic classification (Chen et al, 1990; Kevlahan, 1992; Wray and Hunt, 1990), and, more recently, fractals (Vassilicos and Hunt, 1991) and the wavelet transform (Brasseur

and Wang, 1992; Farge, 1992; Hunt et al., 1993). Each of these techniques breaks down the flow in different ways and places a different emphasis on the various aspects of turbulence (usually velocity, pressure, and their gradients). The question then arises: which methods are best able to detect, classify and describe eddy structures which may contain significant complexity? This paper has two parts: the first is concerned with the identification and eduction of large coherent structures. The second presents and discusses subtler tools capable of identifying small scale complex eddy structure.

We evaluate three common eduction techniques for coherent structures, namely Proper Orthogonal Decomposition (POD), conditional sampling with ensemble statistics, and conditional sampling with conditional statistics by applying each of these techniques to a simple test function that is asymmetric and whose energy is not contained in a single mode (i.e. $f(x) = (a + xb)\exp{-(x^2)}$). Then we assess the strengths and weaknesses of each approach. Some of these techniques have been tested before on actual turbulent flows (e.g. Guezennec, 1989), but the goal here is to assess these techniques on mathematically simple test signals so that the precise differences between the techniques are brought out. Differences between the techniques and the reasons for those differences may be obscured when they are applied to more complex flows. The results show that these techniques can lead to quite ambiguous and erroneous inferences as to the structure of eddies.

In the second part of this paper we address the problem of identifying and analysing eddies with significant internal complexity; none of the traditional approaches described above are capable of giving this sort of information. By 'complex structure' we mean eddies with a self-similar or singular internal structure. The usual Fourier transform can provide some limited information about the existence of such singular regions or structures in the flow. A non-integer power law energy spectrum (e.g. Kolmogorov's $E(k) \propto k^{-5/3}$ for the inertial range of isotropic turbulence) implies that the velocity field must contain singularities 'worse' than discontinuities (Moffat, 1984; Hunt and Vassilicos, 1991; Zel'dovich and Sokolov, 1985). These singular structures could be cusps, accumulating discontinuities or oscillations (e.g. functions of the form $f(x) = r^s \sin(r^{-t})$), fractal functions (e.g. the non-differentiable Weierstrass function $f(x) = \sum_{k=1}^{\infty} \lambda^{(s-2)k} \sin(\lambda^k x)$), or some more complex superposition of these. Both the accumulating and fractal functions are self-similar, however the accumulating functions are self-similar only about a specific point while fractals (characterised by a non-integer Hausdorff dimension) are self-similar everywhere. Accumulating and fractal structures may be considered globally and locally self-similar respectively. Turbulence models have been developed using both these types of structures as building blocks (e.g. the fractal β-model of Frisch et al. (1978) and the strained spiral vortex model of Lundgren (1982)).

To detect whether or not the structure of eddies actually corresponds to that assumed by these models requires a method for unambiguously determining and distinguishing between global and local self-similarity. The differences between
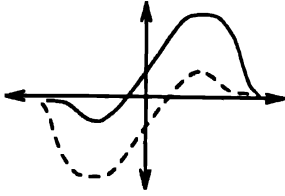
Fig. 1. Typical eddy structure from the test function $u(x) = (a + bx)\exp(-x^2)$.

these classes of self-similar structures are investigated by applying Fourier, wavelet and fractal methods to an accumulating test function as $f(x) = \sin 2\pi/x^t$ (which is locally self-similar) and a related function constructed from the random superposition of its Fourier components (which is globally self-similar). Finally, general analytical methods of distinguishing between locally and globally self-similar structures are proposed.

2. Comparison of Methods for Large Eddy Eduction

In this section we investigate the relative strengths and weaknesses of methods for eduction based on unconditional, or ensemble, statistics compared to those based on conditional sampling by applying each of them in turn to a simple one-dimensional test function.

Methods based on invariants of the deformation tensor and/or pressure (e.g. Wray and Hung, 1990; Chen et al., 1990) are in a different class, since unlike the above approaches they classify each point of the flow in a given realisation and do not extract whole eddy structures. Invariant/pressure methods do, however, have the advantage of being equally applicable to both large and small scale coherent structures. The invariant/pressure approach also requires more sophisticated and physically realistic test signals for evaluation, and for this and the previous reasons these methods are not included in the comparison.

The test function $u(x)$ we use is a simple sum of the Gaussian profile and its first derivative, both having random amplitudes, viz.:

$$u(x) = (a + bx)\exp(-x^2) \tag{2.1}$$

where a and b are normally distributed random variables with zero mean. This is representative of the velocity profile across a flow (e.g. a free shear flow) in which there are different kinds of eddies that are asymmetrical about the centre line $x = 0$ (see Fig. 1). If the eddies are uncorrelated with each other a and b are also uncorrelated. It is assumed that the variances σ_a^2, σ_b^2 of a and b are of similar magnitude. Each of the structure eduction techniques will be judged on its ability to pick out these typical eddies with the least amount of subjective manipulation. This is a more demanding task than in many flows, where the dynamics leads to a selection of a few dominant modes or types of eddy (Hussain, 1988).

2.1. PROPER ORTHOGONAL DECOMPOSITION (POD)

POD decomposes a signal onto a basis of non-specified functions chosen to represent the energy of the signal in the fewest number of modes. This method is completely objective (no possibility of subjective bias or control in the process), and it optimally efficient. The attempt to find the structure that is best correlated (in terms of energy) with the random turbulence field reduces to a problem of maximisation (Aubry et al., 1988). The calculus of variations reduces this maximisation problem to the solution of a Fredholm integral equations of the first kind

$$\int R_{ij}(x, x')\phi_j(x')\,\mathrm{d}x' = \lambda\phi_i(x), \tag{2.2}$$

where $R_{ij}(x, x')$ is the autocorrelation tensor and $\phi_i(x)$ are the eigenfunctions, or modes (which are often interpreted as independent eddy structures). Then the signal $u_i(x)$ may be written as the sum of the eigenfunctions $\phi_i^{(n)}(x)$ with random amplitudes $a^{(n)}$

$$u_i(x) = \sum_{n=1}^{\infty} a^{(n)}\phi_i^{(n)}(x). \tag{2.3}$$

The turbulent kinetic energy is the sum over the n eigenvalues

$$E = \int \langle u_i u_i \rangle \,\mathrm{d}x = \sum_{n=1}^{\infty} \lambda^{(n)}, \tag{2.4}$$

because of the orthogonality of the eigenfunctions and the statistical independence of the amplitudes, i.e.

$$\int \phi^{(n)}\phi^{(m)}\,\mathrm{d}x = \delta_{nm} \quad \text{and} \quad \langle a^{(m)}a^{(n)}\rangle = \delta_{mn}\lambda^r \tag{2.5}$$

where $\langle\ \rangle$ denotes the ensemble average. In the case of discrete data, solving Eq. (2.2) reduces to a matrix inversion problem. Note that although (2.3) converges optimally fast, some signals require many POD modes to capture a significant portion of the energy. POD is only useful for those signals where the energy can be captured in a few modes, or where the coefficients $a^{(n)}$ decrease abruptly after a certain mode.

The correlation function of the test signal (2.1) is

$$R(x, x') = (\sigma_a^2 + \sigma_b^2 xx')\exp(-x^2 - x'^2), \tag{2.6}$$

where a and b are taken to be random uncorrelated variables with standard deviations σ_a and σ_b. For this simple correlation function Eq. (2.2) can be solved analytically by the separable kernel method (Arfken, 1985, p. 872) to give

$$u(x) = a^{(1)}\phi^{(1)}(x) + a^{(2)}\phi^{(2)}(x), \quad a^{(1)} = a^{(2)} = \sqrt{\pi}\,(\sigma_a^2 + \sigma_b^2) \tag{2.7}$$

where the two modes are symmetric and anti-symmetric,

$$\phi^{(1)} = \sqrt{2}\,\pi^{-1/4}x\exp(-x^2), \quad \phi^{(2)} = \pi^{-1/4}\exp(-x^2). \tag{2.8}$$

Note that neither $\phi^{(1)}$ nor $\phi^{(2)}$ describes the asymmetrical form of the general eddy (see Fig. 1). It is evidently misleading to interpret the largest mode, $\phi^{(1)}$, as a typical eddy of the flow. The problem of interpreting the first mode arises here because the energy of the signal is fairly evenly distributed between the two largest modes. If the majority of the energy is not captured by the first mode it is more appropriate to consider the truncated series $\sum_{n=1}^{N} a^{(n)}\phi_i^n$ for which an increase of N by 1 results in little increase in energy, but for which a decrease of N by 1 removes a large portion of the energy. The first N modes together are then interpreted as the typical flow structure. It is important to remember that signals are possible for which even this method of interpreting the POD is not suitable (e.g. the complex eddies studied in Section 3).

2.2. CONDITIONAL SAMPLING WITH ENSEMBLE STATISTICS

The goal in conditional sampling is to estimate $u(x, t)$ given that the velocity at (x', t) assumes a specific value $u(x', t)$. It can be shown (see Adrian et al., 1988) that the best estimate of the profile $u(x, t)$, which is defined as $\hat{u}(x)$, is the *conditional average*

$$\hat{u}(x) = \langle u(x, t) \mid u(x', t)\rangle. \tag{2.9}$$

The conditional average (2.9) can be approximated in terms of second-order (linear) and third-order (non-linear) two-point spatial correlations by

$$\hat{u}_i(x) \sim A_{ij}(x', x)u_j(x') + B_{ijk}(x', x)u_j(x')u_k(x') + O(u^3(x')), \tag{2.10}$$

where A_{ij} and B_{ijk} are found by requiring that the mean-square errors $e_i = \langle (\hat{u}_i(x) - u_i(x))^2 \rangle$ be minima. Setting the derivatives of e_i with respect to A_{ij} and B_{ijk} equal to zero and carrying out the indicated averages gives the following equations for the components of A_{ij} and B_{ijk} for inhomogeneous, anisotropic turbulence

$$A_{ij}(x', x)\langle u_j u_l\rangle(x') + B_{ijk}(x', x)\langle u_j u_k u_l\rangle(x') = \langle u_l(x)'u_i(x)\rangle \tag{2.11}$$

$$A_{ij}(x', x)\langle u_j u_l u_m\rangle(x') + B_{ijk}(x', x)\langle u_j u_k u_l u_m\rangle(x')$$
$$= \langle u_l(x')u_m(x')u_i(x)\rangle. \tag{2.12}$$

In the case of homogeneous, isotropic turbulence these relations simplify to

$$A_{ij}(x', x) = \langle u_j(x')u_i(x)\rangle/u^2, \tag{2.13}$$

$$B_{ijk}(\mathbf{x'}, \mathbf{x}) = 3\langle u_j(\mathbf{x'})u_k(\mathbf{x'})u_i(\mathbf{x})\rangle/2Ku^4 \qquad (2.14)$$

where $u^2 = 1/3\langle u_i u_i \rangle$, and K is the kurtosis. Note that these correlations are *unconditional*, and they are not selected for particular 'eddies'; they are ensemble statistics. The Linear Stochastic Estimation (LSE) for $u(\mathbf{x}, t)$ retains only the first term on the right-hand side of Eq. (2.10).

From (2.10), (2.11), and (2.12) the LSE for our test function is

$$u(x) = \frac{R(x, x')}{\langle u^2(x') \rangle}\, u(x'), \qquad (2.15)$$

which, using (2.6), becomes

$$\hat{u}(x) = \frac{(\overline{\sigma_a^2} + \overline{\sigma_b^2}xx')\exp(-x^2 + x'^2)}{(\sigma_a^2 + \sigma_b^2 x'^2}\, u(x'). \qquad (2.16)$$

This purely statistical estimate may be combined with conditional sampling to determine the form of all eddies whose maximum amplitude is negative, i.e. $u < 0$. Conditional sampling governs how the reference point (in space and time) is chosen. In general, conditions are placed on both the location of the reference point, x', and the value of the velocity at that point, $u(x')$. If the location of the maximum (x_{mx}) is taken as the reference point x' then (2.16) shows that if $u_{mx} < 0$ the point $u = 0$ lies at $x = -\sigma_a^2/(\sigma_b^2 x')$. Therefore the location of the 'zero point' always has the opposite sign to that of the location of u_{mx}. This is a significant improvement over POD: the conditional eddy correctly represents the qualitative characteristics of the typical physical eddy as shown in Fig. 1.

How robust is the conditional eddy to changes in the sampling criteria? Consider a purely conditional approach (not based on the correlation tensor). If the conditional average is based on the criterion $x_{mx} > 0$ then the conditional eddy becomes

$$\langle u(x)^2 \mid x_{mx} > 0 \rangle = \sigma_b^2 x \exp(-x^2). \qquad (2.17)$$

This conditional eddy has lost all information about the symmetrical part of the velocity field (and half the energy)! If we now add an additional criterion $u(0) > 0$ the conditional eddy becomes

$$\langle u(x)^2 \mid x_{mx} > 0, u(0) > 0 \rangle = (\sigma_a^2 + \sigma_b^2)\exp(-x^2). \qquad (2.18)$$

This is again a very different structure from the one obtained by conditioning only on $x_{mx} > 0$. These examples show how sensitive the LSE method can be to the conditions chosen: slight changes in conditions can lead to the identification of completely different eddies.

2.3. CONDITIONAL SAMPLING AND CONDITIONAL STATISTICS

The Coherent Structures method (Hussain, 1986) is an interactive and iterative from of conditional sampling. In this approach one first defines the signal, its nature and the relevant length scales of the coherent structure for there to be a conditional event. The location of the structure is adjusted until an optimal mean structure pattern is obtained. If the spread of structures is too great one reclassifies, introducing more structure classes. This process continues until an optimal mean structure pattern with minimum spread is obtained.

Consider our test signal (2.1). Initially we may decide that there is only one coherent structure, and then filter the signal to remove white noise. On examining the signal we could then split the structures into two classes based on the sign of the maximum velocity: $u_{mx} > 0$ and $u_{mx} < 0$. This classification would still allow too great a spread of structures so we would reclassify further into four groups based on the sign and position of the maximum velocity: $u_{mx} > 0$, $x_{mx} > 0$, $x_{mx} < 0$, $u_{mx} < 0$, $x_{mx} > 0$, $u_{mx} < 0$, $x_{mx} < 0$. These structure classes can be further divided by the magnitude of the maximum velocity: e.g. $1/2 < u_{mx} < 1$, $1 < u_{mx} < 3/2$, $3/2 < u_{mx} < 2$, $2 < u_{mx} < 5/2$, $5/2 < u_{mx}$. Finally, by this iterative, subjective process we have ended up with twenty structure classes. This example shows that the coherent structures approach can require a large amount of manipulation to obtain representative structures, but also permits a great deal of fine control and sensitivity. An advantage of this approach is that, unlike LSE, it is able to separate out the incoherent noise of the signal.

3. Small Scale Complex Eddy Structures

How can small scale structures with complex internal organisation (e.g. the accumulating oscillatory signal from a cut through a spiral vortex) be identified? The continuous spectrum and accumulating structure of these eddies makes them difficult to represent in a few terms of a series (their energy is not concentrated in the first few POD modes). Conditional sampling is also inappropriate since it is difficult to extrapolate on such a highly oscillatory function. New tools are definitely needed to identify and analyse eddies with complex fine scale structure.

In this section we introduce some new tools for the analysis of complex eddy structures and apply them to two test signals: a $\sin(2\pi/x)$ 'spiral' which is an oscillatory locally self-similar function, and the Fourier phase scrambled version which is a globally self-similar fractal function. We use two new tools: the box-counting algorithm and the wavelet transform, and one old tool: the Fourier transform. The problem we address here is how to determine whether turbulence has a locally self-similar ('spiral') structure, or a globally self-similar fractal structure. The long term goal of the analysis of complex eddy structures is to find the relation between the quantities α (the exponent of the self-similar Fourier energy spectrum), $\phi(k)$ (the Fourier phase spectrum), D_K (the Kolmogorov capacity, a measure of
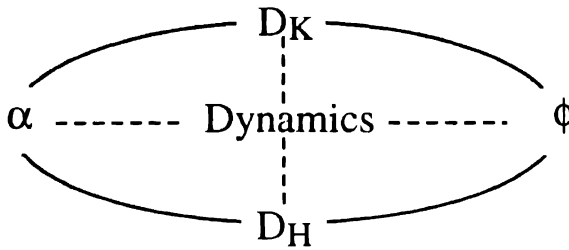
Fig. 2. The relation between quantities important for the analysis of the fine-scale structure of turbulence: the exponent of the Fourier energy spectrum α, Fourier phase spectrum $\phi(k)$, Kolmogorov capacity D_K, and Hausdorff dimension D_H. The solid lines indicate primarily fixed relationships, while the dotted lines indicate that the relationship is determined by the dynamics of the turbulence.

self-similarity), D_H (the Hausdorff dimension, a non-integer Hausdorff dimension defines a fractal) and the dynamics and geometry of the flow (see Fig. 2).

The box-counting algorithm gives a number (the Kolmogorov capacity) which characterises the self-similarity of a signal. A non-integer Kolmogorov capacity means that the signal is in some way self-similar, however both locally and globally self-similar functions will have a non-integer dimension. The Kolmogorov capacity alone cannot tell us whether the turbulence is fractal or spiral.

The general form of our accumulating 'spiral' test function

$$f(x) = x^2 \sin(2\pi x^{-t}) \tag{3.1}$$

is locally self-similar; its zero crossings form a set of points which Hausdorff dimension $D'_H = 0$, but a non-trivial Kolmogorov capacity $D'_K = t(t+1)$ (Hunt et al., 1993). Using the method of stationary phase, one finds that for large k the energy and phase spectra of (3.1) are given by (Hunt et al., 1993)

$$E(k) \propto k^{-2p} \tag{3.2}$$

$$2p = (2s+1)(1 - D'_K) + 1 \tag{3.3}$$

$$\phi(k) \propto k^{D'_K} \tag{3.4}$$

provided that $1 < 2p < 2$, $-t < s < 1$, and $t > 0$.

Orey (1970) showed that Gaussian sample functions with an energy spectrum $E(k) = k^{-2p}$ are fractal and that their zero crossings have a Hausdorff dimension

$$D'_H = \frac{1}{2}(3 - 2p). \tag{3.5}$$

Notice that the two functions just mentioned differ in three aspects: (i) $D'_H = 0$ for (3.1), $D'_H \neq 0$ in (3.5), (ii) they have different relations between p and respectively D'_K and D'_H, (iii) they have different phase spectra – the phase spectrum of a

Gaussian random function is random. A question which then arises is whether the *phase spectrum* can discriminate between local and global self-similarity.

To study the relation between an ordered phased spectrum $\phi(k)$ and the type of self-similar structure we took the Fourier transform of the accumulating function (3.1) with $s = 0$ and $t = 1$, scrambled the phases and then transformed back to physical space. This procedure destroys the spatial organisation of the original signal and produces a function that is quantitatively and qualitatively indistinguishable from a fractal in the Hausdorff sense. The Kolmogorov capacity of the signal was significantly altered by this operation! In fact it is then given by Eq. (3.5) for Gaussian random functions. This property appears to be generally true for power-law spectra with random phase (Osborne and Provenzale, 1989), but may not hold for practical reasons related to the scrambling procedure when $s \neq 0$ in the initial signal. By considering both the scrambled and original versions of the signal we will try to find analytical ways capable of distinguishing between such localised and global self-similar structures that we have the same energy spectra or Kolmogorov capacities, but different phase spectra and Hausdorff dimensions.

3.1. BOX COUNTING ANALYSIS AND KOLMOGOROV CAPACITY

The Kolmogorov capacity (D_K) of a curve is calculated by finding the slope on a log-log graph of the plot of the number of boxes required to cover the curve as a function of the size of the box. The range of length-scales which need to be resolved to calculate D_K is in certain cases much smaller than that required to obtain a good estimate of the exponent of the energy spectrum (Vassilicos and Hunt, 1991).

Thus, the Kolmogorov capacity is a more practical measure of self-similarity than the energy spectrum. Although D_K alone cannot distinguish between the original and scrambled signals, the overall shapes of the curves do differ significantly. In the case of the scrambled signal the transition from a slope of -1.5 (the true dimension of the function) to 0 (caused by the finite number of points in the representation of the function) is very abrupt, while in the case of the original signal the transition is much more gradual (see Fig. 4). This difference is due to the fact that in the original signal the points representing the function are distributed evenly, but the increasingly smaller scales emerge only as one near the origin. The scrambled signal is self-similar at every location, so the box-counting algorithm suddenly saturates everywhere at a particular length-scale whereas in the original signal the saturation occurs at different length-scales at different positions, thus smoothing the transition of the box-counting curve. This result may give a practical way of distinguishing between locally and globally self-similar structures.

The on-off function generated by the zero-crossings, i.e. the function that jumps from 0 to 1 and from 1 to 0 at the zero-crossings, but remains constant elsewhere, has a Fourier power spectrum $\Gamma(k) \sim k^{-2\rho}$, $2\rho = 2 - D'_K$ (Vassilicos and Hunt, 1991), whether the zero-crossings are of a fractal or a spiral signal. Two such different signals with the same value of D'_K will have the same ρ, but different p.
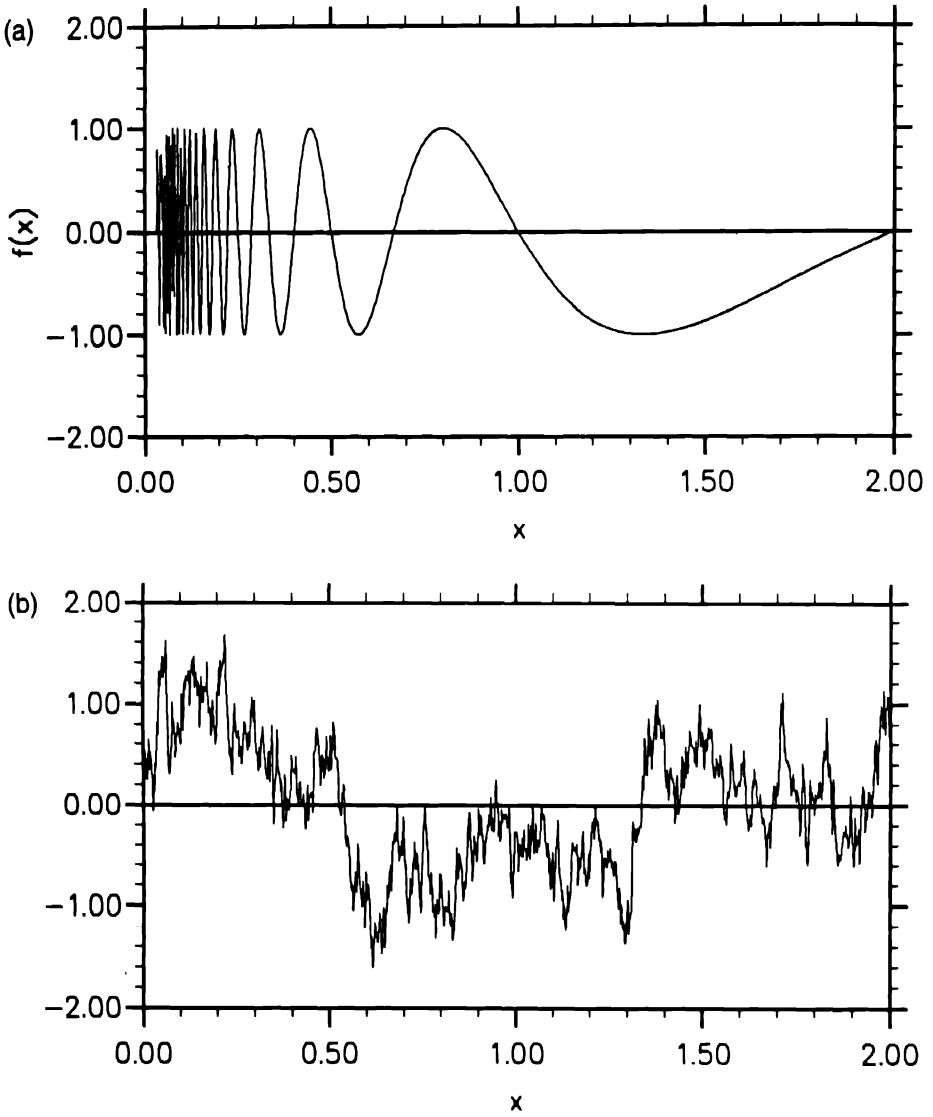
Fig. 3. (a) Original, and (b) scrambled versions of the accumulating function $f(x) = \sin(2\pi/x)$.

In the case of Gaussian sample functions, $p = 2\rho - 1/2$ (see (3.5)); in the case of spiral functions, such as (3.1), the relation between p and ρ is different. A good understanding of this relation may again lead to new practical ways of detecting whether $D'_H = 0$.
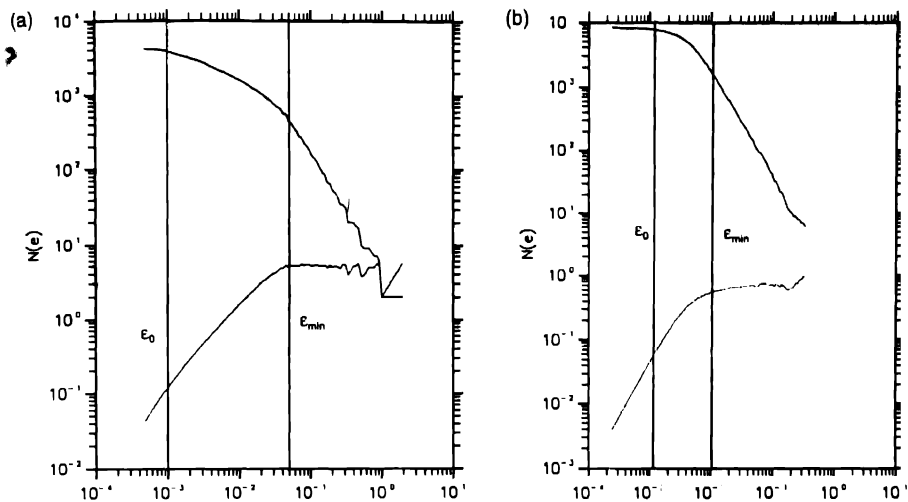
Fig. 4. Calculating the box-counting dimension. (a) Spiral function $\sin(2\pi/x)$, lower curve is $\times \varepsilon^{1.5}$. (b) Scrambled spiral, lower cure is $\times \varepsilon^{1.75}$. Note the much more gradual transition between ε_{min} (the lower limit of the power-law section of the curve) and ε_0 (the minimum, spacing between points in the signal) for the locally self-similar spiral.

3.2. WAVELET ANALYSIS

A more systematic tool for obtaining local information about spectral quantities is the recently developed wavelet transform (Grossman and Morlet, 1984; Farge, 1992)

$$\tilde{f}(\lambda, x_0) = \lambda^{-1/r} \int_{\infty}^{\infty} f(x)\psi^* \left(\frac{x - x_0}{\lambda} \right) \, dx. \tag{3.6}$$

The wavelet transform allows one to investigate the structure of the signal $f(x)$ at different scales λ and different positions x_0 simultaneously. Because we are interested in what are essentially local fractal dimensions and fractal dimensions are related to energy spectra the wavelet transform would seem to be a good way of determining whether a flow contains locally self-similar accumulating functions or global fractal structures. In this section we use the wavelet analysis to develop another way of distinguishing between our locally and globally self-similar test functions.

Using the Morlet wavelet,

$$\psi(x) = e^{ik_g x} e^{-(|x|^2/2)} , \tag{3.7}$$

the squared modulus of the wavelet transform of the $\sin(2\pi x^{-t})$ spiral is

$$|\tilde{f}(\lambda, x_0)|^2 \sim \lambda^{1/2} \lambda^{-((2s+1)(D'_K-1)+1)} \exp \left[\frac{(x_0 - (t\lambda)^{1-D'_K})^2}{2\lambda^2} \right] \tag{3.8}$$

where λ is the length-scale and x_0 is the location. The wavelet transform of the spiral is thus peaked around $x_0 = (t\lambda)^{1-D'_K}$. By contrast, the wavelet transform of the scrambled spiral shows no spatial organisation, although, of course, it reflects the overall distribution of the energy of the signal between different length-scales (see Fig. 5). This difference is brought out most clearly by looking at the local wavelet energy spectra at various locations. The local wavelet energy spectrum is obtained from the modulus of the wavelet transform by taking a slice through length-scale space at a particular location. The difference between the scrambled and spiral test functions is obvious in Fig. 5. The scrambled spiral has essentially the same local energy spectrum everywhere (on average $\propto k^{-((2s+1)(D'_K-1)+1)}$ where D'_K is the capacity of the original spiral), but the spiral test function has different ranges of $k^{-((2s+1)(D'_K-1)+1)}$ spectrum depending on the location. Looking at the way the local energy spectrum varies from position to position may provide another way of determining whether turbulence has a 'spiral' or fractal structure.

It has been claimed that branching in the wavelet transform indicates the signal is fractal (e.g. Arnéodo et al., 1989), however this is not necessarily the case. If a signal holds only one singularity of the type (3.1) and is totally regular elsewhere, then (3.8) shows that the wavelet transform will point towards $x_0 = 0$ since most of the power $|\tilde{f}(\lambda, x_0)|^2$ is concentrated around a curve $x_0 \sim \lambda^{1-D'_K}$ in the $x_0-\lambda$ plane of the wavelet transform. The exponents t and s or D'_K and s characterising this singularity can be extracted from the examination of that curve and of the scaling of the wavelet transform along that curve. Problems arise when the signal carries an unknown distribution of singularities of the type (3.1), thereby producing a plethora of intertwined inverse branchings which may not be easily distinguishable from the branching pattern obtained when a fractal or multifractal signal is wavelet transformed (or even when random noise is transformed). It is then not a trivial task to untangle the local scaling exponents from the wavelet transforms of a complex signal, let alone interpret them. A simple example of the way this sort of fractal-like branching may arise is shown in Fig. 6.

Note also that one must be careful in applying real wavelet transforms to determine scaling exponents (related to Hausdorff dimension). Vergassola et al. (1991) have shown that spurious scaling exponents can be obtained from the Mexican Hat wavelet transform of a fractional Brownian signal. The same conclusion is reached, for other reasons, on the basis of a different example: the spiral accumulation function $\sin 2\pi x^{-t}$. From (3.8) it can be seen that the closer x_0 is to 0, the centre of the accumulation, the smaller the range over which $|\tilde{f}|^2$ is dominated by the power law $\lambda^{1/r}\lambda^{((2s+1)(D'_K-1)+1)}$ rather than by the Gaussian filter. A calculation of the scaling over the wrong range will give misleading results. Furthermore, even in the correct range, the detection of a power law does not prove that the signal is fractal; it can evidently also be a spiral accumulation. These two examples show the difficulty of determining the precise self-similar nature of a signal.
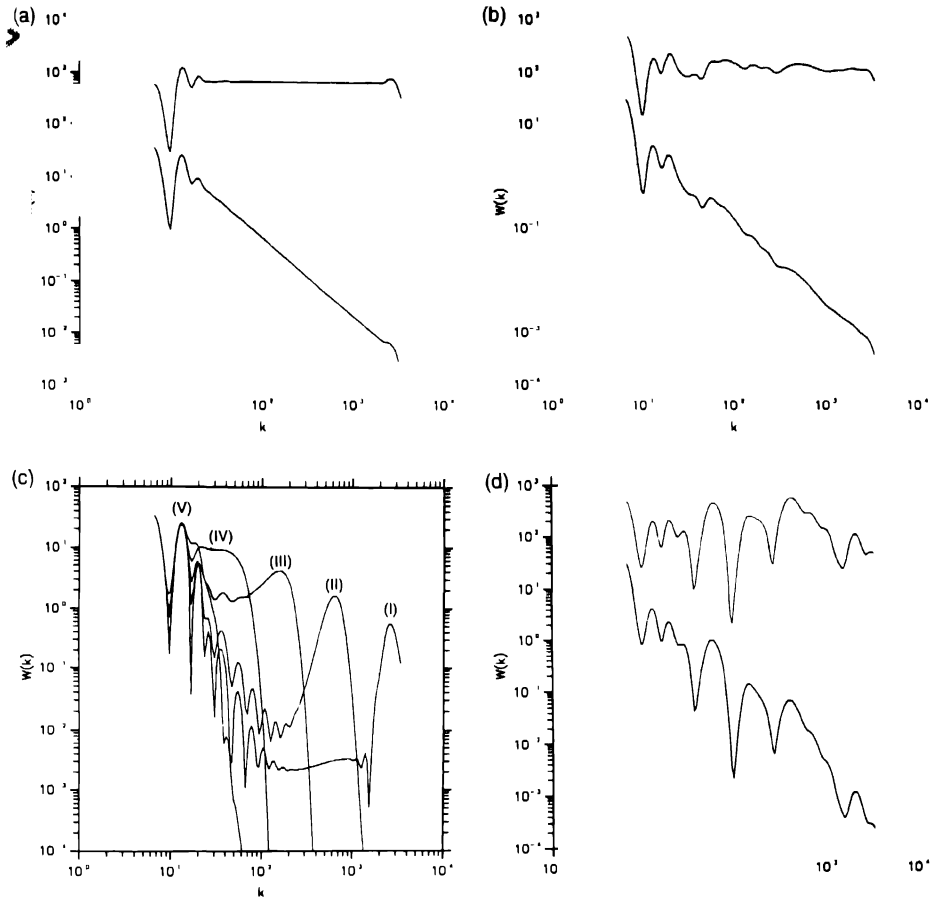
Fig. 5. Distinguishing between locally and globally self-similar signals using the wavelet transform. (a) Wavelet energy spectrum averaged over all locations for the spiral (upper curve is $\times k^{1.5}$). (b) Wavelet energy spectrum averaged over all locations for the scrambled spiral (upper curve is $\times k^{1.5}$). (c) Local wavelet spectra $\times k^{1.5}$ of the spiral at locations (I) 0.05, (II) 0.1, (III) 0.2, (IV) 0.4, (V) 0.8. The flat regions indicate the locations of $k^{-1.5}$ spectrum. (d) Typical local wavelet spectrum of the scrambled spiral at location $x = 0.4$ (upper curve is $\times k^{1.5}$).

4. Conclusions

By applying the POD, conditional sampling with conditional statistics (Linear Stochastic Estimation), and conditional sampling with conditional statistics (Coherent Structures) to a test signal we have clarified the strengths and weaknesses of each approach. First, the physical interpretation of POD is unclear: the first eigenmode will *not* be a typical flow structure unless it contains most of the energy. Secondly, conditional sampling can give a qualitatively accurate physical representation of
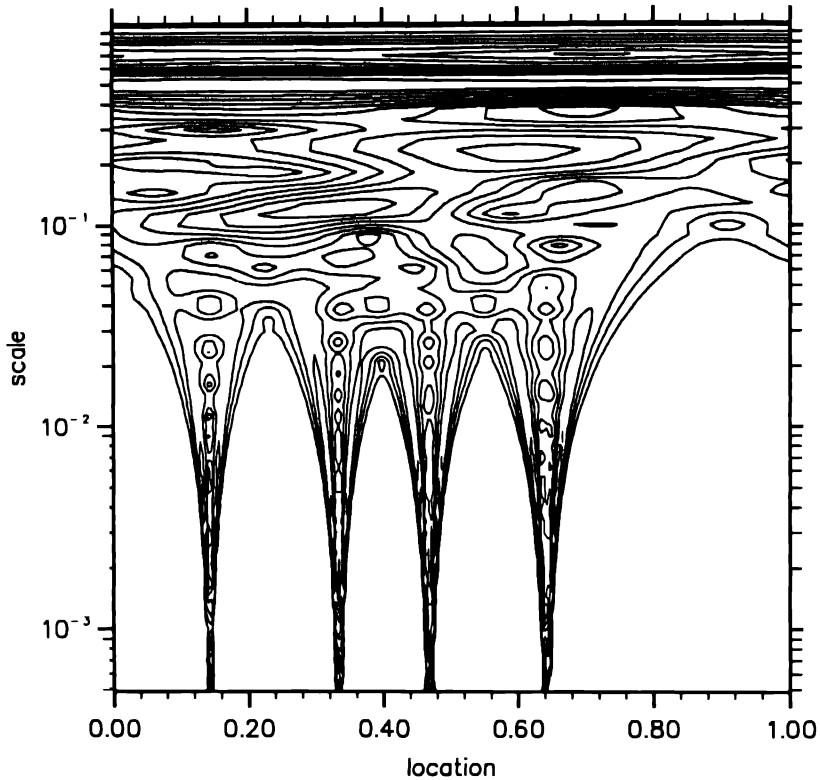
Fig. 6.   Branching pattern in the modulus of the Morlet wavelets transform produced by a random superposition of four $\sin(2\pi/x)$ spirals.

the flow structures, but the resulting eddy may be sensitive to the precise conditions chosen. A combination of ensemble statistics with conditions determining the location (in space and time) of the reference point gives physically realistic results with a minimum of manipulation. Thirdly, the Coherent Structures method requires significant manipulation to obtain representative structures, although the interactive nature of this approach also makes it the most flexible and least liable to misinterpretation. The Coherent Structures approach also gives a way of separating out the incoherent noise of the signal.

Approaches based on invariants of the deformation tensor and pressure can give information about the relative number and location of regions with particular dynamics, but say nothing about their shape or internal structure. No clear way of interpreting invariant plots exists yet!

None of the above methods are incapable of analysing or identifying the local fine-scale structure of the flow.

The new techniques of fractal analysis and the wavelet transform have been applied to the problem of distinguishing between globally ('fractals') and locally

TABLE I. The differences between signals with random and non-random phase spectra

$\phi(k)$ random	$\phi(k)$ non-random
$D_H = D_K = \frac{1}{2}(5 - \alpha)$	D_H, D_K, α – no fixed relation
– no energy cascade	– allows for cascade
– no structures	– allows for structures

('spirals') self-similar signals. The Kolmogorov capacity gives one parameter for describing the average degree of convolutedness within a coherent structure where the fields are self-similar over a range of length scales that may be quite small compared to those necessary for conventional Fourier methods. Alone among the methods examined, the wavelet transform is able to provide a simple functional description in terms of *local* length scales and position of the typically complex distribution of velocity and vorticity within turbulence structures. Three methods of distinguishing between fractals and spirals have been suggested: the first is based on the box counting algorithm (the variation of the range over which a Kolmogorov capacity is clearly defined), the second exploits the difference between the Fourier power spectrum of the original function and the on-off function obtained from the zero-crossings, and the third uses the variation of the local wavelet energy spectrum with position.

The long term goal of the development of new techniques to analyse complex structure is to clarify the relationship between the Fourier energy spectrum (exponent α), the Fourier phase spectrum ($\phi(k)$), the Hausdorff dimension (D_H), and the Kolmogorov capacity (D_K). This knowledge will have far-reaching implications for a deeper understanding of the dynamics of turbulence. A major part of this investigation is a study of the differences between signals with a non-random $\phi(k)$ ('spirals') and those with a random $\phi(k)$ ('fractals'). The phase spectrum of turbulence largely determines its dynamics and structure. For example, if the phases of a DNS are randomised the characteristic small-scale vortex tubes vanish. The nature of the energy cascade also depends crucially on the phase spectrum; in a velocity field with random phases there can be no net cascade of energy. The phase spectrum also changes the relationship between D_K and D_H. In a $\sin 1/x$ spiral $D_K = 1.5$ and $D_H = 1$, while if the phases of the spiral are scrambled $D_K = D_H = 1.75$. The fixed relation between D_H and α given by Orey's formula (3.5) holds for a Gaussian (random phase) signal. It is interesting to note that the Kolmogorov cascade in turbulence implies a non-random $\phi(k)$ which in turn means that D_H in turbulence is probably not given by (3.5), i.e. if $\alpha = 5/3$ then $D_H \neq 2.67$ in three-dimensional turbulence (contrast with results of Procaccia et al., 1991). Some differences between signals with random and non-random phases are summarised in Table I.

This investigation has helped to quantify the differences between the many methods of analysing a turbulent flow into turbulence structures, and has suggested optimum structure types for elucidating the dynamics of turbulence. The results obtained will give greater power and precision to the structural approach to understanding turbulence.

Acknowledgement

References

Adrian, R.J. and Moin, P., Stochastic estimation of organised turbulent structure: homogeneous shear flow. *J. Fluid Mech.* 190 (1986) 531–559.

Arfken, G., *Mathematical Methods for Physicists.* Orlando: Academic Press (1985).

Arnéodo, A., Argoul, F., Bacry, E., Elezgaray, J., Freysz, E., Grasseau, G., Muzy, J.F. and Pouligny, B., Wavelet transform of fractals. In *Wavelets and Some of Their Applications, Proceedings of the Conference held in Marseille-Luminy, June 1989* (1989).

Aubry, N., Holmes, P., Lumley, J.L. and Stone, E., The dynamics of coherent structures in the wall region of a turbulent boundary layer. *J. Fluid Mech.* 192 (1988) 115–173.

Brasseur, J.G. and Wang, O., Structural evolution of intermittency and anisotropy at different scales analysed using three-dimensional wavelet transforms. *Phys. Fluids A* 4(11) (1992) 2538–2554.

Chen, J.H., Chong, M.S., Soria, J., Sondergaard, R., Perry, A.E., Rogers, M., Moser, R. and Cantwell, B.J., A study of the topology of dissipating motions in direct numerical simulations of time-developing compressible and incompressible mixing layers. In: *Studying Turbulence using Numerical Simulation Databases – III. Proceedings of the 1990 Summer Program.* Stanford: CTR (1990).

Falconer, K., Fractal Geometry – Mathematical Foundations and Applications. John Wiley & Sons (1990).

Farge, M., The wavelet transform. *Ann. Rev. Fluid. Mech.* 23 (1992).

Frisch, U., Sulem, P.-L. and Nelkin, M., A simple dynamical model of intermittent fully developed turbulence. *J. Fluid Mech.* 87(4) (1978) 719–736.

Grossman, A. and Morlet, J., Decomposition of Hardy functions into square integrable wavelets of constant shape. *SIAM J. Math. Anal.* 15 (1984) 723–736.

Guezennec, Y.G., Stochastic estimation of coherent structures in turbulent boundary layers. *Phys. Fluids A* 1(6) (1989) 1054–1060.

Hunt, J.C.R., Kevlahan, N.K.-R., Vassilicos, J.C. and Farge, M., Wavelets, fractals and Fourier transforms: Detection and analysis of structure. In: *Wavelets, Fractals and Fourier Transforms: New Developments and New Applications, Proceedings of the IMA Conference at Newham College, Cambridge, December 16–18, 1990* (1993) (to appear).

Hunt, J.C.R. and Vassilicos, J.C., Kolmogorov's contributions to the physical and geometrical understanding of small-scale turbulence and recent developments. *Proc. R. Soc. Lond. A* 434 (1991) 183–210.

Hussain, A.K.M.F., Coherent structures and turbulence. *J. Fluid Mech.* 173 (1986) 303–356.

Lumley, J.L., The structure of inhomogeneous turbulent flows. In: A.K. Yaglom and U.I. Tatarsky (eds), *Proceedings of the International Colloquium on the Fine Structure of the Atmosphere and Its Influence on Radio Wave Propagation, Moscow, June 15–22, 1965.* Moscow: Nauka (1967) pp. 166–176.

Lundgren, T.S., Strained spiral vortex model for turbulent fine structure. *Phys. Fluids* 25(2) (1982) 2193–2203.

Moffatt, H.K., 1984, Simple topological aspects of turbulent vorticity dynamics. In: T. Tatsumi (ed.), *Turbulence and Chaotic Phenomena in Fluids.* Elsevier (1984) p. 223.

Mumford, J.C., The structure of the large eddies in fully developed turbulent shear flows. Part 1. The plane jet. *J. Fluid Mech.* 118 (1982) 241–268.

Orey, S., Gaussian sample functions and the Hausdorff dimension of a level crossing. *Z. Wahrschein-lichkeitstheory verw. Geb.* 15 (1970) 249.

Osborne, A.R. and Provenzale, A., Finite correlation dimension for stochastic systems with power-law spectra. *Physica D* (1989) 357–381.

Procaccia, I., Brandenburg, A., Jensen, M. and Vincent, A., The fractal dimension of isovorticity structures in 3-dimensional turbulence. NORDITA preprint, *Europhys. Lett.* (1991) (submitted).

Vassilicos, J.C. and Hunt, J.C.R., Fractal dimensions and the spectra of interfaces with applications to turbulence. *Proc. R. Soc. Lond. A* 435 (1991) 505–534.

Vergassola, M., Benzi, R., Biferale, L. and Pisarenko, D., Wavelet analysis of a Gaussian Kolmogorov signal. *Proceedings of the USA–French Workshop on 'Wavelets and Turbulence'* (1991).

Vincent, A. and Meneguzzi, M., The spatial structure and statistical properties of homogeneous turbulence. *J. Fluid Mech.* 225 (1991) 1–20.

Zel'dovich, Ya.B. and Sokolo, D.D., Fractals, similarity, intermediate asymptotics. *Sov. Phys. Usp* 28(7) (1985) 608–616.

Topology of Flow Patterns in Vortex Motions and Turbulence

A.E. PERRY and M.S. CHONG
Mechanical and Manufacturing Engineering Department, University of Melbourne, Parkville, Victoria 3052, Australia

Abstract. Some applications of critical point theory are shown for the description and identification of eddying motions in turbulence and in vortex shedding. This includes both large scale and fine scale motions. Difficulties in the interpretations of flow topology are outlined with some examples.

1. Introduction

In turbulence research the term *eddying motions* has long been used without any precise definition in mind and means of identifying and classifying these motions have been arbitrary and ad hoc. It is only in recent times that rigorous mathematical techniques and concepts adopted from topology have been applied to flow fields and eddying motions. In the past we have been forced to examine fields described only with smoke or dye or be content with single point measurements from a small number of probes. However with the aid of massive computers, computer-aided data acquisition systems applied to experiments with scanning probes and rakes and new optical techniques and with full direct numerical simulations (DNS) of the Navier–Stokes equations, entire flow fields for a series of time frames can be generated. In the case of simulations one has the choice of many quantities for describing the field and its eddying motions such as velocity, vorticity, pressure, pressure gradient and the various components of the velocity-gradient tensor. With such an explosion of information one asks, *What do we do with all these numbers? What quantities do we plot? What will give us the best insight into the physical processes occurring?* The answer to some of these questions will be addressed here in the form of case studies.

2. Flow Visualisation and Velocity Vector Fields

The most basic and primitive indicators of flow patterns are smoke and dye. If judicially introduced at places where vorticity is generated (e.g. at solid boundaries in the case of incompressible uniform density fluids) then such dye will follow the vorticity since vorticity like dye or heat is *locked* in the fluid. This of course is true only if we can neglect viscous diffusion and this will be true in the initial roll-up of vortices and in the early stages of development of a jet, wake or boundary layer. Dye then is useful in indicating the position and geometry of vortex sheets

but there are innumerable counter examples where dye is introduced incorrectly, giving erroneous interpretation of the flow field.

Perry and Lim (1978), Perry et al. (1980) and Perry and Tan (1984) were able to relate smoke patterns with phase-sampled velocity vector fields for periodically perturbed coflowing wakes and jets. Provided an appropriate convection velocity was chosen large streamwise lengths of the instantaneous streamline patterns can be related to the smoke patterns. The topology of the velocity fields and instantaneous streamline patterns can be described qualitatively in terms of critical points, i.e. points in the flow field where the velocity is zero and the streamline slope is indeterminate. These critical points have been identified and classified below.

3. Critical Point Classification Using Phase-Plane Techniques

The velocity field u_i about a critical point can be expanded in terms of the space coordinate x_j using a Taylor series. Asymptotically close to the critical point, we can neglect the higher order terms giving

$$\dot{x}_i = u_i = A_{ij}x_j. \tag{1}$$

By integrating this equation with respect to time we obtain solution trajectories in x_i space. This corresponds to instantaneous streamlines for the given A_{ij}. If the eigenvalues of the velocity gradient tensor A_{ij} are all real, then it can be shown that there will exist three planes (which are not necessarily orthogonal) which will contain solution trajectories. These are the osculating planes or eigenvector planes and these will contain saddles or nodes. If the eigenvalues of A_{ij} are complex then there will be only one plane which contains solution trajectories and in that plane we have a focus. In each of these planes we can use simple phase plane analysis, i.e.

$$\dot{\mathbf{x}} = \mathbf{u} = \mathbf{F}\mathbf{x} \tag{2}$$

where $\mathbf{F}$ is a 2×2 matrix. The phase-plane portrait of the critical points can be classified by the two invariants, p and q, of $\mathbf{F}$. The classification of all possible points can be mapped out on the so-called p–q chart (see Perry and Chong, 1987). The eigenvectors may be orthogonal or nonorthogonal. Nonorthogonality can occur if there is vorticity present.

The basic patterns of nodes, foci and saddles can be related to phenomena such as vortex stretching or contraction and the stretching of vortex sheets. This has led to the construction of simplified *vortex skeletons* which describe the patterns in a simple and compact way. Just as Prandtl could describe the essential features of flow about a finite span wing with a vortex skeleton consisting of a bound vortex and two trailing vortices, so also can simple coflowing jets and wakes be described in terms of vortex skeletons (see Perry and Tan, 1984). Perry and Hornung (1984) applied the vortex skeleton technique to three-dimensional separation patterns.
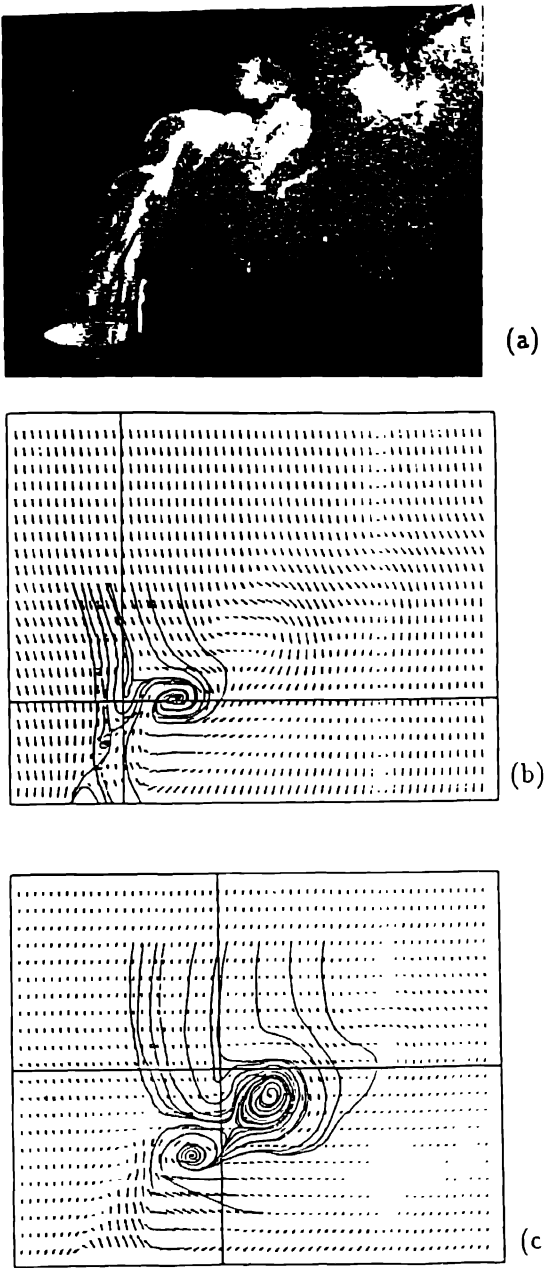
Fig. 1.   (a) Externally illuminated jet in cross-flow. (b) and (c) Instantaneous phase-averaged velocity field and streamline pattern at the same phase as seen by an observer moving at two different velocities. Flying hot-wire measurements. After Kelso (1990).
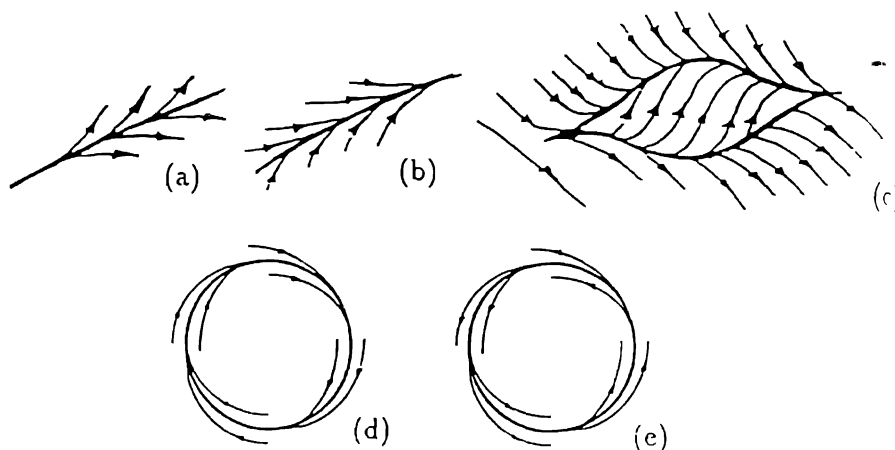
Fig. 2. (a) Positive bifurcation lines. (b) Negative bifurcation lines. (c) A combination of bifurcation lines produced by a vortex close to a surface. (d) Stable limit cycle. (e) Unstable limit cycle.

The important transport properties of the velocity field can be constructed using the Biot–Savart law.

Features of turbulent spots and the statistical features of fully developed wall turbulence can also be described in terms of representative vortex skeletons (e.g. see Perry and Chong, 1982) which serve the same purpose as the representative eddies of Townsend (1976). This has led to the idea that perhaps vorticity might be a much better quantity to study than velocity fields. For a start, the vorticity field is Galilean invariant whereas the velocity field and its associated distribution of critical points depends on the velocity of the observer. It is only when Galilean frame of reference can be found which gives an almost steady velocity field that we have a velocity pattern with some useful physical meaning. Transport processes and other properties can then be correctly interpreted. For example, large streamwise lengths of a Kármán vortex street at moderate Reynolds numbers can yield velocity fields which are steady with a correctly chosen Galilean frame of reference as was shown by Perry et al. (1982). Dye introduced at the source of the vorticity generation tends to align with the eigenvectors of the saddle points and accumulate at the centre points which are the centroids of vorticity. On the other hand, there are patterns, e.g. jets in cross-flow examined by Kelso (1991) where there is no single Galilean frame which can be chosen to see all the eddies at once. Here the eddies are accelerating and for a given frame of reference only local parts of the pattern become steady and eddies appear as foci and then only for a short time (see Fig. 1).

Another salient feature of flow patterns besides critical points are bifurcation lines (Perry and Hornung, 1984) or asymptotic trajectories. In the case of velocity fields these are streamlines to which other streamlines asymptote exponentially. These occur in a variety of free shear flows and in wall turbulence. Figure 2 shows
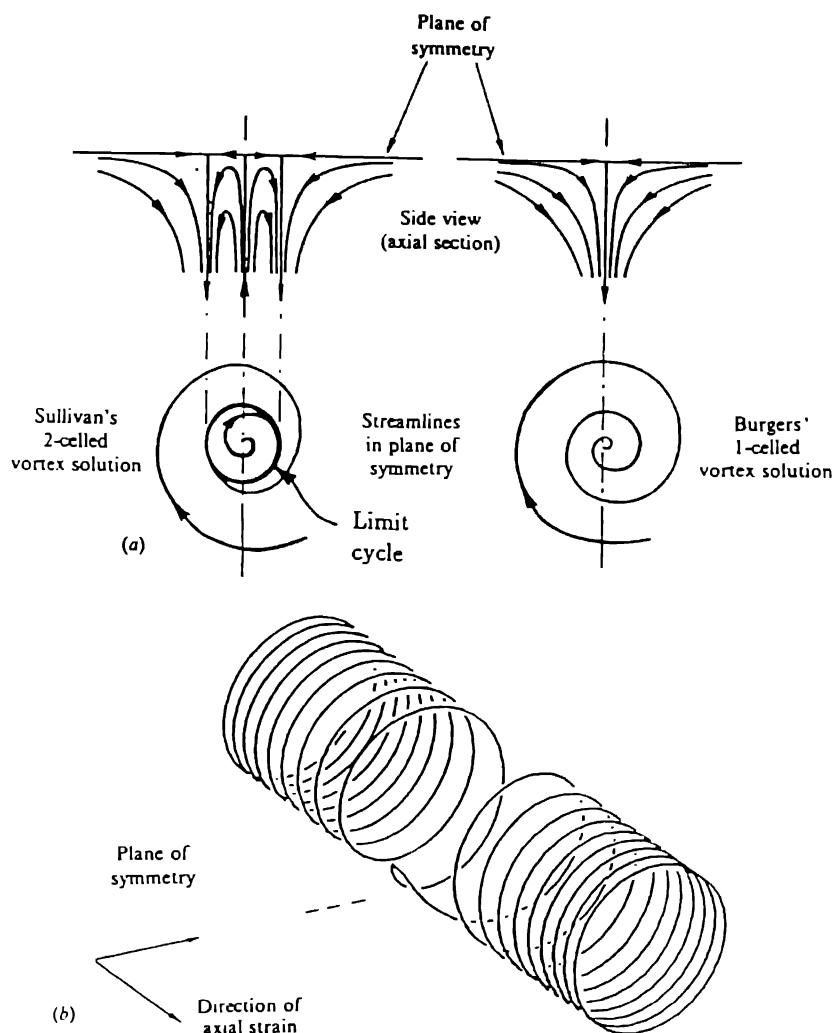
Fig. 3.   (a) Vortex flows for Sullivan's two-celled vortex solution and Burgers' one-celled solution. (b) Typical vortex line for the Sullivan vortex. After Perry and Steiner (1987).

some examples. If the bifurcation line is closed, then we have a limit cycle as shown in Figs 2d and e.

In many of these flow fields taken along planes of symmetry, limit cycles occur in the vortices shed from nominally two-dimensional bluff bodies (e.g. see Steiner and Perry, 1987). A possible explanation is that this may be due to spanwise waviness in the roll-up of the vortex sheets. An example of this is the Sullivan vortex as illustrated in Fig. 3 (see Sullivan, 1959). Perry and Steiner (1987) calculated the integrated vorticity field and one typical vortex line is shown plotted. One can see

that on one side of the plane of symmetry the vortex line is a right-handed helix and on the other side it is a left-handed helix. Such vortex line windings have been observed by Professor Fazle Hussain (private communication). This vortex field feature is consistent with slight spanwise waviness in the vorticity field. It is conjectured that this waviness then becomes magnified as the vortex is formed.

Vorticity vector fields and associated plots of vortex lines have their own set of critical points which have the same basic classification as the velocity field. However, computed vorticity fields tend to be extremely complex which is somewhat disappointing. However, since the induced velocity field a short distance away from a vortex filament is insensitive to detailed complexities, perhaps some form of spatial filtering might be permitted to aid in forming a simpler but essentially correct interpretation. This at least would be valid for the large scale motions. Such fields might give more insights if used in conjunction with the grad p field (i.e. ∇p), where p is pressure, as was done by Chen et al. (1989). One very appealing property of grad p field is that it has the features of an irrotational velocity vector field, i.e. it has zero curl and therefore all associated critical points have real eigenvalues and all eigenvectors are orthogonal. Thus the integrated field, i.e. the lines-of-force field tends to be simple and may reveal features about eddying motions in a more apparent way. Also, such a field is Galilean invariant and being a force field makes it an excellent quantity for forming physical interpretations.

4. Examples of Misinterpretations

In order to know fully the topology of a flow pattern about a critical point it is of great importance to have full three-dimensional information. In some work it has been tempting to simply look at *sectional-streamline* patterns in a plane through a critical point and make physical interpretations on this basis. This is fraught with danger. A sectional-streamline is defined as the integrated vector field of the vectors at the sectioning plane resolved onto the sectioning plane. Figure 4a shows an example of a stretched vortex described by a critical point with complex eigenvalues. There is really only one plane which contains solution trajectories (i.e. the x_1–x_2 plane, $\theta = 0$). This is a plane of symmetry and the stable focus in that plane indicates correctly that we have vortex stretching. As θ is increased, the sectioning plane invariants move down the p–q chart as is shown in Fig. 4b and there are cases where we have an unstable focus, i.e. a focus where trajectories spiral out, which could be incorrectly interpreted as a vortex undergoing contraction. Such problems might occur in particle-image velocimetry. Thus, it is only on planes of symmetry and other eigenvector planes that sectioning streamline patterns can be safely interpreted.

Another example of misinterpretation occurs with the Burgers vortex. This is simply a vortex with a Gaussian distribution of vorticity undergoing axisymmetric stretching in the direction of the vortex axis (Burgers, 1948). A sectioning plane at the plane of symmetry would show a stable focus. If however the sectioning

$$u = \begin{bmatrix} -a & \omega & 0 \\ -\omega & -a & 0 \\ 0 & 0 & 2a \end{bmatrix} x$$

$$\theta = 0$$

$S_1 - S_2$ plane

$$q = \frac{p^2}{4}$$

$$\theta = \frac{\pi}{2}$$
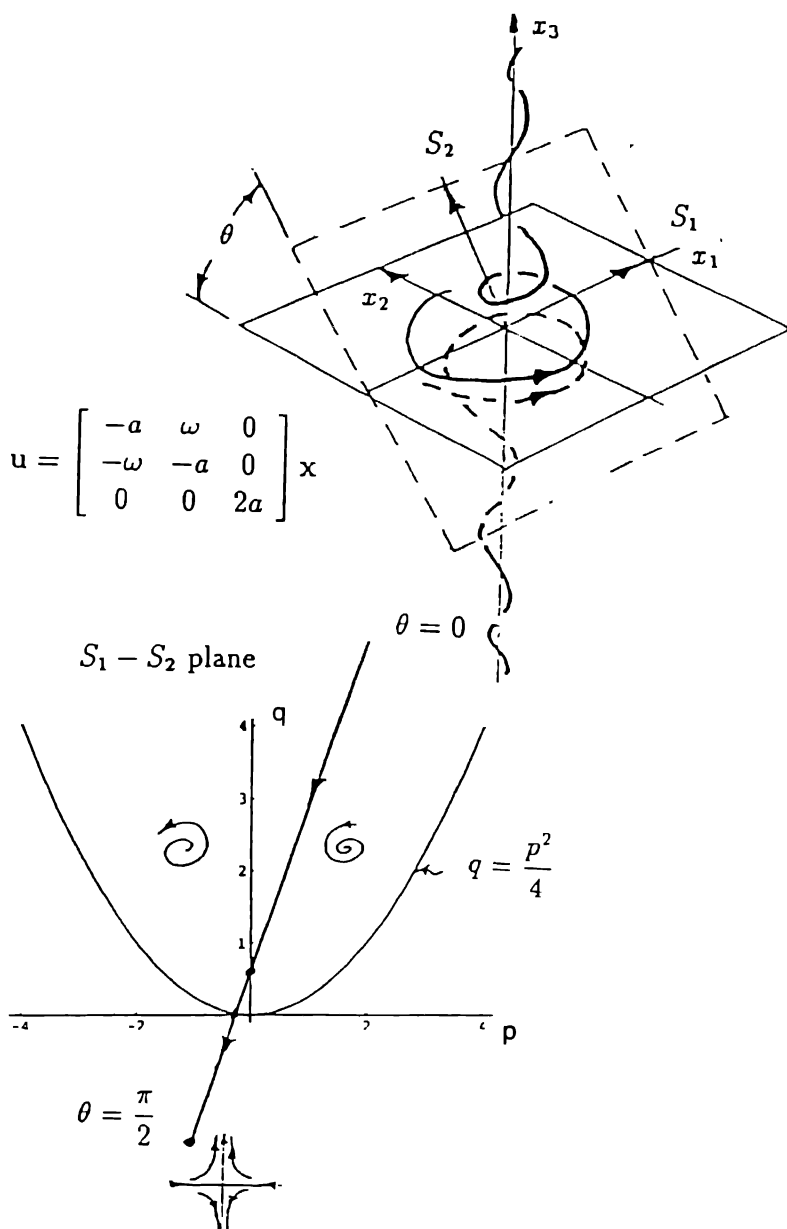
Fig. 4.   (a) Definition of sectioning planes. (b) Variation of sectioning plane invariants as θ increases.

streamline pattern on a plane titled at 60° to the vortex axis is plotted, an unstable focus occurs at the origin surrounded by a limit cycle as shown in Fig. 5 and could be misinterpreted as a Sullivan vortex discussed earlier. This again illustrates that
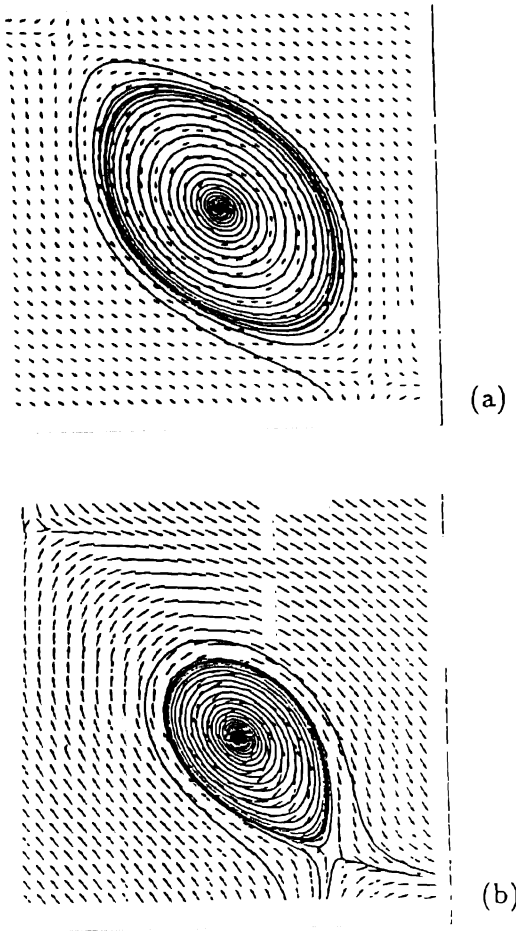
Fig. 5. (a) Sectional velocity field and integrated streamline pattern around a Burgers vortex cut by a sectioning plane through the origin $x_1 = 0$, where x_1 is in the direction of the vorticity. The planes intersect at $60°$. (b) The sectioning plane now intersects the vortex away from the origin, i.e. $x_1 \neq 0$. After Steiner and Perry (1987).

if one is off a plane of symmetry, interpretations from sectional streamlines are most dangerous.

5. No-slip Critical Points and Application of Isoclines

A critical point is a point where the velocity is zero. More importantly it is a point where the streamline slope is indeterminate. This is particularly relevant to no-slip boundaries since all points at a no-slip boundary have zero velocity. At the no-slip boundary we have to use the concept of limiting streamlines or trajectories. These
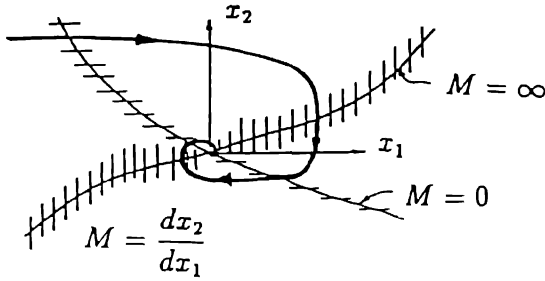
Fig 6. Critical point located by two intersecting isoclines.

are trajectories with directions obtained by approaching the boundary from above and extrapolating to the boundary. Such trajectories correspond to skin friction lines and they are orthogonal to vortex lines at the boundary (see Lighthill, 1963). By Taylor series expanding about a critical point on the boundary, the lowest order term is quadratic in order that the no-slip condition on the boundary is satisfied, i.e.

$$\overset{o}{x}_i = \frac{x_i}{x_3} = \frac{u_i}{x_3} = B_{i,j}x_j \tag{3}$$

where x_3 is the coordinate normal to the boundary (and the orthogonal coordinates x_1 and x_2 define the no-slip boundary). Hence $u_i \to 0$ as $x_3 \to 0$ but u_i/x_3 remains finite for finite x_1 and x_2 as $x_3 \to 0$. $B_{i,j}$ is the appropriate tensor to use in place of $A_{i,j}$ given earlier for *free-slip* critical points and the same rules apply regarding the properties and classification of critical points. The quantity $\overset{o}{x}_i$ could be thought of as a derivative with respect to a transformed time given by $d\tau = x_3\,dt$, where t is real time. On a no-slip boundary, a critical point in velocity is also a critical point in vorticity but this is not true elsewhere.

A useful concept from phase-plane analysis of nonlinear dynamical systems is the *isocline*. This is a curve along which the trajectory slope is constant. Figure 6 shows two isoclines (with trajectory slope $M = \infty$ and trajectory slope $M = 0$) intersecting. The intersecting point must be a critical point since the streamline slope at this point is indeterminate. In the Taylor series expansion solution of the Navier–Stokes equations given in Perry and Chong (1986), in the early stages of development some three-dimensional separation patterns were synthesized by constructing higher order polynomials which gave sets of isoclines as shown in Fig. 7a. By shifting the two ellipses of fixed size and shape relative to each other, the three standard separation patterns (the simple U-separation, the owl-face of the first kind and the owl-face of the second kind) can be generated as shown respectively in Figs 7b, c and d. The flow patterns which occur above the surface have also been computed and are discussed in Perry and Chong (1986).

The authors have often wondered what the limiting instantaneous streamlines would look like in a turbulent boundary layer. Figure 8a shows such a pattern computed using the DNS data of Spalart (1988) for a zero pressure gradient boundary
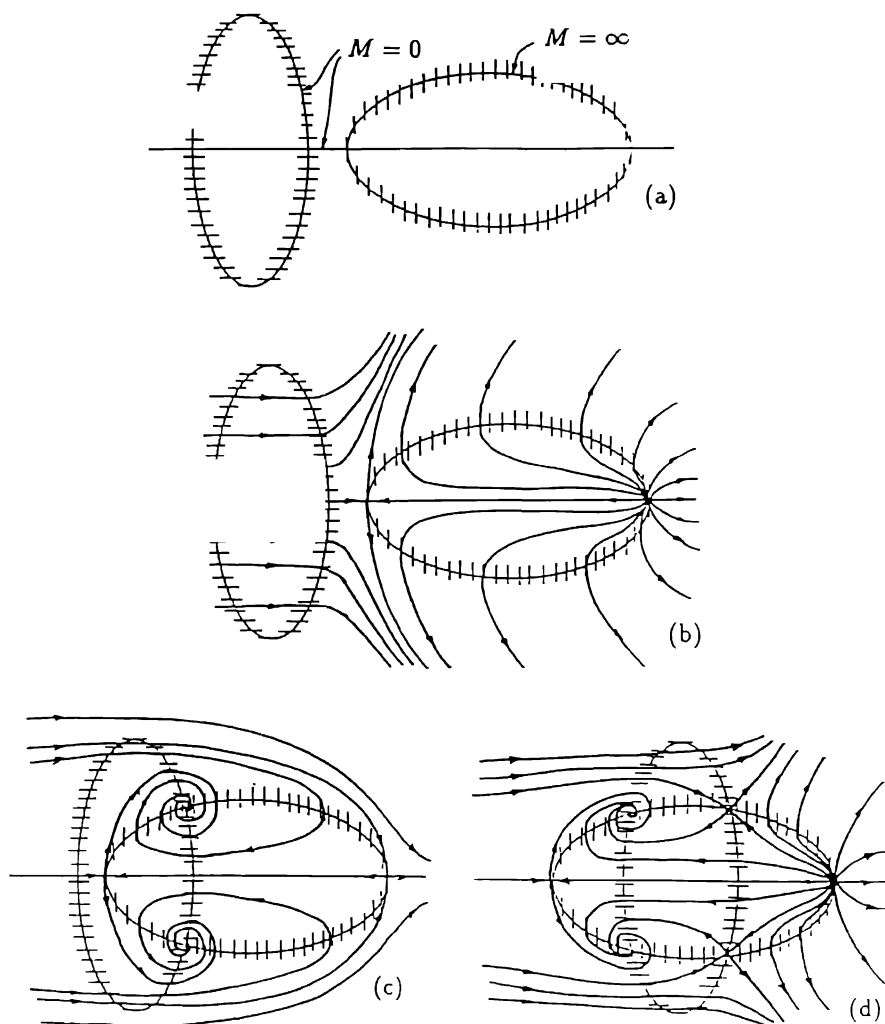
Fig. 7.   (a) Isoclines (ellipses and a straight horizontal line) used to generate simple U-separation, owl-face of the first kind and owl-face of the second kind shown respectively in (b), (c) and (d).

layer. One can see a spectacular display of bifurcation lines. The question is: *do critical points occur?* At such critical points there would exist a streamline at a finite angle to the wall (all limiting streamlines are parallel to the wall except at critical points). Perry and Spalart (unpublished) attempted to locate these critical points. It is very time consuming to seek such critical points, particularly at low Reynolds numbers, but using the isocline method these were located rapidly. At low Reynolds numbers, such points were rare but as the Reynolds number increased from $R_\theta = 670$ to $R_\theta = 1400$, the number of points increased. This is complete-ly consistent with the attached eddy hypothesis of Townsend (1976) as further

External Flow Direction ⟶ (a)

External Flow Direction ⟹ (b)
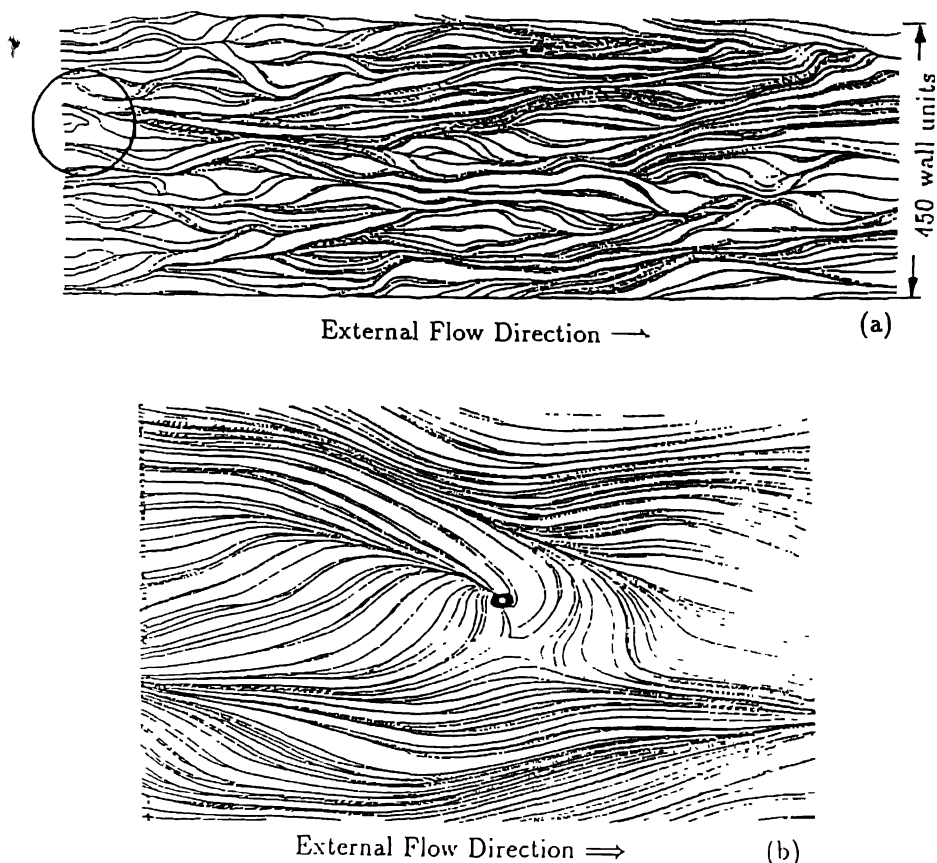
Fig. 8. (a) Instantaneous streamlines in a zero pressure gradient turbulent boundary, $R_\theta = 670$, from Perry and Spalart (unpublished). (b) Blow-up of circled region shown in (a).

developed by Perry et al. (1986). With increasing Reynolds number, the turbulence intensity (based on local mean velocity) at a fixed $x_3 u_\tau/\nu$ in the logarithmic region increases and so flow reversal and critical points at the wall are inevitable. Here u_τ is the friction velocity and ν is the kinematic viscosity. Figure 8b shows critical points which are made clearer by a blow-up of the localized region shown in Fig. 8a.

These surface pattern features are undoubtedly vortical structures which extend away from the boundary as shown in Fig. 9 where some sectional instantaneous streamlines have been plotted. In some recent work by Spalart and Coleman (unpublished), the surface trajectories for an adverse pressure gradient boundary layer were computed and are shown in Fig. 10. Here the critical points are most obvious. There is even the suggestion of owl-faces. The important point which the authors wish
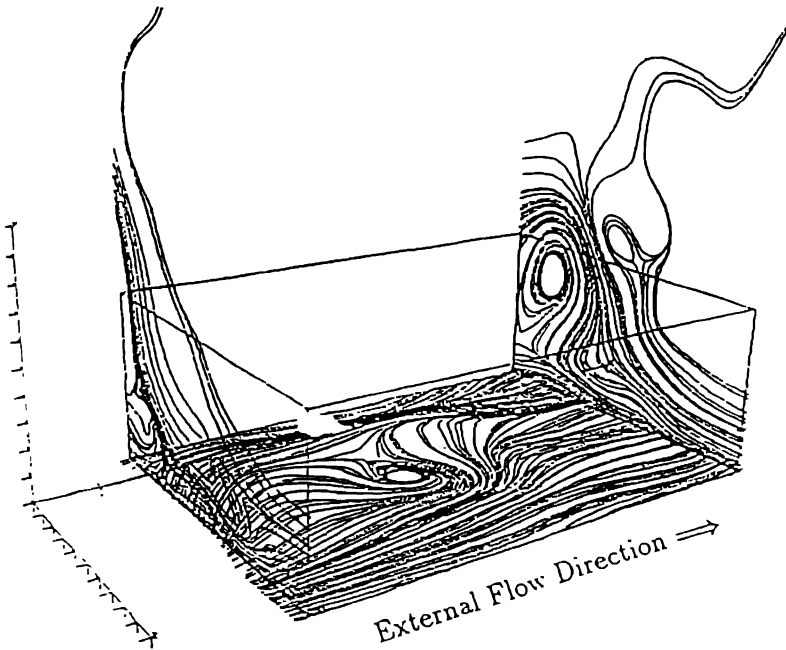
Fig. 9.   Surface streamlines and vertical plane sectional streamlines, from Spalart and Perry (1987) (unpublished).

External Flow Direction ⟹
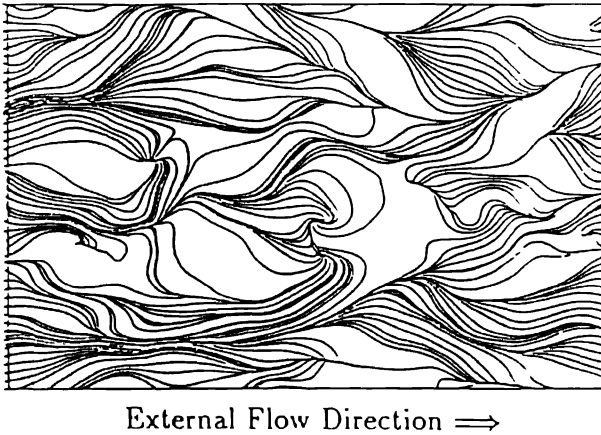
Fig. 10.   Surface streamlines for adverse pressure gradient boundary layers, from Spalart and Coleman (private communication). From simulations given in Spalart and Watmuff (1992).

to make is that a turbulent boundary layer should be looked upon as a forest of three-dimensional unsteady separations.

6. Classification Based on Three Invariants and Application to Turbulent Motions

Critical points have been classified by Perry and Fairlie (1974) using the concept of eigenvector planes and simple phase-plane analysis. However, an alternative approach has been given in a paper by Chong et al. (1990). Here, three invariants of the velocity gradient tensor are used for the general classification of critical points and the various restrictions for compressible and incompressible flows away from and at no-slip boundaries are derived. This analysis shows how important it is to have full three-dimensional information about a flow field before correct topological classification can be made and this reinforces what was stated earlier in Section 3.

The three-invariant topological classification can be applied to every point in the flow field. If an observer moves in a nonrotating frame with any particle in the field, then the flow surrounding the particle can be described in terms of the nine components of the velocity gradient tensor A_{ij}. The velocity gradient tensor may be broken up into a symmetric and an antisymmetric part, i.e. $A_{ij} = \partial u_i / \partial x_j = S_{ij} + W_{ij}$ where $S_{ij} = (\partial u_i / \partial x_j + \partial u_j / \partial x_i)/2$ and $W_{ij} = (\partial u_i / \partial x_j - \partial u_j / \partial x_i)/2$ are the rate-of-strain and rate-of-rotation tensors respectively. The eigenvalues of A_{ij} satisfy the characteristic equation

$$\lambda^3 + P\lambda^2 + Q\lambda + R = 0. \tag{4}$$

The three invariants P, Q and R form a space which is divided into various topological classification and these are Galilean invariant (see Chong et al., 1990). In the P–Q–R space the surface which divides regions with three real solutions for the above characteristic equation and that with one real and two complex solutions is given by

$$27R^2 + (4P^3 - 18PQ)R + (4Q^3 - P^2Q^2) = 0. \tag{5}$$

The above classification serves as an excellent means of defining a vortex core. A region of vorticity need not necessarily be part of a vortex. *When does such a region qualify as being part of a vortex?* It is asserted here that a particle belongs to a vortex core if its velocity gradient tensor A_{ij} has invariants such that it is above the surface shown in the P–Q–R space. This is effectively the same definition used by Cantwell (1978) and later by Vollmers (1983) and Dallmann (1983). Any such point will have a flow pattern with a plane containing trajectories in the form of a focus. Perhaps subconsciously this is what we have all meant by the term *eddying motions*. For some reason inexplicable to the authors, some workers oppose this definition.

For incompressible flow, $P = 0$ and so we are confined completely to the Q–R plane and Fig. 11 from Soria et al. (1992) shows the topological classification on this plane. Below the *tent-like* curves, the eigenvalues are real and the eigenvectors
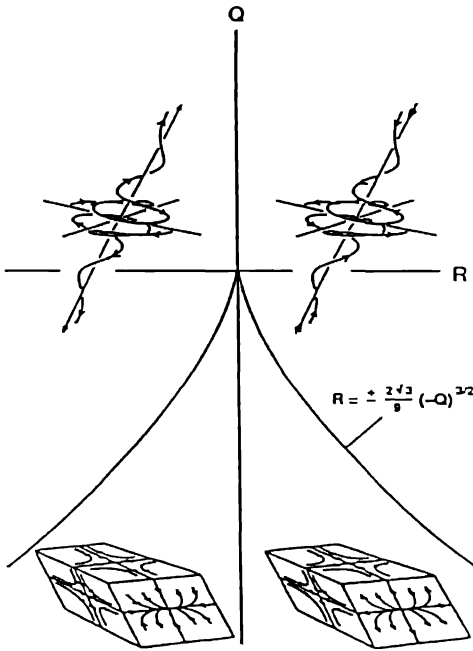
Fig. 11.   Three-dimensional topologies in the Q–R ($P = 0$) plane. From Soria et al. (1992).

are not orthogonal if the flow has vorticity. The classifications shown are (reading from top right corner counter-clockwise) unstable focus/contracting, stable focus/stretching, stable node/saddle/saddle and unstable node/saddle/saddle.

From these basic quantities other quantities can be derived, e.g. the invariants of the rate of strain tensor, P_s, Q_s and R_s, can be formed from S_{ij}. The mechanical dissipation for kinetic energy due to viscous friction is

$$\phi = 2\nu S_{ij}S_{ij} = -4\nu Q_s. \tag{6}$$

Another important quantity is Q_w which is the second invariant of the rate of rotation tensor W_{ij}. This is nonzero and is given by

$$Q_w = -\frac{1}{2} W_{ij}W_{ji} = -\frac{1}{2} W_{ij}W_{ij}. \tag{7}$$

This is proportional to the enstrophy density.

At two recent *Center of Turbulence Research* Summer programs, DNS data for plane mixing layers and other shear layers were examined. The second and third invariants for A_{ij}, S_{ij} and W_{ij} were calculated using all nine components of the velocity gradient tensor for every grid point in the flow field. Scatter diagrams of Q versus R, Q_s versus R_s and $-Q_s$ versus Q_w were produced (see Chen et al., 1990 and Soria et al., 1992). Some typical results are shown in Fig. 12 for a plane mixing layer with Reynolds number of 3000 based on velocity difference and vorticity thickness.
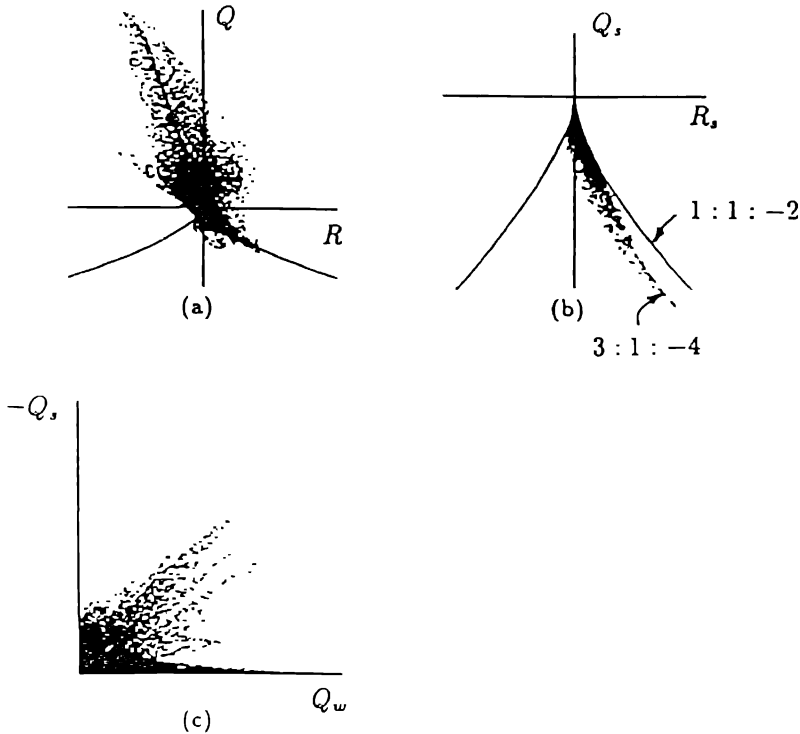
Fig 12.   Scatter plots of (a) Q vs. R, (b) Q_s vs R_s, and (c) $-Q_s$ vs. Q_w for incompressible mixing layer. From Soria et al. (1992).

Large positive values of Q indicate large enstrophy density which dominates over the rate of strain effect. This is because $-S_{ij}S_{ji} = S_{ij}S_{ij}$ is always negative ($= Q_s$) and $W_{ij}W_{ji} = -W_{ij}W_{ij}$ and is always positive ($= Q_w$). One can see from Fig. 12a that such points are most likely to have topology of stable focus/stretching. Motions which have large $-Q_s$ have high dissipation and tend to lie along curves on the Q_s versus R_s plot as shown. Such curves are scaled vertically from the boundary curve and denote curves of constant ratio of the principle rates of strain $\alpha : \beta : \gamma$. The boundary curve is 1 : 1 : -2 whereas the data shown is 3 : 1 : -4. However, from the work of Soria et al. (1992), this result was not found to be universal.

The plot of $-Q_s$ versus R_s is most interesting as shown in Fig. 12c. Figure 13 shows the physical interpretation for various regions of the plot. It can be seen from Fig. 12c that a large number of points appear to belong to vortex sheets but there are a very large number of points which belong to vortex tubes. Figure 14 shows a most intriguing result of Chen et al. (1990) for a plane mixing layer. This flow is slightly compressible but indicates that most of the motion belonging to vortex sheets (i.e. a high enstrophy density also corresponds with a high dissipation).

$$-Q_s = \tfrac{1}{2}S_{ij}S_{ij} \sim \text{Dissipation}$$

Irrotational dissipation

Vortex sheets

Vortex tubes

$$Q_w = \tfrac{1}{2}W_{ij}W_{ij} \sim \text{Enstropy density}$$
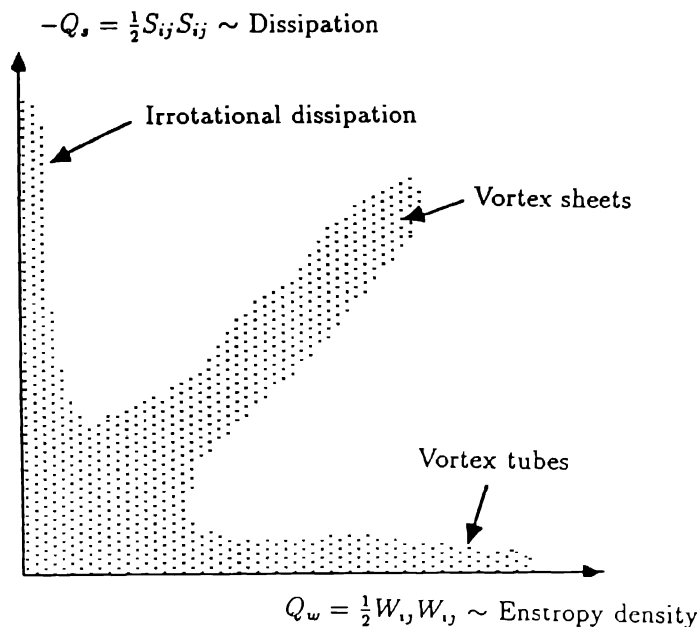
Fig. 13.   Physical interpretation of various regions in the $-Q_s$ vs. Q_w plot.

$-Q_s$

Q_w
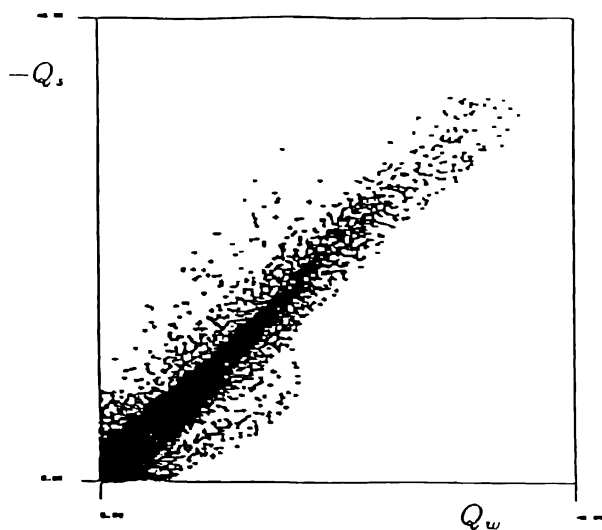
Fig. 14.   Plot of $-Q_s$ vs. Q_w for compressible mixing layer computed by Chen (1990).

Figure 15 shows a plot of $-Q_s$ versus Q_w from some preliminary work on turbulent boundary layers using the DNS data of Spalart. Although the plot has poor resolution (the figure is a blow-up from another plot) it indicates that most
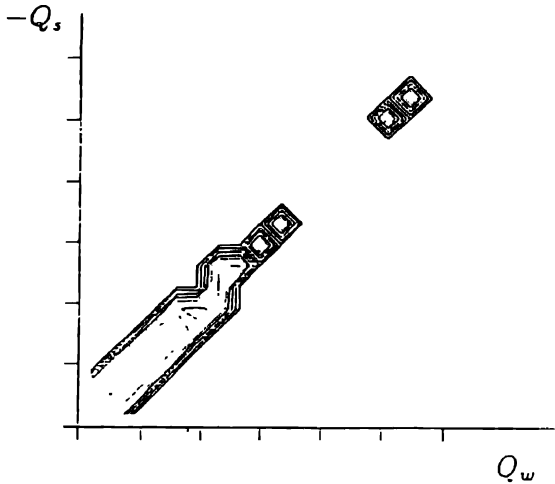
Fig 15. Plot of $-Q_s$ vs Q_w for turbulent boundary layer using DNS data of Spalart.

high velocity gradient motions are sheet like. All these intriguing results should be pursued in future work.

7. Conclusions and Discussion

In the study of the topology of flow patterns and eddying motions, instantaneous streamlines have found considerable use even though they are not Galilean invariant and appear to lose physical meaning if the flow is unsteady. However, cases have been identified where they are of some use in describing the large scale motions of turbulence and the vortex shedding processes. Much of their use stems from the fact that they are the easiest to measure and are the most accurate feature to compute.

The usefulness of other vector fields needs to be explored. Now that we have DNS data almost any quantity can be mapped out and studied. Unfortunately this situation does not hold at the moment with experimental data. With DNS data, not only can the large scale topology be examined but also the fine scale dissipating motions. The concept of critical points for velocity fields can be applied to every point in the flow field by chosing a nonrotating observer fixed to a particle at the chosen point. The local instantaneous streamline patterns give a geometric meaning to the concepts of the symmetric rate of strain tensor and the antisymmetric rate of rotation tensor. By definition, the observer does not need to be specified. Applying this to all points of a DNS data set with scatter diagrams of the tensor invariants has shown some intriguing results which need to be pursued. No matter what vector field is chosen the same critical point concepts outlined here will be needed for describing and understanding what we are looking at and this after all is what our job as researchers is all about.

References

Burgers, J.M., A mathematical model illustrating the theory of turbulence. *Adv. in Applied Mechanics* 1 (1948) 171–199.

Cantwell, B.J., Coherent turbulent structures as critical points in unsteady flow. *Arch. Mech. Strosow.* (Archives of Mechanics) 31 (1978) 707–721.

Chen, J., Cantwell, B. and Mansour, N., The topology and vortex dynamics of a three-dimensional plane compressible wake. *Proceedings of the Tenth Australasian Fluid Mechanics Conference.* University of Melbourne, Australia (1989).

Chen, J.H., Chong, M.S., Soria, J., Sondergaard, R., Perry, A.E., Rogers, M., Moser, R. and Cantwell, B.J., A study of the topology of dissipating motions in direct numerical simulations of time-developing compressible and incompressible mixing layers. *Proceedings of Center of Turbulent Research*, CTR-S90 (1990).

Chong, M.S., Perry, A.E. and Cantwell, B.J., A general classification of three-dimensional flow fields. *Physics of Fluids A* 2(5) (1990) 765–777.

Dallmann, U., Topological structures of three-dimensional flow separations. DFVLR Rep. IB 221-82-A07. Göttingen, West German (1983).

Kelso, R.M., A study of free shear flows near rigid boundaries. Ph.D. Thesis, Mechanical Engineering Department, University of Melbourne (1990).

Lighthill, M.J., Attachment and separation in three-dimensional flow. In: L. Rosenhead (ed.), *Laminar Boundary Layers.* Oxford: Oxford University Press (1963), pp. 72–82.

Perry, A.E. and Fairlie, B.D., Critical points in flow patterns. *Adv. in Geophysics* 18B (1974) 299–315.

Perry, A.E. and Lim, T.T., Coherent structures in coflowing jets and wakes. *J. Fluid Mech.* 88 (1978) 451–463.

Perry, A.E., Lim, T.T. and Chong, M.S., The instantaneous velocity fields of coherent structures in coflowing jets and wakes. *J. Fluid Mech.* 101 (1980) 243–256.

Perry, A.E. and Chong, M.S., On the mechanism of wall turbulence. *J. Fluid Mech.* 119 (1982) 173–217.

Perry, A.E. and Tan, D.K.M., Simple three-dimensional vortex motions in coflowing jets and wakes. *J. Fluid Mech.* 141 (1984) 197–231.

Perry, A.E. and Hornung, H.G., Some aspects of three-dimensional separation. Part II. Vortex skeletons. *Z. Flugwiss. Weltraumforsch.* 8 (1984) 155–160.

Perry, A.E. and Chong, M.S., A series-expansion study of the Navier–Stokes equations with applications to three-dimensional separation patterns. *J. Fluid Mech.* 173 (1986) 173–217.

Perry, A.E. and Steiner, T.R., Large-scale vortex structures in turbulent wakes behind bluff bodies. Part 1. *J. Fluid Mech.* 174 (1987) 233–270.

Perry, A.E. and Chong, M.S., A study of eddying motions and flow patterns using critical point concepts. *Annual Review of Fluid Mech.* 19 (1987) 125–155.

Soria, J., Chong, M.S., Sondergaard, R., Perry, A.E. and Cantwell, B., Topology of time developing incompressible mixing layers. *Proceedings of Center of Turbulence Research*, CTR-SS92 (1992).

Spalart, P.R., Direct simulation of a turbulent boundary layer up to $R_\theta = 1410$. *J. Fluid Mech.* 187 (1988) 61–98.

Spalart, P.R. and Watmuff, J.H., Experimental and numerical study of turbulent boundary layers with pressure gradients. *J. Fluid Mech.* 249 (1992) 337–371.

Steiner, T.R. and Perry, A.E., Large-scale vortex structures in turbulent wakes behind bluff bodies. Part 2. *J. Fluid Mech.* 173 (1987) 271–298.

Sullivan, R.D., A two-celled solution of the Navier–Stokes equations. *Journal of the Aero/Space Sciences* 26 (1959) 767–768.

Townsend, A.A., *The Structure of Turbulent Shear Flow,* 2nd edn. Cambridge University Press (1976).

Vollmers, H., Separation and vortical-type flow around a prolate spheroid. Evaluation of relevant parameters. *AGARD Symposium on Aeordyn. of Vortical Type Flow in Three-Dimensions,* Rotterdam, AGARD-CP 342 (1983) pp. 14.1–14.14.

Topological Visualisation of Focal Structures in Free Shear Flows

JULIO SORIA
Department of Mechanical Engineering, Monash University, Clayton, Vic 3168, Australia

and

BRIAN J. CANTWELL
Aeronautics and Astronautics Department, Stanford University, Stanford, CA 94305, USA

Abstract. This paper describes a method for identifying and visualising the three-dimensional geometry of focal (vortex) structures in complex flows. The method is based primarily on the classification of the local topology as it is identified from the values of the velocity gradient tensor invariants. The identification of the local topology is reference frame invariant. Therefore, focal (vortex) structures can be unambiguously identified in these flows. A novel flow visualisation method is introduced whereby focal structures are rendered using a solid model view of the local topology. This new approach is applied to the identification of focal structures in three-dimensional plane mixing layer and plane wake flows.

1. Introduction

The success in direct numerical simulation (DNS) of three-dimensional free shear flows at moderate Reynolds number has made available large data sets of transitional and turbulent flow fields. Topological methodology has recently been identified as a useful tool in the study of the geometry of the kinematics of these unsteady flows. Examples of studies which have used this approach are Chen et al. (1990) and Sondergaard et al. (1991), who applied this methodology to the study of the local topology of small scale motions in turbulent compressible and incompressible shear flows. Soria et al. (1994), have studied the topology of the dissipating motions in turbulent mixing layers evolving from different initial conditions.

Although the local flow patterns are described using critical point theory (Chong et al. (1990)), one does not have to rely on stationary points in the flow to apply the topological identification and classification to the entire fluid flow. At each instant in the flow field evolution, each point can be considered to be a stationary point if an observer moves in a non-inertial, non-rotating frame with the fluid particle at that point. It is thus possible, to characterise the local topology of the kinematics of the entire fluid flow by calculating the invariants of the velocity gradient tensor at each point and applying the topological classifications proposed by Chong et al. (1990). It is important to note that since the velocity gradient tensor is reference frame invariant, and it is the values of the velocity gradient tensor components which are used for the local topological characterisation of the flow kinematics,

this identification of topological structures is in fact independent of any particular observer.

Note also, that the velocity gradient tensor is not the only quantity that can be used to classify the geometry of the flow kinematics; other quantities such as the vorticity, derived quantities from the rate-of-strain tensor and the rate-of-rotation tensor or the pressure gradient can also be used in the topological analysis of the flow field. The pressure gradient field was used by Chen (1991) to study the topology of a compressible mixing layer. The relative usefulness and applicability of any particular quantity as the input to this type of analysis remains to be explored. This paper considers exclusively the characterisation of the geometry of the kinematics as derived from the velocity gradient tensor for an incompressible fluid flow. The approach of identifying and classifying topological structures in turbulent flows is illustrated by its application to moderate Reynolds number free shear flows.

2. The Local Topology of Three-Dimensional Incompressible Flows

Let the velocity gradient tensor

$$A_{ij} = \frac{\partial u_i}{\partial x_j}(\mathbf{x}) \tag{1}$$

be divided into a symmetric and an anti-symmetric part. The symmetric part is known as the rate-of-strain tensor and is given by

$$S_{ij} = \frac{1}{2}(\frac{\partial u_i}{\partial x_j} + \frac{\partial u_j}{\partial x_i}), \tag{2}$$

while the anti-symmetric part is known as the rate-of-rotation tensor, and it is given by

$$W_{ij} = \frac{1}{2}(\frac{\partial u_i}{\partial x_j} - \frac{\partial u_j}{\partial x_i}), \tag{3}$$

A_{ij}, S_{ij} and W_{ij} are second order tensors. The second order tensor, $\mathbf{A}(\mathbf{x})$ has eigenvalues λ_1, λ_2 and λ_3 and corresponding eigenvectors e_1, e_2 and e_3, given by the eigenvalue problem

$$(\mathbf{A} - \lambda\mathbf{I})\mathbf{e} = 0. \tag{4}$$

The eigenvalues can be determined by solving the corresponding characteristic equation

$$\det[\mathbf{A} - \lambda\mathbf{I}] = 0, \tag{5}$$

which, for a second order tensor yields

$$\lambda^3 + P\lambda^2 + Q\lambda + R = 0. \tag{6}$$

The invariants P, Q and R characterising the $A_{ij}(\mathbf{x})$ tensor are

$$P = -S_{ii}, \tag{7}$$

$$Q = \frac{1}{2}(P^2 - S_{ij}S_{ji} - W_{ij}W_{ji}), \tag{8}$$

$$R = \frac{1}{3}(-P^3 + 3PQ - S_{ij}S_{jk}S_{ki} - 3W_{ij}W_{jk}S_{ki}). \tag{9}$$

Solutions of the characteristic Equation (6) determine the local, linearised flow patterns. It can be shown that in the (P, Q, R) space of the tensor invariants the surface which divides characteristic equations with three real solutions for the eigenvalues from characteristic equations with one real and two complex solutions is

$$27R^2 + (4P^3 - 18PQ)R + (4Q^3 - P^2Q^2) = 0. \tag{10}$$

A detailed discussion of the properties of this surface and a guide to the various possible flow geometries and their terminology which can occur in the entire (P, Q, R) space (includes compressible flows) is given in Chong et al. (1990). At each point $\mathbf{x}$ in a general compressible flow field the values of the triplet (P, Q, R) specify the local topology of the fluid motion.

For an incompressible fluid, $P = 0$ and the (P, Q, R) space is reduced to the (Q, R) plane with $P = 0$. Thus, Equations (7)–(9) reduce to

$$Q = -\frac{1}{2}(S_{ij}S_{ji} + W_{ij}W_{ji}), \tag{11}$$

$$R = -\frac{1}{3}(S_{ij}S_{jk}S_{ki} + 3W_{ij}W_{jk}S_{ki}), \tag{12}$$

and the discriminant of $\mathbf{A}$ can be defined from Equation (10) for $P = 0$ as

$$D = Q^3 + \frac{27}{4}R^2. \tag{13}$$

Figure 1 shows the two-dimensional (Q, R) space with the four possible non-degenerate topologies. The tent-like curve indicated in Figure 1 is a cut through the surface defined by Equation (10) at $P = 0$ and corresponds to $D = 0$. Below this curve the eigenvalues of the velocity gradient tensor are real, while above it the velocity gradient tensor has one real eigenvalue and a complex conjugate pair of eigenvalues.

Strain-rate dominated regions in the flow field are areas which have local topologies denoted by either stable-node/saddle/saddle ($SN/S/S$ – below the tent with $R < 0$) or unstable-node/saddle/saddle ($UN/S/S$ – below the tent with $R > 0$) according to the terminology of Chong et al. (1990). Vortex-like structures
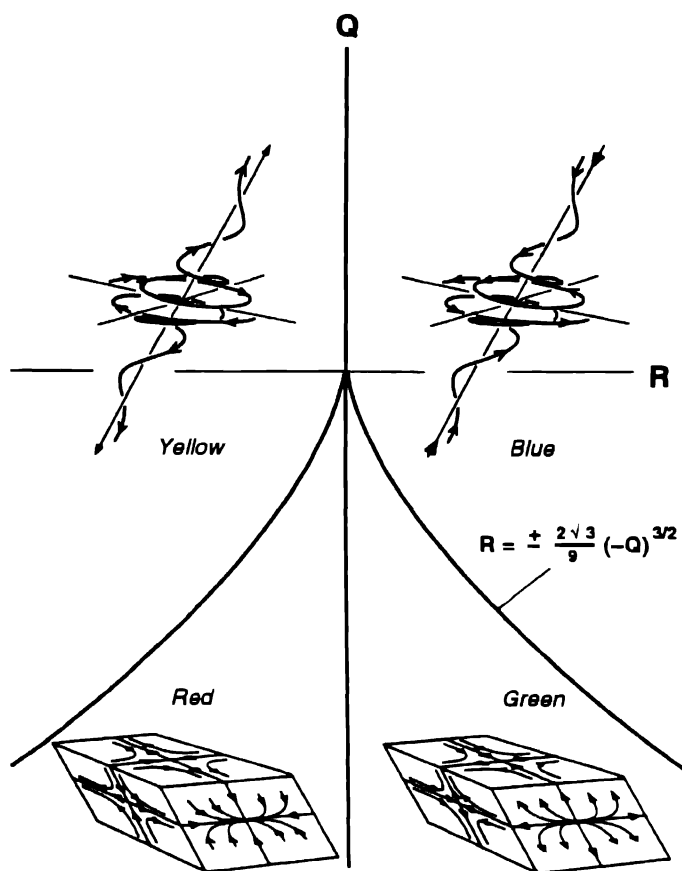
Fig. 1.   Identification of local non-degenerate flow topologies in the plane $P = 0$.

are a conglomerate of local regions which have as their local topology stable-focus/stretching (SF/S – above the tent with $R < 0$) or unstable-focus/contracting (UF/C – above the tent with $R > 0$).

   In the compressible flow considered by Chen et al. (1990) only two additional topologies were found to be vortex-like in nature for this more general flow, namely stable-focus/contracting (SF/C) and unstable-focus/stretching (UF/S). Colour coding the different topologies has been found to be the most appropriate method for the visualisation of the geometry of the different topological structures which exist in the flow. Figure 1 includes the different colours which have been assigned to the four possible non-degenerate incompressible fluid flow topologies.

   In the degenerate case when $R = 0$ which corresponds to two-dimensional flow, regions which are focal in nature can be established from the second invariant

alone. Closer inspection of the second invariant as given by Equation (11), shows that (i) $S_{ij}S_{ji}$ gives a measure of the local strength of the irrotational stretching and is a positive quantity because S_{ij} is a symmetric tensor and (ii) $W_{ij}W_{ji}$ gives a measure of the local strength of the vorticity (enstrophy) and is negative because W_{ij} is an anti-symmetric tensor. Thus, in the restricted case when $R = 0$ focal-like regions exist only if the strength of the local vorticity dominates over the strength of the irrotational stretching. In the more general case when $R \neq 0$ the change from focal to nodal behaviour occurs across the line $D = 0$.

Implicit in this definition of regions which are vortex-like ($focal$) in nature is the concept that whether a region of vorticity appears as a vortex structure or not depends also on its environment, i.e. it depends on the local strain field induced by motions outside the region of interest as pointed out by Chong et al. (1990). Again, it is important to re-emphasise that the present definition of a vortex structure is independent of the observer, since its characterisation depends entirely on the properties of the velocity gradient tensor. Therefore, the classification and identification of focal regions in the flow is unambiguous and accurately calculable from the invariants of the velocity gradient tensor.

3. Application of Local Topological Classification to the Identification of Focal (Vortex) Structures

The topological classification and identification just described can be used as a flow visualisation tool for large DNS data bases. It is quite difficult, if not impossible to load a complete DNS flow field for one instant in time (e.g. more than 2 million data points) into the computer for three-dimensional flow visualisation. The computation of instantaneous streamlines (which are not reference frame invariant and depend on an observer) and the graphical manipulation is a computationally intensive task. Contrast with this, the visualisation of the flow field using one characteristic (e.g. one colour code) per data point. Although this still represents a large amount of data, it is manageable and it is possible to visualise interactively the three-dimensional geometry of the kinematics.

The identification of the geometry of reference frame invariant structures in free shear flows by identifying the local topology at each point in the flow is illustrated by applying it to two numerically computed data bases: one a temporally-developing plane mixing layer and the other a temporally-developing plane wake. In both cases the emphasis is on the identification of focal structures in the flow.

3.1. FOCAL STRUCTURES IN A TIME-DEVELOPING MIXING LAYER

A data base of a time-developing plane mixing layer computed by Rogers and Moser (1990) was used for the visualisation of the topologies and the identification of focal structures in this type of shear flow. The data presented here is for a time frame which corresponds to $Re = 3000$, where Re is based on the velocity

difference and vorticity thickness. At this time frame, the flow has undergone pairing and post-mixing transition.

The simulation was calculated by solving the vorticity equation with periodic boundary conditions of period L_x and L_z in the streamwise (x) and spanwise (z) spatial directions respectively. The domain was doubly infinite in the cross-stream direction with L_x and L_z corresponding to the size of the computational box in the streamwise and spanwise directions. The initial conditions supplied to the simulation comprised a mean velocity profile (a function of y only) plus the corresponding most unstable two-dimensional fundamental eigenfunction plus the sub-harmonic of this fundamental plus streamwise vorticity distributed uniformly in the streamwise direction. The initial Re in this computation was 500. The direct simulation of the Navier-Stokes equations was a fully de-aliased spectral calculation. Further details on this simulation are described in Rogers and Moser (1993).

Figure 2 shows the cross-sectional topology visualisation of this three-dimensional time-developing plane mixing layer. Only topologies with $|\omega| > 0.1|\omega|_{\mathrm{max}}$ are shown. Included in this figure are equally spaced contour lines of vorticity magnitude for $|\omega| \geq 0.5|\omega|_{\mathrm{max}}$. All the regions which are yellow and blue in Figure 2 correspond to focal regions. Note that a significant amount of this flow field has $|\omega| < 0.5|\omega|_{\mathrm{max}}$ but still forms part of a focus.

The topological maps in Figures 2(a) and (b) show two different xy-planes. Figure 2(b) shows streamwise structures which are topologically focal/stretching in nature. In fact, these regions of the flow are dominated by rotation. They contain the largest vorticity magnitude and very little strain as identified by Chen et al. (1990), and correspond to streamwise stretching vortices. Figures 2(c)–(e) show the topologies in yz-planes of this flow. Figure 2(c) corresponds to a cross-sectional cut through the middle of the streamwise stretching vortices. The topological visualisation of these structures shows them to have an elliptical cross-sectional geometry at this yz-plane. In contrast, the cross-sectional geometry of the same structures is circular towards their extremities (Figure 2(e)).

Figure 3 shows a three-dimensional flow visualisation of regions in the flow which are focal in nature by showing iso-surfaces with $|\omega| = 0.3|\omega|_{\mathrm{max}}$. This visualisation clearly identifies the dominant focal structures in this flow as streamwise vortices. It is curious to note the helical nature of these streamwise focal structures at their extremities. At these locations there is an intertwining of topologies which are *SF/S* and *UF/C*. The evolution of the spiralling nature of the streamwise vortices in this mixing layer flow has been the subject of a recent study by Lopez and Bulbeck (1993). A double-helix structure in a plane turbulent mixing layer has previously been observed experimentally by Chandrsuda et al. (1978) and more recently in direct numerical simulations studies of the mixing layer by Comte and Lesieur (1990). These double-helix structures were associated in both investigations with helical vortex pairing of the spanwise Kelvin-Helmholtz vortices. In
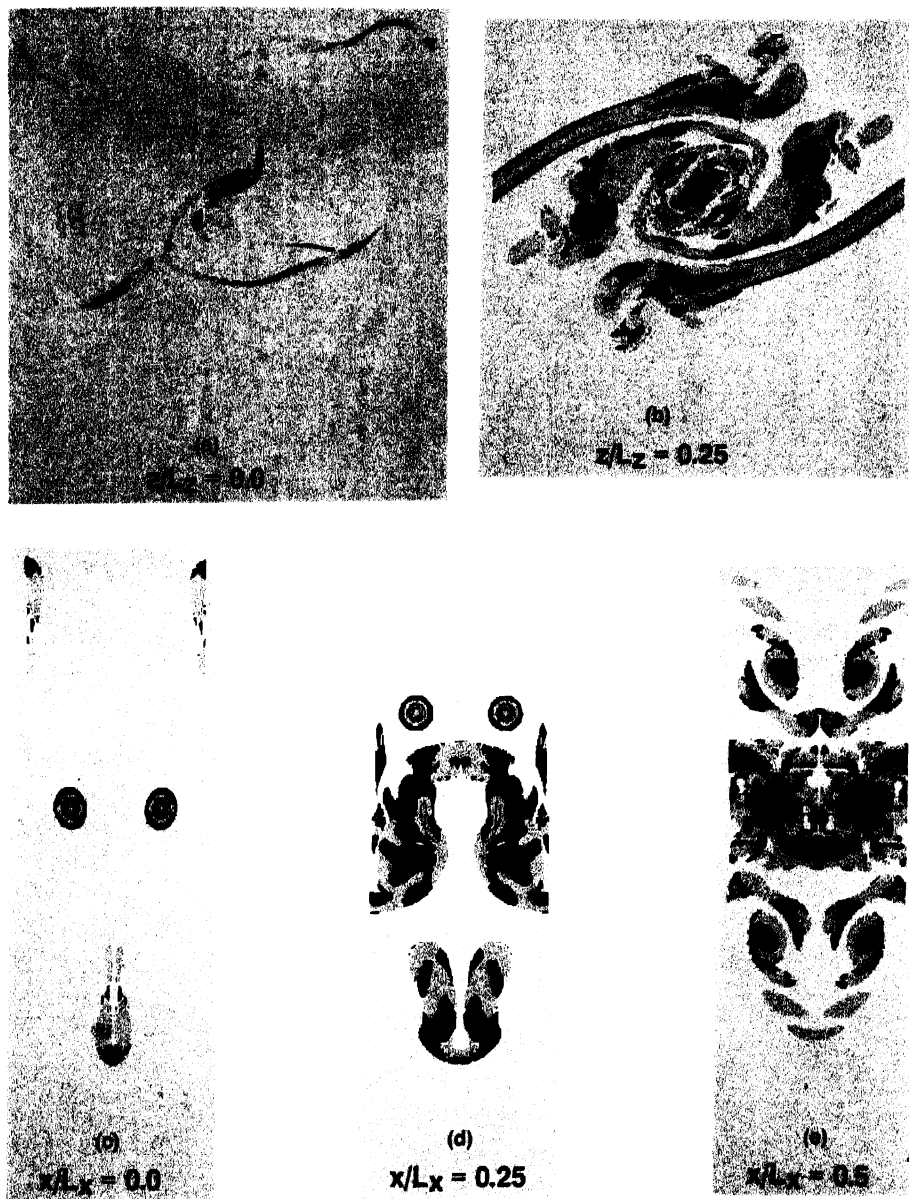
Fig. 2. Topology map of xy-planes (a)–(b) and yz-planes (c)–(e) showing the local topology of the plane mixing layer for $|\omega| > 0.1|\omega|_{max}$. Black lines denote equally spaced $|\omega|$ contour lines for $|\omega| \geq 0.5|\omega|_{max}$.
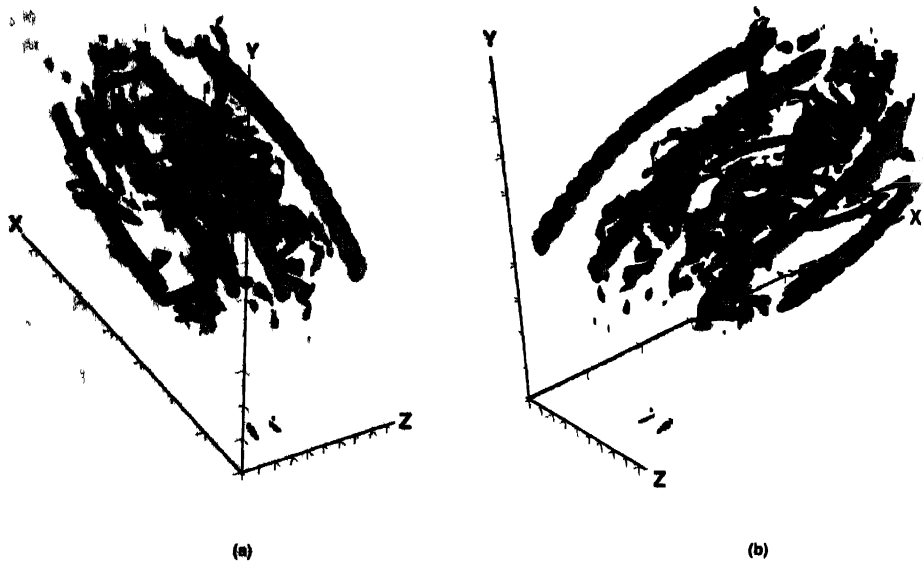
(a)   (b)

Fig 3   Visualisation of *SF/S* and *UF/C* focal (vortical) structures in the plane mixing layer
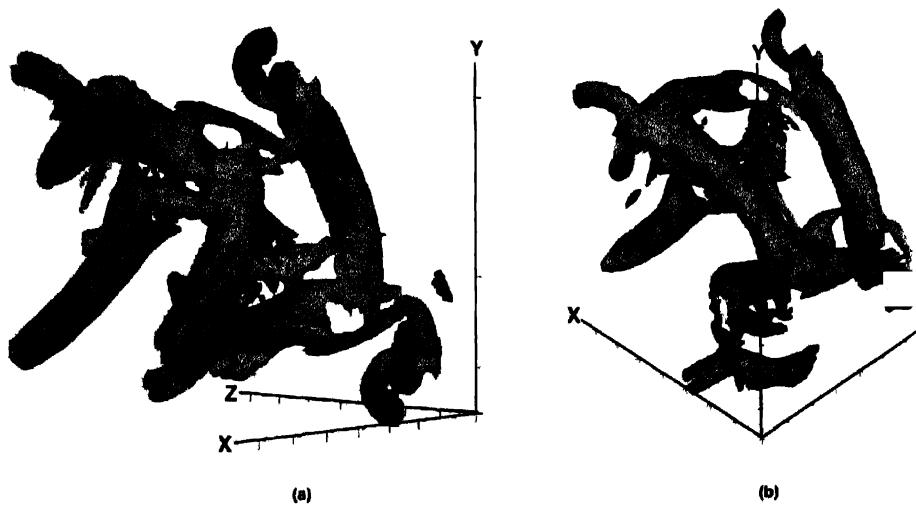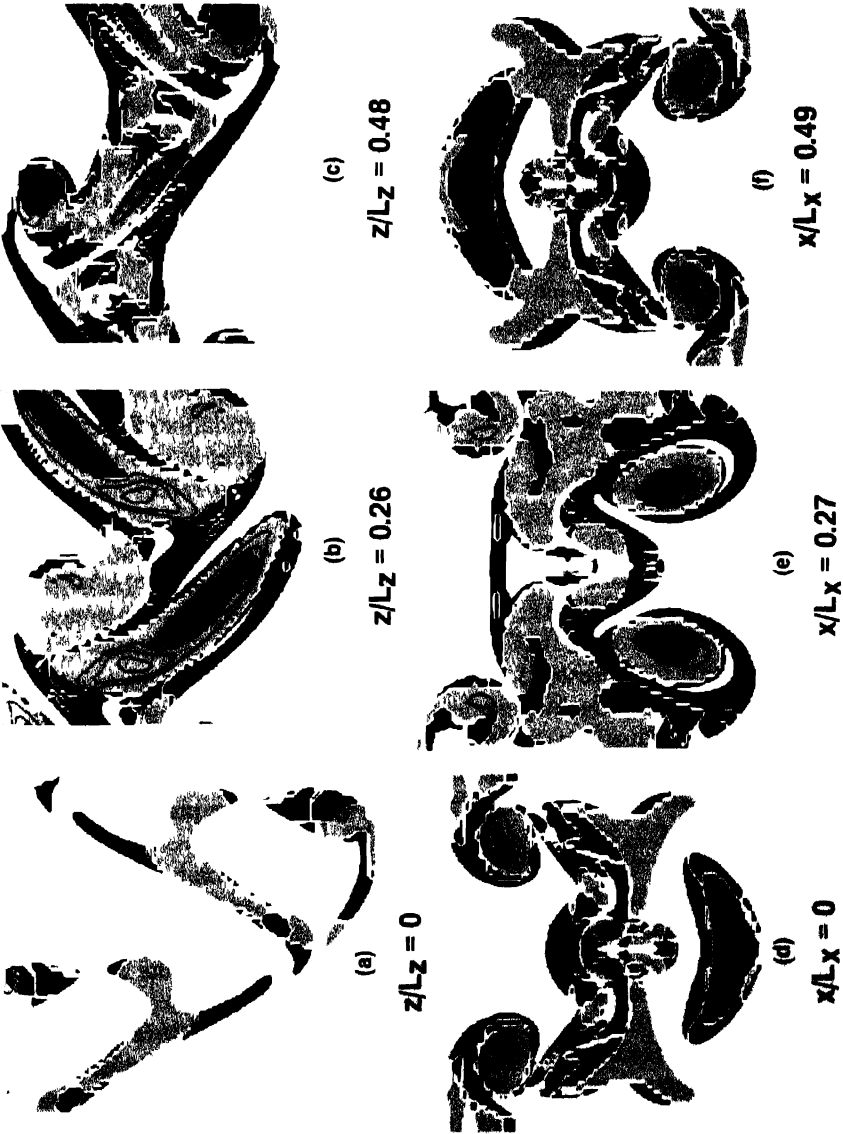shown as iso-surfaces with $|\omega| = 0\ 3|\omega|_{max}$

(a)   (b)

Fig 5   Visualisation of *SF/S* and *UF/C* focal (vortical) structures in the plane wake shown
as iso-surfaces with $|\omega| = 0\ 4|\omega|_{max}$

Fig 4 Topology map of xy-planes (a)–(c) and yz-planes (d)–(f) showing the local topology of the plane wake for $|\omega| > 0.1|\omega|_{max}$ Black lines denote equally spaced $|\omega|$ contour lines for $|\omega| \geq 0.5|\omega|_{max}$

contrast the regions with helical geometry observed here in the Rogers and Moser
mixing layer are associated with the streamwise focal structures.

3.2. FOCAL STRUCTURES IN A TIME-DEVELOPING WAKE

Regions with focal structures in plane wake flows were identified by considering
the data base of a direct numerical calculation of a time-developing plane wake
at a $Re = 500$, where Re is based on the velocity deficit and the displacement
thickness. The initial conditions for this calculation were a Gaussian mean velocity
profile with the corresponding most unstable two-dimensional mode plus an oblique
mode at 45° with the same streamwise wavenumber as the two-dimensional mode.
The numerical calculation was performed by solving the incompressible vorticity
equations using periodic boundary conditions in the streamwise (x) and span-
wise (z) spatial directions with period L_x and L_z respectively. The size of the
computational box was L_x in the streamwise direction and L_z in the spanwise
direction, while in the cross-stream direction the domain was doubly infinite. A
pseudo-spectral numerical code developed by Rogers and Moser (1990) was adapt-
ed for this three-dimensional time-developing plane wake calculation. Details of
the pseudo-spectral numerical method are described in Spalart et al. (1991). The
numerical calculation was performed with $64 \times 128 \times 64$ Fourier/Jacobi modes.

Figure 4(a)–(c) shows the topology map of the wake in xy-planes at a certain
time frame in its evolution. Flow is left to right in the positive x-direction. The
topology of the flow is shown only for regions with vorticity magnitude such that
$|\omega| > 0.1|\omega|_{max}$. This threshold value was chosen so that only regions of the flow
are shown which contain at least 10% of the maximum vorticity magnitude. It is
important to stress that this threshold value does not affect the local topology of
the flow directly, the effect of the magnitude of the local vorticity in characterising
the local topology is via Equations (8)–(9), where the effect of the local strain field
is also taken into account (see also also the discussion in Soria and Chong (1993)).
Equally spaced contours of vorticity magnitude for each of the xy-planes are also
included for $|\omega| \geq 0.5|\omega|_{max}$ in Figure 4.

A close correspondence is observed between the regions of high $|\omega|$ and the
topological regions which are focal in nature. In general, a direct correspondence
between the vorticity magnitude and the local topology of a region in the flow cannot
be drawn. However, if in an incompressible fluid the local strength of the vorticity
is larger than the local strength of the irrotational strain (i.e. when $Q > 0$) then,
the local topology is always focal (hence, vortex-like) in nature because $D > 0$.
The converse is not true, i.e. when the strength of the local strain is larger than the
strength of the local vorticity (i.e. when $Q < 0$), D may be positive of negative
and hence, the local topology may be focal or nodal in character respectively.

Figure 4(c) shows regions of focal topology which can be identified as the
classical spanwise rollers of a wake (i.e. von Karman vortices) and some focal
regions which are *SF/S* which are elongated and tilted in the streamwise direction.

Figure 4(b) also shows regions of *SF/S* which can be identified as part of the span-wise rollers. A large focal structure which is elongated and tilted in the streamwise direction is also identified in Figure 4(b). Figures 4(d)–(f) show the corresponding topology map for yz-planes, clearly showing the streamwise oriented focal struc-tures. Figures 4(d) and (f) also show clearly that (i) the spanwise vortex structures contain significant regions of *UF/C* topology and (ii) that regions with the largest vorticity magnitude are associated with the streamwise vortex structures which are topologically focal in nature.

Much information can be deduced about the geometry of focal structures in this wake flow from planar topology maps. However, all this information and more about the vortex structures in this flow is even better summarised and visu-alised by considering a three-dimensional solid model of the focal structures. This was achieved by an iso-surface visualisation of regions of focal topology with $|\omega| = 0.4|\omega|_{max}$.

On a graphics computer the iso-surface visualisation is easily rotated and hence, provides a great deal of geometric insight into the complex three-dimensional nature of the focal structures in this flow. Some of the views of this visualisation are shown in Figure 5. The spanwise rollers and the streamwise vortices are clearly identified in this visualisation. Curiously, the streamwise vortices in this wake have a helical geometry in the region close to the spanwise vortices. The streamwise vortices consist of topologies *SF/S* with the core consisting of *UF/C*. The helical region of these vortices is made up of intertwining regions of *SF/S* and *UF/C* similar to the helical regions of the streamwise vortices identified in the plane mixing layer. The spanwise focal structures corresponding to the spanwise wake vortices are clearly identified between the pair of streamwise vortical structures.

4. Concluding Remarks

An unambiguous and reference frame invariant method for the identification of focal (vortex-like) regions has been presented. The method is based on the local topology classification determined from the calculation of the velocity gradient ten-sor invariants. The method has been illustrated in incompressible free shear flows, although, its applicability is more general and also encompasses compressible fluid flows.

A novel method of visualisation of the flow geometry has been introduced. A rendition of the geometry of focal structures in any flow can be generated by a solid model view of regions with a focal topology. These focal regions can be determined exactly from the values of the velocity gradient tensor invariants. This method of visualising the geometry of focal structures, and hence, the identification of vortex structures in a complex three-dimensional flow has been illustrated by considering a three-dimensional plane mixing layer flow and plane wake flow. Spanwise focal structures and streamwise oriented focal structures have been identified using this

methodology. In both flows the streamwise vortex structures are found to have an interesting helical geometry towards their extremities.

Acknowledgements

References

Chandrsuda, A., Mehta, R.D., Weir, A.D. and Bradshaw , P., Effect of free-stream turbulence on large structure in turbulent mixing layers. *J. Fluid Mech.* 85 (1978) 693–704.

Chen, J., Chong, M., Soria, J., Sondergaard, R., Perry, A.E., Rogers, M., Moser, R. and Cantwell, B., A study of the topology of dissipating motions in direct numerical simulations of time-developing compressible and incompressible mixing layers. CTR Report SS90, Stanford University, Stanford, CA (1990).

Chen, J.H., The topology of the compressible mixing layer. *Bull. Am. Phys. Soc.* 36(10) (1991) 2615.

Chong, M., Perry, A.E. and Cantwell, B., A general classification of three-dimensional flow fields. *Phys. Fluids A* **2**(5) (1990) 765–777.

Comte, P. and Lesieur, M., Two manners of becoming three-dimensional for mixing layers. In V.V. Kozlov and A.V. Dovgal (eds), *Separated Flows and Jets*, Springer Verlag (1990).

Lopez, J.M. and Bulbeck, C.J., Behaviour of streamwise rib vortices in a three-dimensional mixing layer. *Phys. Fluids A* 5(7) (1993) 1694–1702.

Rogers, M.M. and Moser, R.D., Mixing transition and the cascade to small scales in a plane mixing layer. *Proc. of the IUTAM Sym. on Stirring and Mixing.* UCSD, LaJolla, CA (1990).

Rogers, M.M. and Moser, R.D., Spanwise scale selection in plane mixing layers. Submitted for publication to *J. Fluid Mech.* 247 (1993) 321–337.

Sondergaard, R., Chen, J., Soria, J. and Cantwell, B., Local topology of small scale motions in turbulent shear flows. *8th Sym. on Turbulent Shear Flows, Munich, Germany* (1991) 16.1.1–16.1.6.

Soria, J., Chong, M.S., Sondergaard, R., Perry, A.E. and Cantwell, B.J., A study of the fine scale motions of incompressible time-developing mixing layers. *Phys. of Fluids* 6(2) (1994) 871–884.

Soria, J. and Chong, M.S., The structure of intense focal regions in a direct numerical wake flow calculation. *9th Sym. on Turbulent Shear Flows*, Kyoto, Japan (1993) 3.1.1–3.1.6.

Spalart, P.R., Moser, R.D. and Moser, M.M., Spectral methods for the Navier-Stokes equations with one infinite and two periodic directions. *J. Comp. Phys.* 96 (1991) 297–324.

Identification of Zones in a Free Evolving Vortex Ring

P. ORLANDI and R. VERZICCO
Dipartimento di Meccanica e Aeronautica, Università di Roma 'La Sapienza', Italy

Abstract. A direct numerical simulation of a three-dimensional free evolving vortex ring has been performed to understand some features of the dynamics of vortex rings. In previous experiments, a persistent wake has been observed and the direct simulation has clarified the causes of this wake formation. A kinematic alignment analysis of the vorticity vector with the eigenvectors of the strain-rate tensor, together with vorticity visualisations, have been employed to explain the growth of the 'Widnall' instabilities. The analysis has shown the presence of two different zones, the first characterised by intense vorticity and low strain rate and the second with opposite features. In the former, there is a ring core which maintains its coherence even in the long term, in the latter there are elongated structures contributing to the deformation of the ring.

1. Introduction

There are many practical applications in which round jets play an important role. For example, in combustion chambers the efficiency of combustion is related to the spreading of the jet which increases the mixing of the two reacting fluids. To control the jet, it is important to understand the vorticity dynamics of the basic structures causing the jet to be initially wavy and finally turbulent. Using detailed flow visualisations, Lasheras et al. [1] observed that coaxial jets, at least in their first stage of evolution, can be thought of as an array of vortex rings which interact, deform their structure and by pairing and tearing reach the turbulent status. Vortex rings are then block structures of round jets, therefore an understanding of the evolution of a free vortex ring is necessary for the control of a turbulent jet.

The vortex ring has been experimentally and theoretically investigated in the past. Amongst the numerous experimental studies, Glezer [2] produced flow visualisations of laminar and turbulent vortex rings showing the formation of a wake. A further aspect of the vortex ring dynamics is the so-called 'Widnall' instability associated with the evolution of three-dimensional azimuthal disturbances. The theoretical analysis by Widnall et al. [3], limited to thin inviscid rings, has shown that the wavenumber of the azimuthal instability depends on the vorticity distribution in the ring core.

In the present study, a direct numerical simulation of the Navier–Stokes equations, by a finite-difference scheme, has been performed to understand the reasons for the wake formation and for the azimuthal deformations. The computed instantaneous velocity field allows the calculation of the strain-rate tensor and, as shown by Ashurst et al. [4] in isotropic turbulence, of its eigenvalues and eigenvectors.

Using these quantities the alignment between vorticity vector and eigenvectors of the strain-rate tensor (α, β, γ) is evaluated and this gives an insight into the amount of vortex stretching in the field. The knowledge of $Q_s = S_{ij}S_{ji}$ and of the determinant R_s of the strain-rate tensor $(R_s = \alpha\beta\gamma)$ reveals some features of the flow. For example the sign of R_s indicates whether two eigenvalues are positive or negative. In the case of positive R_s two of the strains are compressive and, from the incompressibility condition $(\alpha + \beta + \gamma = 0)$, it follows that the most intense strain is extensional; the resulting vortex structures are rod-like. For negative R_s one strain is compressive and the vortices are ribbon-like. The ribbon-like structures tend to be unstable and have a tendency to roll up. In the calculation of the previous quantities particular regions of the flow were selected and, within each region, only the points where the vorticity exceeded a prescribed threshold value were used for the statistics. Results have shown that where vorticity is high, i.e. in the core, there is a high probability to have $R_S > 0$ while the opposite occurs in the region close to the axis where the rate of strain is larger than vorticity. This is a condition for a growing instability.

2. The Model

The Navier–Stokes equations, for an incompressible viscous flow in primitive variables and in cylindrical coordinates, have been solved by a finite-difference scheme. The scheme is second order accurate in space and time and locates the unknowns on a staggered grid with the velocities on the faces of the computations cell, the pressure at the centre and the vorticities at the edges. This choice of location of quantities gives the most compact form of *div*, *grad* and *curl* discrete operators and yields solenoidal vorticity and velocity fields within round-off errors. The solution of the equations has been obtained by a fractional step method which evaluates the velocity field in two steps: in the first a non-solenoidal field is obtained then, in the second a scalar Φ is introduced and this allows to project the non-solenoidal field onto a solenoidal one. The quantity Φ is calculated by a Poisson equation which does not require explicit boundary conditions. A third-order Runge–Kutta scheme, with implicit viscous terms and the explicit convective terms, has been used for advancement in time. This consists of three substeps with the calculation of the scalar Φ at each one.

Details of the numerical scheme are given by Verzicco and Orlandi [5] and are not repeated here. It should be noted that the equations have been non-dimensionalised by the ring toroidal radius r_0 and its initial circulation Γ, which lead to the Reynolds number being defined as $\mathrm{Re}_\Gamma = \Gamma/\nu$, where ν is the kinematic viscosity. The results presented here have been obtained at $\mathrm{Re}_\Gamma = 5,500$.

A Gaussian azimuthal vorticity distribution for the ring has been assumed at $t = 0$ and it has been perturbed by a sinusoidal radial displacement of the toroidal axis with $n = 5$ wavenumber. The maximum amplitude of the displacement is $\varepsilon = 0.02 r_0$.

The expression for ω_θ is

$$\omega_\theta = \frac{1}{2\pi} e^{-(\rho/\sigma)^2} \qquad \rho^2 \equiv (z - z_0)^2 + (r - \bar{r}(\theta))^2$$

$$\bar{r}(\theta) = r_0(1 + \varepsilon \sin(n\theta)).$$

This radial displacement does not introduce ω_z, and the radial vorticity component ω_r is evaluated by $\nabla \cdot \omega = 0$.

Preliminary computations in the whole azimuthal span have shown the fulfilment of the symmetries in that direction. Then, a $65 \times 97 \times 129$ grid has been used to discretize the domain of dimensions $2\pi/5 \times 4r_0 \times 6r_0$, respectively. Periodicity has been imposed in z. The field has been replicated in the azimuthal direction for a better visualisation of the field.

Using the velocity components, vorticities and the strain-rate symmetric tensor have been evaluated by:

$$S_{11} = \frac{1}{r} \frac{\partial v_\theta}{\partial \theta} + \frac{v_r}{r}, \quad S_{22} = \frac{\partial v_r}{\partial r}, \quad S_{33} = \frac{\partial v_z}{\partial z},$$

$$S_{12} = \frac{1}{2} \left\{ r \frac{\partial v_\theta/r}{\partial r} + \frac{1}{r} \frac{\partial v_r}{\partial \theta} \right\}, \quad S_{13} = \frac{1}{2} \left\{ \frac{1}{r} \frac{\partial v_z}{\partial \theta} + \frac{\partial v_\theta}{\partial z} \right\},$$

$$S_{23} = \frac{1}{2} \left\{ \frac{\partial v_r}{\partial z} + \frac{\partial v_z}{\partial r} \right\},$$

$$\omega_z = \frac{1}{r} \frac{\partial r v_\theta}{\partial r} - \frac{1}{r} \frac{\partial v_r}{\partial \theta}, \quad \omega_r = \frac{1}{r} \frac{\partial v_z}{\partial \theta} - \frac{\partial v_\theta}{\partial z}, \quad \omega_\theta = \frac{\partial v_r}{\partial z} - \frac{\partial v_z}{\partial r}$$

The eigenvalues and eigenvectors of the S_{ij} tensor have been calculated by a standard Jacobi method.

The skew-symmetric rotation-rate tensor is related to the vorticity components through:

$$R_{12} = \frac{1}{2} \left(\omega_z - \frac{v_\theta}{r} \right) = -R_{21}, \quad R_{13} = \frac{\omega_r}{2} = -R_{31},$$

$$R_{23} = \frac{\omega_\theta}{2} = -R_{32}. \tag{1}$$

3. Results

At $t = 0$ the ring starts the self-induced translation and sheds a vorticity wake. The formation of the wake, in a companion paper [6], was proved to be related to the re-adjustment of the initial Gaussian distribution of ω_θ towards a distribution $\omega_\theta/r = f(\psi)$ which is the solution of the steady Euler equations. This is strictly valid in axisymmetric conditions, which are approximately encountered during the first eddy-turnover time ($t \simeq 15$) when azimuthal disturbances do not sufficiently grow. This wake, with low azimuthal vorticity, is deformed by the strain field in thin
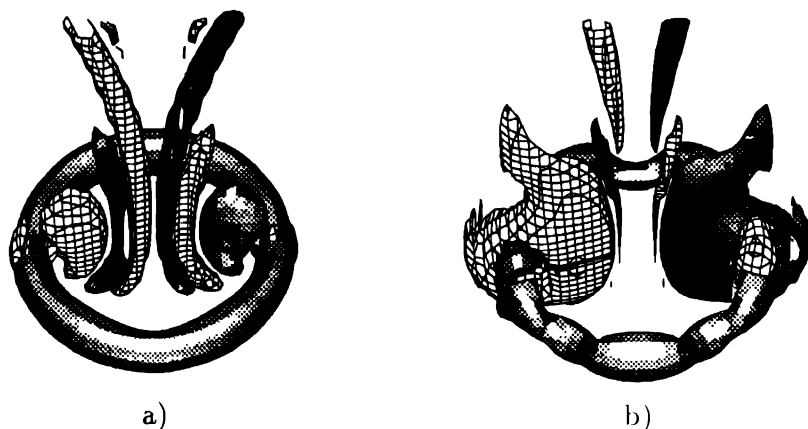
Fig. 1.   Surface contour plots of axial and azimuthal vorticity: (a) $t = 30$, (b) $t = 57$. Light gray for ω_θ, dark gray for positive ω_z, grid for negative ω_z.

and elongated structures with a weak energy content which is rapidly dissipated. As a consequence the wake does not substantially affect the ring during its initial translation.

In Fig. 1a the surface plots of azimuthal and axial vorticities at a value -1.4 and $\pm$ -0.5 at $t = 30$ are shown. It is noted that in producing these plots, we have plotted only two opposite structures for a better visualisation of the vortex dynamics. From this figure it is evident that counter-rotating axial vortices are generated near the core and these, in their turn, induce a hierarchy of oppositely-signed vortices spanning to the axis, where they become small and eventually dissipate by the viscosity. We suppose that these axial vortices could be responsible for the dye accumulation in the ring centre, depicted in the photography by Glezer [2]. These vortices and in particular those with a thicker structure encircling the core, cause the radial deformation of the ring that, at this time, is not appreciable yet. Figure 1b shows that at $t = 57$ the structure of axial vorticity are not visible any longer at the axis of the ring because these have been convected far from the ring and mainly diffused by the viscosity. On the other hand, the positive axial vorticity within the ring core, represented as the white region on the right side of Fig. 1b, is strong enough to substantially deform the ring itself in the radial direction. The amount of ω_z, going from $t = 30$ to $t = 57$ has increased due to the vortex stretching and this intensification causes the birth of oppositely-signed vorticity localised in a large region encircling the ring core (note the black structure on the right side). Similar plots were obtained by superposition of radial and azimuthal vorticity components. If the same levels as those of Fig. 1 are chosen, we observe (Fig. 2a) that the radial vorticity is localised in smaller regions despite the fact that initially the amount of ω_r was larger than ω_z. At $t = 30$, being the maximum value of the vorticity components in the ratio $\omega_\theta : \omega_r : \omega_z = 2.0 : 0.12 : 0.4$, it follows that there are weakly appreciable deformations of the ring. Since radial vorticity
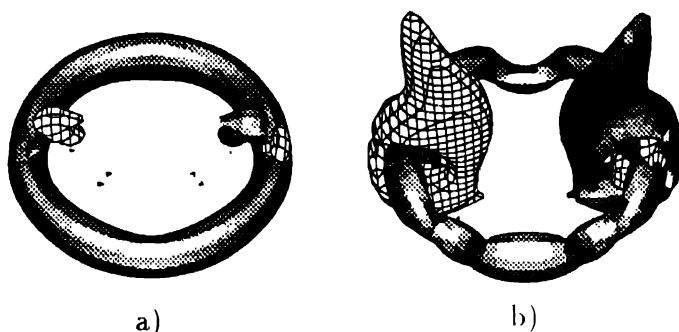
Fig. 2.   Surface contour plots of radial and azimuthal vorticity components: (a) $t = 30$, (b) $t = 57$. Surfaces are as in Fig. 1.

causes deformations in the axial direction, it results that at $t = 30$ deformations in the radial direction are larger than those in the axial direction. On the contrary, at $t = 57.5$ the ratio becomes $2.2 : 0.48 : 0.75$ with the consequence that the deformations are more pronounced and of the same order in both radial and axial directions.

The vortex structures interconnection and their effect on the core was clearly seen in contour plots of velocity vectors in horizontal and axial planes, however these plots are not shown for sake of brevity. Here, we wish instead to present the analysis of the strain field and how it is correlated with the vorticity. This procedure has been used previously to analyse turbulent fields [4] and only in one case, to our knowledge, it was used to analyse the interaction of well-defined vortical structures [7]. In the present case we wish to apply this analysis to the vortex ring, one of the simplest coherent structures in three-dimensional flows which has attracted a large number of theoretical and experimental studies. The eigenvalues α, β and γ of the strain-rate tensor and the eigenvectors $\mathbf{S}_\alpha$, $\mathbf{S}_\beta$ and $\mathbf{S}_\gamma$ allow the estimation of the vorticity-strain alignment and the identification of different zones in the flow. For example, in regions where the vorticity is mostly aligned with $\mathbf{S}_\beta$ the structure is two-dimensional or axisymmetric, whereas in contrast in the zones where ω aligns with $\mathbf{S}_\alpha$ or $\mathbf{S}_\gamma$, high stretching or compression occurs and in these zones large three-dimensionalities grow. Since in the present case the basic state is an axisymmetric vortex ring, significant probability of ω pointing to the α or γ directions indicates the growth of the azimuthal instabilities. As usual the convention is $\alpha > \beta > \gamma$. When $\beta > 0$ ($R_s = \alpha\beta\gamma < 0$) there exist sheet-like regions (ribbons) that are dominant in low Re_Γ isotropic turbulent flows [8] or in near-wall turbulence [9] when turbulence is sustained by growing instabilities.

At present, this analysis can only be pursued thanks to the large amount of data generated by direct numerical simulation, since it is necessary to have vorticity and strain-rate tensor in as many points as possible to compute accurate statistics. By the available measurement techniques it is not readily possible to produce the
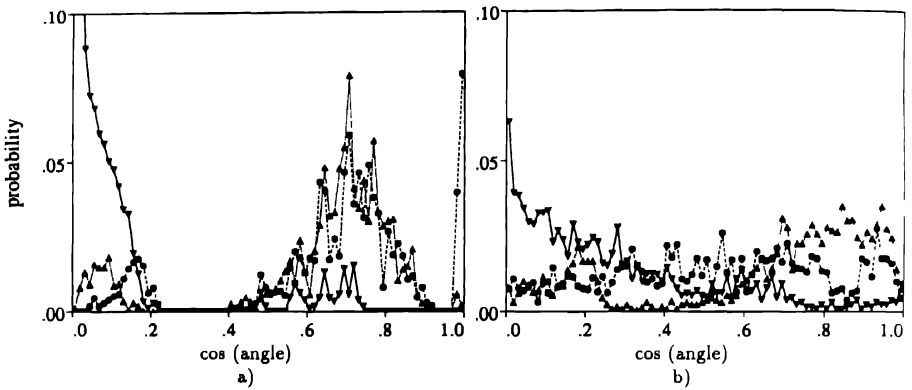
Fig. 3.   Probability distribution of — ▼ — $S_{\alpha\theta}$, - - - ● - - - $S_{\alpha r}$, · · · ▲ · · · $S_{\alpha z}$, with $\omega_M =$ 1.5, (a) $t = 30$, (b) $t = 57$.

same amount of data. Furthermore, direct simulation allows one to select and focus on the region of interest and hence consider only those points where the vorticity magnitude is larger than a threshold value ω_M.

The kinematic analysis of the region around the ring core has been performed by choosing two different values for ω_M. At $\omega_M = 1.5$ we focused our attention on the core and we expect to find results comparable with those found in [4], where regions of very intense vorticity in isotropic turbulence were selected. In fact Fig. 3a shows that at $t = 30$, when the ring is not appreciably deformed, α lies in a $r-z$ plane and in this plane it is preferentially oriented at around 45°. We observe also that there is a probability that the largest strain is directed towards the radial direction and zero probability to be directed along the axial direction. It follows that the ring is deformed more along the radial than along the axial direction. This behaviour is confirmed by the vorticity visualisations (Fig. 1). At $t = 57$, when the deformation has reached a substantial level, Fig. 3b shows the probability that the positive strain α lies in the $r-z$ plane is reduced, and there is not a preferred orientation at 45° any more. As previously mentioned, the radial vorticity is larger than at $t = 30$, then the highest positive strain in the radial direction has largely increased with the consequence to deform the core more in the axial than in the radial direction.

The analysis of the vorticity field has shown that with the constraint $\omega_M > 1.5$, ω_β is the largest component, and it is aligned as shown in [4]. In coherent compact vortices the vorticity is almost completely aligned with the eigenvector of the intermediate strain β [10], therefore ω_β is the largest component of the vorticity vector. The probability distribution of the ratio $\sigma = \alpha/\omega_\beta$ (α is the largest strain) gives information on the relative importance between vorticity and strain-rate in the field. Figure 4a shows that, at $t = 30$ this ratio is small ($\sigma \sim 0.15$) meaning that the vorticity largely overcomes the strain and that the core tends to resist
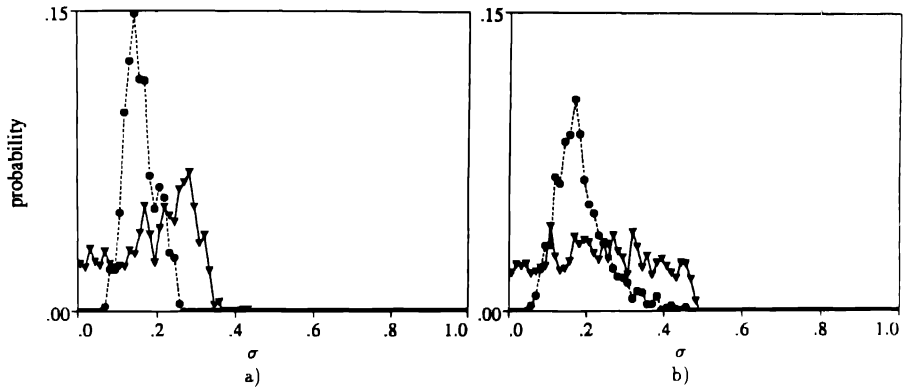
Fig. 4. Probability distribution of — ▼ — $\sigma = |\beta|/\alpha$ and - - - ● - - - $\sigma = \alpha/\omega_\beta$ with $\omega_M = 1.5$, (a) $t = 30$, (b) $t = 57$.

deformation. At $t = 57.5$ the probability is distributed on a broader range (Fig. 4b) and the ring core is less resistant to the strain deformation. Nevertheless the value of σ at which the peak probability occurs is still low as is expected from a structure where a preferential orientation of the vorticity is still visible (Fig. 1b). In Fig. 4a the probability distribution of the ratio between β and α has also been plotted indicating that the shape of the strain tensor is $\alpha : \beta : \gamma = 3 : 1 : -4$ or $4 : 1 : -5$ (probability with peaks at $0.25 < \sigma < 0.30$). These values are in agreement with those found in [4] or by Jiménez [10] for the Burgers vortex at Re ≈ 100. The similarity of the strain-rate tensor, despite the different structures and Reynolds numbers, confirms that the shape of S_{ij} and its alignment with the vorticity is a kinematic mechanism, independent of the dynamical process involved in the generation of the structure.

On the other hand, in the vortex ring low ratios between β and α must be expected also because the core, at $t = 30$, does not largely differ from an axisymmetric configuration in which the ratio between β and α is very low. We wish to recall that for two-dimensional flows β/α is 0, on the contrary in axisymmetric flows ($\beta \equiv S_{11} = v_r/r$) this strain is small (but not 0) in the core region and it can be very large near the axis of symmetry. This quantity gives information about the vortex stretching in the azimuthal direction which is responsible for the increase of ω_θ. At $t = 57$ (Fig. 4b) the probability to have β comparable with α increases, confirming that large perturbations are growing. The probability to have β close to α, is a characteristic of flows without regions of intense concentrated vorticity.

From the comparison between our results and those in isotropic turbulence [4] we believe that in isotropic turbulence the intense vortex tubes (i.e. the so-called 'worms'), deeply analysed in [8] could present deformations similar to those in the first stage of the 'Widnall' instabilities.
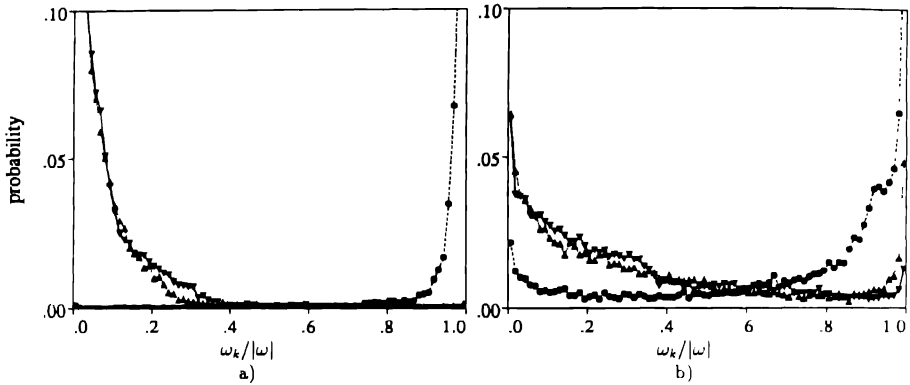
Fig. 5.   Probability distribution of — ▼ — $k = \alpha$, - - - ● - - - $k = \beta$, $\cdots$ ▲ $\cdots$ $k = \gamma$, with $\omega_M = 0.5$, (a) $t = 30$, (b) $t = 57$.

The same computations have been performed by fixing the vorticity threshold at $\omega_M = 0.5$. If we define $\rho_{n/p}$ as the ratio between the number of points where $R_s < 0$ and that where $R_s > 0$, the analysis shows that with the high threshold ($\omega_M = 1.5$) $\rho_{n/p} = 1.03$ which increases up to $\rho_{n/p} = 1.3$ with the low threshold ($\omega_M = 0.5$). Since $R_s < 0$ represents unstable sheet-like vortices, this outcome shows that, the region encircling the ring core contributes to the growth of the azimuthal instabilities.

From this observation we expect that the vorticity alignment ($|\omega| \sim |\omega_\beta|$) holds at the early stages of the evolution (Fig. 5a) when the core of the ring is nearly an axisymmetric structure while in the long term (Fig. 5b) the alignment is less pronounced due to the generation of large deformations. When the deformations are well developed, Fig. 5b shows that there is also a small probability that the vorticity is aligned with the maximum strain α. This is a very interesting situation because this alignment can lead to the occurrence of a finite time singularity in the 3-D Euler equations.

We have also analysed the region near the axis, dominated by ω_z, as shown in Fig. 1a. Since in this region the vorticity level is low (i.e. $(\omega_z)_{\max} = 0.48$) we have selected a threshold level of $\omega_M = 0.2$. Figure 6a shows that the intermediate strain β is poorly aligned in the radial and azimuthal directions and it has large probability of alignment in the axial direction. This result is confirmed by the visualisation of Fig. 1a where elongated structures of axial vorticity (aligned with the local intermediate strain) are visible. Although in this region the vorticity level is low, also in this case ω_β is the highest component and ω_α can reach a high level. The ratio α/ω_β in Fig. 6b shows that it is almost equally distributed for $\sigma > 0.25$ while it is zero for smaller values. The associated vortices are not intense enough to resist the strain and they can easily change their shape, as observed in the vorticity visualisations. Also in this case the shape of the strain tensor is approximately
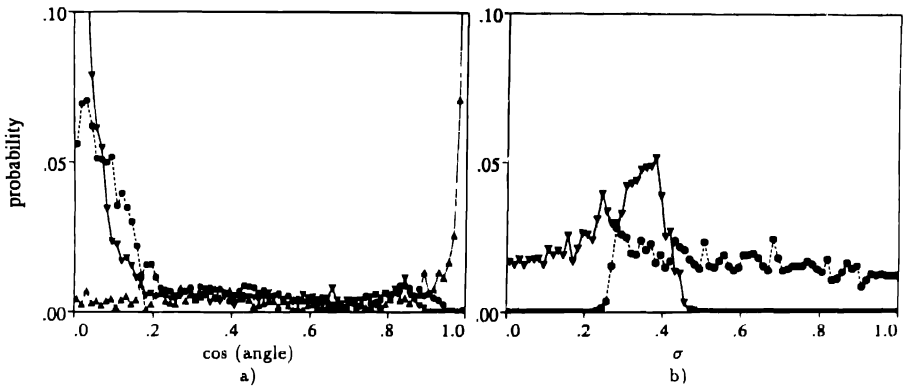
Fig. 6.   Probability distribution in the axis region at $t = 30$ with $\omega_M = 0.2$, (a) of — ▼ — $S_{\beta\theta}$, - - - ● - - - $S_{\beta r}$, $\cdots$ ▲ $\cdots$ $S_{\beta z}$ and (b) of — ▼ — $\sigma = |\beta|/\alpha$, - - - ● - - - $\sigma = \alpha/\omega_\beta$.
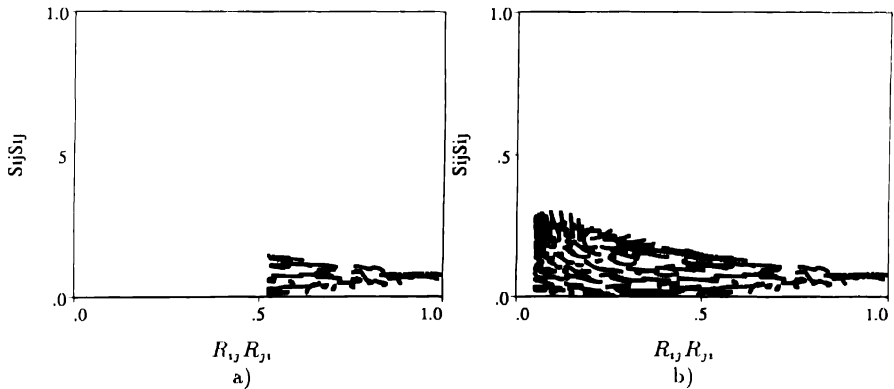
Fig. 7.   Scatter-plots of strain-rate *vs.* rotation-rate at $t = 30$, (a) region of the ring core and $\omega_M = 1.5$, (b) region around the axis and $\omega_M = 0.5$.

$\alpha : |\beta| = 2.5 : 1$ with a zero probability of almost equal intermediate and positive strain. This is a configuration related to thick non-circular vortices that easily deform.

The analysis has also shown that in this region there is a large number of points with $S_{ij}S_{ji}$ larger than $R_{ij}R_{ji}$, a further proof of the instability of the inner region of the ring. This is shown in Figs 7a–b, where scatter-plots of $S_{ij}S_{ji}$ versus $R_{ij}R_{ji}$ indicate that inside the core vorticity is intense and low levels of strain do not appreciably influence the structure. This does not hold in the region near the axis where the vorticity is low and strain-rates are quite high. In the long term, azimuthal instabilities increase in amplitude and at $t = 57$ we observed that the effect of the strain-rate is sensible also inside the ring core (see Fig. 8).
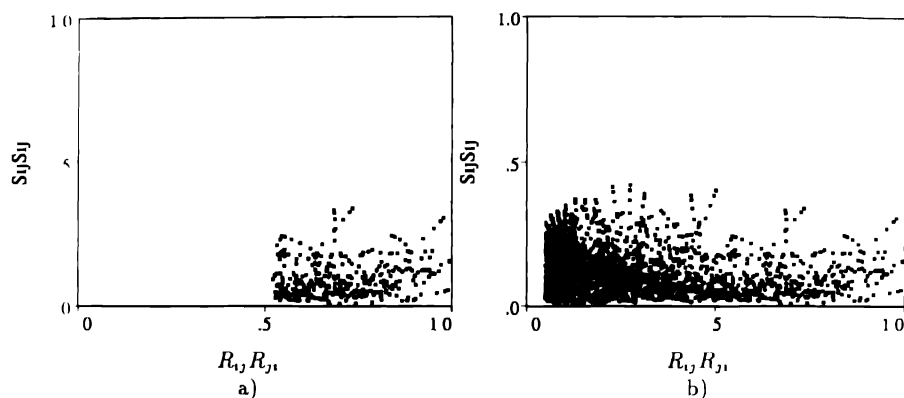
Fig. 8   The same as Fig 7 at $t = 57$
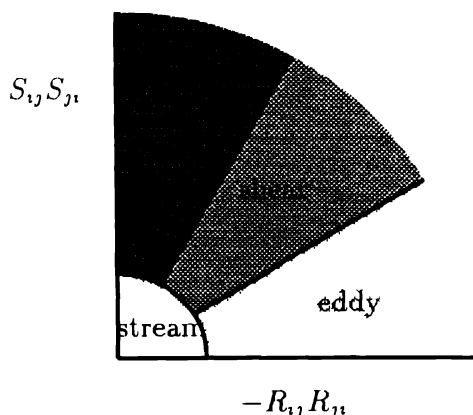
Fig 9   Schematic draft of the regions in the $R_{ij}R_{ji}-S_{ij}S_{ji}$ plane stream, eddy, shear and convergence

Different zones within the flow field can be characterised by the rate of deforma-
tion tensor A_{ij} which can be decomposed in a symmetric S_{ij} and an anti-symmetric
R_{ij} tensor. According to the definition given by Chong et al. [11] we are in the pres-
ence of an eddy region when R_{ij} is the dominant part of A_{ij}, ($-S_{ij}S_{ji}/R_{ij}R_{ji} \ll$
1). From Eq. (1) it follows that an eddy region is characterised by intense vorticity
and low strain. A similar classification was used by Kevlahan et al. [12] which
divides the field into an eddy region ($-S_{ij}S_{ji}/R_{ij}R_{ji} < \sqrt{3}/3$), a shear region
($\sqrt{3}/3 < -S_{ij}S_{ji}/R_{ij}R_{ji} < \sqrt{3}$), a convergence region ($S_{ij}S_{ji}/R_{ij}R_{ji} > \sqrt{3}$)
and a stream region where $R_{ij}R_{ji}$ and $S_{ij}S_{ji}$ are both small (Fig. 9) (e.g. as Fig. 6
of [12]).
   By a procedure similar to that used by Wray and Hunt [13] we have identified
different zones in the ring. In this case, instead of considering a single plane of
the 3-D field we evaluated the average of $-S_{ij}S_{ji}/R_{ij}R_{ji}$ in θ to have a global
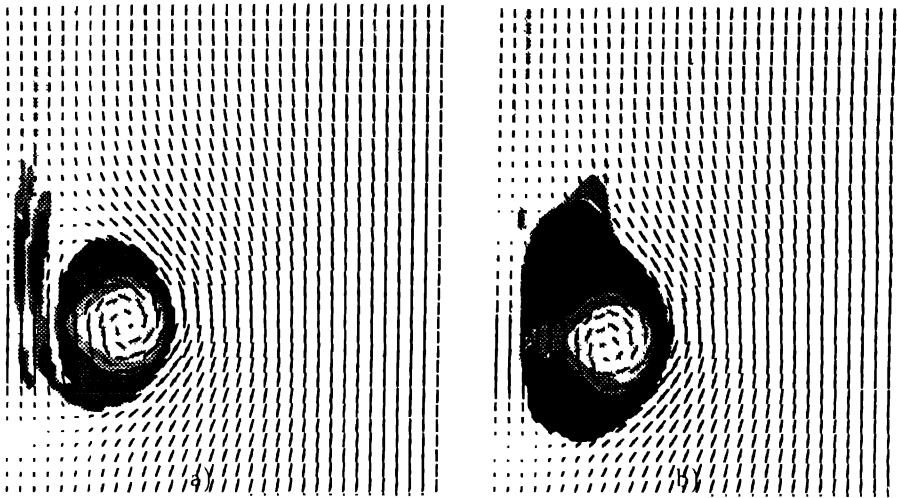
Fig. 10.   Contours of $\Omega(r, z)$ and velocity vectors, (a) $t = 30$, (b) $t = 57$. For gray tones see Fig. 9 (The ring translates downward.)

picture of the ring. Figure 10 shows $\Omega(r, z) = \overline{-S_{ij}S_{ji}/R_{ij}R_{ji}}$, at $t = 30$ and $t = 57$, together with the averaged vectors in a frame moving with the ring. In both cases there is an eddy region in the core of the ring which is characterised by an almost solid body rotation. This region represents the inner part of the core, where the vorticity is very intense, and maintains its strength in time. The shear region is a thin transitional zone between the eddy and the convergence zone and it does not play a significant role. On the contrary, growth of the convergence zone characteristic of the instabilities, shows that large strains are induced and these, in their turn, produce further deformations. Figure 10b shows that the deformations in the downstream part of the ring are larger than those upstream. The effects of the thick structure, shown in Fig. 1b, are represented by the thicker convergence zone in the inner part of the ring.

4. Conclusions

In this paper the direct numerical simulation has been used to analyse the vorticity and strain fields of a free vortex ring. This analysis gives insights impossible to obtain by flow visualisation in real experiments. The vortex ring has been chosen for its coherence and because it can be considered as the basic structure in several flows of practical importance. By visualisation of the vorticity field, the wake formation and the growth of azimuthal instabilities is explained. The flow structures were also investigated by kinematic considerations on the alignment between the eigenvectors of the strain-rate tensor and the vorticity vector. The choice of different zones and different values of the threshold vorticity ω_M, to condition the alignment

analysis, has shown that the field can be divided into two regions. The first is constituted by high level coherent vorticity, strongly aligned with the intermediate strain where the structure is mainly axisymmetric. In the second region, with a smaller vorticity, there is a reduced probability of alignment between vorticity and intermediate strain and higher probability of negative R_S. This means that regions of low vorticity are more unstable and less resistant to external strain. This result is consistent with the findings of Jimènez [10] in homogeneous turbulence. The similarity between the core of the ring region and the intense vorticity structures in isotropic turbulence, brought us to draw the tentative conclusion that in isotropic turbulence intense vortex tubes should have instabilities similar to those in vortex rings. Results have also shown that the coherence of regions with high vorticity is decreased in time. This indicates the tendency to generate the smaller structures present in turbulent rings.

The limitation of this work, as usual for the direct simulation, is in the Reynolds number. Before performing simulations at higher Reynolds numbers where we expect to have the ring in a turbulent state, we intend to focus our attention on the interaction between two rings, giving insights to vortex pairing in a round jet, which is known to be the mechanism largely contributing to the spreading of the jet.

Acknowledgements

References

1. Lasheras, J.C., Lecuona, A. and Rodriguez, P., Three-dimensional structures of the vorticity field in the near region of laminar co-flowing forced jets'. In: Jimènez (ed.), *The Global Geometry of Turbulence*. Plenum Press (1991).
2. Glezer, A., The formation of vortex rings. *Phys. Fluids* 31 (1988) 3532–3542.
3. Widnall, S.E., Bliss, D.B. and Tsai, C.Y., The instability of short waves on a vortex ring. *J. Fluid Mech.* 66 (1974) 35–47.
4. Ashurst, W.T., Kerstein, A.R., Kerr, R.M. and Gibson, C.H., Alignment of vorticity and scalar gradient with strain rate in simulated Navier–Stokes turbulence. *Phys. Fluids* 30 (1987) 2343–2353.
5. Verzicco, R. and Orlandi, P., A finite different scheme for direct simulation in cylindrical coordinates. Presented at the ICOSAHOM 92, Montpellier, 1992. *J. of Comp. Phys.* 274 (1994) 1–25.
6. Shariff, K.R., Verzicco, R. and Orlandi, P., A numerical study of three-dimensional vortex ring instabilities: Viscous corrections and early non-linear stage. *J. Fluid Mech.* 274 (1994) 1–25.
7. Borotav, O.N., Pelz, R.B. and Zabusky, N.J., Reconnection in orthogonally interacting vortex tubes: Direct numerical simulations and quantifications. *Phys. Fluids. A* 4 (1992) 581–605.
8. Jimènez, J., Wray, A.A., Saffman, P.G. and Rogallo, R.S., The structure of intense vorticity in isotropic turbulence. *J. Fluid Mech.* 255 (1993) 65–90.

9. Jimènez, J. and Orlandi, P., The rollup of a vortex layer near a wall. *J. Fluid Mech.* 248 (1993) 297–313.
10. Jimènez, J., Kinematic alignment effects in turbulent flows. *Phys. Fluids A* 4 (1992) 652–654.
11. Chong, M.S., Perry, A.E. and Cantwell, B.J., A general classification of three-dimensional flow fields. *Phys. Fluids A* 5 (1990) 765–777.
12. Kevlahan, N., Mahesh, K. and Lee, S., Evolution of the shock front and turbulence structures in the shock/turbulence interaction. *Proceedings of the 1992 Summer Program*, Centre for Turbulence Research NASA.
13. Wray, A.A. and Hunt, J.C.R., Algorithms for classifications of turbulent structures. In: Moffat and Tsinober (eds), *Topological Fluid Mechanics, Proceedings of the IUTAM Symposium*. Cambridge (1989).

Applied Scientific Research

Author Index, Volume 53 (1994)

Further Developments in Turbulence Management

edited by **K. Krishna Prasad**

The thrust of modern research on turbulence in fluids is concerned with coherent structures and modelling. Riblets have been shown to reduce drag, and the papers presented in this volume tackle the main question of the mechanism responsible for this behaviour in turbulent flow.
The contributions in this volume were presented at the Sixth Drag Reduction Meeting held at Eindhoven during November 1991.
This volume will be a useful reference work for engineers, physicists and applied mathematicians interested in the topic of fluid turbulence.

Contents and Contributors
1. Bursting and Structure of the Turbulence in an Internal Flow Manipulated by Riblets; *S. Tardu, T.V. Truong, B. Tanguay.* **2.** On Near-Wall Turbulence-Generating Events in a Turbulent Boundary Layer on a Riblet Surface; *Y.P. Tang, D.G. Clark.* **3.** Friction Velocity and Virtual Origin Estimates for Mean Velocity Profiles above Smooth and Triangular Riblet Surfaces; *A.D. Schwarz-van Manen, A.F.M. van Geloven, J. Nieuwenhuizen, J.C. Stouthart, K.K. Prasad, F.T.M. Nieuwstadt.* **4.** Viscous Sublayers Analysis of Riblets and Wire Arrays; *P. Luchini.* **5.** Riblet Flow Calculations with a Low Reynolds Number K – ɛ model; *L. Djenidi, R.A. Antonia.* **6.** On the Prediction of Riblet Performance with Engineering Turbulence Models; *B.E. Launder, S.P. Li.* **7.** Modelling the Time Dependent Flow over the Viscous Wall Region; *S. Tullis, A. Pollard.* **8.** Possibility of Drag Reduction using d-Type Roughness; *K.S. Choi, N. Fujisawa.* **9.** The Drag of Three-Dimensional Rectangular Cavities; *E. Savory, N. Toy, P.J. Disimile, R.G. DiMicco.* **10.** Turbulence Structure of Dilute Polymer and Surfactant Solutions in Artificially Roughened Pipes; *H.-W. Bewersdorff, H. Thiel.* **11.** Effect of External Manipulators on the Heat Transfer on a Flat Plate Turbulent Boundary Layer; *A. Hamdouni, J.P. Bonnet.*

KLUWER ACADEMIC PUBLISHERS

Applied Scientific Research

Contents of Volume 53 (1994)

Vol. 53   Nos. 1–2   September 1994

Special Double Issue

A Tribute to Mårten T. Landahl

Guest Editors

P. HENRIK ALFREDSSON, FRITZ H. BARK & ARNE V. JOHANSSON

Special Double Issue

Selected Papers from a IUTAM Symposium entitled
"Eddy Structure Identification in Free Turbulent Shear Flows",
held at Poitiers, France, 12–14 October 1992

Guest Editors

J.P. BONNET & M.N. GLAUSER   .